Transactions of the ASME®

Transactions of the ASME, Journal of Engineering for Gas Turbines and Power (ISSN 0022-0825) is published quarterly (Jan., Apr., July, Oct.) for $120 per year by The American Society of Mechanical Engineers, 345 East 47th Street, New York, NY 10017. Second class postage paid at New York, NY and additional mailing offices. POSTMASTER: Send address change to Transactions of the ASME, Journal of Engineering for Gas Turbines and Power, c/o The AMERICAN SOCIETY OF MECHANICAL ENGINEERS, 22 Law Drive, Box 2300, Fairfield, NJ 07007-2300.
CHANGES OF ADDRESS must be received at Society headquarters seven weeks before they are to be effective. Please send old label and new address.
PRICES: To members, $29.00, annually; to nonmembers, $120.00.
Add $12.00 for postage to countries outside the United States and Canada.
STATEMENT from By-Laws. The Society shall not be responsible for statements or opinions advanced in papers or ... printed in its publications (B 7.1, para. 3).

INDEXED by Applied Mechanics Reviews and Engineering Information, Inc.

Journal of Engineering for Gas Turbines and Power

Published Quarterly by The American Society of Mechanical Engineers
VOLUME 112 • NUMBER 1 • JANUARY 1990

TECHNICAL PAPERS

(Contents continued on p. 20)

(Contents Continued)

ANNOUNCEMENTS

Chemical Aspects of Deposition/ Corrosion From Coal-Water Fuels Under Gas Turbine Conditions

R. A. Wenglarz

R. G. Fox, Jr.

Allison Gas Turbine Division,
General Motors Corporation,
Indianapolis, IN 46206

A staged, subscale turbine combustor based on a promising rich-quench-lean combustion approach to reduce NO_x emissions was used to evaluate deposition, erosion, and corrosion (DEC) from coal-water fuels (CWF). This combustor was operated with three CWF at conditions of a recuperated turbine. Specimens were exposed in two test sections at temperature conditions of the first stator vanes and first rotor blades of the recuperated turbine. The resulting deposits were chemically analyzed. Deposit-covered segments of specimens were placed in a furnace to extend their exposure to the potentially corrosive deposits. The deposits produced at higher temperature first stator conditions differed significantly from those produced at lower temperature first rotor conditions. The rates of formation of the higher temperature deposits were high and the deposit chemistries were similar to the coal ash chemistry. The rates of formation of the lower temperature deposits were one to two orders of magnitude less and deposit chemistries were not the same as the coal ash chemistry. Some corrosion of a CoCrAlY coating was detected after a few hours of exposure in the DEC tests. Corrosion penetration up to one-half of the coating thickness was observed after an additional 460 h furnace exposure. Much more testing is needed to explore whether the deposition and corrosion produced by the fuels evaluated are typical of this fuel form and to assess benefits of alternate turbine protection measures.

Introduction

Direct coal-fired turbines for locomotives were evaluated in U.S. and Australian programs from the 1940s to the 1960s (Smith et al., 1966; Interdepartment Gas Turbine Steering Committee, 1973). Turbine flowpath degradation due to coal ash and contaminants was found to be the major technology barrier to successful operation. Although deposition was experienced with some coals, the primary flowpath degradation was erosion. Significant corrosion was not experienced.

Major technology advances related to coal fuels have occurred since the early coal-fired turbine programs. These include improved coal cleaning processes to remove ash and contaminants, development of coal-water suspensions as a fuel form, staged combustion for NO_x control, and greater understanding of the turbine deposition, erosion, and corrosion (DEC) degradation processes and their control (Wenglarz, 1987a). Renewed activity to develop coal-fired turbines using these technology advancements has emerged in recent years (Crouse, 1986). A major consideration is again turbine flowpath life. However, the turbine degradation experience of the early coal-fired turbine projects provides little information directly applicable to modern turbines operated with coal. This is because of major differences in the flowpath conditions of modern turbines compared to the older vintage machines tested with coal. Maximum gas velocities relative to airfoils, maximum gas temperatures, and maximum surface temperatures are up to 240 m/s (800 ft/s), 360°C (650°F), and 250°C (450°F) higher, respectively, in modern turbines.

Consequently, the insignificance of corrosion and the lesser role of deposition compared to erosion observed in the early coal-fired turbine programs cannot be assumed for modern high-temperature turbines operated with coal. The higher gas and surface temperatures affect the chemistry and phases (solid, liquid, or gas) of ash and contaminant compounds delivered to turbine surfaces and tend to increase the interaction (sticking, corrosion) of these compounds with the airfoil surfaces. The following describes results of deposition, erosion, and corrosion tests of coal-water fuels at typical temperature conditions representative of the first two airfoil rows (first stator and first rotor) of aero-derivative turbines. Deposition and corrosion chemistry factors are emphasized. Physical factors have been reported in detail elsewhere (Wenglarz and Fox, 1990) and will only be summarized here.

Test Facility

The facility used to evaluate deposition, erosion, and corrosion (DEC) characteristics of coal-water fuels is illustrated

Contributed by the International Gas Turbine Institute and presented at the 34th International Gas Turbine and Aeroengine Congress and Exhibition, Toronto, Ontario, Canada, June 4–8, 1989. Manuscript received at ASME Headquarters February 1, 1989. Paper No. 89-GT-207.

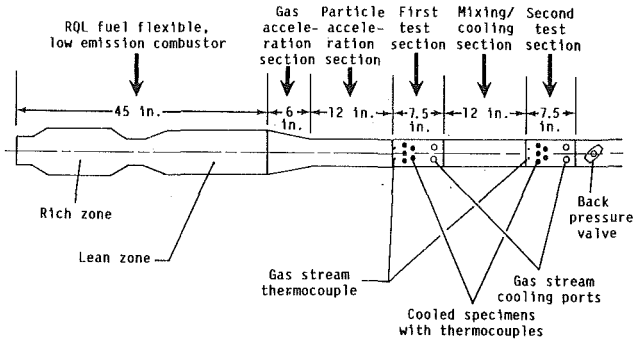

Fig. 1 DEC test facility

in Fig. 1. A description of this facility has been reported in detail elsewhere (Wenglarz, 1987b) and will be summarized here. A fuel-flexible, staged, rich-quench-lean (RQL), subscale turbine combustor was operated with coal-water fuels. Earlier tests demonstrated that this combustor concept offers promise for achieving high combustion efficiencies and NO_x control in future turbines operating with alternate fuels (Novick and Troth, 1981; Wilkes et al., 1985). Products of combustion (POC) from the RQL combustor were accelerated in a transition duct to enter the test sections at a representative turbine inlet velocity of about 183 m/s (500 ft/s). Five wedge-shaped specimens were exposed to the POC in each of two downstream test sections. The combustor exit temperature was adjusted to produce a gas temperature entering the first test section typical of a turbine first stator vane (vicinity of 1100°C [2000°F]). Air was injected at the exit of the first test section to lower the gas temperature entering the second test section to a typical inlet value (vicinity of 980°C [1800°F]) of first rotor blades.

Specimens in both test sections were internally cooled to establish maximum surface temperatures of aero-derivative turbine first stator vanes (980°C [1800°F]) and first rotor blades (900°C [1650°F]). Some specimens were cooled to 100°C (180°F) lower values to explore surface temperature effects on DEC. One uncooled SiC ceramic specimen in each test section was used to evaluate the DEC performance of this candidate future turbine material. The remaining specimens were fabricated from IN 738 turbine alloy covered with a CoCrAlY coating. Such coatings have demonstrated corrosion/erosion resistance in past coal-fired, pressurized fluidized bed combustor tests at relatively lower temperatures (maximum of 870°C [1600°F]) as described by Stringer et al. (1985).

Tests

DEC tests were conducted with three coal-water fuels (CWF). These fuels were formulated from a single batch of bituminous coal cleaned to 1.25, 0.97, and 0.69 percent ash levels (coal analyses are shown in Table 1) and slurried at about 50 percent coal concentration with water and additives to control settling and flow behavior. A single batch of coal was used for these fuels to explore the effect of ash cleaning while minimizing the uncertainty of feedstock variation. The three fuels varied in maximum coal particle size (40 μm for fuel 1 and 15 μm for fuels 2 and 3) and additive levels (twice the viscosity inhibiting additive in fuel 3 than in fuels 1 and 2). However, these differences did not appear to produce major differences in the products of combustion particle sizes or DEC (Wenglarz and Fox, 1990). The durations of DEC tests for fuels 1, 2, and 3 were 5, 1.7, and 4.3 h, respectively.

Deposit—Physical Characteristics

Physical descriptions of the deposits from the CWF are described in detail by Wenglarz and Fox (1990). In summary, deposits formed on all specimens for all fuels. Consequently, underlying specimen surfaces appeared to be protected from

Table 1 Fuel properties

Ultimate analysis--wt % dry			
Element	Fuel 1	Fuel 2	Fuel 3
Carbon	82.76	82.79	82.89
Hydrogen	5.19	5.20	5.22
Nitrogen	2.11	2.08	2.15
Chlorine	0.19	0.15	0.17
Sulfur	0.91	0.96	0.71
Ash	1.25	0.97	0.69
Mineral analysis of ash--wt % of ash			
Phosphorus	0.88	0.57	0.23
Silicon	12.00	11.48	7.50
Iron	20.40	21.90	23.14
Aluminum	14.24	13.92	10.94
Titanium	0.83	0.83	1.00
Manganese	0.02	0.03	0.04
Calcium	3.82	3.37	4.73
Magnesium	0.82	0.98	1.40
Potassium	1.19	0.98	0.87
Sodium	0.58	0.73	0.98
Oxygen and trace elements	Balance	Balance	Balance

significant erosion. At high gas temperatures (vicinity of 1100°C [2000°F]) of the first test section, the level of deposition was approximately proportional to fuel ash level. However, at the lower gas temperatures (vicinity of 980°C [1800°F]) of the second test section, increased levels of ash removal may not have yielded a proportionate reduction in deposition.

Deposition was highly sensitive to gas temperature. Deposition increased by one to two orders of magnitude (depending on specimen surface temperature) when the gas temperature increased from 980 to 1100°C (1800°F to 2000°F). Deposition increased with increasing surface temperature at a 1100°C (2000°F) gas temperature. However, no clear trend in deposition with surface temperature was discernible at 980°C (1800°F) gas temperature. For other candidate turbine coal fuels, the boundary temperatures between high and lower rates of deposition may be above or below the value observed for the fuels evaluated here. This temperature depends on fuel ash chemistry of the specific fuel, which affects the ash compounds released and formed in the combustion process and their melting points.

Deposition rates on the simple geometry specimens using CWF were referenced to rates in past deposition tests at 1100°C (2000°F) gas temperature using simple geometry specimens and a residual oil, which had successfully operated in utility gas turbines. Deposition rates on specimens at 980°C (1800°F) gas temperature were comparable to the past residual oil deposition rates even though the CWF ash levels were 25 times those of the residual oil. CWF deposition rates at 1100°C (2000°F) gas temperature were much higher than residual oil deposition rates at the same gas temperature. For both gas temperatures, CWF deposit hardness and tenacity after cooldown appeared to be much greater than for residual oil deposits.

Both the deposition rates and deposit tenacity observed in the CWF tests may well have been affected by incomplete combustion efficiency, which typically ranged approximately from 90 to 95 percent. This resulted in carbon mass levels more than four times the ash levels in the product of combustion (POC) particulate. This unburned carbon can significantly increase the gas stream particle size distribution and thereby increase the rates of delivery of ash material carried to surfaces by the carbon. Probability of particle sticking upon arrival to build up deposits can be enhanced by any remaining volatile carbon (which would be sticky), increased particulate and deposit surface temperatures due to burning carbon, and de-

pressed ash melting points in reducing environments in the vicinity of the burning carbon.

Deposit Chemistry Characteristics

Analytical Methods. Deposit chemistry and its relation to fuel ash chemistry were explored with the objective of identifying critical ash species affecting deposition (and corrosion). Standard techniques such as energy dispersive X-ray (EDAX) and atomic absorption (AA) were used to investigate very small area and bulk chemistry, respectively. However, most of the deposit analyses utilized secondary ion mass spectroscopy (SIMS). This method ionized a thin layer of deposit (1/2 μm in depth and about 200 μm in diameter for the analyses described here) and then used mass spectroscopy to analyze the resulting plasma.

SIMS was particularly useful in analyzing the low-temperature test section deposits for which insufficient mass was available for accurate AA analysis. The SIMS approach offered advantages over EDAX of much higher accuracy (especially for critical elements such as sodium) and ability to analyze larger areas. The overall chemistry of the nonuniform deposit is difficult to determine using EDAX since its measurement area of a few square microns is smaller than many of individual particles of widely varying chemistry from which the deposit was formed.

Analytical Results. Tables 2, 3, and 4 give deposit and fuel ash analyses for the fuels used in DEC tests 1, 2, and 3, respectively. The element percentages neglect oxygen and trace elements in the coal ash. Consequently, the ash analysis for each fuel in Tables 2, 3, and 4 differs from that in Table 1 (which considers oxygen and trace elements) by a constant factor. SIMS analyses at two locations on the same specimen from the test of fuels are shown in Table 2. Agreement between the two readings is good considering the typical variability of deposit composition with location. SIMS analyses of two locations on the same high-temperature test section specimen from the fuel 2 test are also shown in Table 3. Agreement is not as good as shown in Table 2, especially for Na, which differs between the two readings by a factor of 30 for the same specimen. The higher reading for Na might be suspect since the AA analysis shown in Table 3 of the bulk deposit spalled from the same specimen gives an Na value more consistent with the lower SIMS reading. Furthermore, as will be discussed later, the high Na measurement was more than a factor of 4 greater than the highest reading for any other of the high-temperature test specimens used in all of the three DEC tests.

The gas and surface temperatures at which the specimens were exposed are given for the specimen analyses shown in Tables 2, 3, and 4. Gas temperatures of 1100°C (2000°F) indicate specimens in the higher temperature test section. Gas temperatures of 980°C (1800°F) indicate specimens in the downstream lower temperature section. SIMS analyses on low-temperature test section specimens were obtained on the outer surfaces of the relatively thin deposits on the specimens. SIMS analyses for the high-temperature test section specimens were usually obtained on the relatively thin deposits remaining on the specimens after spallation during test shutdown. In a few cases the SIMS analysis was obtained on the spalled pieces at surfaces adjacent to the specimen. Consequently, the location of the SIMS analyses on specimens were typically on a deposit surface less than 100 μm from the specimen surface. AA analyses are also given for the bulk spalled pieces from three of the high-temperature test section specimens.

Tables 2, 3, and 4 show very high sodium (Na) levels on some specimens compared to levels in the fuel ash. Concentrations of Na on a number of specimens are more than 5 times (up to 30 times) the concentrations in the fuel ash. The highest sodium level approaches 40 percent (Table 3) of the deposit, neglecting oxygen. These increased concentrations of Na in deposits near the specimen surface are significant because sodium is a well-known corrodent, which is typically specified to less than 1 ppm levels in oil-derived turbine fuels. Na can cause accelerated corrosion because it tends to form low melting point aggressive compounds. Such molten phases can also increase deposition by increasing sticking fractions of particles arriving on surfaces and forming deposit bonding media.

Vanadium (V) is another species that can form molten compounds at relatively low temperatures to contribute to corrosion and deposition. V, like Na, is a recognized turbine corrodent, which is typically specified to less than 1 ppm in oil-derived fuels. Examination of Tables 2, 3, and 4 indicates that levels of V in the deposits are lower than many other elements. However, V levels in all of the thin deposits analyzed by SIMS are several orders of magnitude higher than in the fuels. On the other hand, V levels in all spalled bulk deposits analyzed by AA are comparable to levels in the fuels. Because the AA analyses were supplemented with the graphite furnace procedure for the detection of V, the AA readings for V in Tables 2, 3, and 4 are expected to be reasonably accurate. Consequently, the data suggest a great enrichment in vanadium near the specimen surfaces, which is not apparent in the deposits farther from those surfaces.

Most of the deposit chemistries shown in Tables 2, 3, and 4 appear to fall in one of two categories. The first category (high Na deposits) is characterized by the following:

- high Na percentages in the deposits more than 2.5 times (up to 30 times) Na percentages in the fuel ash
- Si, Al percentages in the deposits substantially lower (usually a factor of 2 or more) than percentages in the fuel ash
- relatively low deposition rates

The second category (low Na deposits) is characterized by the following:

- Na percentages in the deposits comparable to (and usually lower than) percentages in the fuel ash
- Si, Al percentages in deposits comparable (to within 50 percent) to percentages in the fuel ash
- high deposition rates

All of the first category (high Na) deposits (except for the one with a suspect Na reading discussed earlier) occurred on the specimens in the low-temperature test section (gas temperature 980°C [1800°F]). Except for the one suspect Na reading, all deposits in the high-temperature test section (1100°C [2000°F]) were in the second category (low Na). However, two of the ten low-temperature test section deposits described in Tables 2, 3, and 4 were also in the second category. Possible reasons will be discussed in the following interpretation section for the usual association of high Na deposits with low gas temperatures and low Na deposits with high gas temperatures.

Interpretations. Deposits have been produced by other investigators using a turbine-type combustor operating with a physically cleaned CWF similar to those tested in this program (Corman, 1986). An elegant analysis approach indicated that the potassium (K) from the coal ash remained predominantly in the alkali aluminosilicate form of illite after the combustion process. K was not transformed into the well-known alkali sulfate corrodent.

The deposit analyses described in the last section suggest that sodium, unlike potassium, may not be retained in the alkali aluminosilicate forms but may be vaporized during combustion to condense later at lower temperatures. As discussed earlier, the deposits high in Na were typically low in Al and Si compared to the fuel, indicating that much of the Na was probably not mostly associated with aluminosilicates (i.e., Al, Si).

Table 2 Deposit chemical analysis for DEC Test 1

Spec temp--°C (°F) Gas	Surface	Analysis procedure	Si	Fe	Al	Ti	Ca	Mg	K	Na	S	P	V
1093 (2000)	1093 (2000)	SIMS	22.32	35.17	21.92	1.62	7.77	1.09	1.79	0.81	--	0.59	0.23
1093 (2000)	982 (1800)	SIMS	18.34	39.40	18.33	1.14	7.93	1.02	1.30	0.87	0.06	1.29	0.21
1093 (2000)	899 (1650)	SIMS	23.20	33.14	20.20	1.22	11.75	1.27	0.48	0.40	--	1.40	0.03
982 (1800)	982 (1800)	SIMS	12.15	38.03	19.22	1.60	8.78	1.12	2.35	1.41	0.12	3.07	0.35
982 (1800)	899 (1650)	SIMS*	11.96	30.22	14.37	0.89	5.07	0.78	2.50	21.93	0.43	1.86	0.20
982 (1800)	899 (1650)	SIMS*	10.48	32.93	13.29	0.89	5.88	0.85	2.61	23.32	0.65	1.61	0.19
982 (1800)	899 (1650)	SIMS	15.80	38.67	20.38	1.48	9.38	1.27	1.28	1.54	0.11	2.78	0.30
					Fuel ash chemical analysis DEC Test 1								
		AA	21.31	36.22	25.28	1.47	6.78	1.46	2.11	1.03	2.31	1.56	0.0001

*Analysis of same specimen

Table 3 Deposit chemical analyses for DEC Test 2

Spec temp--°C (°F) Gas	Surface	Analysis procedure	Si	Fe	Al	Ti	Ca	Mg	K	Na	S	P	V
1093 (2000)	1093 (2000)	AA	20.29	36.62	25.91	2.11	9.71	1.91	0.96	0.81	0.62	0.28	0.0001
1093 (2000)	982 (1800)	AA*	21.25	38.04	25.44	1.50	8.09	1.86	0.90	0.77	0.74	0.62	0.00003
1093 (2000)	982 (1800)	SIMS*	15.03	47.20	23.60	1.50	6.40	0.86	0.64	0.43	0.006	0.26	0.08
1093 (2000)	982 (1800)	SIMS*	11.68	42.27	14.59	0.91	6.73	1.07	1.12	13.01	0.04	0.46	0.14
982 (1800)	982 (1800)	SIMS	7.36	41.28	10.82	0.76	6.64	0.95	1.50	17.36	0.08	1.04	0.17
982 (1800)	899 (1650)	SIMS	3.36	32.84	5.72	0.39	4.69	0.64	1.35	39.08	0.40	1.34	0.13
982 (1800)	899 (1650)	SIMS	4.46	33.64	6.69	0.49	6.00	0.78	1.61	34.77	0.36	1.08	0.14
					Fuel ash chemical analysis DEC Test 2								
		AA	20.30	38.73	24.62	1.47	5.96	1.73	1.29	1.29	2.60	1.01	0.00008

*Analysis of same specimen

Table 4 Deposit chemical analyses for DEC Test 3

Spec temp--°C (°F) Gas	Surface	Analysis procedure	Si	Fe	Al	Ti	Ca	Mg	K	Na	S	P	V
1093 (2000)	1093 (2000)	AA	18.53	34.00	25.92	2.75	12.73	2.89	0.20	0.59	0.88	0.22	0.00005
1093 (2000)	982 (1800)	SIMS	14.82	35.62	24.92	1.81	10.36	2.13	0.22	0.41	0.05	0.23	0.12
1093 (2000)	899 (1650)	SIMS	12.13	44.61	16.54	1.20	8.25	1.70	1.18	2.77	0.75	0.46	0.09
982 (1800)	982 (1800)	SIMS	11.60	37.17	16.84	1.35	10.10	1.68	0.26	10.26	0.31	0.33	0.12
982 (1800)	899 (1650)	SIMS	4.11	37.88	7.15	0.65	6.69	0.75	0.69	27.44	0.31	0.36	0.07
982 (1800)	899 (1650)	SIMS	5.35	50.56	9.82	0.92	10.54	1.21	0.85	4.64	0.41	0.23	0.10
					Fuel ash chemical analysis DEC Test 3								
		AA	13.88	42.82	20.24	1.85	8.75	2.59	1.61	1.81	4.90	0.43	0.00005

A plausible explanation for the two categories of deposits observed may be as follows. At high gas temperatures (vicinity of 1100°C [2000°F] and above), a significant fraction of gas stream particles larger than a few microns is probably molten. Significant fractions of larger molten particles were very likely necessary for the high sticking fractions and rapid deposit buildup observed in this program for the specimens exposed at 1100°C (2000°F) gas temperatures. One possible molten phase at these temperatures might be illite—the potassium aluminosilicate in CWF deposits produced in the turbine simulation tests described earlier (Corman, 1986). Other investigators (Bryers and Walchuk, 1984) have observed that illite separated from coal ash appears to occur as a melt at temperatures as low as 1000°C (1830°F).

Most of the particles larger than a few microns that were molten at high temperatures could have solidified (frozen) at the lower gas temperatures in the vicinity of 980°C (1800°F) and even lower temperatures of cooled specimen boundary layers for the lower temperature specimens. This could account for the observed one order of magnitude (uncooled specimens) to two order of magnitude (cooled specimens) decreased deposition rates for the low-temperature test section compared to the high-temperature test section. If the previously molten species at high temperatures were Al–Si compounds (such as illite) then particles of these compounds would not tend to stick on impact after freezing at lower temperatures. Consequently, the lower gas temperature deposits would tend to be depleted in Al and Si compared to the higher gas temperature deposits, as was observed.

If nearly all of the frozen larger particles delivered by inertial impaction do not stick upon impact at lower temperatures, then molten species in smaller particles delivered at much lower rates and affected by mechanisms such as condensation, diffusion, and thermophoresis could become important. Should these particles consist of Na complexes (many of which are highly volatile and form low melting point compounds upon condensation), the low gas temperature specimen deposits would be enriched in Na compared to the high gas temperature deposits, as was observed before. Even if condensation and delivery of small molten particles were occurring on the high gas temperature specimens, the relatively low mass concentrations and delivery rates for these particles would be obscured by the much higher mass loadings and delivery rates for larger particles if a significant fraction of larger particles (a few percent) stuck on impact.

Although the condensation and delivery of Na compounds appear to be important for the low gas temperature specimens, the composition of these compounds is not clear. The low levels of sulfur (S) in the deposits relative to Na indicate that most of the sodium could not have formed the dreaded sodium sulfate corrodent. Although the deposits were not analyzed for chlorine, NaCl is one possible condensable, low melting point compound that might be present in the high Na deposits. Whatever the form, the presence of most low melting point Na compounds at a turbine alloy surface would produce an undesirable corrosion environment.

A network parameter model used by glass technologists and ceramists in comparing softening ranges of glasses was explored for deposition evaluations. This model considers glasses to be made up of network formers (e.g., Si, Al) and network modifiers. When network modifiers such as Na and K are added to a glass, the ratio (network parameter) of oxygen ions to network formers increases and the number of bridging oxygen bonds is decreased (some polymer networks are terminated). The resulting shorter linear molecules produce decreased interfacial tension and a lowered glass softening temperature range.

A reasonably high statistical correlation was observed between the value of the network parameter based on deposit chemistry and the specimen gas-to-surface differential (ΔT) as exposed to the RQL products of combustion. This result would be expected if network modifiers Na and K were delivered to the surfaces by thermophoresis, which depends on ΔT.

Corrosion Characteristics

Approach. The approach selected to evaluate the corrosion up to a few hundred hours used specimens with adherent deposits formed during the actual operation of the RQL combustor burning coal slurry. The specimens were exposed in a controlled atmosphere furnace at the same surface temperature as in the RQL deposition, erosion, and corrosion (DEC) tests. The sulfur dioxide–air ratio in the furnace was held at 730 ppm SO_2 to duplicate the molecular concentration of SO_2 in an engine full-pressure RQL combustor gas stream. Because the furnace exposure was at atmospheric pressure while the turbine operates at 10 atmospheres pressure, furnace SO_2 concentrations were increased upward by the ratio of pressures to provide the same molecular concentration of SO_2 (Halstead, 1973). The supply of sodium and potassium was limited to the concentrations in the original deposits and was not renewed. It can be inferred that the alkali concentrations fell off with time during the test due to evaporation at the material test temperature. This rate of evaporation is believed to be low since the alkali cations must diffuse to the deposit-gas interface and then evaporate at 900°C (1650°F). Also, temperature transients, due to throttle excursions and cyclic instabilities at 3–100 Hz that characterize gas turbine combustors, were not duplicated during this furnace test. As a consequence, the thermal stressing of the oxide scale that would be present in an engine was not duplicated in the furnace. Note that both of these relaxations of similitude tend to reduce the rate of corrosion in the furnace relative to the engine.

Eight 1.3 cm (0.5 in.) long pieces of the 4.72 cm (1.86 in.) long test specimens from all three DEC tests were enclosed in a ceramic retort fitted with a bottom gas inlet and top exit. The retort temperature was controlled by a standard metallurgical test furnace at 899°C ± 1.1°C (1650°F ± 2°F) for the test duration. Two specimens were removed at 100 h for a preliminary metallographic estimation of penetration. The remaining six pieces were run to a total of 460 h. The pieces were sliced at 25 and 50 percent of the original length, and the corrosion penetration was evaluated at several points around the mounted section to estimate the anticipated variability in corrosion commensurate with the range in alkali concentrations in the deposits reported earlier (Tables 2, 3, and 4). Penetration depth, percent penetration of the CoCrAlY coating, and width of the corroded area were recorded. The metallurgical preparation showed depletion of aluminum in the coating, which is designed to form an Al_2O_3 protective oxide scale. Since depletion is a precursor of accelerated corrosion, the depth of the depletion region and percent of coating were also recorded. Thickness of adherent deposits close to or on the corrosion site was measured and recorded.

Results. Several of the RQL combustor exposed specimens were examined for corrosion after a 5-h run (DEC Test 1). The onset of corrosion was very rapid with pitting corrosion ranging from no detectable penetration through scattered 0.1 mil fingering to 1.2 mil pits.

The two specimens exposed in the furnace for 100 h showed very little increase in corrosion over the 5 h measurements. Accordingly, attention was concentrated on the 460 h specimens.

The specimens were originally fabricated from 1.27-cm (0.500-in.) diameter cylindrical test bars by grinding two flat surfaces at various included angles, to form a wedge with two leading edge corners. This leading edge was oriented into the gas stream. Figure 2 shows a section of one of the leading edge corners of specimen 23 (50 percent slice). The flat surface is

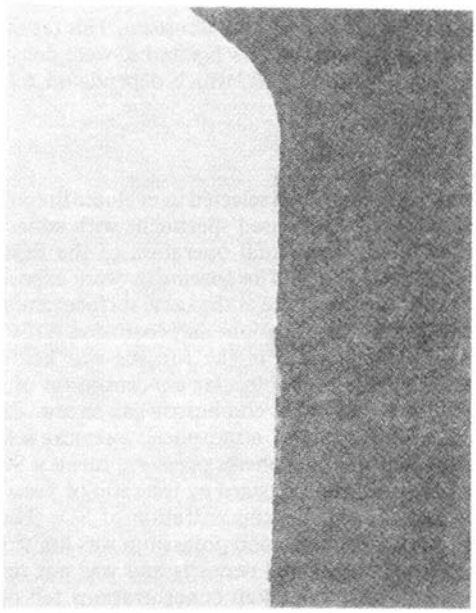

Fig. 2 Leading edge corner, in 738 CoCrAlY Coating: 460-h exposure

vertical with the nose angling up to the left. Three corrosion zones are shown with the white depleted area surrounding each zone. The coating (Co balance, 26 percent by weight Cr, 9 percent by weight Al, 0.3 percent by weight Y) is depleted along the entire gas contact face. Figure 3 shows the corrosion penetration at a leading edge corner for specimen 23 (50 percent) and a flat surface corrosion zone with a shallow pit (without corrosion product) of the type seen at about 5 h in the RQL tests, surrounded by three corrosion zones. Figure 4 shows a leading edge corner SiC specimen with thick ash deposits covering an area of extensive defoliation, or flaking, of the ceramic.

The numerical results for the 460 h furnace specimens are given in Table 5. The penetration of the CoCrAlY coating varies from 0.10 to 2.6 mils while the precursor depletion reaction zone ranges from 0.4 to 2.6 mils in depth. When the table is examined more closely, a bimodal distribution can be seen with a clearly defined cause. The flat surface penetration averages 0.52 mils while the leading edge corners average 1.04 mils. This correlates with the well-known fact that sharp points, edges, and corners are more chemically reactive than surfaces in heterogeneous reactions. Interestingly enough there is no difference in depletion reaction rate between corners and surfaces in the data. (Bulk properties dominate diffusion reactions.) This bimodal distribution clearly identified the potential life-limiting areas for corrosion as the edges and corners of turbine components.

The flaking of the SiC specimens appeared to result from metallographic preparation, which probably caused edge breakdown of the brittle material.

Discussion of Results. The rates of penetration observed in the CoCrAlY coated IN 738 specimens after furnace exposure were very high and would certainly be prohibitive in a gas turbine. This comparison furnace environment was probably less severe than the engine environment in most respects (ash deposits not being replenished, less severe thermal transients).

The tests to date indicate a potential for high rates of corrosion for turbines operating with coal–water fuels. As indicated earlier, some corrosion was observed for the RQL combustor DEC tests even at short durations of 5 h and less.

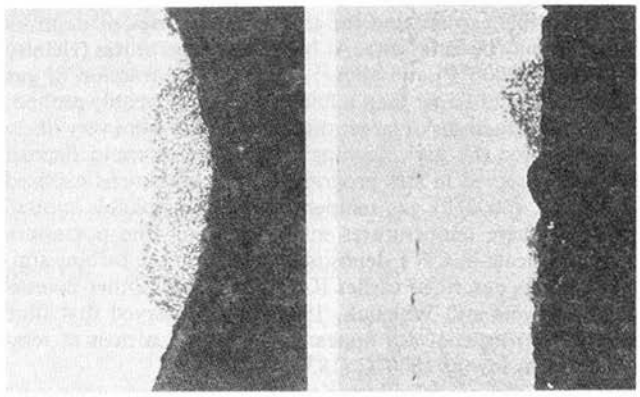

Fig. 3 Leading edge corner specimen 23 (50 percent) flat surface corrosion (right) and in 738, CoCrAlY coatings at 899°C (1650°F): 460-h exposure (left)

Fig. 4 Leading edge corner and sintered silicon carbide, specimen 3 (50 percent): 460-h exposure

In addition, high rates of corrosion were observed in extended exposure furnace tests, which in several respects may have produced less severe corrosion environments than in an engine.

The presence of carbon in deposits has been previously shown to accelerate hot corrosion of turbine alloys (McKee and Romeo, 1973, 1975). The corrosion experienced during the 5-h DEC tests may have been greatly accelerated by carbon in the deposits. Analysis of captured gas stream particulate revealed carbon levels greater than 80 percent. Since measured carbon levels in the deposits after the DEC tests were less than 1 percent, carbon may have been oxidizing (burning) in the specimen deposit. Because most of the carbon had been previously consumed prior to the furnace tests, carbon effects are expected to be less in the furnace test than in the DEC test (Wenglarz and Fox, 1990).

Summary and Conclusions

Specimens were exposed to combustion products from three CWF in two test sections at representative gas and surface temperatures of the first stator and rotor of aero-derivative

Table 5 Corrosion distribution photomicrographs of SO_2/air; 899°C (1650°F) furnace corrosion of RQL adherent deposit specimens (460 h)

Material	Specimen	Penet mils	Penet % CoCrAlY coating	Width mils	Deple mils (1)	Penet % CoCrAlY coating	Comment
CoCrAlY IN 738	8-25%	0.10	3.2	1.1	1.4(2)	45.2	Flat surface, adh dep <0.1 mils
	8-50%	0.20	6.7	2.6	0.5	16.7	Flat surface adh dep 0.10 mils pit (no corrosion products)
SiC	3-25%	Below detect					Leading edge corner, adh dep >0.15 mils
	3-25%	Fract 0.50		<9			Leading edge corner, adh dep 2.0 mils
	3-50%	Fract 0.7		6.5			Flat surface, adh dep 0.8-1.6 mils
CoCrAlY IN 738	23-25%	1.0	31.3	<<9	1.6	46.7	Flat surface, adh dep 0.1-0.15 mils
	23-25%	1.3	43.0	5.8	2.2	73.3	Leading edge corner, adh dep 0.05-0.15 mils
	23-25%	0.8	25.8	4.0	1.3	41.9	Leading edge corner, adh dep 0.05-0.10 mils
	23-25%	0.4	12.5	1.9	1.0	32.3	Flat surface, adh dep <0.05-0.18 mils
	23-50%	0.9	33.3	6.5	1.4	50.0	Flat surface, adh dep <0.05-0.08 mils
	23-50%	0.5	16.7	1.0	0.7	22.6	Flat surface, (prob high Y) adh dep 0.2 mils
	23-50%	1.7	58.2	<9	2.2	82.1	Leading edge corner, adh dep 0.05-0.15 mils
	23-50%	1.0	34.5	4.4	1.5	48.3	Flat surface, adh dep 0.15 mils
CoCrAlY IN 738	29-25%	1.1	33.3	4.3	1.7	51.5	Leading edge corner, adh dep 0.10 mils
	29-25%	0.3	9.2	0.5(3) 0.7	0.6	18.5	Flat Surface, adh dep 0.05-0.10 mils
	29-50%	0.3	9.1	1.4	0.4	12.1	Flat surface, Pit (no corrosion products)
	29-50%	0.9	27.3	2.7	1.3	39.4	Flat surface, adh dep 0.3 mils
		0.2	6.1	1.8	0.6	18.2	Flat surface, adh dep 0.3 mils
		0.9	26.5	5.4	1.7	50.0	Leading edge corner, adh dep 0.15 mils
CoCrAlY IN 738	7-25%	1.1	30.6	8.9	1.4	38.9	Leading edge corner, adh dep 0.10-0.35 mils
	7-25%	0.2	5.5	1.1	4.0	12.1	Flat surface, adh dep 0.15-0.70 mils
	7-25%	0.9	26.5	<9	1.9	55.9	Flat surface, stringer deple., adh Dep 0.05-0.35 mils
	7-25%	1.2	38.1	<9	1.8	55.6	Leading edge corner, adh dep 0.15 mil
	7-50%	0.4	11.4	4.4	0.7	20.0	Flat surface, Pit (no corrosion products) adh dep 0.10-0.40 mils
	7-50%	1.0	29.4	<8	2.2	64.7	Flat surface, stringer deple., adh dep 0.05-0.30 mils
	7-50%	0.2	6.1	1.4	0.5	15.2	Leading edge corner, adh dep 0.05-0.20 mils
CoCrAlY IN 738	25-25%	0.1	3.6	5.2	0.4	14.3	Flat surface, adh dep 0.20-0.70 mils
	25-50%	0.5	16.7	3.8	0.9	30.0	Flat surface, adh dep 0.10 mils
	25-50%	2.6(2)	86.7	0.3	2.6(2)	86.7	Flat surface, stringer corr. and deple, adh dep 0.2 mils

(1) Includes corrosion penetration
(2) Depletion at stringer(s)
(3) Two adjacent areas.

turbines. The deposit formed in the two test sections differed substantially. Deposition rates at first stator conditions were high and deposit chemistry near the specimen surfaces was similar to that of the fuel ash (except for trace elements). Deposition rates at the lower temperature first rotor conditions were up to 100 times lower and deposit chemistry near the specimen surfaces was unlike the fuel ash chemistry. Sodium levels were typically 2.5 to 30 times higher and Si and Al levels were typically 2 times lower in the lower temperature deposits than in the fuel ash.

At the higher first stator temperatures, ash particle sticking to form deposits appears to have been affected mainly by inertial impaction of larger molten particles. These particles probably became frozen at lower first rotor temperatures. Ash sticking at these lower temperatures may have been affected mainly by condensed phases involving sodium, which are delivered to surfaces by diffusion and thermophoresis mechanisms at relatively low rates compared to inertial impaction.

Limited corrosion was detected on some CoCrAlY coated, IN 738 alloy specimens after only about 5 h of exposure to the RQL products of combustion. Further exposure of deposit-coated specimens from the DEC tests in an SO_2 seeded furnace produced significant coating penetration by corrosion after a total of 460 h. The test results suggest a potential for significant corrosion in turbines operating with coal-water fuels.

Coal-fired utility boiler experience has shown a wide range of DEC characteristics for coal fuels. The DEC levels observed in this program were substantially affected by the ash chemistry associated with the specific feedstock and cleaning processes used to formulate the test fuels. Consequently, additional testing will be necessary to determine the range of DEC degradations from candidate CWF used in turbine combustors and to identify fuel ash specifications and systems measures such as hot gas cleanup to minimize those degradations.

Acknowledgments

The DEC tests were sponsored by the Department of Energy

(Morgantown Energy Technology Center [METC]) and Allison Division of General Motors. The direction and encouragement of Janna Thames and Nelson Rekos, METC contracting officer's technical representatives, have been greatly appreciated.

References

Bryers, R. W., and Walchuk, D. R., 1984, "Operating Experience With a Pilot Scale Combustion Facility Used for Studying Slagging and Fouling Characteristics of Coal—Part II: Experimental Results," presented at the Engineering Foundation Conference, Copper Mountain, CO.

Corman, J. C., 1986, "Turbine Utilization of Coal and Coal-Derived Fuels," *Proceedings of New Fuel Forms Workshop*, Washington, DC.

Crouse, F. W., Jr., ed., 1986, *Proceedings of the Third Annual Heat Engine Contracts Meeting*, DOE/METC-86/6041.

Halstead, W. D., 1973, "Calculation on the Effects of Pressure and Temperature on Gas Turbine Deposition," in: *Deposition and Corrosion in Gas Turbines*, A. B. Hart and A. J. B. Cutler, eds., Wiley, New York.

Interdepartment Gas Turbine Steering Committee, 1973, "The Coal-Burning Gas Turbine Project," Australian Government Publishing Service, Canberra.

McKee, D. W., and Romeo, G., 1973, "Carbon Deposition and the Role of Reducing Agents in Hot Corrosion Processes," *Metallurgical Trans.*, Vol. 4, No. 8, pp. 1877–1885.

McKee, D. W., and Romeo, G., 1975, "Effects of Transient Carbon Deposition on Sodium Sulfate-Induced Corrosion of Nickel-Base Alloys," *Metallurgical Trans.*, Vol. 6, No. 1, pp. 101–108.

Novick, A. S., and Troth, D. L., 1981, "Low NO_x Heavy Fuel Combustor Concept Program," NASA CR-165367, DOE-NASA-0148-1.

Smith, J., Strimbeck, D. C., Coates, N. H., and McGee, J. P., 1966, "Bureau of Mines Progress in Developing Open and Closed Coal-Burning Gas Turbine Plants," ASME Paper No. 66-GT/CLC, presented at the International Gas Turbine Conference, Zurich, Switzerland.

Stringer, J., McCarron, R., et al., 1985, "Results From the Turbine Materials Testing Program on the IEA Grimethorpe Experimental PFBC Facility," *Proceedings of 8th International Conference on Fluidized Bed Combustion*, Houston, TX.

Wenglarz, R. A., 1987a, "Direct Coal-Fueled Combustion Turbines," ASME Paper No. 87-GT-269.

Wenglarz, R. A., 1987b, "Turbine Deposition, Erosion and Corrosion Evaluations Using a Simplified Test Approach," ASME Paper No. 87-GT-214.

Wenglarz, R. A., and Fox, Jr., R. G., 1990, "Physical Aspects of Deposition From Coal-Water Fuels Under Gas Turbine Conditions," ASME JOURNAL OF ENGINEERING FOR GAS TURBINES AND POWER, Vol. 112, this issue.

Wilkes, C., Wenglarz, R. A., and Clark, D. W., 1985, "Combustion and Deposition, Erosion and Corrosion Tests of Coal Turbine Fuels," ASME Paper No. 85-JPGC-GT-8.

Physical Aspects of Deposition From Coal-Water Fuels Under Gas Turbine Conditions

R. A. Wenglarz

R. G. Fox, Jr.

Allison Gas Turbine Division,
General Motors Corporation,
Indianapolis, IN 46206

Deposition, erosion, and corrosion (DEC) experiments were conducted using three coal-water fuels (CWF) in a staged subscale turbine combustor operated at conditions of a recuperated turbine. This rich-quench-lean (RQL) combustor appears promising for reducing NO_x levels to acceptable levels for future turbines operating with CWF. Specimens were exposed in two test sections to the combustion products from the RQL combustor. The gas and most surface temperatures in the first and second test sections represented temperatures in the first stators and rotors, respectively, of a recuperated turbine. The test results indicate deposition is affected substantially by gas temperature, surface temperature, and unburned carbon due to incomplete combustion. The high rates of deposition observed at first stator conditions showed the need for additional tests to identify CWF coals with lower deposition tendencies and to explore deposition control measures such as hot gas cleanup.

Introduction

Coal-water fuels (CWF) are being considered for boiler plants and combustion turbines. A major area of technical uncertainty for these applications is component degradation due to deposition, erosion, and corrosion (DEC) from ash in the CWF. Some DEC testing of related boiler applications has been conducted (Jones and Matthews, 1985). However, the DEC behavior of CWF at boiler conditions is probably not representative of the behavior of candidate turbine CWF.

Turbine CWF are expected to be more highly processed to result in lower ash levels (perhaps less than 1 percent) than for boiler fuels (often > 10 percent). An increased level of coal cleaning affects not only the overall level of ash but also the ash chemistry, which could affect the compounds and melting points of particles formed in the combustion process. Combustion intensities and pressures are much higher with much shorter residence times (by one to two orders of magnitude) for typical turbine combustion processes compared to boiler plant combustion. Consequently, kinetic effects in ash transformations during combustion are likely more significant for turbine combustors.

The gas stream conditions and the surfaces that are exposed to the combustion products are different in turbine applications and boiler applications. Gas stream velocities are more than an order of magnitude greater and some surfaces operate at temperatures that are several hundred degrees higher in turbine applications. The higher velocities tend to increase particle delivery rates to surfaces and higher temperatures tend to increase the probability of particle sticking on those surfaces (and probably increase corrosion potential).

Contributed by the International Gas Turbine Institute and presented at the 34th International Gas Turbine and Aeroengine Congress and Exhibition, Toronto, Ontario, Canada, June 4-8, 1989. Manuscript received at ASME Headquarters February 1, 1989. Paper No. 89-GT-206.

The following discusses some results of early coal-water fuel deposition, erosion, and corrosion tests under simulated turbine conditions. Simple geometry specimens were exposed to the combustion stream produced by a rich-quench-lean (RQL), low-NO_x burner. The emphasis in the results to be described is the understanding of critical factors and mechanisms affecting DEC for turbines operating with a CWF. Such understanding is directed to aiding specification of fuel properties and turbine system design and operating conditions for use of coal-water fuels.

Test Facility

A staged, RQL combustor was used for the DEC tests. The RQL Combustion system was developed originally under National Aeronautics and Space Administration (NASA)/DOE sponsorship to investigate the combustion characteristics of a rich-lean combustion process aimed specifically at the reduction of oxides of nitrogen (NO_x) yield from fuel bound nitrogen. The original combustor (illustrated in Fig. 1) has three stages: rich, mixing, and lean zones followed by a dilution zone. Airflow to the rich, mixing, and dilution zones is controlled by three variable geometry mechanisms that can be adjusted independently of each other. The variable geometry feature provides a degree of control of combustion conditions in each zone for the purpose of optimizing overall combustion and emissions performance.

The RQL combustor has demonstrated high combustion efficiency and low NO_x, CO, and unburned hydrocarbon emissions using distillate, heavy petroleum residual, and synthetic coal-derived liquid fuels (Novick and Troth, 1981). Based on results of subsequent tests (Wilkes et al., 1985) with CWF, the combustor lean zone was extended to increase residence time in the lean stage by a factor of 3 to 4 and thereby improve combustion efficiency.

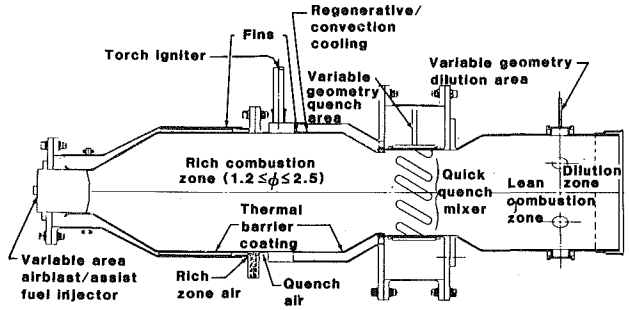

Fig. 1 RQL combustor

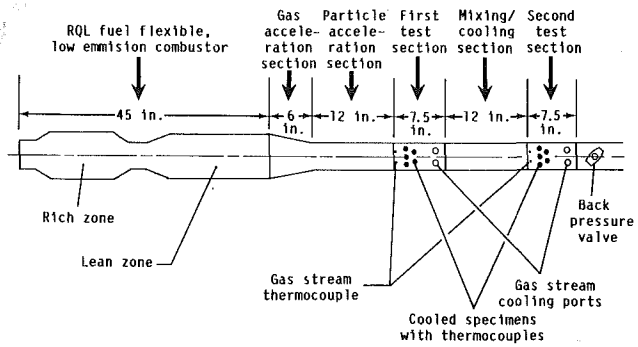

Fig. 2 DEC test facility schematic

The DEC characteristics of products of combustion (POC) from turbine combustors directly fired with CWF are virtually unknown and depend on many variables. Consequently, a new DEC facility was designed and fabricated to control and efficiently explore as many DEC variables as possible with available resources and provide data that can be extrapolated to operating turbines. This has been accomplished by using simple specimen and flow passage geometries, which control product of combustion (POC) particle impact rates, angles, and velocities, utilizing a double test section arrangement, and operating at reduced pressure (310 kPa [45 psia)] while maintaining the same combustor residence time as for a full-pressure engine. The data from this test facility are intended to be used for identification of critical DEC mechanisms and extrapolations using turbine deposition and erosion models to estimate turbine maintenance intervals. Critical factors and mechanisms affecting turbine deposition from CWF are described in this paper. The data extrapolation approach and maintenance interval extrapolations using data from the tests described here are given elsewhere (Wenglarz, 1987; Ahluwalia et al., 1989). The DEC test facility and data extrapolation approach are advancements of those used previously in 600 h of residual oil tests (Whitlow et al., 1982) and 1400 h of coal-derived liquid tests (Spengler et al., 1983).

A schematic for the DEC test facility is shown in Fig. 2. Cooled specimens are exposed to CWF combustion products from the RQL combustor in two test sections. The gas and most specimen surface temperatures of the first and second test sections were representative of the maximum gas and surface temperatures of the first two expander rows (first stator and first rotor) of a recuperated turbine. The gas temperature entering the first test section was nominally 1100°C (2000°F). Air injected immediately downstream of the first test section reduced the gas temperature entering the second test section to about 980°C (1800°F). The transition duct from the combustor to the first test section was designed with sufficient length to accelerate particles to the gas velocity of 183 m/s (500 f/s). The gas velocity then controlled the particle impact velocity on the specimens. The wedge-shaped specimen flat surface orientations controlled the particle impact angles (10, 30, and 45 deg). The surface temperatures for most specimens were 980°C (1800°F) in the first test section and 900°C (1650°F) in the second test section. One specimen in each test section was cooled up to 100°C (180°F) lower surface temperature (than a turbine airfoil) to evaluate possible beneficial effects on deposition and corrosion. One uncooled SiC specimen was also exposed in each test section to evaluate the erosion and corrosion resistance of this potential turbine material. The remaining specimens were constructed of a turbine alloy (IN 738) covered with a CoCrAlY coating of the type that has demonstrated erosion and corrosion resistance in coal-fired PFBC cascade tests (Stringer et al., 1985).

Table 1 Fuel properties

Ultimate analysis--wt % dry			
Element	Fuel 1	Fuel 2	Fuel 3
Carbon	82.76	82.79	82.89
Hydrogen	5.19	5.20	5.22
Nitrogen	2.11	2.08	2.15
Chlorine	0.19	0.15	0.17
Sulfur	0.91	0.96	0.71
Ash	1.25	0.97	0.69
Mineral analysis of ash--wt % of ash			
Phosphorus	0.88	0.57	0.23
Silicon	12.00	11.48	7.50
Iron	20.40	21.90	23.14
Aluminum	14.24	13.92	10.94
Titanium	0.83	0.83	1.00
Manganese	0.02	0.03	0.04
Calcium	3.82	3.37	4.73
Magnesium	0.82	0.98	1.40
Potassium	1.19	0.98	0.87
Sodium	0.58	0.73	0.98
Oxygen/trace elements	balance	balance	balance

Table 2 Carbon levels and size distributions for POC particulate samples

Fuel	Carbon wt-- % in sample	Carbon burn-out eff--%	Avg particle dia (μm)	Vol--% >10 μm	Vol--% 10 to 5 μm
1	81.45	94.4	10.2	51.0	28.6
2	96.56	72.5	8.5	43.3	31.3
3	94.43	90.1	14.5	65.4	20.2

Test Fuels

Table 1 gives properties of the three fuels used in the DEC tests. The fuels were formulated by the one supplier from one batch of coal cleaned to three ash levels (1.25, 0.97, and 0.69 percent). The cleaned coal was slurried with water and the same additives to produce a coal loading of about 50 percent. A common coal feedstock was used to evaluate the effect of the degree of ash removal and eliminate feedstock variation effects on DEC. The largest coal particle size was 40 μ m for fuel 1 and 15 μm for fuels 2 and 3. The viscosity-inhibiting additive level in fuel 3 was about twice that of fuels 1 and 2. The differences in the largest coal particle size and additive level were chosen to explore their effects on atomization, combustion, and resulting DEC.

Although the DEC test duration goal for each fuel was 5 h, factors such as premature shutdowns resulted in deviations from the nominal. The durations for DEC tests of fuels 1, 2, and 3 were about 5.0, 1.7, and 4.3 h, respectively.

Test Results

Product of Combustion (POC) Particulate. Using an isokinetic probe, POC particulates were captured immediately downstream of the RQL combustor. The particulates were rapidly cooled by quenching upon capture to prevent further

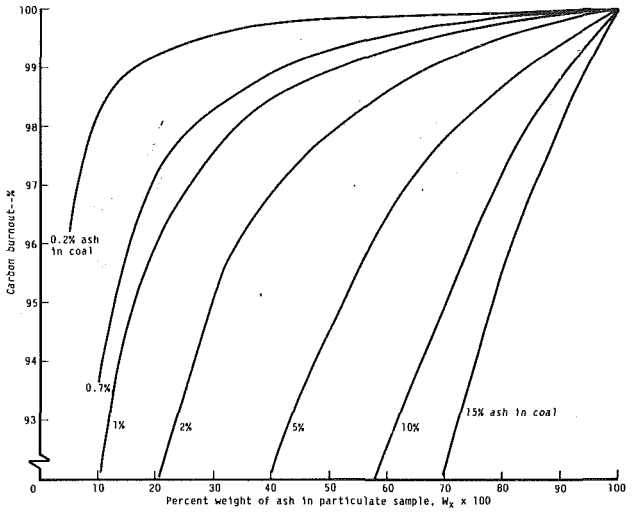

Fig. 3 Carbon burnout versus ash concentration in particulate samples

oxidation. Table 2 gives carbon levels and size distributions for POC particulate samples obtained in combustion tests conducted at the at the same conditions as the DEC tests for three test fuels. The relatively high particulate carbon level shown for the combustor test of fuel 2 was probably lower for the corresponding DEC tests. A partial nozzle air obstruction occurred in the combustion test but was corrected for the DEC test of fuel 2.

Carbon burnout efficiency for the three fuels is also given in Table 2. These were obtained using a formula (applicable to slurry and dry fuels) that obtains fractional carbon burnout by relating the weight fraction W_x of ash in the particulate sample to the weight fraction W_a of ash in the coal from which the fuel was made (Germane et al., 1984):

$$\text{burnout fraction} = (1 - W_a/W_x)/(1 - W_a)$$

Using this formula, Fig. 3 gives carbon burnout efficiencies versus percentage ash in POC particulate for combustion of fuels with several ash levels. Figure 3 shows that relatively high carbon weight fractions greater than 50 percent can occur in POC particulate even at 99 percent carbon burnout efficiencies for fuels containing ash levels ≤ 1 percent. In contrast, POC carbon levels are less than about 5 percent at 99 percent carbon burnout efficiencies for coal fuels containing $\geq$ 15 percent ash such as might be used in coal boiler plants.

The much higher carbon fractions in gas stream particulate for prospective coal-fueled turbine systems compared to convention coal-fired boilers may result in increased deposition. Several factors could increase particulate delivery rates to turbine surfaces and their probability of sticking upon impact to build up deposits:

1 Increased amounts of particulate larger than 10 μm in diameter due to incomplete carbon burnout could result in higher particle delivery rates to turbine surfaces.

2 Volatile carbon that was not released could be sticky at gas stream temperatures to cause particle attachment at impact on surfaces. This effect has been observed in deposition tests (Jones and Matthews, 1985) using CWF at boiler conditions and could be enhanced in turbines due to higher carbon fractions in the particulate.

3 Carbon in the particulate could be burning in the gas stream to increase particle temperatures above gas temperatures and increase the molten fraction of ash carried with the carbon particles. The higher molten fraction would increase the probability of particle sticking upon impact on a turbine surface. At the surface, burning carbon could melt the ash deposit in its vicinity to provide a sticky surface to capture other impacting particles.

Table 3 Impact fraction versus particle size for first stator passage of 5000 hp turbine

	3μm	6μm	9μm	12μm	15μm	25μm
Impact fraction	0.08	0.19	0.30	0.42	0.5	0.84

Table 4 Particulate sample size distribution before and after ashing

	Avg particle dia (μm)		Vol % > 10 μm		Vol %-10 to 5 μm	
Fuel	Before ashing	After ashing	Before ashing	After ashing	Before ashing	After ashing
1	10.2	3.2	51.0	12.2	28.6	19.8
2	8.5	2.9	43.3	9.2	31.3	15.8
3	14.5	2.6	65.4	13.0	20.2	11.7

Table 5 Carbon levels in deposits from DEC test 1

Specimen surface temperature—°C (°F)	Carbon—%
1100 (2000) uncooled	0.02
980 (1800)	0.04
900 (1650)	0.07

4 Burning carbon in the gas stream or at turbine surfaces could result in locally reducing conditions to depress melting points of ash material carried by the carbon or at the impact surfaces.

Analyses were conducted to explore whether the above factors might have contributed to deposition in the DEC tests and whether they might be significant for turbines operating with CWF. Table 3 shows the estimated mass fraction of particles entering first stator passages that impact a stator airfoil surfaces for a turbine size in the 5000–10,000 hp range. These impact fraction versus particle diameter results were obtained with the aid of a turbine inertial impaction particle delivery model. Table 3 shows that the impact fraction increases with particle diameter such that virtually all particles larger than about 30 μm impact the first stator surfaces. Comparison of impact fractions in Table 3 with the size distributions in Table 2 indicates that a significant fraction (>30 percent) of particulate would impact turbine surfaces for the test fuels.

The particulate material described in Table 2, which was captured in combustion gas streams of the test fuels, was ashed. Table 4 compared Coulter Counter size distributions of the ashed particulate to the size distribution as captured in the gas stream in order to obtain an indication of the potential effects of carbon burnout efficiencies approaching 100 percent. The particulate material as captured has significantly larger size distributions than the ashed material with 4–5 times greater fractions of particulate larger than 10 μm.

The effect of incomplete carbon burnout on particle delivery to the first stator surfaces was estimated using the impact fractions and size distributions represented in Tables 3 and 4, respectively. For a turbine combustor assumed to produce the same POC as the test combustor, the incomplete carbon burnout indicated in Tables 2 and 3 could increase the ash impact fraction on the stator vanes by a factor of 2 and higher compared to 100 percent carbon burnout for the three test fuels. Considering the higher overall gas stream particulate loading due to unburned carbon, the projected overall mass delivery to the vanes increases by a factor greater than 10 for the three fuels.

The above results assume little additional consumption of carbon POC between the combustor exit and the stator passages. Analyses conducted have indicated that most of the carbon would not be consumed. Carbon burnout of POC particulate in a furnace at combustor exit temperatures required 2 to 3 min whereas the flight times to vane surfaces (and test specimen surfaces) are a fraction of a second.

Carbon levels were measured in the deposits on some specimens exposed in the high-temperature (1100°C [2000°F] gas) test section from the DEC test of fuel 1. Table 5 shows the percent carbon for three specimens exposed at different surface temperatures. While the gas stream particulate contained

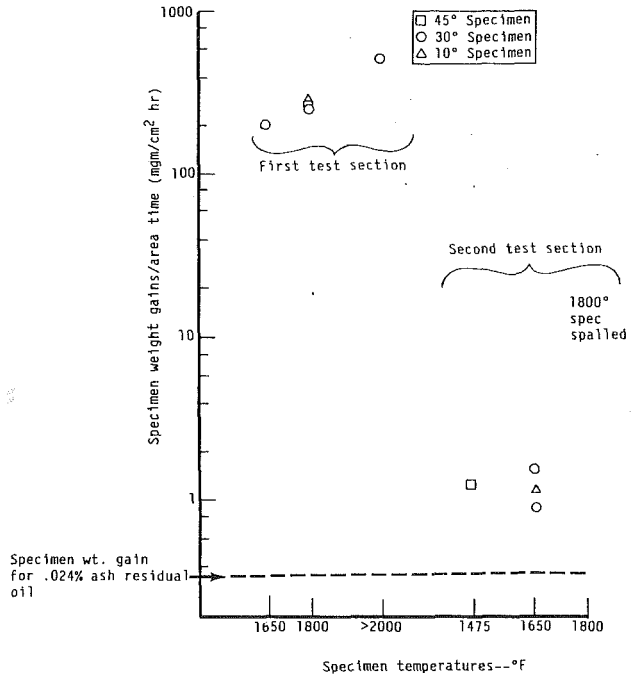

Fig. 4 Deposition rates on specimens for 1.25 percent ash coal-water fuel

over 80 percent carbon (Table 2), the carbon concentrations in the specimen deposits after extended exposure (5 h) were less than 0.1 percent (Table 5). This suggests that the carbon likely oxidized (burned) on its flight to the specimen and, to a much greater extent, in the deposit after impact. Note that decreasing unconsumed carbon content at increasing specimen surface temperatures shown in Table 5 also suggests burning at the surface at higher rates for higher surface temperatures.

In summary, these results support the hypothesis that incomplete carbon combustion efficiency (carbon burnout) could enhance deposition in coal-fueled turbines (and in the DEC tests reported here). Higher temperatures and locally reducing conditions for impacting particles and deposit surfaces due to burning carbon would be expected to increase sticking fractions of particles delivered to turbine surfaces. Even though the carbon is eventually consumed and does not directly contribute to deposit mass, the larger gas stream particle size distributions associated with incomplete carbon burnout could cause an increased fraction of ash material carried to turbine surfaces by the carbon. As shown in the discussions of Fig. 3, the low fuel ash levels expected for direct coal-fired turbines will probably make these combustion inefficiency effects much more significant than has been experienced in the past for conventional coal-boiler plants using high ash coals.

These observations are consistent with results of tests associated with an early coal-fueled turbine program (Morley and Wisdom, 1964). Those experiments showed that the presence of relatively coarse incandescent (burning) coal particles in the gas stream could greatly increase the rate and density of deposit buildup. However, low bulk gas temperatures in downstream turbine rows or low temperatures in the vicinity of highly cooled surfaces could result in insufficient oxidation rates to melt much of the ash carried with gas stream carbon. In that case the greater concentration of larger hard particles due to unburned carbon could reduce net deposit accumulation by eroding deposits formed by softer particles. Such large carbon particles in colder turbine locations could also increase the erosion of vane and blade surfaces.

Deposition. Deposition was the primary short-term degradation observed following the DEC tests. Deposits were observed on all test specimens. Figure 4 shows the specimen weight gain rates per unit area for the DEC test of fuel 1 containing 1.25 percent ash and coal particle sizes smaller than 40 μm. Since some deposits had spalled at test shutdown, the deposit weight gains included material remaining on the surfaces and large spalled pieces matched to specimen spall patterns and collected at the bottom of the test sections. In some cases where spalled pieces were not found, specimen weight gains were adjusted to reflect full surface coverage of the thickness of deposits remaining on the specimens.

As indicated in Fig. 4, the shapes of data point symbols indicate the angle of orientation of specimen flat surfaces with respect to the gas velocity. The data points at the left designate deposit weight gains for specimens exposed in the higher gas temperature (1100°C [2000°F]) test section. Data points at the right indicate specimens exposed at the lower gas temperature (980°C [1800°F]) test section. Specimen surface temperatures are given on the horizontal axis. The gas temperature of 1100°C (2000°F) and surface temperature of 980°C (1800°F) of the high-temperature test section represent maximum gas and surface temperatures of first stator vane passages of aeroderivative turbines. The gas temperature of 980°C (1800°F) and surface temperature of 900°C (1650°F) in the lower temperature test section represent maximum temperatures of first stage turbine rotor blade passages. Three specimens with flat surface orientations of 10 deg, 30 deg, and 45 deg are exposed at these representative stator and rotor temperatures.

Specimen surface orientations are shown in Fig. 4 to have a minor effect on specimen weight gains. The lower temperatures associated with first rotor conditions result in less deposition, by more than two orders of magnitude, than the higher temperatures associated with first stators. For all specimen surface temperatures, the higher gas temperature of the first test section results in much greater deposition than for the second test section. Reduction of gas stream particle loading entering the second test section due to capture in the first test section had only a minor effect on the greatly reduced deposition on the downstream section specimens. This is because the deposit weight gains of first test section specimens accounted for only about 5 percent of the total ash mass throughput in the tests.

The high rates of deposition in the first test section were likely caused by a significant fraction (probably between 1 and 10 percent) of molten or soft particles in the gas stream. The much lower deposition in the second test section probably resulted from freezing of much of this material. The first test section gas temperature (1100°C [2000°F]) was lower than the initial deformation, ash fusion temperature (1170°C [2140°F]) for the ash of fuel 1 measured by the standard ASTM ash cone test; however, evaluations (Borio et al., 1977) have shown that significant ash melting/softening can occur before initial deformation is observed in the ash cone test.

A clear trend in increasing deposition with increasing surface temperature is seen for 1100°C (2000°F) gas temperatures. The deposition at the surface temperature of 1100°C (2000°F) is about 2.5 times greater than at 900°C (1650°F). No trend in deposition with surface temperature was seen at the lower gas temperature. The highest deposition rate on the uncooled SiC specimen at 1100°C (2000°F) gas temperature is probably due to its highest surface temperature and not its difference in material from the coated alloy specimens. Once an initial thin deposit is formed, additional deposition accumulates on underlying deposits and the original surface composition is probably of little consequence.

The dashed line near the bottom of Fig. 4 gives specimen weight gains measured in a past program (Sherlock et al., 1983) using similar sized simple geometry specimens exposed at 1100°C (2000°F) gas temperature and 900°C (1650°F) surface temperature representing first stators of a utility turbine. The fuel was a 0.024 percent ash residual oil, which has been

successfully used in peaking turbines operating at utility power plants. Figure 4 shows that even though the CWF contained 25 times the ash level of the residual oil, deposition rates were comparable at the lower gas temperature. At higher gas temperatures, the deposition rates for the CWF tested in this program are much higher than for residual oil. These results suggest possible deposition benefits for CWF operation at lower expander inlet temperatures in the range of 900°C (1800°F) used in older vintage turbines.

Figure 5 compares normalized mass deposition rates on specimens for the three test fuels. Since specimen surface orientations were seen to have a minor effect on deposition, only data for 30 deg specimen angles are shown. The deposition rates/area in Fig. 5 are normalized to the ash levels in the combustions stream to factor out differences in fuel ash levels and fuel feed rates. The darkened symbols in Fig. 5 indicate first test section specimens exposed at gas temperatures in the vicinity of 1100°C (2000°F). The open symbols designate second test section specimens exposed at gas temperatures in the vicinity of 980°C (1800°F). The square symbols indicate uncooled SiC specimens while the circles designate cooled IN 738 specimens with a CoCrAlY coating.

Figure 5 again shows a major effect of temperature on deposition. The cooled metallic specimens exposed at 1100°C (2000°F) experienced higher deposition rates, by two orders of magnitude, than cooled metallic specimens exposed at 980°C (1800°F). Deposition rates on uncooled SiC specimens were one order of magnitude higher at 1100°C (2000°F) than at 980°C (1800°F). These differences are likely due to higher levels of molten gas stream particles at high gas temperatures, which experience some degree of freezing as they traverse the thermal boundary layer of cooled specimens.

Effects of gas temperature at a fixed surface temperature are indicated by comparing the deposit weight gains for the 980°C (1800°F) surface temperature specimens in Fig. 5. The 120°C (200°F) difference in gas temperature (1100°C versus 980°C [2000°F versus 1800°F]) is seen to result in an order of magnitude difference in deposition. A plausible explanation may be that hotter particles entering the thermal boundary layer of a surface would have a higher temperature at impact and a greater probability of sticking.

Figure 5 shows that since the specimen deposition rates normalized to ash levels in the high-temperature test section are nearly the same for the three fuels, deposit buildup was nearly proportional to the residual ash level after coal cleaning. However, the normalized deposition rates for specimens in the second test section increased with increased removal of ash so that increased cleaning may not have yielded a proportional reduction in deposition. It appears that the cleaning process changes ash chemistry and changes the level of those molten ash constituents that promote particle sticking on impact at lower temperatures.

Figure 5 indicates that little or no deposition benefit was obtained from the smaller coal particle sizes (< 15 um) in fuels 2 and 3, compared to the larger size (<40 um) in fuel 1. This might be expected since the POC particle size distributions in Table 1 for fuels 2 and 3 compared to fuel 1 do not reflect their factor of nearly three lower top coal particle size. It appears that POC particle sizes are determined by fuel atomization droplet size distributions, not coal particle sizes, if maximum coal particle diameters are smaller than maximum droplet diameters. This is consistent with previous tests with CWF at boiler plant conditions (McHale, 1985).

Deposit Tenacity. Although the tenacity of the CWF deposits at high-temperature test conditions was not evaluated, the cooled deposits appeared to be much harder than cooled deposits from residual oil DEC tests (Sherlock et al., 1983). Those CWF deposits from both the high and low-temperature test sections that did not spall on test shutdown were often very tenacious, especially on specimens that had experienced higher surface temperatures.

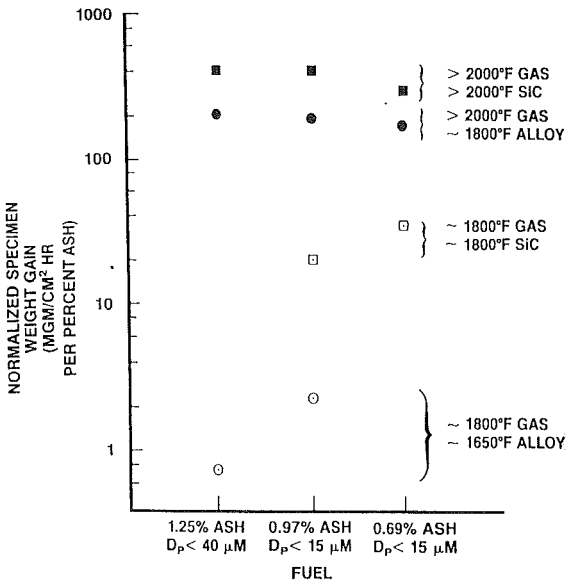

Fig. 5 Normalized weight gains for 30 deg specimens

Summary and Conclusions

Deposition was observed on all specimens for all fuels and was the dominant short-term degradation process. Deposition rates were highly sensitive to temperature. At the higher first test section temperatures representative of a turbine first stator row, deposition rates on coated alloy specimens were about 100 times greater than at the lower temperatures representative of a turbine first rotor row. Higher deposition rates at higher temperatures very likely resulted from a greater fraction of molten particulate delivered to specimen surfaces, which increased particulate sticking fractions.

The deposition rates at the representative conditions of a turbine first rotor row (gas temperature in the vicinity of 980°C [1800°F]) were comparable to deposition rates from past tests at simulated turbine conditions for residual oil, which has been successfully used in commercial utility turbines. At the higher temperatures (gas temperatures in the vicinity of 1100°C [2000°F]) representative of current turbine first stators, deposition rates of the CWF tested in this program were much greater than for residual oil.

At higher temperature first stator conditions, deposition rates were nearly proportional to the ash level and degree of coal cleaning. At lower temperature first rotor conditions, increased cleaning may not have yielded a proportional reduction in deposition. Neither coal particle size nor additive level in the fuels appeared greatly to affect combustion product particle sizes or levels of deposition. The high carbon levels (compared to past coal experience) in the combustion product particulate resulting from combustor inefficiency of low ash CWF will likely increase rates of particulate delivery to turbine surfaces, the probability of ash sticking on those surfaces, and resulting deposition.

The transition temperatures between the high and lower rates of deposition observed in the tests described here are very likely sensitive to the coal feedstock ash chemistry and cleaning process. Consequently, feedstock/cleaning process combinations may well be found that result in fuels with ash melting/softening temperatures above the temperatures in turbine first stator passages. If such fuels were available, deposition rates comparable to those at lower temperatures of this program might be more representative. Those rates are of the

same order of magnitude as commercial turbines operating on residual oils.

Acknowledgments

The DEC tests were sponsored by the Department of Energy (Morgantown Energy Technology Center, METC) and Allison Gas Turbine Division of General Motors. The direction and encouragement of Janna Thames and Nelson Rekos, the METC contracting officer's technical representatives, have been greatly appreciated.

References

Ahluwalia, R. K., Im, K. H., and Wenglarz, R. A., 1989, "Flyash Adhesion in Simulated Coal-Fired Gas Turbine Environment," ASME JOURNAL OF ENGINEERING FOR GAS TURBINES AND POWER, Vol. 111, pp. 672-678.

Borio, R. W., Goetz, G. J., and Levasseur, A. A., 1977, "Slagging and Fouling Properties of Coal Ash Deposits as Determined in a Laboratory Test Facility," presented at the ASME Winter Annual Meeting, Combustion Engineering publication TIS-5155.

Germane, G. J., et al., 1984, "Space Resolved Coal-Water Mixture Combustion and Pollutant Formation Studies in a Laboratory Scale Furnace," *Sixth International Symposium on Coal Slurry Combustion*, Orlando, FL.

Jones, A. R., and Matthews, K. J., 1985, "The Ash Deposition Characteristics of Twelve Coal-Water Mixtures," Second European Conference on Coal-Liquid Mixtures, *I Chem E Symposium Series 95*.

McHale, E. T., 1985, "Review of CWF Combustion Technology," *Energy Progress*, Vol. 1, No. 5.

Morley, W. J., and Wisdom, J. C., 1964, "Brown Coal Ash Deposition in the Open-Cycle Gas Turbine." *Journal of the Institute of Fuel*, Vol. 37, No. 280, pp. 187-200.

Novick, A. S., and Troth, D. L., 1981, "Low NO_x Heavy Fuel Combustor Concepts Program," NASA Report CR-165367, DOE-NASA-0148-1.

Sherlock, T. P., Wenglarz, R. A., et al., 1983, "Combustion-Turbine Design Guidelines Based on Deposition-Corrosion Considerations," Residual Fuel Oil Studies, EPRI Report AP-2739, Vol. 1.

Spengler, C. J., Wenglarz, R. A., et al., 1983, "Corrosion and Deposition Results From Pressurized Passage Tests With Heavy Ash Bearing Fuels From the SRC II Process," ASME Paper No. 83-GT-85.

Stringer, J., McCarron, R., et al., 1985, "Results From the Turbine Materials Testing Program on the IEA Grimethorpe Experimental PFBC Facility," *Proceedings of 8th International Conference on Fluidized Bed Combustion*, Houston, TX.

Wenglarz, R. A., 1987, "Turbine Deposition, Erosion, and Corrosion Evaluations Using a Simplified Test Approach," ASME Paper No. 87-GT-214.

Whitlow, G. A., Wenglarz, R. A., et al., 1982, "Combustion Turbine Deposition Observations From Residual and Simulated Residual Oil Studies," ASME Paper No. 82-GT-7.

Wilkes, C., Wenglarz, R. A., and Clark, D. W., "Combustion and Deposition, Erosion and Corrosion Tests of Coal Turbine Fuels," ASME Paper No. 85-JPGC-GT-8.

C. F. Smith[1]
Graduate Research Assistant.

P. E. Sojka
Assistant Professor.

Gas Turbine Combustion Laboratory,
Thermal Sciences and Propulsion Center,
School of Mechanical Engineering,
Purdue University,
West Lafayette, IN 47907

J. M. Thames[2]
U.S. Department of Energy,
Morgantown Energy Technology Center,
Morgantown, WV 26505

The Influence of Fluid Physical Properties on Coal-Water Slurry Atomization

This study reports the atomization behavior of coal-water slurries (CWS) at conditions typical of a gas turbine combustor. Slurry atomization characteristics were determined for a plain-jet airblast research nozzle and six slurries. Atomization quality is reported in terms of the spray's Sauter mean diameter (SMD) and the radial distribution of fuel mass flux (patternization). The drop size data demonstrate that SMD can be predicted from a knowledge of slurry velocity, the relative velocity between the airblast air and the slurry, the air-to-fuel mass flow ratio (AFR), and the slurry rheology. Slurry rheology is represented here by a power law expression.

Introduction

Coal-water slurry (CWS) has proved to be a particularly promising alternative fuel since it retains the economic advantages of coal while possessing the handling convenience of a liquid. The viability of CWS for use in boilers and furnaces has been demonstrated and its application to stationary gas turbine combustion is currently in the research phase. This paper presents results describing the atomization of six CWS fuels sprayed through a plain-jet airblast nozzle under conditions characteristic of a gas turbine combustor.

Detailed knowledge of the atomization process is of particular importance to the combustion of CWS in gas turbines since atomization is known to play a key role in the determination of flame speeds, flame stability, and ignition limits (Farmayan et al., 1984). In order to improve understanding of the slurry atomization process, CWS has been sprayed through several types of nozzles. Plain-orifice and pressure swirl atomizers were unable to generate shearing forces of sufficient magnitude to cause slurry jet breakup, resulting in large mean drop sizes and poor spray quality (Sojka and Lefebvre, 1986). Air-assist nozzles were found to atomize CWS effectively, but the external compressor required to supply the necessary high-pressure air can be a disadvantage. Airblast atomizers, however, make use of the pressure drop across the combustor liner to provide high-velocity atomizing air without the complication of an external air supply. An airblast nozzle was employed in this study.

There have been numerous previous investigations of CWS atomization with the majority employing air-assist (Allen et al., 1985; Borio et al., 1984; Gillberg et al., 1983; Knell et al., 1983; Knell and Tsai, 1985; Pohl et al., 1985; Winters et al., 1985) or airblast nozzles (Cronin et al., 1985; Smith et al., 1984, 1985). Synthesis of the results of these studies shows nozzle air-to-fuel (AFR) mass flow ratio, through the quantity

$$(1 + 1/\mathrm{AFR})^N \tag{1}$$

to be an important parameter in determining spray mean drop size. In particular, Pohl et al. (1985) and Knell and Tsai (1985) both reported a dependence of SMD on $(1 + 1/\mathrm{AFR})^N$. Pohl et al. determined N to be 0.5 using one nozzle and four slurries, while Knell and Tsai reported values of N between 0.09 and 1.35, depending on the slurry and nozzle used. Data from several other studies also suggest that SMD is proportional to $(1 + 1/\mathrm{AFR})^N$; however, values of N were not stated (Allen et al., 1985; Borio et al., 1984; Cronin et al., 1985; Gillberg et al., 1983; Knell et al., 1983; Smith et al., 1984, 1985; Winters et al., 1985).

Some researchers have investigated the effects of slurry viscosity on SMD (Farthing et al., 1983; Gillberg et al., 1983; Knell and Tsai, 1985; Pohl et al., 1985; Winters et al., 1985). Several investigators reported no consistent effect of slurry viscosity on drop size (Farthing et al., 1983; Knell and Tsai, 1985; Pohl et al., 1985) although Winters et al. (1985) noted a slight increase in spray mean diameter with slurry viscosity and Gillberg et al. (1983) determined that spray mean diameter was dependent on fuel viscosity to the power 0.3, with the viscosity being measured at a strain rate of 450 s^{-1}. In none of the previous studies was a predictive equation quantifying the relationship between slurry SMD, slurry velocity, the relative velocity between the slurry and the airblast air, tank pressure, and slurry rheology presented. For this reason, plus the rising importance of CWS as an alternative fuel, a study was undertaken to determine the effects of these key variables on CWS atomization.

Experimental Apparatus

The effects of relative velocity, air pressure, air-to-fuel mass flow ratio (AFR), and slurry rheology on SMD were investigated using the test facilities shown in Figs. 1 and 2. The main

[1]Current address: Allison Gas Turbine Operations, General Motors Corporation, Indianapolis, IN.

[2]Current address: General Electric Aircraft Engines, Cincinnati, OH.

Contributed by the International Gas Turbine Institute for publication in the JOURNAL OF ENGINEERING FOR GAS TURBINES AND POWER. Manuscript received at ASME Headquarters February 8, 1989.

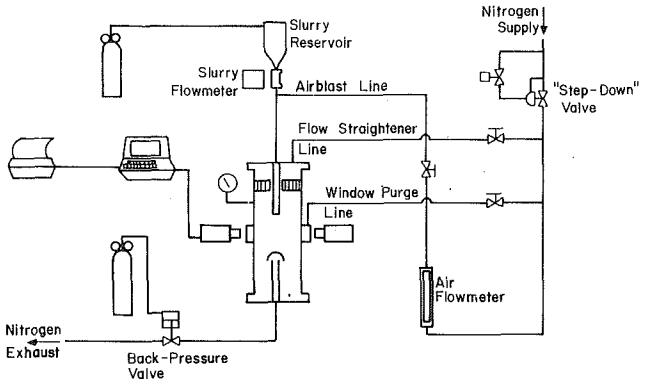

Fig. 1 The experimental facility

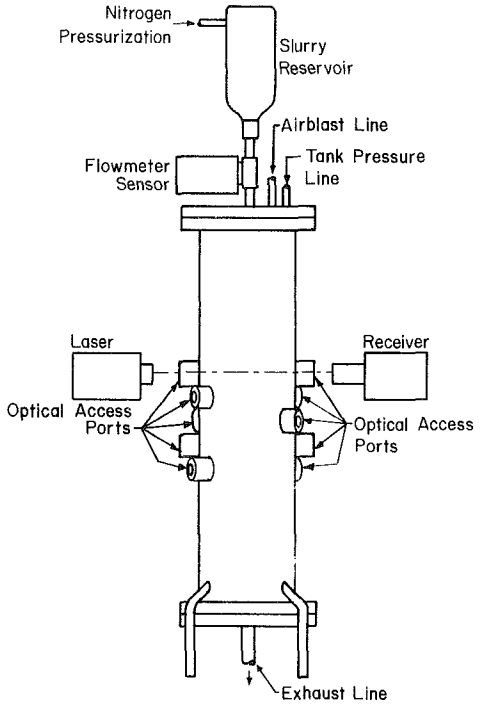

Fig. 2 Atomization pressure vessel

component is a cylindrical pressure vessel, 130 cm tall and 25 cm in diameter, mounted on a stand with its axis in the vertical position. The atomizer under investigation was located centrally at the top of the vessel and sprayed downward. The tank was pressurized to the desired level (between 100 and 2000 kPa) using nitrogen tapped from a large storage/evaporator facility. Drops produced during testing were swept downward by a

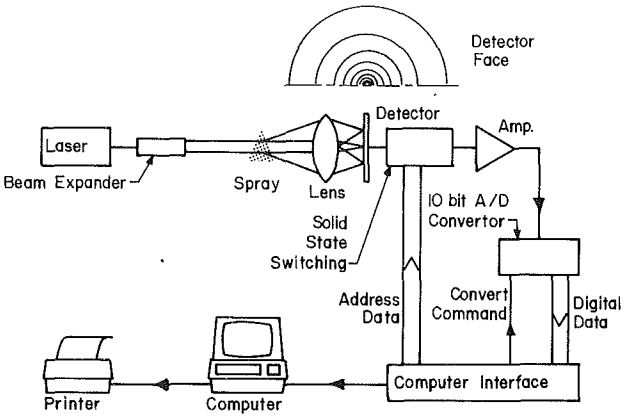

Fig. 3 Malvern 2600 HSD block diagram

flow of nitrogen ($2 < U < 4$ m/s), collected in a chamber at the bottom of the tank, and exhausted. Flow straighteners were positioned in the upper and lower sections of the tank to minimize recirculation of sprayed particles.

The tank is fitted with several pairs of diametrically opposed quartz windows to provide optical access at varying distances downstream of the atomizer. The windows were kept free of spray contamination by a flow of pressurized nitrogen.

Sauter mean diameters and drop size distributions were measured 16 cm downstream of the nozzle using a commercially available Malvern Spray Analyzer, as shown in Fig. 3. The instrument was calibrated using a standard reticle (Hirleman, 1983) and published calibration procedure (Dodge, 1984a). Sauter mean diameter values for this instrument were within 2 percent of the accepted reticle value (Hirleman, 1986).

In nondilute sprays, the data obtained by the drop sizing instrument can be inaccurate due to multiple scattering of the incident laser beam as it traverses the spray. Multiple scattering becomes significant when the spray transmissivity falls below 40 percent. When this occurred, the data were corrected using the empirical relation developed by Dodge (1984b).

The effects of AFR, relative velocity, air pressure, and slurry rheology on spray SMD were determined using the plain-jet airblast nozzle shown in Fig. 4. The nozzle consists of a centrally located slurry delivery tube constructed of 316 stainless steel surrounded by a coaxial annular passage for high-velocity, coflowing air. An exit contraction accelerates the airblast air.

A plain-jet airblast nozzle was chosen for two reasons. First, the dynamics of drop formation and the factors affecting drop size have been exhaustively investigated using plain-jet airblast nozzles and conventional liquid fuels (Lefebvre, 1980). Second, this type of nozzle permits a straightforward determination of the impact of fuel physical properties and airblast parameters on SMD, thus isolating the unique effects of CWS fuels.

Nomenclature

A, B, a, b, c, d, f = constants in SMD equation
AFR = air-to-fuel mass ratio
d_o = diameter of atomizer fuel exit orifice, mm
K = flow consistency index, cP-s^{n-1}
le = log error, error criterion
n = flow behavior index
p_A = air pressure (in Jasuja's equation), Pa
p_T = tank or combustor pressure, Pa
$\Delta p/p_T$ = combustor pressure drop, percent
SMD = Sauter mean diameter, μm
U_A = air velocity (in Jasuja's equation), m/s
U_L = atomizer liquid velocity, m/s
U_R = relative velocity between atomizing air and liquid, m/s
$\dot{\gamma}$ = fluid strain rate, s^{-1}
μ = liquid viscosity (in Jasuja's equation), cP
ρ_A = air density, kg/m^3
ρ_L = liquid density (in Jasuja's equation), g/cm
σ = surface tension (in Jasuja's equation), dyne/cm

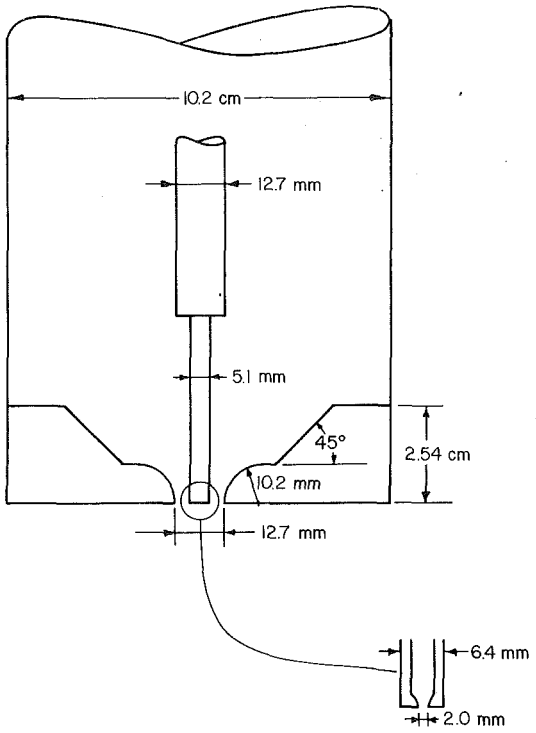

Fig. 4 Plain-jet research atomizer

Slurry was supplied to the nozzle from a reservoir bottle located directly above it. The slurry mass flow rate was controlled by pressurizing its free surface with nitrogen and was monitored using a Micromotion flow meter. Nitrogen mass flow rates were controlled using regulating valves and measured using float-type flow meters.

Results

The experimental operating conditions covered the range typical of a gas turbine combustor: Relative velocity varied from 50 to 160 m/s, nozzle AFR varied from 0.5 to 5, and tank pressure varied from 0.1 to 2.0 MPa. The effect of slurry rheology was investigated through the use of six slurries. The slurries had coal loadings between 50 and 70 percent (by weight) and were rheologically characterized over a wide range of strain rates by their manufacturers. Values of non-Newtonian flow behavior index (n) between 1.05 and 1.67 and of non-Newtonian consistency index (K) between 6.9 and 460 cP-s^{n-1} were provided by the manufacturer when the slurries were purchased. No further rheological characterization was attempted.

Slurry properties are summarized in Table 1, with water properties included for comparison. Rheological data, in the form of n and K, were available for all slurries. However, not all slurries were rheologically characterized at the high strain rates (approximately 10,000 s^{-1}) typical of the nozzle used in this study. Extrapolations from low strain rate behavior were made in the cases where high strain rate data were lacking.

Representative spray data are presented in Figs. 5 through 7. The data of Fig. 5 show the dependence of SMD on AFR and on the relative velocity between the air and fuel exiting the nozzle. These data were obtained using a single slurry and nozzle configuration and, as such, the factor N in the quantity $(1 + 1/\text{AFR})^N$ is a constant. Sauter mean diameter is expected to increase as the quantity $(1 + 1/\text{AFR})$ increases because this reflects a decrease in the air blast momentum and energy available for slurry jet breakup.

The change in relative velocity is related to the air pressure drop across the combustor liner, represented here by the term

Table 1 Coal-water slurry characteristics

Slurry	1*	2*	3*	4*	5*	6**	Water
Coal loading (Weight-percent)	68.0	57.1	55.0	57.4	50.4	70.5	--
Coal top size (μm)	150	35	35	45	35	300	--
Coal mean size (μm)	26.0	14.0	14.0	9.0	14.0	12.5	--
Consistency index (cP-sec^{n-1})	40	45	67	6.9	460	417	1.00
Flow behavior index (dimensionless)	1.67	1.54	1.44	1.20	1.05	1.16	1.00

*Donated by AMAX Extractive Research and Development courtesy of Dr. K. Bahsin, K. Anast, and M. Bergren.

**Donated by Atlantic Research Corp. courtesy of Dr. E. T. McHale.

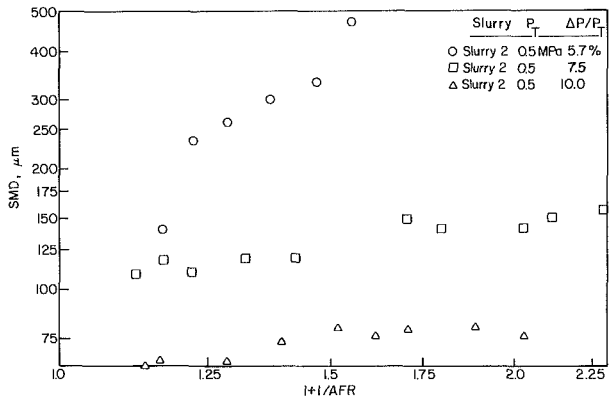

Fig. 5 Sauter mean diameter versus (1 + 1/AFR), showing the effect of air velocity

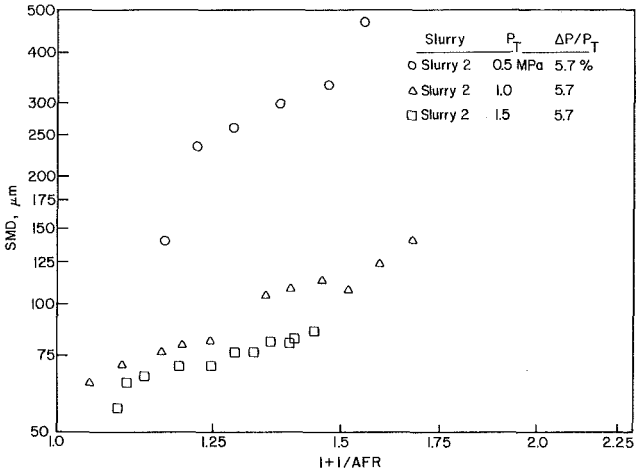

Fig. 6 Sauter mean diameter versus (1 + 1/AFR), showing the effect of pressure

$\Delta p/p_T$. For conventional gas turbines this ratio ranges from 2.5 to 5.0 percent; however, this ratio may need to be increased when burning CWS as evidenced by the improvement in atomization quality at 10 percent $\Delta p/p_T$. Sauter mean diameter is expected to decrease with increasing relative velocity due to an increase in the airblast momentum and energy available for slurry jet breakup.

Figure 6 illustrates the effect of air density, or tank pressure, on SMD. An increase in tank pressure results in an increase in the shear between the air and CWS streams and a decrease in SMD. The test data plotted in Fig. 6 also demonstrate that

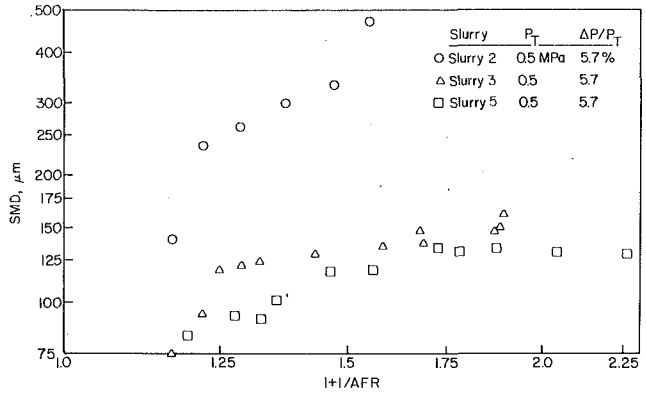

Fig. 7 Sauter mean diameter versus (1 + 1/AFR), showing the effect of slurry type

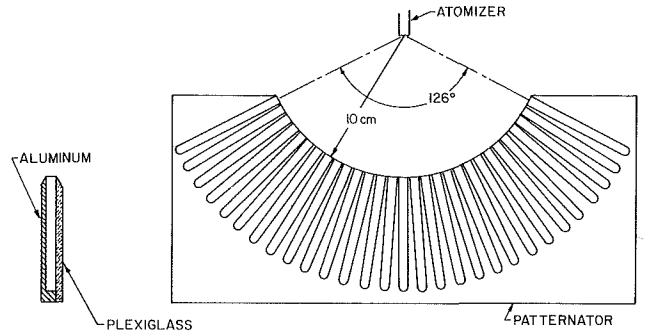

Fig. 8 Patternator schematic

the effect of pressure lessens as the pressure is increased. A 50 percent decrease in SMD was noted as the air pressure increased from 0.5 to 1.0 MPa; when the air pressure was further increased to 1.5 MPa, Sauter mean diameter decreased by only 10 percent.

A comparison of the spray characteristics of slurries having the same coal particle size distribution (slurries 2, 3, and 5) is presented in Fig. 7. Figure 7 shows that SMD increased with coal loading and flow behavior index, but decreased with consistency index.

Mean drop size data for slurries 1, 4, and 6 have been reported in a previous paper (Smith et al., 1984). In that study, it was concluded that the atomization of these slurries was characterized by a decrease in SMD with increases in AFR, tank pressure, and air velocity. It was also clear that the rheology of these slurries had a marked influence on drop size, wholly counteracting the effect of atomizing air parameters in some cases.

The results for all six slurries indicate that the atomization behavior of a particular slurry is strongly influenced by its rheology. Examination of the data for slurries 2, 3, and 5 indicates that the relative drop sizes of different CWS sprays are weakly dependent on coal particle size distribution. Since it is not clear at this time how to model the mechanism through which particle size distribution influences atomization, the data have been analyzed neglecting the effect of particle size distribution and describing slurry rheology in terms of a power law expression. Note that data from all six slurries were included when developing the expression for SMD.

Spray cone angle measurements were made in addition to drop size measurements. Spray cone angle information is in the form of patternation data and presents the mass flux distribution downstream of the nozzle. The impact of AFR on spray cone angle was assessed.

Patternation was measured using the patternator shown in Fig. 8. It consists of a series of cells, or slots, machined in an

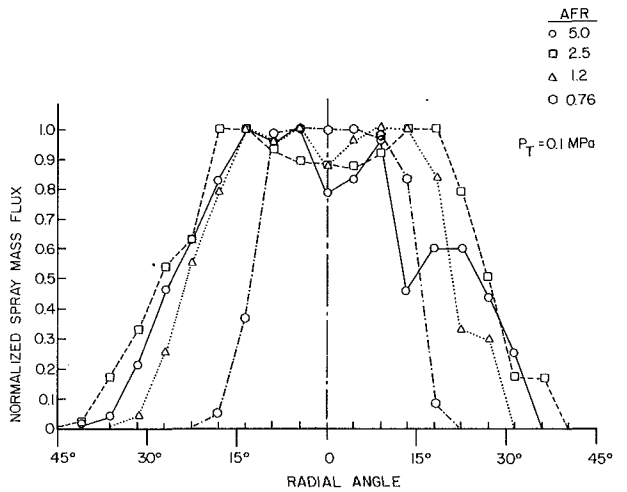

Fig. 9 Radial coal-water slurry mass flux distribution versus air-fuel ratio

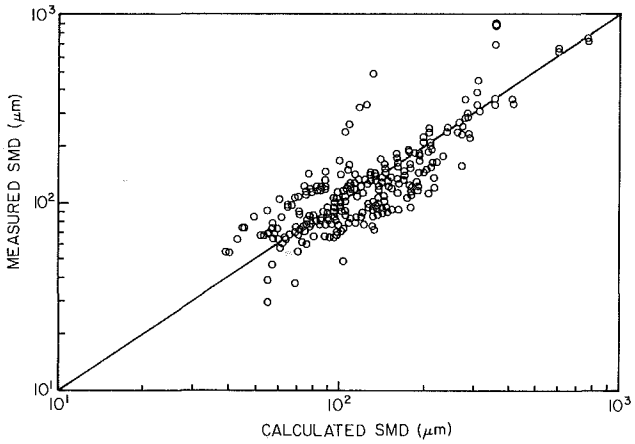

Fig. 10 Comparison of measured Sauter mean diameter to Sauter mean diameter calculated using equation (4)

aluminum plate. The spray nozzle was positioned at the apex of the patternator and sprayed downward into it. The height of fluid in each patternator cell represented the relative spray mass flux at the corresponding radial location. The results are shown in Fig. 9. The spray pattern is largely symmetric and, as would be expected, the mass flux is greatest within about 15 deg of the nozzle centerline. The mass flux falls off rapidly outside this region.

The effect of AFR on mass flux can also be seen in Fig. 9. Little change in fuel distribution occurred when AFR decreased from 5.0 to 2.5. A small decrease in cone angle was observed when AFR decreased further to 1.2. The cone angle decreased by 50 percent when AFR was reduced from 1.2 to 0.75.

These results indicate that the mechanisms controlling patternation are much the same for conventional fuels and CWS. When AFR decreases, less air momentum is available per unit mass of slurry. The cone angle decreases as the mixing of air and fuel becomes less thorough and tangential transport of fuel decreases. It is significant that the CWS mass flux is only slightly affected by AFR when AFR is greater than 1.2.

Analysis

A systematic evaluation of the data from all six slurries indicates that an equation similar to that suggested by Jasuja (1982) will predict CWS SMD. Jasuja studied the plain-jet airblast atomization of petroleum fuels, including residual fuel oil, under the following range of conditions:

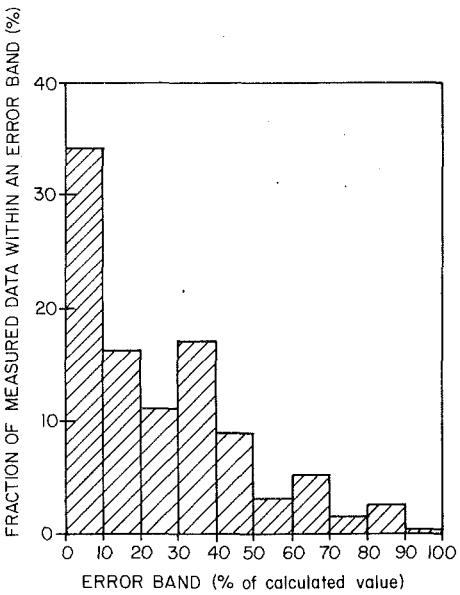

Fig. 11 Error frequency distribution

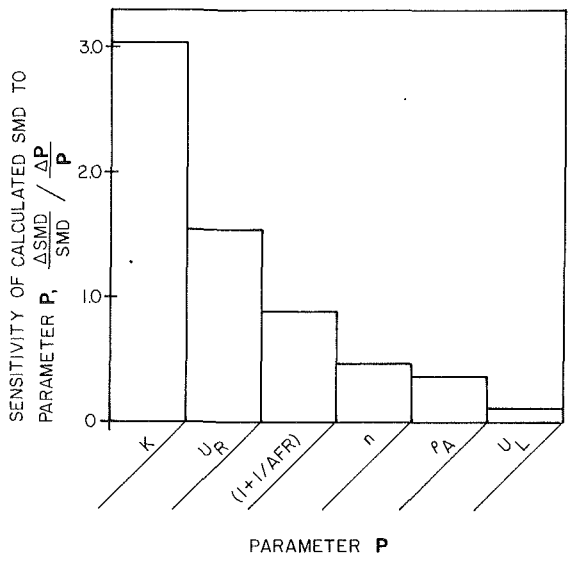

Fig. 12 Sensitivity of calculated Sauter mean diameter to individual parameter variations

Atomizer AFR	$2 < \text{AFR} < 12$
Air velocity (m/s)	$55 < U_A < 150$
Air pressure (MPa)	$0.1 < p_A < 1.4$

The equation developed to relate SMD to liquid physical properties and combustor operating conditions was

$$\text{SMD} = 0.022 \left(\frac{\sigma_L}{U_R^2 \rho_A}\right)^{0.45} \left(1 + \frac{1}{\text{AFR}}\right)^{0.5} + 14.3 \times 10^{-4} \left(\frac{\mu_L}{\sigma_L \rho_L}\right)^{0.4} \left(1 + \frac{1}{\text{AFR}}\right)^{0.8} \quad (2)$$

The dimensions of the parameters are as listed above, with density in units of kg/m^3. Equation (2) was chosen as the basis for this work because the range of viscosities was the greatest of any such relation.

In developing a relationship describing coal-water slurry atomization data, the surface tension and liquid density terms were omitted, as these properties vary little among the CWSs tested here. The viscosity term is replaced with the equivalent power law expression to account for the non-Newtonian rheology of these fluids. (The applicability of power law expressions when describing CWS rheology has been discussed by McHale, 1985, and Smit et al., 1984). Therefore, the form of the equation used to describe CWS SMD data is

$$\text{SMD} = A \frac{\left(1 + \frac{1}{\text{AFR}}\right)^a}{U_R^b \rho_A^c} + B(K(\dot{\gamma})^{n-1})^d \left(1 + \frac{1}{\text{AFR}}\right)^f \quad (3)$$

This expression was fit to the data from all six slurries (a total of 272 points) using a combination of least squares and iterative algorithms. This resulted in

$$\text{SMD} = 2.12 \times 10^6 \frac{\left(1 + \frac{1}{\text{AFR}}\right)^{0.3}}{U_R^2 \rho_A^{0.5}} + 1.08 \times 10^2 \frac{\left(K\left(4\frac{U_L}{d_o}\right)^{n-1}\right)^{2.9}}{U_L^{0.8}} \left(1 + \frac{1}{\text{AFR}}\right)^{2.0}$$

The strain rate is that experienced at the minimum area of the liquid orifice (assuming Poiseuille flow) and was calculated to be

$$\dot{\gamma} = \frac{4U_L}{d_o} \quad (5)$$

The inclusion of the slurry velocity in the second term was found to improve the correlation significantly.

Equation (4) is consistent with the findings of Pohl et al. (1985) and Knell and Tsai (1985), since the dependence of SMD on (1 + 1/AFR) encompasses their results. Equation (4) is also consistent with the findings of Gillberg et al. (1983).

The dimensions of the parameters of equation (4) are the same as for equation (3). The units of consistency index are $(\text{N/m}^2)\text{s}^{n-1}$ and those of strain rate are s^{-1}.

A graph of measured versus theoretical SMD, calculated using equation (4) and data from all six slurries, is presented in Fig. 10. The correlation coefficient is 0.83 and the logarithmic error is 0.24, with the logarithmic error defined as

$$le = \frac{\Sigma(\ln(\text{SMD}_{\text{measured}}) - \ln(\text{SMD}_{\text{calculated}}))}{n} \quad (6)$$

The error frequency distribution (Fig. 11) shows that 50 percent of the data are within 20 percent of the calculated SMD, and 88 percent of data are within 50 percent of the calculated value. Figure 12 shows that CWS SMD is particularly sensitive to rheology, especially the consistency index.

One limitation of equation (4) is the paucity of rheology data from which the power law constants K and n are derived. These data do not always cover the range of strain rates typical of atomization. Also, no account is taken of coal particle size distribution. As noted above, SMD values for slurry 5 are similar to those of slurries 2 and 3, despite differences in rheology. Note that these slurries have the same particle size distribution, which may be a key factor in atomization. Alternatively, these three CWSs could have similar rheological properties at very high strain rates. Both explanations are currently under investigation.

Conclusions

The drop size data demonstrate that coal-water slurry (CWS) spray Sauter mean diameter (SMD) can be predicted from a knowledge of the slurry velocity, the relative velocity between the airblast air and the slurry, the air-to-fuel mass flow ratio (AFR), and the slurry rheology. Slurry rheology is represented

here by a power law expression. For plain-jet airblast atomizers, under the conditions

Flow behavior index	$1.05 < n < 1.67$
Atomizer AFR	$0.5 < \text{AFR} < 5$
Air velocity (m/s)	$50 < U_A < 160$
Air pressure (MPa)	$0.1 < P_A < 2.0$

the expression for SMD is

$$\text{SMD} = 2.12 \times 10^6 \frac{\left(1 + \frac{1}{\text{AFR}}\right)^{0.3}}{U_R^2 \rho_A^{0.5}} + 1.08 \times 10^2 \frac{\left(K\left(4\frac{U_L}{d_o}\right)^{n-1}\right)^{2.9}}{U_L^{0.8}} \left(1 + \frac{1}{\text{AFR}}\right)^{2.0}$$

The cone angle of CWS sprays produced by the plain-jet airblast atomizer was found to be constant above an AFR of 1.2. Below an AFR of 1.2, the cone angle decreased markedly.

The authors would like to express their appreciation to Mr. E. Dunagan for his excellent technical assistance throughout the program, and to Professor A. H. Lefebvre for many helpful discussions and much advice. The authors would also like to thank Chevron (CFS, for fellowship support) and Mobil Research and Development Corp. (PES, for equipment). This work was funded by Dept. of Energy Contract No. DE-AC21-83MC204 through the Morgantown Energy Technology Center.

References

Allen, J. W., Rennie, A. G., and Welbourne, M. C., 1985, "Atomization of Coal Water Mixtures," *Proceedings of the Seventh International Symposium on Coal Slurry Combustion and Technology*, New Orleans, LA, pp. 392–401.

Borio, R. W., Smith, D. A., and Laflesh, R. C., 1984, "Development and Comparative Testing of Commercial Scale Atomizers for Slurry Fuels," *Proceedings of the Sixth International Symposium on Coal Slurry Combustion and Technology*, Orlando, FL.

Cronin, L. J., Sojka, P. E., and Lefebvre, A. H., 1985, "The Effect of Fuel Film Thickness on Coal Water Slurry Atomization," SAE Paper No. 852086.

Dodge, L. G., 1984a, "Calibration of the Malvern Particle Sizer," *Appl. Opt.*, Vol. 23, No. 14, pp. 2415–2419.

Dodge, L. G., 1984b, "Change of Calibration of Diffraction-Based Particle Sizers in Dense Sprays," *Opt. Engr.*, Vol. 23, No. 5, pp. 26–30.

Farmayan, W. F., Walsh, P. M., Teare, J. D., and Beer, J. M., 1984, "Coal-Water Slurry Ignition and Flame Stability: Mechanisms and Effects of Major Input Variables," ASME Paper No. 84-WA/HT-94.

Farthing, G. A., Daley, R. D., and Vecci, S. J., 1983, "EPRI Coal-Water Mixture Evaluation Program," presented at the American Flame Research Committee International Symposium on Combustion Diagnostics, Akron, OH.

Gillberg, L., Larsson, N., Mathiesen, M., Nystrom, O., and Persson, J.-E., 1983, "Some Rheological Data and Atomization Behavior of CWM's Containing 68 to 83% Coal," presented at the Fifth International Symposium on Coal Slurry Combustion and Technology, Tampa, FL.

Hirleman, H. D., 1983, "On Line Calibration Techniques for Laser Diffraction Droplet Sizing Instruments," ASME Paper No. 83-GT-232.

Hirleman, H. D., 1986, private communication.

Jasuja, A. K., 1982, "Plain-Jet Airblast Atomization of Alternative Liquid Petroleum Fuels Under High Ambient Air Pressure Conditions," ASME Paper No. 82-GT-32.

Knell, E. W., Muzio, L. J., and Arand, J. K., 1983, "Combustion Characteristics of Occidental Coal-Water Mixtures," presented at the American Flame Research Committee International Symposium on Combustion Diagnostics, Akron, OH.

Knell, E. W., and Tsai, S. C., 1985, "Rheology and Its Effects on Atomization of Coal Water Slurry," *Proceedings of the Seventh International Symposium on Coal Slurry Combustion and Technology*, New Orleans, LA.

Lefebvre, A. H., 1980, "Airblast Atomization," *Prog. Energy. Comb. Sci.*, Vol. 6, No. 27, pp. 223–261.

McHale, E. T., 1985, "Review of CWF Combustion Technology," *Engr. Prog.*, Vol. 5, No. 1, pp. 15–24.

Pohl, J. H., Sepulveda, J., and Rothfeld, L. B., 1985, "Correlation of the Spray Characteristics of Coal-Water-Fuels," *Proceedings of the Seventh International Symposium on Coal Slurry Combustion and Technology*, New Orleans, LA, pp. 357–376.

Smit, F. J., Anast, K. R., and Bahsin, A. K., 1984, "Properties of Ultra-Clean Coal-Water Slurry Fuels for Direct-Fired Gas Turbines," ASME Paper No. 84-JPGC-GT-5.

Smith, C. F., Sojka, P. E., and Lefebvre, A. H., 1984, "Investigation of Spray Characteristics of Coal Water Slurry Fuels," *Proceedings of the Sixth International Symposium on Coal Slurry Combustion and Technology*, Orlando, FL.

Smith, C. F., Sojka, P. E., and Lefebvre, A. H., 1985, "Plain-Jet Airblast Atomization of Coal Water Slurry Fuels," SAE Paper No. 852085.

Sojka, P. E., and Lefebvre, A. H., 1986, "Investigation of Spray Characteristics of Coal Water Slurry Fuels," Final Report to DOE Contract No. DE-AC21-83MC204.

Winters, P. J., Bailey, R. T., and Olen, K. R., (1985), "The Effect of Fuel Formulation on the Atomization Characteristics of Coal-Water Mixtures," *Proceedings of the Seventh International Symposium on Coal Slurry Combustion and Technology*, New Orleans, LA, pp. 430–439.

A Small Air Turbine Power Plant Fired With Coal in an Atmospheric Fluid Bed

R. W. Foster-Pegg
Independent Consultant,
Cape May, NJ 08204

An efficient, indirectly heated, steam-injected air turbine power or cogeneration plant, fired with coal in an atmospheric fluid bed, is described. The plant will meet all environmental standards and will generate about 35 MW. The plant offers a high power-to-steam ratio without requiring a condensing steam turbine and can operate efficiently without any export steam. Eliminating a condensing steam turbine, cooling tower, etc., reduces the capital cost and produces a low $/kW installation. If necessary, most of the water injected into the air turbine can be recovered from the exhaust air and reused. All the equipment for the plant is commercially available.

Introduction

Because of high capital cost, coal-fired plants are only applicable for base load, and for base load, efficiency is of sufficient importance for gas turbine plants to require some kind of a combined cycle to be competitive.

Vejtasa (1986) gives the specific cost ($/kW) of a combined cycle as twice that of a simple-cycle gas turbine. The power output of the steam turbine of a combined cycle is typically half the power of the gas turbine, from which the specific cost of the steam portion of the combined cycle is found to be four times the specific cost of the simple gas turbine [(2*1.5-1)/0.5 = 4]. A significant reduction in cost of base load gas turbine plants can be made by replacing the high-cost condensing steam turbine system with lower-cost steam injection of the gas turbine.

Steam-Injected Air Turbine Cycle (Fig. 1)

Steam is injected at the outlet of the air compressor. The gas turbine working fluid is 80–90 percent air with 10–20 percent steam and is heated in a heat exchanger, which for simplicity is called an air heater. The coal is burned in a circulating fluid bed of stone at atmospheric pressure and about 1700°F and the air heater is heated by the circulated hot stone. After transferring heat to the air heater, the stone is reheated by recirculating through the coal combustion zone.

To accommodate the additional volume of the steam in the expander of the air turbine, the pressure is raised by a topping compressor driven by a turbine through which the steam passes before injection and blending with the compressed air.

Steam is produced in two boilers, one recovering heat from the exhaust of the coal combustor and the other recovering heat from the exhaust of the air turbine.

The power of the air turbine is increased from 16,230 to 34,560 kW (113 percent) by the steam addition.

A plant for a cogeneration application is shown in Fig. 1. The depicted plant is designed around the Canadian Westinghouse CW 191 gas turbine. Canadian Westinghouse agrees with the estimated performance.

The air turbine compresses 256 lb/sec of air through a pressure ratio of 6.5. The topping compressor raises the pressure of the air leaving the air turbine compressor by a ratio of 1.4. The pressure entering the expander is increased by 20 percent and the pressure ratio of the main gas turbine compressor is reduced by approximately 20 percent, thus reducing the power to drive it.

Steam equal to 15 percent of the airflow (38 lb/sec) is expanded to air heater inlet pressure in a steam turbine producing 6380 kW mechanical, which drives the topping compressor and exhausts to the air heater. The steam then mixes with the compressed air leaving the compressor and passes through the air heater, expander, heat recovery boiler, and stack.

The air and steam are heated to 1450°F in the air heater and expand in the expander of the air turbine from 120 psia to 15 in. of water gage and 753°F. After deducting compressor power and losses, 34,560 kW is output from the generator.

The air heater consists of tubes submerged in hot fluidized stone granules. The stone after transferring heat to the tubes returns to the combustion bed for reheating. The stone is heated to about 1700°F while being suspended and elevated by the combustion gas. The stone is separated from the gas in cyclones and flows by gravity through the air heater. The bed in the air heater is fluidized with fresh air so the tubes are surrounded by strongly oxidizing air.

The gaseous products of combustion separate from the circulating granular stone in the cyclones, and flow through the steam superheater, a boiler, and a combustion air heater. They are cooled to about 250°F. The flue gas passes through a bag filter for particulate removal, is repressured in an inducing fan, and is exhausted through the stack.

Steam is evaporated at 650 psig, 25 lb/sec in the fired boiler and 27 lb/sec in the air turbine heat recovery boiler. All steam is superheated to 900°F in the coal-fired boiler. Steam at 150

Contributed by the International Gas Turbine Institute and presented at the 34th International Gas Turbine and Aeroengine Congress and Exhibition, Toronto, Ontario, Canada, June 4-8, 1989. Manuscript received at ASME Headquarters February 1, 1989. Paper No. 89-GT-216.

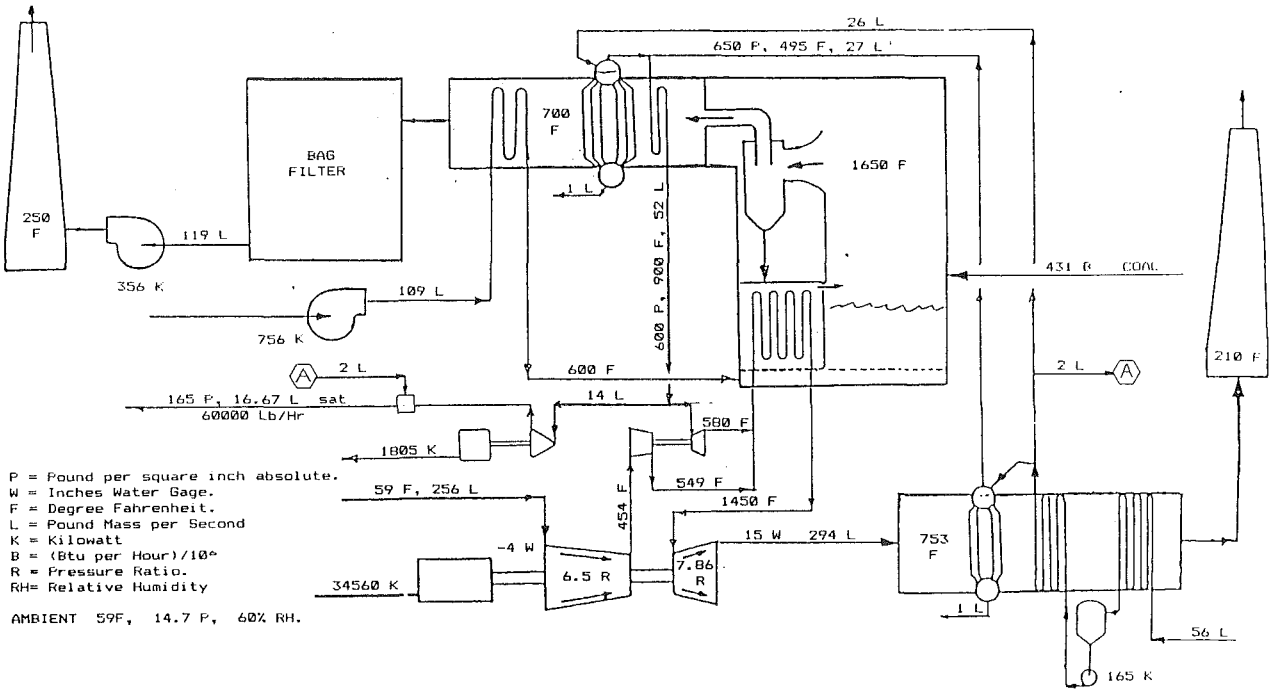

Fig. 1 Schematic of the coal-fired steam-injected air turbine cycle

psig, saturated, is exported for cogeneration and is obtained by expanding 13.8 lb/sec of the 900°F steam from 600 psig to 150 psig in a back pressure turbine generating 1805 kW. This steam is then desuperheated to dry saturated producing 16.67 lb/sec for export.

There are no combustion products in the gas flowing through the air turbine or its heat recovery boiler. The air turbine exhaust is clean air and steam. The heat recovery boiler evaporates 55 percent of the steam and heats all the feed water. Its stack temperature is 210°F. With the makeup water entering at 59°F water will condense on the colder tubes of the economizer. The water leaves the low economizer at about 250°F for deaeration and is afterward pumped to 650 psig before it enters the high economizer.

Coal Combustion System. Before being fed into the combustor, the coal is crushed to minus 0.25 in. and blended with 25 percent minus 0.125 in. limestone ($CaCO_3$) to give a ratio of 3 mol of calcium per mol of sulfur. 90 percent of the sulfur combines with the stone to form calcium sulfate and is removed with the ash. The low and uniform combustion temperature and staged introduction of combustion air produce little NO_x and all regulations to mitigate acid rain are satisfied.

The pressure rise of the forced draft fan is 60 in. water primarily for fluidization. The induced draft fan raises pressure by 20 in. water to provide atmospheric pressure in the combustion chamber where the coal is fed. In the case shown in Fig. 1, 120 percent of chemically correct combustion air is preheated to 600°F in a recuperative heater by the departing flue gas cooling to 250°F.

The stone in the compressed air heater is fluidized at low velocity. The bed in the combustor is fluidized at higher velocity to entrain and elevate the heated stone into the cyclones. The stone then flows by gravity through the air heater bed and back to the combustion chamber for reheating.

A portion of the sulfated stone is drained from the outlet of the air heater and replaced by fresh stone entering with the coal. Thus the captured sulfur is removed as calcium sulfate.

The flue gas passes through a bag house filter for particulate removal before entering the induced draft fan. The combustion system is generally similar to previous proposals (e.g., Foster-Pegg, 1983).

As with any boiler, the areas of the heat transfer surfaces must be proportioned carefully to obtain the required air and steam temperatures and flows. To best capture sulfur in the coal, the temperature in the combustor should be about 1600–1700°F, which determines the temperatures entering the

Nomenclature

air turbine = an open-cycle gas turbine operating on indirectly heated air

equivalent heat rate = [(total heat input)-(heat input for process steam)]/[(total power)+(power needed for process steam)]

expander = component of a gas turbine in which a gas expands to produce power

STIG = Steam Injected Gas Turbine

stone = the mixture of noncombustible particles of limestone (calcium carbonate), sulfated limestone (calcium sulfate), and ash that constitute a fluid bed

Conversions to SI

Pascals = 6895*psi

Degrees Centigrade = (°F−32)/1.8

Joules = 1056*Btu

kg = 0.4536*lb

mm = 25.4*in.

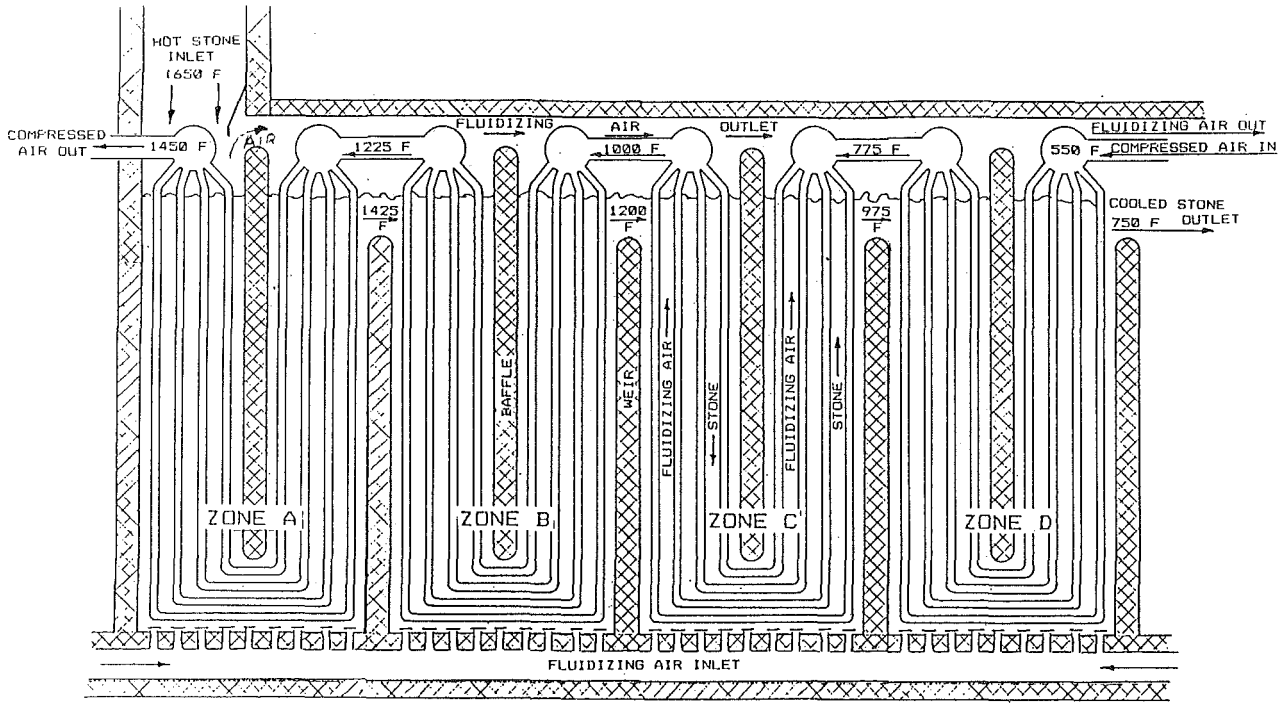

Fig. 2 Schematic arrangement of the fluid bed air heater

boiler and the air heater. In the base case this temperature is 1650°F.

Air Heater (Fig. 2). The compressed air heater is the one component of the air turbine system not found in other familiar power plants. Its design is important because the required high-temperature materials can lead to high cost, and because the high temperatures at which the heat transfer materials must operate combined with the undesirable constituents in coal can cause corrosion if improperly implemented. Therefore means of avoiding these dangers are proposed.

Above approximately 1600°F inlet temperature, the expander of a gas turbine must be cooled, causing some loss of efficiency and some additional cost. At a higher temperature the materials of the heater would be more costly and the areas would be increased, incurring additional cost on both counts. This is unlike a fired turbine in which a hotter combustor is not materially more expensive. Because of the added cost of both expander cooling and hotter air heater an expander inlet temperature requiring expander cooling in an air turbine is probably uneconomical.

Ceramic heaters are being proposed to allow higher temperatures. For the above reasons, and because the temperature of the sulfur capture reaction is limiting, the use of ceramic materials appears constricted for this application.

Thus an air temperature of 1450–1550°F is thought to be the most cost effective.

In the circulating bed air heater, the compressed air is heated from 550°F to 1450°F by stone entering at 1650°F. The stone passes through the heater counterflow to the air at a constant 200°F approach temperature, thus leaving the heater at 950°F. The mass flow rates of the stone and the air are in the same relationship as their specific heats or 0.86 lb of stone for each lb of air. Counterflow is accomplished by a multipass arrangement in which the fluidized stone flows parallel to the air tubes over and under a series of weirs, as shown in Fig. 2.

At each plane in the counterflow path of the air and stone the stone is about 200°F hotter than the air and the tube temperature is about a mean of the temperatures of air and stone. The flow of stone cannot be reduced much below the 0.86 ratio and still achieve the desired air temperature. However, it could be increased at the cost of larger stone separators and higher draft loss.

The higher flow of stone would raise the stone leaving temperature but not the inlet temperature. The tube temperature at the cold end of the heater would be increased and the cold end surface area reduced, but only the least expensive surface would be reduced.

The weirs for the fluidized stone separate the air heat into temperature zones. The most cost-effective tube material would be selected for each temperature range as in a steam boiler and superheater. Temperatures and possible selections of alloys for the tubes in each zone are listed in Table 1. Final selection of the most cost effective alloys must await detailed design and cost analysis of the complete system.

The air heater with circulating solids allows the heat transfer tubes to be constructed into similar banks and be top supported in the bed with feedom to expand.

The separate banks of tubes terminate in headers above the bed surrounded by the fluidizing air leaving the beds. The heat transfer from gas to tube is much lower than from the bed material so the headers will be essentially at the lower temperature of the compressed air inside the headers.

This arrangement facilitates the joining of different alloys and the replacement or temporary plugging of a leaker. The separation of the surface into separate banks by the headers and baffles corresponds with the zones of Table 1.

Avoiding Corrosion of the Air Heater. Previous investigations of fluid bed air turbine and steam cycles are mostly with bubbling beds in which both combustion and heat transfer occur simultaneously.

With bubbling beds corrosion and erosion of the heat transfer surface has occurred frequently in test units. Corrosion would occur in susceptible alloys if the partially oxidized and hence reducing gas existing during the combustion reaction combined with the protective oxide layer on the surface of the particular alloy. When this occurred the protective oxide would be stripped from the surface exposing the base metal, which would then be attacked by sulfur, chlorine, and other

corrosive constituents of coal (Godfrey, 1981; Wright, 1982; Rocazella, 1983; Moskowitz, 1983).

The fluidizing velocity in bubbling beds is relatively high, dictated by the flow of air required for combustion, and has led to erosion of the in-bed tubes. The preponderance of investigations of systems with bubbling combustion beds has associated corrosion and erosion with heat transfer surface in fluid beds.

This situation does not occur with circulating fluid beds because combustion and heat transfer processes are separate. Also the heat transfer bed is essentially free of combustibles and fluidized at low velocity with clean air, ensuring a surplus of oxygen and avoiding reducing conditions. Thus the erosion and corrosion phenomena are eliminated in circulating-type fluid beds.

Even for service in bubbling beds in the presence of combustion, several alloys withstand the conditions. The benefit of the elimination of combustion from the air heater lies in the double assurance of freedom from corrosion and the ability to use less costly alloys and thus in the potential reduction in the cost of the heater.

Air Turbine (Fig. 3). The air turbine in the base case is a Canadian Westinghouse 191 gas turbine with volutes for the compressed air and with the combustors omitted. Other less obvious modifications include changes to the plumbing of the expander rotor cooling air, the rotor shaft sealing, and thrust balance systems.

The blade path and aerodynamics of the normal gas turbine engine are unaltered. The 20 percent higher volume flow resulting from the steam input is accommodated by the topping compressor increasing the pressure at the inlet to the expander. The topping compressor raises the pressure by 40 percent. Four percent is absorbed by pressure losses into and out of the topping compressor, the expander pressure is raised by 20 percent, and the balance of the topping compressor pressure rise reduces the compression ratio of the air turbine compressor.

The power of the expander is increased by 35 percent due to the greater flow and expansion ratio and the power absorbed by the compressor is decreased by 9 percent from the reduced compression ratio. The net power is increased by 113 percent to about 35 MW.

The major stress in a blade is from centrifugal force and the 35 percent increase in power of the expander will increase the combined stress in the blades by about 10 percent.

To accommodate the higher than normal power due to the steam injection, the 191 reduction gear and generator are replaced with the corresponding components designed for the CW 251, which rotates at the same speed and produces more power than the steam-injected 191. The design of other higher-power components of the 251 (like the spool connecting the expander and compressor, the compressor to reduction gear shaft, and bearing) can also be taken from the 251.

Table 1 Air heater data

Air Heater Zone	A	B	C	D
Air at Outlet F	1450	1225	1000	775
Air at Inlet F	1225	1000	775	550
Stone at Inlet F	1650	1425	1200	975
Stone at Outlet F	1425	1200	975	750
Tube at Air Outlet F	1550	1325	1100	875
Tube at Air Inlet F	1325	1100	875	650

Possible Materials

Zone A. Incolloy 800 H, Haynes 188, Inconel 617, Sandvik 253 MA.

Zone B AISI 310, AISI 304 H, Type 405, T 9.

Zone C AISI 304, .25 Mo.

Zone D Carbon

Feed Water Treatment. The feed water will be chemically treated as recommended by the Boiler Manufacturers' Association for the boiler pressure. Oxygen-scavenging chemicals containing sulfur or other constituents that could harm high temperature alloys of the air heater and expander will be avoided. Hydrazine (N_2H_4) is a suitable sulfur-free oxygen scavenger.

The precipitated solids will be discharged by approximately 4 percent blowdown from the steam drums. Carryover of any remaining impurities in droplets will be minimized by droplet separation from the steam using the best available technology.

The steam in the air turbine plant will be at a pressure at which the solubility of silica is small. Also the steam will be above 500°F throughout the steam and air turbine so silica will not be deposited (Hamer, 1960). There is thus no need to remove silica from the injected steam and expensive demineralization of feed water is unnecessary and will be avoided.

The major source of impurities in condensing steam plants is condenser leaks, a source that does not exist in a STIG plant.

Recovery of Injected Steam. At atmospheric pressure the dew point of the mixture of steam and air that constitutes the

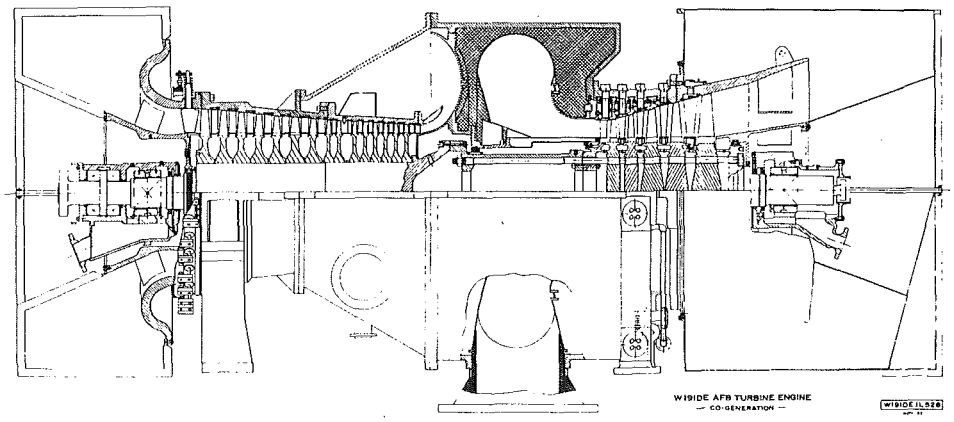

Fig. 3 The CW 191 air turbine

working fluid is about 140°F and steam will condense if the mixture is cooled below this temperature. The exit temperature of the air–steam leaving the heat recovery boiler is 210°F without water recovery. By cooling the exhaust to about 100°F by any of various methods, approximately 70 percent of the injected water can be condensed, recovered, and reused.

With indirect heating of the working fluid, the collected water will not be contaminated in any way.

Operation and Control

This type of plant will normally be base loaded at maximum continuous rating corresponding to the rated outlet temperature of the air heater. The air heater outlet temperature will be automatically controlled by regulating the combustor temperature by the coal and combustion air inputs.

The quantity of steam produced will be adjusted primarily by the over fire air rate. Steam pressure will be uncontrolled and will vary with output.

Most efficient operation at part load will be obtained by closing the compressor inlet guide vanes. This reduces the flows through the equipment while maintaining full temperature.

This mode of control provides faster response to load changes because temperature change and thermal inertia are minimized.

The plant will be started by first firing up the coal combustor using the motor-driven fans and pumps. When the air heater is warmed sufficiently to prevent condensation, steam produced in the convection passes of the fired boiler will be introduced to the topping turbine. The topping compressor will induce air flow through the system and crank the CW 191. With hot air from the air heater the 191 will accelerate and the generator will be synchronized and the breaker closed. The steam-injected air turbine requires no mechanical cranking device.

Prevention of overspeed is by governor-initiated short circuit of the air heater with a trip effected by blow-off of compressed air.

Parametric Performance Studies

The performance calculations assume ISO site conditions of sea level, 59°F, and 60 percent relative humidity. In each study, only one condition is varied while others remain at the base value.

The following thermodynamic quantities of the base case are maintained throughout the parametric studies unless varied for the particular investigation.

Pressure Losses

Total product 0.85

Polytropic Efficiencies

Main compressor	0.86
Topping compressor	0.80
Main expander	0.88
Steam turbine	0.75

Heat Losses

1 percent of exchanger duties

Air Heater Outlet Temperature

1450°F

Air Flow

256 lb/sec

Induced Steam

15 percent of airflow, 38 lb/sec, 137,000 lb/hr.

Coal

Sulfur 2.6 percent, moisture 12 percent, ash 9.7 percent, HHV 11,950 Btu/lb, LHV 11,433 Btu/lb.

Combustion System

Ca/S mol ratio 3.0, unburned carbon 1 percent. Combustion air 120 percent of chemically correct.

Fan Pressures

Forced draft 60 in. water. Induced draft 20 in. water.

Steam

H.P. 600 psig, 900°F. 137,000 lb/hr.
Process, 150 psig, saturated, 60,000 lb/hr.

Heat Rate. Quoted heat rates are "equivalent," and are calculated from heat and power values obtained by deducting the heat input and adding the power output that would be required to produce the process steam in a separate boiler. The efficiency and power requirement per unit of heat of the separate steam boiler are assumed the same as the boiler of the cogeneration plant.

The credits for the 60,000 lb/hr of 150 psi process steam are 69.66 million Btu/hr and 155 kW. Heat rates are quoted first as higher followed by lower in parentheses. The equivalent heat rates of the base case are 10,140 Btu/kWh (9700) and equivalent power is 34,880 kW.

Variation of Combustion Air. Assuming the combustion efficiency would not change, variation of combustion air from 10 to 30 percent excess over chemically correct changes the heat rate by 5 (4.8) Btu/kWh per percentage point change in excess air. Since the lower air would probably increase carbon loss and decrease combustion efficiency, the overall effect of excess air in this range is probably small. An increase in combustion air shifts heat into steam production and can be used for control without an appreciable effect on heat rate.

Variation of Steam Flows. Figures 4, 5, and 6 give the results of this investigation.

Heat rates with different amounts of steam injection and with and without export of 60,000 lb/hr of process steam are compared in Fig. 4.

Export of 60,000 lb/hr of steam improves the heat rate by 1000–1500 Btu/kWh and power is increased by the power of the back pressure steam turbine exhausting to process by 1800 kW.

Total production of steam must be at least 10 percent for effective recovery of heat exhausted from the air turbine and boiler and best efficiency.

The base export of steam is about 5 percent of airflow requiring injection of about the same amount for the lowest heat rate of 9600 (9185) Btu/kWh. Injection of less steam gives a higher heat rate because surplus heat must then be discarded.

With cogeneration, injecting more than 5 percent steam requires burning additional coal and increases heat rate somewhat. Each percent steam injection in excess of the best heat rate increases heat rate by about 47 (45) Btu/kWh.

Without cogeneration, heat rate is almost constant at 11,400 Btu/kWh above 10 percent steam injection.

Each 1 percent of airflow of added injection steam increases the generator output by about 8.5 percent as seen in Fig. 5.

Eighty-five percent of the increase in power of the air turbine as a result of steam injection is due to increased output of the expander, and 15 percent is due to a reduction in compressor power absorption. The power of the expander is increased by the added masss flow of steam and the increased pressure ratio required to pass the added flow. The power absorbed by the main compressor is decreased because the topping compressor reduces the outlet pressure of the main compressor. These relationships are shown in Fig. 5.

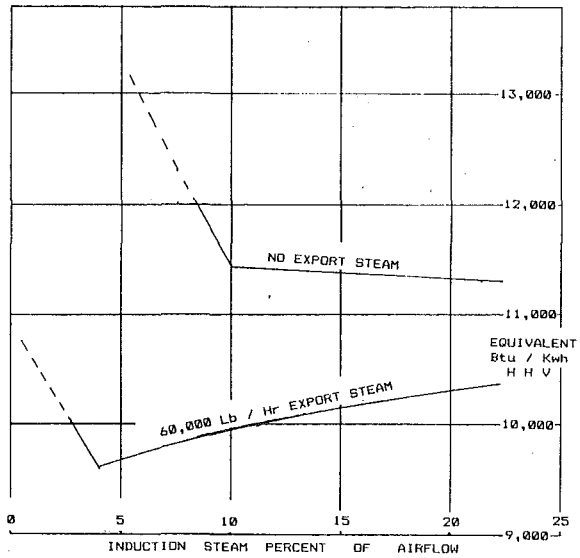

Fig. 4 System heat rate versus percent injected steam

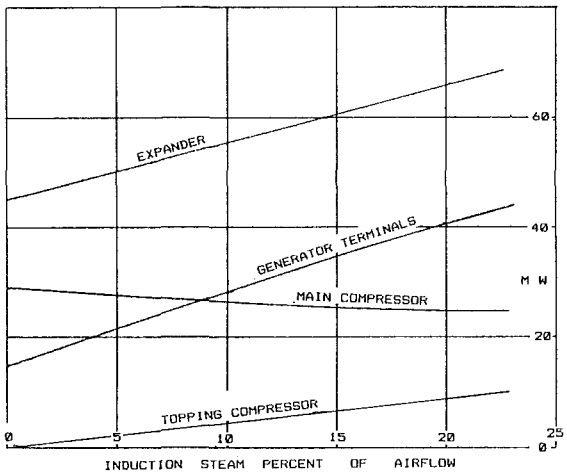

Fig. 5 Powers versus percent injected steam

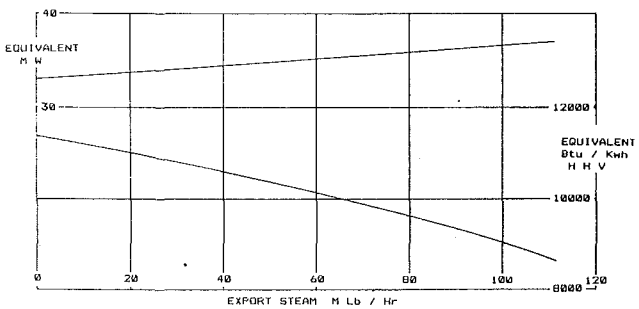

Fig. 6 Equivalent power and heat rate versus exported steam

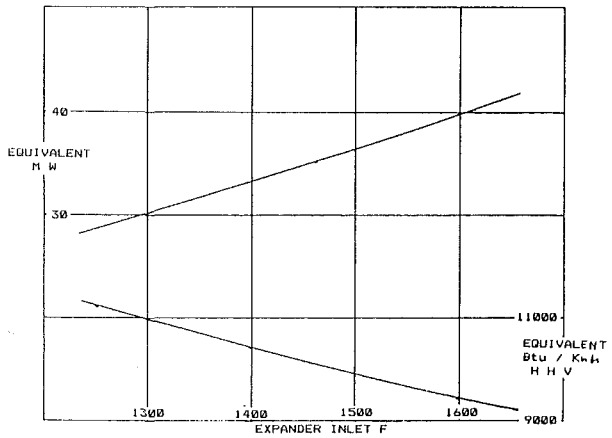

Fig. 7 Equivalent power and heat rate versus expander inlet temperature

The effect of varying export steam with injection steam constant at the basic 15 percent of airflow is shown in Fig. 6. Heat rate improves and power increases as export is increased because of the high thermodynamic efficiency of the back pressure expansion process.

Variation of Expander Inlet Temperature. The effect of different expander inlet-air heater outlet temperatures on performance is illustrated in Fig. 7.

Each degree Fahrenheit increase of expander inlet temperature reduces heat rate by about 5 (4.8) Btu/kWh and increases power by about 0.3 percent.

Available materials for the air heater have the potential of uprating to 1500°F after experience has been gained at the conservative 1450°F initial temperature.

Current Position of the Concept

The proposed power plant—while novel—includes only technology that has been tested.

The beneficial novelty in the proposal is the combination of coal firing, indirect heating, and steam injection of a gas (air) turbine, expected to offer more economical small power generation in the right circumstances.

Indirect heating has been used with *closed*-cycle gas turbines for decades (Bammert, 1983) and recently with fluid bed heating (Stambler, 1987). The air heater for an open cycle is intrinsically an easier technical exercise than for closed cycles because of the lower pressures in open cycles. The thinner pressure parts allowed by the lower pressures reduce thermal stresses and facilitate provision for thermal expansion.

Steam injection is "old hat." An extensively H_2O injected gas turbine operated in 1906 (Brown-Boveri, 1939). The gas turbine was designed by Armengaud and Lemale and it was the first gas turbine to achieve sustained operation.

Steam injection has been used commercially for many years (Bultzo, 1969) and recently has been applied more extensively receiving wide attention in technical literature (Brown and Cohn, 1981; Messerlie and Strother, 1984; Pequot, 1987; Soroka et al., 1987).

Potential problems with combustion arising from the high proportion of steam are avoided by indirect heating. Blending of the injected steam with the air is simplified by passage through the air heater compared to internal combustion.

The separation of the steam-laden air from combustion of fuel avoids potential corrosion should condensation of combustion products occur. Mixing the injected steam with only clean air allows recapture of the water (Laar et al., 1988) without contamination with combustion products.

A detailed cost comparison of a steam-injected air turbine, and its main competitor, an all-steam plant, is necessary for a proper assessment of the concept and is presently not available. Back-of-the-envelope type cost comparisons suggest that the air turbine may have a worthwhile economic advantage arising from a combination of better efficiency and lower capital cost.

A credible conclusion with respect to the merits of the proposed system requires parallel detailed design and cost estimates of air and steam turbine systems.

References

Bammert, K., 1983, "Twenty-Five Years of Operating Experience With the Coal-Fired, Closed-Cycle Gas Turbine Cogeneration Plant at Coburg," ASME JOURNAL OF ENGINEERING FOR POWER, Vol. 105, pp. 806–815.

Brown, D. H., and Cohn, A., 1981, "An Evaluation of Steam Injected Combustion Turbine Systems," ASME JOURNAL OF ENGINEERING FOR POWER, Vol. 103, pp. 13–19.

Brown-Boveri, 1939, Review, Asea Brown Boveri, Baden, Switzerland, June.

Bultzo, C., 1969, "Steam Injection: A Source of Incremental Power," ASME Paper No. 69-GT-68.

Foster-Pegg, R. W., and Davis, J. S., 1983, "A Coal Fired Air Turbine Cogeneration System," ASME Paper No. 83-GT-181.

Godfrey, T. G., and DeVan, J. H., 1981, "Corrosion of High Temperature Materials in AFBC Environments, Part 2 (4500 hr Tests)," Oak Ridge National Laboratory, TM-7734/P2, Aug.

Hamer, P., 1960, "Present Day Feed Water Treatment for High-Pressure Boilers," *Proc. IMechE*, Vol. 174, No. 1, 1960.

Laar, J. A., Wendorf, A. W., Cohn, A., Esposito, N. T., and Foster-Pegg, R. W., 1988, "Site Assessment of STIG and Combined Cycle Plants," ASME Paper 88-JPGC-Pwr-21.

Messerlie, R. L., and Strother, J. R., 1984, "Integration of the Brayton and Rankine Cycle to Maximize Gas Turbine Performance, a Cogeneration Option," ASME Paper No. 84-GT-52.

Moskowitz, S., Mullen, J., and Vanderlinden, S., 1983, "A Coal Fired Gas Turbine Using an Air Cooled Fluidized Bed Combustor," ASME Paper No. 83-GT-165.

Pequot, 1987, "Water Injection Can Add 50 Percent to Gas Turbine Power," *Gas Turbine World*, Pequot Publishing Inc., Fairfield, CT, May–June.

Rocazella, M. A., Wright, I. G., and Holt, C. F., 1983, "The Corrosive Environment in the Fluidized-Bed Heat-Exchanger for CCGT Service," ASME Paper No. 83-GT-249.

Soroka, G., and Kamali, K., 1987, "Modular Remotely Operated, Fully Steam-Injected Plant for Utility Application," presented at the ASME Joint Power Generation Conference.

Stambler, I., 1987, "Closed Cycle Plant With AFB Design Nears Full Load Test," *Gas Turbine World*, Pequot Publishing Inc., Fairfield, CT, Sept.–Oct.

Vejtasa, S., 1986, *Technical Assessment Guide, Vol. 1. Electricity Supply*, P-4463-SR, Electric Power Research Institute, Box 10412, Palo Alto, CA.

Wright, I. G., and Minchener, A. J., 1983, "Materials Selection for Metallic Heat Exchangers in Advanced Coal-Fired Heaters," ASME JOURNAL OF ENGINEERING FOR POWER, Vol. 105, pp. 446–451.

The Performance of a Compact Oil-Designed Utility Boiler When Firing Coal-Water Fuel

D. M. Rankin
New Brunswick Power,
Fredericton, New Brunswick, Canada

H. Whaley

P. J. Read
Energy Mines and Resources Canada,
Ottawa, Canada

D. J. Burnett
MBB Mechanical Services Ltd.,
Dartmouth, N.S., Canada

The Canadian coal-water fuel technology development program has been in progress since 1980. This phase of the work is the final stage in the demonstration of practicability of burning coal-water fuel in a boiler designed to burn oil. Early tests in small coal-capable front-wall and tangentially fired utility boilers have shown that two of the major problems to be addressed are both burner related: atomizer durability and poor carbon conversion performance. The present paper describes tests that were conducted in a 20 MWe compact, oil-designed boiler. Five burners were modified to burn coal-water fuel and oil with minimum changeover time. No changes were made to the boiler heat transfer tubes or to the flat furnace bottom to facilitate ash removal. The addition of a fabric filter bag house to contain fly ash emissions is the subject of another paper at this conference. The performance of the unit on coal-water fuel and oil is compared and evidence given that the derating was not as severe as had been predicted. The commercial burner supplied did show some atomizer wear, part of which could be attributed to manufacturing deficiences. It is suggested that the performance of this small unit should be applicable to larger units in the 100 MWe range.

Introduction

The use of coal to replace imported oil is a goal of the Canadian Energy Policy. This replacement has been inhibited by the inconvenience of handling solid fuel and by its environmental implications. The current state of world oil prices is likely to delay the commercial implementation of new coal combustion technologies. It is however, worthwhile to bring coal-water fuels (CWF) and their use to a state of commercial readiness, so that, if economic or environmental reasons demand, these technologies can be implemented quickly. A program of development and commercialization of fuels made from mixtures of coal and liquids, with the objective of easy, economic handling and minimized environmental impact, has therefore formed an integral part of Canada's energy strategy the last ten years.

Until satisfactory combustion of coal-water fuel has been demonstrated at a large enough scale, utilities and industries that might use coal-water fuel are generally not in a position to switch. With this in mind the first major demonstration was initiated in 1982 to demonstrate the preparation and combustion of coal-water fuel in two utility boilers at Chatham, New Brunswick, which were originally designed to burn coal (see NB Power, 1985). The results of this first demonstration have prompted the continuation of the program with the testing of burners and the demonstration of coal-water fuel in a 20 MWe compact, oil-designed utility boiler.

Contributed by the Fuels and Combustion Technologies Division and presented at the Joint ASME/IEEE Power Generation Conference, Miami Beach, Florida, October 4-8, 1987. Manuscript received at ASME Headquarters July 9, 1987. Paper No. 87-JPGC-FACT-1.

The 20 MWe boilers at the Maritime Electric Co. Ltd. (MECL) Generating Station in Charlottetown, PEI, are not in regular use and their compact nature is a challenge to the new fuel, which will indicate its potential for most other units designed to burn oil. These boilers are an appropriate size for the demonstration and the modification necessary will be beneficial to the station's future operation.

A collaborative agreement was signed among Energy Mines and Resources Canada (EMR), New Brunswick Power (NB Power), Cape Breton Development Corporation (CBDC), and Maritime Electric Company Limited (MECL) to convert a 20 MW oil-fired utility boiler to burn coal-water fuel and to assess the performance and economics of the conversion. Under the agreement, EMR provides financial and technical support for the production of coal-water fuel and the conversion and demonstration of the fuel in the MECL boiler. CBDC supplies coal-water fuel from its preparation plant in Sydney, Nova Scotia. NB Power provides technical support based on its experience during the burning of about 6000 tons of coal-water fuel in the Chatham, New Brunswick boilers. MECL provides the utility boiler plant and support facilities for the demonstration.

The main objectives of this program are:

1 to manufacture, transport, handle, and burn a substantial quantity of coal-water fuel.

2 to evaluate the minimum maintainable derating when firing coal-water fuel under normal operating conditions in an oil-designed utility boiler.

3 to evaluate the performance of a fabric filter when firing coal-water fuel and oil in combination and separately.

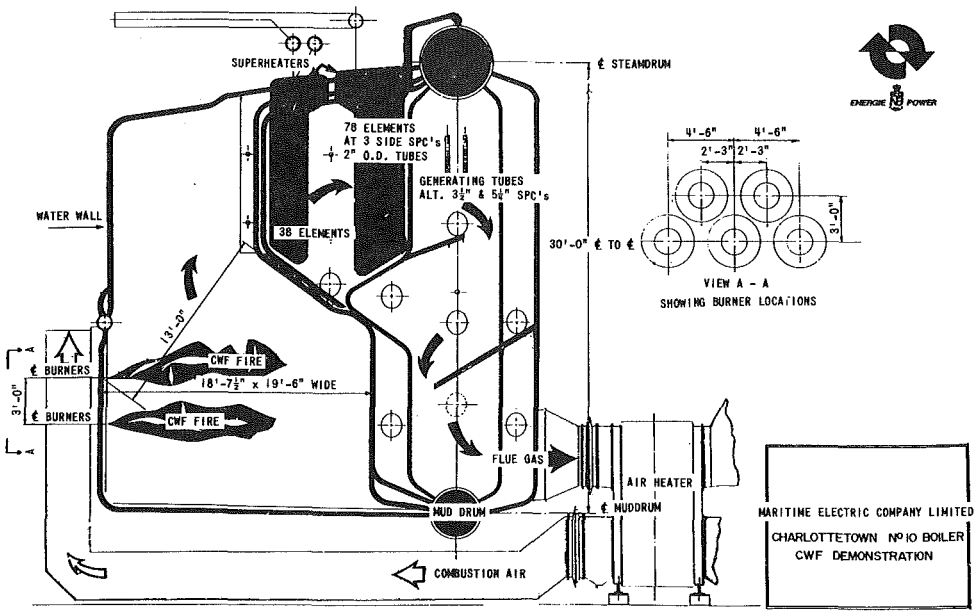

Fig. 1

4 to upgrade the storage capacity and control systems at the CBDC coal-water fuel preparation plant.

Part of the program included the development of fuel specifications designed to insure the consistency of fuel supplied to the project and a basis of checking the quality of fuel upon receipt.

One of the first tasks undertaken was the installation of additional storage capacity at the fuel preparation plant, as well as additional instrumentation and controls, which were designed to improve the quality and consistency of fuel. Two new storage tanks with a total capacity of approximately 1000 tons were installed. After manufacture the fuel was stored in these tanks to provide a buffer between the supply and variable demand. When the project required, the fuel was loaded into clean road tankers and trucked about 600 km to Charlottetown, PEI, where the fuel was off loaded either into a 200 ton day tank or into rail cars, which were set up to serve as temporary storage.

An evaluation of alterntaive methods of transportation of the fuel showed road tankers to be the most convenient and economical method of transporting the fuel from Sydney, NS, to Charlottetown, PEI.

From previous work it was learned that it is extremely important that the fuel be blended to ensure a homogeneous mixture. Therefore the 200 ton day tank at the MECL plant included a mixer for blending the various loads of fuel as part of its equipment.

The fuel is supplied by variable-speed, progressive cavity pumps, through a strainer to the burner front header. Selection of an appropriate strainer proved to be critical to satisfactory operations. Air-operated diaphragm pumps are used to unload the road tankers and to transfer the fuel from the rail car storage to the day tank.

Boiler

The Charlottetown #10 boiler is a Babcock Wilcox, two drum boiler of Stirling design. The furnace is integral with an exit screen, followed by a secondary and primray superheaters. The flue gas enters the steam-generating bank and finally exits into a regenerative air heater. The unit is bottom supported. Five burners fire through the front wall in two horizontal rows. Ignition is by propane gas. It should be noted that the secondary superheater has a sideways clear spacing of 25 mm and the gas entering this area is expected to be in the region of 980°C. As the boiler was originally of pressurized design, an induced draft fan was added to convert the boiler to balanced draft.

The Charlottetown #10 boiler has most of the features of an oil-fired boiler that make it extremely difficult to burn pulverized coal. As may be noted in Fig. 1, the furnace volume is small: approximately 100 m^3. The bottom is nearly flat with no facilities for ash removal. The screen tubes are very close (4 m) to the throat of the upper burners and have very narrow (25 mm) spacing between them. No changes were made to the tubes or to the furnace shape for the purposes of the demonstration.

Modifications were made to fuel delivery system to the boiler to allow easy alternation of #6 oil and coal-water fuel. The burners were changed but no alteration was made to the burner port diameter or wind box. Two soot blowers were added in front of the screen tubes. Viewing ports were added on the side and front walls of the furnace to give visual access to the flames, furnace bottom, and water walls. A fabric filter system was also installed to remove particulates from the flue gas, as there was no means of flue gas cleanup on the original installation. At the burner front, the piping arrangement has been modified to include supplies of flushing water, atomizing steam for oil, atomizing steam for coal-water fuel, #6 bunker oil, coal-water fuel, and propane for ignition.

As originally installed, the boiler controls were designed for manual operation. For the CWF demonstration automatic controls were installed for both oil and coal-water fuel burner operation as well as for the fabric filter. The adjustment of the electronic control system has proved to be very time consuming and caused a considerable number of trips. All systems are now operating properly.

Burners

During previous work, it was noted that there is a drastic difference between operating a burner on coal-water fuel in a test furnace and operating that same burner in a utility boiler. Criteria were therefore established that a burner manufacturer must demonstrate a burner of the same size using the same fuel in a manner that represents conditions typical of the Charlottetown boiler.

As a result, three suppliers were selected to have their pro-

totype burners tested and witnessed. From these tests the Coen burner designed by Coen Burners Inc. of Burningham, CA, was chosen. Five burners to provide a capacity of 20 MWe were purchased from Coen Canada Ltd. Montreal. These burners have fixed vanes to control the primary combustion air swirl and adjustable vanes to control the swirl of the secondary combustion air. The amount of combustion air as well as the proportion of primary to secondary combustion air is controllable within limits. The burners are set well into the furnace wall to allow the refractory quarl to provide radiant heat for flame stabilization. Ignition is by propane igniters (capacity about 1 GJ/h).

A burner developed by EMR, Canada, in collaboration with the National Research Council, has proved to be quite versatile in that it can operate on either coal-water fuel or #6 fuel oil. At the early stages of the Charlottetown project this burner was not commercially available. Since that time, however, arrangements have been made to manufacture the burners and efforts are now underway to install a complement of the EMR Burners.

Initially one burner will be installed, to operate along with four of the Coen Burners. After proving systems associated with one burner, plans are to proceed immediately with a full conversion to the EMR Burners.

Environmental

As the Charlottetown thermal plant is situated in a scenic downtown location, sulfur oxide and particulate emission are of prime concern. Steps have therefore been taken to select equipment and institute operating procedures and concepts that will contain these emissions.

A six-module fabric filter dust collector has been installed at Charlottetown. Five modules are required for full load operation while a spare is available for cleaning or maintenance. The ash is removed by screw conveyers to enclosed bins. These bins are then taken to an approved site for disposal of the ash.

Observations—Boiler

At the time of writing the following observations can be made. These may not be indicative of the conclusions drawn at the completion of the demonstration.

Normal practice is to bring the boiler to operating condition (at least 5 MWe) using oil, then switch to coal-water fuel. The switch is made by changing burner guns. Once the switch has been made and the fire stabilized (usually 15 to 20 min) the igniters can be removed.

The initial Coen burners provide good quality atomization with a ratio of fuel to atomizing steam between 4:1 and 5:1. With proper adjustment the fire is bush shaped, very stable with no sparklers. Good carbon burnout has been achieved. Analysis of the ash shows about 50 percent carbon when the average ash content of the fuel is 1.8 percent (see Table 1).

Although the burners have worked quite well, the nozzle wear rates appeared initially to be intolerably high. Design changes made by the manufacturer have not yet been evaluated in the long term.

The furnace bottom is flat and covered by refractory with embedded water tubes. Any ash or unburned fuel that is not entrained in the combustion gases falls to the bottom of the furnace. After firing about 2400 tonnes of fuel with 1.8 percent ash the total accumulation of ash on the furnace bottom is less than 1 tonne, the balance being entrained with the flue gas and collected by the fabric filter.

Table 1 Typical data (preliminary)

	CWF	#6 oil
Electrical load	18.5-19.5 MWe	20 MWe
CWF flow	10,404 kg/h	5705 kg/h
Fuel pressure	1379 kPa	910 kPa
Atomizing steam pressure	1586 kPa	1117 kPa
CWF temperature	19°C	90°C
Windbox pressure	279 mm	229 mm
Furnace pressure	−12.7 mm	−12.7 mm
Flue gas O_2	1.4 percent	1.03 percent
Combustion air temperature	221°C	213°C
Carbon conversion	>98 percent	>99 percent

No slagging or fouling has been observed in the boiler. A small quantity of slag built up on uncooled refractory where the flame impinged as the result of a poorly aligned or partially blocked fuel nozzle.

Soot blowing has been on a regular basis at least every 12 hours, not to maintain heat transfer, but rather to avoid plugging of the dust collector ash system. The flyash, when sampled, was found to have a bulk density of about 400 kg/m^3 (less than half that of the comparable pulverized coal flyash).

Inspection of the boiler in early March 1987 showed no signs of erosion on the boiler tubes. Some small deposits of light fluffy ash were found in corners of the boiler and on some of the tubes. The air heater baskets were clean.

The performance fabric filter was described in another paper at this conference (see Read et al., 1987b).

Conclusion

Fuel has been transported by tanker truck and burned without difficulty.

The storage and control systems at the CBDC fuel processing plant have ben upgraded and are now operational.

The fabric filter has worked well in containing particulate emissions from the Charlottetown plant.

Based on the results to date, it is concluded that coal-water fuel technology can be applied to many boilers designed to burn oil with far less derating penalty than originally predicted (Read et al., 1987a; Rankin, 1986).

References

New Brunswick Electric Power Commission, 1985, "Coal-Water Fuel Pilot Production Plant and Burner Development," Report No. 1, June.

Rankin, D. M., Read, P. J., and Whaley, H., 1986, "Coal-Water Fuel Test at Maritime Electric Company Limited's Charlottetown Plant," Energy Technology Conference, Mar.

Read, P. J., Whaley, H., and Rankin, D. M., 1987a, "Performance of an Electric Utility Boiler Designed for Oil But Burning Coal-Water Fuel," Third European Conference Coal Liquid Mixtures, Sept.

Read, P. J., Rankin, D. M., Thanish, M. R., and Whaley, H., 1987b, "Fabric Filter Performance During Combustion of Coal-Water Fuel for Electric Power Generation," 10th Annual Energy Source Technology Conference and Exhibition.

Indianapolis Resource Recovery Facility: Community Efforts and Techology Required for a Successful Project

P. L. Stevens
Director,
Indianapolis Department of Public Works,
Indianapolis, IN 46204

J. S. Henderson
Staff Power Engineer,
CRS Sirrine, Inc.
Research Triangle Park, NC 27709

R. Tulli
Project Manager,
Ogden Martin Systems of Indianapolis,
Fairfield, NJ 07607

There are many community needs. Refuse is an abundant byproduct of our civilization. The disposal of this byproduct has become a major problem for our cities. This paper describes one community's efforts to turn a community problem, refuse disposal, into a community asset. The paper describes the many aspects of effort and technology required to develop the Indianapolis Resource Recovery Facility. This facility required the cooperation of the public and private sectors to blend technology into a successful project. Special efforts were required to match appropriate technology to specific community needs and produce a successful and economically sound project. Five basic activities are presented. The first four activities are essential steps for any community to assure the right project fit to community needs. The areas presented are: (1) defining community needs, (2) technology evaluation (approaches evaluated), (3) feasibility studies (economic studies), (4) project implementation (bids and contracts), and (5) a description of the Indianapolis Resource Recovery facility. A review of these five areas places a real world perspective on refuse as an alternative fuel and source of resource recovery.

Background

The City of Indianapolis. Indianapolis is a capital city, the state's largest city, and the 14th largest in the nation. In 1970 Indianapolis became one of the first cities in the nation to establish a consolidated form of city government. The marriage resulted by combining most of the City and Marion County functions and sharing the same boundaries.

Changing National Laws. The 1972 Water Pollution Control Act and the 1976 Resources Conservation and Recovery Act each contributed to the need for a resource recovery facility. In 1972, in response to the Water Act, planning started on upgrading the two City wastewater treatment plants. The planning quickly revealed the need to dispose of approximately 1000 tons-sludge-cake/day. In response to the Recovery Act, the City's 15 landfills were coming under increasingly strict operating rules. Considering the sludge quantities the strict rules, and the Recovery Act led community leaders to question the future of landfilling.

Task Force. In 1976 Mayor Hudnut established a Solid Waste Task Force to find a workable, long-range solution for sludge and solid waste disposal. The Task Force consisted of representatives from key community groups: technical, business, utility, City-County councilors, and citizens' groups. The Task Force reviewed the extensive technical information available on solid waste disposal, including incineration. Facilities in both the U.S. and Europe were reviewed. The evaluation process, the findings, the economics, the selection process, and the final facility overview are presented in this paper. Figure 1 pictures the final Indianapolis Resource Recovery Facility (IRRF).

Contributed by the Fuels and Combustion Technologies Division and presented at the Joint ASME/IEEE Power Generation Conference, Miami Beach, Florida, October 4–8, 1987. Manuscript received at ASME Headquarters June 30, 1987. Paper No. 87-JPGC-FACT-3.

Technology and Community Interests Merged

Community interest focused on a number of issues:

Siting. Prior to the 1985 request for proposals (RFP), well-organized and vocal opposition developed against the four possible locations for the landfill site. The new landfill was to receive bypass wastes for the IRRF. Results: *No* environmentally acceptable site existed within the county. Therefore, a resources recovery facility must be located in a less sensitive area and sized to reduce by passed quantities and dependence on landfills. The wastewater treatment plant property was selected as a candidate. Figure 2 documents the relationship of the proposed IRRF to the surrounding city. The site possessed a number of distinct advantages:

- Area used for industry and commerce
- General area has few homes and no homes within 1/2 mile
- The only remaining landfill within one mile

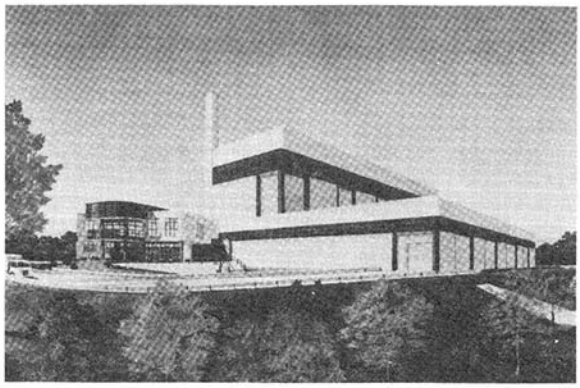

Fig. 1 Overview of the Indianapolis Resource Recovery Facility

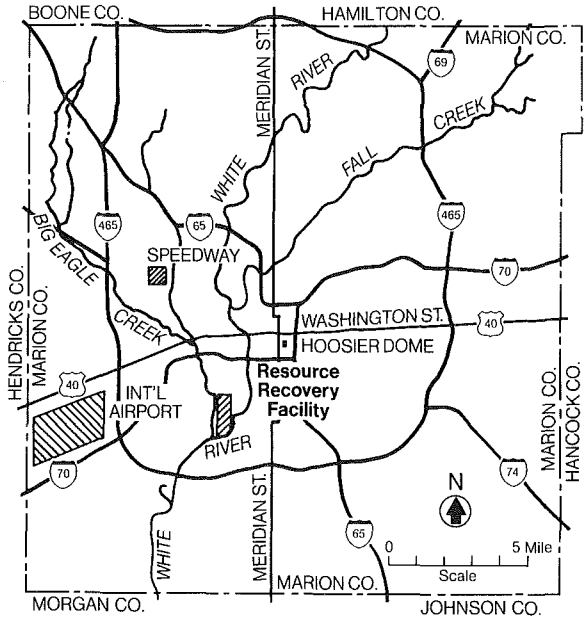

Fig. 2 Area map of Indianapolis Resource Recovery Facility

Figure 3A
Primary Selection

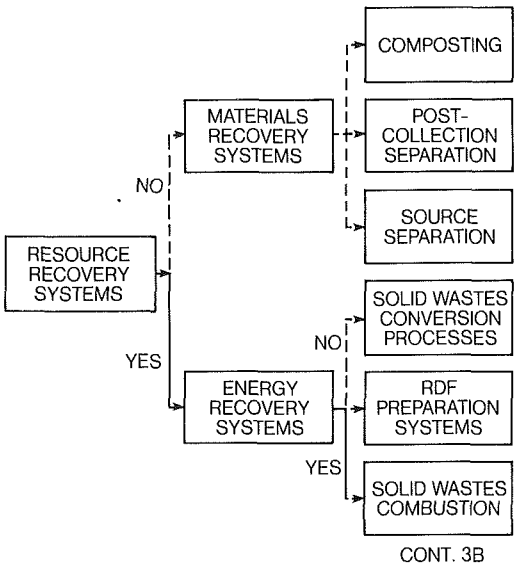

Figure 3B
Secondary Selection

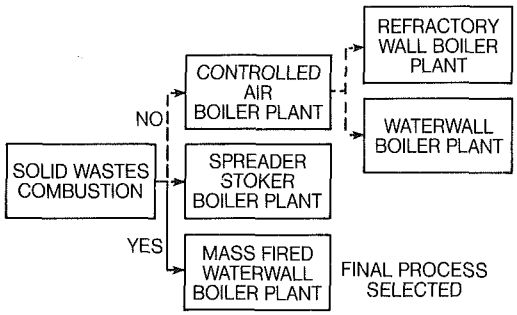

Fig. 3 Task force technology selection studies

- Small change to existing refuse truck traffic
- Site is a former landfill

Air Quality Control. The environmental task group focused on a broad range of issues, especially on dioxins. Several workshop sessions were dedicated specifically to the issue. Studies focused on information from EPA, other plants, and the Swedish government. These efforts lead to critical input in the request for proposals (RFP) and project performance requirements.

Community Relationships and Inputs. To assure project responsiveness to citizen concerns, key task force committees were established. Each committee contributed the following:

- Environmental: Performance criteria in operating agreement (gas temperature 1800°F + /2 s)
- Private haulers: Industrial and commercial pickups early hours; integral, tipping floor transfer station to avoid driver detour and alternate destination
- Legal: City/vendor risk allocation table in RFP (request for proposal)
- Financial: Established RFP financial requirements; review vendor finances
- Citizens: Long-term committee to monitor implementation and operation

Community Education. One final, but crucial link was completed during 1984 and 1985: community education. The Department of Public Works drew from the critical information developed by the task force to present the Resource Indianapolis Recovery Facility story. Approximately 50 talks, slide shows, and videotape displays encouraged community confidence and support. Interested citizens were reached in church groups, service clubs, political clubs, and Chamber of Commerce committees.

Task Force and Technology Evaluation

Many Alternatives Considered. The Indianapolis Solid Waste Task Force assumed complete responsibility for technology evaluation. The Task Force mission concentrated on selecting the optimum process based on:

- Successful commercial operation
- Greatest on-line reliability
- Capability to burn waste sludge

Figure 3(A) presents the selection route for the primary processes, and Fig. 3(B) presents the secondary selection process. The review process encompassed a two-year span and included a number of activities, such as:

- Manufacturer presentations: all types of equipment
- On-site inspections: of technology in the U.S. and key European facilities
- All types of equipment were included.

Table 1 Task force technology decisions

Technology Options	Decision
Energy Recovery vs. Materials Recovery	*The Technology Selected Must Have:* • A Proven Operational Record, • Be Economically Feasible And • Reduce The Dependency On Landfills The Three Materials Recovery Systems Studied; Composting, Post-Collection Separation And Source Separation, Each Depend To A Greater Extent On Landfilling (30 to 60% Reduction) Than Energy Recovery. Markets For Recycled Materials And Composted MSW Are Spotty And Revenues Are Less Than For The Sale Of Energy.
Solid Waste Combustion vs. RDF Preparation And Conversion Processes	RDF Preparation Systems Studied; Wet Pulping And RDF Processes Both Relied Upon A Series Of Mechanical Processes Each Of Which Lowered The Overall Reliability Of The Entire System. RDF Systems Have Since Shown To Be Dangerous. Solid Waste Conversion Processes Were Relatively New Technologies With No Proven Operating Record. In General Those Processes Have Proven Not To Be Effective On MSW.
Mass Fired Water Wall vs. Spreader Stoker And Controlled Air Boilers	Spreader Stokers Can Operate On Either RDF/Coal Mix Or All RDF. Some Type Of Front End MSW Preparation Is Required And These Plants Had No Proven Operational Record. Controlled Air Boilers Depend On Starved Air Conditions With Auxiliary Fuel Fired Afterburners. Units Available Were Of Small Capacity (150 TPD) And Had No Long Term Operational Record.
Mass Fired Water Wall Boilers	Were Ultimately Selected Because Of The System's Demonstrated Durability And Long Term Record Of Worldwide Success In Commercial Operation.

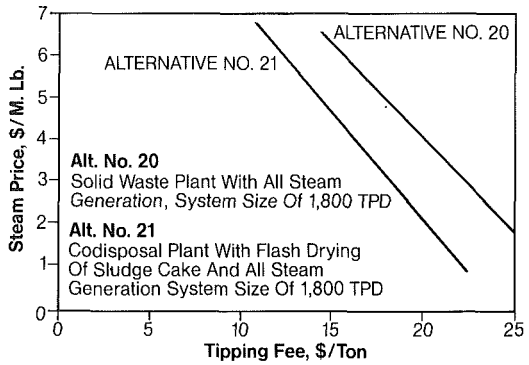

Fig. 4 Comparison of tipping fees with steam price, 1980

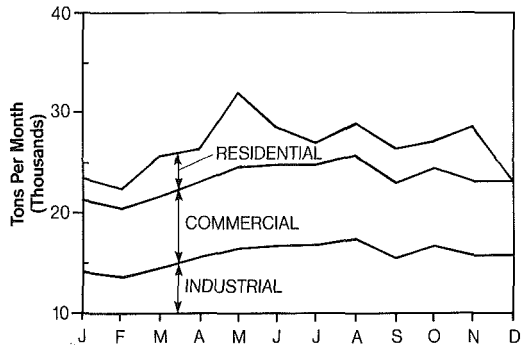

Fig. 5 Breakdown of monthly solid waste generation, 1984

Task Force. The task force was composed of a diverse group of prominent community leaders and citizen groups. Table 1 outlines the criteria used as the basis of technology selection. Their 1979 findings stood the challenge. During the next five years the findings served the community well during project implementation.

Task Force Results and a ReStart

First Results (1981). After adding support from several experts, the first task force results were published in 1981:

- The annual solid waste quantity averages 1800 tons per day (TPD) with 4500 Btu per lb.
- The facility should consist of three 600 TPD boilers with the capacity for drying wet sludge cake.
- The plant should generate only steam for sale to the downtown district steam loop, operated by Indianapolis Power and Light (IPL).
- The City should develop its own 200 acre landfill for waste in excess of 1800 TPD.
- The plant will be constructed through a full service vendor to design, construct, and operate. Financing should be through industrial revenue bonds with the vendor taking a 25 percent equity interest.
- The City should continue to evaluate alternate sludge drying technologies, including indirect steam dryers.
- Resulting tipping fee prices are highly dependent upon sale price of steam. See Fig. 4 for comparison of tipping fees with steam price.

Restart. An RFP was issued in 1981 and three vendors were short listed. However, conflicts developed with the EPA over funding of sludge disposal costs. Indiana's Pioneer Energy Bill caused rethinking of the proposed IRRF project. In 1984 the task force findings were updated to include cogeneration under the new legislation and new waste quantity and composition studies:

- The low electricity sale price of $0.025/kWh (1984 dollars) makes cogeneration not cost effective.
- Compared to an all-landfill option, resource recovery with steam production will be more cost effective around the year 2000. Estimated landfill fees were priced at the $17+ range for the year 2008.
- Waste quantities increased slightly and equaled the national average in composition. Figure 5 presents the monthly breakdown.

As the Department of Public Works revised the RFP and developed the 200 acre landfill recommendation, strong public opposition to the landfill developed. Clearly public opinion favored an enlarged IRRF and minimal dependence on a landfill. At the same time the DPW conducted a successful pilot test on an indirect steam-heated sludge dryer. The conclusion was reached not to use flue gas drying. The indirect dryer produced sludge with an average moisture of 10 to 15 percent. The required IRRF sludge burning capacity was reduced to 60 TPD. In 1984 the RFP was reissued with the proposed plant configured with:

- Storage, pit with 5 day retention at 1800 TPD and stack flues for four boilers
- Three boilers in the initial procurement
- Total plant capacity (with no sludge), 2175 TPD at 5200 Btu/lb, and 2362 TPD at 4500 Btu/lb

The addition of this data allowed the final selection process to continue with issuing of the RFP, evaluation of proposals, and selecting the final full service vendor for the IRRF.

Final Selection Process

Relationships. Defining the City's needs and acceptable technology made up the key first step. The key second step becomes getting the IRRF facility constructed. A number of very important factors separate the IRRF from a typical private industry, capital project. For example, when XYZ Company needs a new plant, decision are made not only within a single enterprise unit, but also within a single sector of enterprise. To achieve the IRRF, decisions and cooperation spanned three sectors of enterprise: public (City of Indianapolis), private developer (Ogden Martin Systems of In-

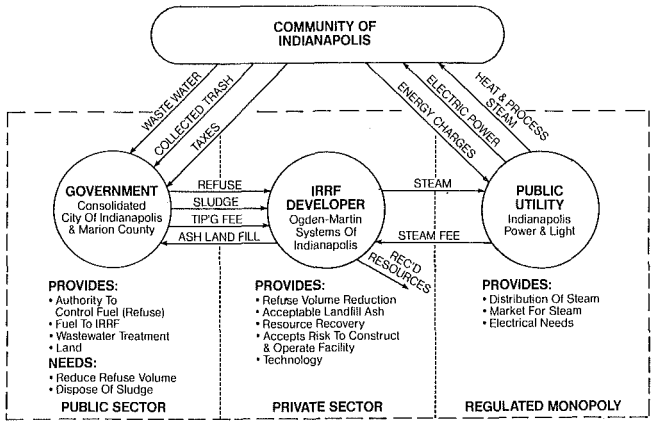

Fig. 6 Relationship diagram

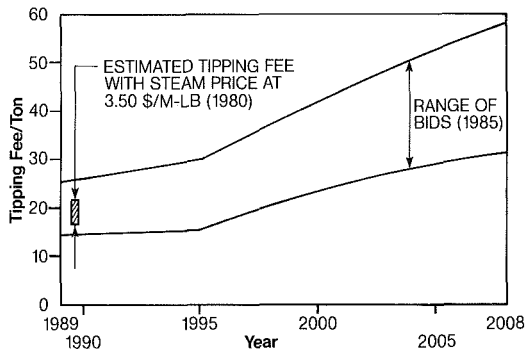

Fig. 7 Financial model confirmed: 1980 estimate versus bids 1985

dianapolis, OMSI), and a regulated monopoly (Indianapolis Power and Light, IPL). In effect the fuel (the refuse) is public; the operator and technology supplier is private (OMSI); and the steam distributor is a regulated public utility (IPL). A number of relationships and activities have and must take place between these three entities. Figure 6 illustrates the relationships between the three sectors of enterprise.

Selection Criteria. The interests of the City extend beyond technology in selecting the "Full Service" supplier and operator of the IRRF. The final selection process began with a RFQ (request for qualifications) in Nov. 1984. From the initial screening of 11 submittals, four qualified suppliers were selected to receive the RFP (request for proposals). For proposal evaluation, the task force established four pivotal areas for evaluation: technical, financial, management/legal, and environmental. A system was then developed for evaluation of each proposal on a common criteria. A Task Force subcommittee was assigned to each area. Table 2 summarizes the selection criterion developed and used by each subcommittee for evaluation. The task force established the division of group weight between the four areas, as technical. The total of the group weights adds up to one (1.0). The selection criteria for each area were developed by each subcommittee and assigned a weight from zero to one. The criteria weight multiplied by the group weight results in the overall weight assigned to each specific criteria. The far right column (Table 2) reflects these values as a percentage. Based on the comprehensive evaluation of the Task Force, Ogden Martin Systems of Indianapolis (OMSI) was selected to be the full service supplier for the IRRF. As part of the IRRF team, OMSI had submitted and the Task Force accepted CRS Sirrine (Research Triangle Park, N.C.) as the engineering design consultant and J. A. Jones (Charlotte, NC) as the general contractor.

Table 2 Resource recovery steering committee selection criteria

Group	Criteria	Group Weight	Criteria Weight	Overall Weight
TECHNICAL		0.20		
	Design			
	Solid Waste		.50	10.0%
	Sludge		.20	4.0%
	Residue		.10	2.0%
	History Of Operation Of Similar Plants			
	Design/Build		.10	2.0%
	Operate		.10	2.0%
FINANCIAL		0.44		
	Life Cycle Disposal Fees For Guaranteed Throughput		0.77	33.9%
	Life Cycle Disposal Fees For Excess Waste Quantities		0.09	4.0%
	Sensitivity To Changing Economic Assumptions		0.14	6.2%
MANAGEMENT/ LEGAL		0.16		
	Risk		0.29	4.6%
	Management Concepts		0.15	2.4%
	Management Plan For Construction		0.138	2.2%
	Management Policies		0.122	2.0%
	Operating Personnel		0.10	1.6%
	Design And Engineering Personnel		0.12	2.0%
	Residue Marketing		0.08	1.3%
ENVIRONMENTAL		0.20		
	Combustion Parameters		0.20	4.0%
	Particulate Control Equipment Sizing		0.20	4.0%
	Acid Gas Control Equipment Sizing		0.22	4.4%
	Wastewater Quantities And Strengths		0.09	1.8%
	Safety Provisions		0.09	1.8%
	Reduction Of Landfill Requirements		0.14	2.8%
	Aesthetics		0.06	1.2%

Financial Model Confirmed. With a 3.50 $/M-lb steam price, Fig. 4 illustrated a tipping fee range of 17 to 21.50 $/ton, in 1980 dollars. With zero for inflation, the low bid 1989 tipping fee (startup year) is well below the 1980 projected range of tipping fees. Figure 7 compares the 1980 projected tipping fee with the bid tipping fees. The bids were submitted in 1985.

Contracts

Overview. As illustrated in the relationship diagram (Fig. 6), many complex activities exist between the three "sector" partners. Contracts become the legal mechanisms to facilitate the IRRF operations. The Service Agreement binds the City and Ogden Martin Systems of Indianapolis (OMSI), and the Steam Service Agreement binds OMSI to IPL. The following discussion highlights the contract ingredients that enable the IRRF to function.

Service Agreement. In simple terms the developer, OMSI, agrees to provide equity, build, and operate (for 20 years) the IRRF, for a service fee. The City agrees to provide a lease for the site, refuse, and loan the proceeds from bond sales to finance a portion of the facility. The long-term nature of the Agreement focuses on six major areas: facility construction, facility operation, City's landfill, service fees, and schedules (related to functional details, not calendar time).

Facility Construction. This section details topics as progress monitoring, facility price ($83.8 million), easements to and from site (provided by City), facility acceptance (and testing), and risk sharing. One of the factors contributing to lower capital cost of the IRRF is risk sharing. The City–contractor (OMSI) relationship allocated risk on a "best qualified" basis, as the right-of-way risk. Table 3 presents the City/OMSI risk sharing arrangement.

Facility Operations. One of the most obvious and *most* critical items is outlined. The City commits to deliver acceptable wastes. A main contributing factor underlying a successful IRRF is: The City *does* control the disposal location for solid wastes generated within the county and has the authority to *cause* the refuse to be delivered to the IRRF. This is a distinct *advantage* of the combined, *consolidated form of government.*

Other Major Areas. Areas covered by the agreement in-

Table 3 Risk allocation table

Risk Category	Risk Area	City	Contractor
Capital Cost	Project Delay		X
	Construction Cost Overrun		X
	Post Construction Remedies To Achieve Operational Performance		X
	New Pollution Equipment Required By New Legislation	X	
	Sludge Drying	X	
	Bond Interest Rate	X	
	Steam Line Easement	X	
O&M Costs	Low Solid Waste Quantities Due To Overestimating	X	
	No/Low Solid Waste From Strike	X	X
	Sludge Drying Facility		X
	Guarantee Of Plant Capacity And Energy Performance		X
	Plant Down Time In Excess Of Guaranteed Amount		X
	Hazardous Waste	X	X
	Work Stoppage Or Slowdown At Facility		X
	Utilities		X
	Failure To Operate In Compliance With Existing Laws		X
Energy Income	Changes In Waste Composition And Heating Value	X	X
	Overestimating Of Energy Recovery		X
Disposal Fee Income	Minimum Waste Quantity	X	
	Prevent Waste Diversion To Other Disposal Site	X	
Energy Market	Withdrawal Of Energy Customer After Start Of Operation	X	X
Ash	Disposal In Acceptable Landfill	X	X
Bypass Waste	Disposal Of Waste In Excess Of Plant Capacity	X	X
Uncontrollable Circumstance	Unforeseen Event	X	X
Tax Law Change	Before Contract Signing	X	
	After Contract Signing		X

clude: startup operations and testing, operation of facility, service coordinator, facility safety and maintenance, wastes delivered on a spot basis, and visitors and inspections.

Landfill. This section details procedures for handling toxic wastes delivered to the facility and access to city landfill.

Service Fee. The details of the service fee are detailed. The form of the service fee formula is: Service Fee = Debt Service + O&M Charge + Pass Thru − Recovered Resources Credit.

Schedules. The "schedules," all 23 sections, contain the many and very necessary details supporting the agreement. Each schedule deals with a particular topic such as: facility technical specifications, performance guarantees, and maximum allowed utility consumptions (natural gas, water, electricity). The facility process guarantees are based on a fuel value of 4,500 Btu/lb-refuse and two process time periods: 15,710 tons-refuse-/7-days or 718,300 tons-refuse/year.

Steam Purchase Agreement. The agreement is between OMSI and IPL and required the approval of the Public Service Commission. The document encompasses some 28 articles. A few of the nonlegal, focal point items will be discussed.

Operating Committee Key Link. The IRRF and the Perry K plant (of IPL) are physically connected via a new 8600 ft export steam line plus the IPL steam distribution network. It is in the best interest of all to allow *fast* response and close cooperation between the two facilities. An Operating Committee with a small number of representatives performs this task. The committee implements the procedures for dispatching the project steam.

Operating Numbers. Several benchmark numbers are referenced:

- Standard steam unit: Defined as "Standard M-lb" and is equal to steam with a heat content of 1294 Btu/lb-steam.

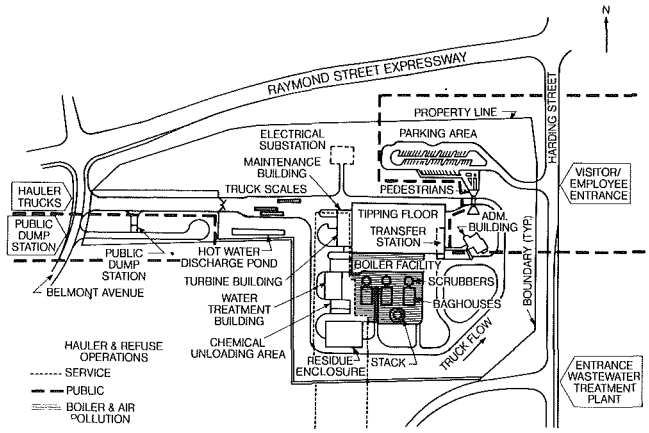

Fig. 8 Access and uses separated

- Minimum steam to IPL during November to March: 134,400 M-lb/month.
- IPL maximum down time (cannot accept steam): 570 hours/year.

Steam Sales Rates. Three rates exist:

- Primary rate for steam to heating district: set at $3.50/Mlb-steam (1985 dollars) for first 2,400,000 M-lb and $2.87/M-lb thereafter.
- Secondary rate for steam in excess of district demand and delivered to the Perry K turbines: This rate is $0.78/M-lb-steam (1985 dollars).

Indianapolis Resource Recovery Facility

Highlights and Task Force Input

Overview. Three areas deserve special emphasis: (1) facility interface with traffic access and uses, (2) plant description and the future provisions, and (3) visitors' welcome.

Traffic Use and Interface. Four groups require noninterfering access:

- Hauler trucks (and refuse operations)
- Visitors and employees (with parking)
- Recovered resources pickup & service
- Public spot trash disposal

Physical separation of these access needs allows for smooth functions. *Figure 8* illustrates the arrangement and separation zones for each access or use. This type of arrangement places the boiler in the center or at the "hub" of operations.

Hauler Traffic. In a typical 8-hour day, 500 truck deliveries occur. Three computerized scales facilitate truck weight in and out. Truck traffic enters on the plant west side, passes through the scales, circulates counterclockwise, unloads in the tipping area (directly into the pit), and exits through the scale on the west.

Public Separated From Truck Traffic. Public access for either the public dumping station or visitors (and employees) is physically separated from the intense "hauler" traffic. The public dump facility has a separate entrance/exit from the hauler traffic (plant west side). The visitor/administrative area is located to the northeast. Visitor parking is outside the truck loop, and the administrative building is inside the loop, connected by an underpass. In this way visitor/employee access is physically separated from truck traffic and operations.

Service Area. This area consists of plant maintenance, contained chemical delivery area (for water treatment plant), and resource recovery area (contained within the residue enclosure).

Plant Description and the Future. Figure 9 presents an

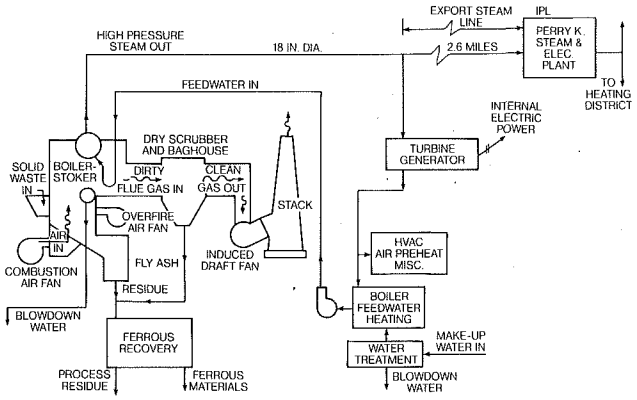

Fig. 9 Simplified proces flow diagram

Table 4 IRRF basic configuration

Facility Item	No. Or Units	Value
BOILERS, EACH		
- Number Of Units	No.	3
- Refuse Capacity (4500 Btu/lb)	TPD	600
- Sludge (Co-Fired With Above)	TPD	33
- Steam Output 510 psig & 71 deg	M-lb/hr	163
REFUSE CRANE, CAPACITY	2@ Tons/Lift	13.5 Ea.
ASH SYSTEM	TYPE	
- Bottom Ash	Main, Vibrating Emer'y, Belt	
- Fly Ash	Screw To Discharger	
- Transfer To Residue Building	Belt Following Grizzly	
- Distribution Within Building	Vibrating	
FLUE GAS CLEANING		
- Gas Absorption	Dry Scrubber With Limestone	
- Particulate	Bag House	
STACK	Ht. X O.S. Dia., Ft.	290 X 30
- Type	Steel Outer & Inner Shell	
- Height, Ft.		

overview of the process. Basic refuse is consumed in the boilers, and steam is produced for export (to IPL). The turbine generator serves two basic internal needs. The high-pressure steam passes through the turbine generator to produce electric power (for internal use, not sale). After passing through the turbine generator the steam is used to heat boiler feedwater. Table 4 summarizes the basic plant configuration and data for the IRRF.

Environmental Controls. Air emissions are controlled directly. Wastewater streams receive pretreatment before discharge to the City waste treatment plant. Air emission control equipment and function consists of:

- Negative pressure tipping building: unloading dust odors contained and incinerated in furnace.
- Furnace high-temperature combustion controls: destruction of organic gases within flue gas.
- Dry scrubber with lime injection: collection of flue gases, such as sulfur dioxide.
- Baghouse fabric filter: flue gas particulate collection.
- Paved access roads and covered conveyors: minimize fugitive dust.

Wastewater pretreatment systems consist of:

- Neutralization: for dealkalizer (boiler water) plant.
- Grit chamber: for suspended solids removal, and grit from floor drains.
- Containment area: for storm water runoff in outside equipment areas.
- Hot water discharge pond: cooling deaerator overflow.

Future Perspective. A number of provisions have been made to allow for a future IRRF expansion. Table 5 outlines the key components that have been added to allow a smooth expansion in the future.

Table 5 Future provisions

Facility Item	Future Provisions
Refuse Pit	Constructed For Fourth Boiler
Site	Space Allocated For Fourth Boiler
Auxiliary	Ash System, Deaerator, & Feedwater Pumps Sized For Fourth Boiler
Stack	Fourth Boiler Flue Installed
Export Steam Line	Sized For Fourth Boiler
Residue Enclosure	Arranged For Future Expansion
Sludge System	Storage Bin & Transport System Installed
Internal Transfer Station	Provides Transition Facility To Fourth Boiler Start-Up

Easy Access for Visitors. Because of the community relationship to and identity with the IRRF, public interface and ease of access are important. The following accommodations insure these requirements:

- Visitor/employee parking lot with a capacity for fifty cars and four buses.
- Access to the administrative building via a pedestrian tunnel leading through a landscaped and planted area

Administrative Building. The floor level arrangement accommodates visitors without interfering with plant operations:

Floor Level	Function	Facilities
First	Employee activities	Employees entrance, change facilities, building mechanical
Second	Visitors	Reception, conference with audiovisual
Third	Administrative and cafeteria	Offices, food cafeteria service, facility overlook

Plant Access. Unusual provisions provide for visitor access to the plant interior:

- Covered walk between administrative building and boiler building.
- Clear ground floor access isle at grade to passenger elevator to central control room and firing floor.
- Firing isle floor area improvements including finished concrete floor at boiler front and grate area coordinated to allow visitor inspection.

These efforts reflect an Ogden concern for good citizenship and concern for public communications.

Summary

The focus of this paper has been to highlight the community efforts of Indianapolis to assess the community need for refuse disposal and to apply the most appropriate technology to City needs. Environmentally acceptable disposal of community refuse presents a continuing problem to every community. The successful completion of the Indianapolis Resource Recovery Facility relies on the following critical steps:

1 The changing laws on energy, environmental control, and conservation must be continually evaluated during project planning.

2 Early recognition of the refuse disposal problem and decreasing landfill space avoided crisis circumstances. Early recognition allowed important citizen inputs, technology assessment, and sound economic planning for the project.

3 Seeking broad and informed community input through the working Task Force allowed:

- Detailed evaluation of needs
- Appropriate tailoring of available technology
- Adequate planning for built-in future expansion to meet long-term community needs

4 The task force process selected mass-fired waterwall boiler technology after evaluating a range of technology options.

5 Considerable attention was applied to nontechnical project areas as finances and contracts. The results include:

- Export steam sales and not electricity sales aid project financial success
- Best-qualified risk sharing reduced project and tipping fee costs to the City
- The bid tipping fees were confirmed by the financial model estimated for the project

6 The plant arrangement provides for separation of basic facility functions to minimize traffic congestion and assure smooth access to the facility.

7 The successful IRRF project results have relied on cooperation between three separate community sectors: the City of Indianapolis (public), OMSI (private), and IPL (monopoly).

These efforts have resulted in a facility designed to meet community needs now and in the future.

A. J. Scalzo
Technical Director, Combustion Turbine Operations,
Westinghouse Electric Corporation,
Orlando, FL 32826-2399

W. T. Sharkey
Production Supervisor,
Power I and Power II,
Dow Chemical, USA,
Plaquemine, LA 70765-0150

W. C. Emmerling[1]
Design Engineer, Combustion Turbine Operations,
Westinghouse Electric Corporation,
Orlando, FL 32826-2399

Solution of Combustor Noise in a Coal Gasification Cogeneration Application of 100-MW-Class Combustion Turbines

The field conversion of two W501D5 combustion turbines to burn medium Btu fuel gas supplied by a Dow Chemical coal gasification process at Plaquemine, LA resulted in excessive 105-Hz airborne sound and a corresponding unacceptable nonsynchronous engine vibration when burning natural gas. A joint Westinghouse and Dow Chemical corrective action program is described including field tests. Test results indicated that the combustion noise phenomenon was related to the strength of the primary air scoop recirculation pattern and its compatibility with the fuel and steam momentum vectors. A design was selected that eliminated the nonsynchronous combustion noise generated vibration and reduced the 100-Hz third-octave noise from 115 db to 97 db, an intensity reduction of 64 to 1.

Introduction

Dow Chemical, USA, contracted Westinghouse Electric Corporation to modify two existing 104 MW-W501D5 combustion turbines to burn medium Btu synthetic fuel gas produced by a 2400 ton per day coal gasification facility at the Dow petrochemical plant in Plaquemine, LA. The Dow Syngas Project is a 160-MW Integrated Gasification Combined Cycle (IGCC) power plant. Scalzo et al. (1981) indicated that the W501D5 combustion turbines were designed to permit field changeover to burn medium Btu synthetic fuel gas. The combustion turbines were placed in service in 1982 and 1983 burning natural gas fuel with the first unit being converted to burn synthetic fuel gas in late 1986. Fisackerly and Sundstrom (1986a) have previously described the overall DOW Gasification Project. Hendry and Pillsbury (1987) discussed the basic retrofit and combustor development program. The retrofitted combustion turbines are designed to operate on natural gas, synthetic fuel gas, or a mixture, together with steam injection for NO_x control and power augmentation.

After a unit was retrofitted to burn syngas, severe engine vibration and airborne noise were experienced when burning natural gas with steam injection. A severe nonsynchronous 105-Hz rotor and casing vibration as well as engine noise was found to be a strong function of load and steam flow. The load and steam threshold for no 105-Hz signal was 85 MW and about 10,000 lb per hour of steam. The unit that was not modified did not exhibit the 105-Hz noise problem.

Past experience with Westinghouse combustion turbines indicated that a discrete frequency of 209 Hz was common, but there was no former experience with the 105-Hz frequency. Since the physical dimensions of diameter and length were similar and the velocities and temperatures were also similar, the only changes that could alter combustor acoustics were the new syngas nozzle and combustor basket.

This paper discusses the joint Dow Chemical and Westinghouse field investigation, field tests, and design changes required to restore combustor stability and to eliminate objectionable combustion noise and the resulting nonsynchronous engine vibration. Operating experience with the modified combustion system including combustor wall temperatures and emissions is discussed by Morrison and Pillsbury (1989).

Synthetic Fuel Gas Conversion

Fisackerly and Sundstrom (1986b) have noted that the synthetic fuel gas produced at the DOW chemical petrochemical plant in Plaquemine, LA is a medium Btu coal gas with a lower heating value of 238.44 Btu per standard cubic foot. The retrofit program scope included replacement of fuel nozzles and combustor baskets and modification of control functions. Design specifications included natural gas starting, and burning natural gas or a mixture of natural gas and synthetic gas together with steam injection for NO_x control and power augmentation. Since the synthetic fuel gas increases mass flow to the turbine, a maximum synfuel and steam injection limit based on compressor surge was required, as shown in Fig. 1. This limit did not pose an operational problem since the plant output was 160 MW and the two W501D5 combustion turbines were each rated at 104 MW. In addition, since the W501D5 has a single row 1 turbine vane, a change in vane

[1] Current address: Naval Air Propulsion Center, Trenton, NJ.

Contributed by the International Gas Turbine Institute and presented at the 34th International Gas Turbine and Aeroengine Congress and Exhibition, Toronto, Ontario, Canada, June 4–8, 1989. Manuscript received at ASME Headquarters February 1, 1989. Paper No. 89-GT-217.

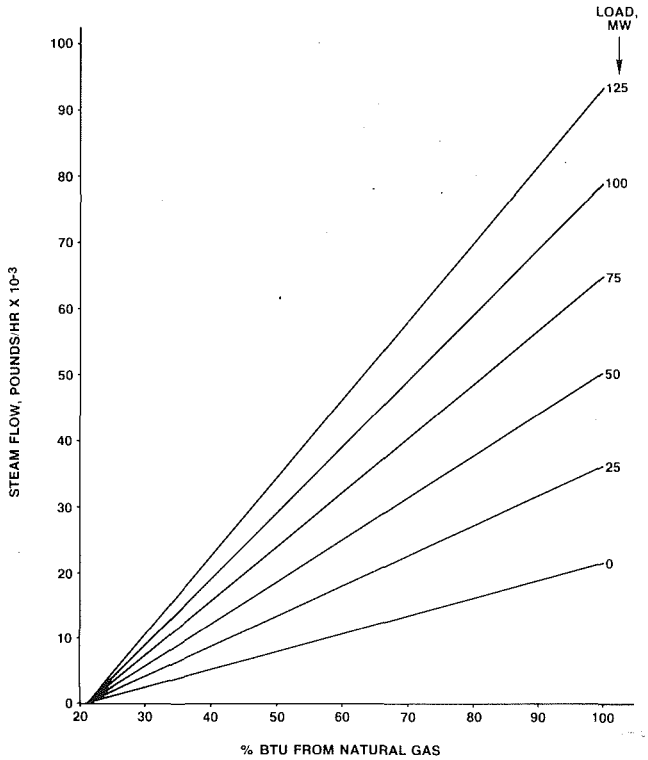

Fig. 1 Permitted steam injection as a function of load and percent Btu from natural gas

stagger angle could easily be selected in future manufactured sets to enable 100 percent synthetic fuel gas capability, if desired. Dow had anticipated a future conversion to synthetic fuel gas and had the two W501D5 units shipped with oversized fuel gas manifolds, thereby eliminating the need for a costly fuel gas manifold replacement.

Combustor Noise Phenomenon

Dow installed the synthetic fuel gas nozzles and baskets on one W501D5 unit and initiated operation on natural gas from the Dow Chemical coal gasification process in late 1986. Just before the new year holiday a severe nonsynchronous rotor and casing vibration together with objectionable airborne sound was encountered when burning natural gas with steam injection. Airborne sound and mechanical vibration level was a strong function of load and steam flow. Figure 2 displays rotor vibration data for the converted unit when operating at 100 MW on natural gas with 10,000 lb/h of steam. The unfiltered seismic is 5 mils double amplitude while the filtered seismic is only 2.5 mils and the absolute rotor vibration is 5 mils. A harmonic expansion of the unfiltered seismic "X" signal is shown in Fig. 3. Note the significant magnitude of the 105-Hz vibration component compared to the 60-Hz signal. This confirmed that a major percentage of the rotor vibration was a 105-Hz nonsynchronous forced vibration. Further investigation using accelerometers revealed that a high 105-Hz nonsynchronous vibration was also present at the exhaust end of the engine. Since it existed on both sides of the cloth expansion joint, it was apparent that airborne pressure pulsations were the source of the stimulus. A noise meter measured an acoustical signal over 112 db in the 100-Hz third octave. It was apparent from this evidence that the source of the nonsynchronous vibration and noise was the combustion system. Furthermore, since the 105-Hz signal did not exist with the original configuration of this unit or then with the unmodified unit, it was clear that it was the result of the installed syngas

EXHAUST END

	X	Y	
FILTERED	1.7	3.0	SEISMIC
FILTERED	2.5	1.4	RELATIVE
UNFILTERED	5.-7.	3.-5.	SEISMIC
UNFILTERED	3.0	2.0	RELATIVE
UNFILTERED	5.0	4.0	ABSOLUTE

INLET END

FILTERED	.85	1.1	RELATIVE
FILTERED	1.0	.85	SEISMIC
UNFILTERED	1.3	1.8	RELATIVE
UNFILTERED	3.0	2.5	SEISMIC
UNFILTERED	2.5	2.5	ABSOLUTE

Fig. 2 Rotor vibration data for modified unit in mils double amplitude

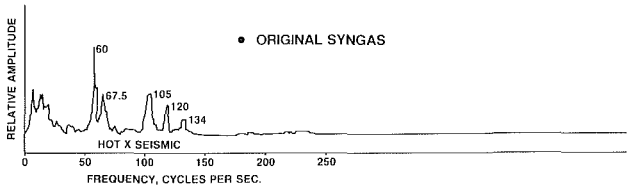

Fig. 3 Harmonic expansion of "X" seismic vibration signal

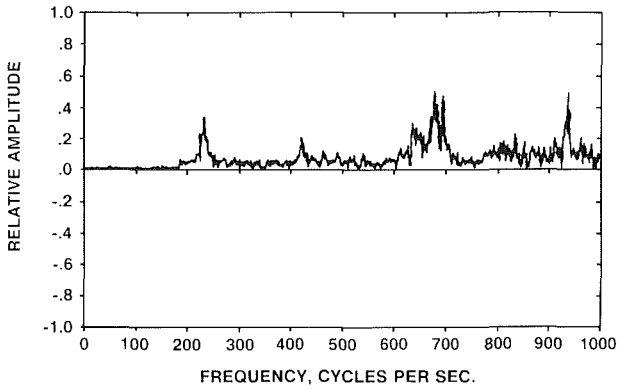

Fig. 4 Accelerometer frequency spectrum on standard combustor basket-burning natural gas at idle

nozzles and baskets. Usually a noise level below 98 db is typical inside the engine enclosure.

Traditionally, combustion noise of Westinghouse combustion turbines when burning natural gas has been encountered at idle if the nozzle pressure drop is low and is less than the pressure fluctuations in the combustor head end. The resulting combustion instability was improved in past units by closing the variable inlet guide vanes (IGV) to increase nozzle pressure drop to restore stability and reduce noise at idle. Figure 4 displays a typical accelerometer reading on a standard combustor basket when burning natural gas at idle. Note the strong signal at 209 Hz but no response at 105 Hz. The standard solution to this problem is to close the IGV's at idle and open them at minimum load. In some extreme cases, a reduction in orifice size was required to increase nozzle pressure drop. Figure 5 displays 250-Hz third-octave noise for the standard basket burning natural gas at idle as a function of IGV closure. At full closure, noise drops to about 96 db, which is below the 98 db encountered at base load.

To put the noise intensity level in perspective, the ratio of sound intensity or energy level should be considered. Since sound intensity is doubled for every 3-db increase, as shown

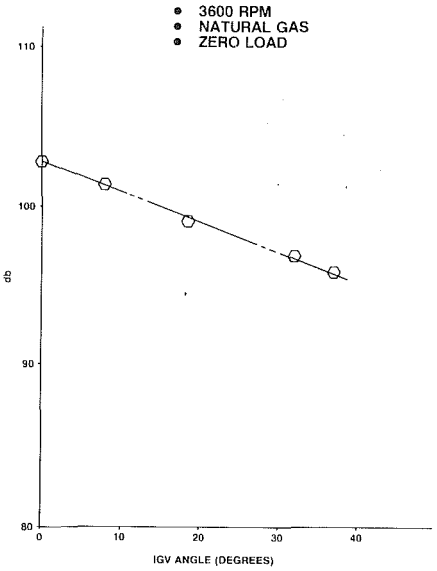

Fig. 5 250-Hz third-octave noise as a function of inlet guide vane position

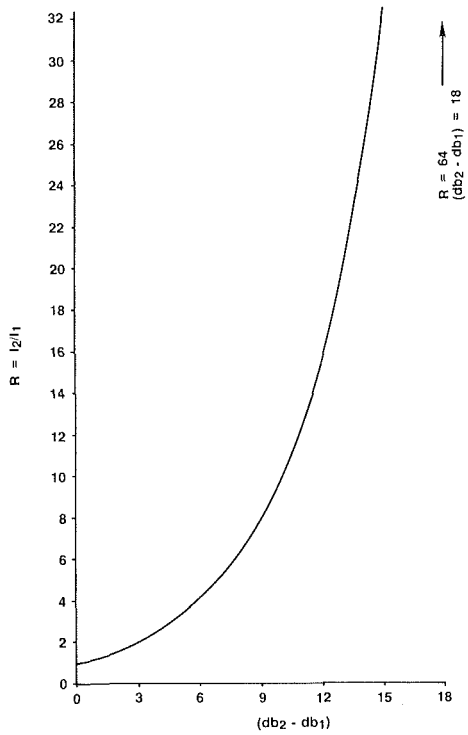

Fig. 6 Sound intensity ratio as a function of change in decibels

by the log function of Freeberg and Kemler (1949), the ratio of sound intensities (I_2/I_1) can be approximately expressed as

$$\frac{I_2}{I_1} = 2^{(db_2 - db_1)/3}$$

This is plotted in Fig. 6 and indicates that for a rise from 97 to 112 db, or a change of 15 db, the noise intensity has been increased by a factor of 32, which provides a more quantitative feel for the severity of the problem.

Understanding Combustor Noise

Dickson (1981) provided insight into the combustion noise phenomenon by treating it as a vibrating column of air. Assuming either a velocity-driven or pressure-driven wave front, i.e., an open or closed-end pipe, the standing wave can change from a half to a quarter wavelength as shown in Figs. 7 and 8. From Fig. 7, it can be seen that a velocity-driven or open-ended pipe creates a half wavelength, and that the standing wave is probably formed at the l_3 location, since the

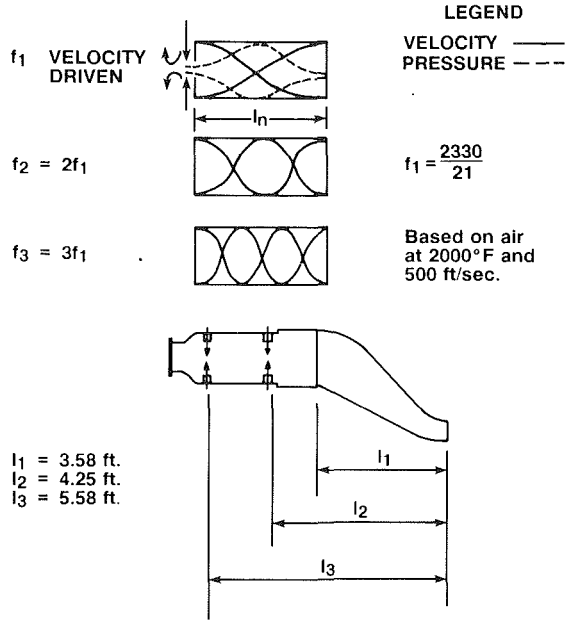

	l_1	l_2	l_3
f_1	325	274	209
f_2	651	548	418
f_3	976	822	626

Fig. 7 Open pipe acoustic frequencies in the combustion system

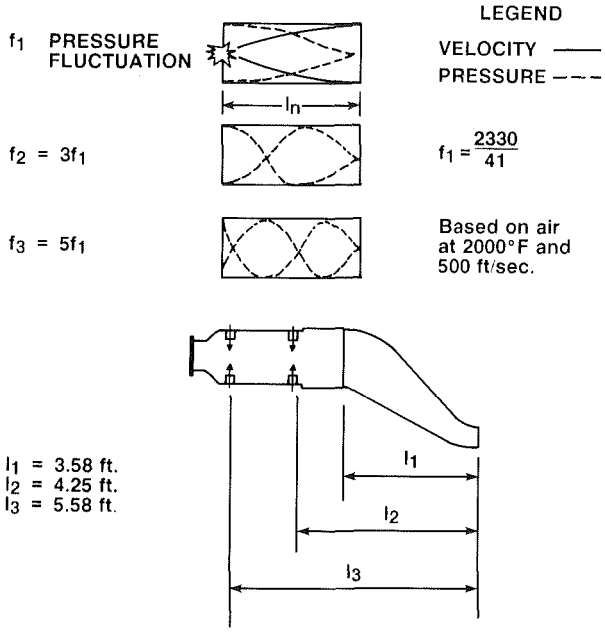

	l_1	l_2	l_3
f_1	163	137	104
f_2	488	411	312
f_3	814	685	520

Fig. 8 Closed pipe acoustic frequencies in the combustion system

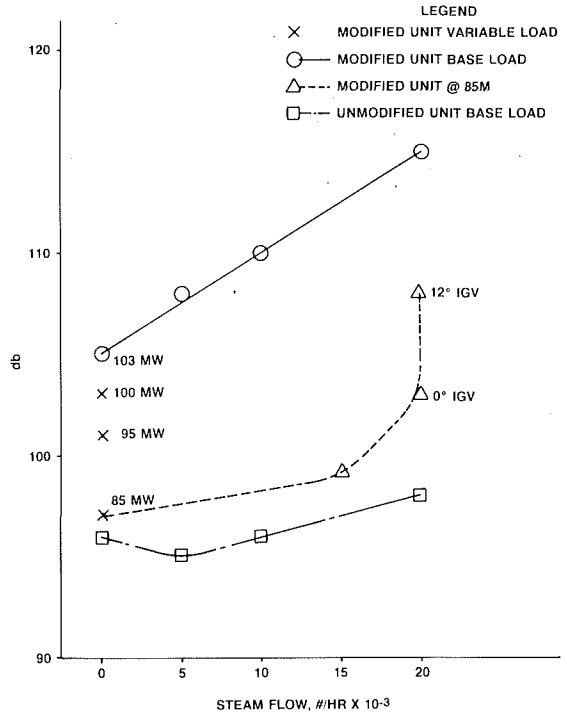

Fig. 9 100-Hz third-octave noise test results: modified unit versus standard unmodified unit

209-Hz natural frequency correlates well with past experience. The noise spectrum shown in Fig. 4 also contains higher frequencies in the 400 and 600 Hz range that compare well with the f_2 and f_3 frequencies. Therefore, it would appear that Westinghouse traditional combustor noise relates to a velocity-driven or open-ended system with the standard wavelength equal to the distance from the primary scoops to the row 1 vane.

The closed-end pipe or quarter wavelength system is shown in Fig. 8, where a pressure-driven system is present. Again, as in the open-ended discussion, it appears that the l_3 frequency of 104 Hz compares very well with the measured noise frequency with the synthetic fuel system provided at Plaquemine. A 412-Hz frequency response was also measured, which relate to the higher modes, such as the second mode of an open-ended l_3 or the second mode of a closed-end l_2. Since the closed-end fundamental is predominant, the most likely source for the 412 Hz is the second mode of an l_2 standing wave. Apparently the velocity-driven or open-ended acoustics was changed to closed-end or pressure-driven acoustics by the synthetic fuel gas nozzle and basket. Understanding the mechanism for this change was necessary in order to provide the information to obtain a solution.

First-Phase Test Program

The first priority was to develop a short-range program to enable the unit to operate while a long-range program was developed. The short-range program included rotor balance, noise measurements, and also tests to determine the effect of IGV closure on the 105-Hz noise.

One balance plug was applied at the compressor balance plane to determine its effect on turbine end vibration. Past experience indicated that this will provide about a one mil response at the opposite end; however, one balance plug produced a response greater than three mils, indicating a significant degree of decoupling from the response due to unbalance and the nonsynchronous response to combustion noise. Total rotor vibration at the turbine end was reduced to less than three mils compared to over six mils before rotor balancing.

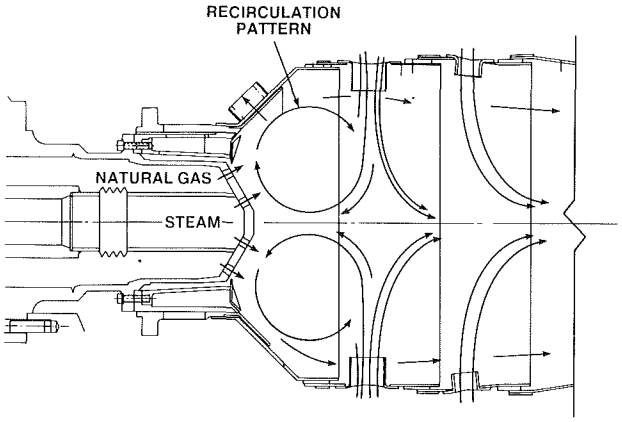

Fig. 10 Steam and natural gas vector relationships with essential recirculation primary air system with standard natural gas nozzle

Moreover, the 105-Hz shaft vibration was now only one mil double amplitude at minimum steam flow.

Noise level tests were conducted on both W501D5 units to develop diagnostic trend data and to determine suitable operating conditions. Figure 9 displays noise data for the converted unit as well as the standard unit. The zero steam data are very significant because 105-Hz signal persists until the load is reduced to 85 MW. Since the fuel pressure drop is increased by 60 percent in going from 85 MW to 103 MW while the shell pressure is increased less than 10 percent, it strongly suggested that the fuel momentum vectors were probably breaking down the primary air recirculating system above 85 MW. The 85-MW plot as a function of steam flow also indicates that at this fuel flow, or more precisely fuel momentum, the system can tolerate 10,000 lb/h of steam before reaching 98 db. The lower curve displays the standard unit 100-Hz third-octave noise as a function of steam flow for base load and illustrates the expected level of 98 db at 20,000 lb/h of steam. The 115-db 100-Hz third-octave noise achieved at base load and 20,000 lb/h of steam with the modified combustion system is 17 db higher than the standard unit. From Fig. 6 this corresponds to an intensity level increase of over 32 to 1.

Another point of interest in Fig. 9 is the effect of the IGV at 85 MW with 20,000 lb/h of steam. The IGV was closed from 0 to 12 deg and the noise level increased by 5 db. This illustrates the consequence of reducing shell pressure and subsequently reducing primary recirculating air. Therefore, the strength of the recirculating primary air flow plays a key role in combustion acoustics together with the fuel and steam momentum vectors. Furthermore, the resulting increase in nozzle pressure drop increased noise rather than decreasing it, as expected. This is further proof that the noise mechanism is a pressure-driven phenomenon.

Nozzle and Basket Influence on Noise

The essential recirculation stabilization flow system provided by the primary scoop air flow is shown in Fig. 10. The original nozzle, also shown in Fig. 10, provides steam in the center orifices and natural gas on the outer orifices. The included angles of the fuel and steam vectors provide good mixing but do not directly oppose the recirculating flow. Raw fuel from the natural gas orifices is mixed with the recirculating air and is carried into the six-lobed pattern provided by the six scoops to be ignited and to flow back to ignite new fuel. Steam also is mixed and drops the flame temperature, thereby reducing NO_x.

The syngas nozzle is shown in Fig. 11 together with the recirculating primary air flow. Note that the center hole fuel vector directly opposes the recirculating air pattern and that

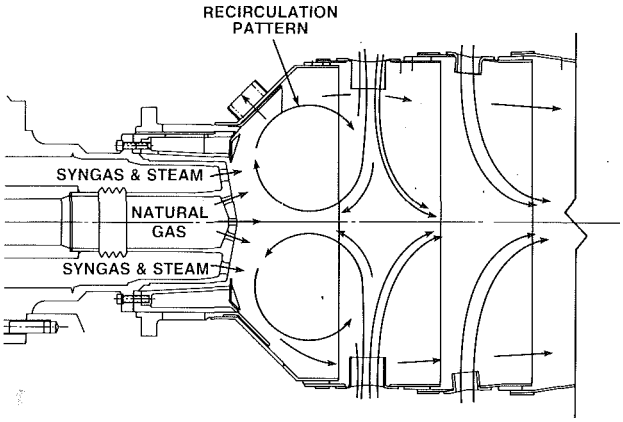

Fig. 11 Steam and natural gas vector relationships with essential recirculation primary air system with original syngas nozzle

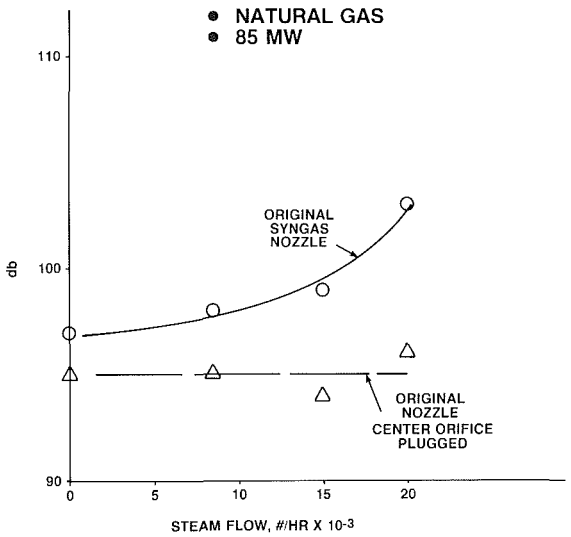

Fig. 12 100-Hz third-octave noise for original syngas nozzle and original with center orifice plugged at 85 MW

the reduction of the angle for the syngas/steam orifices provides more mixing but also more opposition to the recirculating air flow. It would appear from this comparison that the change in orientation of the fuel and steam vectors relative to the essential recirculation primary air flow pattern resulted in a strong mixing design, but also excessive opposition to the required flow patterns. A balance of mixing and support of the recirculating primary flow appeared to be essential in maintaining combustion stability and controlling noise. Fuel and steam flow momentum vectors that directly oppose the required recirculating primary air flow system could therefore be a key factor in the generation of the 100-Hz third-octave noise.

Second-Phase Test Program

To confirm the influence of the fuel gas momentum vectors on the 100-Hz third-octave noise, the center hole of the natural gas orifice system was plugged and sound noise measurements were taken inside the turbine enclosure at the exhaust end. Figure 12 displays the airborne sound data as a function of a steam flow with mass flow and load held constant at 800 lb/s and 85 MW respectively. The reduction from 103 db to about 95 db is an intensity ratio of 6 to 1 as seen in Fig. 6. For the trend of noise as a function of load with zero steam, the plugged center maintained a level 3 db lower than the original syngas nozzle.

The other component changed was the combustor basket,

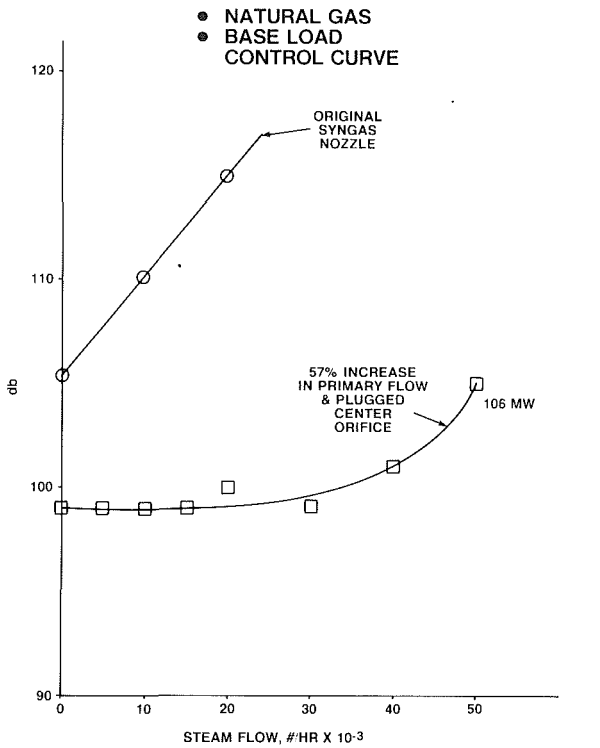

Fig. 13 100-Hz third-octave noise for original syngas nozzle and plugged center orifice with 57 percent increased primary airflow

where dome cooling was increased with a compensating reduction of 12 percent in primary air flow to maintain the original combustor pressure drop. Since it has been established that the traditional approach to combustion noise, i.e., reducing primary air flow by use of the inlet guide vane (IGV), is invalid for the original syngas system, it suggested that an increase in primary air flow would be desirable, especially in view of the importance of this flow as shown in the prior discussion of Figs. 10 and 11. Earlier designs for dual fuel (oil and gas) W501D5 units had 57 percent more primary air than the syngas and were actually used by Dow Plaquemine instead of the standard gas design used by the Dow W501D5 units in Freeport, TX. The rich primary installed at Dow Freeport corrected a flame-out problem at idle. To verify the influence of the primary air recirculating flow, the original baskets (57 percent more primary flow) were re-installed and a noise test was conducted. Results shown in Fig. 13 indicate a reduction of 15 db at 20,000 lb/h of steam, an intensity ratio of 32 to 1. However, the rise to 105 db with 50,000 lb/h of steam indicated that additional improvement was required, but the basic importance of the primary air recirculation in controling combustor noise was clearly demonstrated.

Redesign and Final Test

The earlier tests confirmed the importance that recirculating primary scoop flow and fuel gas momentum vectors had on combustion noise. Reviewing Fig. 11 and test results, it is apparent that the center hole must be plugged, orifices resized, and the injection angles increased, thereby returning to a relationship similar to Fig. 10. However, since the steam orifices are also the syngas orifices, and these were supported by the success of the increased primary air flow test, they were not changed because of the expected impact on basket wall temperature. This new nozzle shown in Fig. 14 was tested together with the high flow primary basket, and the results are shown in Fig. 15. The new system resulted in a 100-Hz third-octave level of 97 db at base load and was independent of

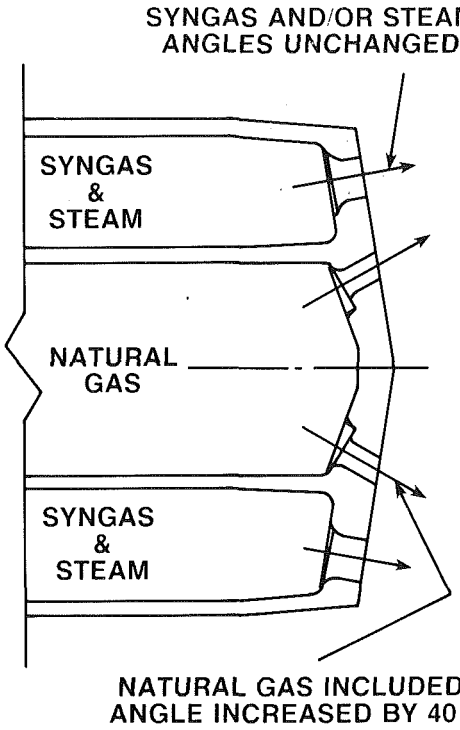

Fig. 14 New syngas nozzle

steam mass flow, compared to 115 db at 20,000 lb/h of steam with the original configuration, an intensity reduction of 64 to 1. The 97 dB level is comparable to the original natural gas system.

During accelerating and loading, the relative and seismic journal vibration signals were monitored at both compressor and turbine ends. No evidence of any nonsynchronous vibratory component was observed, as seen in Fig. 16. This is contrasted with a 3-mil level of nonsynchronous vibration during the original syngas test with the 105 Hz corresponding to the closed-end scenario. Also, the corresponding casing vibration was eliminated.

Summary and Conclusions

The conversion of two Westinghouse W501D5 combustion turbines to burn synthetic fuel gas produced by a Dow Coal Gas Gasification Process in Plaquemine, LA, resulted in unacceptable combustion noise and nonsynchronous engine vibration. A joint Westinghouse and Dow Chemical corrective action program included a series of field noise tests. Test data demonstrated the influence that fuel and steam momentum vectors as well as the primary air scoop recirculation flow had on the noise phenomenon and provided the necessary data base to eliminate the problem

Interpretation of the test data provides the following conclusions:

- Undesirable combustion noise and nonsynchronous engine vibration were associated with a pressure driven closed-end standing wave of one quarter wavelength.
- Acceptable combustion noise was associated with a velocity-driven open-ended standing wave of one half wavelength that was in agreement with historical data for Westinghouse combustion turbines.
- Fuel and steam momentum vectors that oppose the primary air scoop recirculation pattern can result in a closed-end noise phenomenon.
- Fuel and steam momentum vectors that are in sympathy with the primary air scoop recirculation pattern support an open-end noise phenomenon.
- Selecting a strong primary air scoop recirculation flow with compatible fuel and steam momentum vectors eliminated the closed-end noise phenomenon and associated engine nonsynchronous vibration.
- The new combustion system reduced the 100 Hz third-octave noise from 115 db to 97 db, an intensity reduction of 64 to 1.

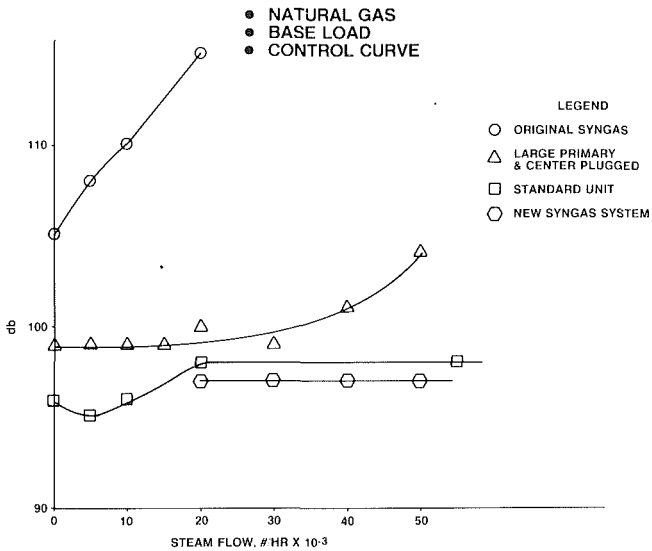

Fig. 15 100-Hz third-octave noise of new syngas system relative to standard unit and various syngas systems

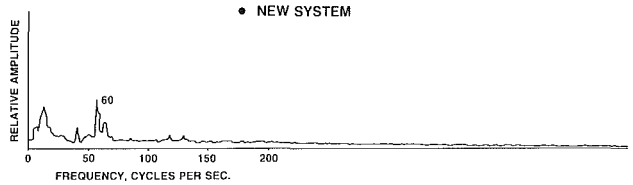

Fig. 16 Harmonic analysis of "X" seismic shaft vibration for new syngas system

Acknowledgments

This synthetic fuel project is proceeding in part due to an incentive provided by a price guarantee from the U.S. Department of the Treasury (formerly from the U.S. Synfuels Corp.).

References

Dickson, W. H., 1981, "Estimate of Combustor System Acoustic Frequencies," Westinghouse Internal Memo, Orlando, FL.

Fisackerly, R. H., and Sundstrom, D. G., 1986, "The Dow Syngas Project—Project Overview and Status Report," *Proceedings of the EPRI 6th Annual Conference on Coal Gasification*, Palo Alto, CA, Oct. 15-16.

Freeberg, C. R., and Kemler, E. N., 1949, *Elements of Mechanical Vibration*, Wiley, New York-London, pp. 151-152.

Hendry, R. L., and Pillsbury, P. W., 1987, "Commercial Demonstration of the Dow Gasification Process in an Integrated Combined Cycle Cogeneration Application," *Proceedings of the American Power Conference*.

Morrison, E. M., and Pillsbury, P. W., 1989, "Coal Generated Synthetic Gas Operating Experience With Two 100-MW-Class Combustion Turbines," ASME Paper No. 89-GT-257.

Scalzo, A. J., Holden, P. C., and Howard, G. S., 1981, "The Westinghouse 501D Combustion Turbine Engine," ASME Paper No. 81-GT-32.

Influence of the Continuous and Dispersed Phases on the Symmetry of a Gas Turbine Air-Blast Atomizer

V. G. McDonell

G. S. Samuelsen

UCI Combustion Laboratory,
UCI Institute for Combustion and
Propulsion Sciences and Technology,
University of California, Irvine,
Irvine, CA 92717

Current trends in liquid-fueled practical combustion systems are leaving less tolerance for fuel injection deficiencies such as poor spray field symmetry. The present paper evaluates the symmetry of the flowfield produced by a practical air-blast atomizer. Specifically, the influence of both the continuous phase and dispersed phase on the spray field symmetry is assessed. In the present case, asymmetry in volume flux is associated principally with disparities in the injection of the dispersed phase, which is manifested by a maldistribution of larger drops. Asymmetries observed in the continuous phase without the dispersed phase are reduced in magnitude by the presence of the dispersed phase, but still contribute to asymmetry in radial spread of the dispersed phase.

Introduction

The need to assess spray field symmetry in liquid-fueled combustion systems is gaining importance for several reasons. First, the move to fuel flexible systems and smaller geometries leaves less tolerance for local variation in combustor performance due to atomizer asymmetry. Second, the current development of numerical codes for liquid-fueled systems is predicated on the assumption of spray field symmetry. Third, the measurement of droplet size and velocity typically assumes spray symmetry with the concomitant acquisition of data along a single radius rather than a full diameter. The interpretation of such data is jeopardized in the absence of atomizer symmetry.

The spray fields produced by air-assist or air-blast atomizers are a result of considerable two-phase interaction. Therefore, it is important to assess the role of *each phase* in order to understand the generation of any asymmetry present. Recently introduced modern diagnostics, coupled with conventional methods, portend the capability of providing the needed assessment of symmetry of the dispersed phase in both isothermal and combustor environments. Recent results have demonstrated the potential of these modern diagnostics in both environments (e.g., McDonell et al., 1987).

The objective of the research reported in the present paper is to explore the extent to which the dispersed *and* continuous phases contribute to the symmetry of an air-blast atomizer using modern methods in an isothermal environment. This study provides a baseline against which the performance of the same atomizer under reacting conditions may be compared.

Contributed by the International Gas Turbine Institute and presented at the 34th International Gas Turbine and Aeroengine Congress and Exhibition, Toronto, Ontario, Canada, June 4-8, 1989. Manuscript received at ASME Headquarters February 21, 1989. Paper No. 89-GT-303.

Experiment

Atomizer. The atomizer selected for characterization, shown in Fig. 1, is a production air-blast atomizer for use in a production helicopter gas turbine engine (Mongia and Reider, 1985). The atomizer features swirled, centrally injected air and, via an outer shroud, swirling external air. The fuel is filmed onto a circular surface (via six ports, which inject the fuel tangentially in the same direction as the swirled air) and sheared between the two air passages.

Methanol is the liquid fuel used in the present study. It was selected due to suitability of the resultant data for modeling. In particular, the methanol vapor has nearly the same density as air (1.33 versus 1.2 kg/m^3) and, when injected at $-10°C$ ($-10°C$ is the wet bulb temperature at test conditions), evaporates isothermally and thereby eliminates density gradients in the gaseous environment and temperature gradients within the droplets. The atomizer is operated at an air-to-fuel ratio of 1.0 and a mass flow of 0.0021 kg/s for each phase. The pressure drops across the atomizer are 5600 Pa and 125 Pa for the fuel and air, respectively.

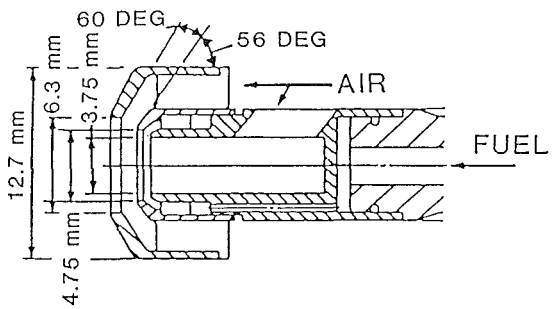

Fig. 1 Fuel injector

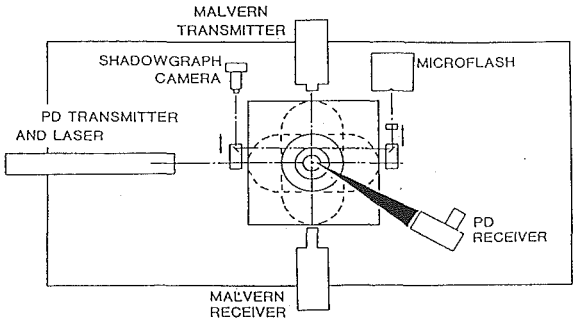

Fig. 2 Facility

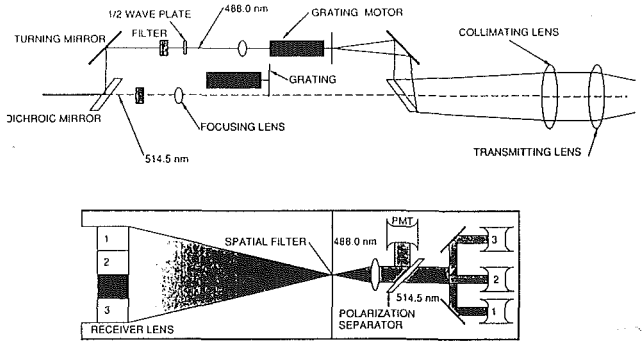

Fig. 3 Two-component phase Doppler transmitter and receiver

Spray Characterization Facility. A schematic of the test facility is shown in Fig. 2. The diagnostics remain fixed, oriented about a square cutout in the optical table that measures 900 × 900 mm. The test article is directed downward from the end of a 28-mm tube, which supplies fuel and atomizing air to the atomizer. This tube is connected to a vertical traverse to provide translation in the axial direction. The entire axial traversing system is attached to the bottom of the table via a two-dimensional horizontal traverse system. Hence, three degrees of translational freedom are available to the test article. In addition, the fuel tube can be rotated about the axial centerline to any degree of atomizer orientation.

A plexiglass and flexible plastic enclosure surrounds the entire traversing/support system and ensures a stagnant environment by isolating the flowfields studied from room perturbations. This structure also permits seeding of the air entrained by the flowfields, thereby enabling unbiased measurements of the gas phase to be made. Air introduced into the structure is removed via an exhaust system located in the fuel collection plenum. A stainless mesh separates the exhaust entrance from the structure to ensure that the exhaust suction is distributed over the large area of the plenum.

Diagnostics. Measurements of mean and fluctuating velocities for each phase are made using a two-component phase/Doppler system (Aerometrics Model 2100-3). The principle of operation of the instrument has been described in detail elsewhere (Bachalo and Houser, 1984). A schematic of the transmitter and receiver is shown in Fig. 3. The measurement of the size of spheres is based upon a linear relationship between the spatial phase shift of the scattered fringe pattern and the diameter of the scatterer. The velocity is determined from the frequency of the swept fringe pattern. Comparative studies with diffraction (e.g., McDonell et al., 1987; Dodge et al., 1987), visibility (Jackson and Samuelsen, 1987), and extinction (Young and Bachalo, 1987) techniques have demonstrated good size measurement capability. In most cases, the phase/Doppler approach demonstrated advantages over the other techniques.

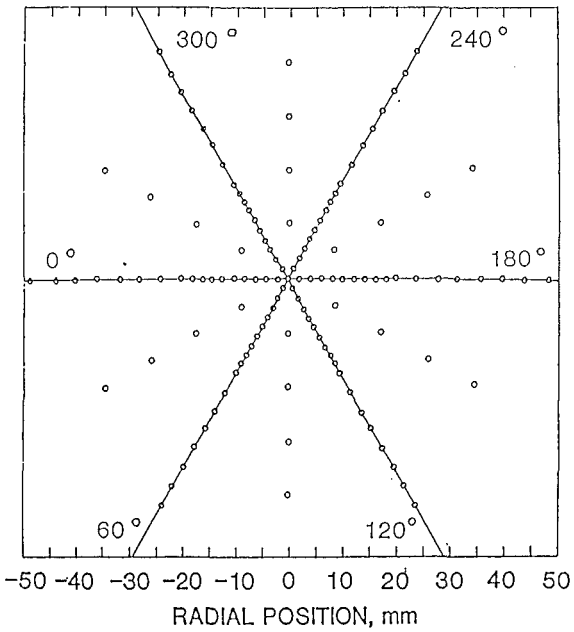

Fig. 4 Measurement locations for each axial station

Discrimination of the continuous and dispersed phases is achieved by sizing all particles, including the seed particles used to track the continuous phase. Al_2O_3 (nominally 1.0 μm) is used to seed the air streams. The seed particles produce size measurements less than 3 μm. Using these scores and those from droplets less than 3 μm in diameter, statistics for the continuous phase are generated. This approach has been applied successfully in previous studies of both monodispersed (e.g., Bluzan, 1988; Mostafa et al., 1988) and polydispersed (e.g., McDonell and Samuelsen, 1988; Rudoff and Bachalo, 1988) flows. In the regions of the flowfield studied in the present work (50 mm and further downstream), particles smaller than 3 μm in diameter track the flow to a good degree.

In addition, the instrument utilizes information from the signals obtained to generate an in-situ measurement of the probe volume cross section. Recent studies have shown that (1) developments in the methods to deduce the sampling cross section have resulted in accurate volume flux calculations in high number density flows (Bachalo et al., 1988), and (2) the values of mass flux correspond in magnitude and trend with those obtained through typical intrusive sampling techniques such as patternation (e.g., McDonell et al., 1987). In the present study, the optical technique alone is used for the volume flux measurement in lieu of a physical probe since the equivalent information is obtained with regard to fuel distributions and, in addition, details are provided with respect to size and velocity distributions. It would not be practical to conduct a detailed mapping such as the one done in the present study if volume flux were the sole quantity sought. In this case, a well-developed patternation system (e.g., McVey et al., 1987) would be more appropriate.

Approach

The approach taken in the current study is to characterize precisely the flowfield produced by a production air-blast atomizer. The first step is to conduct a three-dimensional characterization of the single-phase flow produced by the injector when running the nominal atomization air flow in the absence of fuel. Next, the flowfield with the injected liquid is characterized in the same three-dimensional manner. The two-phase characterization includes the mapping and measurements of statistics for both the liquid and dilute

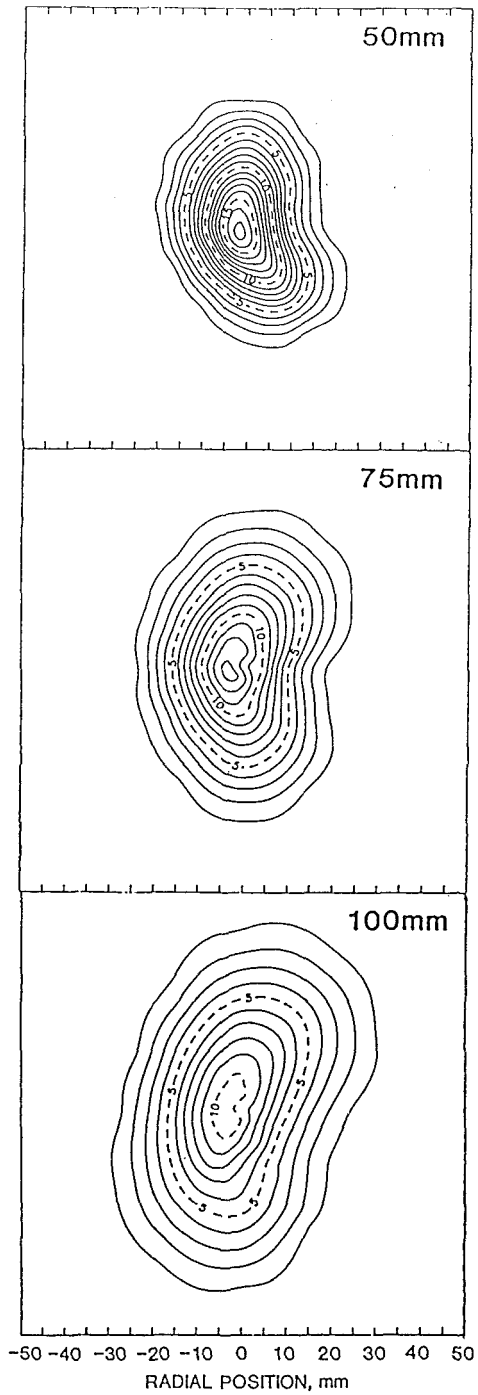

Fig. 5 Isopleths of single-phase axial velocity (m/s)

phase. The trends associated with the single and two-phase flows are then examined in detail to (1) provide understanding of the two-phase interaction and (2) give insight as to the cause and perpetration of asymmetries present in the flow. The characterization consists of measurements of axial and azimuthal velocity for each phase present, and particle size distribution of the dispersed phase, when present. The measurements are conducted at three axial stations (50, 75, and 100 mm), and at six angular orientations of the atomizer (0, 60, 120, 180, 240, and 300 deg) at each axial station. In addition, measurements of partial profiles are conducted at 30 deg increments to ensure adequate coverage of the flowfield. Data are acquired at between 10 and 20 radial stations at each axial station depending on the radial extent of the spray field.

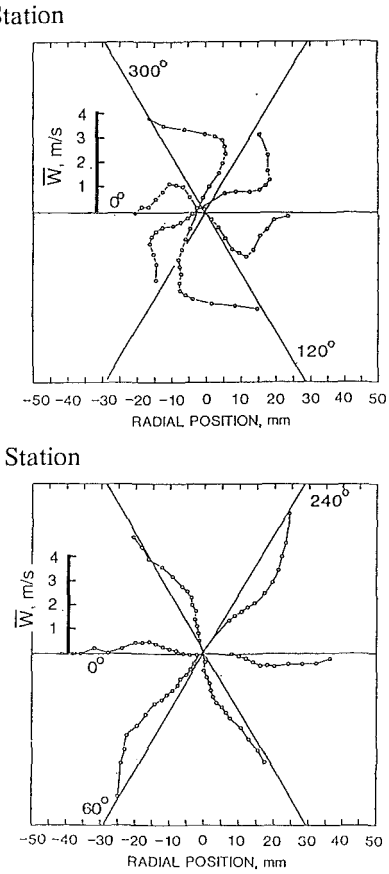

Fig. 6 Single-phase mean azimuthal velocity profiles

Figure 4 shows the locations at which measurements were conducted at each axial station, and provides a reference for the location of each angular orientation.

Results

Results are presented first for the single-phase flow, followed by the continuous phase in the two-phase flow, and finally for the dispersed phase in the two-phase flow. Results are presented in either three dimensions or two dimensions. In the cases where two dimensions are presented, the results are obtained by averaging the data acquired for the six orientations unless explicitly stated as being a profile obtained from a particular orientation.

Symmetry of the Single-Phase Flow. The flowfield symmetry of the atomizer was first characterized in the absence of liquid phase injection to provide a baseline against which to compare the two-phase flow results. Figure 5 shows isopleths of the mean axial velocity at three axial stations: 50, 75, and 100 mm. The plots have an elliptical shape at each location. For the 50-mm case, the major axis of the elliptical shape runs from 300 to 120 deg. The ellipsoidal shape moves through approximately 40 deg of rotation with increasing axial distance. The rotation is due to the azimuthal component of velocity imparted by the swirl vanes in the atomizer.

Figure 6 presents profiles of the mean azimuthal velocity for the six angular orientations of the atomizer studied. Figure 6(*a*) presents the data for the 50-mm axial station. The extension of the ellipsoid is correlated to the presence of an asymmetry in the azimuthal velocity. Note that the azimuthal velocities associated with the 120 and 300 angular orientations are significantly higher. The 0-deg orientation has the least amount of radial spread and it also possesses the lowest

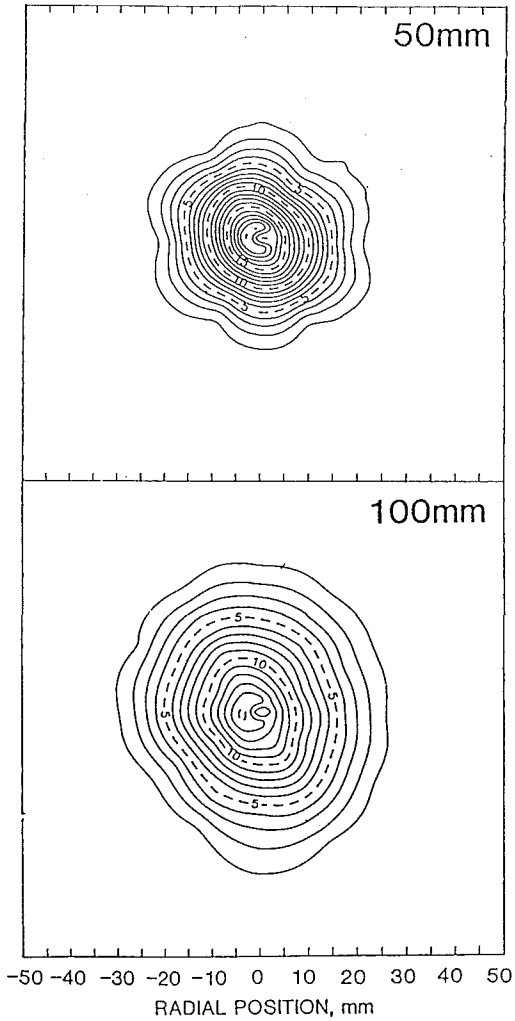

Fig. 7 Isopleths of continuous phase axial velocity (m/s)

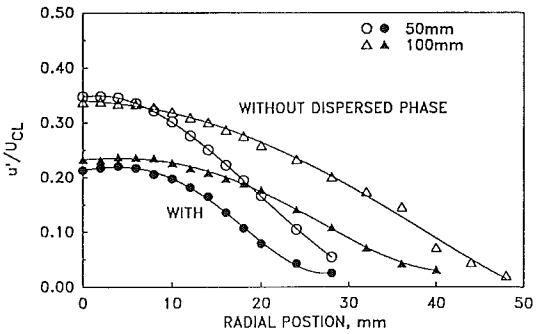

Fig. 8 Continuous phase turbulence intensity

azimuthal velocities. By 100 mm, as shown in Fig. 6(*b*), the local peaks in azimuthal velocity have rotated clockwise to the 240 and 60-deg orientations. Again, the radial spread at these orientations is greater than that at the other orientations. At 100 mm the asymmetry in azimuthal velocity is still noticeable, but is substantially damped out.

Symmetry of the Two-Phase Flow

Continuous Phase. Figure 7 presents isopleths of the mean axial velocity for the continuous phase in the methanol spray field. Note that the presence of the liquid ("dispersed") phase has virtually eliminated the asymmetry present in the single-phase axial velocity field. The flowfield at 50 mm is nearly circular, and the elliptical behavior exhibited by the single-phase flow in the absence of liquid injection is not discernable. Note that the axial velocities associated with the two-phase flow are greater at the centerline region and less at the outer edge, indicating that the presence of the spray increases the gradients in the continuous phase axial velocity.

Figure 8 presents radial profiles (averages of each of the seven orientations) of the axial turbulence intensity based upon the centerline value of the mean velocity at each axial station. The presence of the dispersed phase decreases the turbulence intensity of the continuous phase by 30 percent, resulting in decreased velocity decay and spread in the flow.

Figure 9 presents the azimuthal velocity profiles associated with the axial velocity isopleths of Fig. 7. The 50-mm axial station exhibits reasonable symmetry in the azimuthal velocities, a result consistent with the symmetric axial velocity field. However, the azimuthal velocities at 120 and 300 deg are slightly higher, a result that is consistent with the single-phase flow.

The azimuthal velocities at 100 mm are presented in Fig. 9(*b*). Note that the azimuthal velocities for the two-phase flow are slightly greater than the single phase flow at 100 mm (Fig. 6). The swirl is maintained a greater axial distance in the presence of the dispersed phase due to (1) the decrease of turbulence and (2) the momentum transfer between phases (the methanol is injected with swirl, concurrent with the air). At 100 mm, the peak azimuthal velocities occur at 240 deg. and the minimum at 0 and 180 deg orientations, again reflecting results obtained for the single-phase flow. It is noteworthy that the relatively strong azimuthal velocities at 60 deg for the single-phase flow are not present in the two-phase flow, suggesting that the disparity in the two-phase case is affected by

a) 50 mm Axial Station

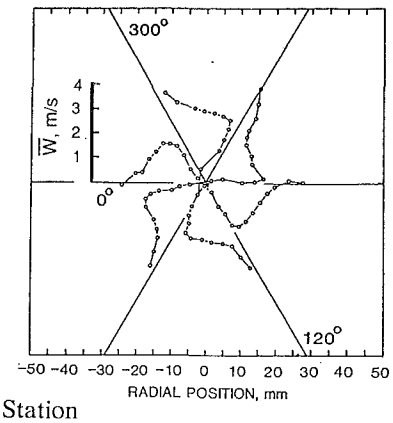

b) 100 mm Axial Station

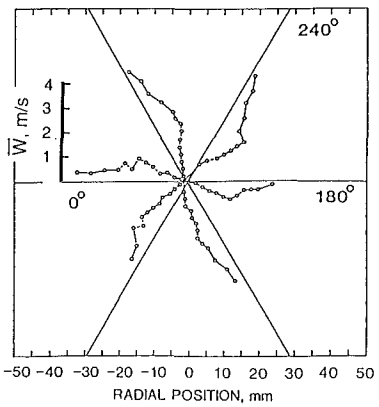

Fig. 9 Continuous phase mean azimuthal velocity profiles

a) 50 mm Axial Station

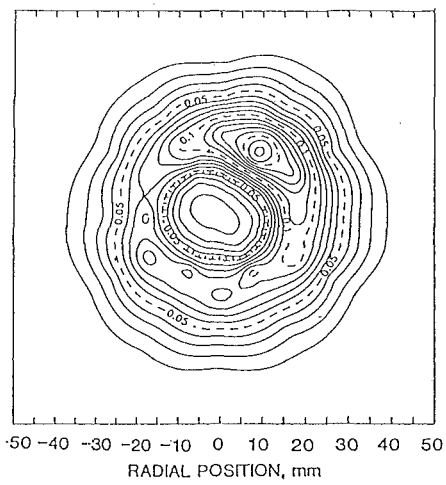

b) 100 mm Axial Station

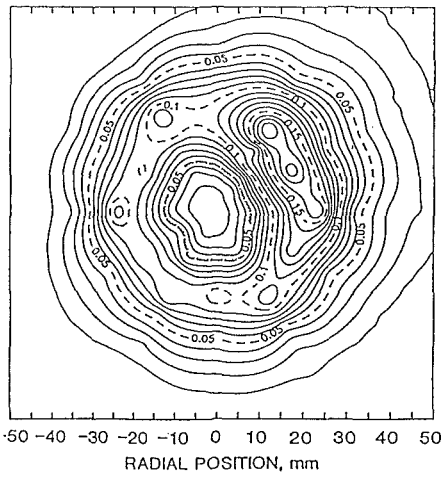

Fig. 10 Isopleths of volume flux (cc/cm^{2}s)

a) 50 mm Axial Station

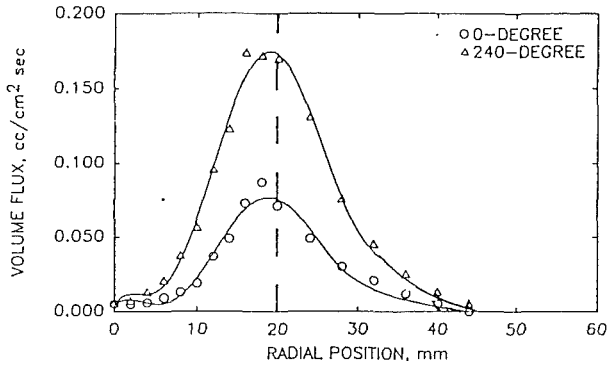

b) 100 mm Axial Station

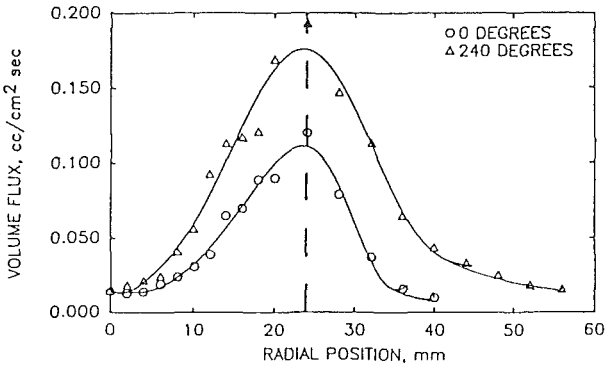

Fig. 11 Radial profiles of volume flux

the presence of the dispersed phase. These results demonstrate that, in the present case where equal mass is present each phase, the continuous phase is strongly influenced by the presence of the dispersed phase. One trait that persists from the single to the two-phase flow is the location of peak azimuthal velocities.

Dispersed Phase. Isopleths of the volume flux at the 50 and 100-mm stations are presented in Fig. 10. The hachure marks on the figure indicate the direction of negative gradients. Thus, the contours nearest the centerline are of lower value than those farther from the centerline. The hachure marks in this case indicate that the nozzle is hollow-cone in nature. The results at 50 mm (Fig. 10*a*) show the uniformity in radial spread of the dispersed phase. Note also that the volume flux peaks at the 240-deg orientation. The same results are presented in Fig. 10(*b*) at the 100-mm axial station. By 100 mm, the uniformity in radial spread has degraded. The regions from 120 through 270 deg have considerably more radial spread than do the other regions. The location of the increased radial spread corresponds to the highest value azimuthal velocity profile (240 deg) in both the single and two-phase flows. In addition, the local peak in volume flux has rotated slightly and elongated, showing the rotation and spreading induced by the swirl.

To check the accuracy of the flux measurement, the volume under the contour surface is calculated to provide the total flow rate at each axial station. At 50 mm, the integrated flow is 30 percent of the measured flow to the atomizer. At 100 mm, it is 93 percent of the measured flow to the atomizer. The value at 100 mm indicates good conservation of mass, especially if evaporation effects are considered. The value at 50 mm, however, does not indicate mass conservation. The possible reasons for this in the present flow are numerous, and include (1) the three dimensionality of the flow, which may lead to erroneous sample area determinations, and (2) relatively high concentration of droplets at the 50-mm station, which leads to erroneous rejection of samples. A smaller sampling volume at 50 mm would likely reduce the error due to the latter reason.

Examination of the 240 and 0-deg Profiles. To understand better the relationship between the phases and the local peak in volume flux, individual profiles are now examined. Results are presented for the 240 and 0-deg orientations, since the greatest disparity in volume flux and radial spread occurs between these orientations. In particular, drop distribution means and drop distributions are examined to understand the volume flux differences better. Additional insight regarding radial spread is also provided by examination of the air/droplet velocity relationships.

Volume Flux. Figures 11(*a*) and 11(*b*) present the individual radial profiles obtained for the volume flux at the orientation of greatest disparity. At 50 mm and 100 mm, the maximum flux occurs for either orientation from between 10 and 30 mm radially. The peak flux occurs at 20 and 24 mm for 50 and 100 mm, respectively. To examine the data with respect to percentage differences, plots of the volume flux at 240 deg divided by the volume flux at 0 deg are presented in Fig. 12. From this figure, the disparity between orientations is clearer.

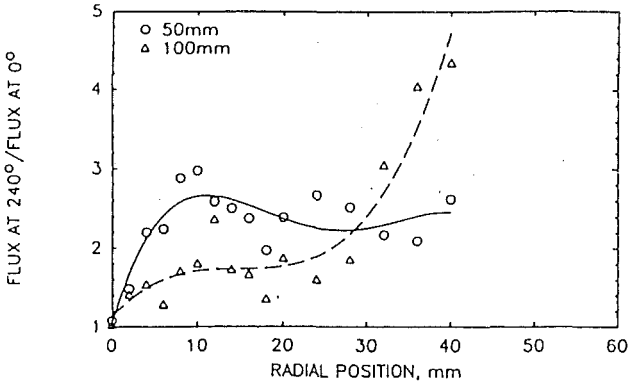

Fig. 12 Ratio of volume flux at 240 deg to volume flux at 0 deg

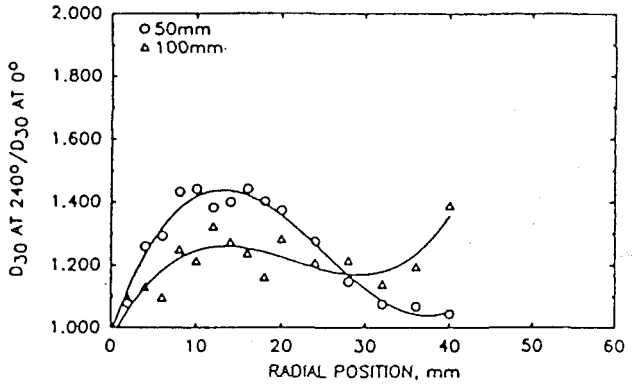

Fig. 13 Ratio of D_{30} at 240 deg to D_{30} at 0 deg

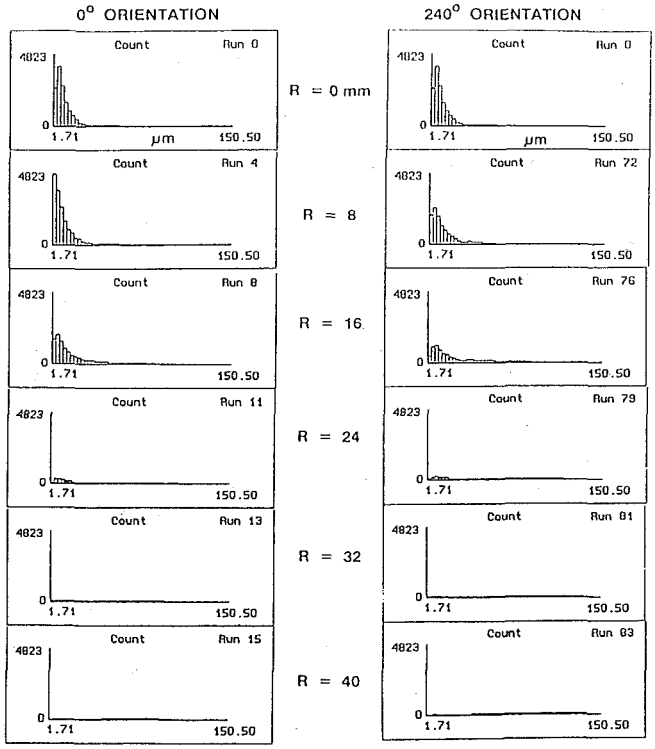

Fig. 14 Normalized droplet size distributions (100 mm)

From two to three times more flux is present at the regions of maximum flux (radial positions between 10 and 30 mm) for 50 mm and from one to two times more at 100 mm. At 100 mm,

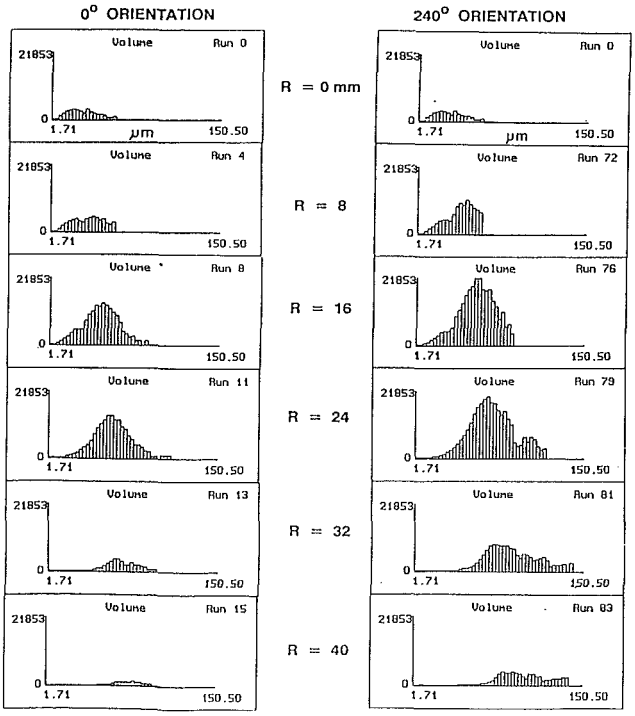

Fig. 15 Normalized droplet volume distributions (100 mm)

the disparity increases beyond 30 mm radially, with up to four times more flux occurring for the 240-deg orientation.

At least two factors affect the volume flux directly: drop size and number of drops. Each of these factors is now examined in order to deduce the importance of each on generating the disparity between these two orientations.

i. Drop Size. In the consideration of disparities in volume flux, the best description of the drop size is the distribution at each point of the volume mean diameter or D_{30}. Radial profiles at 50 and 100 mm of the ratio of the volume mean at the 240-deg orientation to the 0-deg orientation are presented in Fig. 13. At both 50 mm and 100 mm, the discrepancy in the volume mean does not exceed 40 percent at any given radial position. At 50 mm, the distribution volume mean at 240 deg is between 20 and 40 percent higher than that at 0 deg at radial locations corresponding to the greatest volume flux (between 12 and 28 mm). This corresponds to 73 to 173 percent more volume flux at the 240-deg orientation. These differences nearly account for 150 percent greater volume flux at the 240-deg orientation. At 100 mm, the volume mean at the radial locations of greatest flux is 20 to 25 percent higher for the 240-deg orientation, corresponding to 70–95 percent more volume flux. These differences account for the 60 to 80 percent more volume flux on the 240-deg orientation between 12 and 28 mm radially. However, at radial locations beyond 28 mm, the difference in volume mean is not enough to account for the difference in volume flux.

ii. Drop Population. To identify the extent to which various droplet size groups are responsible for the disparity in volume flux, droplet size distributions and droplet volume distributions are presented in Figs. 14 and 15, respectively. The distributions presented are normalized to account for variation in collection time, probe volume area, and system sensitivity as a function of drop size. As a result, the distributions presented reflect identical sensitivity and collection time, and can be used to assess the relative number of drops and volume of drops from point to point.

Figure 14 presents the normalized droplet distributions

a) 0-Degree Orientation

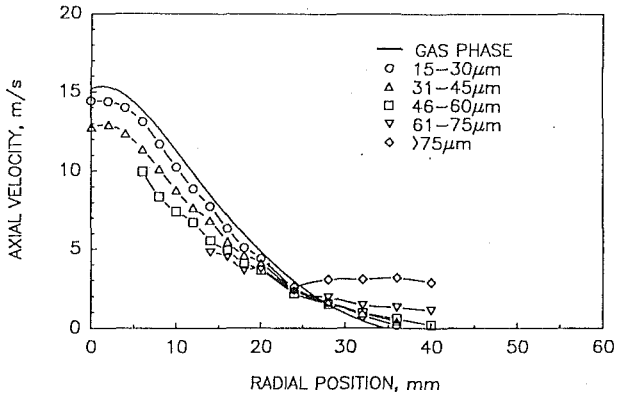

b) 240-Degree Orientation

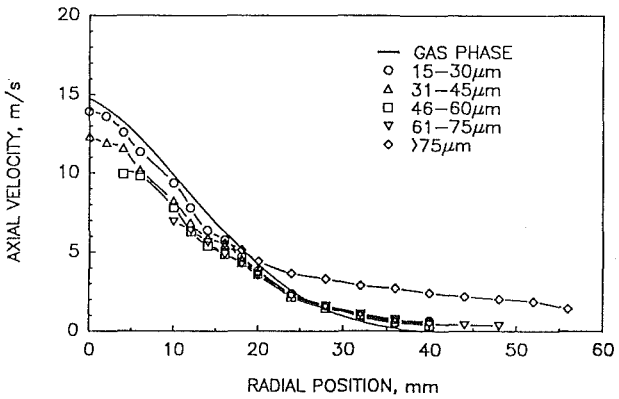

Fig. 16 Gas and droplet velocity profiles (100 mm)

from select radial positions along the 0 and 240-deg orientations. The results show that the greatest population of droplets occurs at the centerline, and that these droplets tend to be small. In the region of greatest dispartity in volume flux (radial positions greater than 16 mm), relatively few drops exist. It is noteworthy that the 0-deg orientation possesses *more* droplets overall than does the 240-deg orientation.

Since the absolute number of droplets may not significantly affect volume flux, the count distributions in Fig. 14 are presented in Fig. 15 as volume distributions. Figure 15 shows that despite the fairly high numbers of small droplets at the centerline, relatively little volume is contributed by these drops. Examination of the volume distributions in the region of greatest volume flux disparity (radial positions greater than 16 mm) indicates that a considerably greater number of large drops are present along the 240-deg orientation. Farther from the centerline, it is observed that the droplets present in this region are large, and that they are considerably larger and more numerous on the 240-deg orientation. This disparity in droplet distribution accounts for the flux differences not explained by the difference in size.

Drop Velocity. Figure 16 presents radial profiles of the gas and droplet mean axial velocities as a function of droplet size. Data are presented at locations where more than 100 drops within the size groupings selected were sampled (10,000 total droplets were sampled at each point). Hence, regions on Fig. 16 where no data are presented for droplets indicate statistically insufficient number of drops of a given size range at that point.

Figure 16 shows that for droplets less than 75 μm in diameter, the profiles for either orientation are similar. The trends for drop size versus axial velocity are consistent, with smaller drops attaining the gas velocity sooner near the centerline. In regions away from the centerline (radial positions greater than 25 mm), the droplets present possess enough momentum to exceed the gas velocity. In these regions, primarily larger drops exist, which (1) have adequate momentum to overcome entrained air and travel away from the centerline, and (2) have the largest influence on the volume flux. The profile for the drops greater than 75 μm on the 240 deg traverse indicate that these drops are responsible for the greater radial spread in volume flux associated with this orientation. Hence, in the present case, the production of larger drops (diameters greater than 75 μm) existing along the 240 deg traverse is responsible for the increased radial spread in volume flux along that orientation.

Little dependency on size exists for the azimuthal component velocity (not presented for brevity); thus it appears that the slightly higher gas azimuthal velocity associated with the 240-deg orientation may also contribute to the increased radial spread. However, decoupling the two effects is not possible without further investigation.

Summary

A precise study of the symmetry of the single and two-phase flow produced by a practical air blast atomizer is conducted using phase/Doppler interferometry. By conducting measurements of two velocity components and drop size distributions for each phase in a three-dimensional manner, the degree of symmetry may be assessed, and the sources of asymmetries may be evaluated.

Conclusions drawn from this study are as follows:

- Two-component phase/Doppler interferometry is capable of distinguishing and measuring statistics for each phase in practical spray fields.
- In the present case, the single-phase flow produced possesses a significant asymmetry, which is considerably damped by the addition of liquid drops in a mass loading of 1.0.
- The addition of the second phase reduces the turbulence and spread of the continuous phase.
- The asymmetry in the volume flux in the present flowfield is mostly due to a disparity in the fuel injection distribution, which is manifested primarily in greater numbers of large drops which have sufficient momentum to travel far from the centerline. Note that the size of the drops alone cannot account for the volume flux disparity.
- Variation in the gas azimuthal velocity field may influence the radial spread of the droplets and causes disparity in radial distribution of the fuel.
- The nature of the asymmetry in azimuthal gas velocity is different in the single and two-phase flows, indicating that, although correlation exists between greater drop radial spread and high azimuthal gas velocities, direct correspondence between the two cases does not exist.
- It is necessary to measure statistics for both phases in two-phase flows to provide the information necessary to understand the transport processes occurring in flows of this type.

Overall, the study demonstrates the complexity of the two-phase interaction and, in addition, shows that the tools necessary to understand the interaction are becoming available. In the present case, the dispersed phase dominates the continuous phase, and is clearly responsible for high local flux at 240 deg. The disparity in radial spread is attributed to both dispersed and continuous phase asymmetry. In cases where air-to-fuel ratios of greater than one are considered, the influence of the continuous phase would become more important. The typical practice of line of sight average drop size, or even of making spatially resolved measurements of drop size, does not provide necessary details regarding phase interaction. Also, steps should be taken to assess symmetry (via patterna-

tion for quick results) before data from a single profile are used to represent the overall behavior of the spray. Without such steps, conducting measurements along a single radial profile at several axial stations within practical flowfields presumes far too ideal a flow.

Acknowledgments

This work was supported, in part, by NASA Contract No. NAS3-24350 (J. D. Holdeman, Contract Monitor) in cooperation with the Allison Gas Turbine Division of General Motors. The participation of Brian Bird in the collection and analysis of the data is gratefully acknowledged. Howard Crum is to be applauded for assistance in the development and maintenance of the facility. Also, the help of Dr. W. D. Bachalo in the specialized development and application of the instrument and software modifications is appreciated.

References

Bachalo, W. D., and Houser, M. J., 1984, "Phase Doppler Spray Analyzer for the Simultaneous Measurement of Droplet Size and Velocity Distributions," *Optical Engineering*, Vol. 23, p. 583.

Bachalo, W. D., Rudoff, R. C., and Brena de la Rosa, A., 1988, "Mass Flux Measurements of a High Number Density Spray System Using the Phase Doppler Particle Analyzer," AIAA Paper No. 88-0236, 25th Aerospace Sciences Meeting, Reno, NV.

Bulzan, D., 1988, "Particle-Laden Weakly Swirling Free Jets: Measurements and Predictions," NASA TM 100881.

Dodge, L. G., Rhodes, D. J., and Reitz, R. D., 1987, "Drop-Size Measurement Techniques for Sprays: Comparison of Malvern Laser-Diffraction and Aerometrics Phase Doppler," *Applied Optics*, Vol. 26, p. 2144.

Jackson, T. A., and Samuelsen, G. S., 1987, "Droplet Sizing Interferometry: A Comparison of the Visibility and Phase Doppler Techniques," *Applied Optics*, Vol. 26, p. 2137.

McDonell, V. G., Cameron, C. D., and Samuelsen, G. S., 1987, "Symmetry Assessment of an Air-Blast Atomizer," AIAA Paper No. 87-2136, 23rd Joint Propulsion Conference, San Diego, California; to appear in the *AIAA Journal of Propulsion*.

McDonell, V. G., and Samuelsen, G. S., 1988, "Evolution of the Two-Phase Flow in the Near Field of Air-Blast Atomizer Under Reacting and Non-reacting Conditions," *Proceedings, Fourth International Symposium on Applications of Laser Anemometry to Fluid Mechanics*, Lisbon, Portugal.

McDonell, V. G., Wood, C. P., and Samuelsen, G. S., 1987, "A Comparison of Spatially Resolved Drop Size and Drop Velocity Measurements in an Isothermal Chamber and a Swirl Stabilized Combustor," *Twenty-First Symposium (International) on Combustion*, pp. 685–694.

McVey, J. B., Russell, S., and Kennedy, J. B., 1987, "High Resolution Patternator for the Characterization of Fuel Sprays," *AIAA Journal of Propulsion*, Vol. 3, p. 202.

Mongia, H. C., and Reider, S. B., 1985, "Allison Combustion Research and Development Activities," AIAA Paper No. 85-1402, 21st Joint Propulsion Conference.

Mostafa, A. A., Mongia, H. C., McDonell, V. G., and Samuelsen, G. S., 1988, "On the Evolution of Particle-Laden Jet Flows: A Theoretical and Experimental Study," to appear in the *AIAA Journal,*.

Rudoff, R. C., and Bachalo, W. D., 1988, "Measurements of Droplet Drag Coefficients in a Polydispersed Turbulent Flow Field," AIAA Paper No. 88-0235, 25th Aerospace Sciences Meeting, Reno, NV.

Young, B. W., and Bachalo, W. D., 1987, "The Direct Comparison of Three In-Flight Droplet Sizing Techniques for Pesticide Spray Research," *Proceedings, International Symposium on Optical Particle Sizing: Theory and Practice*, Rouen, France.

Fuel Molecular Structure and Flame Temperature Effects on Soot Formation in Gas Turbine Combustors

Ö. L. Gülder

B. Glavinčevski

M. F. Baksh

National Research Council of Canada,
Division of Mechanical Engineering, M-9,
Ottawa, Ontario K1A OR6, Canada

A systematic study of soot formation along the centerlines of axisymmetric laminar diffusion flames of a large number of liquid hydrocarbons, hydrocarbon blends, and aviation turbine and diesel fuels was made. Measurements of the attenuation of a laser beam across the flame diameter were used to obtain the soot volume fraction, assuming Rayleigh extinction. Two sets of hydrocarbon blends were designed such that the molecular fuel composition varied considerably but the temperature fields in the flames were kept practically constant. Thus it was possible to separate the effects of molecular structure and the flame temperature on soot formation. It was quantitatively shown that the smoke point height is a lumped measure of fuel molecular constitution. The developed empirical relationship between soot volume fractions and fuel smoke point and hydrogen-to-carbon ratio was applied to five different combustor radiation data, and good agreement was obtained.

Introduction

In gas turbine combustors, the dominant mode of heat transfer to the combustor liner is thermal radiation, mainly caused by the presence of soot particles. The combustor liner temperature is dependent on the radiant emission from the flame, and the combustor life is directly related to its temperature. Therefore, the soot particle concentration in a given combustor as a function of fuel chemical structure and flame temperature is one of the major concerns. Recently, we have shown (Gülder et al., 1988) that a single fuel parameter (like smoke point, hydrogen content, or aromaticity) cannot adequately represent the sooting propensities of aviation turbine fuels. Since the amount of soot formed from a particular fuel has a very complex dependence on the overall combustion process, there exists no one characteristic parameter that can define the amount formed per unit mass of fuel burned (Glassman, 1988).

The ASTM smoke point, the minimum flame height at which soot just escapes from a laminar diffusion flame tip generated by a standard wick burner, has been used for decades to predict the soot formation tendency of aviation gas turbine fuels. In recent years, hydrogen content has been proposed as a better predictor of the sooting tendency of aviation fuels (Blazowski, 1979; Naegeli and Moses, 1980; Bowden et al., 1984). Also, total aromatic content of the fuel and polycyclic aromatic content have been used by some investigators to describe the soot radiation in combustors (Clark, 1984; Rosfjord, 1984). Each of these available sooting tendency predictors is being widely criticized because none of them are fully capable of describing the soot radiation encountered in gas turbine combustors.

It is almost clear that in diffusion flames, when physical effects are isolated, the soot formation rate is governed by the fuel chemical structure and the flame temperature (Glassman and Yaccarino, 1981; Gülder et al., 1988; Glassman, 1988). The fuel pyrolysis mechanism, as governed by the fuel's molecular structure and temperature, plays a dominant role in determining the soot formation rate. Since there is no oxidative attack on the fuel molecules in diffusion flames, the higher the flame temperature, the greater the soot formation rate.

This work constitutes the second part of previously reported results (Gülder et al., 1988). The present study focuses on the influence of hydrocarbon fuel molecular structure, in terms of carbon type distribution, and flame temperature on soot formation in diffusion flames in which physical effects are controlled. The experiments were designed such that the fuel structure and temperature effects can be differentiated. The appearance of soot, and the soot volume fraction in the core of the diffusion flames of liquid hydrocarbons, were determined from laser extinction measurements, and quantitatively related to fuel parameters defining molecular constitution and flame temperature.

The soot formation rate and mechanism in turbulent diffusion flames are complex and dynamic phenomena not governed by a single property of fuel or fuel-oxidant system, but by the fluid mechanics and thermodynamic conditions of the system as well as the molecular composition of the fuel. Therefore, it is suitable to lump the various effects into two classes: physical and chemical. In a gas turbine combustor, the major physical effects are spray characteristics, swirl/tur-

Contributed by the International Gas Turbine Institute and presented at the 34th International Gas Turbine and Aeroengine Congress and Exhibition, Toronto, Ontario, Canada, June 4-8, 1989. Manuscript received at ASME Headquarters February 14, 1989. Paper No. 89-GT-288.

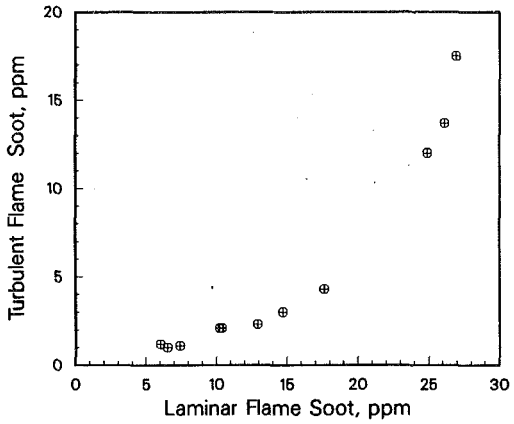

Fig. 1 Correlation of turbulent flame and laminar flame smoke point characteristic soot volume fractions; adapted from Kent (1987)

bulence structure, pressure, and combustor configuration. The molecular constitution of the fuel is responsible for the chemical part for a given temperature and equivalence ratio. This means that, for a given fuel, the response of different engines can be expected to be different (see, e.g., Rudey and Grobman, 1978). But for a given set of engine conditions, any change in soot formation rate will be mainly a function of the molecular structure of the fuel. Therefore, a comprehensive understanding of the effects of fuel molecular structure on soot formation rate and mechanism is essential in order to understand the soot formation in turbulent diffusion flames.

The most fundamental knowledge about the tendency of a fuel to soot can be obtained only from flame systems that are laminar in character. Apart from providing insights into soot formation and oxidation processes and helping the development of models, laminar diffusion flame studies are potentially of practical value in connection with radiant energy transfer and smoke emissions from turbulent flame systems (Markstein, 1988). Also, it is interesting to note that a good correlation has been shown to exist between maximum soot volume fractions of laminar diffusion flames and their turbulent counterparts, as shown in Fig. 1 (Kent, 1987).

Experimental Approach

A standard smoke point burner assembly (ASTM, 1980) was modified for the present experimental work. This burner provides an atmospheric pressure, overventilated diffusion flame in which the fuel is fed through a cylindrical wick. The burner consists of two closely fitting concentric tubes. The inner tube (wick tube) has an internal diameter of 4.7 mm and an external diameter of 6 mm. The external diameter of the outer tube is 9.9 mm. Flame height, and hence the fuel mass burning rate, is controlled by the up and down movement of the wick tube by a rack and pinion drive. The ends of the 80-mm-dia cylindrical burner housing (in which the burner tube is projected vertically from the lower side of the cylindrical surface and perpendicular to the housing centerline) were fitted with glass windows to provide optical access. Further details of the burner can be found in the ASTM Standard Test Method (1980), and it is very similar to the one used by Olson et al. (1985). The burner/reservoir assembly was mounted on a positioning platform with accurate vertical and horizontal movement capability.

The line of sight average soot volume fractions along the centerline of the flames were measured by the extinction of a He-Ne ($\lambda = 632.8$ nm) laser beam. The burner/reservoir assembly was moved vertically while keeping the optics stationary to obtain measurements over the flame length. The soot volume fraction can be calculated as follows, assuming Rayleigh extinction:

$$F = \frac{\lambda/L}{\mathrm{Im}\{(m^2-1)/(m^2+2)\}6\pi} \ln(I/I_0) \quad (1)$$

where λ is the laser wavelength, and I_0 and I are the incident and emerging laser light intensities, respectively. The complex refractive index of the soot particles, m, was taken as $m = 1.89 - 0.48i$ from Lee and Tien (1981). L is the optical path length, which is the visible flame diameter, at the flame height where extinction measurements are being made. L was determined from the flame photographs. Intensities of incident and emerging beams were measured by a photodiode detector, and background noise due to flame radiation was nullified.

The fuel mass burning rates of the flames at their smoke point were determined by weighing the burner/reservoir assembly at suitable intervals. Smoke points were determined as defined by ASTM (1980).

At this point, we define the different carbon atom types in hydrocarbon molecules for the purpose of characterizing the average molecular constitution of the fuel. This is essential for several reasons. The most important ones are that each member of a homologous series of hydrocarbons does not have the same sooting characteristics as the other members of the series (Olson et al., 1985), and that the identification and quantification of several hundreds of hydrocarbon components in a given transportation fuel are very arduous and time consuming, if at all possible. The carbon types that con-

Nomenclature

A = constant, equation (4)
a = constant, equation (3)
a_i = constants, equation (5), $i = 1, 2, \ldots, 8$
b = constant, equation (3)
C_{a1} = fraction of carbon atoms in condensed aromatic rings
C_{a2} = fraction of carbon atoms in monoaromatic rings
C_c = fraction of carbon atoms at β position; and CH and CH_2 carbons at γ, δ positions to aromatic rings, and of paraffinic carbons
C_d = fraction of methyl (CH_3) carbon atoms at γ, δ position to aromatic rings, and of paraffinic hydrocarbons
C_i = fraction of the ith type carbon atoms, $i = a1, a2, o, \alpha, c, d$
C_o = fraction of olefinic carbon atoms
C_α = fraction of carbon atoms at α position to aromatic rings
E = overall activation energy
F = line of sight soot volume fraction along the centerline
F_{max} = line of sight maximum soot volume fraction
H_i = hydrogen types, Fig. 2; $i = a1, a2, o, \alpha, c, d$
h = axial coordinate (along the flame axis)
I = attenuated laser beam intensity
I_o = incident laser beam intensity
L = laser light path length
m = complex refractive index of soot
$\dot{m}_f$ = fuel mass burning rate at smoke point
R = correlation coefficient
R_o = universal gas constant
S = smoke point flame height
T = soot temperature
Z = nondimensional axial coordinate, unity at visible flame height $= h/S$
λ = laser wavelength
ψ = atomic hydrogen-to-carbon ratio of the fuel

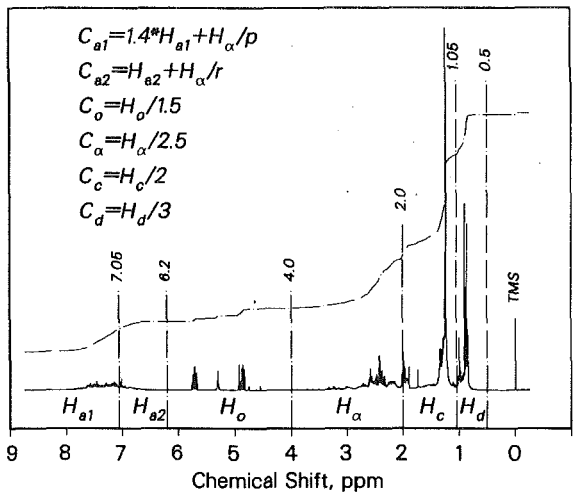

Fig. 2 A typical ^{1}H NMR spectrum showing six regions for the different hydrogen types of a hydrocarbon fuel, and the estimation of carbon type fractions from hydrogen distribution. The values of p and r are determined from the relative amounts of C_{a1} and C_{a2} assuming equal degrees of substitution on mono- and di-cyclic aromatic rings. The dot-dash line shows the integral of the proton spectrum.

stitute the basic structural groups of the global fuel characterization were selected after inspecting the sooting tendencies of different hydrocarbons reported in the literature, and our previous approach (Gülder and Glavinčevski, 1986a, 1986b) that was used to describe the ignition characteristics of complex hydrocarbons. We classify the carbon types in a hydrocarbon molecule as follows:

C_{a1}: carbon atoms in condensed aromatic rings;
C_{a2}: carbon atoms in monoaromatic rings;
C_0: olefinic carbon atoms;
C_α: carbon atoms at α position to aromatic rings;
C_c: carbon atoms at β position; and CH and CH_2 carbons at γ, δ positions to aromatic rings, and CH and CH_2 carbon atoms of paraffinic (*n-*, *iso*, and *cyclo-*) hydrocarbons;
C_d: methyl (CH_3) carbon atoms at γ, δ positions to aromatic rings, and CH_3 carbon atoms of paraffinic hydrocarbons.

In the present study, measurements were made with 51 fuels. Nine of them were transportation fuels, 12 were pure hydrocarbons, and 30 were mixtures blended from pure hydrocarbons. The rationale for the design of blends will be explained in the next paragraph. The characterization of the nine transportation fuels in terms of carbon types was made by proton nuclear magnetic resonance (^{1}H NMR). The spectra were determined at 90 MHz on a Varian EM-390 spectrometer using concentrations of approximately 50/50 by volume of sample to D-chloroform and 1 percent tetramethylsilane (TMS). The proton resonance signals of the fuels were divided into six regions of chemical shift values and the signals in each region were assigned to various types of hydrogen relative to TMS. The relative number of hydrogen atoms in each region was determined from the integral of the signals of the corresponding region. A typical ^{1}H NMR spectrum showing the six hydrogen regions, denoted by H_{a1}, H_{a2}, H_o, H_α, H_c, and H_d, with respect to TMS, and the method of estimation of carbon type fractions from hydrogen type distribution, are given in Fig. 2.

To separate the effects of fuel structure and flame temperature, two groups of fuels were blended from pure hydrocarbons such that the fuels have differing compositional features but the hydrogen-to-carbon ratio of the first group is 1.8, and that of the second group is 1.54. The adiabatic flame temperature of the fuels in group one is around 2270 ± 4 K, and for group two fuels around 2290 ± 4 K. The components of the hydrocarbon blends and their mole fractions are given in Table 1 along with the hydrogen-to-carbon ratios, and hydrogen type distributions of all 51 fuels.

For each fuel listed in Table 1, the smoke point, smoke point fuel mass burning rate, line of sight average light extinction, and optical path length along the flame centerline were determined. Maximum soot volume fractions, smoke points, and mass burning rates are tabulated in Table 1.

Results and Discussion

Soot Volume Fractions. Before discussing the soot volume fraction profiles, we will briefly show here the adequacy of the fuel hydrogen-to-carbon ratio control to fix the temperature field within the flame. The soot particle temperatures measured in liquid hydrocarbon diffusion flames by Olson et al. (1985) correlate very well with the hydrogen-to-carbon ratio. Since gas and soot particle temperatures should be within about 10 K for soot particles smaller in diameter than 0.1 μm in atmospheric flames (Olson et al., 1985), soot emission temperatures are representative of the gas temperatures. Also the equilibrium adiabatic flame temperatures for similar hydrocarbons have been shown to be a function of hydrogen-to-carbon ratio (Gülder, 1986). Although the rates of change of the two temperature values are not exactly the same, adiabatic flame temperatures, and in turn hydrogen-to-carbon ratios, adequately represent the relative magnitude of the actual flame temperatures. One precautionary remark here is in order. The adiabatic flame temperatures of the low carbon number gaseous alkynes and alkenes do not follow the adiabatic flame temperature trends of the liquid fuels listed in Table 1. These hydrocarbons have substantially higher flame temperatures than those of alkanes, aromatics, and high carbon number liquid alkenes.

The maximum soot volume fractions of the two groups of fuels with constant hydrogen-to-carbon ratios of $\psi = 1.8$ and $\psi = 1.54$ (fuels 1 to 17, and 18 to 25, respectively, in Table 1) are plotted versus smoke point heights in Fig. 3. Also included in Fig. 3 are the data for $\psi \approx 1.2$ and $\psi = 0.92$. The emission temperatures were calculated from the group-averaged soot parameter values measured by Olson et al. (1985). These temperatures provide a check on the constancy of flame temperature for the given constant hydrogen-to-carbon ratio. The nontrivial variation of maximum soot volume fraction, for a fixed hydrogen-to-carbon ratio, with fuel molecular structure clearly demonstrates the effect of fuel chemistry on soot formation in laminar diffusion flames. To our knowledge, this is the first time that the effects of fuel type and flame temperature on soot formation have been clearly and quantitatively differentiated for a broad range of liquid hydrocarbons. The extensive data reported by Olson et al. (1985) do not provide this separation due to the fact that the hydrocarbons selected exhibit a strong correlation between their smoke points and the hydrogen-to-carbon ratios, resulting in an overlap of the two effects.

Line of sight average soot volume fractions reach a maximum around $Z \approx 0.5$ (Fig. 4), which is consistent with the previous measurements (Kent, 1986; Olson et al., 1985). The unusual soot volume fractions for fuels 6 and 17 for $Z < 0.2$ are the result of absorption of light by heavy hydrocarbon vapors (Fig. 4), most probably by α-methylnaphthalene vapor in fuel 6, and by fluorene vapor in fuel 17. As can be seen from the soot volume fraction profiles of other fuels in Fig. 4, diphenylmethane, naphthalene, and cyclohexylbenzene vapors cause the absorption of light near the burner rim. From an inspection of the boiling points of the hydrocarbons that were used as fuels or blending components, it was found that those with boiling point temperatures higher than approximately 440–450 K absorb light significantly. With the hydrocarbons with boiling points near this temperature region (e.g.,

Table 1 Hydrogen-to-carbon ratios (ψ), smoke points (S, mm), smoke point fuel mass burning rates ($\dot{m}_f$, mg/s), line of sight average maximum soot volume fractions (F_{max}, ppm), and carbon type distributions of hydrocarbons, hydrocarbon blends, and transportation fuels used in this study

fuel#	Comp.[a]	ψ	S	$\dot{m}_f$	F_{max}	C_{a1}	C_{a2}	C_o	C_α	C_c	C_d
1	A/C/G[b]	1.8	17.	0.6	14.	0.	0.346	0.	0.116	0.304	0.234
2	C/G	1.8	21.	0.75	12.9	0.	0.357	0.	0.119	0.419	0.105
3	A/F	1.8	18.	0.64	13.8	0.	0.376	0.	0.063	0.21	0.351
4	A/D/F[c]	1.8	21.	0.75	12.6	0.	0.405	0.	0.068	0.286	0.241
5	A/E	1.8	22.5	0.81	12.5	0.	0.429	0.	0.	0.214	0.357
6	A/H	1.8	12.	0.42	16.2	0.244	0.	0.	0.025	0.274	0.457
7	A/G/H[d]	1.8	15.	0.53	14.5	0.135	0.15	0.	0.064	0.244	0.407
8	C/F	1.8	20.	0.71	13.2	0.	0.399	0.	0.067	0.428	0.107
9	B/E	1.8	28.	1.01	11.2	0.	0.415	0.	0.	0.418	0.167
10	B/F	1.8	22.	0.79	12.5	0.	0.364	0.	0.061	0.411	0.164
11	C/J	1.8	18.	0.64	13.6	0.	0.262	0.	0.087	0.53	0.122
12	H/N	1.8	14.	0.49	14.9	0.317	0.	0.	0.032	0.284	0.366
13	G/H/O[e]	1.8	15.	0.53	14.8	0.126	0.139	0.	0.059	0.338	0.338
14	K	1.8	22.5	0.81	12.3	0.	0.	0.	0.	1.	0.
15	A/B/E[f]	1.8	26.	0.94	11.6	0.	0.291	0.	0.	0.248	0.413
16	A/G/H[g]	1.8	14.	0.49	15.3	0.191	0.074	0.	0.044	0.259	0.432
17	C/F/Q[h]	1.8	21.	0.75	12.8	0.042	0.319	0.	0.057	0.466	0.116
18	U	1.54	13.3	0.47	16.7	0.	0.462	0.	0.077	0.385	0.077
19	C/R	1.54	10.5	0.36	17.6	0.414	0.	0.	0.035	0.441	0.11
20	A/P	1.54	11.	0.38	17.3	0.398	0.	0.132	0.066	0.152	0.253
21	C/F	1.54	15.	0.53	16.0	0.	0.603	0.	0.101	0.237	0.059
22	A/E	1.54	17.	0.6	15.3	0.	0.627	0.	0.	0.14	0.233
23	B/E	1.54	19.5	0.7	15.2	0.	0.619	0.	0.	0.272	0.109
24	A/H	1.54	9.	0.31	17.9	0.411	0.	0.	0.041	0.206	0.343
25	A/D/F[i]	1.54	13.5	0.47	16.8	0.	0.611	0.	0.102	0.156	0.131
26	B/T	2.03	31.	1.12	11.2	0.127	0.	0.	0.	0.623	0.249
27	A/T	2.08	25.	0.9	12.1	0.096	0.	0.	0.	0.339	0.565
28	C/T	2.03	31.	1.12	11.3	0.119	0.	0.	0.	0.705	0.176
29	A/F	1.72	14.7	0.52	14.5	0.	0.437	0.	0.073	0.184	0.306
30	A/F	1.91	20.2	0.72	13.3	0.	0.291	0.	0.049	0.248	0.413
31	A/F	2.04	25.8	0.93	12.	0.	0.184	0.	0.031	0.294	0.491
32	A/F	2.1	30.2	1.09	11.1	0.	0.129	0.	0.021	0.319	0.531
33	R	0.92	5.	0.16	22.	0.923	0.	0.	0.077	0.	0.
34	V	1.4	10.	0.34	17.2	0.	0.6	0.	0.1	0.2	0.1
35	W	1.4	10.	0.34	17.8	0.	0.6	0.	0.1	0.1	0.2
36	X	1.4	9.	0.31	17.2	0.	0.6	0.	0.1	0.1	0.2
37	S	1.33	9.	0.31	18.7	0.	0.5	0.	0.083	0.417	0.
38	P	1.22	7.	0.23	18.9	0.667	0.	0.222	0.111	0.	0.
39	L	1.2	8.	0.27	19.	0.	0.6	0.	0.2	0.2	0.
40	F	1.14	9.8	0.34	19.2	0.	0.857	0.	0.143	0.	0.
41	A	2.25	42.8	1.56	9.7	0.	0.	0.	0.	0.375	0.625
42	Y	2.	41.	1.49	9.9	0.	0.	0.25	0.	0.625	0.125
43	Z	1.81	15.	0.53	14.7	0.09	0.072	0.	0.084	0.565	0.189
44	Z	1.75	15.	0.53	14.8	0.062	0.077	0.	0.069	0.593	0.199
45	Z	1.97	21.	0.75	12.5	0.068	0.063	0.	0.055	0.571	0.243
46	Z	2.01	26.	0.94	11.4	0.063	0.052	0.	0.048	0.575	0.262
47	Z	2.02	25.	0.9	11.1	0.056	0.055	0.	0.047	0.577	0.265
48	Z	1.99	26.	0.94	11.3	0.08	0.069	0.	0.054	0.546	0.251
49	Z	1.93	22.5	0.81	12.	0.09	0.058	0.	0.059	0.567	0.239
50	Z	1.94	22.	0.79	12.	0.081	0.072	0.	0.065	0.541	0.241
51	Z	1.83	15.	0.53	15.	0.	0.317	0.033	0.097	0.311	0.241

[a] A : isooctane; B : n-heptane; C : n-decane; D : n-hexadecane; E : benzene; F : toluene; G : p-xylene; H : α-methylnaphthalene; J : indan; K : cis-decalin; L : tetralin; N : heptamethylnonane; O : 2-methylpentane; P : α-methylstyrene; Q : fluorene; R : diphenylmethane; S : cyclohexylbenzene; T : naphthalene; U : 1-phenylheptane; V : n-butylbenzene; W : iso-butylbenzene; X : sec-butylbenzene; Y : 1-octene; Z : transport.fuels

[b] mole fractions : 0.3/0.24/0.46

[c] mole fractions : 0.35/0.177/0.473

[d] mole fractions : 0.651/0.2/0.149

[e] mole fractions : 0.185/0.138/0.677

[f] mole fractions : 0.275/0.303/0.422

[g] mole fractions : 0.691/0.099/0.21

[h] mole fractions : 0.582/0.372/0.046

[i] mole fractions : 0.191/0.096/0.713

butylbenzenes, *n*-decane, and indan), attenuation of the laser beam was very small near the burner rim, and presence of fuel vapor absorption was only noticeable after comparisons with the soot volume fraction profiles of the relatively lighter hydrocarbon flames. In the case of transportation fuels (43 to 51 in Table 1), only the flame of fuel 51 did not cause any measurable attenuation near the burner (Fig. 4), whereas the flames of all other transportation fuels, which contain condensed aromatic ring hydrocarbons (see Table 1), did attenuate the laser beam. Although these fuels were not analyzed for the presence of nonaromatic heavy hydrocarbons, estimated molecular weights and the distillation curves in-

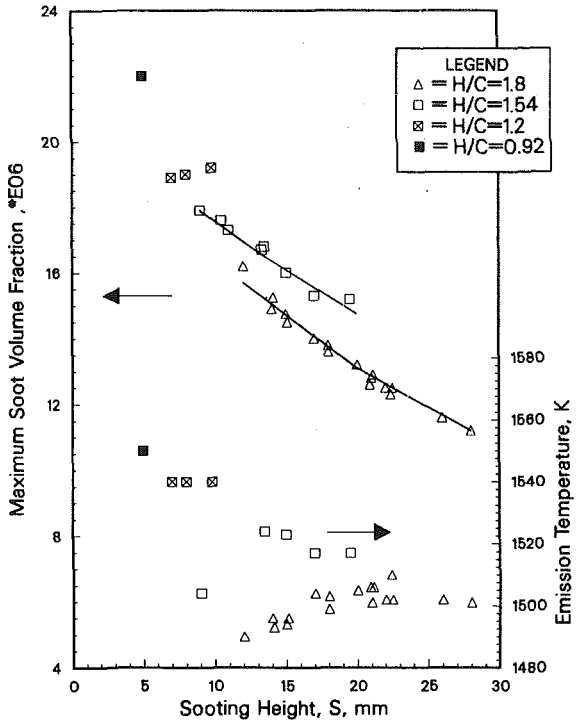

Fig. 3 Variation of the maximum soot volume fraction with smoke point of the fuel for $\psi = 1.8$, 1.54, ≈ 1.2, and 0.92; emission temperatures were computed from the data given by Olson et al. (1985)

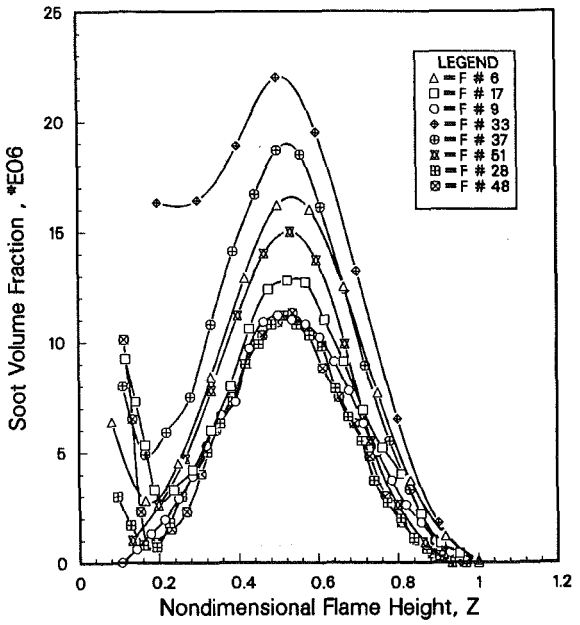

Fig. 4 Line of sight average soot volume fraction profiles along the centerline of the flames of fuels 6, 9, 17 ($\psi = 1.8$), and fuels 28, 33, 37, 48, and 51

dicate the presence of heavy saturated hydrocarbon components. However, for a definitive picture, experiments including fluorescence and direct space resolved sampling measurements should be conducted with liquid hydrocarbon flames.

Soot volume fraction profiles (shown in Fig. 4) were normalized such that the normalized soot volume fraction is F/F_{max}, where F_{max} is the maximum soot volume fraction for a given flame. Eliminating the data points due to heavy hydrocarbon fuel vapor light absorption ($Z < 0.2$), we obtain the normalized soot volume fraction profiles as a function of

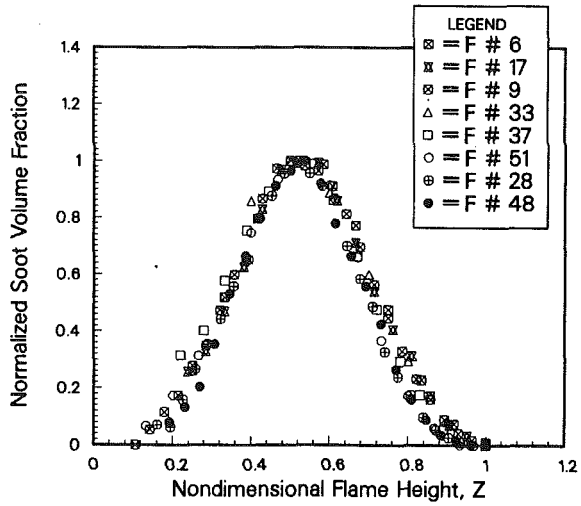

Fig. 5 Normalized soot volume fraction profiles along the centerline of the flames (same data as in Fig. 4)

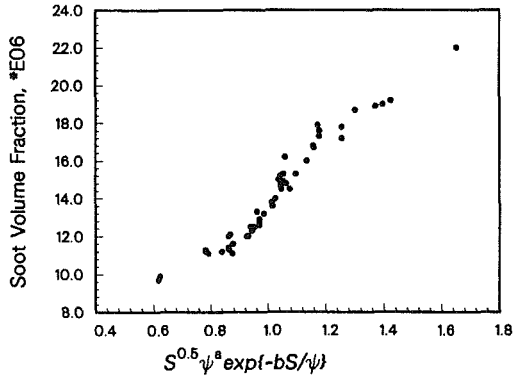

Fig. 6 Correlation between the line of sight average maximum soot volume fraction and the function k, equation (3); the correlation coefficient is $R = 0.985$; constants are as follows: $a = -1.18$ and $b = 0.0738$

Z (Fig. 5). It should be noted here that the data in Fig. 5 represent normalized soot volume fractions ranging from 11.3 ppm to 22 ppm (fuels 28 and 33, respectively). Normalized soot volume fractions for different fuels coincide very well (Fig. 5), supporting the proposition of profile similarity (Kent, 1986) along the flame axis.

Soot Formation Rate and Smoke Point. Assuming that the rate of formation of soot in diffusion flames can be globally represented by an Arrhenius type rate expression, i.e.,

$$\frac{dF}{dt} \propto f(T)\exp\{-E/R_0T\} \tag{2}$$

and that the residence times of laminar diffusion flames burning at their smoke point conditions are proportional to the square root of the visible flame height (Roper, 1977), we can write that the maximum soot volume fraction is

$$F_{max} \propto k = S^{0.5}\psi^{a}\exp\{-bS/\psi\} \tag{3}$$

Equation (3) further assumes that the activation energy E is proportional to molecular constitution represented by the smoke point height S (this will be quantitatively shown to be true later), and that the temperature field can be represented by the hydrogen-to-carbon ratio ψ for given initial conditions. The last assumption is restricted to the liquid fuel hydrocarbon classes and their complex mixtures considered in this work, which cover a broad range of petroleum based transportation fuels. The constants a and b are to be determined from experimental data. Data presented in Table 1 were used to estimate the constants a and b. Figure 6 shows the correlation

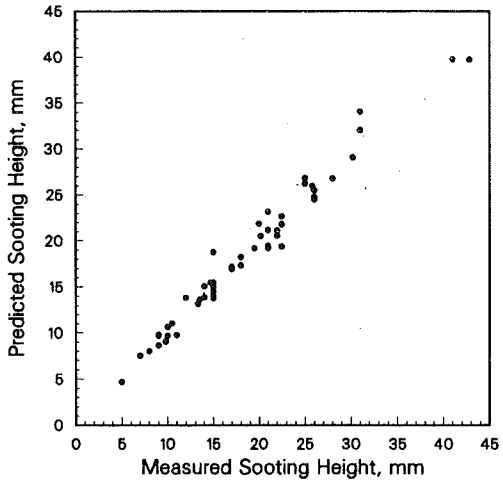

Fig. 7 Predicted smoke point heights versus measured ones; all data points in Table 1 are included; correlation coefficient is $R = 0.987$

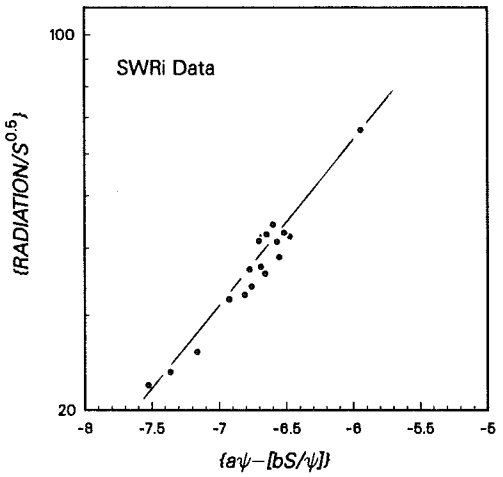

Fig. 8 Correlation of flame radiation to the function given by equation (3); experimental data from Naegeli and Moses (1980), obtained on a T-63 combustor

between F_{max} and the function k. A strong correlation ($R^2 = 0.985$) implies that the fuel molecular constitution and the hydrogen-to-carbon ratio dominate the soot formation in laminar diffusion flames.

The following expression relates the smoke point to the six carbon types and the hydrogen-to-carbon ratio. Since a physical or chemical model is difficult to propose at this stage, we tried polynomial, power law, and exponential expressions to fit the data. Based on a *goodness of fit* analysis, we selected the exponential dependence of S on C_i and ψ, i.e.,

$$S = A \cdot \exp\{f(C_i; \psi)\} \tag{4}$$

The form of the function f in terms of C_i and ψ was selected through an optimization procedure using multivariate regression techniques. To start the optimization procedure, f was assumed to be presented by a linear combination of polynomials containing ψ^n and C_i^n (where $n = 1, 2, 3$). Those terms that do not contribute significantly to the value of S as compared to the other terms were eliminated. This procedure resulted in the following expression:

$$f(C_i; \psi) = a_1\psi^2 + a_2 C_{a1} + a_3 C_{a2} + a_4 C_o + a_5 C_\alpha + a_6 C_\alpha^2 + a_7 C_c + a_8 C_d \tag{5}$$

Adjustable constants A and a_i were determined using the data given in Table 1 as $a_1 = 0.651$, $a_2 = -5.144$, $a_3 = -4.583$, $a_4 = -4.563$, $a_5 = -9.94$, $a_6 = 13.733$, $a_7 = -5.456$, $a_8 = -6.394$, and $A = 618$. The significance of these fitting parameters was verified by checking the t- and F-statistics, and they were shown to represent a confidence interval of 98 percent or better. With these constants, equations (4) and (5) represent the data obtained in this work with good accuracy (Fig. 7). The expected error in predictions of F_{max} by equations (3)–(5) is less than 5 percent.

An inspection of equation (5) and the coefficients of the variables show the degree of contribution of each carbon type to the soot volume fraction. Although the behavior of the C_α carbon in equation (5) is nonlinear, for possible fractions of C_α, at a given ψ value, we observe the following, in order of decreasing contribution to maximum soot volume fraction:

$$C_\alpha > C_d > C_c > C_{a1} > C_{a2} \approx C_o \tag{6}$$

Of course, this is an unexpected result. This expression, equation (6), indicates that, for a given constant ψ value, the carbon types C_α and C_d contribute to soot volume fraction levels more than the aromatic ring carbons, C_{a1} and C_{a2}, and olefinic carbons, C_o. Discussion of this result is reported in detail elsewhere (Gülder, 1988).

Implications for Gas Turbine Combustors. It has been shown that a linear relationship exists between smoke point heights and the smoke point heat release rates (Markstein, 1987), and the radiative fraction of heat release rate at the smoke point has been found to be strongly correlated with smoke point characteristics of the diffusion flame (Markstein, 1988). Kent (1986) and Gülder (1988) have presented formulations to demonstrate that radiant emissions from a soot-laden flame can be described by smoke point maximum soot volume fraction F_{max} and other fuel properties. Since equation (3) expresses maximum soot volume fraction in terms of smoke point height and the hydrogen-to-carbon ratio, we have used equation (3) for describing the radiation heat flux in combustors by employing the independent data sets from combustors. Although equation (3) is semi-empirical in nature, it is more sound in principle than the form of the empirical expression we used previously (Gülder et al., 1988).

Flame radiation data obtained in a T-63 combustor by Naegeli and Moses (1980) have been used to correlate the measured flame radiation to the function given by equation (3). The result is shown in Fig. 8.

The function given by equation (3) has also been used to correlate the flame radiation data obtained in a Tyne combustor by Carrier and Wetton (1988), and data obtained in a generic combustor by Rosfjord (1984); results are shown in Figs. 9 and 10, respectively.

The significance of the results shown in Figs. 8 to 10 is that the same function, in terms of smoke point and hydrogen-to-carbon ratio of the fuel, can describe the radiative heat transfer in different gas turbine combustors. Of course, the values of the adjustable constants, a and b, are different for the three combustors (Table 2).

Two other sets of data on flame radiation in combustors have also shown reasonable agreement with equation (3). The first set of data is from a J79-17A combustor (Gleason et al., 1979). The radiant heat flux versus equation (3) is shown in Fig. 11 for the three operating conditions. Although the agreement is not as good as the previous data shown in Figs. 8 to 10, the fit in Fig. 11 is superior to either of the correlations of radiant heat flux to the smoke point or to the hydrogen content. The second data set is from a Pratt and Whitney combustor (PT6A-65 engine, Gratton et al., 1987). The result is shown in Fig. 12. Again, the fit in Fig. 12 ($R = 0.93$) is superior to either of the correlations of radiant heat flux to the smoke point ($R = 0.75$) or to the hydrogen content ($R = 0.6$).

Equations (4) and (5) prove that the smoke point is an indicator of the fuel molecular structure. Equation (3) shows that hydrogen-to-carbon ratio and smoke point of the fuel

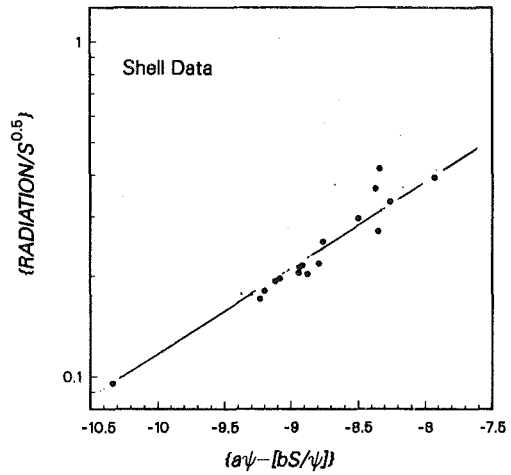

Fig. 9 Correlation of normalized flame radiation to the function given by equation (3); experimental data from Carrier and Wetton (1988), obtained on a Tyne combustor

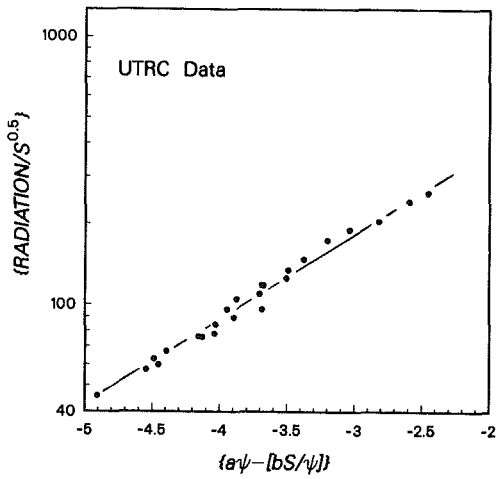

Fig. 10 Correlation of flame radiation to the function given by equation (3); experimental data from Rosjford (1984), obtained on a generic gas turbine combustor

Table 2 Values of the adjustable constants of equation (3) for the three combustor radiation data, and for the laminar flame maximum soot volume fraction data of this work. Last column of the table gives the correlation coefficient R between the terms in $\{\text{Radiation}/S^{0.5}\}$ and $\{a\psi - [bS/\psi]\}$.

Data Source	a	b	R
Naegeli and Moses (1980)	-3.21	0.092	0.98
Carrier and Wetton (1987)	-4.31	0.052	0.96
Rosfjord (1984)	-1.75	0.064	0.99
Laminar Flame Data	-1.18	0.074	

should be used concomitantly to describe the sooting propensity of a given hydrocarbon fuel. Of course, this point seems to be in sharp contrast to most previous studies in which the flame properties related to soot have been correlated either to the smoke point or to the hydrogen-to-carbon ratio. This stems from the fact that for distillate aviation turbine fuels obtained from conventional sources, hydrogen-to-carbon ratios are generally correlatable to smoke points. This implies that, in terms of fuel carbon type structure, C_α/C_{a1}, C_α/C_{a2}, and C_c/C_d ratios do not vary much from one fuel to the other. However, for unconventional fuels obtained from tar sands, shale oil, or coal liquids through different processes, including hydrogenation, these structural parameter ratios vary considerably, to the extent that hydrogen-to-carbon ratios and smoke points display a very poor correlation.

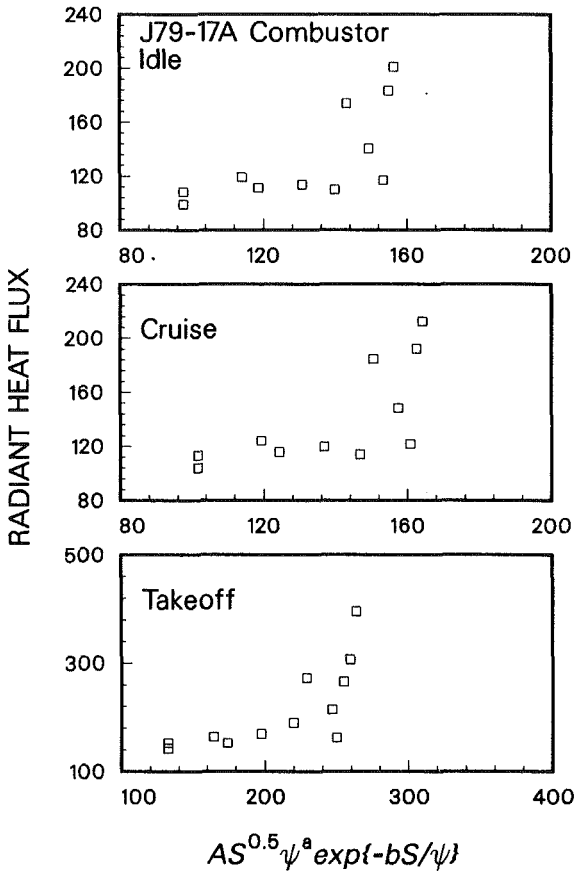

Fig. 11 Correlation of flame radiation data to the function given by equation (3); experimental data from Gleason et al. (1979), obtained on a J79-17A combustor

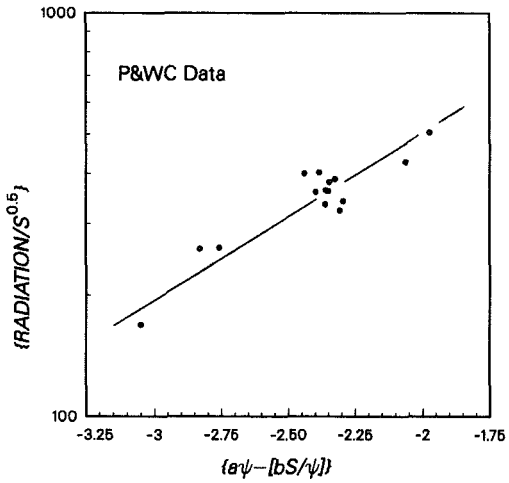

Fig. 12 Correlation of flame radiation data to the function given by equation (3); experimental data from Gratton et al. (1987), obtained on a PT6A-65 engine combustor

Concluding Remarks

It has been shown that the smoke point of a complex hydrocarbon mixture is a lumped measure of the fuel molecular structure. Carbon groups that have a dominant effect on the soot formation characteristics of hydrocarbon fuels have been identified. A fast and reliable technique of characterizing the fuel molecular structure in terms of these carbon types has been described.

The soot yields of diffusion flames with two groups of fuels with constant hydrogen-to-carbon ratios of 1.54 and 1.8 showed that the sooting tendency of hydrocarbon fuels cannot be described by a single fuel property like hydrogen-to-carbon ratio, smoke point, or aromaticity. Smoke point and hydrogen-to-carbon ratio are complementary to each other in describing the sooting propensities of complex hydrocarbon mixtures. This has been further tested sucessfully by using five sets of independent flame radiation data obtained by other investigators on gas turbine combustors. These results strongly support our proposition that in diffusion flames the soot formation rate and soot yields are controlled by the fuel molecular composition indicated by the smoke point and hydrogen-to-carbon ratio.

References

ASTM, 1980, *Standard Test Method for Smoke Points of Aviation Turbine Fuels*, 1975 (reapproved 1980).

Blazowski, W. S., 1979, "Dependence of Soot Production on Fuel Blend Characteristics and Combustion Conditions," ASME JOURNAL OF ENGINEERING FOR POWER, Vol. 102, pp. 403–408.

Bowden, T. T., Pearson, J. H., and Wetton, R. J., 1984, "The Influence of Fuel Hydrogen Content Upon Soot Formation in a Model Gas Turbine Combustor," ASME JOURNAL OF ENGINEERING FOR GAS TURBINES AND POWER, Vol. 106, pp. 789–794.

Carrier, D. M., and Wetton, R. J., 1988, "Prediction of Combustion Performance of Aviation Kerosines Using a Novel Premixed Flame Technique," ASME JOURNAL OF ENGINEERING FOR GAS TURBINES AND POWER, Vol. 110, pp. 100–105.

Clark, J. A., 1984, "Fuel Property Effects on Radiation Intensities in a Gas Turbine Combustor," *AIAA Journal*, Vol. 20, No. 2, pp. 274–281.

Glassman, I., 1988, "Soot Formation in Combustion Processes," *22nd Symposium (Int'l) on Combustion*, Vol. 22 (in press).

Glassman, I., and Yaccarino, P., 1981, "The Temperature Effect in Sooting Diffusion Flames," *18th Symposium (Int'l) on Combustion*, Vol. 18, pp. 1175–1183.

Gleason, C. C., Oller, T. L., Shayeson, M. W., and Bahr, D. W., 1979, "Evaluation of Fuel Character Effects on J79 Engine Combustion System," AFAPL-TR-79-2015, Wright-Patterson Air Force Base, OH.

Gratton, M., Critchley, I., and Sampath, P., 1987, "Alternative Fuels Combustion Research," AFWAL-TR-84-2042, Wright-Patterson Air Force Base, OH.

Gülder, Ö. L., 1986, "Flame Temperature Estimation of Conventional and Future Jet Fuels," ASME JOURNAL OF ENGINEERING FOR GAS TURBINES AND POWER, Vol. 108, pp. 376–380.

Gülder, Ö. L., 1988, "Influence of Hydrocarbon Fuel Structural Constitution and Flame Temperature on Soot Formation in Laminar Diffusion Flames," *Combustion and Flame* (in press).

Gülder, Ö. L., and Glavincevski, B., 1986a, "Prediction of Cetane Number of Diesel Fuels From Carbon Type Structural Composition Determined by Proton NMR Spectroscopy," *Industrial and Engineering Chemistry Product Research and Development*, Vol. 25, pp. 153–156.

Gülder, Ö. L., and Glavincevski, B., 1986b, "Ignition Quality Determination of Diesel Fuels From Hydrogen Type Distribution of Hydrocarbons," *Combustion and Flame*, Vol. 63, pp. 231–238.

Gülder, Ö. L., Glavincevski, B., and Das, S., 1989, "Effect of Molecular Structure on Soot Formation Characteristics of Aviation Turbine Fuels," ASME JOURNAL OF ENGINEERING FOR GAS TURBINES AND POWER, Vol. 111, pp. 77–83.

Kent, J. H., 1986, "A Quantitative Relationship Between Soot Yield and Smoke Point Measurements," *Combustion and Flame*, Vol. 63, pp. 349–358.

Kent, J. H., 1987, "Turbulent Diffusion Flame Sooting—Relationship to Smoke-Point Test," *Combustion and Flame*, Vol. 67, pp. 223–233.

Lee, S. C., and Tien, C. L., 1981, "Optical Constants of Soot in Hydrocarbon Flames," *18th Symposium (Int'l) on Combustion*, Vol. 18, pp. 1159–1166.

Markstein, G. H., 1987, "Radiant Emission and Smoke Points for Laminar Diffusion Flames of Fuel Mixtures," *21st Symposium (Int'l) on Combustion*, Vol. 21, pp. 1107–1114.

Markstein, G. H., 1988, "Correlations for Smoke Points and Radiant Emission of Laminar Hydrocarbon Diffusion Flames," *22nd Symposium (Int'l) on Combustion*, Vol. 22 (in press).

Naegeli, D. W., and Moses, C. A., 1980, "Effect of Fuel Molecular Structure on Soot Formation in Gas Turbine Engines," ASME Paper No. 80-GT-62.

Olson, D. B., Pickens, J. C., and Gill, R. J., 1985, "The Effects of Molecular Structure on Soot Formation. II. Diffusion Flames," *Combustion and Flame*, Vol. 62, pp. 43–60.

Rosfjord, T. J., 1984, "Role of Fuel Chemical Properties on Combustor Radiative Heat Load," AIAA Paper No. AIAA-84-1493.

Rudey, R. A., and Grobman, J. S., 1978, "Impact of Future Fuel Properties on Aircraft Engines and Fuel Systems," Paper No. 6, AGARD Lecture Series, No. 96, *Aircraft Engine Future Fuels and Energy Conservation*, AGARD LS-96.

Spray Characterization and Turbulence Properties in an Isothermal Spray With Swirl

A. Breña de la Rosa

W. D. Bachalo

R. C. Rudoff

Aerometrics, Inc.,
Sunnyvale Technology Center,
Sunnyvale, CA 94089

The present work reports an experimental study of the effect of swirl on the dynamic behavior of drops and on the velocity and turbulence fields of an isothermal spray using a two-component Phase Doppler Particle Analyzer (PDPA). It represents the first phase of an effort to investigate the effect of swirl on the structure of liquid spray flames, the stability of the flame, and its effect on the emission of pollutants. A vane-type swirler was placed on the liquid supply tube of a pressure atomizer and tested in the wind tunnel under specified conditions. Mean velocity and turbulence properties were obtained for the gas phase. In addition, drop velocity and drop size distributions, particle number densities, and volume flux were measured at different locations within the swirling flow. Large differences in the spatial distribution of the drops over its size, velocity, and number density are observed when the spray in coflowing air with the same axial velocity is compared with the atomizer spraying into the swirling flow field. Large drops seem to be recirculated into the core of the swirling flow, while rather small drops surround this central region. The radial distribution of particle number density and the liquid volume flux are also different when the atomizer spraying into the coflowing air and into the swirling field are compared. Particle number densities for the latter exhibit higher peak values close to the nozzle; but show almost the same peak values as in the coflowing case but at a different radial location further downstream. The velocity of specific drop sizes was also obtained. Drops as large as 5 μm are seen to follow closely the mean velocity of the gas. The turbulence properties of the swirling flow show significant influence on the dynamic behavior of the drops. Radial distributions of turbulence kinetic energy, normal Reynolds stresses, and Reynolds shear stresses exhibit double peak values, which delineate the boundaries of the central recirculation region and the external free stream. Within these boundaries the radial distribution of both particle number density and volume flux are seen to attain their maximum values.

Introduction

Swirl generation is by far the most extensively used mechanism for stabilizing the flame and for controlling the efficiency and generation of pollutants in combustion systems (Gupta et al., 1984). While swirl burners have been used widely in combustion, it is only recently that a major effort has been put into understanding the basic mechanisms that govern swirl flows (Sislian and Cusworth, 1986; Cameron et al., 1988; to name but a few). Both innovative diagnostic techniques and analytical/numerical studies are needed to be able to predict and control with a reasonable degree of success the combustion efficiency and the concentration levels of various pollutant species such as NO_x, CO, soot, and other particulates generated in the combustion process.

One of the major obstacles in the study of swirl flows has been the difficulty in obtaining turbulence data, mainly because of the limited instrumentation available for the analysis of these highly complex flows. Many excellent papers have dealt with swirl flows in both isothermal and reactive fields, the majority of which have investigated gaseous fuels. Because of the inherent complexity of having a liquid phase in the form of small drops coupled to the gaseous phase, liquid swirling flows have been studied less comprehensively.

The present paper differs from the previous work in its scope. It is intended to investigate the coupling of the liquid phase to the gaseous phase and the response of the spray drops to the swirling field. Thus, the main interest is in the influence that swirl has on the velocity and turbulence gas fields, and its overall effect on the properties of an isothermal spray, i.e., on the spatial distribution of drops, on their number density, and on their velocity field. It is also intended for these studies to provide a data base from which modelers in spray combustion

Contributed by the International Gas Turbine Institute and presented at the 34th International Gas Turbine and Aeroengine Congress and Exhibition, Toronto, Ontario, Canada, June 4-8, 1989. Manuscript received at ASME Headquarters February 14, 1989. Paper No. 89-GT-273.

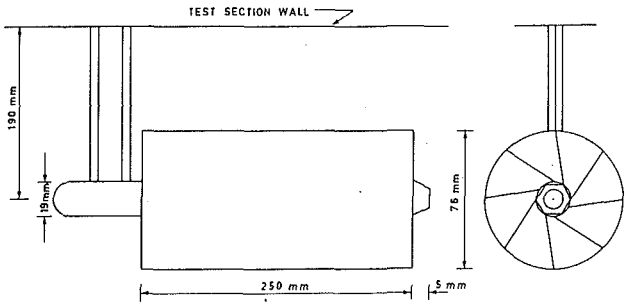

Fig. 1 Schematic of the swirl vane assembly fitted to the liquid supply tube of the atomizer inside the wind tunnel test section.

systems can extract the necessary information for their numerical codes. The present investigation is not a comparison study; a few measurements in coflowing air have been included to emphasize the effect that swirl has on the spray.

Experimental Setup

The experiments were carried out in a 46×46 cm wind tunnel using a vane-type swirler fitted to the liquid supply tube (12.5 mm i.d.) of a commercial pressure swirl atomizer. The swirl nozzle assembly was positioned at a downstream distance where the flow conditioner and screens produced a homogeneous flow with the cross-sectional area of the wind tunnel.

The swirler tested in this investigation consisted of a hub with 19 mm i.d. and eight straight vanes welded equidistantly to it, forming an angle of 20 deg with the longitudinal axis of the swirler. The set of vanes and the hub were placed inside a tube with 76 mm i.d. and 250 mm in length and the whole assembly fitted to the nozzle supply tube (see Fig. 1). The length of the swirl vanes varied according to their angle of inclination, but they blocked the whole cross-sectional area of the swirl housing, such that it was not possible to see through the swirl assembly.

The measurements were obtained with an Aerometrics two-component Phase Doppler Particle Analyzer (PDPA) and the axial, radial, and tangential velocity components of the swirling field evaluated with the airflow seeded with micron size particles only, with the seed particles and the spray drops simultaneously in the flow, and with the spray alone in the swirling field. The 20 deg vane swirler gave a nominal swirl number of $S = 0.26$ [8]. Radial scans of the flow field were taken at six different axial locations, namely, $X = 10$, 20, 50, 100, 150, and 200 mm downstream from the face of the atomizer to evaluate the velocity and turbulence fields. At these same positions (except at $X = 10$ mm where only velocity information was obtained), measurements of drop size, drop velocity, size-velocity correlations, number density, and volume flux were obtained for a water spray in the swirling field. At each axial position the radial measurements were obtained at 2-mm intervals from the centerline of the nozzle to the periphery of the flow field. For comparison purposes, measurements of these properties were also obtained for the same pressure swirl atomizer spraying water in coflowing air with the same free-stream velocity, $U_{fs} = 20$ m/s.

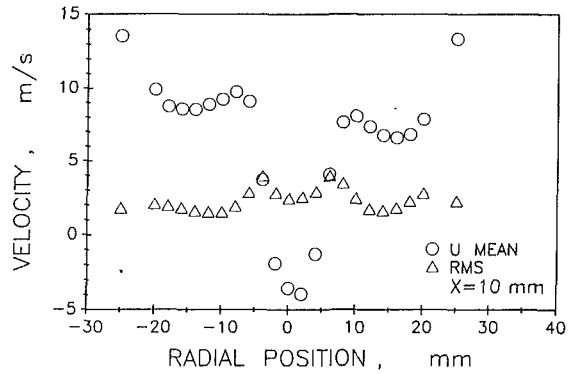

Fig. 2 Axial mean velocity and rms velocity of the seed particles obtained at $X = 10$ mm downstream of the 20 deg vane swirler, $S = 0.26$

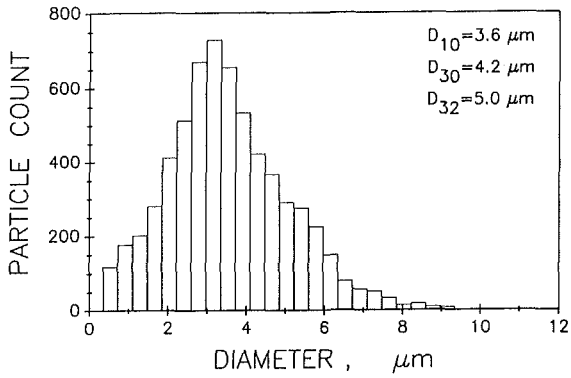

Fig. 3 Histogram of particle sizes and average diameters obtained for the seed particles used in the present investigation

Results and Discussion

The nozzles used in the present investigation were two Hago 45 deg solid cone, pressure swirl atomizers of 0.5 GPH and 3.0 GPH nominal flow rates, respectively. Only the measurements using the 3.0 GPH nozzle are reported here, which was operated at a pressure of $P_a = 415$ kPa. The wind tunnel free-stream velocity was set at $U_{fs} = 20$ m/s in all the experiments reported here.

In order to investigate the symmetry of the velocity field produced by the 20 deg vane swirler, a diametral scan of the mean and rms velocities was obtained at an axial distance of $X = 10$ mm from the face of the atomizer (without spraying) with the flow seeded with particles only (see Fig. 2). The size of the seed particles was also investigated. It is a common statement in the literature to report 1 μm size particles as the "maximum size" of the particles contained in the seed size distribution. This is actually quite uncommon, since the seed particles are distributed over a much larger size range than what is nominally quoted. Figure 3 is a histogram of sizes of the seed particles produced by the vaporizer used in the present study. The particles were introduced upstream of the swirler to form a homogeneous cloud of vapor over most of the cross-sectional area of the test section.

Nomenclature

D = internal diameter of swirl vane assembly
N_d = particle number density
R = radial position
S = degree of swirl
u', v', w' = axial, radial, and tangential fluctuating components of velocity
$\bar{u}, \bar{v}, \bar{w}$ = axial, radial, and tangential mean components of velocity
u, v, w = axial, radial, and tangential instantaneous components of velocity
X = axial distance from nozzle

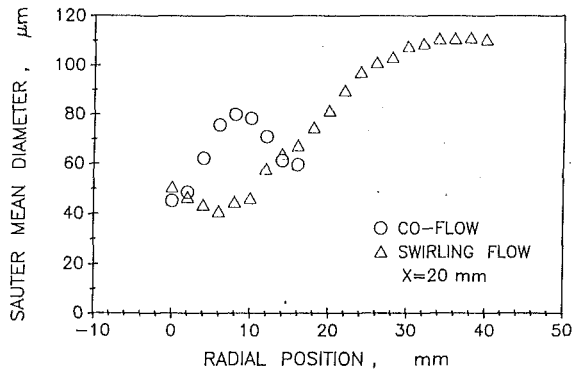

Fig. 4 Distribution of the Sauter mean diameter at $X = 20$ mm for a 3 GPH, 45 deg solid cone pressure atomizer spraying in coflowing air and downstream of a 20 deg vane swirler, $S = 0.26$; free-stream velocity $U_{fs} = 20$ m/s, atomization pressure $P_a = 415$ kPa

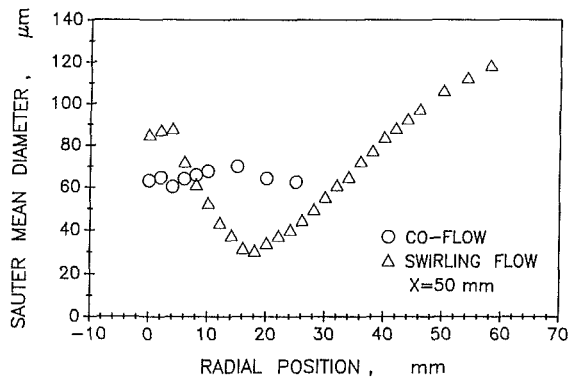

Fig. 5 Distribution of the Sauter mean diameter at $X = 50$ mm; same conditions as in Fig. 4

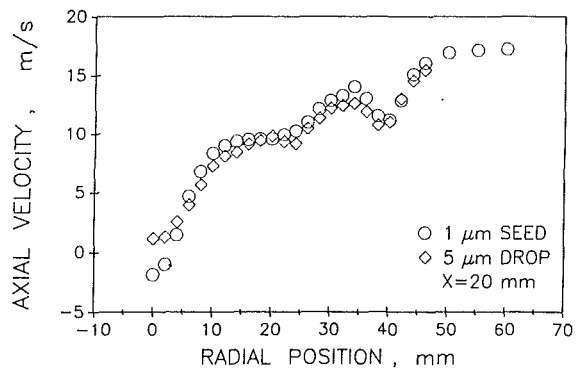

Fig. 6 Distribution of the average axial velocity of 1 μm seed particles and 5 μm drops at $X = 20$ mm; same conditions as in Fig. 4

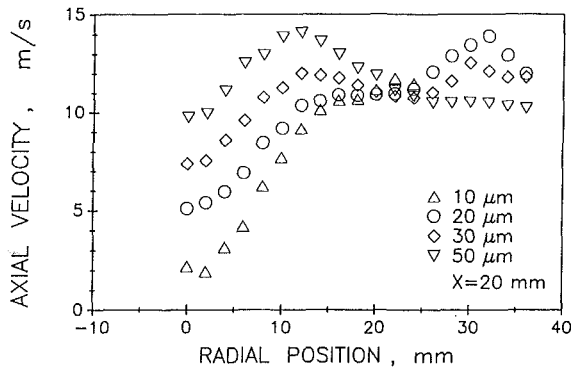

Fig. 7 Distribution of the average axial velocity for drop sizes of 10, 20, 30, and 50 μm diameter at $X = 20$ mm; swirling flow, $S = 0.26$; same conditions as in Fig. 4

Figures 4 and 5 show the radial distribution of Sauter mean diameter at various positions downstream from the atomizer. Figure 4, which is a comparison of the Sauter mean diameter D_{32} obtained for the nozzle spraying in coflowing air and in the swirling field, shows that smaller drops are observed in the central core region for the swirl/nozzle configuration due to the vigorous mixing induced by the swirler. Some very large drops were also observed in the core, evidencing the effect of large drops being recirculated from the periphery of the spray back into the central core. At an axial location of approximately $X/D = 0.66$ ($X = 50$, $D = 76$ mm) (Fig. 5), relatively big drops were observed in the core of the swirling field, yielding higher values of D_{32}. The radial distribution of D_{32} at this axial position decreased from its centerline value to a minimum at approximately $R/D = 0.25$ and subsequently increased toward the periphery of the spray. In contrast, the spray in coflowing air shows, as expected, a narrower distribution of drop sizes in the core with progressively wider distributions and larger values of D_{32} toward the periphery of the spray. Farther downstream at $X/D = 1.97$ and $X/D = 2.63$ ($X = 150$, $X = 200$ mm), not shown, away from the effect of the swirler, small drops are found in the core with increasing concentration of the larger ones at increasing radial distance and the shape of the profiles becomes similar for the spray in coflowing air and in the swirling field.

Experiments taken with the seed particles and the spray simultaneously in the flow show the liquid drops of sizes up to 5 μm in diameter following, to a reasonable accuracy, the fluctuations of the gas flow about its mean property values. The mean axial velocity of 1 μm seed particles was compared with the mean axial velocity of 1, 2, 3, and 5 μm drops at three axial stations: $X = 20$, 50, and 100 mm. Figure 6 shows the results obtained at $X = 20$ mm. With the exception of those velocities at radial locations very close to the centerline (within $R = 4$ mm) the 5 μm drops showed velocities within 6 percent of the mean velocity of the 1 μm seed particles. Values of the turbulence intensity were also obtained for the seed particles and the drops. The largest difference observed was 5 percent between the 5 μm drops and the 1 μm seed particles.

The presence of the swirler has the effect of widening the spray cone angle showing low concentration of drops in the core moving at very low average velocities. Average axial, radial, and tangential velocities of the drops in the swirling field have also been obtained for specific drop sizes at various axial locations from the atomizer. Figures 7 and 8 show the radial distributions of average axial and tangential velocities for drops of 10, 20, 30, and 50 μm in diameter obtained at $X = 20$ mm. Of the drop sizes shown in these figures, the 10 μm drops followed the air flow velocity more closely, as was expected. Axial drop velocities in the central region of the swirling field have higher values as particle size increases, they reach a maximum, and subsequently decrease and seem to converge at a radial location of $R/D = 0.33$. This same trend was evident, although less pronounced, at $X = 50$ mm.

The angle of trajectory of selected drop sizes was obtained at all axial locations. Figures 9 and 10 show the angle of trajectory at $X = 20$ and 50 mm downstream for drop sizes of 10, 20, 30, and 50 μm in diameter (the 50 μm drop size is not shown in Fig. 10 for the sake of clarity). Closest to the nozzle the trajectories of the drops seem to be well defined by their size, especially with increasing radial position. At $X = 50$ mm the drops change their trajectory abruptly but seem to converge to the same directon of travel within a few millimeters from the centerline. This effect was present farther downstream but the angle of trajectory of the drops was not as steep close to

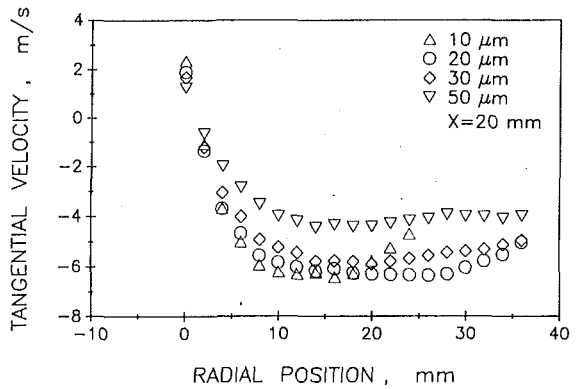

Fig. 8 Distribution of the average tangential velocity for drop sizes of 10, 20, 30, and 50 μm diameter at X = 20 mm; swirling flow, S = 0.26; same conditions as in Fig. 4

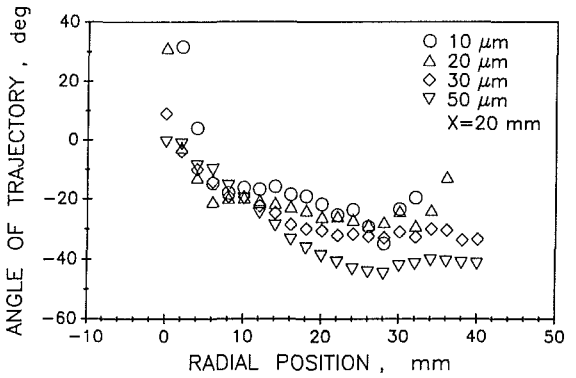

Fig. 9 Angle of trajectory for drop sizes of 10, 20, 30, and 50 μm at X = 20 mm; pressure atomizer 3 GPH, 45 deg solid cone, swirl number S = 0.26, U_{fs} = 20 m/s, P_a = 415 kPa

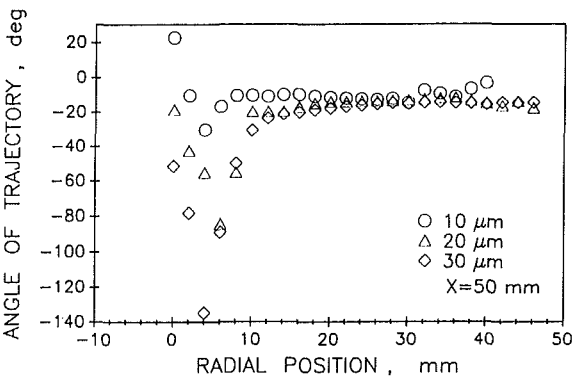

Fig. 10 Angle of trajectory for drop sizes of 10, 20, and 30, μm at X = 50 mm; pressure atomizer 3 GPH, 45 deg solid cone, swirl number S = 0.26, U_{fs} = 20 m/s, P_a = 415 kPa

centerline and the different drop sizes quickly followed the same direction at increasing radial positions.

Particle number density N_d was obtained for both the spray in coflowing air and the swirling spray at various axial locations. The expression used to calculate the particle number density is given by

$$N_d = \sum_{i=1}^{50} \frac{1}{|v_i|} \sum_{j=1}^{50} n_{ij} \left(A_j \sum_{k=2}^{n_{ij}} \Delta t_{ijk} \right)^{-1} \qquad (1)$$

where v_i is the velocity of the ith bin in the velocity histogram composed of 50 bins, A_j is the probe area of the jth size bin, n_{ij} is the total number of particles of size j in the ith velocity

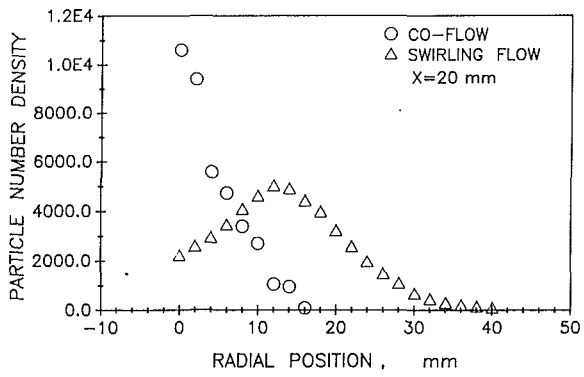

Fig. 11 Distribution of particle number density at X = 20 mm; same conditions as in Fig. 4

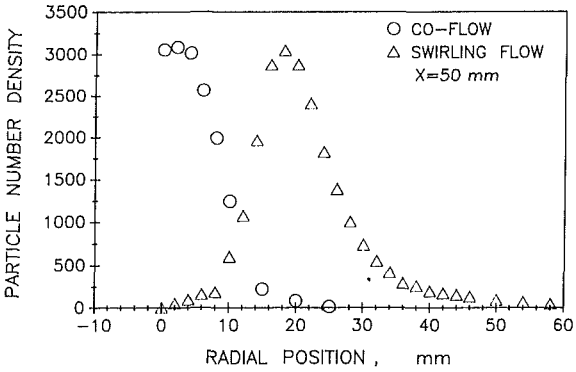

Fig. 12 Distribution of particle number density at X = 50 mm; same conditions as in Fig. 4

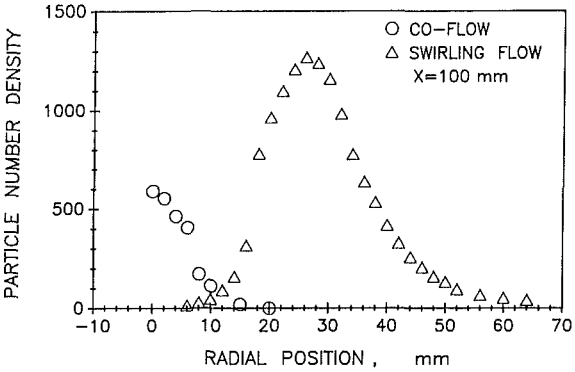

Fig. 13 Distribution of particle number density at X = 100 mm; same conditions as in Fig. 4

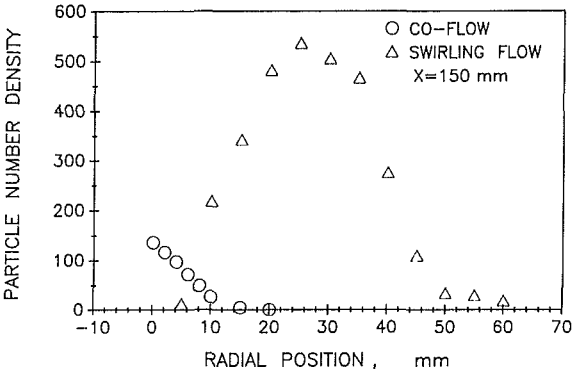

Fig. 14 Distribution of particle number density at X = 150 mm; same conditions as in Fig. 4

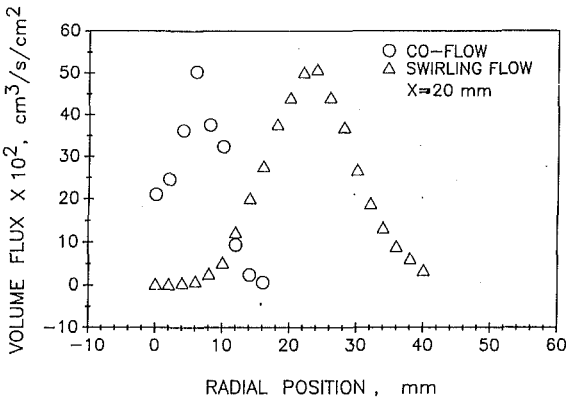

Fig. 15 Distribution of liquid volume flux at $X = 20$ mm; same conditions as in Fig. 4

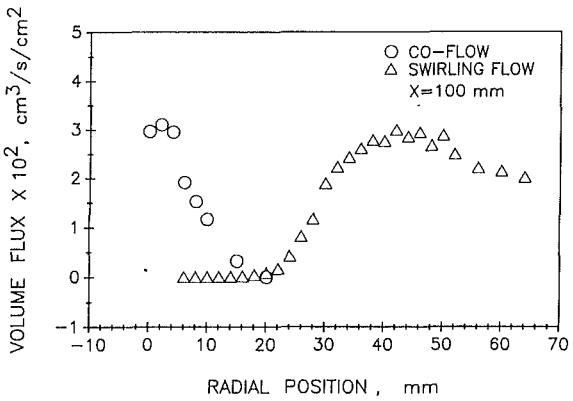

Fig. 17 Distribution of liquid volume flux at $X = 100$ mm; same conditions as in Fig. 4

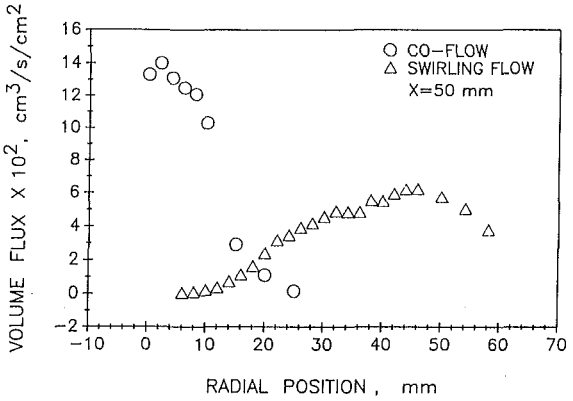

Fig. 16 Distribution of liquid volume flux at $X = 50$ mm; same conditions as in Fig. 4

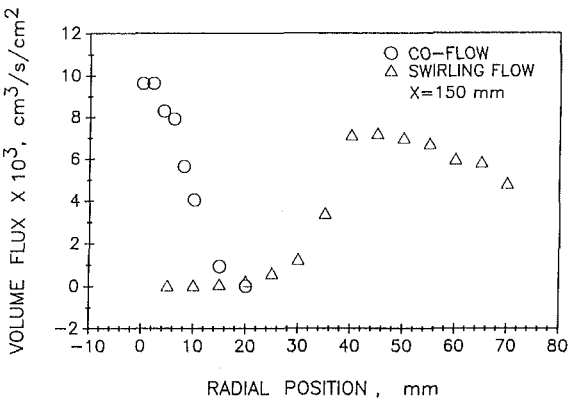

Fig. 18 Distribution of liquid volume flux at $X = 150$ mm; same conditions as in Fig. 4

bin, and Δt_{ijk} is the interarrival time between the kth and $(k-1)$th particles of size j within the ith velocity bin.

Figures 11–14 represent a plot of the radial distribution of particle number density at $X/D = 0.26$, 0.66, 0.76, and 1.97, respectively. There are several interesting points that can be highlighted from these figures. First, at $X = 20$ mm the peak value of the particle number density of the spray in coflowing air is higher than that of the swirling spray. Farther downstream at $X = 50$ mm, however, the two peak values are almost the same. At even larger axial locations, $X = 100$ and $X = 150$ mm, the distribution of particle number density of the spray in coflowing air peaks at the centerline and decreases toward the periphery of the spray. The swirling spray, however, exhibits a Gaussian distribution, which peaks at about $R/D = 0.35$, indicating a "hollow cone" effect on the spray caused by the swirler. This effect was clearly visible during the experiments. Notice also that peak values of N_d are much higher for the swirling spray than for the spray in coflowing air at these locations, with the former spreading more in the radial direction. Second, the particles observed in the swirling spray show relatively high concentrations of small and intermediate size drops, forming a sheath, which surrounds the central core of the swirling field. Because the spray cone angle is widened by the effect of the swirler, the radial distribution of particle number density peaks at an outer radial location than for the spray in coflowing air. Third, the maximum values of particle number density for the swirling spray peak almost at the same radial locations where the radial distribution of the Sauter mean diameter attains its minimum value at the corresponding axial locations. This is no coincidence, since the strong mixing induced by the swirl produces regions in the flow where high concentrations of relatively small particles can be found. Finally, in the swirling field, extremely low concentrations of particles are seen in the central region at increasing axial locations.

Liquid volume flux was determined for the spray in coflowing air and the swirling spray at various axial stations (Figs. 15–18). Both sprays exhibit the same peak value of volume flux closest to the nozzle, $X = 20$ mm, but at different radial locations. Farther downstream the liquid volume flux shows higher values for the spray in coflowing air, except at $X = 100$ mm. In the swirling spray the peak values of the volume flux distribution shift to outer radial locations with increasing axial distance, where the intermediate and large size drops are found. Comparisons of liquid volume fluxes obtained with the PDPA with patternator data or with integrated values with flow rates to the nozzle were not attempted in this study because the accuracy of this type of measurement has already been assessed for a quiescent spray (Bachalo et al., 1988c). It is believed that the accuracy of liquid volume flux calculations in the present measurements remains unaltered.

Turbulence damping by the drops is also a topic of current interest and one that has been discussed by Bulzan (1988) in particle-laden swirling free jets. It is believed that such a study is not practical to be considered here because it would be very hard to determine whether the drops induce production or dissipation of turbulence kinetic energy. Suffice it to say that the injection of the spray particles into the swirling field modifies the flow, inducing air entrainment and momentum exchange with the gaseous phase.

Turbulence properties were obtained of the swirling field with the seed particles in the flow at axial locations of $X = 10$, 20, 50, 100, 150, and 200 mm from the atomizer. Radial traverses consisted of measurements taken at 2-mm intervals

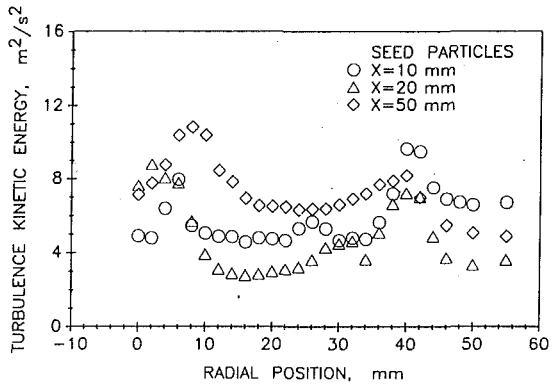

Fig. 19 Distribution of turbulence kinetic energy at $X = 10$, 20, and 50 mm downstream of a 20 deg vane swirler, $S = 0.26$, free-stream velocity $U_{fs} = 20$ m/s

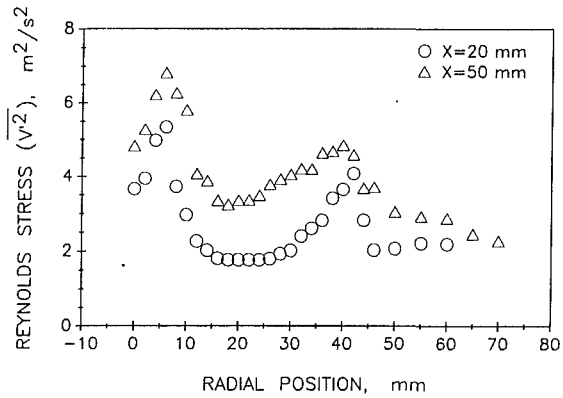

Fig. 21 Distribution of normal Reynolds stresses $\overline{v'^2}$ at $X = 20$ and $X = 50$ mm; $S = 0.26$, $U_{fs} = 20$ m/s

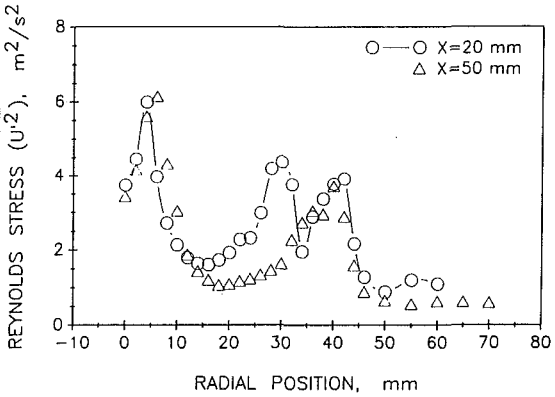

Fig. 20 Distribution of normal Reynolds stresses $\overline{u'^2}$ at $X = 20$ and $X = 50$ mm; $S = 0.26$, $U_{fs} = 20$ m/s

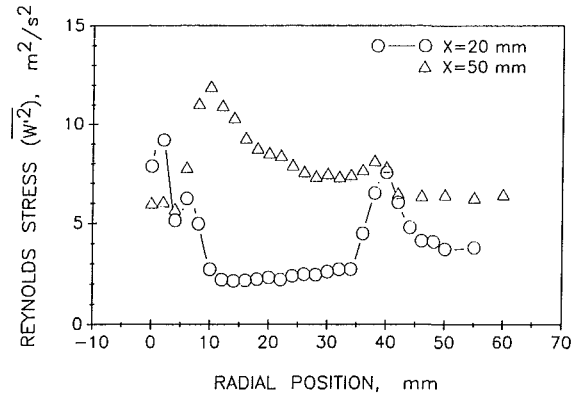

Fig. 22 Distribution of normal Reynolds stresses $\overline{w'^2}$ at $X = 20$ and $X = 50$ mm; $S = 0.26$, $U_{fs} = 20$ m/s

at $X = 10$, 20, and 50 mm and at 5-mm intervals at $X = 100$, 150, and 200 mm. Figure 19 shows the radial distributions of turbulence kinetic energy at three axial locations. The two peaks that are appreciable in these distributions are located in the shear layer of the recirculation region in the inner core and in the boundary of the swirling field with the free-stream high-velocity air. It is also interesting to note that the highest values of turbulence kinetic energy were measured at $X/D = 0.66$ ($X = 50$) mm.

The normal Reynolds stresses $\overline{u'^2}$, $\overline{v'^2}$, and $\overline{w'^2}$ are shown in Figs. 20–22 at axial distances of $X = 20$ and $X = 50$ mm downstream. Double peak values of the normal stresses are observed near the swirler, a characteristic that has also been reported by Sislian and Cusworth (1986) and by Fuji et al. (1981). These peaks are produced in regions where high gradients of mean velocity are found. The dip in the radial profile of $\overline{u'^2}$ occurring at $X = 20$ mm and $R = 34$ mm is not fully documented; however, it is present in a region where the edge of the swirl housing seemed to create a small-scale turbulence zone, an effect that was observed when small spray particles from the 0.5 GPH atomizer were seen moving in different directions.

There is some indication that the inner peak values of normal Reynolds stresses are located close to the zero streamline (i.e., near the edge of the recirculation region), although this observation is planned to be verified with the aid of flow visualization. The outer peak values are due to the shear layer at the edge of the swirling flow with the free-stream air. These double peak values, which persist up to a distance of approximately $X/D = 1.97$ ($X = 150$ mm), decay rapidly with increasing axial distance.

The shear stresses $\overline{u'v'}$ and $\overline{u'w'}$ have been obtained at $X = 10$, 20, 50, 100, 150, and 200 mm from the nozzle. To avoid confusion in the interpretation of the data, Figs. 23 and 24 show these turbulence properties at $X = 20$ and $X = 50$ mm only. Compared to the values of the normal Reynolds stresses, the values of the Reynolds shear stresses are appreciably smaller and also exhibit the double peak values of the profiles at the same radial locations, i.e., the inner peak being near the edge of the recirculation region and the outer peak being near the edge of the swirling field. The radial locations of the peak values of $\overline{u'v'}$ coincide with those of the normal stress $\overline{u'^2}$ at axial locations of up to approximately $X/D = 1.97$. The negative maxima of the $\overline{u'v'}$ shear stress are near the edge of the recirculation zone and subsequently move radially outward at increasing axial locations.

Conclusions

Measurements of the drop size and drop and velocity distributions, particle number density, volume flux, and angle of trajectory have been presented for a pressure swirl atomizer spraying into a low swirling field of $S = 0.26$. In an attempt to emphasize the differences between a spray moving in coflowing air and one immersed in a swirling field, the measurement of the relevant parameters in a spray were carried out and the results reported here for both cases.

In fact, the results bear little resemblance. The spatial distribution of sizes and velocities, particle number density, and volume flux of the spray are strongly influenced by the dynamics imposed by the swirling field. Close to the nozzle, for example, the radial distribution of particle number density in the swirling field exhibits peak values lower than the ones measured for the spray in coflowing air. Liquid volume flux, however, exhibited similar peak values for both flows closest

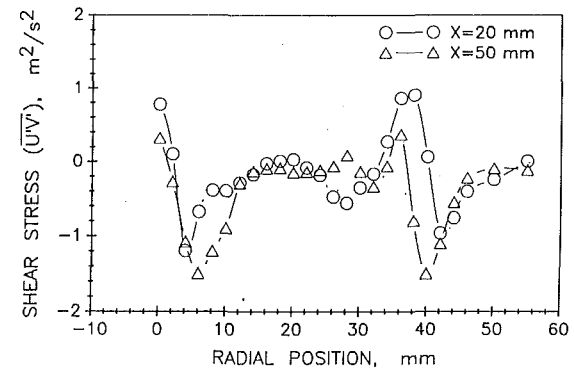

Fig. 23 Distribution of Reynolds shear stresses $\overline{u'v'}$ at $X=20$ and $X=50$ mm; $S=0.26$, $U_{fs}=20$ m/s

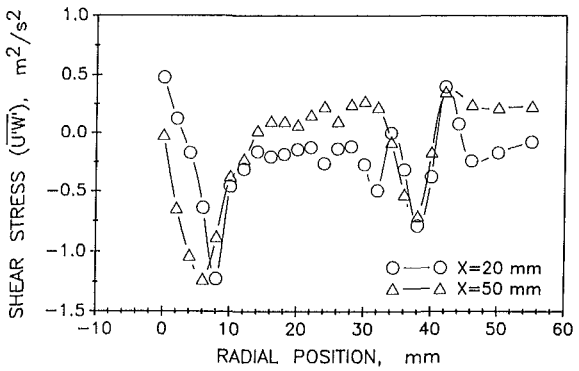

Fig. 24 Distribution of Reynolds shear stresses $\overline{u'w'}$ at $X=20$ and $X=50$ mm; $S=0.26$, $U_{fs}=20$ m/s

to the nozzle. These prevailing conditions near the atomizer, however, differ greatly farther downstream away from the effect of the swirler.

Measurement of the velocity and turbulence parameters of the swirling field using seed particles was also performed. Air velocities were compared with the velocity of drops of 1–50 μm diameter. The results show that drops as large as 5 μm follow the air velocity reasonably well. In addition, turbulence intensity values obtained for the 1 μm seed particles and the 5 μm drops differ only slightly. Plots of the turbulence kinetic energy, normal Reynolds stresses, and Reynolds shear stresses show double peak radial distributions, which indicate regions in the flow where high gradients of mean velocity are found. This double peak distribution deteriorates and decays, obviously, with increasing downstream distance. Although the swirl reported in this work is low, $S=0.26$, close to the nozzle the small drops are seen to recirculate back within the central region of the flow and exhibit negative axial velocities. Within the region surrounding the recirculating zone, the drops are subject to relatively high tangential velocities up to distances of about $X/D=2.63$ ($X=200$ mm).

Future work will be extended to various degrees of swirl and will include an experimental setup which resembles more closely that of a gas turbine combustor. Ultimately, it is the effect of swirl on the combustion efficiency, flame stabilization, and emission of pollutants that is being sought.

Acknowledgments

The authors gratefully acknowledge the support of this work by the NASA Lewis Research Center, Contract No. NAS2-25204, Ms. Valerie Lyons contract monitor.

References

Bachalo, W. D., Breña de la Rosa, A., and Rudoff, R. C., 1988a, "Diagnostic Development for Spray Characterization in Complex Turbulent Flows," ASME Paper No. 88-GT-241.

Bachalo, W. D., Breña de la Rosa, A., and Rudoff, R. C., 1988b, "Advances in Diagnostics for Complete Spray Characterization," *Proceedings of the 4th International Conference on Liquid Atomization and Spray Systems*, Sendai, Japan, Aug. 22—24.

Bachalo, W. D., Rudoff, R. C., and Breña de la Rosa, A., 1988c, "Mass Flux Measurements of a High Number Density Spray System Using the Phase Doppler Particle Analyzer," Paper No. AIAA-88-0236, AIAA 26th Aerospace Sciences Meeting, Reno, NV, Jan. 11-14.

Beer, J. M., and Chigier, N. A., 1983, *Combustion Aerodynamics*, Robert E. Krieger Publishing Company, New York, p. 111.

Bulzan, D. L., 1988, "Particle-Laden Weakly Swirling Free Jets: Measurements and Predictions," NASA TM, 100881.

Cameron, C. D., Brouwer, J., Wood, C. P., and Samuelsen, G. S., 1988, "A Detailed Characterization of the Velocity and Thermal Fields in a Model Can Combustor With Wall Jet Injection," ASME Paper No. 88-GT-26.

Fujii, S., Eguchi, K., and Gomi, M., 1981, "Swirling Jets With and Without Combustion," *AIAA Journal*, Vol. 19, No. 11, pp. 1438–1442.

Gouldin, F. C., Depsky, J. S., and Lee, S-L., 1985, "Velocity Field Characteristics of a Swirling Flow Combustor," *AIAA Journal*, Vol. 23, No. 1, pp. 95–102.

Gupta, A. K., Lilley, D. G., and Syred, N., 1984, *Swirl Flows*, Abacus Press, New York.

Lilley, D. G., 1988, "Lateral Jet Injection Into Swirling Combustor Flowfields," AIAA Paper No. AIAA-88-3183, AIAA/ASME/SAE/ASEE 24th Joint Propulsion Conference, Boston, July 11-13.

Nejad, A. S., Favaloro, S. C., Vanka, S. P., Samimy, M., and Langenfeld, C., 1988, "Application of Laser Velocimetry for Characterization of Confined Swirling Flow," ASME Paper No. 88-GT-159.

Sislian, J. P., and Cusworth, R. A., 1986, "Measurements of Mean Velocity and Turbulence Intensities in a Free Isothermal Swirling Jet," *AIAA Journal*, Vol. 24, No. 2, pp. 303–309.

Improvements to the Performance of a Prototype Pulse, Pressure-Gain, Gas Turbine Combustor

J. A. C. Kentfield

L. C. V. Fernandes

Department of Mechanical Engineering,
University of Calgary,
Calgary, Alberta, Canada

A description is given of a simple, prototype, pulse, pressure-gain combustor for a gas turbine. The work reported was targeted at alleviating problems previously observed with the prototype combustor. These were related to irreversibilities, causing a performance deficiency, in the secondary flow passage. The work consisted of investigating experimentally the effect of tuning the secondary-flow path length, adding a flow restrictor at the combining-cone entry station, and redesigning the combining cone itself. The overall result was to eradicate the previously noted performance deficiency, thereby increasing the maximum pressure gain obtained in the gas turbine from 1.6 to 4.0 percent of the compressor absolute delivery pressure.

Introduction

The results of tests carried out on a prototype valveless, pulse, pressure-gain combustor on, and off, a small gas turbine have been reported previously (Kentfield and Yerneni, 1987; Kentfield and O'Blenes, 1987). A conclusion from the earlier work was that the pressure-gain combustor, when installed on the gas turbine as a substitute for the conventional steady flow combustor, was capable of generating a small stagnation pressure gain, in the region of 1.5 percent of the compressor delivery pressure, at a combustor (stagnation) temperature ratio of approximately 2.2:1 (Kentfield and O'Blenes, 1987). It was known from the earlier work (Kentfield and Yerneni, 1987; Kentfield and O'Blenes, 1987) that impediments to obtaining a superior performance were irreversibilities, and hence pressure losses, associated with the packaging of the valveless pulse combustor that drives the system. The work reported here deals with performance improvements resulting, primarily, from a systematic, experimentally based investigation of the secondary flow ducting incorporated in the pressure-gain combustor.

The pulsating nature of the operation of a valveless pulse combustor is essentially a consequence of the geometry of the device, which, in steady flow terminology, is an unstable self-excited system. The rapid combustive reaction of fuel and air in the combustion zone of a pulse combustor results in a transient pressure rise therein, with consequent outflow from the combustion zone into a long tailpipe and a short inlet pipe, each communicating with the combustion zone. Inertia of the gas column in the tailpipe is sufficient to stop the outflow from the combustor inlet and to cause a flow reversal resulting in an air inflow from the surroundings entering the combustor. This air then mixes with fuel, supplied under pressure through fuel jets in the combustion zone, with subsequent ignition from residual high-temperature products of combustion remaining in the combustion zone. The cycle then repeats automatically. In the gas turbine application the air supply to the pulse combustor comes from the steady-flow delivery of the gas turbine compressor. The products of combustion are ducted into the turbine at a slightly higher stagnation pressure than that of the air flow leaving the compressor.

The benefit, in terms of improved cycle efficiency, of using a pressure-gain combustor, rather than a conventional steady flow combustor, is implied in Fig. 1, which shows a simple gas turbine cycle on the temperature ~ entropy plane with and without combustion-driven pressure gain. A quantification of the performance improvements obtainable has been presented previously (Kentfield, 1988). Typically about a one to two percent increase in net power output, with a corresponding reduction in specific fuel consumption, can be expected for each one percent reduction in combustor pressure loss or increase in combustor pressure gain.

The particular type of pressure-gain combustor considered here does not incorporate any moving parts. The secondary flow, which serves to cool the pulse combustor consituting what is essentially the primary zone, is pumped by means of flow leaving the pulse-combustor inlet. The original sugges-

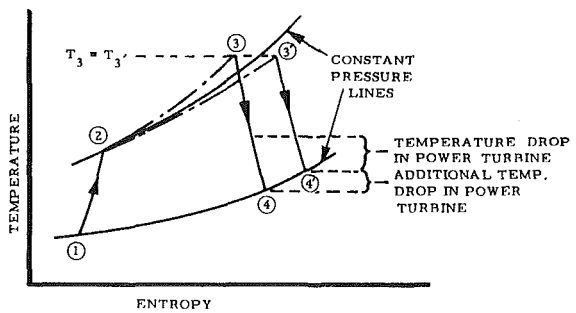

Fig. 1 Simple cycle gas turbine: cycle 1, 2, 3′, 4′ with combustor pressure loss; cycle 1, 2, 3, 4 with combustor pressure gain

Contributed by the International Gas Turbine Institute and presented at the 34th International Gas Turbine and Aeroengine Congress and Exhibition, Toronto, Ontario, Canada, June 4–8, 1989. Manuscript received at ASME Headquarters February 14, 1989. Paper No. 89-GT-277.

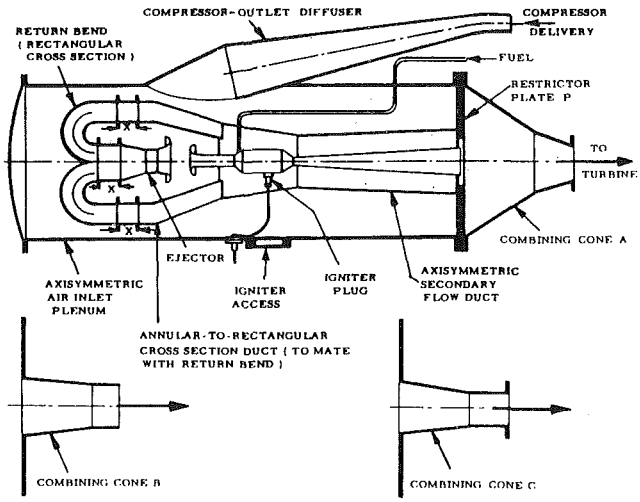

Fig. 2 Configuration of prototype pulse, pressure gain, combustor (diagrammatic); the lengths X are adjustable; three alternative combining cones were provided, A, B, and C

tion of employing a valveless pulse-combustor as a substitute for the conventional steady flow combustor of a gas turbine appears to be credited to Reynst (Thring, 1961).

Pressure-Gain Combustor Configuration

Figure 2 shows, diagrammatically, the arrangement of the propane-fueled, prototype pulse, pressure-gain combustor. The unit was of the appendix type and was connected to the turbomachinery (Cussons P.9000 small, educational, gas generator) at the compressor delivery and turbine-inlet stations. The valveless (or aerovalved) pulse combustor was of relatively small diameter. It carries the igniter plug used only at start-up. Fuel under pressure was supplied, continuously, to the head of the combustor. The secondary flow duct surrounds the enlarged combustion zone and the tailpipe of the pulse combustor. Secondary flow is pumped from the plenum chamber, encompassing the apparatus, into the ejector by means of the intermittent backflow of products of combustion emerging from the pulse-combustor inlet. The plenum chamber serves as a capacity, or settling tank, to prevent the gas turbine compressor from receiving significant pressure surges caused by the cyclic, nonuniform flows entering the ejector and pulse-combustor inlet.

The products of combustion leaving the pulse-combustor tailpipe combine, or mix, with the secondary flow surrounding the tailpipe in the combining cone, at the downstream end of the unit, prior to entering the turbine of the gas generator. The variables changed during the course of the experiments reported here were the:

(*a*) adjustable tuning lengths X (Fig. 2) of the secondary flow ducts and ejector,

(*b*) hole size at the center of the downstream secondary-flow duct restrictor-plate P,

(*c*) configuration of the combining cone. Three alternative cone designs were tested labeled A, B, and C; these are shown schematically in Fig. 2.

The secondary-flow duct tuning-length adjustments were carried out with the combustor mounted on the gas turbine since such testing takes place at the correct temperature. The tests involving adjustment and optimization of the secondary flow duct restrictor plate orifice and combining cone configuration were made with the combustor off, or dismounted from, the gas turbine.

Tuning of Secondary-Flow Channel

The path length of the secondary flow channel was expected to be an optimizable variable because, it seemed from earlier work (Kentfield et al., 1977), the pulses arriving in the combining cone from the pulse combustor tailpipe and the secondary-flow duct should do so in antiphase (i.e., alternatively) rather than in phase (i.e., together). The opportunity had not previously arisen, in earlier testing (Kentfield and O'Blenes, 1987), to carry out experimentally the fine-tuning process associated with varying the lengths X (Fig. 2). The earlier tests (Kentfield and O'Blenes, 1987) of the unit illustrated in Fig. 2 had all taken place with the minimum possible value of X, i.e., $X=0$, and with no restrictor plate P, using only combining cone A.

Two sets of ducts were available, allowing, when $X=0$ is included, three distinct secondary-flow duct path lengths to be tested. The corresponding increases in flow-path length were 7 and 19 percent relative to the shortest flow path. The appropriate tests were carried out with the combustor mounted on the gas turbine.

The stagnation pressure gain ΔP was established from the turbine experiments by measuring the mean static pressure gain using Validyne pressure transducers, one connected to a static tapping in the compressor-diffuser outlet/combustor inlet, the other in the combustor outlet/turbine inlet. To each mean static pressure was added the (small) mean theoretical local dynamic pressure based on the engine, and engine plus fuel, mass flows; known flow cross-sectional areas at the measuring stations and the known corresponding local gas conditions.

Nomenclature

A = cross-sectional area
C_D = flow coefficient applicable to outflow
C_P = specific heat at constant pressure
$\bar{F}$ = time-averaged thrust (atmospheric testing)
H = lower calorific value of fuel
K = constant
$\dot{m}$ = combustor time-averaged outflow rate (atmospheric testing)
$\dot{m}_{FUEL}$ = time-averaged fuel-flow rate (atmospheric testing)
n = number of outflow pulses per cycle (see Fig. 6)
N = rotor speed, rpm
P_{AMB} = ambient pressure
P = total pressure
$\dot{q}$ = time-averaged heat loss rate (through structure)
R = characteristic gas constant for outflow
T_{AMB} = ambient temperature
T = stagnation temperature
u = outflow velocity
X = secondary-flow duct extension length (see Fig. 2)
ΔP = pressure gain $\equiv (P_3 - P_2)$ on gas turbine
Δt_i = duration of ith outflow period
Δt_{PER} = duration of combustor cycle
η = combustion efficiency
ρ = flow density
ϕ = fraction of Δt_{PER} over which outflow occurs

Subscripts

1, 2, 3, 4 = stations within the gas turbine (see Fig. 1)
OUT = outflow
D = pulse-combustor combustion zone

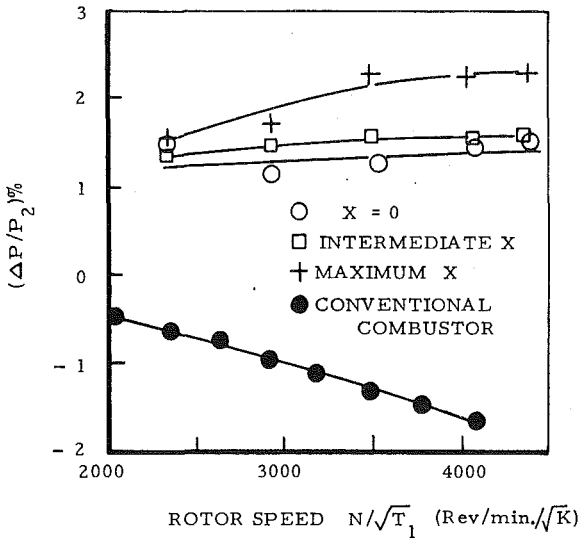

Fig. 3 Influence of length X on stagnation pressure gain; no restrictor plate, combining cone A, turbine load setting 0

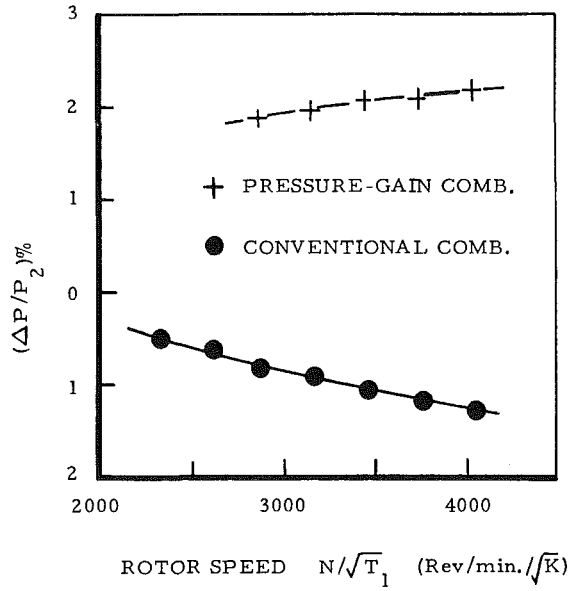

Fig. 4 Stagnation pressure gain with maximum X for turbine load setting 2; no restrictor plate, combining cone A

The influence of secondary-flow duct path length on pressure-gain performance is indicated in Fig. 3 for minimum loading of the gas generator (load setting 0). The loading was adjusted by manipulation of a butterfly valve in the gas generator turbine exhaust; the unit was not provided with a power turbine. It can be seen that the longest available secondary-flow duct path length increased the maximum recorded stagnation pressure gain from about 1.5 percent to about 2 percent of the compressor absolute delivery pressure. Further gains may, it seems, have been possible had it been feasible to increase X yet further. During these tests the gap between the pulse-combustor-inlet bell-mouth and that on the ejector was maintained constant, since earlier work (O'Blenes, 1987) indicated that this dimension was already approximately optimized. The lower curve of Fig. 3 shows the stagnation pressure loss experienced by the conventional, steady flow, propane-fueled combustor constituting an original component of the Cussons P.9000 gas generator.

The pressure gain with the maximum secondary-flow duct length (i.e., maximum X) is shown for loaded operation (load setting 2, which represents the maximum loading of the gas generator) in Fig. 4. It can be seen that here also a stagnation

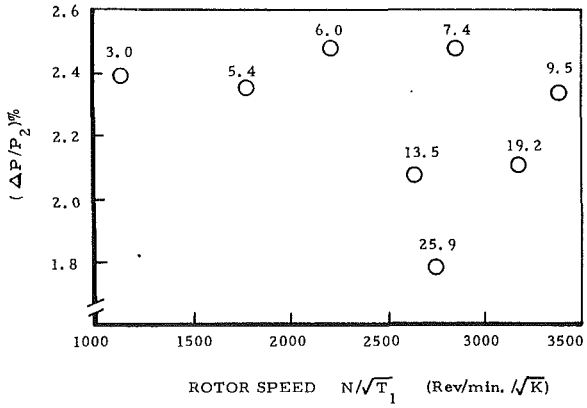

Fig. 5 Transient pressure gain, turbine load setting 0, no restrictor plate, combining cone A, maximum X; numbers on diagram are minutes after starting from cold

pressure gain of just over 2 percent was achieved compared with about 1.6 percent for this load setting from the earlier tests (Kentfield and O'Blenes, 1987) with $X=0$.

Another observation made during the course of the tests to establish the influence of X was that a higher pressure gain was achievable with cold operation, immediately after start-up, than could be sustained later with the engine and combustor fully warmed up. Figure 5 shows, for the maximum value of X, this transient behavior for the minimum load setting of the gas generator. A similar observation had been made during the course of earlier testing (Kentfield and O'Blenes, 1987; O'Blenes, 1987) but no detailed measurements were taken. It can be seen that for short periods following a cold start it was possible to achieve a maximum pressure gain greater than 2.5 percent. It appeared that the transient performance phenomenon was associated with the turbine lubricating oil temperature rather than the temperature of the combustor itself since the latter component is known, from much combustor test rig experience, to attain a steady-state working temperature very quickly. It was possible that with low oil temperature, the plain bearings of the turbocompressor served as a dynamometer and hence the turbocompressor was loaded differently from the back-pressuring resulting from normal, steady-state operation using the butterfly throttle valve. It was not possible, because of an inadequate cooling water supply, to run the turbomachine over extended periods with a low oil temperature. The observed phenomenon was not regarded as sufficiently significant to warrant expensive alterations to the test equipment when other, probably more worthwhile, development remained to be undertaken.

To investigate development of the downstream portion of the secondary-flow system where the secondary flow and the exhaust from the combustor tailpipe combine, or mix, it is desirable to remove the combustor from the gas turbine and operate it independently. This is relatively simple with the pulse combustor since the device is self-aspirating. Independent operation in this way then provides easy access to the outlet region of the combustor. It will be shown that it is possible to correlate, at least to a first approximation, the thrust produced by the independent combustor with pressure-gain potential. Hence an exercise targeted at maximizing thrust generation tends to result in maximizing the pressure-gain potential of the combustor.

Correlation of Thrust With Pressure Gain

A correlation of thrust measurements, in conjunction with corresponding fuel flow rate and temperature measurements, allows the pressure-gain potential of the pulse combustor to be estimated in at least an approximate manner. The thrust

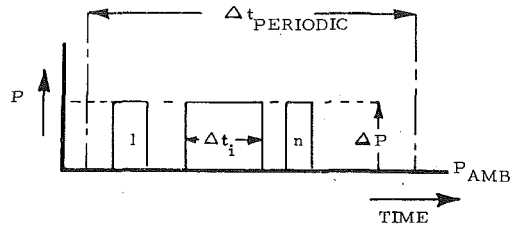

Fig. 6 Diagrammatic representation of outflow pulses (see equation (1))

measurements are, conveniently, made with the combustor intake stagnation pressure equal to the ambient pressure with the combustor self-aspirating. This situation results in an outflow static pressure also equal to ambient pressure, the resulting stagnation pressure gain then being the increase above the ambient intake pressure of the outflow from the combustor. A few simplifying assumptions are applicable to the analysis given here.

Assumptions

(*i*) Pressure during outflow is uniform and outflow occurs for a fraction ϕ of the periodic time Δt_{PER} (see Fig. 6).

(*ii*) Outflow is isentropic.

(*iii*) The relationship between velocity and pressure in the combustor outflow is incompressible, implying a small pressure gain and a relatively low gas Mach number.

Fundamental Relationships. From Fig. 6

$$\phi \equiv \sum_{i=1}^{n} \Delta t_i / \Delta t_{\text{PER}} \tag{1}$$

The energy equation applied to the combustor is

$$\dot{\bar{m}} C_P (T_{\text{OUT}} - T_{\text{AMB}}) + \dot{\bar{q}} = \dot{\bar{m}}_{\text{FUEL}} \eta H \tag{2}$$

Continuity can be written in the form

$$\dot{\bar{m}} = \rho_{\text{OUT}} (A_{\text{OUT}} C_D) u \phi \tag{3}$$

Momentum (subcritical flow as per assumption (*iii*))

$$\bar{F} = \rho_{\text{out}} u^2 (A_{\text{OUT}} C_D) \phi \tag{4}$$

From application of Bernoulli's equation to the combustor outflow

$$\Delta P \equiv (P_{\text{OUT}} - P_{\text{AMB}}) = \rho_{\text{OUT}} u^2 / 2 \tag{5}$$

Derivation. From equations (4) and (5)

$$\Delta P / P_{\text{AMB}} = \bar{F} / 2 (A_{\text{OUT}} C_D) P_{\text{AMB}} \phi \tag{6}$$

From equations (2) and (3)

$$u = \frac{\dot{\bar{m}}_{\text{FUEL}} \eta H - \dot{\bar{q}}}{\rho_{\text{OUT}} (A_{\text{OUT}} C_D) \phi C_P (T_{\text{OUT}} - T_{\text{AMB}})} \tag{7}$$

From manipulation of equations (1) to (7), and also invoking the characteristic gas constant, it can be shown that

$$\frac{\Delta P}{P_{\text{AMB}}} = \frac{T_{\text{OUT}} \bar{F}^2}{2R} \left[\frac{C_P \left(1 - \dfrac{T_{\text{AMB}}}{T_{\text{OUT}}}\right)}{\dot{\bar{m}}_{\text{FUEL}} \eta H - \dot{\bar{q}}} \right]^2 \tag{8}$$

When all variables on the right-hand side of equation (8), other than the time-averaged thrust $\bar{F}$, are invariant it can be seen that the pressure gain $\Delta P / P_{\text{AMB}}$ is directly proportional to the square of $\bar{F}$. This implies that for such circumstances $\bar{F}$ should, therefore, be maximized. A less dramatic approximation can be made for cases in which $\dot{\bar{q}} \to 0$ and the combustion efficiency η and T_{OUT} can both be regarded as constant, in which case

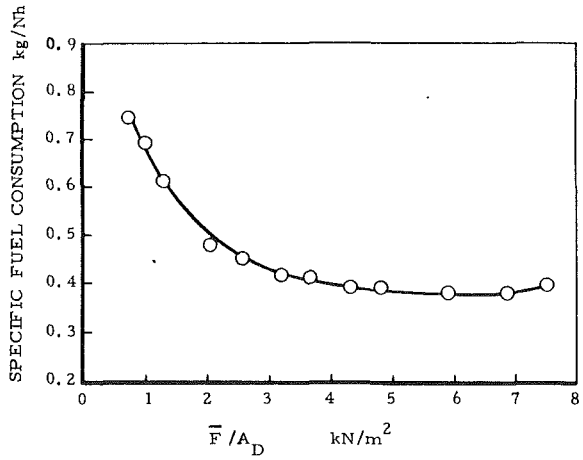

Fig. 7 Thrust performance of isolated combustor

$$(\Delta P / P_{\text{AMB}}) = K (\bar{F} / \dot{\bar{m}}_{\text{FUEL}})^2 \tag{9}$$

The right-hand side of equation (9) is identifiable as the inverse of the specific fuel consumption of the pulse combustor as a thrust generator. When correlating off-engine test results with predicted on-engine performance $\Delta P / P_{\text{AMB}} = (P_3 - P_2)/P_2$ or $\Delta P / P_2$ where, in the latter case, ΔP is the pressure gain under engine operating conditions.

Off-Engine Testing

In order to explore the influence of reducing the cross-sectional area of the secondary flow duct to increase the flow velocity, it was decided to make this modification locally, by means of an easily changed restrictor plate, at the downstream end of the secondary-flow passage at the station where mixing of the combustor tailpipe and secondary flow commences. The initiative to restrict the secondary-flow passage cross-sectional area, due to the second author, was based in part on the supposition that difficulties noted in earlier work (Kentfield and O'Blenes, 1987) with the flow in the secondary-flow duct and combining cone may have been due to too low a flow velocity. The ratio of the area of the secondary flow passage to that of the tailpipe exit was 7:1 in the original configuration (Kentfield and O'Blenes, 1987). This value was arrived at by taking into account in a quasi-steady manner the relative mass flows and flow velocities in the two flow channels.

Influence of Restrictor Plate. Because of the difficulty of gaining access to the region in question, it was decided to investigate the influence of the restrictor plate P by means of off-engine testing with the combustor operating in the self-aspirating mode. The thrust measurements required for assessing pressure-gain potential were made using thrust plates (O'Blenes, 1987). The basic performance of the isolated pulse combustor, that is with the plenum chamber cover, combining cone, intake return bend and ejector removed, with two thrust plates employed, one at the inlet end of the machine the other at the tailpipe exit end, is presented in Fig. 7. The specific thrust referred to is based on the arithmetic sum of the intake back-flow and tailpipe thrusts. The result shown in Fig. 7 is presented as a dotted curve in Fig. 8. Figure 8 shows the results obtained with the inlet ejector and return bend installed but with the combining cone (item *A* in Fig. 2) removed. Only one thrust plate, at the tailpipe end of the system, was required since all the flow exited the combustor in one direction.

As can be seen from Fig. 8, throttling the secondary flow increased the performance of the system, as a thrust producer, quiet effectively. The maximum usable blockage without resultant overheating of the combustor appeared to be in the

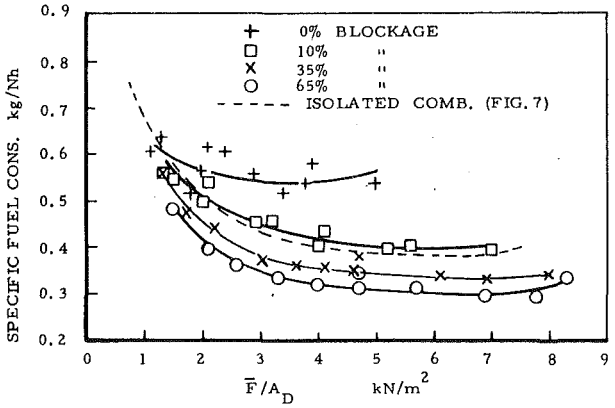

Fig. 8 Thrust performance with restrictor plate *P* (no combining cone)

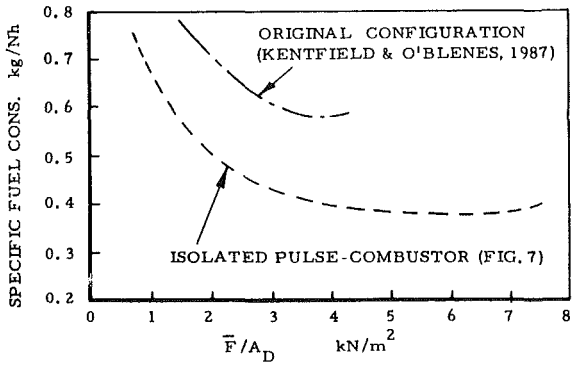

Fig. 9 Comparison of thrust performances of isolated combustor and original configuration of complete system

region of 65 percent, although fine-tuning of the secondary flow blockage ratio was not attempted. With 65 percent blockage the specific thrust and specific fuel consumption were greater and less, respectively, than those obtainable from the isolated combustor. Since the intake back-flow ejector can be shown to act, inherently, as a thrust augmenter (Lockwood, 1961), the latter result is not altogether surprising, although it does represent a very gratifying improvement over the unblocked situation.

For application of the combustor to the gas turbine it is, of course, necessary to provide some form of connection to the turbine inlet. This function is performed by the combining cone component, the original design of combining cone is represented by item *A* in Fig. 2. The influence on performance of cone design was also subjected to experimental study.

Influence of Combining Cone Geometry. The degradation of thrust-producing performance using the original combining cone (i.e., item *A* of Fig. 2) and the unthrottled secondary flow passage is indicated in Fig. 9, which compares the results obtained with that configuration with the performance of the isolated combustor (Fig. 7). The configuration of cone *A* was derived experimentally from an earlier attempt to optimize the combining cone design in conjunction with the use of the unthrottled secondary flow passage (O'Blenes, 1987). Figure 10 shows the consequence of using cone *A* in conjunction with the 65 percent blockage restrictor plate. As can be seen the overall thrust-producing performance of the combustor was degraded relative to that obtainable using cone *A* without the restrictor plate. It would appear that this result is essentially a consequence of the increase in the area ratio of the sudden enlargement at the junction of the combining cone with the combustor tailpipe and secondary flow passage (Fig. 2). This suggested the desirability of redesigning the combining cone region to minimize this loss.

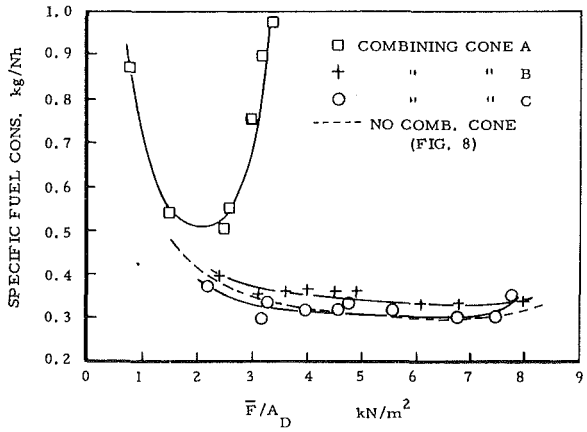

Fig. 10 Thrust performance using 65 percent restrictor plate in conjunction with combining cones *A*, *B*, and *C*

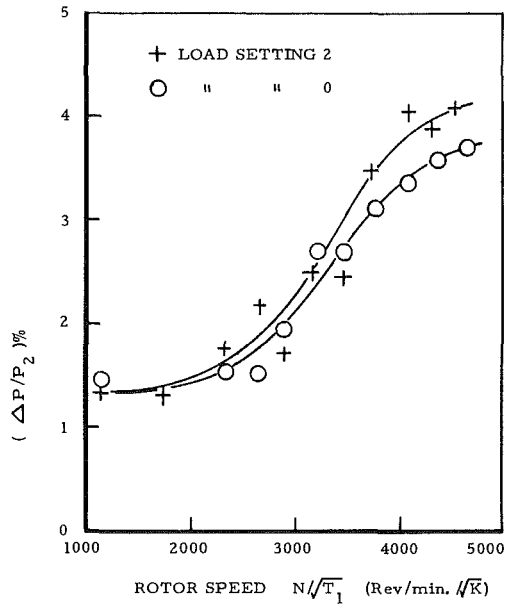

Fig. 11 Pressure gain performance of turbine for load settings 0 and 2; maximum *X*, 65 percent restrictor plate and combining cone *C*

The lower curves (solid lines) of Fig. 10 show the results obtained using combining cones employing smaller upstream diameters and, consequently, very much reduced sudden-enlargement area ratios. Based on the outside diameter of hole in the 65 percent blockage restrictor plate the sudden enlargement area ratio was 1.56 for cone *B* and 1.10 for cone *C*. The exit area divided by the combustor tailpipe exit area was 2.32 for cone *B* and 1.25 for cone *C*.

Since cones *B* and *C* resulted in similar performances, only slightly poorer than that obtainable using the 65 percent blockage restrictor plate without a tailcone, fine details of the mixing cone geometry appear, to a first approximation, to be relatively unimportant. Cone *C* was selected for the test running of the revised combustor on the gas turbine since the exit of this cone was designed suitably for direct attachment to the gas turbine inlet and also the specific fuel consumption was generally lower than that obtained using cone *B*.

Performance on Turbine

The pressure-gain performance of the turbine equipped with the revised combustor, that is using the longest secondary-flow path length, the 65 percent blockage restrictor plate, and tailcone *C*, is presented in Fig. 11 for load settings "0" and "2." It can be seen that with the first load setting the max-

imum steady (i.e., nontransient) stagnation pressure gain was approximately 3.7 percent and for the second load setting it was 4 percent. These results represent an increase in the maximum pressure gain of approximately 150 percent relative to the pressure gain obtainable prior to incorporating the three modifications identified above. The corresponding expected increase of pressure gain based on equation (9) for off-engine testing (applied to the maximum thrust ends of the dotted curve of Fig. 9 and the curve for cone *C*, Fig. 10) is approximately 180 percent.

Development Potential

It is doubtful that the rather coarse and localized tune-up work described here has resulted in a truly optimized configuration, although it is certainly much improved, based on a performance comparison, relative to the original (Kentfield and O'Blenes, 1987). Hence some additional increase in pressure gain may yet be possible by further modification of the current equipment. Any such modifications should, it would seem, be focused on the embryonic secondary flow system rather than the core pulse combustor since the latter is a relatively highly developed configuration from the French National Aeroengine Company, SNECMA, and Lockwood (Lockwood, 1962).

An inherent problem of the work reported here is the very small size of the Cussons P.9000 gas generator. The mass flow rate is only in the region of 0.15 kg/s ($\cong$0.33 lbm/s). It has been shown previously that the pressure-gain performance of pulse combustors improves with increasing unit size (Kentfield et al., 1980). Hence application of the present technology to an engine similar to the P.9000 but of 10 to 20 times the mass flow should, according to the experimentally based prediction procedures already available (Kentfield et al., 1980), result in a stagnation pressure gain of approximately 6–7 percent.

Conclusions

A significant performance improvement has been made to a pulse, pressure-gain combustor applied to a small gas turbine gas generator. The improved performance resulted in increasing the maximum pressure gain from 1.6 to 4 percent of the compressor absolute delivery pressure.

Acknowledgments

The writers wish to thank the Natural Sciences and Engineering Research Council of Canada for financial assistance, which made this work possible. The aid was in the form of operating grant No. A7928 awarded to the first author.

Thanks are also due to the technical staff of the Department of Mechanical Engineering, University of Calgary, for vital assistance with the work.

References

Kentfield, J. A. C., Rehman, M., and Marzouk, E. S., 1977, "A Simple Pressure Gain Combustor for Gas Turbines," ASME JOURNAL OF ENGINEERING FOR POWER, Vol. 99, No. 2, pp. 153–158.

Kentfield, J. A. C., Rehman, A., and Cronje, J., 1980, "The Performance of Pressure-Gain Combustors Without Moving Parts," AIAA *Journal of Energy*, Vol. 4, No. 2, pp. 56–63.

Kentfield, J. A. C., and O'Blenes, M. J., 1987, "The Application of a Second Generation Pulse, Pressure-Gain, Combustor to a Small Gas Turbine," AIAA Paper No. AIAA-87-2156.

Kentfield, J. A. C., and Yerneni, P., 1987, "Pulsating Combustion Applied to a Small Gas Turbine," *International Journal of Turbo and Jet-Engines*, Vol. 4, No. 1–2, pp. 45–53, Nijhoff/Freund Joint Publishing.

Kentfield, J. A. C., 1988, "The Feasibility, From an Installational Viewpoint, of Gas-Turbine Pressure-Gain Combustors," ASME Paper No. 88-GT-181.

Lockwood, R. M., 1961, "Interim Summary Report on Investigation of the Process of Energy Transfer From an Intermittent Jet to Secondary Fluid in an Ejector-Type Thrust Augmenter," Report No. ARD-286, Hiller Aircraft Co., Palo Alto, CA.

Lockwood, R. M., 1962, "Summary Report on Investigation on Miniature Valveless Pulsejets," Report No. ARD-307, Hiller Aircraft Co., Palo Alto, CA.

O'Blenes, M. J., 1987, "A Small Gas Turbine Equipped With a Second Generation Pulse Combustor," M.Sc. Dissertation, University of Calgary, Calgary, Alberta, Canada.

Thring, M. W., ed., 1961, *Pulsating Combustion, The Collected Works of F. H. Reynst*, Pergamon Press Ltd., London, Chap V.

The Influence of Dilution Hole Geometry on Jet Mixing

J. F. Carrotte
Research Assistant.

S. J. Stevens
Professor of Aeronautical Propulsion.

Department of Transport Technology,
University of Technology,
Loughborough, United Kingdom

Measurements have been made on a fully annular test facility, downstream of a row of heated dilution jets injected normally into a confined crossflow at a momentum flux ratio of 4. The investigation concentrated on the consistency of mixing between the jets, as indicated by the regularity of the temperature pattern around the crossflow annulus. When the heated air was supplied from a representative feed annulus, the exit velocity profile across each plunged hole was significantly altered and caused a distortion of the temperature distribution in the ensuing jet. The degree of distortion varies in a random manner, so that each jet has its own mixing characteristics, thereby producing irregularity of the temperature pattern around the annulus. With the same approach and operating conditions some of the plunged dilution holes were modified, and tests on this modified sector indicated a significant improvement in the circumferential regularity of the temperature pattern. Further tests showed that these modifications to the dilution holes had a negligible effect on the values of the discharge coefficients.

Introduction

A jet fluid injected normally into a crossflow occurs in numerous situations and has therefore led to a large number of theoretical and experimental studies that have been conducted over many years. This investigation involves a row of jets being injected into a confined crossflow and therefore simulates the mixing processes that occur in the dilution zone of gas turbine combustion chambers. Relatively cold jets of air are injected at the rear of a combustor to dilute the hot mainstream flow, and are therefore a major factor in ensuring an outlet temperature distribution that is consistent with the integrity of the downstream turbine stage.

Many workers have undertaken research related to this specific application, investigating the relative significance of the large number of aerodynamic and geometric variables involved in defining the dilution process. A comprehensive study of the mixing of air jets injected into a rectangular duct has been conducted by Holdeman et al. (1977–1987), in which jet diameter and spacing, mixing duct geometry and velocity, and temperature ratios were varied. It was concluded that the most important parameter influencing the mixing process is the jet-to-crossflow momentum flux ratio, this being confirmed independently by the results of Sridhari (1970) when investigating the mixing of air jets injected into a circular duct. Although much of the experimental work has been conducted on jets injected from one side toward an opposite wall, experiments by Kamotani and Greber (1974) and Holdeman et al. (1984) have indicated that the wall may be regarded as a plane of symmetry and that results should apply equally well to combustors with directly opposed dilution jets. However, for this to be true it is important that the velocities of the two opposing jets be closely matched and that allowance be made for the enhanced rate of mixing of the directly opposed jets due to the change in the effective mixing duct geometry.

With the exception of the work of Crabb and Whitelaw (1979), nearly all of the published work has concentrated on the mean radial temperature profile, but of equal importance is the consistency of the temperature pattern around the annulus. The localized mixing of each dilution jet with that of the combustion gases produces a change in temperature, and the avoidance of variations in these temperature patterns around the annulus is particularly important since this can have a detrimental effect on engine performance and durability of the nozzle guide vanes and turbine blades. However, as indicated by Shaw (1981), even in experiments with carefully controlled primary zone exit distributions such irregularities do occur, often in a random manner, and they vary in magnitude and position with different combustors built to the same design. Moys (1983) found that only when the combustor casing was removed and the dilution air supplied from a plenum chamber were the temperature irregularities removed. One possible source of such irregularities is variations in the behavior of the dilution jets, and this experimental program has therefore been concerned with the consistency of the temperature pattern downstream of a row of jets injected into a confined crossflow. The experimental investigation being conducted has already shown how differences in the mixing characteristics of individual dilution jets can occur (Carrotte and Stevens, 1987, 1988), and the present paper investigates modifications to the dilution hole geometry that are designed to produce a more regular temperature pattern at the combustor exit.

Contributed by the International Gas Turbine Institute and presented at the 34th International Gas Turbine and Aeroengine Congress and Exhibition, Toronto, Ontario, Canada, June 4–8, 1989. Manuscript received at ASME Headquarters February 14, 1989. Paper No. 89-GT-292.

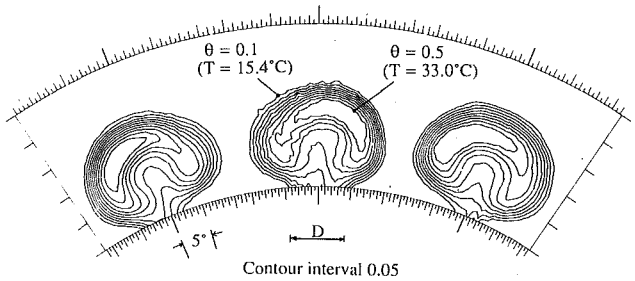

Fig. 1 Temperature distribution (standard hole, *X/D* = 2.0)

Review of Previous Work at Loughborough

Previously published work by the authors (1987) has described and quantified the irregularities observed in the behavior of dilution jets when air is supplied from a representative feed annulus to a row of standard plunged dilution holes. The temperature distribution of a three-hole sector, two hole diameters downstream of the injection plane (Fig. 1), illustrates the differing degrees of distortion or apparent "twisting" of each jet about its center plane. It is this effect that is responsible for the irregular temperature pattern observed around the annulus.

The importance of the feed conditions to the dilution holes makes it necessary to simulate the annulus formed by the combustor liner and casing, so that the approach flow direction is approximately perpendicular to the axial centerline of each hole. The deflection of the flow and its separation from the casing wall as it passes from the feed annulus through the dilution hole has a major influence on the velocity profile across the exit plane, producing an extremely complex flow field in the ensuing jet. As illustrated by the three velocity profiles shown (Fig. 2) these complex flow features may be in the form of vortices or regions of reverse flow, and may vary in a random manner from one jet to another.

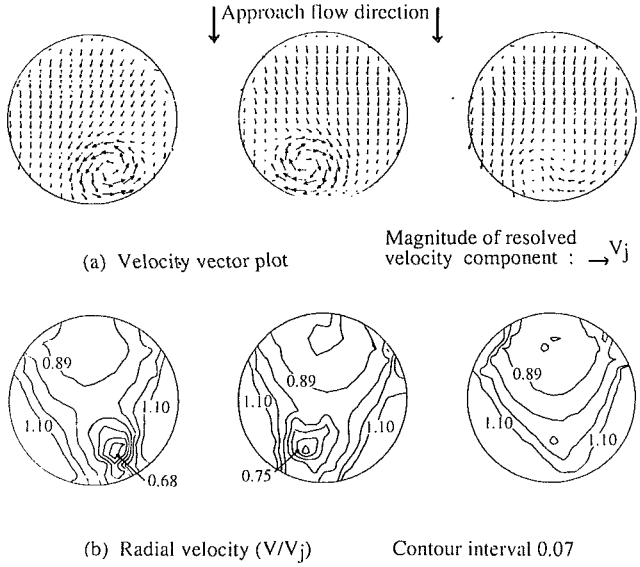

Fig. 2 Velocity distributions across the exit planes of dilution holes (standard holes, *Y/D* = 0.05)

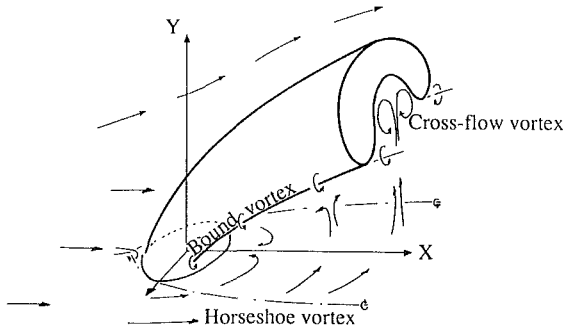

Fig. 3 Multiple jets in a crossflow

Characteristics of Jets in a Crossflow

A detailed study (Carrotte and Stevens, 1988) involving both velocity and temperature measurements has indicated the structure of a dilution jet and the mixing processes that develop as the jet progresses downstream. As each jet of fluid issues from a dilution hole it creates a blockage in the crossflow, and as a consequence the flow immediately ahead of the jet decelerates causing an increase in pressure. Downstream a rarefraction occurs and this, combined with the increased upstream pressure, provides the force that deforms the jet. Intensive mixing between the cross flow and jet fluid results in the rapid development of a turbulent shear layer around the periphery of the jet. The more curved trajectory of this lower momentum fluid at the sides of the jet contributes to the development of the characteristic "kidney"-shaped jet profile. Downstream of the injection plane the flow field is dominated by several vortex systems (Fig. 3) and it is these that mainly control the entrainment and mixing of the crossflow and jet fluid.

A horseshoe vortex system is formed by the oncoming vorticity associated with the boundary layer on the injection wall being deflected around the jet, a feature that is analogous to the case when flow is deflected around a cylinder mounted on

Nomenclature

A = geometric area of dilution hole
C_d = hole discharge coefficient ($m_h = C_d A[2\rho(P-p_\alpha)]^{0.5}$)
D = reference diameter of standard holes
J = momentum flux ratio = $\rho_j V_j^2/\rho_c V_c^2$
m_h = mass flow through dilution hole
P = total pressure in feed annulus
p_α = hole discharge plenum pressure
r = radius
r_i = inner radius of crossflow annulus
r_n = nondimensional radius = $(r-r_i)/(r_o-r_i)$
r_o = outer radius of crossflow annulus
S = distance between dilution holes
T = corrected temperature
T_c = reference crossflow temperature = 11°C
T_j = reference jet temperature = 55°C
T_{max} = maximum temperature in traverse plane
V_c = crossflow velocity
V_j = mean jet velocity
X = coordinate measured from hole center in downstream direction
Y = coordinate measured from injection wall in radial direction
θ = nondimensional temperature = $(T-T_c)/(T_j-T_c)$
θ' = nondimensional temperature profile $(T_{max}-T_c)/(T_j-T_c)$
ρ = density
σ = sector standard deviation
σ_j = jet distortion
φ = angle

a flat surface. However, as outlined by Andreopoulos and Rodi (1984), its effect on fluid mixing is relatively small in comparison with the high regions of vorticity that are generated at the interface of the initially orthogonal jet and crossflow. Streamwise vorticity is generated by the high radial velocity gradients at the sides of the jet, the fluid rolling up to form a pair of bound vortices that are located at the lobes of each jet and therefore enhance the kidney shaped profile of the jet as it progresses downstream. In the case of multiple jets issuing into a confined crossflow, the bound vortex system decays rapidly, and farther downstream ($X/D > 1.0$) the flow field is dominated by vortices formed by crossflow fluid that passes between the jets and into the wake region. Close to the wall the fluid moves in a predominantly lateral direction with very little axial momentum, the inward movement of fluid being assisted by the bound vortex system. This fluid becomes entrained by the jet and rolls up to form two crossflow vortices in the jet wake.

The mechanisms by which the crossflow and jet fluids mix are significantly modified by the velocity profile across the exit plane of a dilution hole. Jet fluid that has been deflected by the crossflow is forced to pitch over or yaw around the complex flow field issuing through the rear of the hole and this leads to a variation in trajectory of the fluid either side of the jet. This is a major factor in producing the distortion or apparent "twisting" of the temperature contours observed about the hole centerplane. The velocity profile across the exit plane of each hole also influences the amount and trajectory of jet fluid at the lateral edges of the jet where the bound and cross flow vortex systems develop. These control the mixing of the fluid in the wake of the jet and thus enhance the distortion of the temperature distribution. Each jet therefore has its own individual mixing characteristics that are related to its exit velocity profile, giving rise to the observed distortions of the kidney-shaped temperature profiles that vary in both magnitude and direction from one jet to another.

To improve the temperature pattern around the annulus, it is necessary to overcome these effects produced by the feed conditions to the dilution holes, so that each jet has virtually the same mixing characteristics in the dilution annulus.

Test Facility

The test facility (Fig. 4) is comprised of three vertically mounted concentric Plexiglass tubes 9.5 mm thick, the space between the inner and center casing forming the dilution hole feed annulus of 35.8 mm height, and the space between the center and outer casing forming the crossflow annulus of 76.2 mm height. Air is drawn from the atmosphere by a centrifugal fan into the crossflow annulus via a plenum chamber, a bell-shaped inlet flare, and a honeycomb flow straightener. A heater mounted on top of the plenum chamber is supplied from a second fan, which draws air from the laboratory. The heated air (55°C) then passes via a pipe and an annular nozzle into the dilution hole feed annulus. Supplying heat in this way gives information on the mixing of the jet fluid, as well as identifying the trajectory of the high-temperature core. Furthermore, by mounting the facility in the vertical plane the influence of buoyancy on the penetration of the jets is eliminated. An annular wedge is located on the inner wall of the feed annulus adjacent to the dilution holes and is designed to reduce the passage height from 35.8 mm to 10.4 mm. In this way the rise in pressure across the face of the holes due to diffusion is reduced and the flow instabilities described by Lefebvre (1983) minimized. No attempt is made to simulate the flow of air used for flame tube and turbine blade cooling that normally passes down the annulus between the liner and combustor casing.

Flow angles and velocities were measured with pressure probes consisting of a cluster of five tubes with 0.25 mm bore,

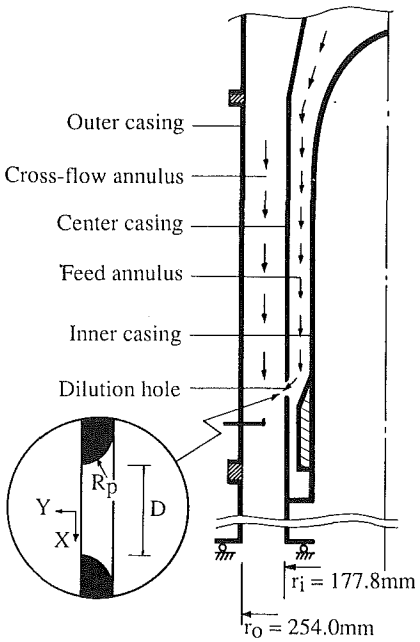

Fig. 4 Test facility

overall diameter 1.73 mm, and were used in the non-nulled mode using the calibration procedure outlined by Wray (1986). All pressure readings were corrected to a reference jet dynamic head of 50 mm water gage and the data derived from the five hole probe measurements are presented in terms of velocity distributions. Resolved components of velocity in the traversing plane are presented in the form of vectors, where the flow direction and magnitude of velocity at points in the plane are indicated by the direction and length of the arrows. The instrumentation has been calibrated to measure local flow directions relative to the probe of up to ±35 deg in both pitch and yaw.

Chromel/alumel thermocouples connected to Comark digital thermometers were used to record temperatures both in the dilution zone and upstream of the injection plane in both the crossflow and feed annuli. Corrections for minor variations in rig operating temperatures were made on the basis that at a fixed momentum flux ratio the nondimensional temperature θ remains constant at a given location. Results are presented as contours of nondimensional temperature θ or values of corrected temperature T, which are derived from a linear interpolation of the experimental data. Accuracy of measurement is limited by the positional error associated with the thermocouples, and in regions of high temperature gradients this has been estimated to be approximately 0.5°C at the measurement plane ($X/D = 2.0$).

All the data presented are based on measurements time-averaged over a period of 5 seconds prior to being committed to the memory of a DEC LSI 11/23 microcomputer. Measurements in planes perpendicular to the center casing were conducted at $X/D = 2.0$, the data being collected at nominal radial spacings of $0.1D$ and 0.5 deg intervals around the annulus, which resulted in over 900 data points being recorded per jet. Measurements recorded in planes parallel to the center casing had a nominal spacing of $0.06D$ between data points.

The datum rig configuration has 16 equispaced plunged dilution holes ($R_p/D = 0.375$) of conventional design, which were used to investigate the irregularities in the temperature pattern around the annulus. The two modified geometries of dilution hole tested were obtained using the existing casing containing the standard plunged holes, which were recontoured using cellulous filler as a lining material. In this way the

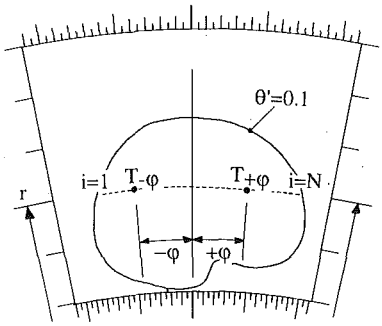

Fig. 5 Jet distortion parameter

modified designs were subjected to virtually the same approach conditions in the feed annulus as were present in the tests on the standard hole geometry. It should be noted however that each hole had to be individually shaped to obtain the desired hole profile, and that the modified designs will cause a change in hole area.

The investigation was conducted at the same operating conditions at which the previously published data was obtained. All dilution measurements were performed at a jet-to-crossflow momentum flux ratio of 4 and a mean jet velocity (V_j) of 29.5 m/s.

Mixing Parameters

The measured temperature distributions are corrected using the nondimensional parameter θ, where

$$\theta = \frac{T - T_c}{T_j - T_c} \tag{1}$$

for reference conditions of $T_j = 55°C$ and $T_c = 11°C$.

The parameters used to assess the consistency of mixing are based on the concept of standard deviation obtained by comparing the differences in the temperature distributions of each jet. Variations in the dilution mass flow are accounted for by evaluating the mixing parameters only within each jet, where the jet boundary is defined using the nondimensional temperature profile

$$\theta' = \frac{T - T_c}{T_{\max} - T_c} = 0.1 \tag{2}$$

The distortion of a single jet is reflected by differences in the temperature distribution either side of the hole centerplane. At any radius, the temperature recorded at a given ($\varphi°$) can be compared with the corresponding ($-\varphi°$) value on the other side of the jet (Fig. 5), and these differences can be summed to give the jet distortion

$$\sigma_j = \frac{2}{N}\sqrt{\left[\sum_{i=1}^{N/2} (T_{\varphi_i} - T_{-\varphi_i})^2\right]} \tag{3}$$

where N is the number of data points ($\theta' > 0.1$) at that radius.

As a means of assessing the circumferential consistency of the flow around the annulus, the concept of a block distribution is introduced (Shaw, 1981), the physical size of which corresponds to the minimum geometric segment repeated around the annulus. In the case of these experiments the 16 dilution holes mean that each jet is located within a 22.5 deg segment of the annulus, and for each traverse position a block temperature T_b is obtained by averaging the temperatures measured in each segment at the same position relative to each dilution hole (Fig. 6). By calculating the block values at each traverse location a temperature distribution can be obtained that represents the mean temperature pattern around the annulus. For an eight-hole sector measurements are made in the

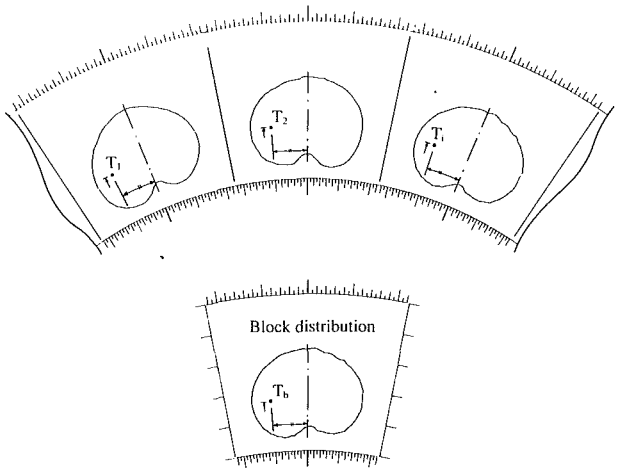

Fig. 6 Block temperature distribution

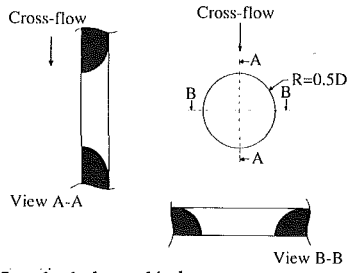

(a) Standard plunged hole

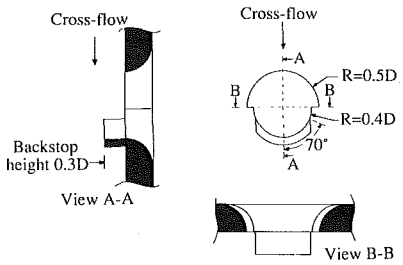

(b) Modified hole - Design A

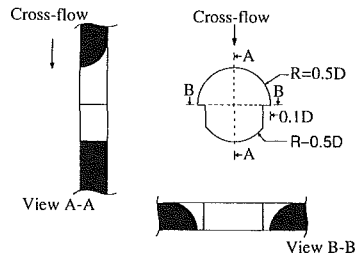

(c) Modified hole - Design B

Fig. 7 Dilution hole geometry

six center segments, and so each block temperature is an average of six recorded temperatures.

Within a specified sector and at the same position relative to each dilution hole, the temperature of each jet can be compared with the relevant block value to obtain a standard deviation. Thus, the total standard deviation within a specified sector from that of its block temperature distribution reflects the consistency of the temperature pattern. For sector tests involving six jets, the total standard deviation at any radial location is given by

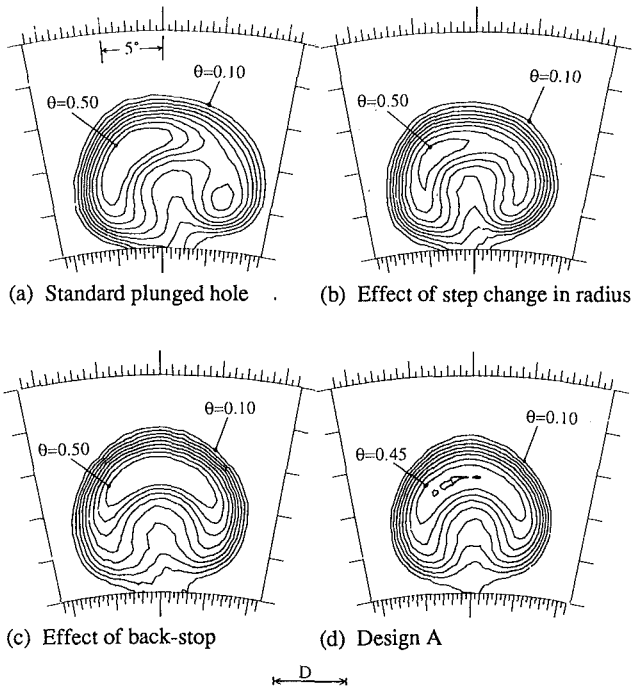

(a) Standard plunged hole (b) Effect of step change in radius

(c) Effect of back-stop (d) Design A

Fig. 8 Temperature distributions (X/D = 2.0)

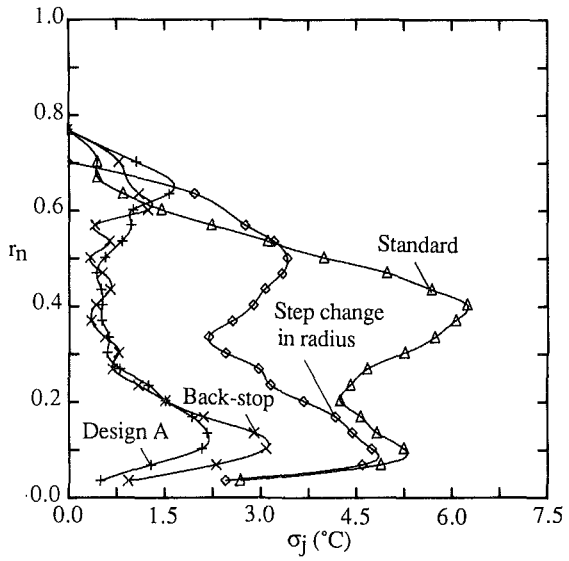

Fig. 9 Jet distortion

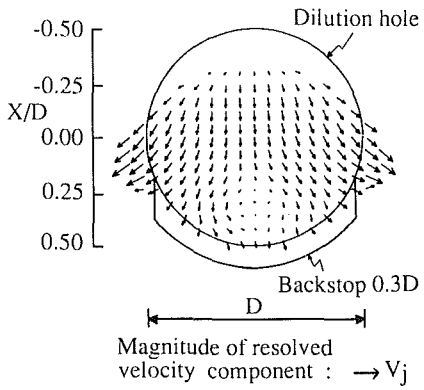

Fig. 10 Velocity vector plot for standard hole with backstop (Y/D = 0.35)

$$\sigma = \left(\frac{1}{6}\right)\left(\frac{1}{N}\right)\sqrt{\left[\sum_{j=1}^{6}\sum_{i=1}^{N}(T_i - T_{b_i})_j^2\right]} \quad (4)$$

where N is the number of data points ($\theta' > 0.1$) at that radius and where the maximum block temperature is used in evaluating the boundary of the jet.

It should be noted that both equations (3) and (4) are functions of r, but whereas the total standard deviation (σ) compares the local temperature pattern of a number of jets with their associated block distribution, the jet distortion parameter (σ_j) reflects the symmetry of a single jet about its own centerplane.

Results and Discussion

To make the development of a jet insensitive to the effects of the approach flow in the feed annulus, it is necessary to control the trajectory of the jet fluid issuing through the rear of the dilution hole, while also influencing the development of the downstream vortex flow field. Two types of dilution hole have been designed with these aims in mind (Fig. 7).

Three-Hole Sector Tests. Initial tests were undertaken with only three out of the 16 holes modified to the selected designs with the mixing characteristics of the jet at the center of the sector being investigated. For the purpose of comparison, the same three holes were modified in each test and compared with the results obtained for the standard geometry.

(*a*) *Design A.* In addition to the test conducted on the complete design, the individual modifications to the standard hole were tested to assess their contribution to the overall performance. Thus, a standard hole with backstop was tested, as was a plunged hole incorporating a step change in radius ($R = 0.4\ D$) around the rear 180 deg of the hole. The smooth temperature contours reflect the accuracy of measurement and high density of experimental data points (Fig. 8) and indicate a reduction in the distortion of the temperature pattern associated with these modifications that is also quantified using the jet distortion parameter (Fig. 9).

Incorporating a step change in radius at the lateral edges of the hole is designed to trip the bound vortices that are known to develop at this location. In addition, the fluid issuing through the rear of the hole has less influence on the lower momentum fluid at the sides of the jet. The hot core formed by the fluid issuing through the rear of the hole however is still distorted (Fig. 8*b*). This is virtually eliminated when a small (0.3*D*) backstop is tested with a standard plunged hole (Fig. 8*c*), so that deflected jet fluid must pitch over or yaw around this component as illustrated by the velocity distribution at $Y/D = 0.35$ (Fig. 10). This dominates any influence on fluid trajectory that the complex flow field has, the location of which has been centralized at the rear of the jet by the backstop. Since this component is present only around the rear 140° of the hole, hot jet fluid can be deflected into the vortex development region either side of the jet and therefore assists in setting up a downstream vortex flow field that is symmetric about the hole centerplane (Fig. 11). Several different lengths of backstop were tested, and to have the required influence on jet mixing at the operating conditions stated the backstop must not be less than 0.2*D*, with the nominal value of 0.3*D* being selected for the tests reported here. Further increases in length result in greater penetration of the jet into the dilution annulus without any significant improvement in the distortion parameter.

When the step change in radius and backstop components are tested individually, an improvement in the jet mixing parameter is obtained when compared with the standard design (Fig. 9). Combining these components to form Design A produces a further reduction in temperature distortion, particularly close to the injection wall. Whereas for the standard

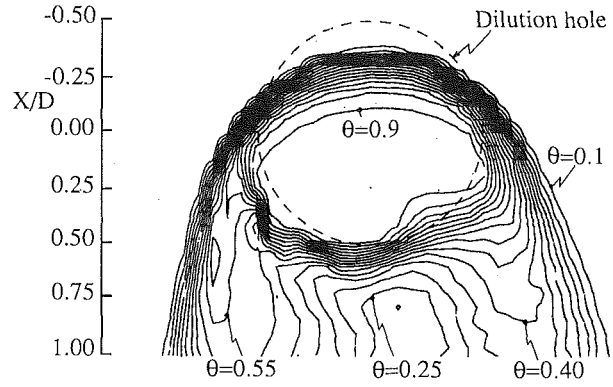

(a) Standard plunged hole (Y/D = 0.30)

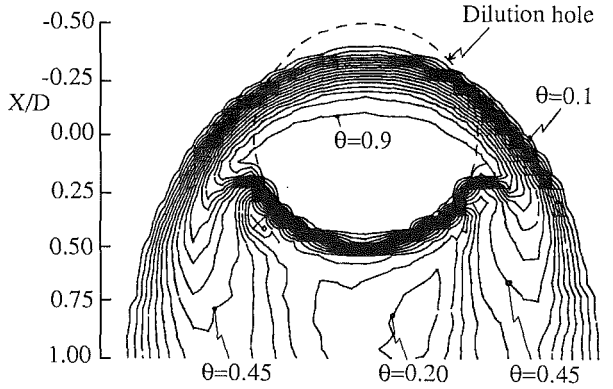

(b) Effect of backstop (Y/D = 0.35)

Fig. 11 Temperature distributions

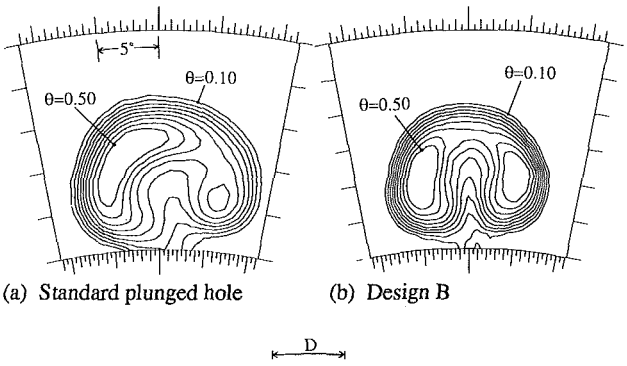

(a) Standard plunged hole (b) Design B

Fig. 12 Temperature distributions (*X/D* = 2.0)

design the maximum distortion of the jet about its centerplane is associated with hot core fluid ($r_n = 0.4$), this has been virtually eliminated by Design A with the peak distortion ($r_n = 0.1$) now being associated with the vortex controlled mixing region close to the injection wall.

The results indicate that these modifications have made the mixing characteristics of the jet less sensitive to the effects of the approach flow conditions.

(*b*) *Design B.* Previously published work by the authors (1987) has shown how jet fluid is deflected as it passes through a dilution hole due to the influence of the crossflow. The zero plunging radius around the rear 180 deg of the hole is therefore designed to influence the way the jet is fed and the deflection of the fluid as it passes from the feed annulus into the crossflow. Furthermore, the change in hole geometry at the lateral edges of the jet is designed to modify the vortex flow field that develops at this location.

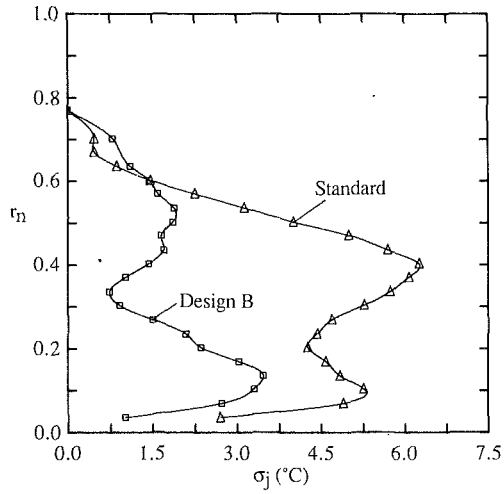

Fig. 13 Jet distortion

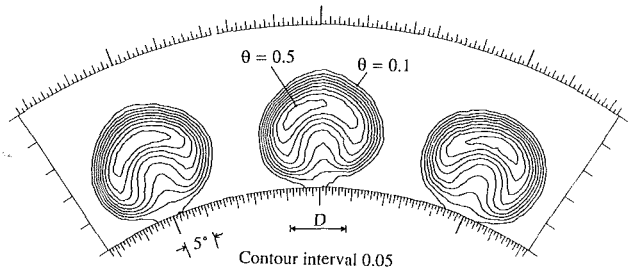

Fig. 14 Temperature distribution for center three jets of modified eight-hole sector (Design A, *X/D* = 2.0)

The temperature distribution associated with this design indicates a distinct change in the mixing characteristics of the jet (Fig. 12) and although some asymmetry is present there is still a significant improvement from that of the standard plunged hole (Fig. 13). The bifurcated temperature distribution is thought to indicate an increase in the strength of the downstream vortex flow field, probably due to the generation of vorticity being concentrated immediately downstream of the step change in radius by the straight sides of the hole.

Eight-Hole Sector Test. Investigation of a single jet has indicated that changes can be made to its mixing characteristics by modifications to the geometry at the injection plane. These results however must be repeated by a number of holes to calculate the effect on the consistency of the temperature pattern around the annulus. Modifications were therefore carried out on eight dilution holes with temperature measurements being made downstream of the six jets in the center of the sector. The results for Design A are compared with the temperature pattern produced in the same sector by the standard holes. Although the complete sector temperature distribution has not been reproduced, comparing the temperature patterns associated with three of the holes (Fig. 14) with the standard geometry results presented earlier (Fig. 1) indicates the more uniform mixing characteristics of the modified dilution jets. The improved overall mixing of the six jets is quantified using the standard deviation for the sector from that of its block distribution (equation (4)), the value of which has been reduced by approximately 50 percent across the annulus (Fig. 15). As was indicated by the jet distortion parameter, the asymmetry associated with the core of each jet about its own center plane is reduced by the modified hole design, and this leads to a significant improvement in the consistency of the temperature pattern around the sector. The maximum circumferential temperature deviation occurs at the same radial

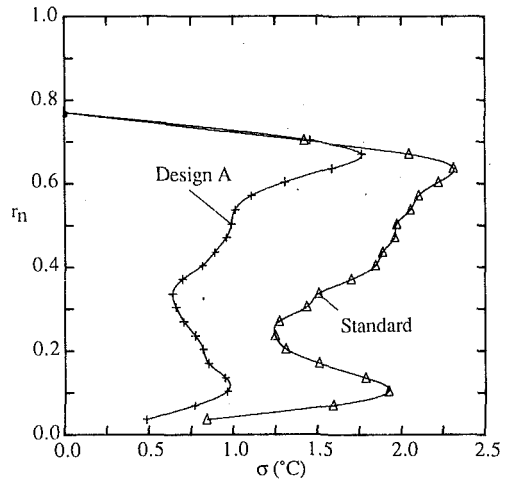

Fig. 15 Total standard deviations for modified and standard hole sectors

location ($r_n \approx 0.65$) for the two types of hole being compared and is associated with differences in the overall penetration of each jet. It would appear that the improved mixing characteristics of each jet core also produce a more uniform penetration of the jets.

Further eight-hole sector tests incorporating Design B have yet to be conducted.

Hole Discharge Coefficients. The outer casing of the test facility was removed so that the jets effectively discharged into a plenum, with the discharge coefficients of the new hole design being calculated from measurements made in the center of a three-hole sector. The mass flow through a hole was obtained by traversing a five-hole probe across the exit plane, although for Design A this meant removal of the backstop protruding from the injection wall. The mass-flow weighted pressure drop across the casing was obtained from a five-tube pitot rake in the feed annulus. To check the accuracy of the experimental method, results for standard holes (Table 1) are compared with empirical data for the same operating conditions and hole geometry, but obtained using a more conventional test technique. Although there is some discrepancy from the previous data, it is thought the experimental method is of sufficient accuracy to indicate that the modified hole designs do not incur a significant penalty in terms of reduced C_D. The test data have indicated that discharge coefficients are sensitive to the leading edge hole profile where separations can take place. Since the flow entering the rear half of the hole is almost axial, modifications can be made to the hole geometry in this region that appear to have minimal effect on C_D.

Conclusions

An experimental investigation has been conducted into the temperature distribution produced by heated dilution jets being injected into a confined annular crossflow. The following conclusions have been drawn.

1 Large distortions of the temperature pattern around the dilution annulus are observed when a row of standard plunged dilution holes is supplied from a representative feed annulus.

Table 1 Dilution hole discharge coefficients

HOLE TYPE	C_d
Straight faced dilution hole (t/D = 0.375)	0.72 (0.69)
Standard plunged dilution hole (R_p/D = 0.375)	0.90 (0.91)
Design A	0.90
Design B	0.90

( ) Denotes values obtained using conventional techniques

2 Two modified hole designs have been tested and have illustrated how the mixing of dilution jets can be controlled by changes in geometry at the injection plane.

3 Results from an eight-hole sector test incorporating one of the modified designs has demonstrated a substantial improvement in the consistency of the temperature pattern around the annulus when compared with the standard hole configuration.

4 At the operating conditions tested, the modified hole designs exhibit virtually the same discharge coefficient values as those of the standard plunged holes.

Acknowledgments

This work was supported by The Ministry of Defence, Royal Aircraft Establishment, Pyestock, Farnborough, Contract No. D/ER1/9/4/2170/113/RAE(P). The authors also wish to express their appreciation to Messrs. G. Hodson, R. Marson, and D. Glover for their assistance in the design and construction of the test rig.

References

Andreopoulos, J., and Rodi, W., 1984, "Experimental Investigation of Jets in a Crossflow," *J. Fluid Mech.*, Vol. 138, pp. 93–127.

Carrotte, J. F., and Stevens, S. J., 1987, "The Influence of Dilution Hole Aerodynamics on the Temperature Distribution in a Combustor Dilution Zone," AIAA Paper No. AIAA-87-1827.

Carrotte, J. F., and Stevens, S. J., 1988, "Experimental Studies of Combustor Dilution Zone Aerodynamics," AIAA Paper No. AIAA 88-3274.

Crabb, D., and Whitelaw, J. H., 1979, "The Influence of Geometric Asymmetry on the Flow Downstream of a Row of Jets Discharging Normally Into a Free Stream," ASME *Journal of Heat Transfer*, Vol. 101, p. 183.

Holdeman, J. D., Walker, R. E., and Kors, D. L., 1977, "Mixing of a Row of Jets With a Confined Crossflow," *AIAA Journal*, Vol. 15, No. 2, pp. 243–249 (see also NASA TM X-71426).

Holdeman, J. D., Srinivasan, R., and Berenfeld, A., 1984, "Experiments in Dilution Jet Mixing," *AIAA Journal*, Vol. 22, No. 10, pp. 1436–1443 (see also NASA CR-168031 and NASA CR-174624).

Holdeman, J. D., and Srinivasan, R., 1986, "Modeling Dilution Jet Flowfields," *Journal of Propulsion and Power*, Vol. 2, No. 1, pp. 4–10 (see also NASA CR-175043).

Holdeman, J. D., Srinivasan, R., Coleman, E. B., Meyers, G. D., and White, C. D., 1987, "Effects of Multiple Rows and Noncircular Ofirices on Dilution Jet Mixing," *Journal of Propulsion and Power*, Vol. 3, No. 3, pp. 219–226 (see also NASA TM-86996).

Kamotani, Y., and Greber, J., 1974, "Experiments on Confined Turbulent Jets in Cros-Flow," NASA CR-2392.

Lefebve, A. H., 1983, *Gas Turbine Combustion*, McGraw-Hill, New York.

Moys, R. H., and Stevens, S. J., 1983, "Asymmetric Jets in an Annulus," Loughborough University, Dept. of Transport Technology, TT83R02.

Shaw, D., 1981, Rolls Royce Ltd., Report PD 2181.

Sridhara, K., 1970, "Gas Mixing in the Dilution Zone of a Combustion Chamber," National Aeronautical Laboratory, India TN30.

Wray, A. P., 1986, "The Use of a 5-hole Probe as a Non-nulled Instrument and the Analysis of Test Data Using the Computer Program, 5HP1, 5HP2 and 5HP3," Loughborough University, Dept. of Transport Technology, TT86R02.

Flow Guiding and Distributing Devices on the Exhaust Side of Stationary Gas Turbines

F. Fleischer

C. Koerner

J. Mann

G&H Montage GmbH,
Ludwigshafen, Federal Republic of Germany

Following repeated cases of damage caused to exhaust silencers located directly beyond gas turbine diffusers, this paper reports on investigations carried out to determine possible remedies. In all instances, an uneven exhaust gas flow distribution was found. The company's innovative approach to the problem involved constructing a scale model of a complete gas turbine exhaust system and using it for flow simulation purposes. It was established for the first time that, subject to certain conditions, the results of tests conducted on a model can be applied to the actual turbine exhaust system. It is shown that when an unfavorable duct arrangement might produce an uneven exhaust flow, scale models are useful in the development of suitable flow-distributing devices.

1 Reasons for the Development of Flow Guiding Devices

At the beginning of the 1970s, when the first 60–90 MW gas turbines were put into operation, damage to exhaust silencers always occurred when the silencers were located directly beyond the gas turbine diffuser. In those cases splitter silencers were always involved. The splitters were made of perforated steel plate and had mineral wool infills wrapped in glass silk cloth.

The glass silk cloth was damaged, the mineral wool was partially pulverized, and some of it was actually drawn out through the holes of the perforated steel plate. This damage occurred only in some areas, whereas other areas showed no signs of damage.

In gas turbine installations with the gas exhausts in an axial direction, damage occurred mostly in a circular area at the inlet to the silencer. This apparently occurred due to extreme flow velocities in conjunction with strong turbulence in this area.

In order to confirm the problem as well as to determine possible solutions, different arrangements of gas turbine diffusers, exhaust ducts, and silencers were set up in a scale model and the flow conditions investigated (DeLank and Poetz, 1976). In all cases the tests confirmed the suspicion gained from the reports on cases of damage to silencers that there was a completely uneven flow distribution in front of and inside the silencers.

In those areas of the actual system where damage occurred, air velocities of more than double the mean were recorded. The mean velocity is calculated out of the nominal throughput and the free section of the exhaust duct.

Especially in square or rectangular silencer sections behind circular gas turbine diffusers, boundary zones were discovered that manifested flow velocities of almost zero or even negative values (recirculation).

In light of the above it was clear why steps to improve the silencer splitters by means of special covering material for the mineral wool infill, such as extra dense mats or stainless steel wire mesh, were not an acceptable long-term solution. Silencer splitters with a mineral wool infill in hot and turbulent exhaust gases are only usable up to velocities of 50 m/s.

Uneven velocity profiles in the exhaust duct are not only responsible for damage to the silencers, but also make it impossible to ascertain the real pressure loss of the silencer.

A silencer with an uneven flow profile will manifest a higher pressure loss than one with even flow conditions. Just as important as the pressure loss is the problem of self-generated noise of silencers with uneven flow profiles, as the latter only tend to even out to a minor extent through the length of the silencer. In light of ever more exacting demands with regard to noise reduction, with very large exhaust gas flow rates (of over 1000 m^3/s) and correspondingly large duct cross sections, the flow noise at the outlet of a silencer is a factor that cannot be ignored when designing gas turbine silencers. Because the sound power level of the flow noise increases by 50 to 60 times the log of the flow velocity, a doubling in the velocity means an increase in the sound power of such flow noise of 15 to 18 dB(A).

2 Development of Flow Guiding Devices

(a) Model Laws. Due to the extremely complex limiting conditions applying to ducts, silencers, and the flow guiding devices, analytical-mathematical calculations do not yield usable solutions.

Experiments to determine suitable flow guiding equipment are rather labor intensive but produce realistic results that are

Contributed by the International Gas Turbine Institute and presented at the 34th Internatioanl Gas Turbine and Aeroengine Congress and Exhibition, Toronto, Ontario, Canada, June 4–8, 1989. Manuscript received at ASME Headquarters February 1, 1989. Paper No. 89-GT-214.

Table 1 Reynolds number $\mathrm{Re} = \dfrac{v \cdot d \cdot p}{\mu}$; $\nu = \mu/p$

v = velocity of the medium, m/s
d = main dimension, m
p = density of the medium, kg/m^3
μ = dynamic viscosity, Pa•m
ν = kinematic viscosity, m^2/s
$\nu = 16 \times 10^{-6}$ m^2/s, air 300 K
$\nu = 80 \times 10^{-6}$ m^2/s, air 800 K

Table 2 Pressure loss in model and in original; $p_o = p_m \times M^4 \dfrac{T_m}{T_o} \times \dfrac{Q_o^2}{Q_m}$

p_o = pressure loss of the original
p_m = pressure loss of the model
M = mode scale
T_o = exhaust temperature of the actual system
T_m = exhaust temperature of the model
Q_o = exhaust flow rate of the actual system
Q_m = exhaust flow rate of the model

applicable in practice. The high costs do not allow experiments on full-size gas turbines.

Effective results can also be gained with small model tests if the conditions under which the aerodynamic laws are comparable are respected. These laws say that the flow profiles of two geometrically similar objects located within an air flow are also geometrically similar if their Reynolds number is the same.

The Reynolds number is a dimensionless number resulting from a combination of all characteristic parameters of a flow as listed in Table 1. These parameters are:

- flow velocity
- major dimension
- density of the flow medium
- dynamic viscosity

With the same Reynolds number for model and actual system the flow geometries wll be similar, i.e., the model and the actual system will have the same flow profiles with wake and maximum velocities at the same positions. The direction and strength of the flow will also be the same. Also the pressure loss coefficient as a coefficient of the total pressure difference and the dynamic pressure are the same in the model as in the original.

If one can achieve the same flow velocities during wind tunnel tests with the model as with the actual system, the scale factor is then determined only by the temperature-related kinematic viscosity of the flowing medium. This kinematic viscosity changes, e.g., for a temperature difference from 300 K to 800 K by the factor five. Models of scale 1:5 are easy to build.

If, however, the temperature differences between the model and the actual system are too small or when the necessary air velocity is not achievable in the model, the case can occur that the Reynolds number of the actual system cannot be realized in the model. However, this is not that critical because as long as a fully turbulent flow remains, i.e., the Reynolds number is larger than 3×10^5, the model results are still easily transferable to the full size installation.

If the Reynolds numbers for the model and the original are the same, one can calculate the pressure loss of the original on the basis of the pressure loss measured in the model according to the formula set out in Table 2.

In Table 3 data of the full-size installation and of the model for a typical 125 MW gas turbine are given as an example. During the last 15 years flow tests on models have been made

Table 3 Example

	Original	Model
Intake air temperature [°C]	15	20
Exhaust gas temperature [°C]	580	40
[K]	853	313
Exhaust gas volume [m3/s]	1030	3,81
Kinematic viscosity [m²/s]	115 x 10^{-6}	16 x 10^{-6}
Reference diameter d [m]	3,477	0,3
Exhaust gas velocity [m/s]	147,6	73,3
Reference cross section F [m^2]	6,98	0,052
Reynolds number Re	4,46 x 10^6	1,37 x 10^6
G + H MONTAGE GmbH		

modelling of a gasturbine hub diffusor

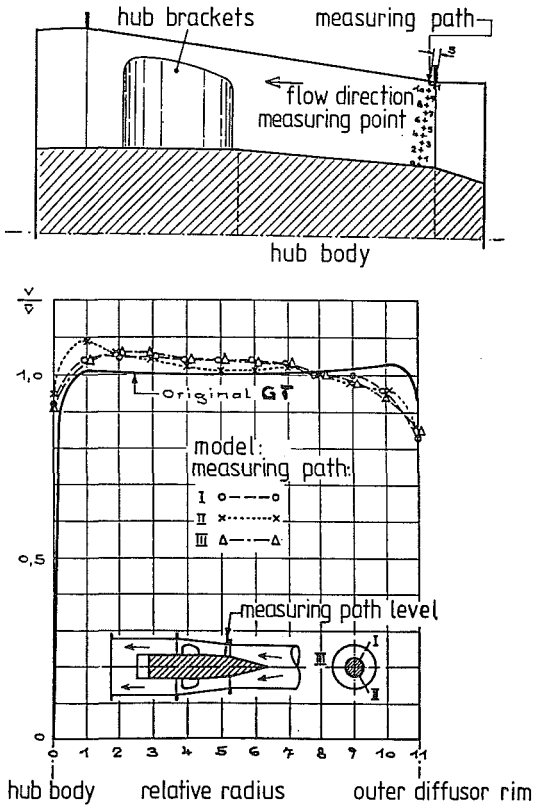

Fig. 1 Flow velocity profile gained by model tests in a gas turbine exhaust diffuser (BBC Hemweg)

in the laboratory on more than 30 gas turbine exhaust systems with silencers.

For these tests models were built up to a scale factor of 1:12 with Reynolds numbers always greater than 10^6.

The following will show how the model tests were carried out.

At the beginning of the testing all relevant technical data of the actual turbine in question are summarized. The data for the model are chosen according to the characteristics of the available wind tunnel and the scale of the model with a view to achieving an equal Reynolds number.

If the flow profile at the diffuser end of the gas turbine is known it is adopted in the model (see Fig. 1)

Often such a profile is not available, in which case an exact replica of the original gas turbine diffuser has to be integrated into the model to ensure that the flow profile obtained in the model tests is equal to the flow profile in the actual full size system. All other parts such as exhaust plenum, ducting, and silencers are built according to the scale of the model.

In order to control the flow velocity and the pressure loss, the total pressure in front of the model is determined in the wind tunnel by means of a matrix measuring method. The flow rate is calculated from static pressure and temperature, the figures of which are determined with a nozzle at the entrance to the wind tunnel.

The target is to obtain flow velocity profiles at the silencer entrance. The velocities are measured with a Prandtl static tube. The result is a velocity profile in the cross-sectional area of the duct.

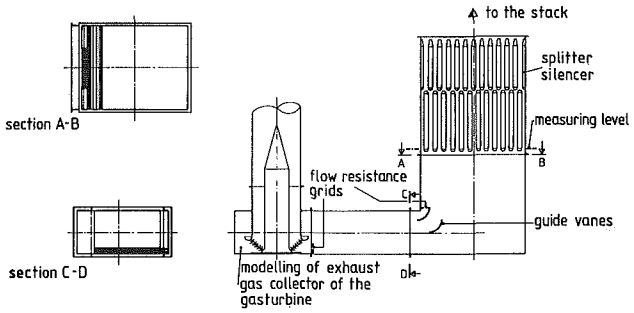

Fig. 2 Model of a horizontal exhaust system for a 120 MW gas turbine

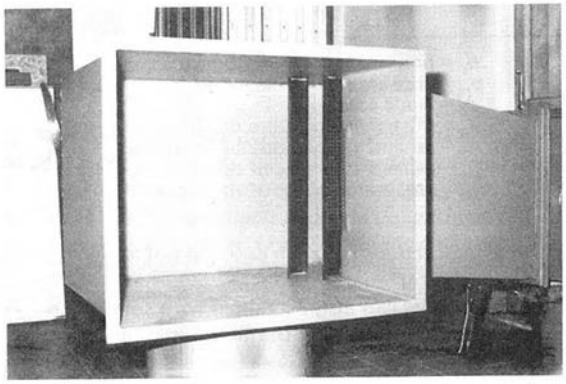

Fig. 4 Flow directing installations in the exhaust system shown in Fig. 2

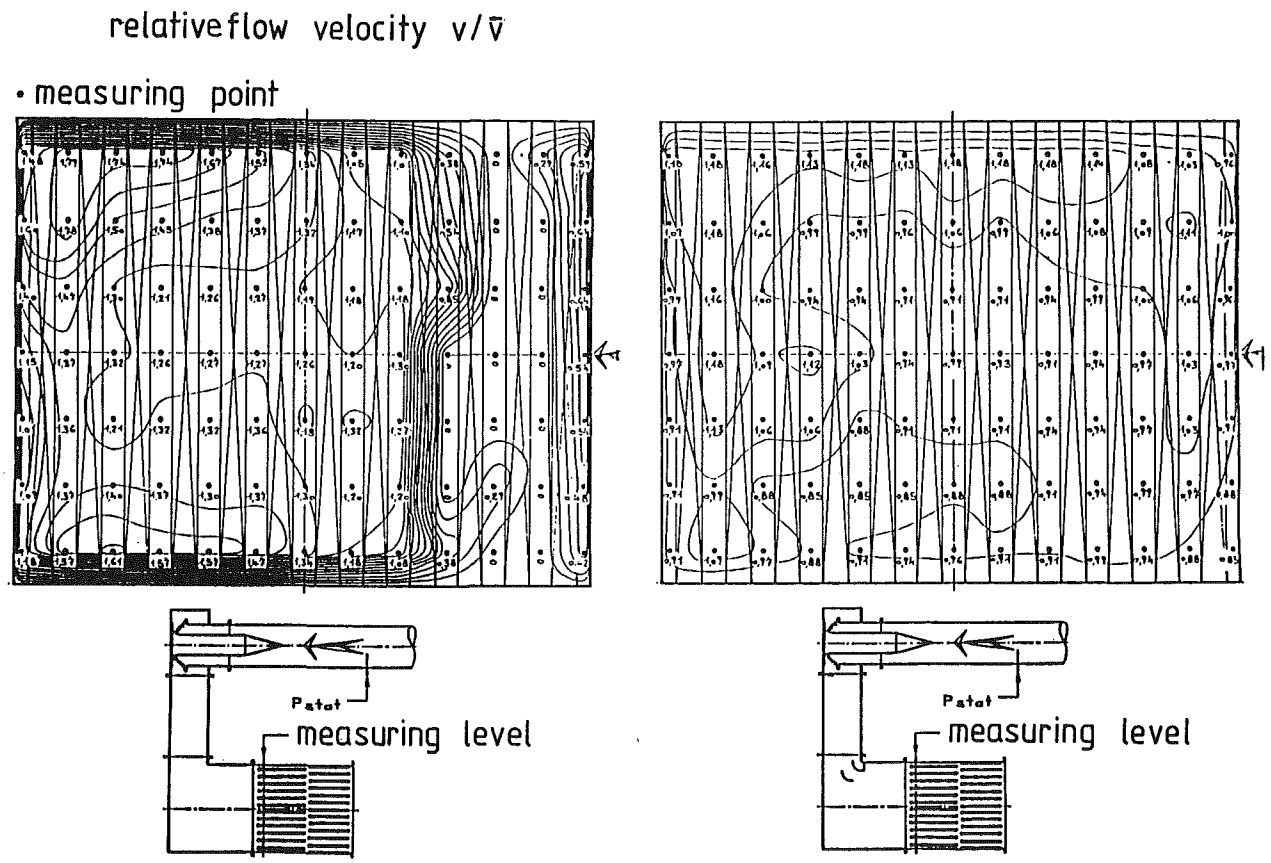

Fig. 3(a) Fig. 3(b)

Fig. 3 Isotachs (= lines of equal flow velocities) in the silencer level for the gas turbine unit of Fig. 2 without (a) and with (b) the flow guiding installations

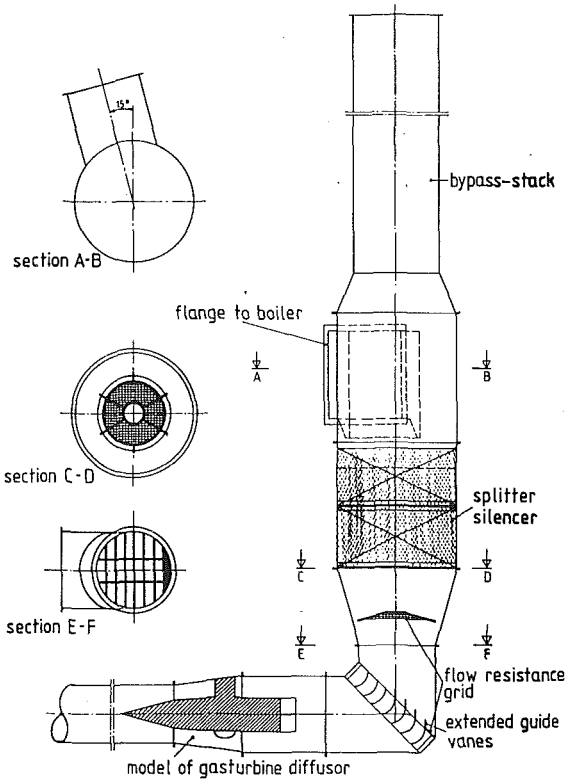

Fig. 5 Arrangement of the horizontal gas turbine diffuser, stack, and silencer of a 150 MW gas turbine

These measurement data are most clearly presented in the form of isotach fields (= lines of equal flow velocities).

Appropriately all data are referred to the calculated mean velocity, and the coefficients of local velocity and mean velocity are demonstrated graphically (see Figs. 3*a*, *b*).

(b) Model Tests. Due to lack of space, most gas turbine installations do not allow the creation of an ideal flow situation between gas turbine diffuser and silencer as well as in the further ductwork (which would be possible if long stretches of ducting with gradually increasing cross section were available). To overcome this limitation, flow guiding devices must be installed in the duct between diffuser and silencer to smooth the flow to an acceptable degree. It has been shown that so-called quasi-permeable flow arresters manufactured

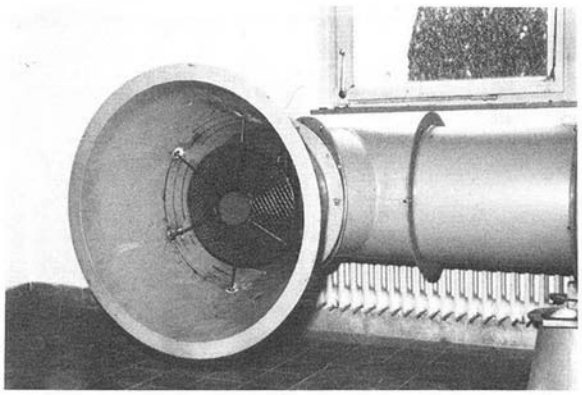

Fig. 7 Flow directing installations for the gas turbine unit as shown in Fig. 5

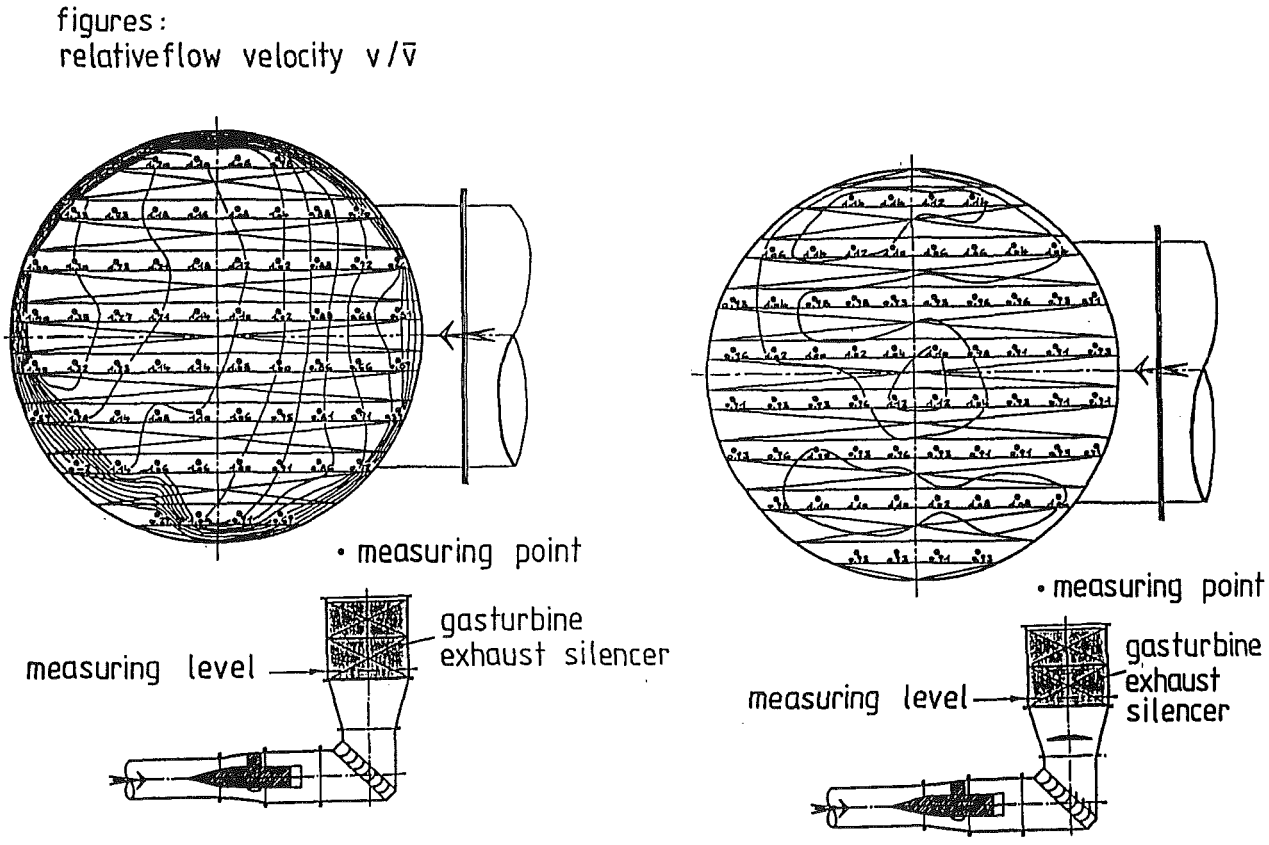

Fig. 6(*a*) Fig. 6(*b*)

Fig. 6 Isotachs in the silencer level of the unit shown in Fig. 5 without (*a*) and with (*b*) the flow directing devices

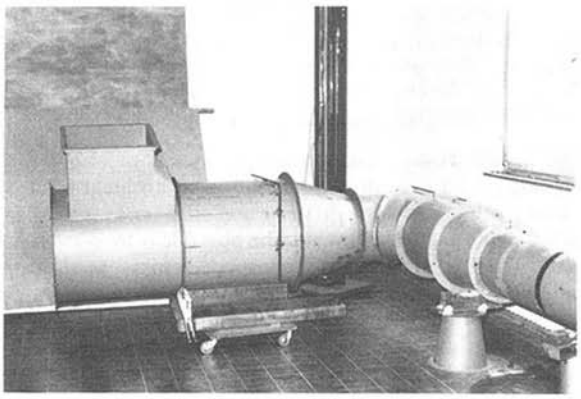

Fig. 8 View of the complete model of the exhaust system depicted in

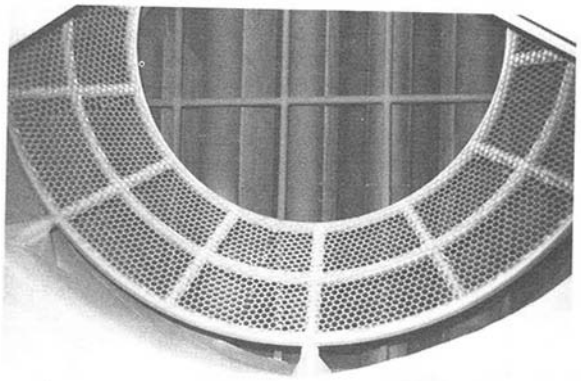

Fig. 10 Mild steel flow resistance grid between turbine diffuser and silencer of a 60 MW gas turbine

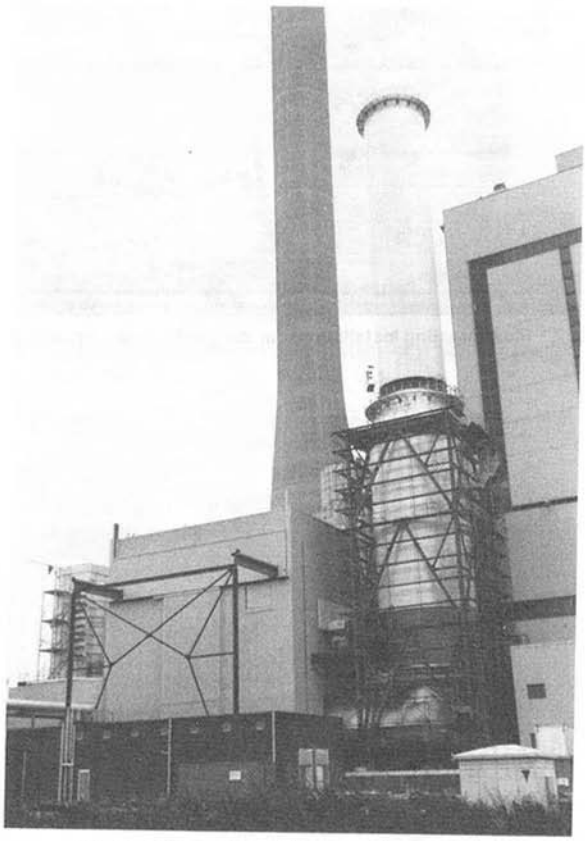

Fig. 9 Actual stack of the unit shown in Fig. 5

from perforated steel plate or grids are very helpful in reducing peaks in the flow velocities. The pressure losses that are created by such flow guiding devices are fully compensated for in most cases by a pressure recovery due to the improved filling of the ducts (i.e., utilization of the whole duct space) with exhaust gas together with a higher directioning efficiency and lower pressure loss in the silencers.

The flow tests have quite frequently revealed deficiencies in customer-designed flow deflectors, e.g., guide vanes. For the model tests these deflectors were initially copied from the design used by the customer. In several cases significient improvements of the flow conditions were achieved by means of slight modifications of the customer-designed flow deflectors.

The following examples show how effective the installation of flow guiding devices can be. In addition to the spatial situation, an isotach field in the plane of the silencer is compared before and after installation of flow correcting devices.

For the model shown in Fig. 2 with a horizontal exhaust duct and a 180 deg bend, the flow profile without the installation of flow guiding devices is given in Fig. 3(a). This flow profile shows peaks up to 1.79 times the mean velocity, zones with back-flow ($v/vm = 0$), and areas with steep gradients of flow velocity.

With the flow directing devices shown in Fig. 4, the flow is significantly smoothed, as shown by the flow profile of Fig. 3(b). This flow profile shows the situation in the measuring plane at the silencer entrance. The biggest deviations from the mean velocity are here reduced to maximum 18 percent. Normally variations of the mean flow velocity of between 10 and 20 percent are acceptable.

This improvement was achieved with semipermeable guide vanes made of perforated steel plate and those made of solid steel plate. In addition small flow resistance grids were installed to reduce the peaks in the flow velocity.

A further example is given where the exhaust gas of a 150 MW gas turbine is directed by a horizontal hub diffuser into a stack with a built-in silencer (N.N., 1988).

The increase of the duct cross section behind the guide vanes at the foot of the stack in the direction of the silencer was originally specified but found to be unfavorable in view of the flow distribution.

Therefore the existing flow distribution had to be improved (Figs. 5 and 6). These guide vanes were designed according to the theories published in the relevant technical literature.

By modification of the existing guide vanes and by installing a circular flow resistance grid an improved flow situation was achieved (Fig. 7). A view of the model and of the actual system is given in Figs. 8 and 9.

3 Application of the Scale Model Results to the One-to-One Scale

(a) Constructional Problems. When applying the test results, one must consider certain technological constraints to prevent damage to the turbine.

The differing thermal expansions and contractions of ducting and built-in items require that the built-in items are flexibly mounted to accommodate such movements.

The initial idea of using flow resistance installations made of wire mesh was not successful. These stainless steel wire mesh grids chafed through under constant use.

Flow directing installations made of 8–10-mm-thick heat-resistant perforated steel plate welded to a suitable framework proved to be satisfactory.

For the model tests, perforated steel plates with a flat surface are used.

In the 1:1 scale the plates must be bent to achieve stiffness against vibrations:

Figure 10 shows such a circular flow resistance grid, which is used directly behind the hub diffuser of a 60 MW gas turbine.

(b) Experience With Previously Installed Flow Guiding Devices. Gas turbine exhaust systems fitted with the previously described flow guiding devices have been used since the mid-1970s. These devices were fitted for turbines from 10 to 150 MW.

The company thus has more than a decade of experience with flow deflecters. Over this period cases of damage to silencer splitters have almost totally ceased. No instances of damage to the absorption material infill of the silencer splitters were recorded even in those cases where silencers were located only a few meters beyond the diffuser of gas turbine installations with a hub diffuser and after 30,000 hours of operation (e.g., BBC turbines type 13 at Najaf Power Station Iraq, BBC turbines type 13 at Mainz-Wiesbaden Power station FRG).

Damage to installed flow guiding devices now no longer occurs since the quasi-permeable flow deflecters are made of perforated plate instead of wire mesh.

4 Summary

A decade of experience has proved that it is important and profitable to investigate the flow characteristics of gas turbine exhausts using scale models.

This prevents damage to silencers and helps to make the self-generated noise controllable where requirements for noise reduction are stringent.

Flow-directing devices developed using a scale model have proved to be highly efficient over many years when installed in actual gas turbine exhaust systems.

References

De Lank, G., and Poetz, F., 1976, "Primary and Secondary Measures to Protect Silencers From Damage Where They Are Installed Directly Behind Gas Turbines," *VGB Kraftwerkstechnik 50*, Vol. 11, pp. 687–692.

N. N., 1988, "Flow Directing Installations for the Exhaust System of the 150 MW Gas Turbine in the Hemweg Power Station," *Motortechnische Zeitschrift*, Vol. 6, p. 226.

The Design and Performance Optimization of Thermal Systems

M. R. von Spakovsky
École Polytechnique Fédérale de Lausanne,
Départment de Mécanique,
Laboratoire d'énergétique industrielle,
Lausanne, Switzerland

R. B. Evans
Georgia Institute of Technology,
The George W. Woodruff School
of Mechanical Engineering,
Atlanta, GA 30332

Optimization techniques are, in general, still not used today in the design and performance analysis of thermal systems and their components. The engineer's search for the best system configuration is based solely on rules-of-thumb and not on a systematic, analytical determination of what the optimal design or performance should be. In addition, economic factors are not directly tied to thermodynamic ones; therefore, the economic ramifications of thermodynamic changes to the system are not usually, if ever, immediately apparent. A general analytical approach that directly determines the optimum thermodynamic and econmic behavior of thermal systems is discussed and illustrated using Rankine cycles. Utilizing the Second Law and typical Second Law costing techniques, this method provides for the creation of mathematical models that balance a cycle's operating costs and capital expenditures. Such models can be solved numerically, subject to various constraints, for the optimum design and performance of thermal systems.

Introduction

The concepts of "Thermoeconomic Functional Analysis" (Evans et al., 1983; Frangopoulos, 1983; von Spakovsky, 1986) and "Thermoeconomic Isolation" (Evans, 1980; Frangopoulos, 1983; von Spakovsky, 1986) form the foundations of the analytical approach presented here. The first concept, based on Second Law analysis (e.g., entropy generation as a precise measure of energy utilization) and typical Second Law costing techniques, is used in an example of a nonidealized Rankine cycle to demonstrate how a thermal system's thermoeconomic "basis" model is established and then optimized. Such a model simultaneously describes both the economic and thermodynamic behavior of the system by balancing operating costs and capital expenditures and by requiring the functional breakdown of each of the system's physical components into either a conversion or a transmission function. The term "basis" indicates that little if any detail about the internal configuration of the system components is used. Conversion functions apply to components such as a boiler, turbine, reheater, condenser, pump, or feedwater heater and define a device having one and only one primary function or purpose. A transmission function, on the other hand, applies to a component such as a pipe. It may have one or more primary functions since it, in fact, carries or transports some or all of the different quantities used to define the various constraints utilized in the model.

In such a model, operating costs are based on the Second Law quantities that each component requires in order to perform its function. Such Second Law quantities are discussed in detail below. These component functions relate the entropy generated in each physical process to the Second Law quantities that each component buys from and/or sells to the rest of the system in order to satisfy the Second Law and overcome the irreversibilities present in each cycle. It is this use of the Second Law that accurately describes the true nature of each physical process taking place and serves as a common means of comparison not possible when using the First Law. An accurate picture of where the cycle inefficiencies exist is, therefore, directly incorporated into the mathematical model of the system, and the operating costs that relate to the costs of entropy generated at each point in the cycle can be found using mathematical methods of nonlinear programming. These costs, along with their corresponding Second Law quantities, represent the economic and thermodynamic interactions, respectively, that occur between cycle components.

In addition to the operating costs, capital expenditures (which also appear in the model) are formulated mathematically to depict the actual costs of the initial investment, depreciation, interest, insurance, tax, replacement, and maintenance for each piece of equipment. These costs vary with changes in the thermodynamic operation of the system and are important from the standpoint of the worth or weight in capital that each component operation has relative to the other component operations in the system. Balancing these capital expenditures with the operating costs for each component and summing them together results in a mathematical model that includes an objective function that describes a system's cost of ownership and operation. It is the minimization of this function, subject to various constraints (i.e., the thermodynamic interactions mentioned above) that yields an optimum set of performance variables corresponding, for example, to a given power plant load. Such a set results in the best overall cycle efficiency consistent with a minimum cost of ownership and operation.

Finally, if in the development of the "basis" model for a system and its components the concept of "Thermoeconomic Isolation" is combined with that of "Thermoeconomic Functional Analysis," then the model's optimization results not only in a minimum system cost and a minimum cost for each

Contributed by the Advanced Energy Systems Division for publication in the JOURNAL OF ENGINEERING FOR GAS TURBINES AND POWER. Manuscript received by the Advanced Energy Systems Division August 26, 1988.

component but also in a "stable economic environment" around each function or component in the system. Such an environment allows each component to be optimized in greater detail, isolated from the system, while at the same time maintaining an optimum design for the system as a whole. A discussion of the "detailed" thermoeconomic models used in such environments is beyond the scope of this paper. However, stable economic environments for individual components do place requirements on the development of the "basis" model. For this purpose, the concept of "Thermoeconomic Isolation" is briefly covered in the following discussions.

Thermoeconomic Functional Analysis

The thermoeconomic optimization of a thermal system must first begin with a determination of the function(s) of the system and each of its physical components (hence the name "Thermoeconomic Functional Analysis"). The function(s) of the system correspond to any products that cross the system boundaries to the surroundings and are then sold at some price to a buyer. These system products are designated as "benefits," and an example is the sale of electrical power and process steam from a cogeneration plant to some outside agency.

The function(s) of a physical transmission component depend on the nature of the interconnection(s) between conversion components and, as such, are known once these interconnection(s) are established. The function of each physical conversion component, on the other hand, is determined by examining the outputs of each and deciding which of these exhibit the primary purpose or nature of the component in question. For example, in a steam power plant, a turbine's primary function is to produce shaft power, that of a boiler feed pump is to produce high-pressure feedwater, and that of a feedwater heater is to heat the feedwater. A steam generator, however, can have two primary products, i.e., superheated steam for a high-pressure turbine and reheated steam for an intermediate pressure turbine. In "Thermoeconomic Functional Analysis," each conversion component has one and only one primary function so that the steam generator described above actually consists of two components, a boiler unit with superheated steam as its primary product and a reheater unit with reheated steam as its primary product.

With few exceptions the main function of each conversion component in a thermal system is obvious, and the number of components making up the system (not including transmission components) is at least initially consistent with one primary product per conversion component. This initial number increases when certain physical characteristics of the operation of the thermal system require "staging." By "staging" it is meant that a component with one primary function is broken down into multiple components, each with one primary product, the sum of which equals the primary product of the original component. As an illustration, a steam turbine with reheat and multiple regeneration is chosen. The turbine component with one primary product will have one stage before and one after reheat and one stage for each feedwater heater extraction after the first. Each stage will then correspond to a single component. Of course, the steam extractions, the main steam flow to the next component, or the steam for reheat act only as secondary outputs for each stage so that the primary product of each turbine component is still the generation of shaft power.

Once the components of the system, their functions, and primary outputs are determined, the next two steps in the functional analysis of a thermal system require the separation of a component's secondary outputs from its primary function(s) and a determination of the inputs necessary for each component's thermoeconomic operation. The process of finding the inputs is best served by a concrete example, which is presented later in the analysis of a Rankine reheat cycle. For now we assume the inputs are known. The separation of secondary outputs can, however, be generalized to the use of branches and is necessary since the performance of a component's primary purpose or purposes does not require these outputs. By inserting a branch for each of them, every secondary output is separated from its component's function(s) and, in turn, made an output of a branch. In this way, each component in the system, both conversion and transmission, consists only of its function(s), each function's product, and all the inputs required for the performance of its function(s). Thermoeconomically, each component's operation can now be fully described by a balance between the cost rates associated with each of its inputs, function(s), and product(s).

Up to this point, the functional breakdown of a thermal system has been described; and in a general way, the thermoeconomic operations of each function have been represented. The next step is to establish the interconnections between all system components. These interconnections introduce the use of junctions, help pin down the inputs required for each function, and determine the functional opera-

Nomenclature

$B, \dot{B}$ = benefit cost function and cost rate
i = original total investment or purchase cost
i_b = original base investment or purchase cost
$\dot{K}, K$ = fixed cost rate or cost, e.g., surcharges
L = Lagrangian
P = pressure
s = entropy per unit mass
T = temperature
TTD = terminal temperature difference
U = overall heat transfer coefficient
$\dot{W}$ = rate of work or power
x = decision or design variable; quality (mass)
Y = essergy (all forms) input stream
y = essergy (all forms) output stream
$Z, \dot{Z}$ = capital cost function and cost rate
$\Gamma, \dot{\Gamma}$ = cost function and cost rate
η, η_M = mechanical efficiency
η_{II} = Second Law efficiency or effectiveness
λ = Lagrange multiplier or unit cost (marginal)
ϕ = primary stream or performance variable

Subscripts

a = condenser cooling water inlet
B = boiler
b = condenser cooling water outlet
BFP = boiler feed pump
CND = condenser
CP = condenser cooling water, circulating pump
FWH = feedwater heater
G = generator
HP = high-pressure turbine
IP = intermediate-pressure turbine
LP = low-pressure turbine
M = mechanical
n = iteration
o = environment
R = reheater

Superscripts

*, opt = optimum

tion of each transmission component and the system as a whole. As a part of this step, the main mass flow of the thermal system with its associated cost rates is chosen as the basis for the component interactions. Any component functions either branch off of the main flow or join the main flow with a junction.

The result of all branches and junctions is that the component interconnections as represented by the main mass flow and any secondary mass flows exist as a separate entity apart from that of the component functions and their inputs and outputs. Branches and junctions simply tie these two separate entities together. In this way, the functional nature of each component is maintained even while interacting with the system as a whole. Of course, establishing the component interconnections does not establish the nature of the interconnections, i.e., their measure or measures, nor their direction. A set of interconnections, which appears at equilibrium points in thermal systems, is the one representing the "potential work" interactions that occur between most ordinary system components. "Thermoeconomic Functional Analysis" suggests the Second Law quantity essergy or "essential energy" as a measure. This quantity was shown by Evans (1968, 1969) to be the only consistent and most general measure of potential work. As such, it applies to nonequilibrium points, thereby describing the interactions between all possible thermal components. All other measures such as exergy, availability, available energy, etc. are simply special equilibrium cases. Component interconnections not represented by a potential work interaction are measured by other forms of essergy such as negentropy. As with potential work, the negentropy interconnections represent interactions occurring between all of a system's thermal components. Any additional component interconnections require measures of essergy other then the ones mentioned above and may also be limited to interactions that occur between only some of the system's components, i.e., between those where the measure plays a crucial decision role. Such interactions are called "accommodation constraints or costs" (von Spakovsky, 1986) and may lead to a further functional breakdown of one or more components. Their purpose is related to the degree of disjointness or thermoeconomic isolation of each component and are beyond the scope of this paper.

The use of essergy as a measure gives an indication of each component's ability to utilize or "consume" the potential work represented by each stream in a thermal cycle. In other words, essergy and its associated cost rates show how well each component's function operates thermoeconomically in overcoming its energy dissipations and producing its "product(s)." The choice of negentropy and its associated cost rates results from the terminal component, which is explicitly or implicitly part of any thermal system (e.g., the condenser and cooling tower in a Rankine cycle). Its function is to rid the system of heat in conformance with the Second Law, and Smith (1981) showed that this was equivalent to selling an absolute form of essergy called negentropy to the rest of the cycle. Not only are the irreversibilities of the terminal component related to the cost of negentropy at the system's boundary, but so are the irreversibilities of each of the other components. All irreversibilities within the cycle, therefore, contribute to the cost of negentropy (or heat) rejected to the environment since, in essence, each of them cannot, according to the Second Law, exist within the cycle without the function of the terminal component. As a result, each component must pay the terminal one for removing the entropy that each accumulates.

Establishing the component interconnections as two parallel streams of essergy (potential work as a special case of) and negentropy (as a special case of essergy) also establishes these costs as transmission component products and helps pin down where most of the component inputs within the system occur. If essergy (both mechanical and thermal) or negentropy represent the interconnections between components, then there is usually one input for each type of interconnection per component interacting with the main flow, plus one additional input per component for each secondary flow of essergy or negentropy with which the component interacts. An exception to the above rule applies to the essergy interconnection for a purely mechanical type of component such as a pump or compressor, which adds potential work to the system by the input of mechanical essergy from some outside source. This type of outside resource and others are the only additional inputs needed by the system. Further examples are fuel and air, which are "resources" required by a boiler and reheater, and for which the component or system must pay some outside agency. In addition, the cost of removing exhaust gases from the boiler and reheater is an input required for the performance of the boiler and reheater functions. Its cost rate is opposite to the direction of flow of the exhaust gases; and as can be seen with this last example, the mass flow of an input or for that matter of any of the component interconnections is not necessarily in the same direction as its corresponding cost rate flow. In the example of the Rankine cycle and with the exception of the exhaust gases, the interconnections defined by essergy are in the direction of mass flow, and those defined by negentropy are opposite to the direction of mass flow.

All steps in the functional analysis of a thermal system that have been outlined in the preceding paragraphs lead to the next part of "Thermoeconomic Functional Analysis," the drawing of a "Functional Diagram." In order to illustrate this and the discussions to this point, the Rankine reheat cycle with regeneration as shown in Fig. 1 is used as a specific example. It consists of a steam generator, a turbine, a terminal condenser and cooling towers, a boiler feed pump, and two high-pressure, three-zoned feedwater heaters. The "Functional Diagram" representing this cycle is presented in Fig. 2 and does not include any transmission components. In this diagram, the steam generator is broken into boiler (II*a*) and reheater (II*b*) functions and the turbine into high (I*a*), intermediate (I*b*), and low (I*c*) pressure turbine stage functions. The system boundary is not shown explicitly but is the point at which the outside "resources," Y_4 through Y_7, and the system "benefits," y_1 through y_3, enter and exit the system. The solid-line loop represents the main "essergy cost rate" component interconnection while the dotted-line loop represents the primary "negentropy cost rate" component interconnection. In general, all solid-line flows including inputs, outputs, and secondary streams correspond to essergy cost rates and all dotted-line flows to negentropy cost rates.

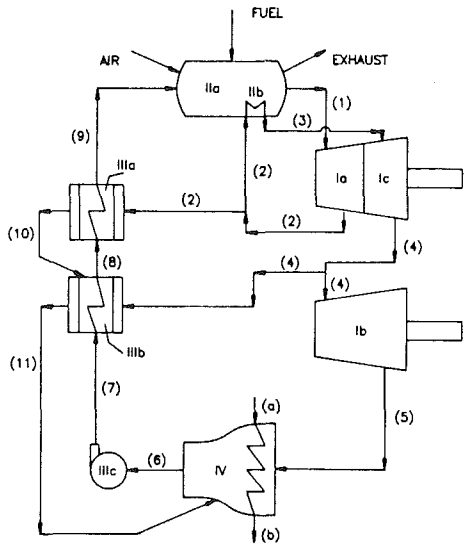

Fig. 1 Diagram of a Rankine reheat cycle with regeneration

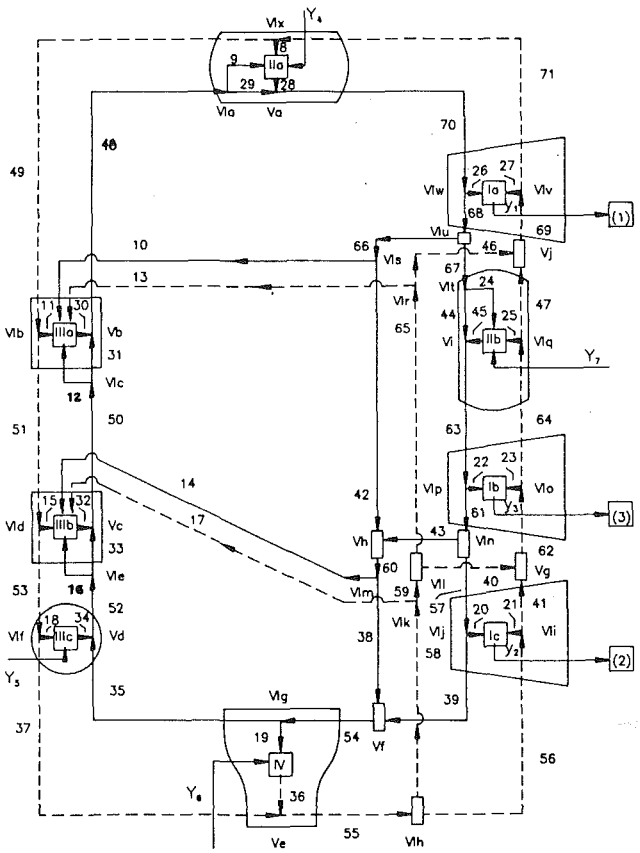

Fig. 2 "Functional Diagram" of a Rankine reheat cycle with regeneration

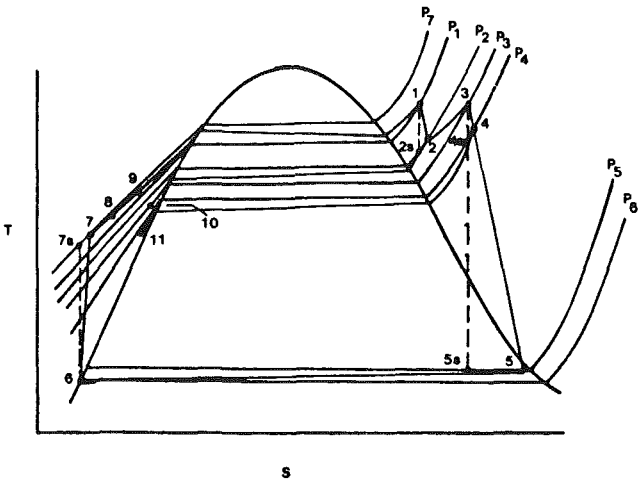

Fig. 3 *T-s* diagram of the Rankine reheat cycle with regeneration in Fig. 1

In order to resolve the "Functional Diagram" into its corresponding set of thermodynamic (and cost) equations, the relationship of the cycle's thermodynamic states to the cost rate flows of essergy and negentropy must be determined. This is done with a *T-s* diagram (Fig. 3) describing the various thermodynamic states of the cycle as they appear on Fig. 1. Table 1 is a cross-reference between the states on the *T-s* diagram and the streams on the "Functional Diagram" corresponding to them. In general, the states of a cycle only correspond on a one-to-one basis with some of the streams on a "Functional Diagram," the remaining being the result of more than one thermodynamic state. Also note that in many cases essergy cost rates correspond to flow essergy cost rates and at other times to the cost rate forms of essergy used to overcome flow

Table 1 Cross reference of thermodynamic states and streams for the cycle of Figs. 1 and 2

THERMODYNAMIC STATE	FIGURE 1 STREAM #	FIGURE 2 ESSERGY STREAM #	FIGURE 2 NEGENTROPY STREAM #
(1)	(1)	(70)	(71)
(2)	(2)	(68,67,66)	(47,46,69)
(3)	(3)	(63)	(64)
(4)	(4)	(61,43,57)	(62,40,41)
(5)	(5)	(39)	(56)
(6)	(6)	(35)	(37)
(7)	(7)	(52)	(53)
(8)	(8)	(50)	(51)
(9)	(9)	(48)	(49)
(10)	(10)	(42)	(65)
(11)	(11)	(38)	(58)

friction in a heat exchanger or pipe or used to represent the shaft power of a turbine, pump, or compressor. For an illustration of how the "Functional Diagram's" thermodynamic interconnections are resolved, refer to von Spakovsky and Evans (1987) and von Spakovsky (1986).

The thermodynamic equations that result from a resolution of the "Functional Diagram" form the basis of the "formalized" constraints, which are derived as part of a thermal system's overall thermoeconomic model. These constraints combined with the thermal system's thermoeconomic "objective" function form the foundation from which the system's thermoeconomic optimization equations are found. The "objective" function represents the total cost rate of ownership and operation of the thermal system. The general set of equations for this function and its constraints is as follows:

$$\text{minimize } \dot{\Gamma}_{sys} + \sum_{c=1}^{P} \dot{B}_c = \sum_{c=1}^{C} \dot{Z}_c + \sum_{c=P+1}^{R} \dot{\Gamma}_c + \dot{K}_c \tag{1}$$

subject to:

Benefits:

$$Y_j = Y_j(\mathbf{x}_c) \equiv Y_j,\ j=1, \ldots, P;\ c=1, \ldots, P \tag{2a}$$

Components:

$$y_j = Y_j(\mathbf{x}_c, \mathbf{y}_c) \equiv Y_j,\ j=P+1, \ldots, N;\ c=I, \ldots, C \tag{2b}$$

Junctions:

$$y_j = Y_j(x_c, y_c) \equiv Y_j = f_j y_c,\ j=N+1, \ldots, N+N_j;$$

$$c=C+I, \ldots, J \tag{2c}$$

Branches:

$$y_j = Y_j(\mathbf{y}_c) \equiv Y_j = \Sigma \mathbf{y}_c,\ j=N_j+1, \ldots, F;$$

$$c=J+I, \ldots, B \tag{2d}$$

In equation (1), $\dot{K}_c$ is a constant that represents any additional fixed cost rates, such as surcharges, not included in any of the other terms of the equation. $\dot{\Gamma}_{sys}$ is the net cost rate of owning and operating the system; and the $\mathbf{x}$'s and $\mathbf{y}$'s in equations (2) are the set of design or decision variables and the set of outputs, respectively, for benefit, component, junction, or branch "c." The capital expenditure, outside resource, and benefit cost rates in equation (1) are defined as follows:

$$\dot{Z}_c = Z_c(\mathbf{x}_c, \mathbf{y}_c) \equiv Z_c, \quad c=I, \ldots, C \tag{3a}$$

$$\dot{\Gamma}_c = \Gamma_c(\mathbf{y}_c) \equiv \Gamma_c, \quad c=P+1, \ldots, R \tag{3b}$$

$$\dot{B}_c = B_c(\mathbf{x}_c) \equiv B_c, \quad c=1, \ldots, P \tag{3c}$$

Note that only components have capital cost rates, and only component and benefit functions exhibit any decision variables. Z_c, Γ_c, and B_c are the mathematical representation of the capital cost rate "c," outside resource cost rate "c,"

and system benefit cost rate "c," respectively. Also notice that the only input, output, and component interconnection cost rates, i.e., stream cost rates, left in the objective function are those for the outside resources. All stream cost rates internal to the system cancel each other out since the cost rate output (excluding system benefits) of each component, junction, or branch is an input to some other component, junction, or branch.

If the general equation for an objective function, equation (1), is applied to the Rankine cycle of Figs. 1 and 2, the equation that results is written as follows:

minimize:

$$\dot{\Gamma}_{\text{sys}} + \dot{B}_1 + \dot{B}_2 + \dot{B}_3 = \dot{Z}_{1a} + \dot{Z}_{1b} + \dot{Z}_{1c} + \dot{Z}_{\text{II}a} + \dot{Z}_{\text{II}b} + \dot{Z}_{\text{III}a} + \dot{Z}_{\text{III}b} + \dot{Z}_{\text{III}c} + \dot{Z}_{\text{IV}} + \dot{\Gamma}_4 + \dot{\Gamma}_5 + \dot{\Gamma}_6 + \dot{\Gamma}_7 + \dot{K}_{\text{sys}} \quad (4)$$

The minimization, of course, is subject to the various "formalized" constraints of equations (2). To derive these equations, the expressions that result from a resolution of the "Functional Diagram" must be modified. The first step in this process is the determination of the decision variables for the system and each of its components or functions. The following set is chosen for the cycle of Figs. 1 and 2:

$$\mathbf{x} = \{T_1, T_5, T_8, T_9, P_4, \eta_{\text{II}B}, \eta_{\text{II}R}, \eta_{\text{II}HP}, \eta_{\text{II}IP}, \eta_{\text{II}LP}, \eta_{\text{II}BFP}\} \quad (5)$$

where for this choice of variables it should be noted that the fuel essergy rates associated with the boiler and reheater efficiencies are also allowed to vary. Many other sets of variables could have been chosen. However, efficiencies were used here because of the design as opposed to the operational nature of the optimization problem being presented. For a more complete discussion refer to von Spakovsky (1986). On a per component basis, the sets of decision variables are as follows:

$$\mathbf{x}_{1a} = \{T_1, T_5, T_8, T_9, P_4, \eta_{\text{II}HP}, \eta_{\text{II}IP}, \eta_{\text{II}LP}, \eta_{\text{II}BFP}\} \quad (6)$$

$$\mathbf{x}_{1b} = \mathbf{x}_{1c} = \mathbf{x}_{\text{III}a} = \mathbf{x}_{\text{III}b} = \mathbf{x}_{\text{III}c} = \mathbf{x}_{\text{IV}} = \mathbf{x}_{1a} \quad (7)$$

$$\mathbf{x}_{\text{II}a} = \{T_1, T_5, T_8, T_9, P_4, \eta_{\text{II}B}, \eta_{\text{II}HP}, \eta_{\text{II}IP}, \eta_{\text{II}LP}, \eta_{\text{II}BFP}\} \quad (8)$$

$$\mathbf{x}_{\text{II}b} = \{T_1, T_5, T_8, T_9, P_4, \eta_{\text{II}R}, \eta_{\text{II}HP}, \eta_{\text{II}IP}, \eta_{\text{II}LP}, \eta_{\text{II}BFP}\} \quad (9)$$

In addition, several other design parameters exist but are not included in the above list since all are functions of the variables of equation (5). These parameters along with their dependencies are given below.

$$T_3 = f(T_1) = T_1, \quad (10)$$

$$P_3 = f(\eta_{\text{II}IP}, T_3) \quad (11)$$

$$T_2 = f(\eta_{\text{II}HP}, P_2) \quad (12)$$

$$P_2 = f(P_3) = 1.07527 P_3 \quad (13)$$

$$n = f(T_5) = \ln[(T_5 - T_a)/(T_5 - T_b)] \quad (14)$$

$$P_5 = f(T_5) \quad (15)$$

$$\text{TTD}_{\text{CND}} = f(T_5) = T_5 - T_b \quad (16)$$

$$P_6 = f(P_5) = P_5 - 0.1267 \text{ MPa} \quad (17)$$

$$T_6 = f(P_6) \quad (18)$$

$$T_7 = f(\eta_{\text{II}BFP}, P_7) \quad (19)$$

$$P_{10} = f(P_3) = P_2 \quad (20)$$

$$P_{11} = f(P_4) = P_4 \quad (21)$$

With equations (5) through (9), the mathematical functions for the Y_j's in equations (2a) and (2b) can be developed in terms of the component and benefit decision variables, $\mathbf{x}_c$'s, and the component products, $\mathbf{y}_c$'s. An illustration of this process and a summary of the resulting constraint equations are given by von Spakovsky and Evans (1987) and von Spakovsky (1986).

Once the constraint equations are formulated, each term in the objective function, equation (1), must be determined with respect to the functional representation of equations (3) and cost data found in the literature. These cost data may be in the form of "cost equations," which are functions of geometric and manufacturing variables. "Costing equations" that depend on performance and stream variables are easier to use and interpret in "Thermoeconomic Functional Analysis"; therefore, any "cost equations" are converted to "costing equations" (El-Sayed and Tribus, 1983). Beginning with the capital cost, the use of "costing equations" in the development of the cost functions of equation (3a) is illustrated in the following discussions. According to Singer (1981) and Bartlett (1958), the annualized capital cost rate of a component can be expressed in terms of a capitalization ratio (also called carrying charge or fixed charge rate) and the original investment or purchase cost,

$$\dot{Z}_{ac} = (C/100) i_c \quad (22)$$

C is the percent capitalization ratio, which includes return on investment; federal, state, and local income taxes; depreciation; interim replacements; insurance, real estate, personal property and state capital stock taxes; etc. (Bartlett, 1958). $\dot{Z}_{ac}$ is the annualized capital cost rate in \$/yr and i_c the original investment or purchase cost of component c in \$. However, the capital cost rate of component c must include maintenance and operating costs. Equation (22) is therefore modified by a fixed percentage, maintenance/operating factor f_{mc}, and the number of operating hours per year N (Frangopoulos, 1983). Equation (3a) becomes

$$\dot{Z}_c = Z(\mathbf{x}_c, y_c) \equiv Z_c = (C/3.6 \times 10^{-5}\text{N}) f_{mc} i_c, \; c = I, \ldots, C \quad (23)$$

where $\dot{Z}_c$ is in \$/s and C is a percentage. The choice of a fixed f_{mc} is a simplification since in actuality $f_{mc} = f(\mathbf{x}_c, \mathbf{y}_c)$.

The purchase cost or original investment for each component i_c in equation (23) is based on each component's performance and stream variables, i.e., $\mathbf{x}_c$ and $\mathbf{y}_c$. In order to convert any "cost equations" for purchase cost in the literature to "costing equations," two methods are available: one proposed by El-Sayed and Tribus (1983) and a modification of the first by Frangopoulos (1983) and Garceau (1982). The latter was chosen because the "costing equations" can be derived more directly. The form taken by this method is a power function of the primary stream or performance variable of component "c," which is set equal to the component's "base" purchase cost i_{bc}. In equation form

$$i_{bc} = a_c (\phi_c)^{(s_c)} \quad (24)$$

which, in fact, is one of the forms, i.e., log/log plots and First Law quantities, given in the literature for the components of thermal cycles. Thus, a conversion from "cost equations" to "costing equations" is sometimes not necessary. However, since "Thermoeconomic Functional Analysis" does require Second Law quantities (Frangopoulos, 1983; von Spakovsky, 1986), a conversion of the base purchase cost equation's First Law quantities must be carried out.

The relationship between the "final" purchase cost i_c, and "base" purchase cost i_{bc}, for each piece of equipment is a set of correction factors. These are specific to each type of component and in the literature are usually in terms of First Law quantities so that a conversion to Second Law quantities is required. The general form of the final and base purchase cost relationship is

$$i_c = i_{bc} \prod_{i=2}^{m} f_{ic} \tag{25}$$

where f_{ic} is the ith base purchase cost correction factor for component c and m the number of factors plus one.

Of course, the final determination of equation (25) from the cost literature is specific to the type and use of equipment in the thermal system and is only applicable within certain ranges of some of the system design parameters both fixed and variable. Therefore, the fixed system parameters should be specified prior to the formulation of the purchase cost for each component, and any limitations on these and the variable system parameters should be noted during the formulation. For an illustration of the development of a capital cost function and for a complete list of the "costing equations" used to obtain the results presented in this paper refer to von Spakovsky and Evans (1987) and von Spakovsky (1986).

To complete the thermoeconomic objective function, equation (1) or (4), expressions for the outside resources and system benefits must be found. A linear combination of the essergy value associated with each benefit and resource and some corresponding unit cost is chosen. For the cycle of Figs. 1 and 2, these resource and benefit equations take the following form:

$$\Gamma_4 = a_4 y_4, \quad \Gamma_5 - a_5 y_5, \quad \Gamma_6 = a_6 y_6, \quad \Gamma_7 = a_7 y_7 \tag{26}$$

$$B_1 = a_1 y_1, \quad B_2 = a_2 y_2, \quad B_3 = a_3 y_3 \tag{27}$$

where y_1 through y_7 are determined from the constraint equations and the coefficients or unit costs, a_4 through a_7, have the following values:

$$a_4 = a_7 = 3.259228 \ \$/10^6 \text{ kJ} \tag{28}$$

$$a_5 = a_6 = 11.11 \ \$/10^6 \text{ kJ} \tag{29}$$

The unit costs, a_4 and a_7, include both the cost of fuel and the capital expenditures for the coal handling, coal firing, and lighter oil systems (Southern Co. Serv., 1983a, 1983b, 1983c; Potter, 1959). The fuel used is eastern bituminous coal @ \$0.0798/kg (Southern Co. Serv. 1983a, 1983b). The unit costs, a_5, and a_6, are the cost of electrical power from an outside source (Peters and Timmerhaus, 1980); and a_1, a_2, and a_3 are the unit costs of power production determined during the optimization of the cycle.

Thermoeconomic Isolation

With the "Thermoeconomic Functional Analysis" equation of total purchase cost for each component of a cycle, the capital cost rates can be formulated. Then determining expressions for the outside resource cost rates and benefit cost rates, the cycle thermoeconomic optimization equations for the "basis" model can be set up. However, in addition to optimizing the system as a whole, separate or "isolated" component optimizations using "detailed" models are also of interest. The term "isolated" optimization does not refer here to the individual optimization of a system component resulting from the optimization of the system as a whole. It is the opposite process of isolating components, optimizing their design, and then letting them interact in a system in order to obtain an optimum for the system. These separate optimizations, however, required some sort of decentralization procedure with a fairly high degree of disjointness, i.e., the design or decision variables of one component do not significantly affect the design or performance of other components within the system.

A concept called "Thermoeconomic Isolation," first introduced by Evans (1980) and further developed by Frangopoulos (1984), Frangopoulos and Evans (1984), and von Spakovsky (1986), achieves the kind of disjointness required. This concept is used in the sense of "economically" isolating a "thermodynamic" function (component) from the other functions in a thermal system, i.e., establishing "stable economic environments." Such environments require three things:

1 that an adequate functional breakdown of the system exists, i.e., there are no important functions that have been left out;
2 that the system and component cost equations and constraints are all based on Second Law quantities;
3 that the system and component costing equations are linear with respect to each corresponding component (function) product.

On a more rigorous basis, the "unit" or "marginal" cost associated with each "formalized" constraint in the "basis" model must be a constant. Representing each unit cost by λ_j results in the following definition for "Thermoeconomic Isolation":

$$\lambda_j = \text{const} \tag{30}$$

where

$$\lambda_j = f_1(Y_j) \tag{31}$$

$$Y_j = f_2(\mathbf{x}_c) \tag{32}$$

Items one and two above are achieved through "Thermoeconomic Functional Analysis," and are directly related to the number and type of formal constraints for the system and, thus, to the degree of disjointness. The third item requires the linearization of the constraint equations and the total purchase cost equation for each component or function with respect to its product. For a general outline of the procedure to linearize and for a listing of the final resulting component capital cost equations for the system refer to von Spakovsky and Evans (1987) and von Spakovsky (1986).

Thermoeconomic Optimization

To derive the system of thermoeconimc optimization equations for a cycle, Lagrange's Method of Undetermined Multipliers is applied to the objective function, equation (1), and its constraints, equation (2). This transforms a constrained optimization into an unconstrained one in which the relative value of each constraint can be assessed. The method is applied by first forming the Lagrangian using the functional form of each type of cost rate. In general form,

$$L \equiv L(\mathbf{x}, \mathbf{y}) = \Gamma_{\text{sys}} + \sum_{c=1}^{P} B_c - \sum_{j=1}^{R} \lambda_j (y_j - Y_j) \tag{33}$$

Optimizing equation (33) with respect to the vectors $\mathbf{y} = (y_1, \ldots, y_F)$, $\mathbf{x} = (x_1, \ldots, x_n)$, and $\lambda = (\lambda_1, \ldots, \lambda_F)$ results in

$$(\partial L / \partial y_j)_{j \neq s, \mathbf{x}, \lambda} = 0, \quad j = 1, \ldots, F \tag{34}$$

$$(\partial L / \partial x_i)_{x_i' s, \mathbf{y}, \lambda} = 0, \quad i = 1, \ldots, n \tag{35}$$

$$(\partial L / \partial s_j)_{\lambda_k s, \mathbf{x}, \lambda} = 0, \quad j = 1, \ldots, F \tag{36}$$

where n is the number of decision variables for the system. The partial derivatives of the Lagrangian with respect to the various Langrange multipliers, the λ_j's, result in the constraints, equations (2) or for the cycle of Figs. 1 and 2, equations (43), (44), and (45) in von Spakovsky and Evans (1987). Equations (34) give the λ_j values for the system and are the unit or marginal costs associated with each essergy and negentropy stream. They are marginal costs because they represent the cost of increasing each essergy or negentropy stream by one "unit" (Humphreys and Katell, 1981). From a mathematical standpoint, the λ_j's are also called "shadow prices" since they represent the partial derivatives of the cost

function with respect to the constraint variables (Reklaitis et al., 1983).

Equations (34), (35), and (36) describe the general form of the optimization equations for a cycle. Those specific to the cycle of Figs. 1 and 2 are found through the application of these equations to the Lagrangian formed from equations (4) and equations (43), (44), and (45) in von Spakovsky and Evans (1987). Once established, they can be solved simultaneously for the optimum solution vectors, $\mathbf{x}^{OPT}$, $\mathbf{y}^{OPT}$, and λ^{OPT}. These are the vectors at which the cost of ownership and operation of the cycle is a minimum.

Solution Methods

Several different solution algorithms were utilized in the creation and optimization of the thermoeconomic model presented in this paper. Each step in this process presented certain difficulties of time, convergence, and error recovery, which in turn dictated the nature of the solution approaches used. For a discussion of these solution algorithms refer to von Spakovsky and Evans (1987) and von Spakovsky (1986).

Discussion of Results

The optimum solution vectors, $\mathbf{x}^*$, λ^*, and $\mathbf{y}^*$, were found for the thermoeconomic model of the cycle of Figs. 1 and 2. However, because of the difficulties arising from the use of Newton's method in conjunction with numerical differentiation, a certain degree of uncertainty exists in the optimum values found. In addition, the solution for a reduced decision set is given here. By employing fixed ΔT's of 4.44°C and 15.56°C on the tube side of each feedwater heater, respectively, it is possible to drop the feedwater exit temperatures, T_8 and T_9, from the decision set of equation (5). Likewise, the steam extraction pressure P_4 at the exit of the intermediate pressure turbine is removed by fixing it at a constant value of 775.996 MPa. The reduced set is

$$\mathbf{x} = \{T_1, T_5, \eta_{IIB}, \eta_{IIR}, \eta_{IIHP}, \eta_{IIIP}, \eta_{IILP}, \eta_{IIBFP}\} \quad (37)$$

Using the fixed parameters given below:

$$\left.\begin{aligned}
&P_1 = 12{,}492.0 \text{ MPa}, \quad T_0 = 15.6°\text{C}, \quad P_0 = 76.0 \text{ MPa}\\
&P_a = 90.667 \text{ MPa}, \quad T_a = 15.6°\text{C}, \quad T_b = 43.3°\text{C}\\
&P_b = 76.0 \text{ MPa}, \quad \eta_{MHP} = \eta_{MIP} = \eta_{MLP} = 98.3 \text{ percent}\\
&\eta_{BFP} = 86 \text{ percent}, \ \eta_{CP} = 71.4286 \text{ percent}, \quad \dot{W}_T = 818 \text{ MW}\\
&\eta_G = 98.7 \text{ percent}, \quad U_{IV} = 2571.328 \text{ W/m}^2\text{K}, \quad x_5 = 0.93\\
&U_{IIIa} = U_{IIIb} = 3191.04 \text{ W/m}^2\text{K}, \quad x_{10} = x_{11} = 0.0\\
&P_8 = f(P_7) = 0.9575 P_7\\
&P_9 = f(P_7) = 0.9575 P_8\\
&P_1 = f(P_7) = 0.9192 P_9
\end{aligned}\right\} \quad (38)$$

the optimum values for the x's along with their estimated uncertainty were found. They are presented in Table 2.

Only selected values of the unit cost and product essergy/negentropy solution vectors are shown in Table 3. The unit costs of power production are λ_1, λ_2, and λ_3. Transmission costs for the essergy and negentropy are not included in the solution of this model. Table 3 is given below as is Table 4, which shows the properties fixing the thermodynamic states of the optimum cycle. The mass flow rates for the optimum cycle are 2,080,721 kg/h exiting the boiler, 149,248 kg/h extracted at the exit of the high-pressure turbine, and 64,813 kg/h extracted from the intermediate pressure turbine. The total heat rate to the cycle and the plant's overall thermal efficiency are 2,016,651 kJ/s and 40.56 percent, respectively.

The distributions of capital and resource costs are shown in Table 5. The capital costs are approximately 16.55 percent of the total optimum cost rate for the cycle.

Finally, though separate or "isolated" optimizations are not part of this paper (refer to von Spakovsky and Evans, 1988, and von Spakovsky, 1986, for a discussion of these), it might be of interest to examine the economic environment around one of the feedwater heaters by observing the behavior

Table 2 Reduced optimum decision variable vector x^*

$\underset{\sim}{x}^*$		ESTIMATED UNCERTAINTY
T_1	= 523.092°C	± 10.0
η_{IIHP}	= .964	± .001
η_{IIR}	= .400	± .001
η_{IIIP}	= .964	± .001
η_{IILP}	= .945	± .002
T_5	= 46.346°C	± .1
η_{IIBFP}	= .795	± .001
η_{IIB}	= .395	± .001

Table 3 Value for the optimum unit cost and product essergy/negentropy vectors, λ^* and y^*

STREAM #	$\underset{\sim}{\lambda}^* 10^5$ ($/kJ)	$\underset{\sim}{y}^*$ (kJ/sec)
1	1.2306671	262,632.10
2	1.2336937	424,145.14
3	1.1988841	131,270.64
4	.3259	2,128,931.75
8	.1256633	839,321.27
9	2.4144557	851.23
29	2.4144557	35,456.04
28	1.0293486	842,024.40
5	1.111	17,266.11
18	.1256633	3,027.31
34	1.9179758	11,821.54

Table 4 Thermodynamic states of the optimum cycle

STATE	P(MPa)	T(°C)	QUALITY
1	12,490.53	523.09	
2	1,866.27	252.49	
3	1,773.00	523.09	
4	776.00	398.85	
5	7.71	46.34	.93
6	7.55	46.02	.0
7	14,821.52	48.09	
8	14,191.62	70.32	
9	13,588.46	103.65	
10	1,866.27	223.69	.0
11	776.00	181.33	.0

Table 5 Optimum cycle capital and resource cost rates

COMPONENT #		$\dot{Z}$ ($/sec)	% Of $\dot{Z}_{Total}$	RESOURCE #	$\dot{\Gamma}$ ($/sec)
IIIc	(BFP)	.0421786	2.47	5	.191836
IIa	(B)	.751240	43.93	4	6.93867
Ia	(HP)	.171834	10.05		
IIb	(R)	.0882307	5.16	7	1.48630
Ib	(IP)	.0858878	5.02		
Ic	(LP)	.317481	18.57		
IIIa	(FWH)	.0029242	.17		
IIIb	(FWH)	.0017593	.10		
IV	(CND)	.248414	14.53	6	.003118
	TOTAL:	1.70995		TOTAL:	8.61992
	PLANT TOTAL:		10.3299 $/sec		

Table 6 Behavior of the input unit costs of IIIb (FWH)

ITER. #	$\lambda_{14} \cdot 10^5$ ($/kJ)	% VARIATION	$\lambda_{15} \cdot 10^5$ ($/kJ)	% VARIATION
n	1.06508094	.007	.12565884	.004
n+1	1.06491694	.009	.12565785	.004
n+2	1.06502766	.002	.12570590	.034
n+3	1.06571771	.066	.12647605	.647
n+4	1.06578530	.073	.12632242	.525
n+5	1.06524949	.022	.12591919	.204
n+6	1.06516797	.015	.12571179	.039
n+7	1.06500415	.001	.12566773	.004
n+8	1.06510113	.008	.12567007	.005
n+9	1.06502330	.001	.12566446	.001
SOLUTION	1.06501088		.12566328	

ITER. #	$\lambda_{16} \cdot 10^5$ ($/kJ)	% VARIATION	$\lambda_{17} \cdot 10^5$ ($/kJ)	% VARIATION
n	1.76453582	.050	.12565887	.003
n+1	1.76327877	.018	.12565783	.004
n+2	1.77303265	.540	.12570579	.034
n+3	1.75979288	.220	.12647613	.650
n+4	1.76810968	.260	.12632241	.520
n+5	1.76530426	.100	.12591924	.200
n+6	1.76698535	.190	.12571175	.005
n+7	1.77200558	.480	.12566774	.004
n+8	1.76367987	.005	.12567004	.005
n+9	1.76620098	.150	.12566446	.001
SOLUTION	1.76359502		.12566325	

of its input unit costs. For several iterations prior to final convergence, Table 6 shows the variations of the heater's unit costs from their optimum values. The variations in the essergy and negentropy inputs are not included but are one to two and one half orders of magnitude greater than those for the unit costs which correspond to them.

Conclusions

One of the obvious advantages of this and any other Second Law approach is that it can present an accurate picture of where the true cycle inefficiencies exist since it provides a common basis for comparison not inherent in any First Law approach. One obvious strength of the particular method presented here is that it also provides for a high degree of decentralization. Utilizing a greater amount of detail than that present in the "basis" model for the overall cycle, this decentralization allows for *isolated*, individual component optimizations consistent with some overall system optimum. The use of "detailed" component models completes the design aspects of the thermal system, aspects not handled by the "basis" model optimization of the cycle. For a discussion of these detailed model optimizations, the reader is again referred to von Spakovsky and Evans (1988) and von Spakovsky (1986).

Another strength of this method is that the thermoeconomic basis model can be created not only for various Rankine cycle configurations but, more generally, for any type of thermal system. Such models, once optimized, allow the performance and design engineer to know under what set of economic and thermodynmic conditions a particular cycle should operate. Although the performance analysis presented in this paper primarily involves the design of a thermal system, the method can handle optimizing the operation of an existing system in which equipment investment costs may already be sunk and the equipment design fixed. This type of application requires additional performance constraints on the operation of each piece of equipment. A discussion of these constraints is left for another paper.

Still another point that should be made is that the cost rates and operating points determined from the performance analysis of a system seem at first glance to be very dependent on the values of the capital cost functions found in the literature. In fact, costs vary on a yearly basis (or shorter duration), and cost functions are subject to change. However, the methods described here are not intended for "accounting" purposes but are meant to give the relative and not absolute worth of each component's operation to the operations of the other components in the system. So, although their absolute cost might change significantly, their approximate relative costs or weights are much less likely to change. Thus the model is less dependent on variations in the cost literature than is at first apparent.

Finally, the basic principles of "Thermoeconomic Functional Analysis" are general and could, in fact, be applied to nonthermal systems, e.g., to the stability and control problem of a robotic device. Investigations into these other areas may be of interest.

References

Bartlett, R. L., 1958, *Steam Turbine Performance and Economics*, McGraw-Hill, New York.

El-Sayed, Y. M., and Tribus, M., 1983, "Strategic Use of Thermoeconomics for Process Improvement," *Efficiency and Costing*, R. A. Gaggioli, ed., ASC, Washington, DC.

Evans, R. B., 1968, "The Formulation of Essergy," *Thayer News*, Thayer School of Engineering, Dartmouth College, Hanover, NH.

Evans, R. B., 1969, "A Proof That Essergy is the Only Consistent Measure of Potential Work," Ph.D. Thesis, Dartmouth College, Hanover, NH.

Evans, R. B., 1980, "Thermoeconomic Isolation and Essergy Analysis," *Energy: The International Journal*, Vol. 5, No. 8-9, pp. 805-821.

Evans, R. B., Hendrix, W. A., and Kadaba, P. V., 1983, "Essergetic Functional Analysis for Process Design and Synthesis," *Efficiency and Costing*, R. A. Gaggioli, ed., American Chemical Society.

Frangopoulos, C. A., 1983, "Thermoeconomic Functional Analysis: A Method for the Optimal Design or Improvement of Complex Thermal Systems," Ph.D. thesis, Georgia Institute of Technology, Atlanta, GA.

Frangopoulos, C. A., 1984a, "Thermoeconomic Functional Analysis: An Innovative Approach to the Optimal Design of Thermal Systems," *Second Law Aspects of Thermal Design*, ASME HTD-Vol. 33, New York.

Frangopoulos, C. A., and Evans, R. B., 1984b, "Thermoeconomic Isolation," *Second Law Aspects of Thermal Design*, ASME HTD-Vol. 33, New York.

Graceau, R. M., 1982, "Thermoeconomic Optimization of a Rankine Cycle Cogeneration System," M.S. Thesis, Georgia Institute of Technology, Atlanta, GA.

Humphreys, K. K., and Katell, S., 1981, *Basic Cost Engineering*, Marcel Dekker, Inc., New York.

Peters, M. S., and Timmerhaus, K. D., 1980, *Plant Design and Economics for Chemical Engineers*, McGraw-Hill, New York.

Potter, P. J., 1959, *Power Plant Theory and Design*, 2nd eds., Wiley, New York.

Reklaitis, G. V., Ravindran, A., and Ragdale, K. M., 1983, *Engineering Optimization: Methods and Applications*, Wiley, New York.

Singer, J. G., 1981, *Combustion Fossil Power Systems*, 3rd ed., Combustion Engineering, Rand McNally, CT.

Smith, M. S., 1981, "Effect of Condenser Design Upon Boiler Feedwater Essergy Costs in Power Plants," M.S. Thesis, Georgia Institute of Technology, Atlanta, GA.

Southern Company Services, Inc., 1983a, *SCS 818 MW Power Plant Model Fossil Scope and Cost Document*, Birmingham, AL.

Southern Company Services, Inc., 1983b, *1983 Power Plant Component Escalation Guide*, Cost Engineering Department, Birmingham, AL.

Southern Company Services, Inc., 1983c, "Boiler Model Data," private communication, Atlanta, GA.

von Spakovsky, M. R., 1986, "A Practical Generalized Analysis Approach to the Optimal Thermoeconomic Design and Improvement of Real-World Thermal Systems," Ph.D. thesis, Georgia Institute of Technology, Atlanta, GA.

von Spakovsky, M. R., and Evans, R. B., 1987, "The Optimal Design and Performance of Thermal Systems and Their Components," *Analysis and Design of Advanced Energy Systems: Fundamentals*, ASME AES, Vol. 3-1, New York.

von Spakovsky, M. R., and Evans, R. B., 1988, "The Optimal Design and Performance of Components in Thermal Systems," *Second-Law Analysis in Heat/Mass Transfer and Energy Conversion*, ASME, AES-Vol. 6, HTD-Vol. 97, New York.

Comparative Thermodynamics for Brayton and Rankine Cycles

E. W. Beans
Professor of Mechanical Engineering,
The University of Toledo,
Toledo, OH 43606

The thermal efficiency, work per unit mass, and work per unit volume of the simple Rankine and Brayton cycles are expressed in terms of seven independent variables using a simplified thermodynamic model. By requiring equal efficiency, equal work conditions, and the same maximum cycle temperature for both cycles, two necessary relationships are established between the seven independent variables. These two relationships along with two maximum work conditions produce a method for comparing required and selected properties. These comparisons provide useful guidelines for the selection of the cycle and cycle fluids. The comparison analysis shows that for a given application the more attractive cycle is strongly dependent upon the fluids selected.

Introduction

The ideal Brayton and Rankine cycles have much in common. Both have constant pressure heating and cooling processes, which are connected by isentropic expansions and compressions. Both may be operated as open or closed cycles, with or without regeneration, and with or without reheat. Both are continuous flow engines and have separate devices for "heating," "expansion," "cooling," and "compression."

The major difference between the cycles is that the Rankine cycle is normally operated with a change in phase, while the Brayton cycle operates solely within the gas phase. This condition for the Rankine cycle gives it three important characteristics: (1) The cycle pressures and temperatures are linked by the necessity to operate across the vapor dome. (2) The "compression work" or pump work is small and can be neglected. (3) The expansion process must be in the vapor region or to a point of high quality. Because of their many similar features, the two cycles are frequently candidate cycles for the same application, be it stationary power plants, propulsion, or space power. The two cycles are often joined to form a topping cycle.

The important parameters in determining the selection of one cycle over the other are (1) cycle efficiency (η), (2) the work per unit mass (W_m), and (3) the work per unit volume (W_v). The cycle efficiency is important because it determines the size of the input energy supply, be it fuel, a solar collector, or a thermal reservoir. The same is true for the "cooler," be it a condenser or a radiator.

The work per unit mass is a measure of the required mass flow for the working fluid and is a measure of the size of the power plant. An engine with a high work per unit mass will require smaller inlet and exhaust areas and contain less mass for the working fluid in a closed cycle.

The work per unit volume is used in this analysis because it is a better measure of the size of the power plant. For example, two engines with the same work per unit mass require the same mass flow rate to produce the same power. If the exhaust fluid density of one engine is lower than the other, its ducts, expander, and exhaust heat exchanger (if any) will be larger in volume and probably more massive than those for the higher density engine. Volume and mass of the entire power plant are of primary importance in engines for transportation and space applications. The work per unit volume for the cycle will be based on the fluid density as it leaves the expander. This is the lowest density state for both cycles. The work per unit volume is essentially a mean effective pressure.

The relations for the cycle efficiency and the work are tied to the thermodynamics of the two cycles and the properties of the fluids used in each cycle. The objective of this paper is to use the principles of thermodynamics to make a comparison between the two cycles. Comparisons of equal efficiency, equal work per unit mass, and equal work per unit volume result in expressions that relate the cycle parameters and the thermodynamic properties of the fluids for each cycle.

The approach used in this study is similar to the one used for parametric studies of aero-propulsion systems. The most notable contribution to this approach is by Dugger (1969). The approach is used to optimize the cruise speed for a ramjet by Hattingh (1981). Approaches similar to the one presented here have been used to analyze refrigeration cycles (Chang and Roux, 1985). The approach has been used to analyze steam power cycles (Naimanov, 1986; Barilovich et al., 1985; Manokova, 1984). In these papers the Rankine cycle performance parameters are analyzed in terms of thermodynamic properties such as pressure and enthalpy of vaporization.

Model for Thermodynamic Properties and Cycle

To make a thermodynamic comparison, one needs a model for the fluid properties and the cycle. A simple model will be used for the properties and an ideal cycle will be used for the cycle. This was done to simplify the analysis and to make the results easy to interpret. It is recognized that this approach introduces some error into the results. However, it is felt that this error is not sufficient to change any general conclusions. At the very worst, the results will point to the need for a more detailed analysis.

Contributed by the Advanced Energy Systems Division for publication in the JOURNAL OF ENGINEERING FOR GAS TURBINES AND POWER. Manuscript received by the Advanced Energy Systems Division January 25, 1989.

The model used in the analysis is based on the following assumptions:

1 For vapor or gas c_p = const, $pv = RT$

2 For liquid c = const, ρ = const

3 For liquid-vapor h_{fg} = const

4 For the Rankine cycle the exhaust state is a saturated vapor.

5 All component efficiencies are unity (100 percent).

6 No reheat or regeneration.

Assumptions 1 and 2 are reasonable for all gases and liquids at moderate temperatures and pressures. For example, for saturated water from $T_r = 0.42$, $P_r = 0.00003$ (the triple point) to $T_r = 0.6$, $P_r = 0.0049$, the change in c_p, c, ρ, h_{fg}, and the compressibility Z is less than 10 percent. For Freon 12 over the same reduced temperature range the change in the above properties is less than 10 percent. The exhaust enthalpy of vaporization will be selected based on the thermal sink temperature. In any case a range of values will be examined. Assumption 4 assures that the Rankine cycle expansion is within the vapor region. Assumption 5 is a result of the ideal cycle model. Assumption 6 limits the comparisons to a simple cycle for both the Brayton and Rankine cycles. This was done also to simplify the analysis. Since the intent of the analysis was to establish direction, a simple cycle should do this. The analysis could be expanded to include reheat and regeneration with much added complexity.

Thermodynamic Analysis

The T-S diagrams for the cycles are presented in Fig. 1. The Brayton cycle is $0\text{-}2_b\text{-}3_b\text{-}4_b$. The Rankine cycle is $1_r\text{-}2_r\text{-}3_r\text{-}4_r$. The subscripts b and r refer to the Brayton and Rankine cycles, respectively. This notation will be used throughout.

Brayton Cycle. For the Brayton cycle, in Fig. 1, the work per unit mass, the work per unit volume, and thermal efficiency are

$$W_{mb} = (h_{3b} - h_{4b}) - (h_{2b} - h_o)$$

$$W_{vb} = \rho_{4b}[(h_{3b} - h_{4b}) - (h_{2b} - h_0)] = \rho_{4b} W_{mb}$$

$$\eta_b = \frac{[(h_{3b} - h_{4b}) - (h_{2b} - h_0)]}{(h_{3b} - h_{2b})}$$

For the assumptions listed above, these relationships become

$$W_{mb} = c_{pb} T_o (\theta_b/\phi_b - 1)(\phi_b - 1) \quad (1)$$

$$W_{vb} = [kp_0/(k-1)]_b (1 - T_0\phi_b/T_{3b})(\phi_b - 1) \quad (2)$$

$$\eta_b = 1 - 1/\phi_b \quad (3)$$

where

$$\phi_b = (p_{2b}/p_0)_b^{\frac{k-1}{k}} \text{ and } \theta_b = T_{3b}/T_0 \quad (4)$$

Rankine Cycle. For the Rankine cycle, in Fig. 1, the same three parameters are

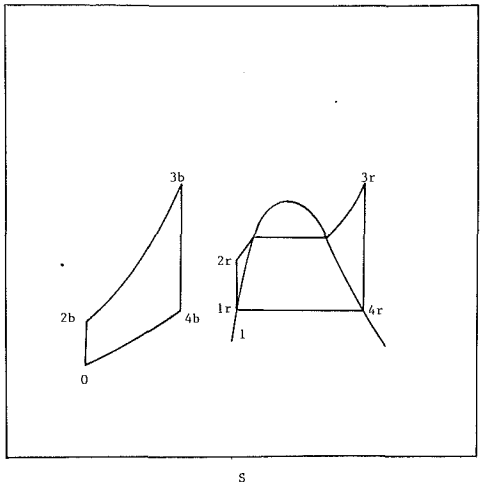

Fig. 1 T-S diagram for ideal Rankine and Brayton cycles

$$W_{mr} = (h_{3r} - h_{4r}) - (h_{2r} - h_{1r})$$

$$W_{vr} = \rho_{4r}(h_{3r} - h_{4r}) - (h_{2r} - h_{1r})$$

$$\eta_r = \frac{(h_{3r} - h_{4r}) - (h_{2r} - h_{1r})}{h_{3r} - h_{2r}}$$

From the model in the previous section, the expressions for the various enthalpies are

$$h_{1r} = h_{4r} - h_{fg}$$

$$h_{2r} = h_{1r} + (p_2 - p_1)_r/\rho_1 = h_{4r} - h_{fg}$$

$$h_{3r} = h_{4r} + c_{pr} T_{1r} (\phi_r - 1)$$

In the second expression above, the pump work, $(p_2 - p_1)_r/\rho_1$, is neglected. The term ϕ_r for the Rankine cycle is defined similarly to ϕ_b for the Brayton cycle. Combining the above enthalpies and the assumptions into the work and efficiency relations

$$W_{mr} = c_{pr} T_{1r} (\phi_r - 1) \quad (5)$$

$$W_{vr} = [kp_1/(k-1)]_r (\phi_r - 1) \quad (6)$$

$$\eta_r = \frac{(\phi_r - 1)}{(\phi_r - 1) + h_{fg}/c_p T_{1r}} \quad (7)$$

In writing equations (5)-(7), it should be recalled that $T_{1r} = T_{4r}$ and $p_{1r} = p_{4r}$, and state 4 is an ideal gas state; see Assumption 1.

Notation. At this point, it is convenient to introduce some useful notation. The Brayton cycle at Point 0 is used as the reference point. The ratio of k and the pressure for the Rankine cycle to those of the Brayton cycle is defined in the following relationship as the *pressure parameter* β:

$$\beta = \left[\frac{k_r/(k_r - 1)}{k_b/(k_b - 1)}\right] \frac{p_{1r}}{p_0} \quad (8)$$

The ratio of c_p for the Rankine cycle to that for the Brayton cycle is defined as the *specific heat parameter* λ

Nomenclature

c_p = specific heat
h = enthalpy
h_{fg} = enthalpy for change in phase
k = ratio of specific heats
p = pressure
T = temperature
W_m = work per unit mass
W_v = work per unit volume
w = mass work ratio
β = pressure parameter
η = thermal efficiency
θ = cycle temperature ratio
θ_s = thermal sink temperature ratio
λ = specific heat parameter
ρ = density
ϕ = isentropic temperature ratio
ψ = enthalpy of vaporization parameter
ω = volumetric work ratio

Subscripts

b = Brayton Cycle
r = Rankine Cycle

$$\lambda = c_{pr}/c_{pb} \tag{9}$$

The following dimensionless "energy" terms are defined:

Specific work ratio

$$w = W_m/c_{pb}T_o \tag{10}$$

Volumetric work ratio

$$\omega = W_v/[p_0 k_b/(k_b - 1)] \tag{11}$$

Enthalpy of vaporization parameter

$$\psi = h_{fg}/c_{pr}T_{1r} \tag{12}$$

In defining the specific and the volumetric work ratios, it is convenient to use the Brayton cycle properties as the reference properties. This is done even when these work ratios apply to the Rankine cycle, i.e., $\omega_r = W_{mr}/c_{pb}T_o$.

The following dimensionless cycle parameters are also defined:

Isentropic temperature ratio

$$\phi = (p_2/p_1)^{\frac{k-1}{k}} \tag{13}$$

Maximum temperature ratio

$$\theta = T_3/T_o \tag{14}$$

Thermal sink temperature ratio

$$\theta_s = T_{1r}/T_0 \tag{15}$$

The terms λ, ψ, and β establish the links between the thermodynamic properties for the two cycles. The term λ is just the ratio of the vapor and gaseous c_p's; see equation (9). The term ψ is the dimensionless enthalpy of vaporization for the Rankine cycle heat rejection process.

The term θ_s is the thermal sink reservoir link between the cycles. In general, a value of one would be used in order to obtain a high thermal efficiency. However, the term θ_s is included in the analysis so that the effect of different lower temperature limits can be examined. The term θ_s is important to the Rankine cycle. Increasing the thermal sink temperature will increase the exhaust pressure and the volumetric work ratio for the Rankine cycle and this may be an advantage. However, this will decrease its thermal efficiency.

The term β is primarily the exhaust pressure link between the cycles. The term is an important one, because it establishes the exhaust pressure for the Brayton cycle. The exhaust pressure for the Rankine cycle is determined by the term θ_s. Therefore, when a required value for β is established by one of the comparisons, the value for the Brayton cycle exhaust pressure p_o is determined.

The terms defined by equations (10)-(14) are subscripted with an r or b to identify the cycle. There are two exceptions. From the assumptions upon which the analysis is based one can see that

$$\phi_r = T_{3r}/T_{1r} = \theta_r/\theta_s$$

where θ_r is the maximum temperature ratio, T_{3r}/T_0, for the Rankine cycle. Since the term ϕ_r is defined in terms of other cycle variables, the isentropic temperature ratio ϕ applies only to the Brayton cycle and will not be subscripted. The term ψ applies only to the Rankine cycle.

Model. Using the above notation in equations (1), (2), (3), (5), (6), and (7), the work ratios and the efficiencies for the two cycles become

$$\omega_b = (1 - \phi/\theta_b)(\phi - 1) \tag{16}$$

$$w_b = (\theta_b/\phi - 1)(\phi - 1) \tag{17}$$

$$\eta_b = 1 - 1/\phi \tag{18}$$

$$w_r = \lambda(\theta_r - \theta_s) \tag{19}$$

$$\omega_r = \beta(\theta_r/\theta_s - 1) \tag{20}$$

$$\eta_r = (\theta_r/\theta_s - 1)/(\theta_r/\theta_s - 1 + \psi) \tag{21}$$

Equations (16)-(21) constitute the model that will be used in the comparative studies.

The model formed by equations (16)-(21) contains six dependent variables (w_b, w_r, ω_b, ω_r, η_b, and η_r) and seven independent variables (β, ψ, λ, ϕ, θ_b, θ_r, and θ_s). One can see from the model that a set of seven independent variables can be selected that gives $\omega_b > \omega_r$ and $\eta_r > \eta_b$ and vice versa. Furthermore, a general comparison of all thirteen variables requires the determination of surfaces in multidimensional space. This task is difficult to visualize and analyze. Accordingly, if the cycles are to be compared there must be a basis for comparison. Hence, additional conditions must be established that will interrelate the various variables.

Three such conditions are:

1 Equal specific work ratio $w_b = w_r$

2 Equal volumetric work ratio $\omega_b = \omega_r$

3 Equal efficiency $\eta_b = \eta_r$

Since cycle performance is tied to maximum cycle temperature a fourth condition is

4 Equal temperature ratio $\theta_b = \theta_r$

Equal Temperature Ratio Relationships

The equal temperature ratio comparisons are applicable to powerplants designed for a known thermal source and thermal sink such as occurs in solar power or OTEC. With the assumption of equal maximum temperature, and either of the other three pairing relations, such as equal efficiency, the model is reduced to five independent variables and three sets of six dependent variables.

The models resulting from pairing condition 4 with each of conditions 1-3 are presented below:

Set I. Equal temperature-equal specific work.

Conditions:

$$\theta = \theta_b = \theta_r; \quad w = w_b = w_r$$

Independent Variables:

$$\theta,\ \theta_S,\ \phi,\ \psi, \text{ and } \beta$$

Dependent Variables:

$$w = (\theta/\phi - 1)(\phi - 1) \tag{22}$$

$$\lambda = [(\theta - \phi)/(\theta - \theta_s)](1 - 1/\phi) \tag{23}$$

$$\omega_b = (\theta/\phi - 1)(\phi - 1) \tag{24}$$

$$\eta_b = 1 - 1/\phi \tag{25}$$

$$\omega_r = \beta(\theta/\theta_s - 1) \tag{26}$$

$$\eta_r = (\theta/\theta_s - 1)/(\theta/\theta_s - 1 + \psi) \tag{27}$$

Set II. Equal temperature-equal volumetric work.

Conditions:

$$\theta = \theta_b = \theta_r; \quad \omega = \omega_b = \omega_r$$

Independent Variables:

$$\theta,\ \theta_S,\ \phi,\ \psi, \text{ and } \lambda$$

Dependent Variables:

$$\omega = (1 - \phi/\theta)(\phi - 1) \tag{28}$$

$$\beta = (1 - \phi/\theta)(\phi - 1)/(\theta/\theta_s - 1) \tag{29}$$

$$w_b = (\theta/\phi - 1(\phi - 1)) \tag{30}$$

$$\eta_b = 1 - 1/\phi \tag{25}$$

$$w_r = \lambda(\theta - \theta_s) \tag{31}$$

$$\eta_r = (\theta/\theta_s - 1)/(\theta/\theta_s - 1 + \psi) \tag{27}$$

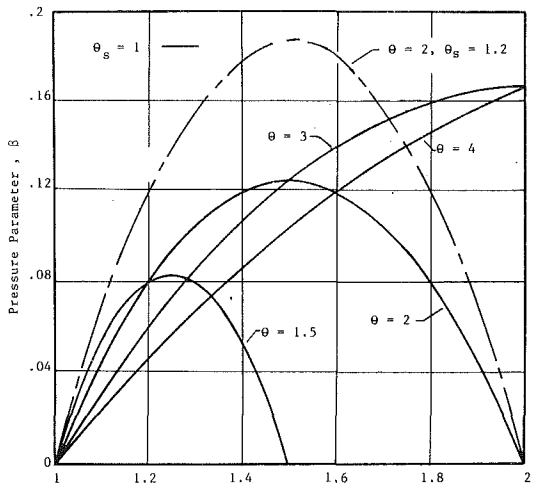

Fig. 2 Pressure parameter relation for equal work volumetric condition

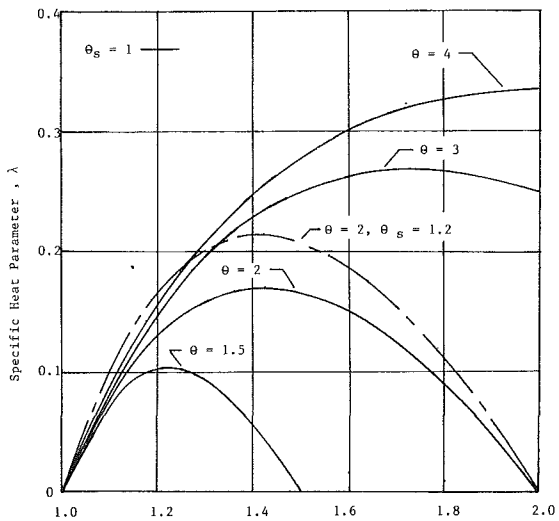

Fig. 3 Specific heat parameter relation for equal specific work condition

Set III. Equal temperature-equal efficiency.

Conditions:

$$\theta=\theta_b=\theta_r; \quad \eta=\eta_b=\eta_r$$

Independent Variables:

$$\theta,\ \theta_S,\ \phi,\ \lambda, \text{ and } \beta$$

Dependent Variables:

$$\eta=1-1/\phi \tag{32}$$

$$\psi=(\theta/\theta_s-1)/(\phi-1) \tag{33}$$

$$w_b=(1-\phi/\theta)\,(\phi-1) \tag{30}$$

$$\omega_b=(\theta/\phi-1)(\phi-1) \tag{24}$$

$$w_r=\lambda(\theta-\theta_s) \tag{31}$$

$$\omega_r=\beta(\theta/\theta_s-1) \tag{26}$$

One can see that each of these three pairings results in a relationship between the independent variables and each of the three property parameters λ, β, and ψ. For example, the condition of equal temperature and equal volumetric work results in a relationship for β, which is equation (29).

The relationship between the pressure parameter β and the isentropic temperature ratio ϕ for the equal volumetric work condition (equation (29)) is presented in Fig. 2 for a range of maximum temperature ratios θ and $\theta_s=1$. The relationship between β and ϕ for $\theta=2$ and $\theta_s=1.2$ is also presented in Fig. 2 as a dashed line. This was done to illustrate the effect of the thermal sink temperature ratio. One can see from Fig. 2 and equation (29) that the pressure parameter β maximizes with ϕ and that $\beta=0$ when $\phi=1$ and when $\phi=\theta$. One can also see from Fig. 2 and equation (29) that the values of ϕ for maximum β and $\beta=0$ are independent of the value of θ_s. The magnitude of β at the maximum condition does increase as θ_s increases.

The interpretation of Fig. 2 is that for a given β and θ the isentropic temperature ratio ϕ must be equal to the value from the curve to establish the equal volumetric work ratio condition. If the value of ϕ is in the region "under the curve," the volumetric work ratio for the Brayton cycle will be greater than that for the Rankine cycle. For example, for $\beta=0.1$ and $\theta=2$ if ϕ is in the range $1.3<\phi\leq 1.5$, the Brayton cycle will have the greater volumetric work ratio. For $\beta=0.1$ and $\theta=2$ if ϕ is in the ranges of $1<\phi<1.3$ or $1.5<\phi<2$, the Rankine cycle will have the greater volumetric work ratio.

The relationship between the specific heat parameter λ and isentropic temperature ratio ϕ for the equal specific work condition (equation (23)) is presented in Fig. 3. The values of temperature ratios (θ and θ_s) presented in Fig. 3 are the same as those in Fig. 2. The results in Fig. 3 and the interpretation of Fig. 3 are similar to those in Fig. 2.

Figure 4 presents the equal efficiency condition equation (33) (ψ versus ϕ) for the same dependent variables as those in Fig. 2 and Fig. 3. The interpretation of Fig. 4 is similar to Fig. 2. The efficiency of the two cycles will be equal if the isentropic temperature ratio ϕ is the value obtained for a given ψ and θ. If the isentropic temperature ratio is greater than this value, the Brayton cycle will have the higher efficiency.

For example, for an air Brayton cycle and a water Rankine cycle with $\theta=2$, $\theta_s=1$, $T_o=300$ K, and $p_o=1$ atm, the values for β and ψ are 0.04 and 4.3, respectively. From equation (29) and equation (33) the values of the isentropic temperature ratio for equal volumetric work and equal efficiency are 1.054 1.233, respectively. This corresponds to a Brayton cycle pressure ratio of 1.202 and 2.079, respectively. If the pressure ratio for the Brayton cycle is 2.079, its volumetric work ratio will be greater than that for the Rankine cycle and the efficiencies will be equal.

For the above example, the value for λ is 1.88. It can be seen from Fig. 3 that no value of ϕ exists for these values of θ and θ_s that will produce this value of λ. Hence, the specific work ratio for the Rankine cycle will be greater than that for the Brayton cycle for any value of ϕ.

The stars in Fig. 4 indicate the point of zero work for the Brayton cycle ($\phi=\theta$). This is, however, the point of maximum efficiency for the Brayton cycle. Operating at an isentropic temperature ratio greater than this limiting value has no physical significance.

A fourth and fifth set of relationships can be obtained by combining the equal efficiency condition with each of the equal work conditions. This will reduce the model for each of these two sets to five independent variables and five dependent variables. The condition of equal specific work w and equal volumetric work ω is not a practical one. This condition requires equal fluid densities at the expander exhaust.

The models for the equal efficiency-equal volumetric work condition and the equal efficiency-equal specific work condition are listed below:

Set IV. Equal temperature-equal efficiency-equal volumetric work.

Conditions

$$\theta=\theta_b=\theta_r; \quad \eta=\eta_b=\eta_r; \quad \omega=\omega_b=\omega_r$$

Dependent Variables:

$$\theta,\ \theta_S,\ \phi,\ \psi, \text{ and } \lambda$$

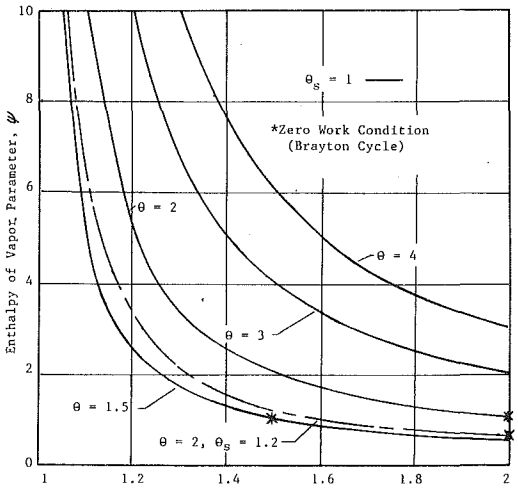

Fig. 4 Enthalpy of vaporization parameter relation for equal efficiency condition

Table 1 Comparison of Rankine and Brayton cycles for the condition of equal temperature-equal efficiency-equal volumetric work

Cycle Ref. Temp.	Water Rankine - Air Brayton 300K				Methanol Rankine - Air Brayton 300K			
Source Temp.	θ=1.5		θ=2.0		θ=1.5		θ=2.0	
θ_S	1.0	1.1	1.0	1.1	1.0	1.1	1.0	1.1
ψ	4.30	3.80	4.30	3.80	2.83	2.55	2.83	2.55
λ	1.88	1.88	1.88	1.88	1.4	1.4	1.4	1.4
φ	1.116	1.096	1.232	1.216	1.177	1.143	1.353	1.321
β	0.060	0.071	0.066	0.103	0.076	0.094	0.114	0.133
λ_{max}	0.101	0.126	0.172	0.191	0.101	0.126	0.172	0.191
p_{1r}(atm)	0.035	0.168	0.035	0.168	0.177	0.72	0.177	0.72
p_o(atm)	0.677	2.77	0.609	1.90	3.61	11.94	2.40	8.38
p_{2b}(atm)	1.0	3.81	1.27	3.76	6.37	19.04	6.93	22.20

Independent Variables:

$$\phi = 1 + (\theta/\theta_s - 1)/\psi \tag{34}$$

$$\beta = [\psi(\theta - 1) - (\theta/\theta_s - 1)]/\theta\psi^2 \tag{35}$$

η is defined in (32); ω in equation (28); w_b in equation (30); and w_r in equation 31.

Set V. Equal temperature-equal efficiency-equal specific work.

Conditions:

$$\theta = \theta_b = \theta_r; \quad \eta = \eta_b = \eta_r; \quad w = w_b = w_r$$

Dependent Variables:

$$\theta,\ \theta_S,\ \psi, \text{ and } \beta$$

Independent Variables:

$$\phi = 1 + (\theta/\theta_s - 1)/\psi \tag{34}$$

$$\lambda = (\theta/\phi - 1)/\theta_s\psi \tag{36}$$

η is defined in equation (32); w in equation (22); ω_b in equation (24); ω_r in equation (26). One can see that these models are just a relisting of selected equations from the previous models. The important difference is that through equations (34) and (35) and equations (34) and (36), two of the previous five independent variables are now dependent variables. For example, for Set IV, any two of the following (θ, θ_S, ϕ, β, and ψ) can be a dependent variable. The variable λ is always an independent variable for Set IV. For Set V, the same is true for the variables (θ, θ_S, ϕ, λ, and ψ). The variable β is always independent for Set V.

A solution for the model Set IV can be obtained by selecting values for θ, θ_c, and ϕ. Then go to Fig. 2 to find the required value for β that makes the volumetric work ratio equal. Then go to Fig. 4 to obtain the required value for ψ that makes the efficiencies equal. A solution to Set V can be obtained in a similar manner by using Figs. 3 and 4.

Selection of Independent Variables

Set IV and Set V are good models for comparing cycles and for selecting the independent variables. The discussion will now center on Set IV, which is the equal temperature-equal efficiency-equal volumetric work. What is said about Set IV is true for Set V except that the roles of variables β and λ are interchanged.

Five of the six independent variables (θ, θ_S, ϕ, β, and ψ) are related by equations (34) and (35). Therefore, for any set of three the remaining two can be determined, which give the cycles equal efficiencies and equal volumetric work ratios. If the efficiency and volumetric work ratio, as determined by equations (32) and (28), are not adequate for the application, the variables, which need to be changed to give the desired result, are known. For example, if the efficiency is too low, the isentropic temperature ratio ϕ can be increased above the value given by equation (34). This will give the Brayton cycle the higher efficiency and make it the preferred cycle for the application.

Of the five independent variables for Set IV, ϕ and β appear to be the most dependent. This is the reason for the forms of equations (34) and (35). The temperature ratios θ and θ_s are usually fixed by temperatures of the available thermal reservoirs. Once the Rankine cycle fluid has been selected the values for ψ and λ become fixed. The variables ϕ and β are pressure terms. There is some flexibility in the pressure range of the Brayton cycle within the limits of the application.

A comparison of Brayton and Rankine cycles is presented in Table 1 for a range of temperature limits (θ and θ_s). The reference temperature is 300 K. Data comparing a water Rankine cycle to an air Brayton cycle and a methanol Rankine cycle to an air Brayton cycle are presented. The model for comparison is equal temperature-equal efficiency-equal volumetric work (Set IV).

To illustrate the procedure, the following data from Table 1 are used to compare a water Rankine cycle and an air Brayton cycle operating between temperature limits of $\theta_s = 1$ and $\theta = 1.5$. For water vapor at $\theta_s = 1$ (300 K) the value for ψ is 4.30. From equations (35) and (34) the required values for β and ϕ for equal efficiencies and equal volumetric work ratios are $\beta = 0.06$ and $\phi = 1.116$. Since the saturation pressure for water at 300 K (p_{1r}) is 0.035 atm the pressure limits for the Brayton cycle are $p_o = 0.677$ atm and $p_2 = 1.0$ atm. If the Brayton cycle operates between 1 and 1.5 atm it will have a greater volumetric work ratio and efficiency than the Rankine cycle.

The value for λ for water and air at 300 K is 1.88. The maximum value for λ as specified by the temperature limits (see equations (34) and (36)) is 0.101. Hence at these temperature limits, the specific work for the Rankine cycle will be greater than that for the Brayton cycle for any value of isentropic temperature ratio.

Increasing the lower temperature limit (θ_s) has the effect of increasing the required values for β and λ and decreasing the required value for ϕ. The reason for this is that the value of ψ decreases with increasing lower temperature limit. The most pronounced effect from increasing the lower temperature limit is the increase in Rankine cycle exhaust pressure, p_{1r}, which is linked to this temperature. Through the variable β, the pressures of the Brayton cycle must be increased with increases in p_{1r}; see Table 1.

A comparison between a methanol Rankine cycle and an air

Brayton cycle is also presented in Table 1. Methanol has a lower enthalpy of vaporization than water, which makes ψ lower and all the required values higher for this comparison. Methanol also has a higher saturation pressure than water at 300 K. This increase in p_{1r} increases the required pressures for the Brayton cycle by a factor of 6 over those for the water comparison. These increases in pressure may shift the preference in favor of the methanol Rankine cycle.

For Refrigerant 12 as a Rankine fluid at 300 K, the value of ψ is 0.75. It can be seen from equation (34) for $\theta = 2$ and $\theta_S = 1$ that the required value for ϕ is 2.325. This is beyond the condition for maximum efficiency for the Brayton cycle ($\phi = \theta$). Hence, for these temperature limits, the efficiency, specific work, and volumetric work for a Refrigerant 12 Rankine cycle will exceed those for an air Brayton cycle.

This example illustrates the effect of thermodynamic properties on cycle selection and cycle variables.

Maxima

As stated earlier the maximum efficiency for an ideal Brayton cycle occurs when $\phi = \theta$. This is the Carnot efficiency. This point is of no practical interest because the cycle work is zero.

One can see from Figs. 2 and 3 and equations (23) and (29) that the variables λ and β and the work ratios w and ω attain a maximum with ϕ for given temperature limits. This is a well-known fact for a Brayton cycle and can be found in many books on gas turbines (Bathie, 1984).

The relationships for maximum specific work and maximum volumetric work are presented below:

Maximum Specific Work Ratio

$$\phi = \sqrt{\theta} \tag{37}$$

$$\eta = 1 - 1/\sqrt{\theta} \tag{38}$$

$$\psi = (\theta/\theta_s - 1)/(\sqrt{\theta} - 1) \tag{39}$$

$$\beta = (\sqrt{\theta} - 1)^2/[\sqrt{\theta}(\theta/\theta_s - 1)] \tag{40}$$

$$\lambda_{\max} = (\sqrt{\theta} - 1)^2/(\theta - \theta_s) \tag{41}$$

$$w_{\max} = (\sqrt{\theta} - 1)^2/\sqrt{\theta} \tag{42}$$

Maximum Volumetric Work Ratio

$$\phi = (\theta + 1)/2 \tag{43}$$

$$\eta = 1 - 2/(\theta + 1) \tag{44}$$

$$\psi = 2(\theta/\theta_s - 1)/(\theta - 1) \tag{45}$$

$$\lambda = (\theta - 1)^2/[2(\theta - \theta_s)(\theta + 1)] \tag{46}$$

$$\beta_{\max} = (\theta - 1)^2/[4\theta(\theta/\theta_s - 1)] \tag{47}$$

$$\omega_{\max} = (\theta - 1)^2/4\theta \tag{48}$$

All these maxima relationships are "Carnot" in nature in that they are dependent only on the temperature limits.

The maximum specific work set gives larger values for ψ, λ, and w. The maximum volumetric work set gives the larger values for ϕ, η, β and ω. The two sets can be used to establish upper and lower bounds.

Equations (37)–(48) can be used to compare cycles quickly in terms of thermodynamic properties. For example, if the fluids for the Rankine and Brayton cycles and the temperature limits have been selected then the values of ψ, λ, and the Rankine exhaust pressure p_{1r} are determined from the thermodynamic properties. From equations (39) and (45) and equations (41) and (45), the upper and lower bound for the required values for ψ and λ can be obtained. If the property values for ψ and λ are greater than the required values for the upper bound, the Rankine cycle will have the lower efficiency and the higher specific work. The reverse is, of course, true if the property values are below the lower bound. Using equations (37) and (40) and equations (43) and (47), one can determine the upper and lower range for Brayton cycle pressures that are required to meet the equal volumetric work condition.

Conclusions

Comparison of the simple Brayton and Rankine Cycles results in the following conclusions:

1 The condition of equal temperature, equal efficiency, and equal volumetric work for the cycles establishes two relationships between the thermodynamic parameters β, λ, and ψ and cycle parameters ϕ and θ_s. These two relationships make two of the six parameters dependent parameters.

2 The condition of equal temperature, equal efficiency, and equal specific work for the cycles establishes two different relationships between the six thermodynamic and cycle parameters.

3 Since thermodynamic properties are strongly dependent upon the cycle fluid, these two sets of relationships provide useful guidelines for selecting fluids as a function of the application.

4 The pressure parameter β and the specific heat parameter λ attain maxima as a function of the temperature limits.

5 The required values for the property parameters λ, ψ, and β have been related to the temperature limits. Comparing these required values to the selected values establishes the preference of cycles and fluids.

References

Barilovich, V. A., Smirnov, Y. A., and Starikov, V. I., 1985, "The Thermal Efficiency of Geothermal Power Stations," *Thermal Eng.*, Vol. 32, No. 11, pp. 627–629.

Bathie, W. W., 1984, *Fundamentals of Gas Turbines*, Wiley, New York, Chap. 5.

Chang, S. C., and Roux, J. A., 1985, "Thermodynamic Analysis of a Solar Zeolite Refrigeration System," ASME *Journal of Solar Energy Engineering*, Vol. 107, No. 3, pp. 189–195.

Dugger, G. L., 1969, *Ramjets, AIAA Selected Reprint Series*, Vol. 6, pp. 8–14, 21–25, June.

Hattingh, H. V., 1981, "Cruise Flight Duration of a Low Mach Number Ramjet," *J. of Aircraft*, Vol. 18, No. 6, pp. 425–430.

Manokova, T. E., 1984, "Analysis of the System of Waste Heat Recovery of a Thermal Power Station by the Method of Comparison of Energy Losses," *Thermal Eng.*, Vol. 31, No. 9, pp. 498–501.

Naimanov, O. S., 1986, "Features of the Selection of Initial Steam Pressure of Geothermal Power Stations With One and Two Evaporation Stages," *Thermal Eng.*, Vol. 33, No. 2, pp. 79–82.

Design and Performance of a Small-Power Clausius–Rankine Process

Z. Shao

M. Malobabic

D. Burhorn

M. Rautenberg

Institute for Turbomachinery,
Hannover University,
Hannover, Federal Republic of Germany

In recent years, an increasing awareness of the shortness of raw materials has led to an improved utilization of the energy input in thermal processes. Utilization of the heat generated in such processes and machinery can improve the overall efficiency of the latter and converse raw materials. In particular, combustion engines have a poor overall efficiency due to the high-temperature exhaust gases they produce. The classical Clausius–Rankine process can be applied to such machines in order to utilize the heat generated so as to provide turbocharging of the latter. The design of such a Clausius–Rankine process in connection with a newly developed steam turbine based upon the Pelton principle is presented. In this design, particular value is placed upon the small size of individual units and a comparability with actual thermodynamic conditions in combustion engines.

Introduction

In recent years, the economic viability of devices and equipment has gained increasing importance. The fact that primary energy resources are becoming limited is reflected in the importance placed upon an improved utilization of such equipment. In the long term, an increased shortage of these energy resources will lead to an increase in the cost of raw materials. The optimization and development of technical machinery in order to attain better energy utilization will thus become unavoidable. An optimization of technical machines already in operation is possible provided their overall efficiency can be increased. This aspect leads to the consideration of converting hitherto unused energy into mechanical or electrical energy, which may be recycled to the machine in question (Papperitz et al., 1981). Where, for example, in the past, bypass valves have been used to reduce or regulate process pressures or mass flows, whereby the working fluid is isenthalpically throttled without further energy utilization, the installation of turboexpanders can make use of a large proportion of the energy previously lost (Fortuin et al., 1979).

Of particular interest in this context are machines that produce heat with a high energy content from combustion processes or other exothermic reactions. Owing to the high temperature of the waste heat of such machines, they exhibit especially low overall efficiency levels.

In the case of combustion engines, for example, which appear to be particularly disadvantageous with respect to the above-mentioned development of the primary energy situation, exhaust temperatures range between 500°C and 900°C. This significant energy potential may be utilized by a heat engine coupled to the primary engine, which can recycle the energy to the latter. For this purpose, the classical Clausius–Rankine process (CRP), which is generally referred to as "Rankine process" in the American and English language, provides a basis for further investigations.

CRP processes, consisting of a feed pump, steam generator, steam turbine, and condenser have been used for a long time to convert heat into mechanical energy. These processes, however, have been primarily considered in relation to large-capacity units in power generating plants. The technical operating behavior of these processes is widely known in relation to stable and transitory operation. In contrast, no results are available concerning the operational behavior of low power CRPs. For the low-power case in particular, however, a wide area of application exists in relation to the utilization of the heat generated in combustion processes.

Application Possibilities for Small CRPs

Owing to their high exhaust gas temperatures, combustion engines appear to be particularly suitable for investigating small CRPs, which may hereby be applied as an alternative to the traditional principles adopted in exhaust gas utilization, for example, turbocharging. This may find application, for example in ship diesel engines, locomotives, and automobile engines. In addition to this area of application, the Clausius–Rankine process may be adopted in other equipment where waste heat is generated. An increasing interest in recent years in low-power solar-heated equipment opens up the possibility of extracting energy by means of a CRP, similar to that described in the present work. A further possible area in which CRP units may be used to recycle energy is in the chemical industry.

The application of the Clausius–Rankine process for utilizing exhaust gas from combustion engines offers significant advantages compared to turbocharging (Tarkir, 1979). Owing to the method of energy conversion in an exhaust gas turbine, the exhaust gas mass flow produced must be led through the turbine. The exhaust gas mass flow thereby builds up in front of

Contributed by the International Gas Turbine Institute and presented at the 34th International Gas Turbine and Aeroengine Congress and Exhibition, Toronto, Ontario, Canada, June 4–8, 1989. Manuscript received at ASME Headquarters February 1, 1989. Paper No. 89-GT-215.

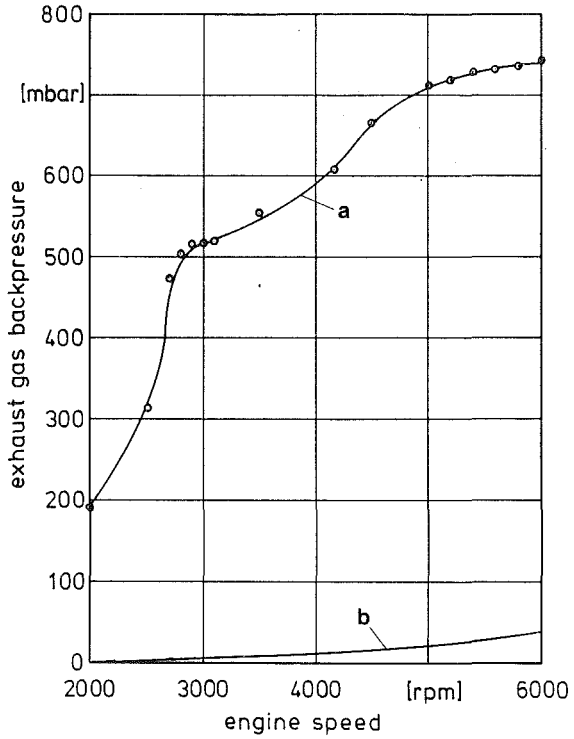

Fig. 1 Comparison of exhaust gas back pressure; (*a*) an exhaust gas turbocharger (measured); (*b*) the tested steam turbocharger (calculated)

the turbine, which results in a high pressure at this location, i.e., behind the combustion engine. It is known that this has a negative effect upon the scavenging loop drop of the engine and consequently upon the filling intensity of the combustion process. The inclusion of a bypass valve in the exhaust gas turbocharger (ETC) to regulate the turbocharger performance leads, however, to isenthalpic expansion of the exhaust gas without energy transfer, and is therefore not a good solution for improving the overall efficiency of the engine.

In a Clausius–Rankine process, on the other hand, only the thermal energy of the exhaust gas is required. If the heat generated by the combustion engine is used to produce steam from water, a small steam turbine may be driven, which, when coupled to a compressor, can again provide turbocharging of the combustion engine. This type of turbocharging was envisaged as long ago as 1984 under the name of "steam turbocharging" (STC) at which time the particular advantages of the STC compared to the ETC were illustrated (Rautenberg et al., 1984a, 1984b). The main advantage is the absence of exhaust gas pressure buildup in front of the turbine, since the exhaust gas mass flow in the case of the steam turbocharger is led through the CRP steam generator without significant pressure losses. By this means, the negative influence of exhaust turbocharging upon the scavenging pressure drop is avoided and there is no need for isenthalpic throttling of the exhaust gas. Figure 1 serves to illustrate to what degree the turbine back pressure using a CRP for turbocharging may be reduced compared to that of a traditional exhaust turbocharger. As may be seen in the figure, the exhaust gas back pressure in the case of steam turbocharging for the given example of a 2.2 liter gasoline engine (Audi, five-cylinder) is only about 5 percent of the value for an exhaust gas turbine regulated by a waste gate. Figure 2 shows the possible way in which a small CRP may be applied for turbocharging. As indicated in Fig. 2, after transferring its thermal energy in a steam generator, the exhaust gas is freely released to the atmosphere. As a closed circuit, the CRP may therefore be operated independently. The energy extracted from the exhaust gas is converted into mechanical energy and can be recycled to the combustion engine by means of a compressor.

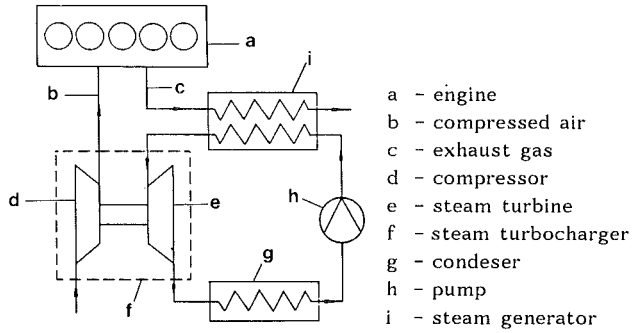

Fig. 2 Scheme of the proposed steam turbocharger system

During the years 1984–1988, small partially admitted steam turbines based upon the Pelton principle have been developed at the Institute for Turbomachinery (IfT), University of Hannover. Their applicability for steam turbocharging has already been repeatedly demonstrated. Meanwhile, it has been possible to increase the efficiency of these small steam turbines to such an extent that they may now be seriously considered as a practical means of utilizing this otherwise wasted energy (Malobabic et al., 1988). In order to be able to test and investigate this utilization under realistic conditions, i.e., in relation to the applicability in combustion engines, a CRP with the necessary components was constructed at the IfT. The layout of this Clausius–Rankine process is thereby oriented toward the thermodynamic conditions that exist in a gasoline or Diesel-powered vehicle engine in the range of about 100 kW. Owing to the fact that the energy supply equipment at the Institute suffered damage at the start of the investigations, thte test rig could not be operated. This meant that the investigation program that had just begun had to be interrupted for an extended period. As a result, it is only possible to present a limited number of initial investigations within the scope of this work. The central theme of this paper concerns the design and detailed description of the individual components of the overall test rig, and initial test results are shown. In future work, it is intended to use the test rig in its present configuration for carrying out further investigations of the Pelton steam turbine. It is thus possible to provide a detailed descrip-

Nomenclature

A = area, m^2
c = velocity, m/s
c_p = specific heat at constant pressure, J/kg K
h = enthalpy, J/kg
k = heat transfer coefficient
$\dot{m}$ = mass flow rate, kg/s
n = rotational speed, rpm
p = pressure, N/m^2
P = power, W
Q = heat, W
$\dot{Q}$ = heat flow, W/s
T = temperature, K

Subscripts

B = bearing
c = compressor
CC = combustion chamber
ex = exhaust gas
i = input
is = isentropic
L = losses
o = output
P = pump
S = steam
SG = steam generator
T = turbine

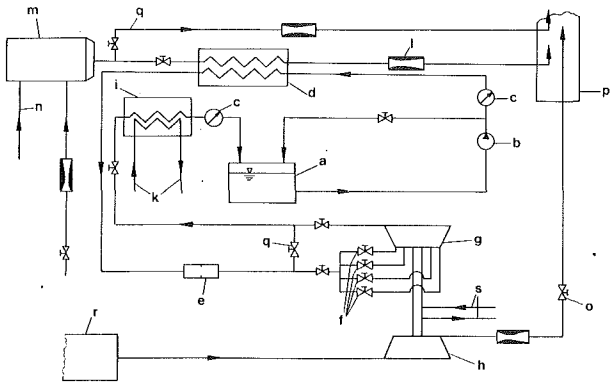

Fig. 3 Schematic view of the test rig

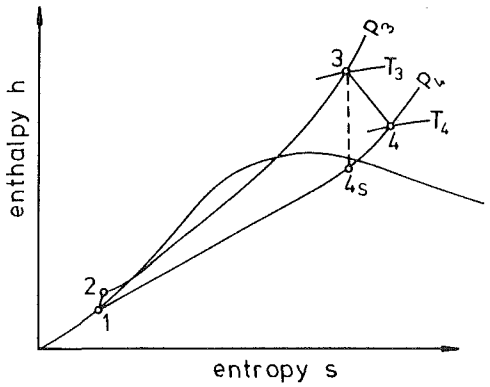

Fig. 4 *h,s*-diagram for the Clausius-Rankine cycle

tion of the experimental equipment and boundary conditions here as a supplement to research that has already been published and to work proposed in the future (Rautenberg et al., 1984b, 1985; Malobabic et al., 1988).

Design of the Clausius-Rankine Process

The layout of the Clausius-Rankine process follows according to the comparability to real conditions as exist in an Otto or Diesel engine and also to the low power associated with this process. It is therefore necessary to be able simultaneously to regulate individual process parameters such as temperature, process pressure, and mass flow in order to obtain a generally valid prognosis concerning the applicability of small CRP engines for utilizing waste heat.

On the basis of these considerations, a combustion chamber was selected as a controllable heat source, which permits the exhaust gas mass flow as well as the gas temperature to be independently varied over a wide range. The combustion chamber temperature could be regulated within the range of 300°C to 1000°C for exhaust gas flows ranging between 0.05 and 0.3 kg/s. Based upon these data values, the equation

$$Q_{CC} = \dot{m}_{ex}[(c_{pex}T_{ex})_i - (c_{pex}T_{ex})_o] \quad (1)$$

gives a value of 120 kW for the maximum available thermal power from the combustion chamber.

Figure 3 shows the test rig setup in schematic form. The adoption of a combustion chamber instead of an engine is justified on the grounds that it is not possible independently to regulate the parameters mass flow ($\dot{m}_{ex}$) and temperature (T_{ex}) in the case of an engine. Since, however, it was intended to investigate the operational behavior of the Clausius-Rankine process in terms of the individual process parameters, independent regulation of the parameters was necessary.

Figure 4 shows the Clausius-Rankine process for the working medium water in the *h,s*-diagram. A high process efficiency may only be obtained provided the upper process temperature as well as the upper process pressure are chosen to be as high as possible while the lower process pressure should be selected as low as possible in order to ensure a high efficiency for the steam turbine. In order to achieve comparability between the test process and the conditions relating to a combustion engine, the upper process temperature and pressure were chosen to be 400°C and 20 bar, respectively. The exhaust gas inlet temperature to the steam generator should therefore be 500°C. As indicated in Fig. 3, the water supply tank is open to the atmosphere, which means that the condenser pressure and thus the turbine outlet pressure is 1 bar (atmospheric pressure). As will be described later in further detail, the lower process temperature has a maximum value of 86°C.

Feed Pump

Owing to the necessity of regulating the working medium mass flow over a wide range, a variable-speed piston feed pump was chosen. This pump design has the great advantage that the mass flow of the working medium is only dependent upon the pump speed and not upon the process pressure. By using this pump in the test rig, the mass flow could be regulated between 0–0.12 kg/s, which corresponds to a pump speed range of 0–800 rpm. As indicated by earlier investigations of steam turbine rotors, a steam mass flow of 0.02–0.04 kg/s is necessary in order to operate the steam turbine at an acceptable efficiency of 50 to 60 percent (Rautenberg et al., 1984b, 1985; Malobabic et al., 1988). The process pressure in the test circuit is adjusted by means of throttle valve installed in the turbine input line (Fig. 3). The most important process parameters are given as follows:

$$0 \text{ kg/s} < \dot{m}_s < 0.04 \text{ kg/s}$$
$$1 \text{ bar} < P_s < 20 \text{ bar}$$
$$86°\text{C} < T_s < 500°\text{C}$$

The performance characteristics of the feed pump according to these specifications are shown in Fig. 5. The feed pump performance characteristics were determined using the test rig shown in Fig. 3. By this means, all losses in this specially designed pipe network are accounted for in the performance characteristics. Depending on the pump performance, these two variables govern the outlet pressure. The work done by the pump in pumping the medium from point 1 to point 2 in the *h,s*-diagram of Fig. 4 is computed from the equation

$$P_P = \dot{m}_P \, \Delta h_P = \int_{P_1}^{P_2} v' dp \quad (2)$$

On the basis of the feed pump performance characteristics, any desired mass flow and process pressure may be quickly obtained as a function of the pump speed. This is of particular interest in relation to the investigation of the transitory operating behavior of the Clausius-Rankine process.

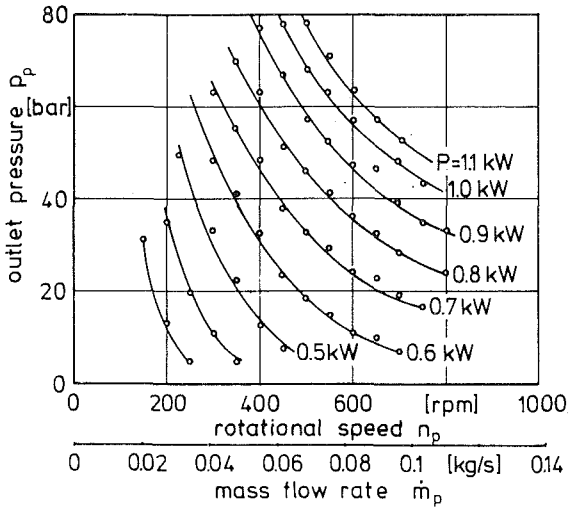

Fig. 5 Pressure ratio and power input of the feed pump

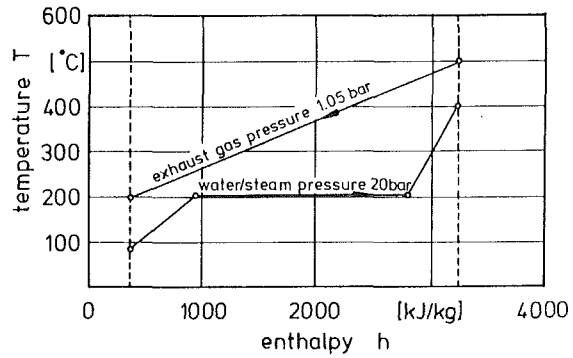

Fig. 6 *T,h*-diagram for the steam generator at design point

Steam Generator

In addition to the previously mentioned boundary conditions for the CRP, the construction size of the steam generator should be kept as small as possible. The main reason for this is that the low-power CRP examined here is representative of an investigation concerning the applicability in combustion engines operating under nonstationary conditions. Furthermore, the steam generator must heat the working medium water from state 2 to state 3 in the *h,s*-diagram (Fig. 4), which comprises the three process stages heating, vaporization, and superheating. The design of the steam generator must thus be oriented to these requirements. For the reasons already given, the inlet temperature of the exhaust gas from the steam generator is limited to 500°C. For the design point of the steam generator, the outlet temperature of the exhaust gas should be fixed at a maximum of 200°C. Together with an exhaust gas mass flow of 0.3 kg/s, a thermal input of 100 kW is obtained from these values at the design point.

From investigations of partially admitted Pelton steam turbines a maximum process temperature of 400°C (see above) and a process pressure of 20 bar appear to provide a good solution (Rautenberg et al., 1984a). The steam mass flow should thereby lie within the limits of 0.02 to 0.04 kg/s. The lower process data, on the other hand, are governed by the condenser and the feed pump. The feed pump inlet temperature is thus limited to a maximum of 86°C for an inlet pressure of 1 bar. Consequently, this is also the state of the process medium at the lower limits of the circuit.

For a process pressure of 20 bar and a steam outlet temperature of 400°C, a specific enthalpy of 3250 kJ/kg is obtained from the *h,s*-diagram for water and steam (Schmidt, 1963). For the lower process pressure of 1 bar, a corresponding enthalpy of 360 kJ/kg is obtained. The relationship between exhaust gas and steam in the steam generator is shown in Fig. 6. According to the equation

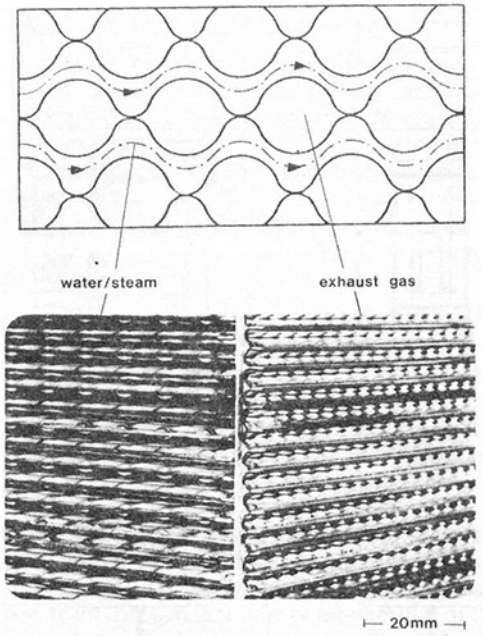

Fig. 7 Plate package of the steam generator

$$\dot{m}_s = \frac{\dot{Q}_{SG}}{\Delta h_{SG}} \tag{3}$$

a process mass flow of 0.035 kg/s is obtained at the design point of the steam generator.

All the thermodynamic boundary conditions for the steam generator are therefore given. As mentioned previously, in selecting a suitable steam generator, the constructional size should be kept as small as possible. About 95 percent of all heat exchangers are based upon either the tubular or plate method of construction. Each of these construction methods has particular advantages and disadvantages. Tubular heat exchangers are especially suitable for high process pressures, baut lead to relatively high pressure losses on the exhaust gas input side. In addition, they also have the disadvantage of a large constructional volume. Both the pressure loss on the exhaust gas side and the large constructional volume are disadvantageous with respect to an application in nonstationary combustion engines. Although plate-type heat exchangers do not have the disadvantages of pressure loss, large volume, and large weight, due to the method of construction, they are not particularly strong and cannot therefore be subjected to high pressures. For the test rig proposed here, a specially built hybrid heat exchanger was therefore selected. The hyprid heat exchanger consists of a plate package from the company Bavaria®, which, due to the special corrugated stamping of the individual plates, represents a combination of the tubular and plate heat exchangers. The construction and form of the plate package is shown in Fig. 7. As indicated in Fig. 7, tubular flow applies to the hot exhaust gas, while the process medium water undergoes plate flow. The individual plates of this package are welded together. In order to provide the steam generator with sufficient pressure resistance for the design pressure of 20 bar, the plate package, which has a rectangular cross section, is fitted into a pressure-resistant frame made of V4A steel. In order to provide additional stiffness, this frame is provided with welded-on ribs. By this means, expansion of the frame under high pressure is prevented. Figure 8 shows the heat generator as installed in the test rig. The heat transfer between the exhaust gas and the process medium is realized in the heat exchanger according to the cross counterflow principle. The hot

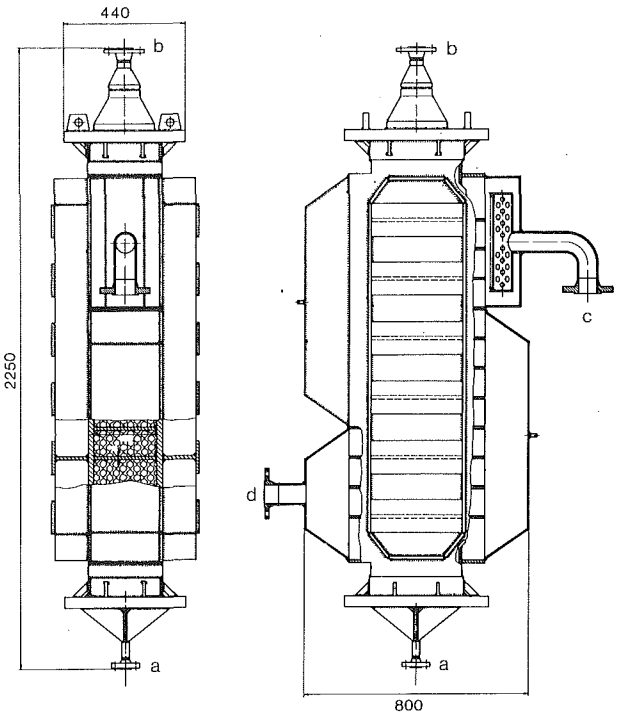

a - water inlet
b - steam outlet
c - exhaust gas inlet
d - exhaust gas outlet

Fig. 8 Design of the steam generator

exhaust gas arriving from the combustion chamber is delivered to the process laterally in the upper region of the steam generator. As may be seen in Fig. 8, a distributor incorporated in the exhaust gas mass flow prevents premature exposure of particular plates directly to the hot exhaust gas flow. This distributor has the effect of distributing the hot exhaust gas over the entire plate cross section, thereby providing an even transfer of heat.

In total, the exhaust gas flows through the heat exchanger three times before leaving laterally in the lower region. The water, on the other hand, enters the lower side of the steam generator in a counterflow direction and leaves as superheated steam from the upper side.

Steam Turbine

The superheated steam arriving from the steam generator is expanded in a partially admitted steam turbine based upon the Pelton principle. For investigating these small-power CRPs, three types of steam turbine rotor have been developed and tested at the Institute for Turbomachinery in recent years (Rautenberg et al., 1984b, 1985; Malobabic et al., 1988). In the turbine, the steam should be expanded from point 3 to point 4 in the h,s-diagram. In designing the turbine, care was taken to ensure that the state at the turbine outlet does not lie in the wet steam phase. Based upon the abovementioned boundary conditions for the CRP, a maximum specific enthalpy of 3250 kJ/kg at $p_s = 20$ bar and a maximum pressure of 1 bar in the condenser, the maximum isentropic enthalpy drop in the steam turbine is found to be 660 kJ/kg (Schmidt, 1963). Although the point 4_s in the h,s-diagram (Fig. 4) lies in the wet steam phase, for real expansion with a turbine efficiency of $\eta_T < 87$ percent the expansion endpoint (point 4) nonetheless lies in the superheated steam phase. In view of the fact that only Clausius-Rankine processes of the low power ($P_T < 20$ kW) should be considered, the turbine output lies in the region of 10 kW. According to the equations for the turbine efficiency and the turbine output power

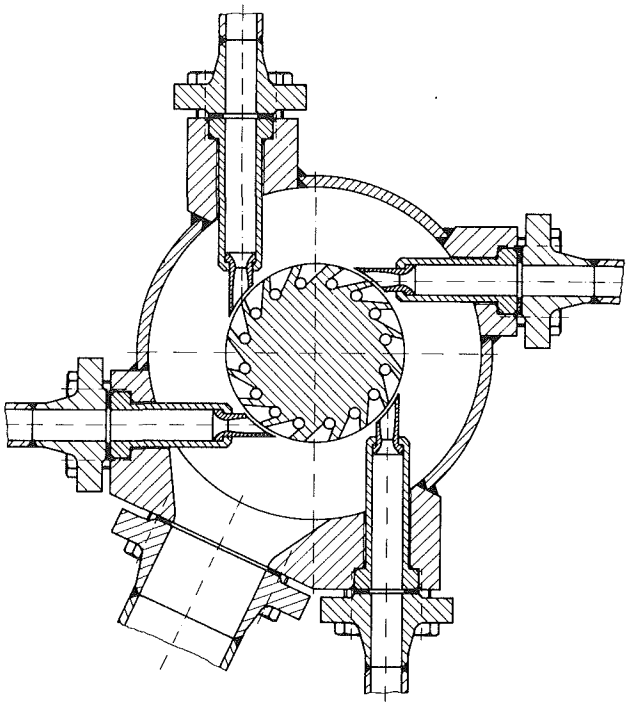

Fig. 9 Casing of the tested turbine

$$\eta_{is,T} = \frac{\Delta h_T}{\Delta h_{is,T}} \tag{4}$$

$$P_T = \dot{m}_s \, \Delta h_T \tag{5}$$

and assuming a turbine efficiency of 50 percent, a turbine mass flow of 0.03 kg/s is computed from the equation

$$\dot{m}_s = \frac{P_T}{\Delta h_{is,T} \eta_{is,T}} \tag{6}$$

As already mentioned, the steam turbine rotors tested in the past and adopted in the present test rig are similar to Pelton turbines. For computing the test rig and steam turbine design data, a turbine efficiency of 50 percent was specified. Since the Pelton turbine is of the constant-pressure type, the superheated steam is expanded in four supersonic nozzles (Fig. 9), which may be independently regulated, and the available enthalpy drop of

$$\Delta h_T = 0.5 \, \Delta h_{is,T} \tag{7}$$

is completely converted into velocity according to the equation

$$\Delta h_T = \frac{c_T^2}{2} \tag{8}$$

The cross sections of three previously tested steam turbine rotors are shown in Fig. 10. Rotor 1, which was developed first, is characterized by radial ending blades, which only permit deflection of the steam jet in the tangential direction. As a result of this, the efficiency of this rotor was only about 30 percent. The logical further development of this rotor is presented by rotor 2. In this rotor type, buckets are integrated into the rotor in place of the blades, which also permit a flow deflection in the radial as well as in the tangential direction. By adopting these measures to achieve better utilization of the available momentum, the turbine efficiency could be raised to about 50–60 percent, depending upon the operating point.

The most recent development in relation to turbine blades is depicted by rotor 3. The bucket shape is replaced by a flow channel that provides an even better flow guide and makes possible a 180 deg deflection of the flow in the tangential direction. This represents the maximum attainable energy

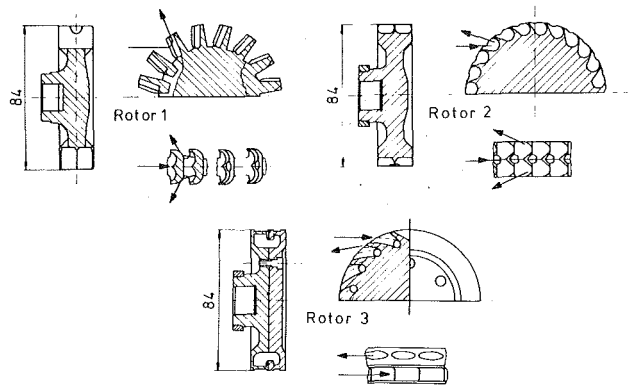

Fig. 10 Comparison of the three different rotor types

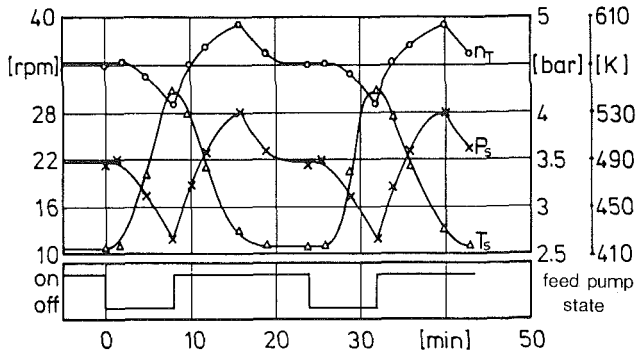

Fig. 11 Transient characteristics of process parameters: (a) turbine speed n_T, (b) steam generator outlet temperature T_S, (c) steam generator outlet pressure p_S

utilization for a Pelton turbine. Further tests have indicated a 5–8 percent increase in efficiency compared to rotor 2.

Since the Clausius–Rankine process proposed here was investigated in relation to the turbocharging of combustion engines, the turbine is coupled to a compressor. In the present case, the turbine and the compressor are mounted on a common shaft. The compressor is a serially produced compressor of Type K26 from the firm Kuehnle, Kopp and Kausch (KKK), as installed in numerous automobile engines over many years. The performance characteristics of this compressor are widely known and shall not be further investigated for this test rig. In the present case, the compressor simply acts as a brake to absorb the power produced by the turbine.

The following relationship thereby holds:

$$P_C = P_T - P_{L,B} - \dot{Q}_T \tag{9}$$

In this equation P_T denotes the turbine power output, $P_{L,B}$ denotes the turbocharger bearing losses including the turbine rotor disk losses, and $\dot{Q}_T$ denotes the turbine heat losses (Kishioka and Osawa, 1972; Malobabic et al., 1988).

Condenser

The task of the condenser is to distill the hot steam expelled from the turbine from point 4 to point 1 in the h,s-diagram (Fig. 4). The boundary conditions for the condenser are governed on the one hand by the state of the process medium at the turbine outlet and on the other hand by the feed pump inlet conditions ($P_P = 1$ bar, $T_P < 86°C$). A tubular heat exchanger was selected that is cooled by a cooling water circuit independent of the CRP. By adopting water cooling for the condenser, which permits a higher specific heat removal compared to air cooling, this can also be kept small in the tubular method of construction. In order to ensure that the entire process closely resembles the conditions met in a conventional engine, this condenser may be replaced by an automobile radiator.

Initial Tests on Transient Operating Behavior

Of particular interest are the stationary and transitory operating behaviors of the Clausius–Rankine process. As is generally known, the circuit is in a state of equilibrium when the individual parameters such as mass flow, steam temperature, process pressure, and turbocharger speed are temporarily constant. It follows that all heat flows and output and input powers are in equilibrium with respect to one another:

$$\sum_i (\dot{Q}_i + P_i) = 0 \tag{10}$$

If one of the process parameters is altered, the system adopts a new equilibrium state. Initial investigations on the CRP test rig presented above were concerned with the process behavior, i.e., with the dynamic response of individual process parameters in relation to the feed water delivered to the process.

Assuming the operating state of the CRP to be stable, the delivery of feed water was interrupted by switching off the water feed pump. Once the feed pump was brought into operation again, the original state of equilibrium of the system re-established itself, whereby the mass flow of the working fluid was identical to the mass flow prior to switching off the feed pump.

The starting point for the investigations concerns the operation of the turbine with three nozzles (Fig. 9). The stationary starting point for the investigations is characterized by the following data:

$$\begin{aligned} n &= 34{,}000\ \text{min}^{-1} \\ P_S &= 3.45\ \text{bar} \\ T_S &= 415\ \text{K} \\ \dot{m}_S &= 0.0163\ \text{kg/s} \\ T_{ex,i} &= 445°C \\ T_{ex,o} &= 130°C \\ \dot{m}_{ex} &= 0.1\ \text{kg/s} \end{aligned}$$

On the basis of this stationary operating point, Fig. 11 shows the interdependence between the process temperature, the process pressure, and the turbocharger speed as a function of time. The state of the feed pump is also indicated.

In Fig. 11, two cycles are illustrated. Between the two cycles and at the end of the second cycle, the stationary state at the start of the test again re-established itself when the feed pump is switched on.

When the feed pump is switched off, water is no longer pumped from the supply tank into the circuit. At the same time, however, the quantity of heat supplied by the combustion chamber remains constant according to equation (1). This leads to a rise in the process temperature due to the fact that the steam generator combines the individual process in the heating, vaporizing, and superheating. If the circuit is continually supplied with heat, water that was previously in the heating-up phase also becomes vaporized. Consequently, the water level in the stream generator drops and the free surface area of the steam generator available for superheating increases. In accordance with equations (11) and (12), for a constant supply of heat (constant exhaust gas mass flow) from the combustion chamber, the process temperature therefore rises

$$\dot{Q}_{SG} = k\,A\,(T_{ex} - T_{SG}) \tag{11}$$

$$T_{SG} = T_{ex} - \frac{\dot{Q}_{SG}}{k\,A} \tag{12}$$

In these equations, k denotes the heat transfer coefficient, which is considered to be constant, and A denotes the free surface area of the steam generator available for superheating. Owing to the rapid rise in temperature, the enthalpy of the

superheated steam also increases. Although on the one hand this must lead to an increase in the pressure p_S, due to the fact that the circuit is open on one side, i.e., at the turbine, the hot steam on the other hand can expand via the turbine nozzles, which leads to a drop in pressure. These two opposing effects become superimposed and result in only a very small drop in the process pressure. In accordance with equation 8, the turbocharger speed is mainly dependent upon the process pressure. Consequently, the variation in speed is similar to the variation in pressure.

Shortly before the system is completely emptied, the process mass flow is again delivered to the circuit by switching on the feed pump. This results in an immediate increase in the process pressure and hence the turbocharger speed. The temperature on the other hand drops. Due to the drop in the steam generator water level with the feed pump switched off, the heat transfer surface of the steam generator is exposed to hot exhaust gas and stores this heat. When the feed pump is switched on, the stored heat is transferred to the process medium until the state of equilibrium found before switching off the feed pump has re-established itself. Thus, both the turbocharger speed and the pressure rise sharply after switching on the feed pump. If the new state of equilibrium slowly becomes re-established, the free surface area available for superheating decreases due to the mass flow delivery. Consequently, the temperature at the steam generator outlet drops and both the pressure and speed decrease again.

The tests carried out here concerning the process behavior for an abrupt cutoff or return of the working fluid supply cause considerable heat stresses and loading of the steam generator. This is caused by exposure of the plate package to hot exhaust gas when the steam generator is almost empty. If the feed pump is then switched on again, the plates come into contact with cold water. Combined with the fact that the plate package and the pressure-resistant frame of the steam generator have different wall thicknesses owing to the technical considerations, these two structural components also have different thermal expansion characteristics. Consequently, there is a danger of cracks forming in the steam generator plate package. Of particular importance, therefore, is the mechanical decoupling of these two structural components by means of a compensator. In the present case, the compensator is installed at the top end of the steam generator between the housing and the plate package and allows the complete plate package to move within the pressure-resistant frame. By this means, thermal stresses are accommodated and damage to the steam generator is avoided.

Summary

In this paper, a comprehensive account of the design and construction of a Clausius–Rankine process for utilizing waste heat is presented. The design of the individual components of this circuit, such as the feed pump, the steam generator, the turbine, and the condenser is described and explained in detail. One of the major aspects of designing the processes was to construct a test rig for converting a small amount of thermal power in the range of 100 kW, as is available, for example, in the exhaust gas of a small combustion engine. The design of the test rig was thus oriented toward the thermodynamic characteristics of such combustion engines. In view of the application of such a small CRP for turbocharging combustion engines, the test rig was equipped with a small partially admitted steam turbine based on the Pelton principle. The power output from this turbine lies in the range of 10 kW. Initial tests concerning the dynamic behavior of this process as a function of the mass flow of the feed water have indicated that the process pressure, the process temperature, and the turbocharger speed response rapidly to changes in the mass flow. No temporal delay could be detected between a change in the mass flow and the correspondingly induced fluctuations of the individual parameters.

Acknowledgments

The research described in this paper was funded by the German Research Association (DFG). The authors would like to thank them for their support. Also the authors wish to express their appreciation for the efforts of Mr. H. Foss and Mr. H. Quietmeyer, who prepared and skillfully operated the test rig. Furthermore the authors are grateful to Mr. T. Merkt and Mr. I. Westwood for their help in preparing the paper and paper layout.

References

Fortuin, J. B., Poolman, P. J., and Siteur, H. W., 1979, "The 'Organic Rankine Cycle' (ORC) Power Conversion System as a Means of Energy Conservation," *Gas Wärme International*, No. 28.

Kishioka, E., and Osawa, K., 1972, "Investigation Into the Problem of Losses of the Pelton Wheel," *Proceedings of the Second International JSME Symposium on Fluid Machinery and Fluidics*, Tokyo.

Malobabic, M., Shao, Z., Burhorn, D., and Rautenberg, M., 1988, "Performance Analysis of a Small Partial Admitted High Speed Steam Turbine," *Proceedings of the 23rd Intersociety Energy Conversion Engineering Conference* (*IECEC*), Denver, CO.

Papperitz, C., Pichler, W., and Roemheld, M., 1981, "Waste Heat Recovery for Electricity Generation," *Turbomachinery International*, Nov. /Dec.

Rautenberg, M., Mobarak, A., Abdel Kader, M., and Meyer, C., 1984a, "Comparison of Different Small Steam Turbines for Steam Turbocharger," ASME Paper No. 84-GT-239.

Rautenberg, M., Malobabic, M., Mobarak, A., and Abdel Kader, M., 1984b, "A Small Pelton Turbine for Steam Turbocharger," *Proceedings of the 19th Intersociety Energy Conversion Engineering Conference* (*IECEC*), San Francisco, CA.

Rautenberg, M., Malobabic, M., Mobarak, A., and Abdel Kader, M., 1985, "Design and Testing of a 10 kW Steam Turbine for Steam Turbochargers," ASME Paper No. 85-IGT-113.

Schmidt, E., 1963, *VDI-Wasserdampftafeln*, 6th ed., Springer-Verlag, Berlin, Federal Republic of Germany.

Tarkir, R. A., 1979, "Application of Rankine Bottoming Diesel Engines to Marine Vessels," SAE Paper No. 790644.

Parametric Analysis of the Kalina Cycle

C. H. Marston
Associate Professor,
Department of Mechanical Engineering,
Villanova University,
Villanova, PA 19085
Mem. ASME

The Kalina Cycle utilizes a mixture of ammonia and water as the working fluid in a vapor power cycle. When the liquid mixture is heated the more volatile ammonia tends to vaporize first and at a lower temperature than does pure water. This property of ammonia–water mixtures makes possible a better match to the enthalpy–temperature curve of a hot gas heat source such as a gas turbine exhaust and also permits circulation of fluids of different composition in different parts of the cycle. Taking advantage of the latter feature, condensation (absorption) can be done at slightly above atmospheric pressure with a low concentration of ammonia, while heat input is at a higher concentration for optimum cycle performance. Computer models have been used to optimize a simplified form of the cycle and to compare results for a more complex version proposed by El-Sayed and Tribus. A method of balancing the cycle was developed and key parameters for optimizing the cycle identified.

1 Introduction

Many thermodynamic cycles have been considered for the utilization of the thermal energy in a hot gas stream in the production of mechanical or electrical work. The most often used cycle is some form of Rankine Cycle, with steam as the working fluid. Heat transfer to the steam takes place in a counterflow heat exchanger, sometimes called the heat recovery steam generator (HRSG).

In the Rankine Cycle more than half of the heat transfer occurs during the boiling process. Since the HRSG operates at essentially constant pressure, temperature is also constant during boiling; the gas at the pinch point, where the water *starts* to boil, must be at a higher temperature than the boiling water (Fig. 1). The pinch point is a limitation on power output because:

1 It can force a higher than otherwise necessary stack temperature.
2 The gas at the point where vaporization is complete will be at a much higher temperature than the steam and the large temperature difference results in a loss of availability.

The Kalina Cycle utilizes a mixture of ammonia and water as the working fluid. When the liquid mixture is heated, the more volatile ammonia tends to vaporize first and at a lower temperature than does pure water (Fig. 2). The temperature of the remaining saturated liquid rises as the ammonia concentration decreases. Thus a better match to the temperature change of the gas is obtained and the potential exists for significant increases in cycle efficiency without the materials problems encountered with high-temperature advanced cycles. Moreover, different parts of the cycle can have different concentrations of ammonia. Thus condensation (absorption) can take place at a pressure slightly above atmospheric, using a relatively low concentration of ammonia, even though a relatively high concentration is appropriate in the boiler.

The cycle was conceived by Kalina (1984) for use in waste heat recovery and combined cycle power generation systems. El-Sayed and Tribus (1985a, 1985b, 1985c) have reviewed and extended data on properties of ammonia–water mixtures and made a theoretical comparison of the Rankine Cycle with a modified form of the Kalina Cycle. A later paper with Kalina (1986a) also addresses mixture properties.

The fluid dynamic design of the turbine is no different than that of a steam turbine since ammonia has almost the same molecular weight as water. However, copper-based alloys are subject to corrosion in the presence of ammonia, so some material substitution may be necessary.

Using the property data compiled by El-Sayed and Tribus, a

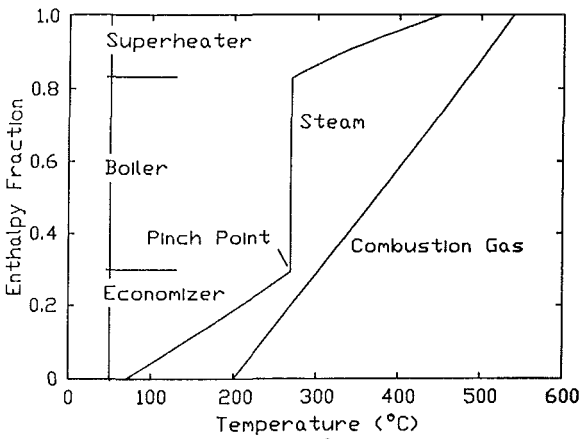

Fig. 1 Enthalpy versus temperature in a heat recovery steam system. Temperature is constant as the water boils. A positive temperature difference must be maintained at the pinch point.

Contributed by the International Gas Turbine Institute and presented at the 34th International Gas Turbine and Aeroengine Congress and Exhibition, Toronto, Ontario, Canada, June 4–8, 1989. Manuscript received at ASME Headquarters February 1, 1989. Paper No. 89-GT-218.

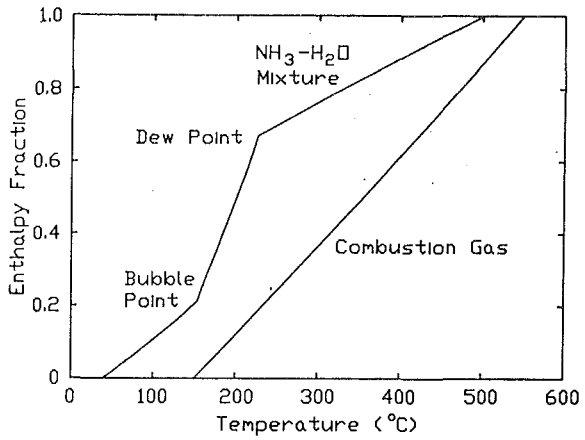

Fig. 2 Enthalpy versus temperature for the Kalina Cycle. Combustion gas exit temperature can be much lower before encountering a pinch point limit.

computer model of the entire cycle has been developed for the purpose of parametric optimization. Another motivation for the work was the preparation of a computer project for an undergraduate course in thermodynamics. A project involving the analysis of some sort of power generation system has been an annual activity since 1983 (Marston, 1986) and the prospect of working on a genuinely new cycle was appealing.

For the student project a simplified version of the cycle was developed, with advice from Dr. Kalina (1986b). The simplified cycle is nearly as efficient as the one studied by El-Sayed and Tribus. It brings out more clearly the key features of the cycle and was therefore studied in some detail.

While the primary application is as a bottoming cycle, this study has focused on a stand-alone cycle. Thus cycle efficiency (net power out divided by thermal energy into the cycle), while higher than for a comparable steam cycle, is relatively low. Kalina and Leibowitz (1987) have shown combined cycle efficiencies in excess of 50 percent (based on higher heating value).

2 Property Data

2.1 Characteristics of Ammonia-Water Mixtures. Analysis of the Kalina Cycle requires property data for ammonia-water mixtures, for which composition (expressed as mass fraction of ammonia in the mixtures) represents a third independent variable. Figure 3 shows plots of temperature and composition of liquid and vapor phases in equilibrium at three pressure levels associated with the cycle.

The dew point temperature is represented by the upper curves and the bubble point temperature by the lower curves. For a pure substance the bubble point and the dew point are identical; hence the curves must meet at the extremes of pure water ($X=0$) and pure ammonia ($X=1$).

Pressure and ammonia mass fraction are sufficient to fix the state of saturated liquid or saturated vapor. For a saturated mixture, temperature is again an independent variable and properties of interest include both those of the mixture and those of the liquid fraction (FL) and the vapor fraction (FG)

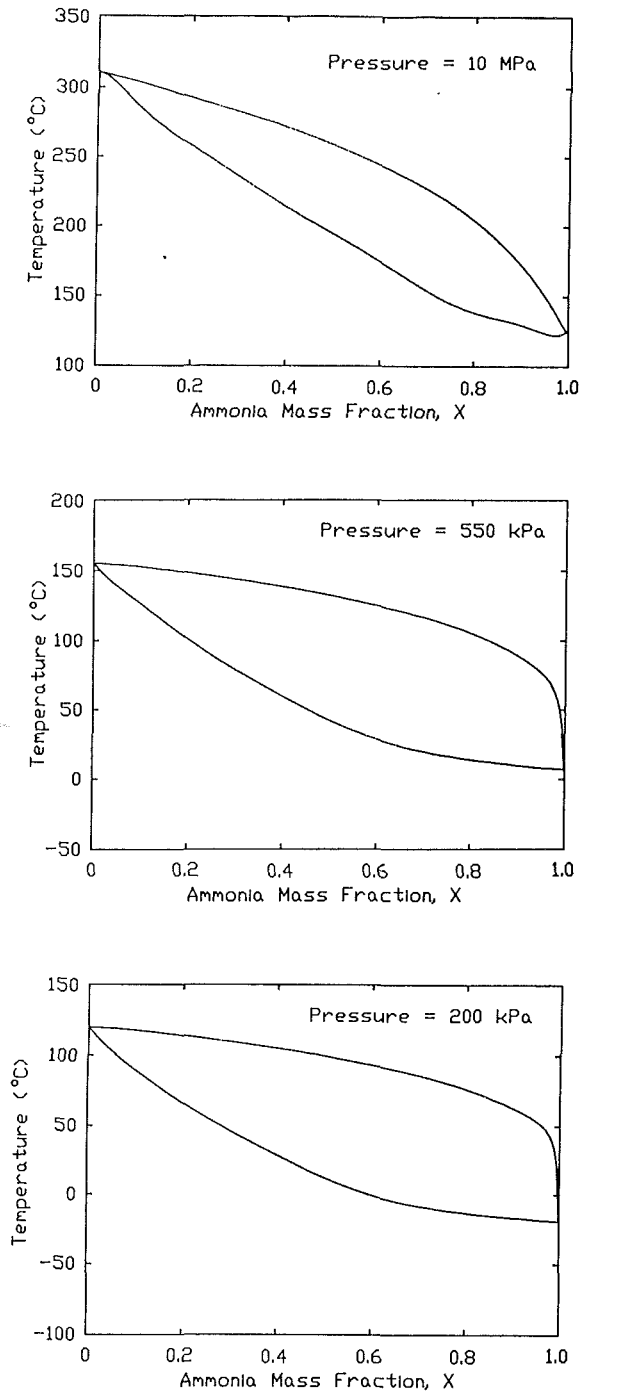

Fig. 3 Phase diagrams for ammonia-water mixtures at three pressure levels. The lower curve is saturated liquid at the bubble point temperature and the upper curve is saturated vapor at the dew point temperature. The curves form the boundaries for three regions: subcooled liquid; saturated mixture of liquid and vapor; and superheated vapor.

Nomenclature

FG = in a saturated mixture of ammonia and water, the fraction of the total mass that is vapor
FL = in a saturated mixture of ammonia and water, the fraction of the total mass that is liquid
h = enthalpy, kJ/kg
KC1 = designation of the computer model for the simplified cycle
KC2 = designation of the computer model for the cycle analyzed by El-Sayed and Tribus
$m(x)$ = mass flow at state x relative to mass flow at the turbine inlet
$P(x)$ = pressure, kPa
s = entropy, kJ/kg-K
$T(x)$ = temperature at state x, °C
$X(x)$ = mass fraction of ammonia in the ammonia-water mixture at state x

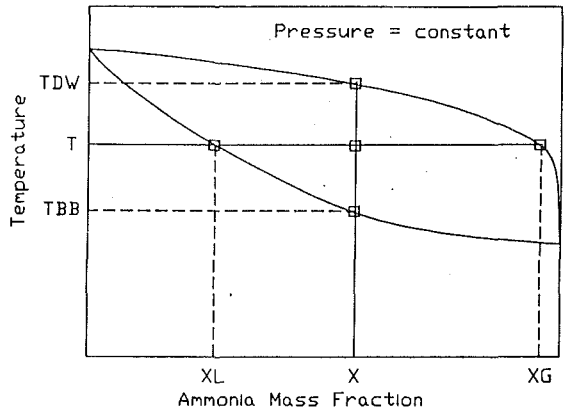

Fig. 4 Relationships among bubble point temperature, dew point temperature, liquid fraction, vapor fraction, and composition for a saturated mixture of ammonia and water

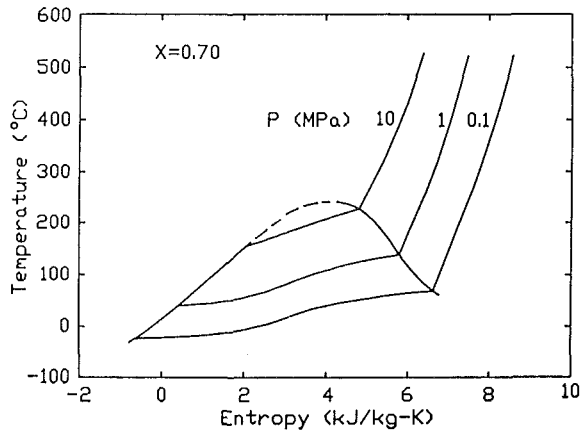

Fig. 5 *T-s* diagram for a mixture of 70 percent ammonia and 30 percent water

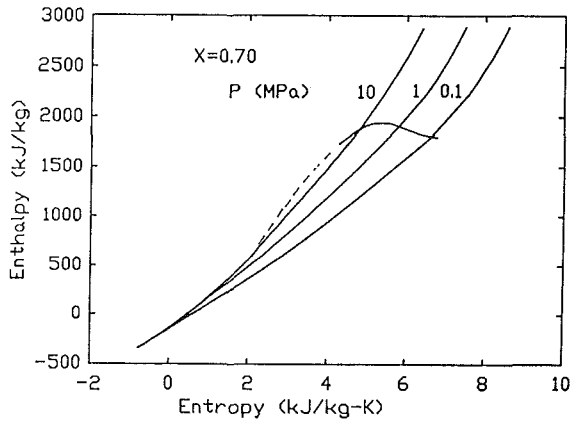

Fig. 6 *h-s* diagram for a mixture of 70 percent ammonia and 30 percent water

separately. Let the state be that indicated by the intersection of the "*X*" line and the "*T*" line in Fig. 4. The liquid fraction has a composition *XL* and the vapor fraction has a composition *XG*, with the mass fractions in each phase determined by species and overall continuity.

Figures 5 and 6 are *T-s* and *h-s* diagrams plotted for $X = 0.7$, which is the composition chosen both by Kalina and by El-Sayed and Tribus for the turbine inlet state. The diagrams are generally similar to equivalent ones for the pure substance. However, not only does temperature along an isobar vary in the saturation region, it varies nonlinearly.

2.2 Computer Implementation of Property Data. The El-Sayed and Tribus (1985a, 1985b) data formed the basis for

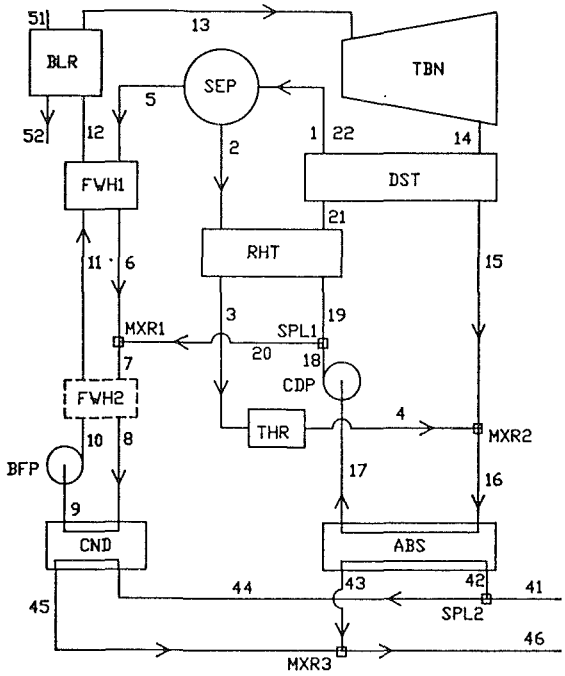

Fig 7 Simplified Kalina Cycle

a set of FORTRAN subroutines. In the process of writing the subroutines, a number of errors were found. Appendix A is a list of corrections. In some cases the correction is obvious. In others, communication with Dr. El-Sayed resolved the problem.

In most cases properties are represented by empirical equations but some tabulated values (El-Sayed and Tribus, 1985a) were used directly, with logarithmic interpolation for pressure and linear interpolation for temperature and mass fraction. INTERFACE subroutines, one for each of the five regions (subcooled liquid, saturated liquid, saturated mixture, saturated vapor, and superheated vapor) can be called as needed. These, in turn, call SOURCE subroutines containing the actual equations or data. The SOURCE subroutines can thus be expanded or upgraded without affecting applications programs. The SOURCE data are in a variety of units but output of the INTERFACE subroutines is in standardized SI or English Engineering units.

3 Analysis of the Simplified Cycle

Figure 7 is a diagram of the simplified cycle. Superheated ammonia-water vapor (13) is expanded in a turbine. The turbine exhaust is cooled, diluted with ammonia-poor liquid, and condensed in a heat exchanger called the absorber. The saturated liquid leaving the absorber (17) is compressed to an intermediate pressure (18) and is then heated and separated into an ammonia-poor liquid stream (2) and an ammonia-rich vapor stream (5). Some of the original condensate is added to the ammonia-rich vapor to obtain the desired ammonia concentration in the working fluid (7), which is then condensed (9), compressed (10), heated, and sent to the boiler (12).

The system was modeled as a network, with each node corresponding to a physical component. Each component is identified by a three-letter mnemonic as shown in Fig. 7 and defined in Table 1. State points 1 through 22 refer to ammonia-water mixtures. State points 41 through 46 refer to cooling water and state points 51 and 52 refer to the hot gas heat source.

3.1 Pressures. For simplicity, pressure drops and heat losses in the piping were ignored, although inclusion of piping

Table 1 Summary of component designations

COMPONENT	SYMBOL	REMARKS
Absorber	ABS	Initial heat rejection.
Boiler Feed Pump	BFP	Irreversibilities are accounted for by specifying an efficiency.
Boiler	BLR	Actually, boiler plus superheater.
Condensate Pump	CDP	Irreversibilities are accounted for by specifying an efficiency. They are somewhat more significant than in an ordinary steam system because the mass flow rate is much larger than the flow rate through the turbine.
Condenser	CND	Additional heat rejection at the intermediate pressure.
Distiller	DST	Counterflow heat exchanger which recovers exhaust heat to vaporize ammonia.
Feedwater Heaters	FWHx	Counterflow heat exchangers which transfer heat to the "feedwater".
Mixers	MXRx	Mixers join two streams. Incoming streams may differ in composition and temperature but must be at the same pressure.
Reheaters	RHTx	More counterflow heat exchangers.
Separator	SEP	Separates a saturated mixture into an ammonia-rich vapor stream and an ammonia-poor liquid stream.
Splitters	SPLx	Splitters divide a single phase flow into two streams. Properties of the incoming and outgoing streams are identical.
Turbine	TBN	Inlet state specified.
Throttle	THR	Necessary to drop the pressure of the liquid stream coming from the separator to the pressure at MXR2.

losses as additional nodes will not be difficult. To this approximation the cycle operates at three pressure levels:

(1) Turbine inlet: Design specification.
(2) Turbine exhaust: Fixed by the temperature and composition of the saturated liquid leaving the absorber (State 17).
(3) Intermediate: Fixed by the temperature and composition of the saturated liquid leaving the condenser (State 9).

3.2 Boiler. The boiler is assumed to be an HRSG with a gas exit temperature determined by the greater of a specified exit temperature or a minimum pinch point temperature difference. The pinch point temperature difference has been taken as 25°C.

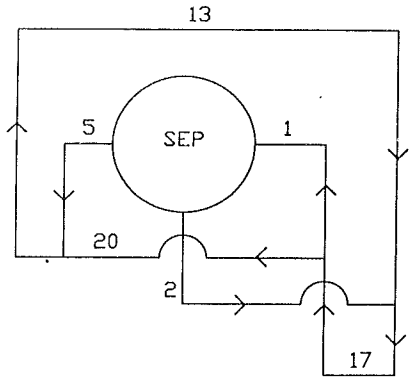

Fig. 8 Topology of the simplified cycle for calculation of mass flows

3.3 Turbine. Turbine inlet state is a design specification. If the energy source is a gas turbine exhaust, typically at 550°C (roughly 1000°F) then a turbine inlet temperature of 500°C is reasonable, as is a turbine inlet pressure of 10,000 kPa (1450 psi). A 70 percent ammonia mixture was chosen by both Kalina and by El-Sayed and Tribus, presumably because at that composition the temperature change from bubble point to dew point is near a maximum, so this value was used for the base case. A turbine efficiency of 90 percent was arbitrarily assumed for most of the calculations but the effect of turbine efficiency on performance was later determined for the range from 85 to 90 percent.

At a heat rejection temperature of 20°C (15°C coolant with a 5°ΔT) the back pressure is above atmospheric, minimizing the need for deaeration.

3.4 Pumps. Pump performance was calculated based on an assumed 60 percent efficiency. The computer model also permits the approximation that temperature is constant through the pump. The latter approach is a convenience when calculating the cycle manually, since the pump exit state can then be determined without the iterative process needed when one of the independent variables is enthalpy or entropy. Assuming that temperature is constant through a pump results in an apparent decrease in entropy but the effect is small.

3.5 Separator. The component that separates an equilibrium mixture into its liquid and vapor components has been designated the separator. Separator pressure is determined by the composition and temperature of the saturated liquid leaving the condenser. Separator temperature is a parameter that varies with mass flow rates but, for a given temperature, there is only one value of ammonia mass fraction at the separator entrance that will satisfy all mass and energy balances.

3.6 Mass Flows. While in practice the mass flows are the variables to be set by the operator, the calculation of cycle performance is more easily accomplished by fixing State 13 and State 1 and then calculating the mass flows (relative to turbine inlet mass flow) from species and overall continuity. This calculation involves only the topology of the ammonia-water circuits, as illustrated in Fig. 8 for the simplified cycle.

Let m symbolize the ratio of mass flow at any point to that at the turbine inlet (13) and let FG be the fraction of total mass flow to the separator that leaves as vapor. Overall conservation of mass and conservation of the mass of ammonia leads to the following relations for mass flow to the separator and "dilution" flow to splitter #1:

$$m(1) = \frac{X(13) - X(1)}{FG*[X(5) - X(1)]} \tag{1}$$

$$m(20) = \frac{X(5) - X(13)}{X(5) - X(1)} \tag{2}$$

Table 2 Input data for the simplified cycle

Item	Base Case Value	Remarks
Logical Switches and run ID		
UNITS	SI	SI or Engl. Engrg.
RUNID	BASE CASE	Up to 25 Character title.
CPMOD	2	Model for combustion gas specific heat; 1 = c_p constant, 2=c_p temperature dependent.
FWH2SW	N	Second feedwater heater; Y = include, N = delete.
Temperatures (°C)		
T(1)	70	Separator inlet.
T(13)	500	Turbine inlet.
T(41)	15	Cooling water inlet.
T(46)	25	Cooling water exit.
T(51)	550	Combustion gas inlet.
T(52)	150	Combustion gas exit (minimum).
TDIFG	25	Minimum difference in the boiler.
TDIF	5	Minimum difference in the ammonia-water heat exchangers.
Pressure (kPa)		
P(13)	10000	Turbine inlet.
Ammonia Mass Fractions		
X(1)	0.4481	Separator inlet; this is the value when T(22)=T(1).
X(13)	0.7000	Turbine inlet.
Efficiencies		
ETAT	0.90	Turbine.
CDPETA	0.60	Condensate pump.
BFPETA	0.60	Boiler feed pump.

3.7 Absorber. Assuming an environment temperature of 15°C (59°F) and allowing for a minimum temperature difference of 5°C, State 17 will be saturated liquid at 20°C. To maintain a low back pressure, the phase diagrams (Fig. 3) show that a low mass fraction of ammonia is desirable. For that reason the ammonia-poor liquid from the separator is mixed with the turbine exhaust. While for purposes of analysis the mixing and condensing processes are shown separately, in practice they are combined and the ammonia vapor is "absorbed" into the liquid: hence the name "absorber."

3.8 Counterflow Heat Exchangers. A minimum temperature difference of 5°C was assumed for the distiller, for the reheater, and for the "feedwater" heaters. The model for the counterflow heat exchangers accounts for the possibility that a pinch point can exist as a result of either:

(1) Transition from subcooled liquid to saturated mixture on the cold side or,
(2) transition from superheated vapor to saturated mixture on the hot side.

When a pinch point occurs, that is where the 5°C minimum temperature difference is applied.

3.9 Addition of FWH2. FWH2 is shown with dashed lines in Fig. 7 to indicate that it was not included in the original simplified cycle. However, when the streams at States 6 and 20 are mixed, the temperature of the mixture exceeds the temperature of both inlet streams! This rather startling result is explained by the fact that stream 6 is almost pure ammonia and, even when cooled, it remains mostly vapor. The mixture at State 7 has a higher bubble point temperature so most of the ammonia from State 6 gives up its enthalpy of vaporization and this shows up as an increase in temperature. FWH2 can take advantage of this phenomenon. FWH2 is subject to the same minimum temperature drop requirements as other counterflow heat exchangers.

3.10 Finding the Balance Point and Completing the Cycle. For a selected separator temperature one must find the ammonia mass fraction at State 1 that will result in an energy balance and mass balance around the cycle. The procedure followed when analyzing the cycle was to fix the temperature and guess the composition at the separator entrance, State 1, then calculate properties around the loop defined by States 2, 3, 4, 16, 17, 18, 19, 21, and 22 and repeat the process until State 22 matched State 1. Generally, if ammonia mass fraction at State 1 is too low, then $T(22) < T(1)$ and vice versa.

Calculation of the remaining states and of cycle efficiency is straightforward. Inclusion of FWH2 in the cycle requires one more iteration loop since $T(6)$ is now dependent on the temperature of the compressed liquid exiting FWH2 at State 11 and $T(6)$ is essential to the calculation of $T(7)$.

3.11 Computer Implementation of Cycle Analysis. The data subroutines described in Section 2.2 were used in two ways. First, simply as a source of property data and then as part of a system code. To generate property data, a menu-driven calling program, AWMENU, was written. It supplies enthalpy and entropy when pressure, temperature, and mass fraction are specified. If the state is known to be saturated liquid or saturated vapor then pressure and mass fraction are sufficient inputs. If pressure, composition, and enthalpy (or entropy) are the independent variables, then an iteration process is needed to obtain the temperature.

Once a workable sequence of calculation steps was established, a system code was prepared. Subroutines were written to model each of the components. Utilities were added to automate the process of finding the state when the region is uncertain or when entropy or enthalpy are one of the independent variables. A main program and some input/output subroutines completed the code, called, collectively, KC1 (Kalina Cycle, Configuration #1).

4 Results for the Simplified Cycle

Table 3 summarizes the input data required, with values for the base case. Table 3 is the output of the system code for the base case. Input data and properties at all state points are shown. Mass flows and heat and work interactions are per unit mass flow at the turbine entrance. Heat and work interactions are tabulated at the state points corresponding the exit state of each component. A comparison of net heat and net work provides a check on internal consistency. A detailed output table for each set of input conditions was printed and retained (Marston, 1987).

The mass flow of fluid circulating through the separator, $m(1)$, and the flow, $m(20)$, which dilutes the nearly pure ammonia at State 6, are the variables subject to direct control during operation. The former affects separator temperature and, to a lesser extent, composition of the fluid at the separator entrance; the latter affects composition at the turbine inlet. However, as has already been pointed out, it is easier analytically to select separator temperature and turbine inlet composition and let mass flows be dependent variables. The influences of $m(1)$ and $m(20)$ are not totally decoupled but, as can be seen in Figs. 9 and 10, the primary effect is indeed dominant.

When separator temperature and turbine inlet composition

Table 3 KC1 system code output; base case: $T(1) = 70°C$, $X(13) = 0.7$, no FWH2

```
RUN ID: BASE CASE - KC1              UNITS: SI   VER:  8.0   FWH2: N

NET HT = 8.709E+02 KJ/KG  NET WRK = 8.709E+02 KJ/KG  CYCLE EFF = 0.3113

TURBINE EFF = 0.900   MIN HX DT =  5.0   MIN BLR DT = 25.0
CONDENSATE PUMP EFF = 0.600
BOILER FEED PUMP EFF = 0.600
CP VARIABLE    MINIMUM STACK TEMPERATURE = 150.
```

STATE	PRESS	TEMP	MASF	ENTH	ENTR
1	5.5391E+02	70.00	0.4481	3.1216E+02	1.4991E+00
2	5.5391E+02	70.00	0.3459	8.2225E+01	7.6995E-01
3	5.5391E+02	25.06	0.3459	-1.1759E+02	1.4359E-01
4	1.9904E+02	25.17	0.3459	-1.1759E+02	1.4494E-01
5	5.5391E+02	70.00	0.9685	1.4828E+03	5.2115E+00
6	5.5391E+02	27.36	0.9685	1.3168E+03	4.7166E+00
7	5.5391E+02	42.92	0.7000	5.5798E+02	2.3138E+00
8	5.5391E+02	42.92	0.7000	5.5798E+02	2.3138E+00
9	5.5391E+02	20.00	0.7000	-1.0775E+02	1.0101E-01
10	1.0000E+04	22.36	0.7000	-8.0337E+01	1.3779E-01
11	1.0000E+04	22.36	0.7000	-8.0337E+01	1.3779E-01
12	1.0000E+04	39.09	0.7000	7.0419E-03	4.0203E-01
13	1.0000E+04	500.00	0.7000	2.7980E+03	6.2771E+00
14	1.9904E+02	118.87	0.7000	1.8972E+03	6.5296E+00
15	1.9904E+02	57.47	0.7000	1.0148E+03	4.0119E+00
16	1.9904E+02	40.15	0.4481	2.0927E+02	1.2746E+00
17	1.9904E+02	20.00	0.4481	-1.5479E+02	4.3865E-02
18	5.5391E+02	20.06	0.4481	-1.5408E+02	4.4688E-02
19	5.5391E+02	20.06	0.4481	-1.5408E+02	4.4688E-02
20	5.5391E+02	20.06	0.4481	-1.5408E+02	4.4688E-02
21	5.5391E+02	52.47	0.4481	1.2933E+01	5.8565E-01
22	5.5391E+02	70.00	0.4481	3.1217E+02	1.4993E+00

STATE	MASS FL	HEAT	WORK	ERROR	MISC
1	2.94871	0.0000E+00	0.0000E+00	0.0E+00	
2	2.46462	0.0000E+00	0.0000E+00	0.0E+00	FL=0.8358
3	2.46462	-4.9247E+02	0.0000E+00	0.0E+00	
4	2.46462	0.0000E+00	0.0000E+00	1.0E-02	
5	0.48409	0.0000E+00	0.0000E+00	0.0E+00	FG=0.1642
6	0.48409	-8.0344E+01	0.0000E+00	0.0E+00	
7	1.00000	0.0000E+00	0.0000E+00	-8.6E-02	
8	1.00000	0.0000E+00	0.0000E+00	0.0E+00	
9	1.00000	-6.6574E+02	0.0000E+00	-1.5E-03	
10	1.00000	0.0000E+00	-2.7418E+01	7.4E-02	SDIF=-.0001
11	1.00000	0.0000E+00	0.0000E+00	0.0E+00	
12	1.00000	8.0344E+01	0.0000E+00	-7.0E-02	
13	1.00000	2.7980E+03	0.0000E+00	0.0E+00	DTPP= 84.23
14	1.00000	0.0000E+00	9.0080E+02	-2.4E-03	SDIF=0.0001
15	1.00000	-8.8236E+02	0.0000E+00	0.0E+00	
16	3.46462	0.0000E+00	0.0000E+00	-3.0E-02	
17	3.46462	-1.2613E+03	0.0000E+00	1.5E-03	
18	3.46462	0.0000E+00	-2.4719E+00	4.9E-02	SDIF=0.0000
19	2.94871	0.0000E+00	0.0000E+00	0.0E+00	
20	0.51591	0.0000E+00	0.0000E+00	0.0E+00	
21	2.94871	4.9247E+02	0.0000E+00	-3.3E-02	
22	2.94871	8.8236E+02	0.0000E+00	-6.7E-02	

COOLING WATER AND HOT GAS :

STATE	TEMP	ENTH	MASS FL	HEAT
41	15.00	6.2760E+01	46.0578	0.000E+00
42	15.00	6.2760E+01	30.1463	0.000E+00
43	25.00	1.0460E+02	30.1463	1.261E+03
44	15.00	6.2760E+01	15.9115	0.000E+00
45	25.00	1.0460E+02	15.9115	6.657E+02
46	25.00	1.0460E+02	46.0578	1.927E+03
51	550.00	8.4673E+02	6.6239	0.000E+00
52	150.00	4.2432E+02	6.6239	-2.798E+03

are treated as the independent variables, composition at the separator inlet, $X(1)$, becomes the single parameter that must be adjusted to balance the cycle. A plot (Fig. 11) of $X(1)$ as a function of $X(13)$ and $T(1)$ is a useful guide during the balancing process.

Efficiency and exergy fraction have been used as the criteria for optimizing performance of the cycle. Recall that these values were calculated for a *stand-alone* cycle, but with input conditions appropriate for a *bottoming cycle* and that combined cycle efficiences exceeding 50 percent appear feasible (Kalina and Liebowitz, 1987).

4.1 Cycle Efficiency. Cycle efficiencies plotted against separator inlet temperature and separator mass flow rate are shown in Figs. 12 and 13, respectively. Not surprisingly, the same trends are apparent in both figures since Fig. 9 shows a close correlation between temperature and flow rate in the separator. These figures are based on calculations in which FWH2 is omitted and stack temperature is fixed at 150°C.

There is a maximum efficiency associated with any particular turbine inlet composition. The maximum efficiency point also corresponds to maximum power output per unit gas flow since none of these cases were limited by a pinch point in the boiler. The falloff in efficiency as separator flow rate is reduced is at least partly a result of a pinch point in the distiller.

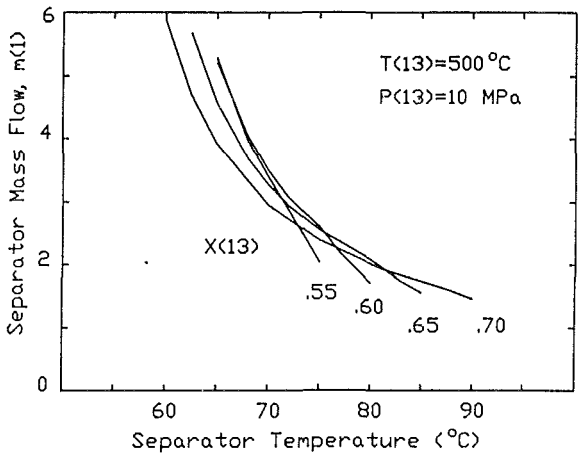

Fig. 9 Separator mass flow, $m(1)$, as a function of separator temperature, $T(1)$, and turbine inlet composition, $X(13)$. Separator mass flow is primarily related to $T(1)$.

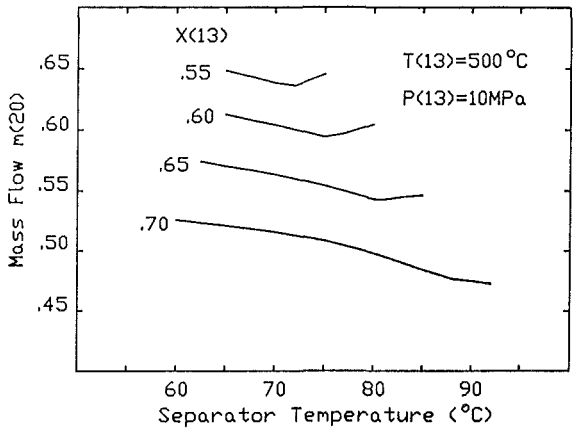

Fig. 10 Dilution mass flow, $m(20)$, as a function of separator temperature, $T(1)$, and turbine inlet composition, $X(13)$. Dilution mass flow is primarily related to $X(13)$.

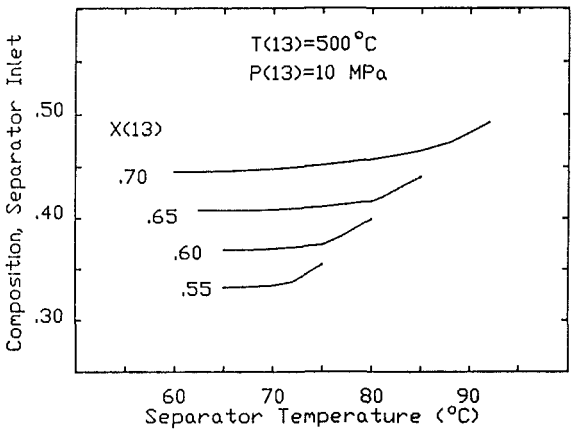

Fig. 11 Separator inlet composition, $X(1)$, required to balance the cycle for specified values of turbine inlet composition, $X(13)$, and separator temperature, $T(1)$.

The choice of 70 percent ammonia at the turbine entrance for the base case was consistent with previous work, both by Kalina (1984) and by El-Sayed and Tribus (1985c). However, the envelope of peak efficiencies suggests that operation with somewhat lower ammonia concentration at the turbine inlet could improve performance, both because efficiency is slightly higher and because efficiency is then less sensitive to small changes in separator mass flow.

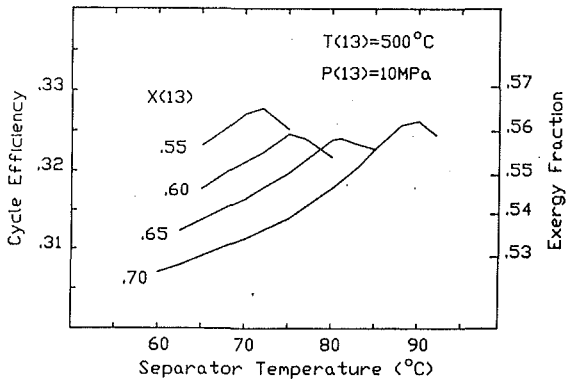

Fig. 12 Cycle efficiency and exergy fraction (150°C stack temperature) as a function of separator inlet temperature, $T(1)$, and turbine inlet composition, $X(13)$

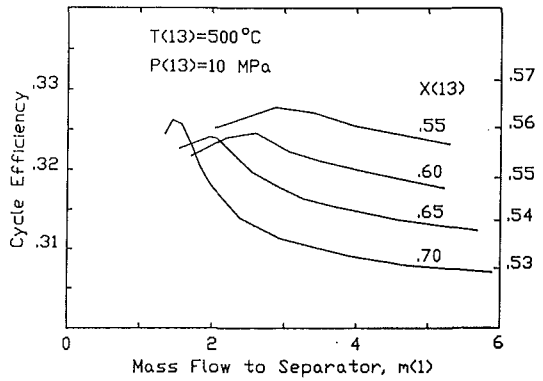

Fig. 13 Cycle efficiency and exergy fraction (150°C stack temperature) as a function of separator mass flow, $m(1)$, and turbine inlet composition, X(13)

While a turbine efficiency of 0.90 was assumed for the curves of Figs. 12 and 13, the influence of lower turbine efficiencies on performance is shown in Fig. 14. To obtain the data for Fig. 14 the base case and the peak efficiency cases at the four levels of turbine inlet ammonia concentration were run for several turbine efficiencies down to 0.85. The effect is essentially linear and very nearly independent of the other parameters, so only two cases are shown. The others fall between the two lines plotted.

4.2 FWH2 Added to the Basic Cycle. Addition of FWH2 to take advantage of the temperature rise that results from mixing the streams entering MXR1 can improve cycle efficiency, as shown in Fig. 15 for a composition at the turbine inlet of 70 percent ammonia. At a separator temperature of 70°C the increase is more than half a point. However, near the point of maximum efficiency the improvement is very slight.

4.3 Exergy. A "second law analysis" can also be performed on the cycle, as was done by El-Sayed and Tribus (1985c). In essence, one compares net work output of the cycle, per kilogram of gas flow, with the "exergy," or maximum theoretical work output obtainable from the hot gas heat source. Neglecting fluid friction and assuming constant composition, exergy is simply the maximum possible change in availability in the gas, where availability is defined as $(h - T_o s)$ and T_o is the sink temperature. Let "exergy fraction" be defined as the ratio of the change in availability as the combustion gas goes through the boiler to the maximum possible change of availability in the gas.

When the gas temperature at the boiler exit is limited by an assumed lower limit on stack gas temperature, the change in availability is constant, and exergy fraction is then directly proportional to efficiency. An exergy scale is therefore included on Figs. 12 and 13.

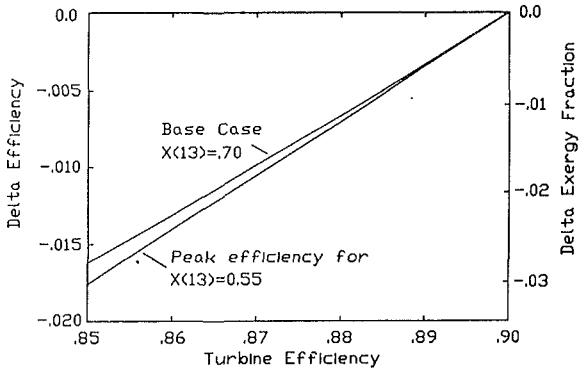

Fig. 14 Effect of turbine efficiency on cycle efficiency and exergy fraction. Other peak efficiency cases fall between the two lines plotted.

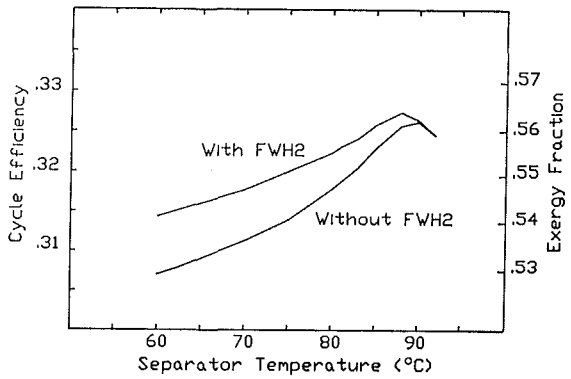

Fig. 15 Effect on efficiency and exergy of adding FWH2 for a turbine inlet composition of 70 percent ammonia and 30 percent water

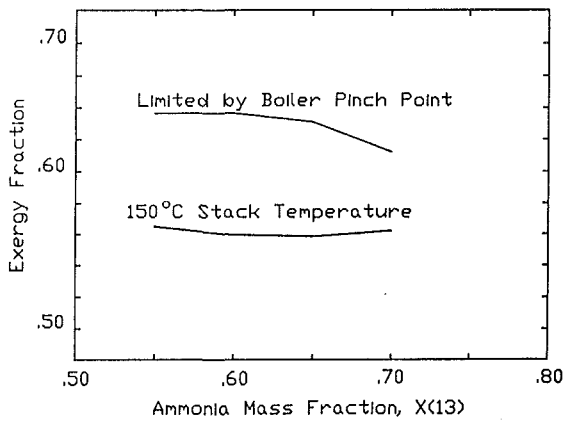

Fig. 16 Envelopes of maximum exergy. The boiler pinch point is an upper bound of varying temperature.

The 150°C stack gas temperature was chosen as a conservative value, safely above the acid dew point, so it represents a reasonable upper bound on stack temperature. A lower bound would be the situation where the gas cooling is limited by a pinch point in the boiler. Figure 16 is a plot of the envelope of maximum exergy fractions as a function of turbine inlet composition.

Since the pinch point temperature difference varies with composition, stack temperature (if it is constrained only by the pinch point) will also vary, as shown in Fig. 17. As ammonia concentration is decreased from the 70 percent value used by Kalina and by El-Sayed and Tribus, the cycle balances at a lower separator temperature so more energy can be trans-

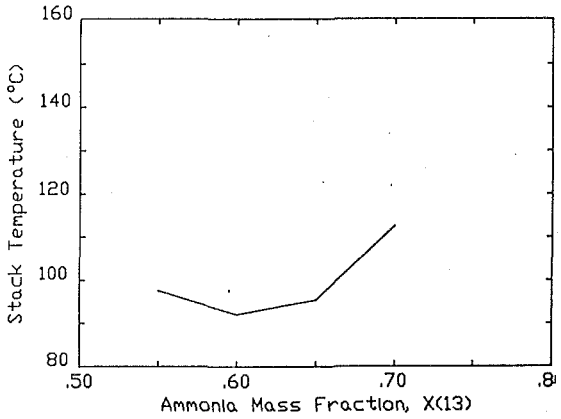

Fig. 17 Combustion gas stack temperature corresponding to the curve of maximum exergy as limited by the boiler pinch point, assuming a minimum temperature difference of 25°C

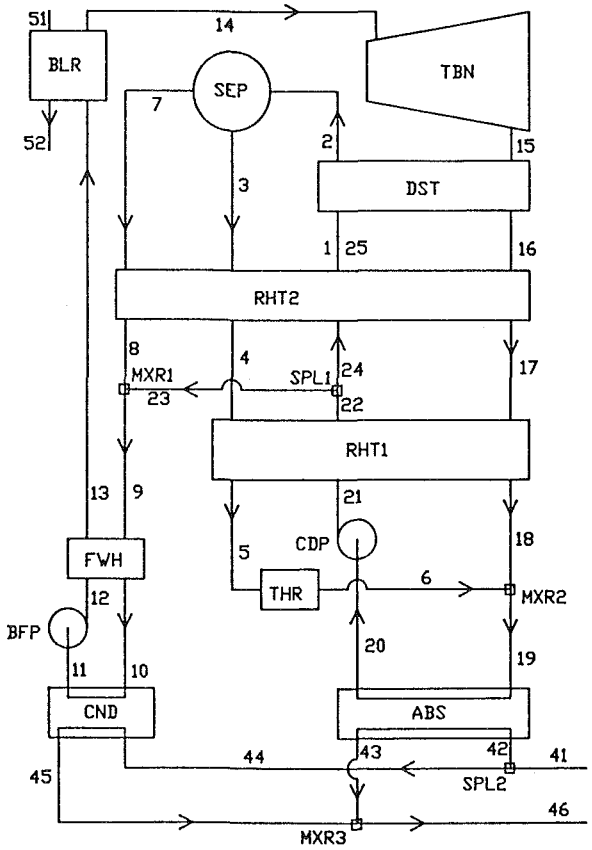

Fig. 18 Cycle configuration analyzed by El-Sayed and Tribus

ferred from the combustion products. For ammonia concentrations below 60 percent the lower volatility of the mixture forces a rise in stack temperature.

5 El-Sayed and Tribus Configuration

The configuration shown in Fig. 18 is that analyzed by El-Sayed and Tribus (1985c). The main program and the input/output routines were suitably modified and designated KC2. A new heat exchanger model was added to the component routines but no change to the data routines was needed.

5.1 Modification of the Computer Model. Modeling of the El-Sayed and Tribus configuration is more complicated because several heat exchangers have more than two streams. A multistream heat exchanger model was coded in which one

Table 4 Results for the El-Sayed and Tribus configuration and comparison with the KC1 base case

Input data: Case	Turbine Eff. (-)	Pump Eff. (-)	Min. Temp Diff. Ht. Exch. (°C)	(°F)	Min. Temp Diff. Boiler (°C)	(°F)	Stack Temp. (°C)	(°F)
1	0.865	¯ 1.0	3.3	6.0	13.3	24.0	70.6	159.0
2	0.865	¯ 1.0	3.3	6.0	13.3	24.0	70.6	159.0
3	0.865	¯ 1.0	3.3	6.0	13.3	24.0	70.6	159.0
4	0.900	0.600	5.0	9.0	25.0	45.0	150.0	302.0
5	0.900	0.600	5.0	9.0	25.0	45.0	150.0	302.0

Case	Conditions at the Separator Inlet Temp. (°C)	(°F)	x_{NH3} (-)	Mass Flow (-)	Bypass Mass Flow to MXR1 (-)	Comb. Gas Mass Flow (-)
1	66.2	151.2	.4167	4.23	0.482	5.691
2	66.2	151.2	.4167	4.359	0.4848	5.667
3	66.2	151.2	.3953	6.366	0.4701	5.663
4	70.0	158.0	.4100	5.043	0.4807	6.478
5	70.0	158.0	.4481	2.949	0.5159	6.624

Case	Net Heat (kJ/kg)	Net Work (kJ/kg)	Cycle Eff. (-)	Max. Availability Change (BTU/lbm)	(kJ/kg)	Exergy Fraction (-)
1	--	--	--	102.	237.4	0.673
2	1105.	921.1	.3313	102.	237.4	0.684
3	939.9	940.1	.3395	102.	237.4	0.699
4	904.0	904.0	.3292	105.4	245.2	0.569
5	870.9	870.9	.3113	105.4	245.2	0.536

Cases: 1. El-Sayed and Tribus results,
2. Closest match to Case 1 using the KC2 computer code.
3. Case 1 input data, balanced (i.e. net heat = net work).
4. KC2 with KC1 base case input conditions.
5. KC1 Base Case.

Notes: 1. Pump efficiency of ¯ 1.0 indicates that temperature was assumed constant through the pump.

2. Maximum availability was based on a sink temperature of 12.78°C (55°F) for cases 1, 2 and 3 and 15°C (59°F) for cases 4 and 5. Calculation of availability utilized c_p=0.25 BTU/lbm (constant) for cases 1, 2 and 3 and $c_p = c_p(T)$ for cases 4 and 5.

primary stream and up to five secondary streams are designated. Temperatures at inlet and exit are specified for the secondary streams. Enthalpy transfer is calculated on the basis of the specified temperatures, but the user must make certain that minimum positive temperature differences have been maintained.

Part of the mass flow from the primary stream can be diverted at a predetermined temperature, so the multistream heat exchanger model can treat RHT1 and RHT2 as a single unit. There is, as yet, no check for internal pinch points in the multistream heat exchanger model.

The process of balancing the cycle is similar to that for the KC1 configuration. The distiller (DST) entrance, States 1 and 25, was chosen as the starting point because the multiple streams in the reheater (RHT2) make it difficult to calculate State 25 without first knowing State 16. However, State 16 is at the exit of the distiller and State 25 is needed to calculate State 16. Starting at the distiller entrance resolves the problem.

As with the KC1 configuration, overall energy balances require that $X(1)$ be adjusted until $T(25)$ matches $T(1)$. During the balancing process the secondary stream temperatures $T(8)$, $T(16)$, $T(17)$, and $T(18)$ must be checked for consistency with the specified minimum heat exchanger temperature drops. Changes to these temperatures affect $T(25)$, which generally requires further adjustment of $X(1)$.

5.2 Results for the El-Sayed and Tribus Configuration. A cross-check on the code was provided by comparing its output with the published results of El-Sayed and Tribus. There is reasonable agreement except at the boiler feed pump. Work done by the pump should result in an increase in enthalpy but El-Sayed and Tribus indicate a slight decrease. A reduction in the ammonia content of the flow to the separator was necessary to obtain a completely balanced cycle. Table 4 presents a comparison with the El-Sayed and Tribus results. A detailed state point comparison is included as Appendix C.

There are a number of minor differences between the El-Sayed and Tribus calculation and the KC2 results. The KC2

code does not yet include piping losses but it does include pump efficiency. Air properties are generated using a piecewise linear fit and agreement with the air tables is very good. El-Sayed and Tribus assumed a constant c_p of 0.25 Btu/lbm-°F, which is also a very good approximation, taken as an average value over the temperature range of interest. There is good agreement in the calculation of maximum change in availability but the corresponding exergy fraction is somewhat higher using the KC2 computer model; see Table 4 (Cases 1 and 2) and Appendix C.

The KC1 cases were run at slightly different input conditions, as indicated in Table 4, so, to obtain a direct comparison between the KC1 and KC2 configurations, KC2 was run using the KC1 inputs. Results are also shown in Table 4 as cases 4 and 5. The more complex KC2 configuration yields slightly less than a two percentage point gain in efficiency over the basic KC1 configuration (excluding FWH2) and about three percentage points in exergy fraction. The lower exergy fractions for cases 4 and 5 are due in part to slightly more conservative assumptions for input data and partly to calculation of maximum availability using a temperature-dependent specific heat.

6 Conclusions

While ammonia–water mixtures have been used for many years in refrigeration cycles, the Kalina Cycle appears to be a genuinely new development for power generation. Efficiencies reported here are modest because they are for a stand-alone cycle with inlet conditions appropriate to a bottoming cycle, but the potential has been shown elsewhere for combined cycle power plant efficiencies as good or better than advanced energy conversion technologies, which depend on a high-temperature topping cycle. Stack temperatures as low as 92°C can be achieved if not limited by other constraints such as plume buoyancy or acid dew point.

Composition at the turbine inlet and temperature at the separator are the key parameters for optimizing the cycle. These can be controlled operationally by adjusting flow rates.

The development of fluid property and component models makes possible extensive parametric studies of cycle configurations to optimize the cycle further.

Actual performance data and a detailed economic analysis will be required to establish viability, but the relative simplicity of the components and compatibility with existing steam turbine design provide room for optimism.

Acknowledgments

The advice and encouragement of Dr. Y. M. El-Sayed, Dr. Myron Tribus, and Dr. A. I. Kalina are gratefully acknowledged. I especially thank Dr. El-Sayed for his assistance in resolving difficulties with the property data.

The work was accomplished using the computer facilities of Villanova University. Interaction with my students was of significant importance in developing the ideas expressed herein.

Table C-1 El-Sayed and Tribus configuration state points

State	Press.	Temp.	Mass Fr. Ammonia	Enthalpy	Entropy	Relative Mass Flow
(-)	(psia)	(°F)	(-)	(BTU/lbm)	(BTU/lbm-°R))	(-)
AMMONIA WATER CIRCUITS						
1	70.82	138.53	0.4167	48.38	0.2135	4.359
2.6	70.1	137.7	0.4167	49.5	0.219	4.23
2	70.82	151.20	0.4167	99.30	0.2989	4.359
2.7	69.9	151.2	0.4167	104.6	0.3113	4.23
3	70.82	151.20	0.3431	28.23	0.1720	3.848
2.8	69.9	151.2	0.34	31.5	0.1809	3.71
4	70.82	128.00	0.3431	3.26	0.1300	3.848
2.10	69.9	126.7	0.34	3.6	0.1343	3.71
5	70.82	66.00	0.3431	-61.79	0.0131	3.848
6	20.01	66.14	0.3431	-61.79	0.0136	3.848
7	70.82	151.20	0.9703	633.63	1.2533	0.5118
2.9	69.9	151.2	0.964	628.	1.245	0.518
8	70.82	128.00	0.9703	604.84	1.2068	0.5118
2.11	69.7	128.	0.964	598.	1.197	0.518
9	70.82	125.45	0.7000	304.37	0.6722	1.0000
10	70.82	103.32	0.7000	238.78	0.5566	1.0000
2.12	69.6	102.8	0.7000	240.2	0.5616	1.000
11	70.82	61.00	0.7000	-54.02	0.0095	1.0000
3	69.6	60.	0.7	-50.7	0.0176	1.000
12	1570.0	61.00	0.7000	-46.19	0.0095	1.0000
3.1	1580.	60.	0.7	-54.1	-0.0039	1.000
13	1570.0	119.45	0.7000	19.41	0.0130	1.0000
4	1580.	121.	0.7	11.02	0.1182	1.000
14	1570.0	950.00	0.7000	1214.6	1.4987	1.0000
1	1570.	950.	0.7	1215.	1.501	1.000
15	20.01	231.98	0.7000	809.78	1.5927	1.0000
2	20.9	222.6	0.7	814.	1.59	1.000
16	20.01	148.50	0.7000	587.81	1.2412	1.0000
2.1	20.7	148.5	0.7	600.	1.259	1.000
17	20.01	126.00	0.7000	455.34	1.0193	1.0000
2.2	20.5	126.	0.7	452.9	1.0144	1.000
18	20.01	80.00	0.7000	302.46	0.7472	1.0000
2.3	20.4	80.	0.7	289.1	0.7227	1.000
19	20.01	79.22	0.4167	13.35	0.1643	4.8476
20	20.01	60.00	0.4167	-74.82	-0.0053	4.8476
21	70.82	60.00	0.4167	-74.63	-0.0053	4.8476
2.4	70.6	60.	0.4167	-75.	-0.0027	4.71
22	70.82	120.00	0.4167	-10.58	0.1118	4.8476
23	70.82	120.00	0.4167	-10.58	0.1118	0.4883
24	70.82	120.00	0.4167	-10.58	0.1118	4.3594
2.5	70.3	120.	0.4167	-9.91	0.116	4.23
25	70.82	142.90	0.4167	66.49	0.2439	4.3594
2.6	70.1	137.7	0.4167	49.5	.219	4.23
COOLING WATER						
41	--	55.00	--	23.00	--	36.01
42	--	55.00	--	23.00	--	21.37
7	15.	55.	--	23.	0.0457	--
43	--	75.00	--	43.00	--	21.37
8	15.	75.	--	43.	0.0838	--
44	--	55.00	--	23.0	--	14.64
7	15.	55.	--	23.	0.0457	--
45	--	75.00	--	43.00	--	14.64
8	15.	75.	--	43.	0.0838	--
46	--	75.00	--	43.00	--	36.01
HOT GAS						
51	14.7	1000.00	--	359.08	--	5.7817
5	15.	1000.	--	242.	0.272	5.691
52	14.7	158.97	--	148.17	--	5.6669
6	15.	159.		31.75	0.0574	5.691

References

El-Sayed, Y. M., and Tribus, M., 1985a, "Thermodynamic Properties of Water-Ammonia Mixtures: Theoretical Implementation for Use in Power Cycle Analysis," Center for Advanced Engineering Study, Massachusetts Institute of Technology, Cambridge, MA, Draft Report.

El-Sayed, Y. M., and Tribus, M., 1985b, "Thermodynamic Properties of Water-Ammonia Mixtures: Theoretical Implementation for use in Power Cycle Analysis," ASME Publication AES-Vol. 1.

El-Sayed, Y. M., and Tribus, M., 1985c, "A Theoretical Comparison of the Rankine and Kalina Cycles," ASME Publication AES-Vol. 1.

Kalina, A. I., 1984, "Combined Cycle System With Novel Bottoming Cycle," ASME JOURNAL OF ENGINEERING FOR GAS TURBINES AND POWER, Vol. 106, pp. 737–742.

Kalina, A. I., Tribus, M., and El-Sayed, Y. M., 1986a, "A Theoretical Approach to the Thermophysical Properties of Two-Miscible-Component Mixtures for the Purpose of Power-Cycle Analysis," ASME Paper No. 86-WA/HT-54.

Kalina, A. I., 1986b, Private Communication, Feb. 20.

Kalina, A. I., and Leibowitz, H. M., 1987, "Applying Kalina Technology to a Bottoming Cycle for Utility Combined Cycles," ASME Paper No. 87-GT-35.

Marston, C. H., 1986, "Three Computer Based Thermodynamics Projects," *Int. J. Appl. Engng. Ed.*, Vol. 2, pp. 115–126.

Marston, C. H., 1987, "Parametric Analysis of the Kalina Cycle," Report, Department of Mechanical Engineering, Villanova University, Villanova, PA.

APPENDIX A

Errata List for "Thermodynamic Properties of Water-Ammonia Mixtures"

The analysis of Kalina Cycle performance was based on properties of water-ammonia mixtures published by El-Sayed and Tribus (1985b). In converting that information to a set of FORTRAN subroutines, a number of errors and misprints were observed. Some of them are minor and the intended meaning is obvious but a number of them that are crucial to correct implementation are not self-evident.

The following list includes all the corrections, however minor, that have come to my attention.

Item	Page	Column	Location/Correction
1	90	2	Assumption 4: . . . temperature
2	91	1	Equation 7: . . .)$d\rho - R(\ln(\rho))$
3	94	2	Equation A-2: . . . $X))^J)($ . . .
4	95	1	fourth constant in the a_i array for the Gibbs free energy departure function: 0.672809
5	95	1	constants following Equation A-4b: $c_2 = -0.0048$
6	95	1	line prior to Equation A-4.5: $P = P(\rho, T)$
7	95	2	line following Equation A-4.5: ρ in kg/m
8	95	1	Equation A-5: . . . $(A)(\rho)^{I-1}$ $(c_1/T$ . . .
9	95	2	first line: . . . VOLUME SPECIFIC HEAT . . .
10	95	2	line following Equation A-8a: T in °C

Note also that:

1 The two-dimensional arrays of coefficients for calculation of the bubble point temperature, the dew point temperature, and the gas state are in row-major order, reading each line from left to right. For example, the C_{ij} for the bubble point temperature calculation are arranged as follows:

$$\begin{matrix} C_{11} & C_{12} & C_{13} & C_{14} \\ C_{15} & C_{16} & C_{17} & C_{21} \\ C_{22} & C_{23} & \ldots & \end{matrix}$$

2 The bubble point temperature to be entered into the equation for specific volume of the liquid should be in °C.

APPENDIX B

Computer Codes

The codes used for this analysis were developed on a VAX minicomputer and are described in more detail elsewhere (Marston, 1987). They have subsequently been transferred to an MS-DOS based computer system using Version 4.0 of Microsoft FORTRAN. Source code for VAX and MS-DOS is now identical. Listings and/or diskettes with the properties data subroutines, menu lookup program, and system programs can be made available.

APPENDIX C

El-Sayed and Tribus Cycle State Points

Table C-1 presents a direct comparison of the KC2 code with results given by El-Sayed and Tribus (1985c). Data in Table C-1 are in English Engineering units for purposes of direct comparison. The first entry at each state point is the KC2 result, keyed to Fig. 18, with input information as close as possible to the El-Sayed and Tribus analysis. The second entry is, with one exception, taken directly from their Table 6, and uses their notation for state points. The exception is the mass flow column, which has been converted from flow per unit gas flow to flow per unit turbine flow to match the corresponding KC2 result.

The KC2 model was run assuming constant temperature through the pumps, as was done by El-Sayed and Tribus. Turbine efficiency was 0.865, minimum temperature drop in counterflow heat exchangers was 6°F, and in the boiler 24°F. However no account was taken of pressure drops in the piping and this may account for some of the differences in output.

Performance Evaluation of Selected Combustion Gas Turbine Cogeneration Systems Based on First and Second-Law Analysis

F. F. Huang
Professor,
Department of Mechanical Engineering,
San Jose State University,
San Jose, CA 95192

The thermodynamic performance of selected combustion gas turbine cogeneration systems has been studied based on first-law as well as second-law analysis. The effects of the pinch point used in the design of the heat recovery steam generator, and pressure of process steam on fuel-utilization efficiency (first-law efficiency), power-to-heat ratio, and second-law efficiency, are examined. Results for three systems using state-of-the-art industrial gas turbines show clearly that performance evaluation based on first-law efficiency alone is inadequate. Decision makers should find the methodology contained in this paper useful in the comparison and selection of cogeneration systems.

Introduction

Cogeneration is an engineering concept involving the production of both electricity and useful thermal energy (steam or process heat) in one operation, thereby utilizing fuel more effectively than if the desired products were produced separately. Since the heart of a cogeneration system is a prime mover with waste heat at a useful temperature, it is not surprising that the requirements of cogeneration may be met in many ways ranging from steam and gas turbines to fuel cells and Stirling engines. An excellent summary of eight kinds of cogeneration systems with unique features of each kind has been given by Bazques and Strom (1983).

Most cogeneration requirements are best met by back pressure steam turbines and combustion gas turbines. The latter are capable of producing significantly more electric power for a given amount of process heat. Since the cost effectiveness of a cogeneration system is directly related to the amount of power it can produce, gas turbines often possess significant advantages over steam tubines. Consequently combustion gas turbines have been widely used in cogeneration applications for many years. This paper is confined to cogeneration systems using combustion gas turbines as the prime movers, and producing thermal energy in the form of saturated steam.

There are many combustion gas turbines on the market today. They differ in power output, cycle efficiency, cycle pressure ratio, firing temperature, exhaust temperature, and exhaust flow rate. An excellent treatment of the thermodynamic performance of combustion gas turbine cogeneration systems has been presented by Rice (1987) in which he has, based on the first law of thermodynamics, developed a unique graphic solution showing the interrelationship of the many relevant parameters involved. This paper, employing the first law as well as the second law of thermodynamics, may be considered as a complement to the work of Rice.

Performance Parameters of a Cogeneration System

The general concept of a cogeneration system is shown in Fig. 1.

The useful products of a cogeneration system are electrical energy ($\dot{W}_{el}$) and thermal energy or process heat ($\dot{Q}_p$). One parameter used to assess the thermodynamic performance of such a system is the fuel-utilization efficiency (η_f), which is simply the ratio of all the energy in the useful products ($\dot{W}_{el}$ and $\dot{Q}_p$) to the energy of fuel input ($\dot{E}_f$). By definition

$$\eta_f = (\dot{W}_{el} + \dot{Q}_p)/\dot{E}_f \tag{1}$$

Since electrical power is worth about three times as much as process heat, the cost effectiveness of a cogeneration system is directly related to the amount of electrical power it can produce for a given amount of process heat. Consequently another parameter commonly used to assess the thermodynamic performance of a cogeneration system is the

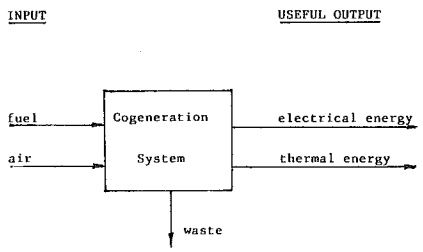

Fig. 1 General concept of a cogeneration system

Contributed by the Advanced Energy Systems Division for publication in the JOURNAL OF ENGINEERING FOR GAS TURBINES AND POWER. Manuscript received by the Heat Transfer Division December 23, 1988.

power-to-heat ratio. By definition, the power-to-heat ratio (R_{pH}) is given by

$$R_{pH} = \dot{W}_{el}/\dot{Q}_p \tag{2}$$

In both the fuel-utilization efficiency and the power-to-heat ratio, power and process heat are treated as equal. This reflects the first law of thermodynamics, which is concerned with energy quantity and not energy quality. Thus the fuel-utilization efficiency is also known as the first-law efficiency. But electrical power is much more valuable than process heat according to the second law of thermodynamics. Exergy, the central concept in second-law analysis, is something that is always consumed or destroyed in any real process. A process is better thermodynamically if less exergy is consumed. Consequently the ratio of the amount of exergy in the products to the amount of exergy supplied is a more accurate measure of the thermodynamic performance of a system. By definition

$$\eta_{II} = (\dot{W}_{el} + \dot{B}_p)/\dot{B}_f \tag{3}$$

where $\dot{W}_{el}$ is all exergy, $\dot{B}_p$ is the exergy content of process heat produced, and $\dot{B}_f$ is the exergy content of fuel input. η_{II} is a second-law efficiency.

Introducing the exergy factor of process heat (ϵ_p) and the exergy factor of fuel input (ϵ_f) by the following expressions

$$\epsilon_p = \dot{B}_p/\dot{Q}_p \tag{4}$$

$$\epsilon_f = \dot{B}_f/\dot{E}_f \tag{5}$$

the second-law efficiency may be given as

$$\eta_{II} = (\eta_f/\epsilon_f)\left[\frac{R_{pH} + \epsilon_p}{R_{pH} + 1}\right] \tag{6}$$

The exergy factor of process heat is always less than unity. In the case of saturated steam, it increases with the pressure of the steam produced. This is consistent with the second law of thermodynamics as the quality of the energy content in high-pressure saturated steam is greater than the quality of the energy content in low-pressure saturated steam. The exergy factor of fuel input is close to unity for most fuels as the chemical energy in fuel is essentially all exergy (Moran, 1982). Thus the second-law efficiency is not very sensitive to the exergy factor of the fuel used in cogeneration systems.

For a typical cogeneration system with process heat in the form of saturated steam, ϵ_p is in the range of 0.25 and 0.4 and

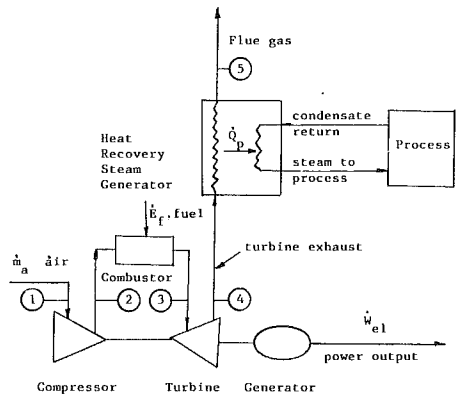

Fig. 2 Schematic diagram of a combustion gas turbine cogeneration system

R_{pH} is usually less than unity. Thus η_{II} is significantly less than η_f. Thus evaluation of the thermodynamic performance of a cogeneration system based on the first-law efficiency alone could be misleading. This important point has also been pointed out by Rosen and Scott (1986). The usefulness of applying the second-law efficiency to the study of gas turbine cogeneration systems has been demonstrated by Stecco and Manfrida (1985a, 1985b), Huang and Egolfopoulos (1985), Huang and Wang (1987), and Huang and Naumowicz (1987).

System Description

The schematic diagram of a combustion gas turbine cogeneration system is shown in Fig. 2.

Fuel input to the system is supplied to the combustor. Hot exhaust from the turbine is the waste heat source for process heat production. The quantity and quality of process heat produced will depend on the temperature of hot exhaust entering and the temperature of saturated steam produced in the heat recovery steam generator, as shown in Fig. 3. With the same pinch point and process steam temperature more process heat will be produced if hot exhaust enters the steam generator at a higher temperature. We thus would expect the pinch point as well as the pressure of process steam to have a significant effect on fuel-utilization efficiency, power-to-heat ratio, and second-law efficiency.

Nomenclature

$\dot{B}_f$ = exergy of fuel input
$\dot{B}_p$ = exergy of process heat
$\dot{E}_f$ = energy of fuel input
F/A = fuel–air ratio used in combustion process
h = enthalpy
h_c = enthalpy of condensate return
h_f = enthalpy of saturated water at process steam pressure
h_g = enthalpy of saturated vapor at process steam pressure
$\bar{h}$ = molal enthalpy
$\bar{h}_4$ = molal enthalpy of gas mixture at turbine exhaust temperature
$\bar{h}_5$ = molal enthalpy of gas mixture leaving heat recovery steam generator
$\bar{h}_{pp}$ = molal enthalpy of gas mixture at pinch point temperature
M = molecular weight of gas mixture
$\dot{m}_a$ = mass flow rate of air in gas turbine engine
$\dot{m}_s$ = mass flow rate of steam
p = pressure (absolute)
pp = pinch point
$\dot{Q}_p$ = amount of process heat production
R_{pH} = power-to-heat ratio, defined by equation (2)
s = entropy
s_c = entropy of condensate return
s_g = entropy of saturated vapor at process steam pressure
T = temperature (absolute)
T_c = temperature of condensate return
T_0 = temperature of the environment
T_p = saturation temperature at pressure of process steam
T_{pp} = temperature of gas mixture at pinch point
T_4 = temperature of gas mixture at turbine exhaust
T_5 = temperature of gas mixture leaving heat recovery steam generator
$\dot{W}_{el}$ = electrical power output of system
y = percent of theoretical air
ϵ_f = exergy factor of fuel input, defined by equation (5)
ϵ_p = exergy factor of process heat, defined by equation (4)
η_f = fuel-utilization efficiency, defined by equation (1)
η_{II} = second-law efficiency, defined by equation (3)
η_{th} = $\dot{W}_{el}/\dot{E}_f$ = cycle efficiency

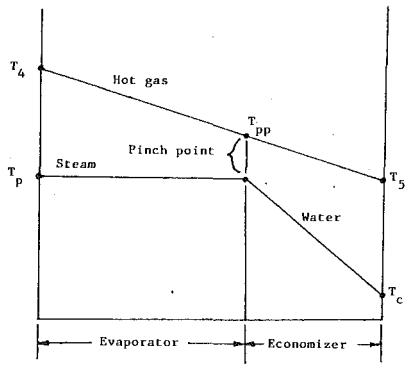

Fig. 3 Temperature profile in heat recovery steam generator

Performance Calculations

The thermodynamic performance of three cogeneration systems using three state-of-the-art industrial gas turbines is studied in this work. Pertinent data for the industrial gas turbines are shown in Table 1. With this information, all that is needed is a procedure to calculate the quantity and quality of process heat produced in order to calculate the fuel-utilization efficiency, power-to-heat ratio, and second-law efficiency.

From an energy viewpoint, the quantity of process heat produced may be given by

$$\dot{Q}_p = \dot{m}_s(h_g - h_c) \tag{7}$$

From an exergy viewpoint, the exergy content of process heat produced is given by

$$\dot{B}_p = \dot{m}_s[(h_g - h_c) - T_0(s_g - s_c)] \tag{8}$$

Combining equation (7) with equation (8), the exergy factor of process heat is given by

$$\epsilon_p = 1 - [T_0(s_g - s_c)/(h_g - h_c)] \tag{9}$$

which indicates that the exergy factor of process heat depends only on steam conditions.

From an energy balance for the evaporator, neglecting heat loss to the surroundings,

$$\dot{m}_s(h_g - h_f) = \dot{m}_a\left(1 + \frac{F}{A}\right)[(\bar{h}_4 - \bar{h}_{pp})/M] \tag{10}$$

Combining equation (10) with equation (7), we have

$$\frac{\dot{Q}_p}{\dot{m}_a} = \left(1 + \frac{F}{A}\right)[(\bar{h}_4 - \bar{h}_{pp}/M](h_g - h_c)/(h_g - h_f) \tag{11}$$

Equation (11) gives the amount of process heat produced per unit mass of air flow. It is necessary to know the composition of the exhaust gas to determine this quantity.

Since the exhaust gas is mainly nitrogen in combustion gas turbines, the effect of different gas turbine fuels on the enthalpy of the exhaust gas will not be significant. Thus the amount of process heat produced is not too sensitive to the kind of fuel burned. For simplicity, the calculations are based on pure methane gas. The combustion equation, on the basis of complete combustion, is then given by

$$CH_4 + (2y)0_2 + (2y)(3.76)N_2 \rightarrow CO_2 + 2H_20 + (2y-2)0_2 + (2y)(3.76)N_2 \tag{12}$$

where y is the percent of theoretical air used.

Knowing y, the mixture composition, M, and F/A may be readily found using equation (12). The values of $(\bar{h}_4 - \bar{h}_{pp})$ may then be found using appropriate data from the literature for the various species in the mixture. The amount of process heat produced per unit mass of air flow may then be calculated using equation (11).

Accordingly, the methodology for performance evaluation of combustion gas turbine cogeneration systems is quite straightforward consisting essentially of the following steps:

1 Making use of power output and cycle efficiency data from Table 1, determine fuel input per unit mass of air flow.

2 Making use of combustion equation and information on excess air, determine M, F/A, and the composition of turbine exhaust.

3 Making use of information on turbine exhaust, determine $(\bar{h}_4 - \bar{h}_{pp})$, then calculate process heat per unit mass of air flow using equation (11).

4 Making use of equation (9), determine ϵ_p for the steam conditions involved.

5 Making use of data determined in the first four steps, calculate η_f, R_{pH}, and η_{II}.

Calculations for this work have been made with the following common characteristics:

Fuel	Methane
ϵ_f, exergy factor of fuel input	1.0
T_0, temperature of the environment	25°C
T_c, temperature of condensate return	100°C

In addition, data from the Gas Tables by Keenan et al. (1980) are used to calculate enthalpy values for the gas mixture.

Table 1 Base-load gas turbine data at International Standards Organization conditions of 15°C, 101.325 kPa, and 60 percent relative humidity (Rice, 1987)

		GT-A GE LM2500PE	GT-C GE LM5000A	GT-E GE PG7111E
1	Power output ($\dot{W}_{el}$), kW	22,007	32,469	77,347
2	Cycle efficiency (η_{th}) percent, LHV	37.0	37.4	32.3
3	Cycle pressure ratio	18.7	30.0	11.7
4	Air flow ($\dot{m}_a$) kg/s	66.9	120.2	274.4
	lbm/s	147.5	265.0	605.0
5	Specific work output ($\dot{W}_{el}/\dot{m}_a$) kJ/kg	328.9	270.3	281.9
	Btu/lbm	141.4	116.2	121.2
6	Turbine rotor inlet temperature °C	1212	1156	1104
	°F	2214	2113	2019
7	Exhaust temperature °C	513	425	538
	°F	955	797	1000
8	Exhaust excess air, percent	226	302	232

Results

The thermodynamic performance of three cogeneration systems using three state-of-the-art industrial gas turbines given in Table 1 is graphically shown in Figs. 4-6. Figure 4 gives the results for the production of saturated steam at 150 psia (approximately 1.0 MPa) while Fig. 5 gives the results for the production of saturated steam at 300 psia (approximately 2.0 MPa). Figure 6 gives the results for systems operating with a fixed pinch point of 20°C.

1 Effect of Pinch Point on System Performance. Figures 4 and 5 show the effect of pinch point on the thermodynamic performance of systems when the pressure of process steam is fixed. From these figures, the following observations can be made:

(*a*) The power-to-heat ratio increases with an increase in the pinch point. This is expected because a larger pinch point will result in a higher temperature for the flue gas according to Fig. 3. Consequently less process heat will be produced when a larger pinch point is used.

(*b*) The fuel-utilization efficiency decreases with increase in the pinch point. This is consistent with the fact that the fuel-utilization efficiency may be given by

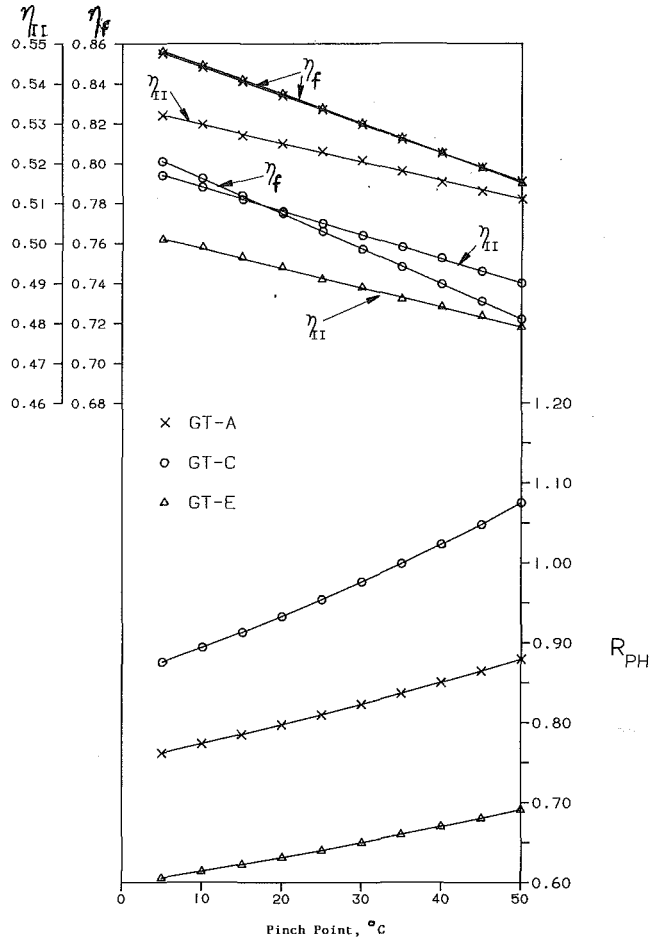

Fig. 4 Effect of pinch point on system performance with saturated steam at 150 psia (approximately 1.0 MPa)

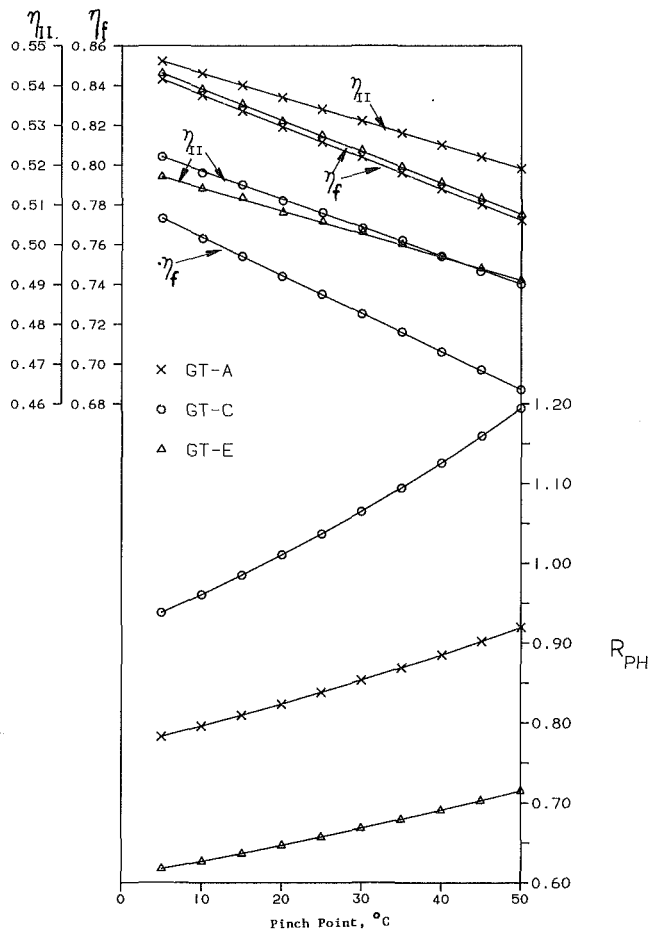

Fig. 5 Effect of pinch point on system performance with saturated steam at 300 psia (approximately 2.0 MPa)

$$\eta_f = \eta_{th}\left(1+\frac{1}{R_{pH}}\right) \tag{13}$$

(*c*) The second-law efficiency decreases with increase in the pinch point. This is consistent with the fact that a larger pinch point would mean larger exergy destruction (entropy generation) for the system.

(*d*) The rates of decrease for both η_f and η_{II} are essentially a constant. But the rate of decrease for η_{II} is smaller than the rate of decrease for η_f by the factor ϵ_p. Since a larger value for the pinch point would mean a smaller (less expensive) heat recovery steam generator but a less efficient system, tradeoffs based on η_f could lead to a wrong decision as the second law efficiency does not decrease as much as the first-law efficiency.

(*e*) Two systems having the same first-law efficiency could have quite different second-law efficiencies and power-to-heat ratios. Consequently the first-law efficiency by itself does not provide the necessary information for decision making.

2 Effect of Pressure of Process Steam on System Performance. Figure 6 shows the effect of pressure of process steam on the thermodynamic performance of systems when the pinch point is fixed. From this figure, the following observations can be made:

(*a*) The power-to-heat ratio increases with increasing process steam pressure. This is as expected because a higher pressure for process steam will increase the temperature of the gas mixture at the pinch point. The result is that the flue gas temperature will be higher according to Fig. 3. Consequently less process heat will be produced at a higher pressure of process steam. But this increase in the power-to-heat ratio is relatively small if the turbine exhaust temperature is relatively high (GT-A and GT-E).

(*b*) The first-law efficiency decreases with an increase in the pressure of process steam. This is expected according to equation (13). But the decrease is relatively small if the turbine exhaust temperature is relatively high (GT-A and GT-E).

(*c*) The second-law efficiency increases quite significantly with an increase in the pressure of process steam if turbine exhaust temperature is relatively high (GT-A and GT-E). If the turbine exhaust temperature is not too high (GT-C), the second-law efficiency will reach a maximum at a steam pressure of about 200 psia (1.38 MPa) in the case of GT-C. Thus a gas turbine engine having a relatively low turbine exhaust temperature is not very versatile for the production of process steam.

Closure

A methodology for performance evaluation of combustion gas turbine cogeneration systems based on first-law as well as second-law analysis has been presented. This methodology is relatively simple and straightforward. Results from applying this methodology to three systems using three state-of-the-art industrial gas turbines show that performance evaluation based on first-law efficiency alone is clearly not adequate. A more meaningful evaluation must include second-law analysis.

It should be noted that the selection of a cogeneration system is a complex decision involving technical as well as economic considerations. Decision makers should find the methodology contained in this paper useful in obtaining im-

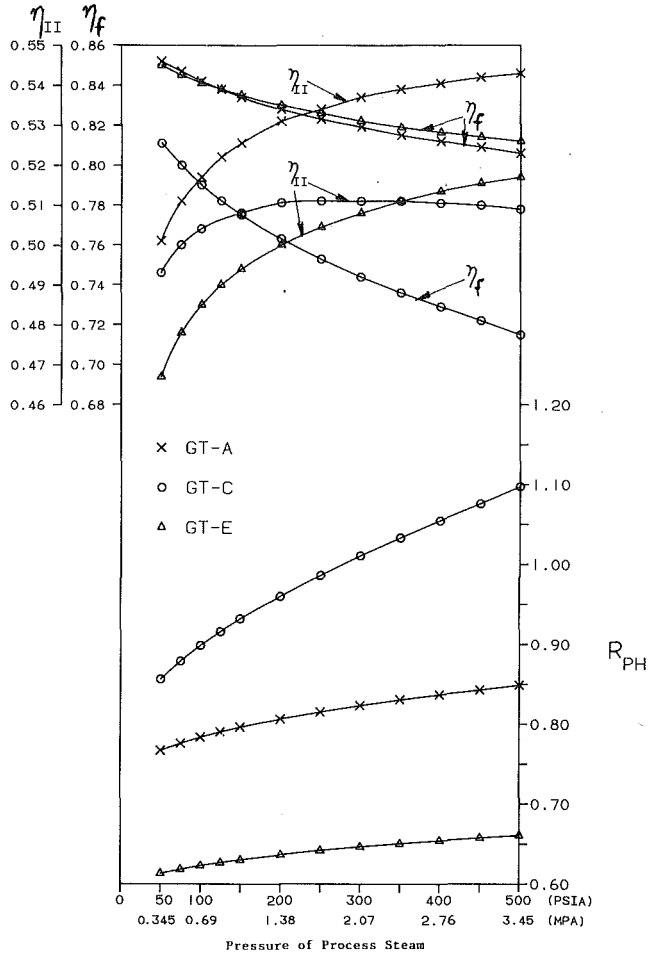

Fig. 6 Effect of steam pressure on system performance with pinch point at 20°C

portant thermodynamic information for proper tradeoffs in the comparison and selection of cogeneration systems. Educators also should find the methodology relevant to the study of this important area in energy engineering.

Acknowledgments

I wish to thank Mr. Tim Naumowicz of NASA-Ames Research Center for his assistance in the production of computer-generated plots of results.

References

Bazques, E., and Strom, D., 1983, "Cogeneration and Interconnection Technologies for Industrial and Commercial Use," *Proceedings of 18th IECEC*, American Institute of Chemical Engineers, pp. 2060–2065.

Huang, F. F., and Egolfopoulos, F., 1985, "Performance Analysis of an Indirect Fired Air Turbine Cogeneration System," ASME Paper No. 85-IGT-3.

Huang, F. F., and Naumowicz, T., 1987, "Thermodynamic Study of an Indirect Fired Air Turbine Cogeneration System With Regeneration," ASME Paper No. 87-GT-34.

Huang, F. F., and Wang, L., 1987, "Thermodynamic Study of an Indirect Fired Air Turbine Cogeneration System With Reheat," ASME JOURNAL OF ENGINEERING FOR GAS TURBINES AND POWER, Vol. 109, pp. 16–21.

Keenan, J. H., Chao, J., and Kaye, J., 1980, *Gas Tables, Second Edition (English Units)*, Wiley, New York.

Moran, M. J., 1982, *Availability Analysis: A Guide to Efficient Energy Use*, Prentice Hall, Englewood Cliffs, NJ, p. 155.

Rice, I. G., 1987, "Thermodynamic Evaluation of Gas Turbine Cogeneration Cycles: Part 1—Heat Balance Method Analysis," ASME JOURNAL OF ENGINEERING FOR GAS TURBINES AND POWER, Vol. 109, pp. 1–7.

Rosen, M. A., and Scott, D. S., 1986, "Comparison of Energy and Exergy Efficiencies for Cogeneration Systems," in: *Computer-Aided Engineering of Energy Systems, Vol. 2: Analysis and Simulation*, R. A. Gaggioli, ed., ASME, New York.

Stecco, S. S., and Manfrida, G., 1985a, "A Rational Efficiency Analysis of Comparison and Trends in Gas Turbines for Cogeneration," ASME Paper No. 85-IGT-13.

Stecco, S. S., and Manfrida, G., 1985b, "Optimal Choice of Gas Turbines for Cogeneration Applications," *Proceedings of 20th IECEC*, Society of Automotive Engineers, Vol. 2, pp. 280–287.

K. Ito
Associate Professor.

R. Yokoyama
Research Assistant.

S. Akagi
Professor.

Department of Mechanical Engineering
for Industrial Machinery
and Systems,
Faculty of Engineering,
Osaka University,
2-1, Yamadaoka, Suita, Osaka, 565 Japan

Y. Matsumoto
Manager,
Technical Research Center,
The Kansai Electric Power Co., Inc.,
3-11-20, Nakoji, Amagasaki, Hyogo, 661
Japan

Influence of Fuel Cost on the Operation of a Gas Turbine-Waste Heat Boiler Cogeneration Plant

The influence of fuel cost on the operation is investigated for a gas turbine-waste heat boiler cogeneration plant by an optimal operational planning method. A planning method is first presented by which the operational policy of each piece of constituent equipment is determined so as to minimize the operational cost. Then, a case study is performed for a cogeneration plant used for district heating and cooling. Through the study, it is made clear how the optimal operational policy and the economic or energy conservative properties are influenced by the costs of purchased electric power and natural gas. It is also shown that the optimal operational policy is superior in economy as compared with other conventional ones.

Introduction

Recently, cogeneration plants have been installed successfully in Japan into commercial and public buildings such as hotels, office buildings, hospitals, and so on. In addition, larger scale plants for district heating and cooling have also been installed into some areas with the redevelopment of cities and improvement in living standards.

The main advantage of introducing cogeneration plants is to be able to reduce operational costs and to save energy by efficient energy utilization. However, these objectives can be realized only if a good operational policy is adopted corresponding to energy demand. As cogeneration plants for industrial purposes have steady energy demand throughout the year, it is rather easy to determine the operational policy rationally. On the other hand, those for commercial and public purposes have an energy demand that fluctuates widely with time and seasons. In such a case, it is considered important at the planning stage to investigate in detail the operational policy corresponding to the fluctuating energy demand.

In the past, the thermal-following or electric-following policies have been adopted as conventional operational policies for cogeneration plants (California Energy Commission, 1982). According to these policies, prime movers are operated to follow the demand for thermal energy or electric power, respectively. However, they have the disadvantage that surpluses or shortages in supplies of electric power or thermal energy occur very often because of the lack of flexibility of operation. In addition, it appears to be irrational to adopt fixed operational policies throughout the year regardless of fuel cost and energy demand. From the economic viewpoint, it is rational to minimize the operational cost by changing the plant's operation flexibly corresponding to fuel cost and energy demand.

The objective of this paper is to propose such an optimal and flexible operational method for a gas turbine-waste heat boiler cogeneration plant. In order to investigate the operational policy of each piece of constituent equipment, it is necessary to take account of the discontinuity of performance characteristic due to the on/off status as well as the variation of efficiency due to the partial loading status (Akagi et al., 1986; Ducrocq, 1985; Nath and Holliday, 1985). As the fuel cost varies widely with its consumption, it is also important to investigate the influence of fuel cost on the operation. In this paper, a detailed investigation is made into the influence of fuel cost on the optimal operational policy and the economic or energy conservative properties through a case study on a cogeneration plant used for district heating and cooling. In addition, the economic and energy conservative properties based on the optimal operational policy are compared with those based on the thermal-following or electric-following ones.

Plant Structure

Figure 1 illustrates the structures of the plants investigated in this paper. The gas turbine-waste heat boiler cogeneration plant (plant A) shown in Fig. 1(*a*) is investigated as a representative type. A conventional energy supply plant (plant B) shown in Fig. 1(*b*) is also investigated to compare with plant A. The equipment symbols in Fig. 1 are explained in the nomenclature. Solid lines, dot-dash lines, two dots-dash

Contributed by the Power Division for publication in the JOURNAL OF ENGINEERING FOR GAS TURBINES AND POWER. Manuscript received by the Power Division December 30, 1988.

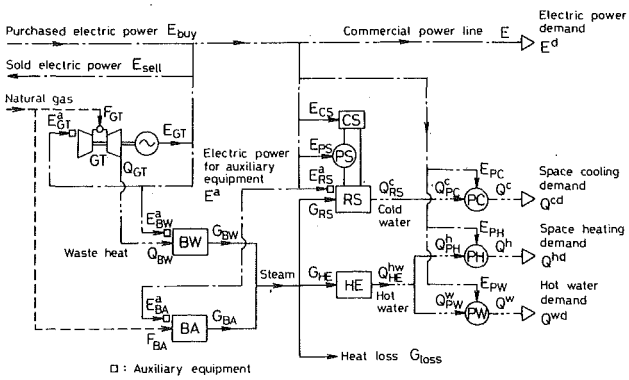

Fig. 1(a) Gas turbine-waste heat boiler cogeneration plant (plant A)

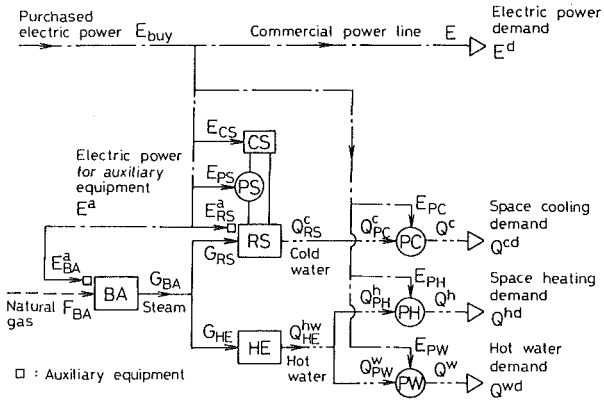

Fig. 1(b) Conventional energy supply plant (plant B)

Fig. 1 Plant structures

lines, and broken lines indicate the flows of steam, electric power, heat, and natural gas, respectively.

Plant A. Electric power is supplied to users by the parallel running of gas turbine generators and purchased electric power from an outside electric power company. The electric power is also used to drive pumps, cooling towers, and other auxiliary equipment in the plant. This plant has the capacity to sell the generated electric power to the outside electric power company. The waste heat generated by the gas turbines is recovered by waste heat boilers, and it is reused for several kinds of thermal energy in a cascade way. The surplus steam generated from wast heat boilers is disposed of through steam dumping, and it is included as heat loss in Fig. 1(*a*). The shortage of steam is supplemented by auxiliary boilers. Steam absorption refrigerators and heat exchangers are installed respectively to supply cold water for space cooling, and hot water for both space heating and hot water supply.

Plant B. Electric power is supplied to users only from purchased electric power, and thermal energy is supplied only by auxiliary boilers. The electric power is also used to drive auxiliary equipment in the plant.

Optimal Operational Planning Method

Formulation of Optimal Operational Planning Problem. As the electric power and thermal energy are supplied independently in plant B, the operational policy can be easily determined corresponding to their demands. On the other hand, as plant A is equipped with gas turbine generators supplying electric power and thermal energy simultaneously, there exist alternatives on the operational policy. In this case, it is difficult to determine the operational policy properly by the trial and error method. In this paper, an optimal operational planning method is proposed from the economic viewpoint, by which the operational policy is determined so as to minimize the operational cost.

A mathematical model is first presented to determine the operational policy. As operational policy, the on/off and par-

Nomenclature

Equipment symbols

BA = auxiliary boiler
BW = waste heat boiler
CS = cooling tower for steam absorption refrigerator
GT = gas turbine generator
HE = heat exchanger
PC = pump to supply cold water for space cooling
PH = pump to supply hot water for space heating
PS = pump to circulate cooling water for steam absorption refrigerator
PW = pump to supply hot water
RS = steam absorption refrigerator

Quantity of energy

E = electric power
F = natural gas consumption
G = steam flow rate
Q = heat flow rate

Other symbols

C_v = annual operational cost
f = monthly or annual load factor
J = objective function
l = annual rate of heat loss
N = number of equipment installed
p, q, r, s = parameters related to performance characteristic of each piece of equipment
Q_p = annual consumption of primary energy
α = unit cost ratio of purchased electric power to natural gas
β = annual rate of energy conservation
γ = reduction rate of annual operational cost
δ = zero-one integer variable expressing on/off status of each piece of equipment
$\sum_t$ = summation over a month, a season, or a year
$\varphi_{elec}, \varphi_{gas}$ = unit costs of purchased electric power and natural gas, respectively
$\underline{(\ )}, \overline{(\ )}$ = lower and upper bounds of input or output energy of each piece of equipment, respectively

Superscripts

a = electric power for auxiliary equipment
c = space cooling
d = demand
h = space heating
w = hot water supply

Subscripts

A = plant A
B = plant B
buy = purchased electric power
loss = heat loss
n = identity number for each piece of equipment
sell = sold electric power

tial loading status are investigated for each piece of constituent equipment. By relating the status respectively with zero-one integer and continuous variables, the optimal operational planning problem is formulated below for the gas turbine-waste heat boiler cogeneration plant shown in Fig. 1 (*a*).

Performance Characteristics of Equipment. The performance characteristics of each piece of equipment is formulated and considered as a constraint in this optimization problem.

(*a*) *Gas turbine generator* (*GT*). The performance characteristics of gas turbine generators can be expressed by relationships between electric power or flow rate of waste heat and natural gas consumption. The relationships can be approximated accurately enough by the following linear equations:

$$\left.\begin{aligned} &E_{GTn}=p_{GTn}F_{GTn}+q_{GTn}\delta_{GTn}\\ &Q_{GTn}=r_{GTn}F_{GTn}+s_{GTn}\delta_{GTn}\\ &\underline{F}_{GTn}\delta_{GTn}\le F_{GTn}\le \bar{F}_{GTn}\delta_{GTn}\\ &\delta_{GTn}\in\{0,\ 1\}\end{aligned}\right\}(n=1\sim N_{GT}) \tag{1}$$

where E, F, and Q denote electric power, natural gas consumption, and flow rate of waste heat, respectively. The coefficients p, q, r, and s denote parameters related to the performance characteristics. The symbols $\underline{\ }$ and $\bar{\ }$ denote lower and upper bounds of input or output energy, respectively. The zero-one integer variable δ expresses the on ($\delta=1$)/off ($\delta=0$) status. The subscripts GT and n indicate that the amount is related to the nth of N_{GT} gas turbine generators. As the performance characteristics of gas turbine generators change with the intake air temperature, the coefficients and bounds in equation (1) are considered as functions of it. In addition, the electric power is needed to drive auxiliary equipment attached to gas turbine generators. It is also approximated by the following linear equation:

$$E^a_{GTn}=p^a_{GTn}F_{GTn}+q^a_{GTn}\delta_{GTn}\quad(n=1\sim N_{GT}) \tag{2}$$

The performance characteristics of other pieces of equipment are similarly approximated by linear equations.

(*b*) *Waste heat boiler* (*BW*).

$$\left.\begin{aligned} &G_{BWn}=p_{BWn}Q_{BWn}+q_{BWn}\delta_{BWn}\\ &E^a_{BWn}=p^a_{BWn}Q_{BWn}+q^a_{BWn}\delta_{BWn}\\ &\underline{Q}_{BWn}\delta_{BWn}\le Q_{BWn}\le \bar{Q}_{BWn}\delta_{BWn}\\ &\delta_{BWn}\in\{0,\ 1\}\end{aligned}\right\}(n=1\sim N_{BW}) \tag{3}$$

(*c*) *Auxiliary boiler* (*BA*).

$$\left.\begin{aligned} &G_{BAn}=p_{BAn}F_{BAn}+q_{BAn}\delta_{BAn}\\ &E^a_{BAn}=p^a_{BAn}F_{BAn}+q^a_{BAn}\delta_{BAn}\\ &\underline{F}_{BAn}\delta_{BAn}\le F_{BAn}\le \bar{F}_{BAn}\delta_{BAn}\\ &\delta_{BAn}\in\{0,\ 1\}\end{aligned}\right\}(n=1\sim N_{BA}) \tag{4}$$

(*d*) *Steam absorption refrigerator* (*RS*), *cooling tower* (*CS*), *and pump to circulate cooling water* (*PS*).

$$\left.\begin{aligned} &Q^c_{RSn}=p_{RSn}G_{RSn}+q_{RSn}\delta_{RSn}\\ &E^q_{RSn}=p^q_{RSn}G_{RSn}+q^q_{RSn}\delta_{RSn}\\ &E_{CSn}=p_{CSn}G_{RSn}+q_{CSn}\delta_{RSn}\\ &E_{PSn}=p_{PSn}G_{RSn}+q_{PSn}\delta_{RSn}\\ &\underline{G}_{RSn}\delta_{RSn}\le G_{RSn}\le \bar{G}_{RSn}\delta_{RSn}\\ &\delta_{RSn}\in\{0,\ 1\}\end{aligned}\right\}(n=1\sim N_{RS}) \tag{5}$$

(*e*) *Heat exchanger* (*HE*).

$$\left.\begin{aligned} &Q^{hw}_{HEn}=p_{HEn}G_{HEn}\\ &0\le G_{HEn}\le \bar{G}_{HEn}\end{aligned}\right\}(n=1\sim N_{HE}) \tag{6}$$

(*f*) *Pump to supply cold water for space cooling* (*PC*)

$$\left.\begin{aligned} &E_{PCn}=p_{PCn}Q^c_{PCn}\\ &0\le Q^c_{PCn}\le \bar{Q}^c_{PCn}\end{aligned}\right\}(n=1\sim N_{PC}) \tag{7}$$

(*g*) *Pump to supply hot water for space heating* (*PH*).

$$\left.\begin{aligned} &E_{PHn}=p_{PHn}Q^h_{PHn}\\ &0\le Q^h_{PHn}\le \bar{Q}^h_{PHn}\end{aligned}\right\}(n=1\sim N_{PH}) \tag{8}$$

(*h*) *Pump to supply hot water* (*PW*).

$$\left.\begin{aligned} &E_{PWn}=p_{PWn}Q^w_{PWn}\\ &0\le Q^w_{PWn}\le \bar{Q}^w_{PWn}\end{aligned}\right\}(n=1\sim N_{PW}) \tag{9}$$

Energy Balance and Supply-Demand Relationships. From the plant structure shown in Fig. 1 (*a*), the following relationships are obtained for each energy flow. They are also considered as constraints.

(*a*) *Electric power.*

$$\left.\begin{aligned} &E_{buy}+E_{GT}=E_{sell}+E^a+E\\ &E_{GT}=\sum_{n=1}^{N_{GT}}E_{GTn}\\ &E^a=\sum_{n=1}^{N_{GT}}E^a_{GTn}+\sum_{n=1}^{N_{BW}}E^a_{BWn}+\sum_{n=1}^{N_{BA}}E^a_{BAn}\\ &\quad+\sum_{n=1}^{N_{RS}}(E^a_{RSn}+E_{CSn}+E_{PSn})+\sum_{n=1}^{N_{PC}}E_{PCn}\\ &\quad+\sum_{n=1}^{N_{PH}}E_{PHn}+\sum_{n=1}^{N_{PW}}E_{PWn}\\ &E=E^d\end{aligned}\right\} \tag{10}$$

(*b*) *Steam.*

$$\sum_{n=1}^{N_{BW}}G_{BWn}+\sum_{n=1}^{N_{BA}}G_{BAn}=\sum_{n=1}^{N_{RS}}G_{RSn}+\sum_{n=1}^{N_{HE}}G_{HEn}+G_{loss} \tag{11}$$

(*c*) *Cold water for space cooling.*

$$\left.\begin{aligned} &\sum_{n=1}^{N_{RS}} Q^{c}_{RSn} = \sum_{n=1}^{N_{PC}} Q^{c}_{PCn} = Q^{c} \\ &Q^{c} = Q^{cd} \end{aligned}\right\} \tag{12}$$

(*d*) *Hot water for space heating and hot water supply.*

$$\left.\begin{aligned} &\sum_{n=1}^{N_{HE}} Q^{hw}_{HEn} = Q^{h} + Q^{w} \\ &Q^{h} = \sum_{n=1}^{N_{PH}} Q^{h}_{PHn} \\ &Q^{w} = \sum_{n=1}^{N_{PW}} Q^{w}_{PWn} \\ &Q^{h} = Q^{hd} \\ &Q^{w} = Q^{wd} \end{aligned}\right\} \tag{13}$$

(*e*) *Waste heat.* Assuming that the plant is equipped with a paired gas turbine generator/waste heat boiler, the following relationship is taken into account:

$$Q_{GTn} = Q_{BWn} \quad (n = 1 \sim N_{GT}) \tag{14}$$

where $N_{GT} = N_{BW}$.

(*f*) *Natural gas.*

$$\left.\begin{aligned} F_{GT} &= \sum_{n=1}^{N_{GT}} F_{GTn} \\ F_{BA} &= \sum_{n=1}^{N_{BA}} F_{BAn} \end{aligned}\right\} \tag{15}$$

Objective Function. The objective function to be minimized is the hourly operational cost, defined by

$$J = \varphi_{elec}(E_{buy} - E_{sell}) + \varphi_{gas}(F_{GT} + F_{BA}) \tag{16}$$

where φ_{elec} and φ_{gas} denote the unit costs of purchased electric power and natural gas, respectively. Considering the case where the electric power company operates the cogeneration plant, the unit cost of sold electric power is assumed to be equal to that of purchased electric power.

The optimal operational planning problem has resulted in a mixed-integer linear programming one (Garfinkel and Nemhauser, 1972), in which the zero-one integer and continuous variables expressing the operational policy are determined so as to minimize J in equation (16) subject to equations (1) to (15).

Solving Method. The branch and bound method is adopted to solve the optimization problem defined above (Garfinkel and Nemhauser, 1972). This method is composed of the following three operations: (*a*) branching: the set of feasible solutions, or the feasible region, is divided into several subsets based on the values of integer variables; (*b*) solving linear programming problems: the suboptimal solution is derived for each subset using the simplex algorithm, in which calculations are carried out by simplex tableaus expressing the objective function and constraints (Dantzig, 1963); (*c*) bounding: by calculating a lower bound of the objective function for each subset, the subset is excluded from the feasible region if it becomes clear that there exists no optimal solution in this subset. Using this mehtod, the optimal solution can be derived more effectively than by the conventional enumeration method. The algorithm used in this paper is based on the Land-Doig method (Land and Doig, 1960; Kuester and Mize, 1973). A detailed explanation of the algorithm is omitted here.

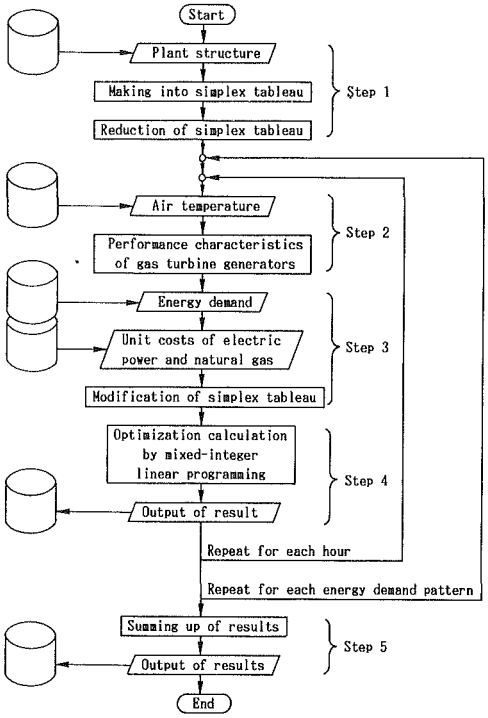

Fig. 2 Systematic procedure to determine the optimal operational policy

Systematic Procedure. Figure 2 shows a systematic procedure organized to determine the optimal operational policy throughout the year by using the above mentioned mathematical model. Each step in the procedure is described below:

Step 1: The input data on the plant structure are made into the simplex tableau required for mixed-integer linear programming. Here, the input data are expressed in the form of character expressions that enable easy and flexible modification of the data with a change of plant structure. Then, for the purpose of the efficient optimization calculation, the size of the simplex tableau is reduced by eliminating dependent variables automatically.

Step 2: The coefficients p_{GTn}, q_{GTn}, r_{GTn}, s_{GTn} and the bounds $\underline{F}_{GTn}$, $\overline{F}_{GTn}$ in equation (1) are determined according to the hourly input data on the air temperature.

Step 3: The simplex tableau is modified according to the hourly input data on energy demand and unit costs of purchased electric power or natural gas.

Step 4: The optimal operational policy is determined by the mixed-integer linear programming method, and the result is stored hourly.

Step 5: The hourly results are summed up for each month, each season, or the year, and the economic and energy conservative properties are estimated.

Steps 2 to 4 are repeated hourly for each energy demand pattern given on a representative day.

Case Study

Input Data. A case study is performed for a gas tur-

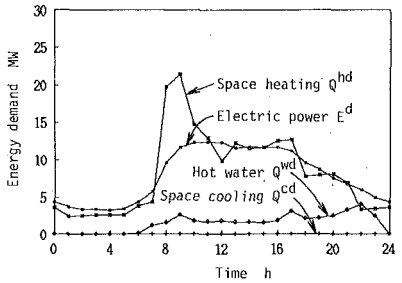

Fig. 3(*a*) Ordinary day in January

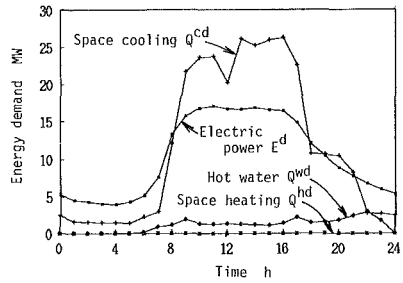

Fig. 3(*b*) Ordinary day in August

Fig. 3 Energy demand patterns

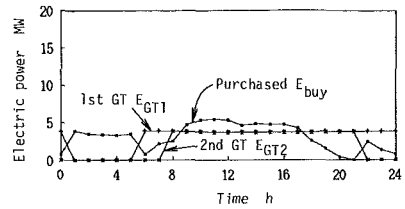

Fig. 4(*a*) Ordinary day in January

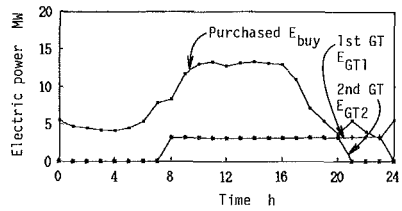

Fig. 4(*b*) Ordinary day in August

Fig. 4 The optimal operational patterns of gas turbine generators and purchased electric power

bine-waste heat boiler cogeneration plant used for district heating and cooling. The area supplied with energy consists of four office buildings and two hotels. Ordinary days, Saturdays, and holidays are considered as representative days for each month; i.e., the operational policy is investigated on 36 representative days throughout the year. Hourly energy demand is given as input data for each representative day. For example, Figs. 3(*a*) and 3(*b*) show the energy demand patterns estimated on the ordinary days in January and August, respectively. Two alternatives on the structure of plant A are investigated here; i.e., one is equipped with one pair of gas turbine generator/waste heat boilers (plant A1), and the other is equipped with two pairs (plant A2). Table 1 shows the number and maximum output of each kind of equipment in-

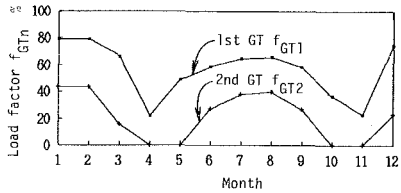

Fig. 5 Seasonal fluctuation of the monthly load factor of gas turbine generators

Table 1 Number and maximum output of each kind of constituent equipment

		Plant		
		A1	A2	B
Constituent equipment	Maximum output	Number	Number	Number
Gas turbine generator (GT)	$\bar{E}_{GTn}$=3.45 MW $\bar{Q}_{GTn}$=7.90 MW (Intake air temp. 17.5℃)	$N_{GT}=1$	$N_{GT}=2$	-
Waste heat boiler (BW)	$\bar{G}_{BWn}$=2.97 kg/s*	$N_{BW}=1$	$N_{BW}=2$	-
Auxiliary boiler (BA)	$\bar{G}_{BAn}$=4.17 kg/s*	$N_{BA}=3$	$N_{BA}=2$	$N_{BA}=3$
Steam absorption refrigerator (RS)	$\bar{Q}_{RSn}$=5.63 MW	$N_{RS}=6$	$N_{RS}=6$	$N_{RS}=6$
Heat exchanger (HE)	$\bar{Q}_{HEn}$=14.7 MW	$N_{HE}=2$	$N_{HE}=2$	$N_{HE}=2$

* 0.490 MPa gauge saturated steam

stalled in plants A1, A2, and B. The details of input data on performance characteristics of equipment are omitted here.

The objective function in equation (16) indicates that the optimal operational policy can be changed by the unit costs of purchased electric power and natural gas. The unit costs of purchased electric power and natural gas vary widely with their demands. In this case study, the investigation is made into the influence of the unit cost ratio of purchased electric power to natural gas on the optimal operational policy and the economic or energy conservative properties. Defining the unit cost as the cost per unit consumption of primary energy, the unit cost ratio α is given by

$$\alpha = \frac{\varphi_{\text{elec}}[\text{Yen/MJ}] \times 0.35}{\varphi_{\text{gas}}[\text{Yen/kg}]/49.60[\text{MJ/kg}]} \tag{17}$$

As expressed in equation (17), the overall thermal efficiency of purchased electric power is assumed as 35 percent. The optimal operational policy and other properties are investigated parametrically with regard to the unit cost ratio α.

Results and Considerations.

Operational Pattern. The optimal operational policy of plant A2 has been first investigated in detail for the case of the unit cost ratio $\alpha = 0.952$. Figures 4(*a*) and 4(*b*) show the optimal operational patterns of gas turbine generators and purchased electric power on the ordinary days in January and August, respectively. Both gas turbine generators are operated at the high loading level in the daytime in January and August because of the high demand for thermal energy. Figure 5 shows the seasonal fluctuation of the monthly load factor of two gas turbine generators given by

$$f_{GTn} = \left(\sum_t E_{GTn}\right) \Big/ \left(\sum_t \bar{E}_{GTn}\right) \times 100 \quad (n = 1 \sim N_{GT}) \tag{18}$$

where Σ_t denotes summation over a month, a season, or a year. The monthly load factor f_{GTn} varies widely throughout the year for both gas turbine generators. The monthly load factor of the second gas turbine generator f_{GT2} is reduced to zero in spring and autumn. Thus, the investigation into the seasonal and time fluctuation of the load factor of prime movers proves to be a very important subject at the planning stage of cogeneration plants for commercial and public purposes.

Influence of Fuel Cost on Operational Policy. Next, an investigation has been made into the influence of the unit cost

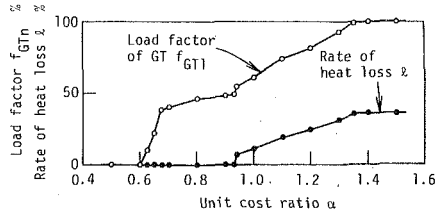

Fig. 6(*a*) Plant A1

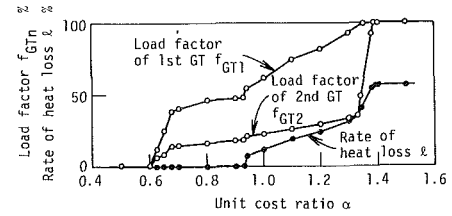

Fig. 6(*b*) Plant A2

Fig. 6 Relationships between the unit cost ratio and the annual load factor of gas turbine generators, or the annual rate of heat loss

ratio α in equation (17) on the optimal operational policy. Figure 6 shows the relationships between the unit cost ratio α and the annual load factor of gas turbine generators f_{GTn} in equation (18), or the annual rate of heat loss relative to the heat recovered by waste heat boilers l given by

$$l=\left(\sum_t G_{\text{loss}}\right)\Big/\left(\sum_t \sum_{n=1}^{N_{BW}} G_{BWn}\right)\times 100 \tag{19}$$

Figures 6(a) and 6(b) correspond to plants A1 and A2, respectively.

The results for plant A1 are described first. In the region of $\alpha \le 0.6$, the annual load factor of the gas turbine generator f_{GT1} becomes zero. This indicates that the conventional operation is superior in economy as compared with the cogeneration operation because of the very low cost of purchased electric power. In the region of $0.6 < \alpha \le 0.93$, f_{GT1} increases with α. Nevertheless, the annual rate of heat loss l is equal to zero. According to this annual total result, the optimal operational policy in this region resembles the thermal-following one. In the region of $0.94 \le \alpha \le 1.35$, f_{GT1} increases gradually with α in spite of the generation of a large amount of heat loss. In this region, several kinds of operational policies coexist with one another; i.e., the conventional or thermal-following policies are dominating during times of low demand for thermal energy, and the electric-following or sending back (i.e., selling the generated electric power to the outside electric power company) policies are dominating during times of high demand for thermal energy. Both the load factor f_{GT1} and the rate of heat loss l increase with α due to the gradual domination of the electric-following or sending back policies. In the region of $\alpha > 1.35$, f_{GT1} amounts to 100 percent.

Next, the results for plant A2 are described. In the region of $\alpha \le 1.33$, the annual load factor of the first gas turbine generator f_{GT1} and the annual rate of heat loss l almost agree with those of plant A1, respectively. As the second gas turbine generator is operated according to the thermal-following policy so as not to generate the heat loss, its annual load factor f_{GT2} is very low. However, in the region of $1.33 < \alpha \le 1.38$, f_{GT2} increases drastically with α due to the domination of the electric-following or sending back policies. In the region of $\alpha > 1.38$, f_{GT2} also amounts to 100 percent. Thus, with the increase in the unit cost ratio α, the optimal operational policy changes gradually by adopting partially the suitable policies from several kinds of operational policy.

Influence of Fuel Cost on Operational Cost. An investigation has been made into the influence of the unit cost ratio α on an economic property. Figure 7 shows the relationship between the unit cost ratio α and the reduction rate of annual operational cost γ defined by

$$\gamma=(C_{vB}-C_{vA})/C_{vB}\times 100 \tag{20}$$

where C_{vA} and C_{vB} denote, respectively, the annual operational cost of plants A and B, given by

$$C_v=\sum_t J \tag{21}$$

Figures 7(a) and 7(b) correspond to plants A1 and A2, respectively. As shown in equation (20), γ indicates how much the annual operational cost can be reduced by employing the cogeneration plant instead of the conventional energy supply plant. In Fig. 7, the optimal operational policy is compared with the thermal-following or electric-following ones. The value of γ increases with α. This is because the cogeneration operation becomes advantageous with the increase in α due to the low cost of natural gas. The thermal-following or electric-following policies approach the optimal one within a partial range of α. However, the optimal one is superior in economy for all values of the unit cost ratio α as compared with other ones.

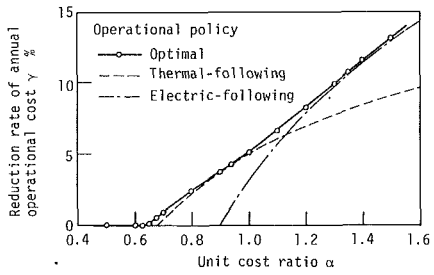

Fig. 7(*a*) Plant A1

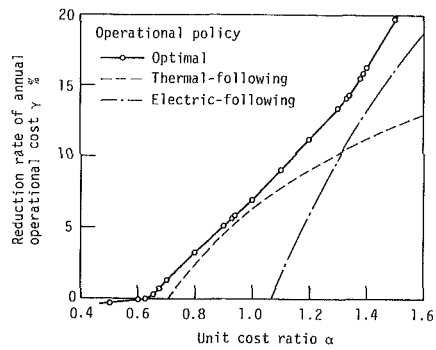

Fig. 7(*b*) Plant A2

Fig. 7 Relationship between the unit cost ratio and the reduction rate of annual operational cost

Influence of Fuel Cost on Energy Conservation. This paper defines the optimal operational policy as the one that minimizes the operational cost. In addition, as the energy conservative property is one of other important estimation indicators for cogeneration plants, it has also been investigated. Figure 8 shows the relationship between the unit cost ratio α and the annual rate of energy conservation β defined by

$$\beta=(Q_{pB}-Q_{pA})/Q_{pB}\times 100 \tag{22}$$

where Q_{pA} and Q_{pB} denote, respectively, the annual consumption of primary energy of plants A and B, given by

$$Q_p=\sum_t \{E_{\text{buy}}/0.35+(F_{GT}+F_{BA})\times 49.60\} \tag{23}$$

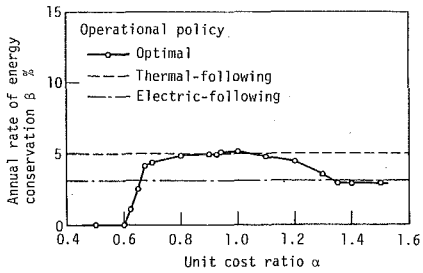

Fig. 8(a) Plant A1

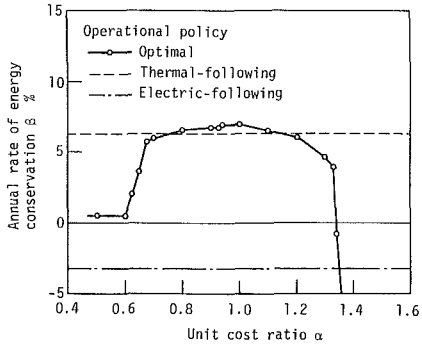

Fig. 8(b) Plant A2

Fig. 8 Relationship between the unit cost ratio and the annual rate of energy conservation

Figures 8(a) and 8(b) correspond to plants A1 and A2, respectively. The optimal operational policy is compared with the thermal-following or electric-following ones, which have a constant value of β due to the independence of the operational policy on α. According to the optimal operational policy, β has a maximum in the vicinity of $\alpha=1$. In the region of $\alpha<1$, β decreases because of the low load factor of gas turbine generators. On the other hand, in the region of $\alpha>1$, β decreases because of the high rate of heat loss. This can be interpreted more exactly as follows. The value $\alpha=1$ indicates that the unit costs of purchased electric power and natural gas are equal to each other. Hence, the objective function defined by equation (16) also indicates the minimization of the consumption of primary energy provided that no generated electric power is sold. Namely, β has a maximum at $\alpha=1$ on the above assumption. In this case study, the value of β at $\alpha=1$ reaches nearly its maximum because of the very little amount of sold electric power. The value of β on the basis of the thermal-following policy is close to the maximum. However, the value of β on the basis of the electric-following policy is far lower, and plant A2 has the negative value of β.

Conclusions

An optimal operational planning method has been proposed for a gas turbine-waste heat boiler cogeneration plant, and by this method an investigation has been made into the influence of fuel cost on the operation. A planning method has been first presented by which the operational policy is determined systematically throughout the year so as to minimize the operational cost. Then, a case study has been performed for a cogeneration plant used for district heating and cooling. The following main results have been obtained:

1 The optimal operational planning method enables easy and rational determination of the operational policy for a cogeneration plant with complex structure.

2 It has been made clear how the optimal operational policy and the economic or energy conservative properties are influenced by the unit cost ratio of purchased electric power to natural gas.

3 The optimal operational policy is superior in economy as compared with the thermal-following or electric-following ones.

Although this paper has dealt with a restricted case study, it appears that the obtained results apply qualitatively to other cases. In addition, the proposed method has the flexibility to apply to investigation into other cases. As a subsequent subject, it will be important to investigate the optimal capacity of cogeneration plants.

References

Akagi, S., Yokoyama, R., and Ito, K., 1986, "Optimal Operation of an Energy Saving Combined Plant for LNG Carriers," *Proceedings of the Japan-U.S.A Symposium on Flexible Automation*, pp. 811-817.

California Energy Commission, 1982, *Cogeneration Handbook*, Resource Dynamics Corporation, McLean, p. 3-4.

Dantzig, G. B., 1963, *Linear Programming and Extensions*, Princeton University Press, NJ.

Ducrocq, J. C., 1985, "Optimal Energy Management in a Complex System With Mixed-Integer Programming," *RAIRO Automatique-Productique Informatique Industrielle*, Vol. 19, pp. 403-413.

Garfinkel, R. S., and Nemhauser, G. L., 1972, *Integer Programming*, Wiley, New York, pp. 7, 111-122.

Kuester, J. L., and Mize, J. H., 1973, *Optimization Techniques With Fortran*, McGraw-Hill, New York, pp. 66-90.

Land, A. H., and Doig, A. G., 1960, "An Automatic Method of Solving Discrete Programming Problems," *Econometrica*, Vol. 28, pp. 497-520.

Nath, R., and Holliday, J. F., 1985, "Optimizing a Process Plant Utility System," *Mechanical Engineering*, Vol. 107, pp. 44-50.

Second-Law Analysis of Diesel Engine Combustion

J. H. Van Gerpen

H. N. Shapiro

Department of Mechanical Engineering,
Iowa State University,
Ames, IA 50011

A second-law analysis of the combustion process in a diesel engine is presented for a single-zone model. Expressions for availability and the availability balance are developed in detail from the energy and entropy balances and applied in a manner that allows the irreversibility due to combustion to be separated from that associated with heat transfer to the walls. Availability is divided into two components: thermomechanical and chemical availability. For the first time, chemical availability of the cylinder contents is dealt with rigorously, which allows for a correct determination of combustion irreversibilities. The analysis is applied in a parametric study of the effects of combustion timing, mass burning rate, and heat transfer rate on the irreversibility and system availability.

Introduction

Engine researchers have long recognized the need for improved understanding of diesel combustion processes to aid in the future design of diesel engines and to explain the behavior of existing engines. Recent developments in the application of ceramic materials and bottoming cycles to diesel engines have shown that past experience cannot be the sole source of design information. This paper extends current single-zone models of diesel combustion by applying second-law analysis to account for the availability supplied to the engine by the fuel. This availability is ultimately transferred from the cylinder as work and heat, or it is destroyed by irreversibilities.

Diesel engine combustion models based on energy balances have been available for many years. Single-zone models such as that proposed by Krieger and Borman have been widely used for studying diesel combustion processes [1]. Shahed et al. [2] have extended this analysis to multiple zones with mixing processes governed by semi-empirical jet-mixing equations. Division of the cylinder into a large number of zones is currently being extended to finite-difference solutions of the complete three-dimensional mass, momentum, and energy equations.

Some attempts have been made to apply second-law analysis to these models. As early as 1964, Patterson and Van Wylen [3] incorporated entropy calculations into a two-zone thermodynamic model for a spark-ignition engine and estimated the magnitudes of availability losses associated with combustion, heat transfer, and exhaust products. Flynn et al. [4–6] studied extensively the characteristics of low heat rejection engines by using a single-zone model and a simplified second-law analysis. However, these studies have not addressed the problem of chemical availability. Moran [7], Brzustowski [8], and Ahrendts [9] present detailed developments of availability that include both thermomechanical and chemical effects. Moran and Brzustowski provide extensive examples of combustion applications, but to date, these concepts have not been applied to engines. In this paper, the availability balance is derived from the energy and entropy balances and applied rigorously to the problem of diesel engine combustion. Then the analysis is applied in a parametric study of the various sources of availability loss and transfer in the engine.

Contributed by the Advanced Energy Systems Division and based on a paper presented at the Advanced Energy Systems Division Symposia, ASME Winter Annual Meeting, Boston, Massachusetts, November 29–December 2, 1987. This paper was awarded the E. F. Obert Outstanding Paper Award. Manuscript received by the Advanced Energy Systems Division July 22, 1988.

Single-Zone Heat Release Model

In this section, governing equations are presented for a single-zone model of diesel engine combustion following Krieger and Borman [1]. Considered are the compression process starting at bottom dead center, the combustion process beginning at a specified crank angle, and the expansion of the combustion products back to bottom dead center. Thus, crank angle θ ranges from -180 deg to 180 deg, where zero degrees is top dead center. Fuel enters the control volume as a liquid at pressure p_f and temperature T_f. No blow-by losses are considered in the present analysis.

Conditions during the combustion process within the cylinder of a diesel engine are highly nonuniform. The injected fuel must vaporize and mix with the air in the cylinder, and regions of burned and unburned gas exist. The single-zone model considered here assumes uniform equilibrium properties within the control volume at each crank angle and ignores many of the details of the actual processes. Instead, a fictitious fuel injection rate, $\dot{m}_f$ is defined that is equivalent to the effective mass burning rate within the cylinder [1]. Fuel is assumed to be injected at this rate and to burn instantly to equilibrium products.

Development of Governing Equations. Neglecting kinetic and potential energy effects, we can write the instantaneous energy balance for the control volume under consideration on a time rate basis as

$$\frac{dU}{dt} = \dot{Q} - \dot{W} + \dot{m}_f h_{\text{fuel}} \tag{1a}$$

In equation (1*a*), U denotes the total internal energy of the mass contained within the control volume.

For a fixed rotational speed of the crankshaft, the time derivatives in equation (1*a*) can be written in terms of the change in crank angle, $d\theta$, as

$$\frac{dU}{d\theta} = Q' - W' + m_f' h_{\text{fuel}} \tag{1b}$$

The total amount of mass in the control volume m changes with θ according to $dm/d\theta = m_f'$. Also, the work term W' can be expressed as the product of the pressure p and the differential rate of change in cylinder volume $dV/d\theta$. By noting that U can be expressed as the product of specific internal energy and mass, equation (1*b*) can be rewritten as

$$m\left(\frac{du}{d\theta}\right) + um_f' = Q' - p\left(\frac{dV}{d\theta}\right) + m_f' h_{\text{fuel}} \tag{2}$$

Attempts have been made to characterize the complicated heat transfer processes that occur within the cylinders of internal combustion engines. The widely used Annand correlation [10] was employed in the present study, where three constant temperatures were chosen for the head, piston, and sleeve, respectively. The correlation plays an important role in the energy balance calculations, but it is less significant in the present second-law analysis because the control volume studied includes only the gases within the cylinder. Because equilibrium states are presumed to exist within the control volume, the heat transfer irreversibilities and availability transferred to the wall are accounted for as losses.

The model is completed by considering appropriate property relations. The state of the gas in the control volume is fixed by the pressure p, temperature T, and equivalence ratio Φ. The equilibrium composition can be expressed in terms of the mole fractions of the various gases present as $x_k = x_k\ (p, T, \Phi)$, where x_k is the mole fraction of species k. Because of the dependence of specific internal energy on the mole fractions, $u = u(p,T,\Phi)$.

Another independent relation is provided by differentiating the ideal gas equation

$$p\frac{dV}{d\theta} + V\frac{dp}{d\theta} = m\bar{R}\left(\frac{1}{M}\frac{dT}{d\theta} - \frac{T}{M^2}\frac{dM}{d\theta}\right) + \frac{\bar{R}T}{M}\frac{dm}{d\theta} \tag{3}$$

Finally, the molar specific internal energies can be evaluated by using

$$\bar{u}_k(T) = \bar{h}_{f,k}^{0\,\text{K}} + \Delta\bar{h}_k^{0\,\text{K}}(T) - \bar{R}T \tag{4}$$

where $\bar{h}_{f,k}^{0\,\text{K}}$ and $\Delta\bar{h}_k^{0\,\text{K}}(T)$ are the enthalpy of formation evaluated at 0 K and the enthalpy change from 0 K to T, respectively, for species k. Equation (4) also applies to the evaluation of the fuel enthalpy. In this way, the energies of all species present within the control volume are calculated relative to the common reference of zero enthalpy for the elements at 0 K.

Solution of the Governing Equations. Equations (2) through (4) can be solved when input relationships for m_f', Q', $dV/d\theta$, an equilibrium property routine for $x_k = x_k\ (p, T, \Phi)$, and initial conditions are all specified. Concerning m_f', the functional form of the relationship used in the present study is a modification of the expressions used by Watson et al. [11]. That is, for $\theta \geq C_2$

Nomenclature

$\mathbf{A}$ = surface area
A = availability
A^{ch} = chemical availability
A^{tm} = thermomechanical availability
c_f = specific heat of the fuel
C_1, C_2, C_3, C_4, C_5 = parameters in mass burning rate function
D = diffusion burning term in mass burning rate function
$\bar{h}_{f,k}^{0\,\text{K}}$ = enthalpy of formation evaluated at 0 K for species k
$\Delta\bar{h}_k^{0\,\text{K}}$ = enthalpy change for species k
h_{fuel} = fuel enthalpy
i = species present in reference environment
I = irreversibility
I' = irreversibility rate, crank-angle basis
j = species not present in reference environment
k = species
m = mass in cylinder
m_f = mass of fuel
$\dot{m}_f$ = fuel injection rate, time basis
m_f' = fuel injection rate, crank-angle basis
M = molecular weight
N_i = number of moles of species i
N_j = number of moles of species j
PR = premixed burning term in mass burning rate function
p = pressure
p_f = fuel supply pressure
p^0 = pressure of system at dead state
q' = heat flux
$\dot{Q}$ = heat transfer rate, time basis
Q' = heat transfer rate, crank-angle basis
$\bar{R}$ = universal gas constant
s_f = fuel entropy
S = entropy
t = time
T = temperature
T_f = fuel temperature
T^0 = temperature of system at dead state
u_k = specific internal energy of species k
U = internal energy
U_o = internal energy of system at dead state
U_e = internal energy of environment
V = volume
V_o = volume of system at dead state
$\dot{W}$ = power, time basis
W' = power, crank-angle basis
x_k = mole fraction of species k
y = dimensionless time parameter in mass burning rate function
θ = crank angle
μ_i = chemical potential of species i
μ_i^o = chemical potential of species i in environment
μ_i^* = chemical potential of species i at restricted dead state
μ_j = chemical potential of species j
μ_j^o = chemical potential of species j in environment
μ_j^* = chemical potential of species j in system at restricted dead state
σ' = entropy production rate, crank angle basis
Φ = equivalence ratio

$$m_f'(\theta) = m_f[C_1 PR(\theta) + (1 - C_1)D(\theta)] \quad (5a)$$

where m_f is the total mass of fuel injected. The premixed portion of the burning rate curve, $PR(\theta)$, is given as

$$PR(\theta) = \frac{5000}{C_3}(C_4 + 1)y^{C_4}\left[1 - y^{(C_4+1)}\right]^{4999} \quad (5b)$$

and the diffusion portion of the burning rate curve, $D(\theta)$, is given as

$$D(\theta) = \frac{6.9076}{C_3}(C_5 + 1)y^{C_5}\ [\exp(-6.9076y^{(C_5+1)})] \quad (5c)$$

with

$$y = (\theta - C_2)/C_3 \quad (5d)$$

The values of the five constants in equation (5) determine the particular characteristics of the mass burning rate function as follows:

C_1 = fraction of fuel burned in premixed portion
C_2 = parameter for specifying start of combustion
C_3 = parameter for specifying duration of combustion
C_4 = shape parameter for premixed burning
C_5 = shape parameter for diffusion burning

The equilibrium properties and enthalpy values used in the present study were determined from a version of the FORTRAN subroutine PER, developed by Olikara and Borman [12], which was modified to calculate entropy values. For all calculations, saturated air at 298.15 K, 1 atm was assumed to fill the control volume at the beginning of compression. The equations of the model were solved by using a fifth-order Runge-Kutta method capable of solving simultaneous, first-order differential equations.

Development of Availability Balance

Availability is the maximum theoretical work output that could be developed in bringing a system into equilibrium with a reference environment. In general, this involves all work that could be obtained by exploiting differences in velocity, potential energy, temperature, pressure, and chemical potential between the system and the environment. When thermal, mechanical, and chemical equilibria are attained and the system is at rest and zero elevation relative to the reference environment, no further potential exists for developing work. In this condition, the system and environment combination is said to be at the *dead state*. The value of the availability depends on both the state of the system and the state of the environment; it is a measure of the system's thermodynamic potential relative to the chosen environment.

In this section, expressions are developed for evaluating availability and other related properties needed to analyze diesel engine combustion. In addition, the availability balance is derived, including a detailed analysis of the chemical aspects of availability. Kinetic and potential energy effects are neglected for the applications considered in this paper. The development begins with the presentation of entropy balance relations.

Entropy Balance. Two forms of the entropy balance presented here are used in the development of the expressions for availability below. First, for a system of fixed mass undergoing an adiabatic process

$$\Delta S = \sigma \quad (6)$$

where ΔS is the change in system availability, and σ is the amount of entropy produced because of irreversibilities within the system during the process.

Next, the entropy balance can be written in rate form, per unit change in crank angle, as follows:

$$\frac{dS}{d\theta} = \frac{q'}{T}\,dA + m_f' s_f + \sigma' \quad (7)$$

In this study, the entropy balance of equation (7) was solved for σ' in order to evaluate the effects of irreversibility. To do so, the equilibrium properties program had to be modified to calculate entropies, and the entropy of the fuel had to be determined. The heat transfer term was evaluated with Annand's correlation, as in the energy balance calculations discussed above. The entropy of the control volume contents was calculated from

$$S = \sum_{k=1}^{n} x_k[\bar{s}_k^{0\,\mathrm{K}}(T) - \bar{R}\,\ln(p_k/p_{\mathrm{ref}})] \quad (8)$$

where $\bar{s}_k^{0\,\mathrm{K}}(T)$ is the molar specific absolute entropy of specie k at temperature T and reference pressure p_{ref}, and p_k is the partial pressure of specie k in the control volume. Values for $\bar{s}_k$ were obtained in the computer program from the JANAF tables [13] within subroutine PER.

The fuel entropy at T_{ref} = 298 K was obtained from [14] and corrected for temperature according to

$$s_f = s_f(T_{\mathrm{ref}}) + c_f\,\ln(T_f/T_{\mathrm{ref}}) \quad (9)$$

where c_f is the specific heat of the fuel, which is assumed to be an incompressible liquid.

Development of Availability. Consider a system at temperature T and pressure p that contains various chemical species, each with chemical potential μ_k. The system is imagined to be enclosed completely in a reference environment at temperature T^0 and pressure p^0; its chemical potentials are μ_k^0 for the environmental components. In general, some species present in the system are also present in the reference environment and some are not.

Consider the combined system consisting of the system of interest and the reference environment. Let the system and environment interact by exchanging mass and energy with each other until equilibrium is reached, but allow no heat or mass transfer across the boundary of the combined system and no change in volume of the combined system. If W_c denotes the work developed by the combined system during equilibration, the energy balance for the combined system is

$$W_c = -(U_o - U) - \Delta U^0 \quad (10)$$

where U = internal energy of system; U_o = internal energy of system at the dead state; ΔU^0 = internal energy change of the environment. The system internal energy can be expressed in terms of other properties by using appropriate thermodynamic relations presented by Moran [7]. Thus

$$U = TS - pV + \sum_{i=1}^{n} N_i\mu_i + \sum_{j=1}^{m} N_j\mu_j \quad (11)$$

where the first summation involves all species within the system that are also present in the reference environment, and the second summation includes those species in the system that are not present in the environment. The composition of the reference environment chosen for this study is listed in Table 1. Note that NO, CO, OH, O, N, and other equilibrium products of combustion that may be present in the system can be reacted to completion with species present in the reference environment.

For the combined system at the dead state, the temperature and pressure equal their respective values in the reference environment, T^0 and p^0. All species remaining are present in the reference environment, and the chemical potential of each species is equal to its chemical potential in the environment μ_i^0. Thus

$$U_o = T^0 S_o - p^0 V_o + \sum_{i=1}^{n} N_{io}\mu_i^0 \quad (12)$$

Table 1 Input parameters

Reference environment: 298.15° K, 101.35 kPa 20.29% O_2, 3.13% H_2O, 0.03% CO_2, 0.90% Ar, 75.65% N_2	
Fuel properties: Liquid dodecane, $C_{12}H_{26}$	
Temperature	40° C
Pressure	35 MPa
Entropy (298.15° K, 101.35 kPa)	2.877 kJ/kg·°K
Availability (298.15° K, 101.35 kPa)	47,037 kJ/kg
Lower heating value	44,111 kJ/kg
Density	734.4 kg/m^3
Specific heat	2.18 kJ/kg·°K
Engine dimensions:	
Bore	114.3 mm
Stroke	114.3 mm
Connecting rod	228.6 mm
Compression ratio	16:1
Operating conditions for baseline case:	
Speed	2000 RPM
Equivalence ratio	0.6
Wall temperatures (case TW1)	
Head	533° K
Piston	478° K
Sleeve	422° K
Initial temperature	298.15° K
Initial pressure	101.35 kPa
Residual fraction	0
Heat release parameters	
$C_1 = 0.25, C_2 = -10, C_3 = 55, C_4 = 3.5, C_5 = 1.0$	

In this equation, the subscript zero denotes extensive properties of the system at the dead state.

For the reference environment

$$\Delta U^0 = T^0 \Delta S^0 - p^0 \Delta V^0 + \sum_{i=1}^{n} \Delta N_i^0 \mu_i^0 \tag{13}$$

The superscript zero is used to designate properties in the environment.

Applying the entropy balance of equation (6) to the process,

$$(S_o - S) + \Delta S^0 = \sigma \tag{14}$$

or

$$S + \sigma = S_o + \Delta S^0 \tag{15}$$

Because the total volume of the combined system is constant, $V_o - V = -\Delta V^0$. When this fact and equations (10), (11), (12), (13), and (15) are combined, the energy balance can be rewritten as

$$W_c = U + p^0 V - T^0 S - \sum_{i=1}^{n} (N_{io} + \Delta N_i^o)\mu_i^o - T^0 \sigma \tag{16}$$

Before completing the development of the expression for availability, the summation in equation (16) is placed in a form more suitable for numerical evaluation. The summation involves changes in the composition of the environment, ΔN_i^o. These terms can be eliminated by considering the stoichiometric relationships that exist between the composition at the initial condition of the combined system and the composition at the dead state. As the system goes to the dead state, any species j (not present in the reference environment) must react with i species (present in the reference environment) to form other i species according to the following reaction:

$$C_j + \sum_{i=1}^{n} v_{ij}^{\mathrm{REAC}}\, C_i \rightleftharpoons \sum_{i=1}^{n} v_{ij}^{\mathrm{PROD}}\, C_i \tag{17}$$

where v_{ij}^{REAC} = the number of moles of environmental reactant i that reacts with one mole of j; v_{ij}^{PROD} = the number of moles of environmental reactant i that results from reaction of one mole of j.

The change in the amount of species i in the system and environment is equal to the difference between the amount of i created and the amount of i destroyed as the system goes to the dead state; that is,

$$(N_{io} - N_i) + \Delta N_i^o = \sum_{j=1}^{m} v_{ij}^{\mathrm{PROD}}\, N_j - \sum_{j=1}^{m} v_{ij}^{\mathrm{REAC}}\, \mathrm{N_j} \tag{18}$$

Multiplying by μ_i^o and summing over all species i results in the following expression:

$$\sum_{i=1}^{n} (N_{io} + \Delta N_i^o)\mu_i^o =$$

$$\sum_{i=1}^{n} N_i \mu_i^o + \sum_{i=1}^{n} \left(\sum_{j=1}^{m} v_{ij}^{\mathrm{PROD}}\, N_j \mu_i^o + \sum_{j=1}^{m} v_{ij}^{\mathrm{REAC}}\, \mathrm{N_j} \mu_i^o \right) \tag{19}$$

Reversing the order of summation in the last term gives

$$\sum_{i=1}^{n} (N_{io} + \Delta N_i^o)\mu_i^o =$$

$$\sum_{i=1}^{n} N_i \mu_i^o + \sum_{j=1}^{m} N_j \left(\sum_{i=1}^{n} v_{ij}^{\mathrm{PROD}}\, \mu_i^o - \sum_{i=1}^{n} v_{ij}^{\mathrm{REAC}}\, \mu_i^o \right) \tag{20}$$

Following Moran [7] and Ahrendts [9], an effective chemical potential in the reference environment for a species not present in the reference environment can be defined on the basis of the equivalence of chemical potentials between reactants and products for the equilibrium reaction given in equation (17). Thus, for any j species

$$\mu_j^o = \sum_{i=1}^{n} v_{ij}^{\mathrm{PROD}}\, \mu_i^o - \sum_{i=1}^{n} v_{ij}^{\mathrm{REAC}}\, \mu_i^o \tag{21}$$

For example, for carbon monoxide, $CO + 1/2\, O_2 \rightleftharpoons CO_2$, so

$$\mu_{\mathrm{CO}}^o = \mu_{\mathrm{CO_2}}^o - 1/2 \mu_{\mathrm{O_2}}^o$$

Similar expressions can be obtained for other nonenvironmental species such as H_2, OH, and the like.

By substituting equation (21) into equation (20)

$$\sum_{i=1}^{n} (N_{io} + \Delta N_i^o)\mu_i^o = \sum_{i=1}^{n} N_i \mu_i^o + \sum_{j=1}^{m} N_j\, \mu_j^o \tag{22}$$

The terms on the right side of equation (21) can each be evaluated with reference only to properties of the system and the reference environment composition.

At this point the availability can be introduced. From the second law of thermodynamics, the last term in equation (16), $T^0\sigma$, always has a positive value when irreversibilities are present within the combined system. Thus, the maximum work that could be obtained corresponds to the case where the process is reversible, $\sigma = 0$. The maximum work is by definition equal to the availability A. Finally, by incorporating equation (22) into equation (16) and setting $T^0\sigma$ equal to zero

$$A = U + p^0 V - T^0 S - \sum_{i=1}^{n} N_i \mu_i^o - \sum_{j=1}^{m} N_j \mu_j^o \tag{23}$$

This expression allows the availability of the system to be evaluated.

Evaluating the Chemical Potentials. The chemical potential μ_k is the partial molar specific Gibbs functions of species k, evaluated at the system temperature and the partial pressure of species k:

$$\mu_k = \bar{g}_k(T, p_k) \tag{24}$$

Since thermodynamic property data are usually tabulated at 1 atm, the chemical potential can be obtained from standard property data (such as the JANAF tables [13]) by using the relation

$$\mu_k = \bar{g}_k(T, p_k) = \bar{g}_k(T, p_{\text{ref}}) + [\bar{R}T \ln(x_k p/p_{\text{ref}}) \tag{25}$$

where p_{ref} is the reference pressure for the property evaluation, typically 1 atm.

Thermomechanical and Chemical Availability. Equations (23) and (25) allow availability to be evaluated for any system at T and p with composition specified by the N_i and N_j values. The availability concept is sufficient for many thermodynamic analyses. However, it is common to consider the availability as consisting of two parts: thermomechanical availability (A^{tm}) and chemical availability (A^{ch}). Thermomechanical availability is associated with work that could be obtained from the combined system by allowing *only* thermal and mechanical interactions between the system and environment. Thus, the combined system achieves a *restricted* dead state condition wherein the system temperature is T^0, the system pressure is p^0, and the system is at an *equilibrium* composition described by N_i^* and N_j^*. At this state, the system and the environment are in thermal and mechanical equilibrium with each other, and the system state is an equilibrium state. No additional potential exists for developing work from the combined system without mass exchange between the system and the reference environment.

The chemical availability is defined as the maximum work that could be developed by the combined system in going from the restricted dead state to the *true* dead state as defined previously. This additional work can, in principle, be obtained by two means. First, species present in the system at the restricted dead state that are also present in the reference environment could diffuse into a work-producing device, such as a Van't Hoff box [7], that exploits the chemical potential difference associated with different species concentrations in the system and the environment. Second, species not present in the reference environment could be allowed to enter into chemical reactions in reversible fuel cells with species from the reference environment to produce environmental species. After these processes occur, the chemical potential of each species in the system would equal its respective chemical potential in the environment, and no further interactions would be possible.

The expressions developed above can be used to evaluate the thermomechanical and chemical availabilities as follows. The expression for chemical availability is obtained by evaluating equation (23) at the restricted dead state

$$A^{ch} = A^* = U^* + p^0 V^* - T^0 S^* - \sum_{i=1}^{n} N_i^* \mu_i^o - \sum_{j=1}^{m} N_j^* \mu_j^o \tag{26}$$

The superscript * denotes extensive properties of the system at the restricted dead state. The expression for thermomechanical availability is obtained by subtracting the chemical availability from the availability

$$A^{tm} = A - A^{ch} = (U - U^*) + p^o(V - V^*) - T^o(S - S^*) - \sum_{i=1}^{n} (N_i - N_i^*)\mu_i^o - \sum_{j=1}^{m} (N_j - N_j^*)\mu_j^o \tag{27}$$

The expression for chemical availability given in equation (26) can be used to calculate the chemical availability of pure fuels. For a fuel that exists alone at the temperature and pressure of the environment, the availability is given by

$$A_f = U_f^* + p^0 V_f^* - T^0 S_f^* - \sum_{i=1}^{n} N_i^* \mu_i^o - \sum_{j=1}^{m} N_j^* \mu_j^o \tag{28}$$

where

$$\sum_{i=1}^{n} N_i^* \mu_i^o$$

can be eliminated because no environmental species are present and

$$\sum_{j=1}^{m} N_j^* \mu_j^o$$

reduces to $N_f \mu_f^0$. Therefore

$$A_f = U_f^* + p^0 V_f^* - T^0 S_f^* - N_f \mu_f^o = N_f[\bar{g}_f(T^0, p^0) - \mu_f^o] \tag{29}$$

where the $\bar{g}_f$ is the molar Gibbs function of the fuel. For a hydrocarbon fuel of composition $C_a H_b$, by using equation (21)

$$\mu_f^o = a\mu_{CO_2}^o + \frac{b}{2}\mu_{H_2O}^o - \left(a + \frac{b}{4}\right)\mu_{O_2}^o \tag{30}$$

The approach given above can be used to evaluate the availability of fuels for which necessary thermodynamic property data are available. Extensive data for pure hydrocarbon fuels are presented in the report of the American Petroleum Institute (API) Research Project 44 [14]. However, for mixtures of pure fuels such as gasoline and diesel fuel, other techniques are necessary. Rodriguez [15] has given correlations for the availability of hydrocarbon fuels and has shown that the availability is typically 4 to 6 percent above the lower heating value of the fuel. If the fuel enters the control volume at a temperature and pressure that is different from p^0 and T^0, respectively, its thermomechanical availability must also be calculated.

The definitions of thermomechanical and chemical availabilities given here are different from the corresponding quantities presented in Moran [7]. The discrepancy arises because of a difference in the definitions of the restricted dead state. Moran assumes the composition of the system to be frozen at the N_i and N_j values existing at T and p, and the system is brought to a nonequilibrium state at T^0 and p^0. Hence, further potential exists for developing work from the combined system if the system is allowed to proceed to its equilibrium composition at T^0 and p^0 without exchanging mass with the environment. This potential is included as chemical availability in Moran's analysis, whereas in the present study, it is part of the thermomechanical availability.

The definitions presented here offer a more fundamental way to distinguish between thermomechanical and chemical availabilities. It is argued that the use of the term "dead state" should imply a condition of zero potential. Using the equilibrium composition of the system at T^0 and p^0 is consistent with this notion. In addition, the concept of thermomechanical availabilty is related logically to work that can be developed through thermal and mechanical interactions between the system and environment. Using the equilibrium composition of the system to define the restricted dead state is also consistent with this emphasis.

Although the distinction drawn here is subtle, it can lead to significant differences in the assignment of thermomechanical and chemical components of the availability. In the case of pure fuels, or processes of pure substances, the definitions become identical. However, in other cases the distinction becomes great, as in the following example. For a system consisting of a homogeneous air and fuel mixture (which for

simplicity is at T^0 and p^0), the mixture would contain no thermomechanical availability with Moran's definition, implying that no work could be obtained solely through thermal and mechanical interactions between the system and the environment. In contrast, if the present definitions were used, the availability would be primarily thermomechanical, since a significant amount of work could be obtained in proceeding to equilibrium products of combustion before allowing mass exchange with the reference environment.

Development of the Availability Balance. The energy and entropy balances presented above are sufficient for analyzing the control volume under consideration from the first- and second-law viewpoints. These balances can be combined to yield a third equation that, while not independent, has the feature that its terms can be identified with availability quantities. This *availability balance* equation allows for a detailed accounting of the availability inputs to the control volume in terms of useful work, losses, and destructions.

To obtain the availability balance equations, the entropy balance is multiplied by T^0 and subtracted from the energy balance. Then, the term $p^0 dV/d\theta$ is added to each side of the resulting equation to give

$$\frac{dU}{d\theta}+p^0\frac{dV}{d\theta}-T^0\frac{dS}{d\theta}=\int q'(1-T^0/T)dA-\left(W'-p^0\frac{dV}{d\theta}\right)+m_f'(h_f-T^0 s_f)-T^0\sigma' \tag{31}$$

To identify equation (31) as an availability balance, the fuel term on the right side and the collection of terms on the left side are considered in turn, beginning with the left side.

Differentiating equation (23) for availability with respect to crank angle

$$\frac{dA}{d\theta}=\frac{dU}{d\theta}+p^0\frac{dV}{d\theta}-T^0\frac{dS}{d\theta}-\sum_{i=1}^{n}\frac{dN_i}{d\theta}\mu_i^o-\sum_{j=1}^{m}\frac{dN_j}{d\theta}\mu_j^o \tag{32}$$

Next, as in Moran [7], specific *flow availability* on a molar basis is defined for a stream entering or leaving a control volume as

$$\tilde{a}_{\text{flow}}=(\tilde{h}-\tilde{h}_0)-T^0(\tilde{s}-\tilde{s}_0)+\tilde{a}^{ch} \tag{33}$$

The expression for fuel chemical availability in equation (29) can be written on a molar basis as

$$\begin{aligned}\tilde{a}_f^{ch} &= \tilde{g}_f(T^0, p^0)-\mu_f^o\\ &= [\tilde{h}_f-T^0\tilde{s}_f]-\mu_f^o\end{aligned}$$

Combining this expression with equation (33) results in the following expression for fuel flow availability $\tilde{a}_{f,\text{flow}}$ if the fuel enters at T^0 and p^0.

$$\tilde{a}_{f,\text{flow}}=\tilde{h}_f-T^0\tilde{s}_f-\mu_f^o \tag{34}$$

With equations (32) and (34), equation (31) can be rewritten as

$$\frac{dA}{d\theta}+\left[\sum_{i=1}^{n}\frac{dN_i}{d\theta}\mu_i^o+\sum_{j=1}^{m}\frac{dN_j}{d\theta}\mu_j^o-\frac{m_f'}{M_f}\mu_f^o\right]=\int q'(1-T^0/T)dA-\left(W'-p^0\frac{dV}{d\theta}\right)+\frac{m_f'}{M_f}(\tilde{a}_{f,\text{flow}})-T^0\sigma' \tag{35}$$

The terms in the square brackets in equation (35) arise because of changes in composition of the control volume associated with two effects: dissociation of i species into j species and fuel addition. In [16] it is shown that these terms cancel identically, resulting in the final form of the availabilty balance

$$\underbrace{\frac{dA}{d\theta}}_{1}=\underbrace{\int q'(1-T^0/T)dA}_{2}-\underbrace{\left(W'-p^0\frac{dV}{d\theta}\right)}_{3}+\underbrace{\frac{m_f'}{M_f}\tilde{a}_{f,\text{flow}}}_{4}-\underbrace{I'}_{5} \tag{36}$$

The numbered terms in this equation can be interpreted as availability quantities as follows:

Term 1: the rate of change of availability in the control volume, including thermomechanical (A^{tm}) and chemical availabilities (A^{ch})

Term 2: the rate of availability transfer associated with heat transfer from the gases to the wall (AQ)

Term 3: net rate of availability transfer to the piston associated with work (AW)

Term 4: rate of availability input to the control volume with the fuel, including the availability input associated with flow work, and the thermomechanical and chemical availabilities of the fuel (AFUEL)

Term 5: rate of availability destruction due to irreversibilities within the control volume (I)

Application to Diesel Engine Combustion

In this section, an availability analysis of diesel engine combustion is presented. The purpose of the analysis is to account correctly for chemical and thermomechanical availabilities and to distinguish combuston irreversibilities from availability transfer to the walls through heat transfer. A baseline case was analyzed, and important operating and model parameters were varied to show their effects on the solution. The parameter values for the baseline case are listed in Table 1. Discussion of the various cases follows.

Overall Availability Balance. Figure 1 shows the values of the terms in the availability balance for the baseline case plotted against crank position. Consider first the curve for availability transfer from the control volume associated with work (AW). During the compression stroke, up to a crank angle of -10 deg, the value of AW is negative and the thermomechanical availability (A^{tm}) increases. In this portion of the cycle there are no irreversibilities, and heat transfer effects (AQ) are negligible. Additionally, the pressure and temperature changes are not enough to cause appreciable dissociation, so the chemical availability (A^{ch}) is virtually constant.

Combustion starts at a crank angle of -10 deg, and there is a corresponding rise in the availability because of fuel addition

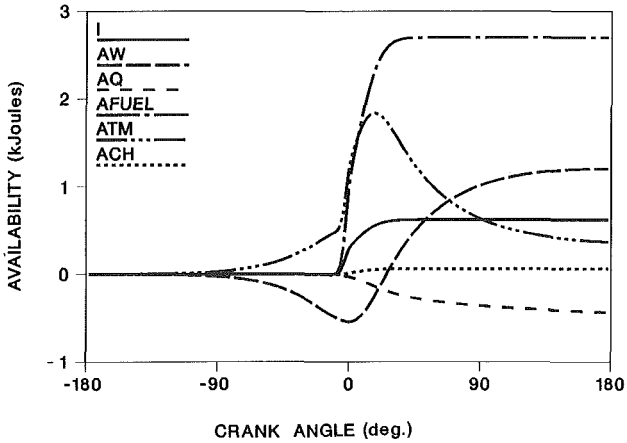

Fig. 1 Terms from availability balance versus crank angle

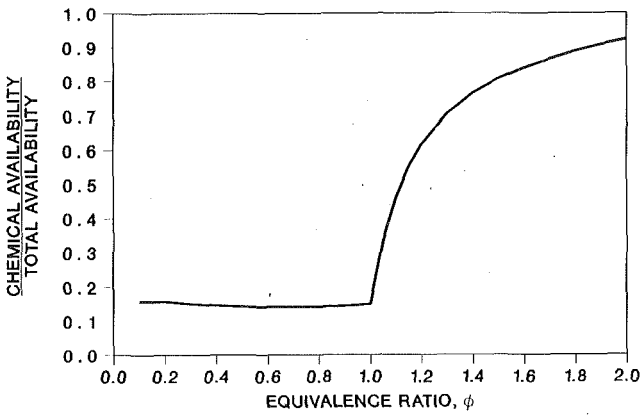

Fig. 2 Ratio of chemical availability to total availability at the end of expansion versus overall equivalence ratio

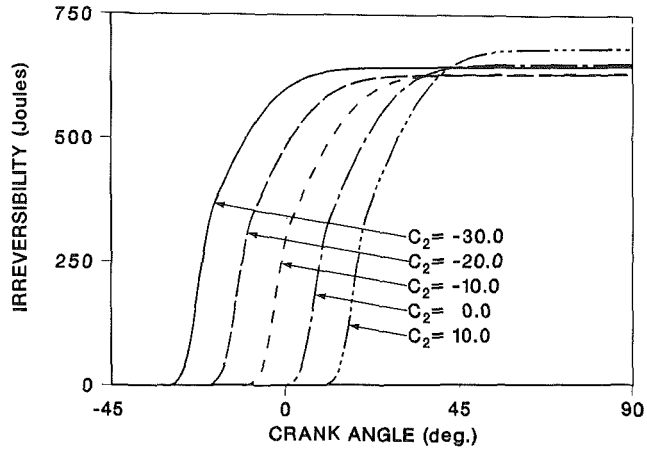

Fig. 3 Effects of timing on irreversibility

(AFUEL). Also, the thermomechanical availability increases rapidly as fuel enters the control volume and burns. The chemical reactions associated with combustion also generate irreversibility as evidenced by the curve labeled *I*. Just after top dead center, the heat transfer term increases in significance because of increasing gas temperatures within the system. The availability associated with fuel addition and the irreversibility does not change for crank angles greater than about 90 deg because combustion has essentially ceased. Heat transfer continues, and the thermomechanical availability decreases as availability continues to leave the system with heat and work.

Contribution of Chemical Availability. The chemical availability contribution to the system availability is small in the base case, constituting about 15 percent of the availability at the end of expansion. However, the contribution increases gradually during the combustion processes as CO_2 and H_2O are produced at levels above their concentrations in the reference environment. The chemical availability is relatively insignificant when the principal constituents of a system are those that are also present in the reference environment. However, under rich conditions or at high temperatures and pressures, significant amounts of species exist that are not present in the reference environment, such as CO and H_2. Under these conditions, the magnitude of the chemical availability can be larger than the magnitude of thermomechanical availability.

Figure 2 illustrates the influence of overall equivalence ratio on the magnitude of the chemical availability contribution at the end of expansion. Under lean conditions, the chemical availability is only about 15 percent of the total and is relatively insensitive to the equivalence ratio. However, under rich conditions the chemical availability can become more than 90 percent of the total because of large concentrations of species not present in the reference environment, which act as fuel species. Some researchers have not included the chemical availability in their second-law analyses. This omission prevents an accurate availability balance from being obtained. If the irreversibility is obtained by difference from the availability balance, errors in calculating the availability would be misinterpreted as irreversibility. This can be a significant source of error under rich conditions such as might be encountered in simulations of spark-ignited engines or in multizone diesel combustion models where zones close to the spray can be very rich.

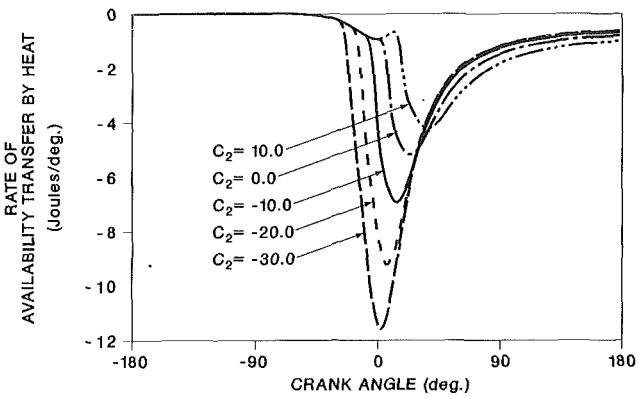

Fig. 4 Effects of timing on the rate of availability transfer by heat

Effects of Combustion Timing. The timing of combustion can have a dramatic impact on the fuel economy and the mean effective pressure and, hence, on the work developed by the engine. The gas temperatures, which change the heat transfer and the availability of the gases at the end of expansion, are also affected.

The effects of combustion timing were investigated by changing the value of the constant C_2 in the burning rate expressions (equation (5)). The constant determines the onset of combustion. This causes the centroid of the mass burning curve to be shifted. Initiating combustion at about -20.0 deg corresponds to centering the heat release at about top dead center. Figure 3 shows the irreversibility as the start of combustion is varied from crank angles of -30 deg to $+10$ deg. The curves indicate that the minimum irreversibility coincides with $C_2 = -20.0$ deg, although the effect is slight. Apparently, the time at which the fuel is burned has little impact on the irreversibility associated with combustion of the fuel.

Some of the availability entering with the fuel is destroyed by irreversibilities. The magnitude of this effect is somewhat insensitive to when the fuel is burned, even though the work varies greatly. Consequently, the availability transfer associated with heat transfer and the availability in the products must vary with the timing of the heat release. Figure 4 shows the rate of availability transfer associated with heat transfer versus crank angle for the same cases as in Fig. 3. It is seen that the availability transferred out of the system increases greatly when combustion is initiated earlier. This increase corresponds to higher temperatures during combustion and greater loss of availability to the surroundings. Because of increased availability loss, less availability is left in the system at the end of the expansion process. Thus, late combustion corresponds to less efficient use of the fuel availability.

Effects of Shape of Heat Release Curve. Figure 5 shows the effects on the irreversibility and on the irreversibility rate of varying the shape of the apparent mass burning rate curve. The shape was varied by changing the value of the parameter

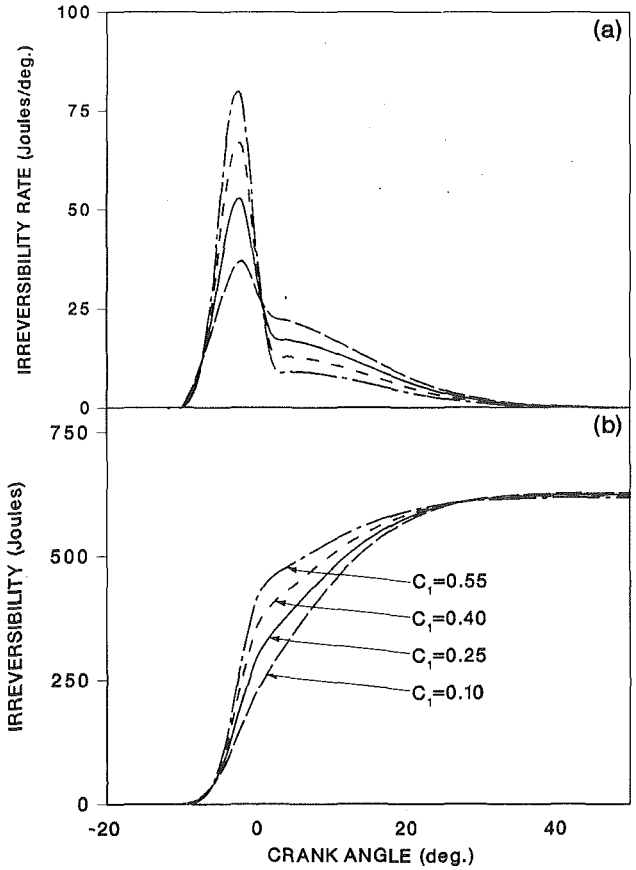

Fig. 5 Effects of premixed burning fraction on irreversibility and irreversibility rate

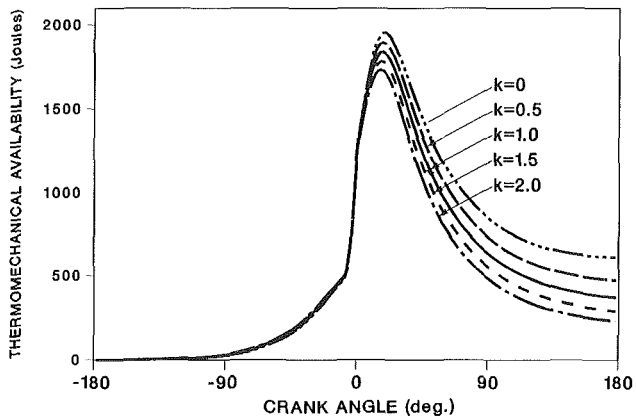

Fig. 6 Effects of heat transfer coefficient on thermomechanical availability

C_1 in equation (5) that represents the fraction of fuel burned in the premixed mode. In an actual engine this could correspond to burning a fuel with different cetane number, causing changes in ignition delay and the proportion of premixed burning. Swirl and injection rate can also affect the fraction of fuel burned in the premixed mode [17]. The fraction of fuel burned in the premixed mode was varied over a wide range that would bracket normal engine operation and extend to high values where excessive noise and nitric oxide emissions would occur. The curves in Fig. 5 show that the effects of the shape of the heat release curve on the overall irreversibility are slight. This reflects the fact that in this model the primary source of irreversibility is chemical reaction, and that changing the shape of the heat release curve affects when the irreversibilities occur, but does not affect the net amount of irreversibility.

Effects of Heat Transfer Correlation Parameters. The effects of varying the heat transfer correlation parameters on the availability balance were explored by varying the heat transfer coefficient. Varying the heat transfer coefficient corresponds to changing engine operating parameters such as swirl or fuel injection pressure, both of which have been shown to affect the heat transfer coefficient [17]. Changing the heat transfer coefficient has a direct effect on the availability loss associated with heat transfer. In addition, the heat transfer coefficient has a significant effect on the thermomechanical availability of the cylinder gases during expansion.

Figure 6 shows the thermomechanical availability for five cases where the heat transfer coefficient predicted by Annand's heat transfer correlation is multiplied by a constant K, which is varied form 0 to 2. The curves are nearly coincidental during compression when the heat transfer rate is low. However, after the start of combustion, significant differences are evident among the cases; the adiabatic case shows about three times more availability in the cylinder gases at bottom dead center than the highest heat transfer case. This high availability is wasted if the gas is simply exhausted from the engine with no provision for an exhaust bottoming device. A turbine could recover some of the availability in the exhaust and use it either to compress air for the engine intake or drive the crankshaft directly.

Conclusion

A second-law analysis of diesel combustion has been conducted with a single-zone model. The analysis includes a detailed development of the availability balance and allows thermomechanical and chemical availability to be separated. The chemical availability, although neglected in many other studies, is shown to be significant and necessary to obtain an accurate estimate of the irreversibility. The shape and timing of the mass burning rate curve were investigated and found to have little effect on irreversibility. Decreasing the heat transfer, by decreasing the heat transfer coefficient, was found to increase the availability of the cylinder gases at the end of expansion.

Acknowledgments

The support of the Iowa State University Engineering Research Institute is greatly appreciated.

References

1 Krieger, R. B., and Borman, G. L., "The Computation of Apparent Heat Release for Internal Combustion Engines," ASME Paper No. 66-WA/DGP-4, 1966.

2 Shahed, S. M., Flynn, P. F., and Lyn, W. T., "A Model for the Formation of Emissions in a Direct-Injection Diesel Engine," *Combustion Modeling in Reciprocating Engines*, J. N. Mattavi and C. A. Amann, eds., Plenum, New York, 1980.

3 Patterson, D. J., and Van Wylen, G., "A Digital Computer Simulation for Spark-Ignited Engine Cycles," *SAE Progress in Technology Series*, Vol. 7, 1964, p. 88.

4 Flynn, P. F., Hoag, K. L., Kamel, M. M., and Primus, R. J., "A New Perspective on Diesel Engine Evaluation Based on Second Law Analysis," SAE Paper No. 840032, 1984.

5 Primus, R. J., Hoag, K. L., Flynn, P. F., and Brands, M. C., "An Appraisal of Advanced Engine Concepts Using Second Law Analysis Techniques," SAE Paper No. 841287, 1984.

6 Flynn, P. F., and Primus, R. J., "Second Law Diagnosis of Engine Performance," *Proceedings of First International Symposium on Advanced Engine Research*, Madison, WI, Sept. 13-14, 1985.

7 Moran, M. J., *Availability Analysis*, Prentice Hall, New Jersey, 1982.

8 Brzustowski, T. A., "Toward a Second Law Taxonomy of Combustion Processes," *Energy*, Vol. 5, 1980, pp. 743-755.

9 Ahrendts, J., "Reference States," *Energy*, Vol. 5, 1980, pp. 667-677.

10 Annand, W. J. D., "Heat Transfer in the Cylinders of Reciprocating Internal Combustion Engines," *Proc. Instn. Mech. Eng.*, Vol. 177, No. 36, 1963, pp. 973-990.

11 Watson, N., Pilley, A. D., and Marzouk, M., "A Combustion Correlation for Diesel Engine Simulation," SAE Paper No. 800029, 1980.

12 Olikara, C., and Borman, G. L., "A Computer Program for Calculating Properties of Equilibrium Combustion Products With Some Applications to I.C. Engines," SAE Paper No. 750468, 1975.

13 *JANAF Thermochemical Tables*, 2nd ed., National Bureau of Standards Publications, NSRDS-N35 37, Washington, DC, 1971.

14 Rossini, F. D., Pitzer, K. S., Arnett, R. L., Braun, R. M., and Pimentel, G. C., *Selected Values of Physical and Thermodynamic Properties of Hydrocarbons and Related Compounds*, American Petroleum Institute Research Project 44, Carnegie Press, Pittsburgh, PA, 1953.

15 Rodriguez, L., "Calculation of Available-Energy Quantities," *Thermodynamics: Second Law Analysis*, American Chemical Society Symposium Series No. 122, R. A. Gaggioli, ed., American Chemical Society, Washington, DC, 1980, pp. 39–59.

16 Van Gerpen, J. H., and Shapiro, H. N., "Second Law Analysis of Diesel Engine Combustion," *Analysis and Design of Advanced Energy Systems: Computer-Aided Analysis and Design*, AES-Vol. 3-3, ASME, New York, 1987, pp. 53–65.

17 Van Gerpen, J. H., Huang, C., and Borman, G. L., "The Effects of Swirl and Injection Parameters on Diesel Combustion and Heat Transfer," SAE Paper No. 850265, 1985.

Thermodynamic Analysis of Indirect Injection Diesel Engines by Two-Zone Modeling of Combustion

D. A. Kouremenos
Professor-Dr.Ing. of Thermodynamics.

C. D. Rakopoulos
Professor Assoc.-Dr.Ing. for I. C. Engines.

D. Hountalas
Dr. Ing., Research Assistant.

Thermal Engineering Section,
Mechanical Engineering Department,
National Technical University of Athens,
Athens 106 82, Greece

This work presents a thermodynamic analysis of a naturally aspirated, four-stroke, diesel engine with a swirl prechamber, under firing conditions during the open and closed part of the cycle. For calculating the heat exchange between gas and walls in both the main chamber and (swirl) prechamber, the relevant characteristic velocities and lengths are calculated by setting up a zero-dimensional energy cascade turbulence model. One-dimensional, quasi-steady, compressible flow with heat transfer inside the throat passageway connecting the two chambers is used. Combustion in both the main chamber and the swirl prechamber is attacked by proposing a two-zone combustion model, and following the movement of the spray plume inside an air solid body rotation environment in the prechamber and its later progression into the main chamber through the connecting throat. To validate the analysis, an extensive experimental investigation is undertaken at the laboratory of the authors on a flexible Ricardo, single-cylinder, swirl chamber diesel engine, and evaluating its performance in a wide range of operating conditions. The experimental results are found to be in good agreement with the theoretical results obtained from the computer program implementing the analysis.

Introduction

Analytical techniques have been developed for predicting the performance and exhaust emissions of diesel engines. The first attempts to simulate the diesel engine cycle substituted the "internal combustion" by "external heat addition" (Obert, 1973; Ferguson, 1986), and later apparent heat release rates were empirically correlated to fuel injection rates (Benson and Whitehouse, 1979) in order to model the transient and heterogeneous character of diesel combustion. For direct injection diesel engines the state of the art of cycle simulation has proceeded from one-zone (Benson and Whitehouse, 1979; Whitehouse and Way, 1969-70) to two-zone (Benson and Whitehouse, 1979; Kouremenos et al., 1986; Kouremenos et al., 1987a) and multizone (Khan et al., 1971; Hodgetts and Shroff, 1975; Whitehouse and Abughres, 1975; Chiu et al., 1976; Hiroyasu et al., 1983; Kouremenos et al., 1987b) modeling, with high predictive powers, but with increased computing time (cost).

However, for indirect injection diesel engines the art of modeling seems to be in its infancy. The main reason is the additional complexity due to flow and heat transfer interactions between the two chambers, which are unknown in many respects, especially under firing conditions. Recent attempts at such modeling have been reported by Watson and Kamel (1979), Kamel and Watson (1979), Mansouri et al. (1982), Kort et al. (1982), Meintjes and Alkidas (1982), and Pinchon and Guillot (1985). All these works concentrate on swirl-type prechambers, the emphasis being on modeling flow and heat transfer processes, while when combustion is treated, it is modeled in a rather simple way, which does not represent the real physical and chemical processes involved.

Detailed combined experimental and theoretical work is reported by Kort et al. (1982) and Mansouri et al. (1982). They used a stochastic model for the combustion and mixing process in the cycle simulation of a swirl chamber diesel engine and verified their model over a certain number of operating conditions (from light to midload). The difficulties of modeling such an engine's (swirl prechamber type) behavior, even for the performance side, can be clearly deduced from their work, which was made harder by the existence of small pressure differences between the two chambers.

For (plain) precombustion chamber diesel engines, an experimental work has appeared by Yoshida et al. (1982), while Kouremenos et al. (1987c) model the processes in the cylinder of such an engine under motoring conditions for the closed cycle only. A recent work by the present authors (Kouremenos et al., 1988) gives a simulation program of the cycle of a plain precombustion chamber, naturally aspirated, four-cylinder, four-stroke diesel engine, under firing conditions, where the basic mechanisms are recognized and represented in the analysis. For the combustion period a modification of the Whitehouse-Way monozone model was used (Whitehouse

Contributed by the Advanced Energy Systems Division and presented at the ASME Winter Annual Meeting, Chicago, Illinois, November 27–December 2, 1988. Manuscript received by the Advanced Energy Systems Division January 25, 1989; revision received June 6, 1989.

and Way, 1969-70). The results of the analysis were validated with experimental data from a MAN engine at the authors' laboratory.

Going one step further, the present work gives a thermodynamic analysis of a monocylinder, naturally aspirated, four-stroke diesel engine with a swirl prechamber, under firing conditions, during the open and closed part of the cycle. For the calculation of the heat exchange between gas and walls in both main chamber and (swirl) prechamber, the relevant characteristic velocities and lengths are calculated by setting up a zero-dimensional energy cascade turbulence model (Kouremenos et al., 1988). One-dimensional, quasi-steady, compressible flow with heat transfer inside the throat passageway connecting the two chambers is used. Combustion in both the main chamber and the swirl prechamber is attacked by proposing a two-zone combustion model, following the movement of the spray plume inside an air solid body rotation environment in the prechamber and its later progression into the main chamber through the connecting throat.

It is felt that such a rigorous analysis is needed for predicting the quite peculiar behavior of indirect injection diesel engines performance-wise, which differs from that of direct injection engines (Heywood, 1988), while at the same time paving the way for emission predictions from such engines. At this point it is mentioned that the results of recent multidimensional codes of flow in diesel engines (Butler et al., 1981; Kouremenos et al., 1987d) may be used insofar as they can assist in the elucidation of flow processes, mainly in the swirl prechamber (Meintjes and Alkidas, 1982) and fuel spray trajectory.

To validate the analysis, an extensive experimental investigation was undertaken at the authors' laboratory on a flexible Ricardo E-6 (Kouremenos and Rakopoulos, 1986), single-cylinder, swirl chamber diesel engine, evaluating its performance in a wide range of operating conditions.

In comparing experimental and theoretical results, the rather high pressure difference encountered between the two chambers (from full to midload) of the present engine led to useful pressure indicator diagrams. A sensitivity analysis, presented at the end of the paper, shows a high insensitivity of the overall model predictions, when changing the calibration constants over a wide range.

Readers may be interested in a related work by the present authors confirming that this model is very successful with respect to emission for the same type of engine (Kouremenos et al., 1989a). For these emission predictions, the present model is supplemented with the successful NO kinetics scheme of Lavoie et al. (1970) and the net soot formation model of Hiroyasu et al. (1983), while keeping the same set of calibration constants.

General Description of the Model

In the present analysis the closed and open part of the cycle of an indirect injection (IDI) diesel engine is examined. The analysis models the processes occurring in the four control volumes (main chamber, prechamber, inlet, and exhaust manifolds) by treating them as open thermodynamic systems that are continuously exchanging mass, heat, and work among them. Its main purpose is to predict accurately the influence of major operating conditions (such as speed, load, and injection timing) upon the engine performance (brake mean effective pressure, specific fuel consumption, maximum pressures).

The combustion process is attacked by separating the prechamber and the main chamber into two control volumes each: a burning zone and a pure air zone. This kind of two-

Nomenclature

a = major axis of jet cross section ellipse, m
a_m = constant in turbulent diffusivity expression, m^{-1}
A = cross-sectional area, m^2
A_{eq} = equivalent area, m^2
(AFR) = actual air fuel ratio
$(AFR)_{st}$ = stoichiometric air fuel ratio
b = minor axis of jet cross section ellipse, m
b_m = exponent of velocity in turbulent diffusivity expression
B = mass of injected fuel per pump stroke and injector hole, mg
c = penetration coefficient
c' = radiation constant, W/m^2K^4
c_d = discharge coefficient
CR = compression ratio
d = diameter, m
d_{eq} = equivalent diameter, m
d_{inj} = injector hole diameter, m
D_t = turbulent diffusivity constant in mixing model, s^{-1}
E = mean flow kinetic energy, J
E_c = reduced activation energy, K
E_{kin} = kinetic energy in prechamber, J
E_ω = kinetic energy of swirling flow, J
F = wall surface area, m^2
h = specific enthalpy, J/kg
h_{tr} = gas specific enthalpy change due to heat exchange in the throat, J/kg
J = momentum, kg m/s
k = turbulent kinetic energy, J
K = burning rate coefficient, $K^{1/2}\ bar^{-1}\ s^{-1}$
l = characteristic length or thermohydraulic diameter, m
m = mass, kg
$\dot{m}$ = mass flow rate, kg/s
n = exponent in jet velocity expression
N = engine rotational speed, rpm
P = pressure, N/m^2
$\bar{P}_{mf}$ = friction mean effective pressure, bar
P_{O_2} = partial pressure of oxygen, bar
Q = heat transfer to walls, J
r_{eq} = equivalent radius of main chamber jet or prechamber jet cross sectional area, m
r_{eqo} = as above, but at the beginning of the jet, m
r_i = distance along the wall jets, m ($i = 5$ or 6)
r_k = radius of cross section of prechamber, m
r_{oi} = wall jets transition length, m ($i = 5$ or 6)
r_p = spherical prechamber radius, m
s = spray tip trajectory, m
SMD = Sauter mean diameter, m
t = time, s
T = absolute temperature, K
u = velocity, m/s
$\bar{u}$ = mean gas velocity, m/s
u' = turbulent velocity component, m/s
u_d = mean flow velocity, m/s
u_{inl} = inlet flow velocity in a control volume, m/s
u_o = initial velocity of main chamber jet, m/s
V = volume, m^3
w = wall jet velocity, m/s
w_o = initial wall jet velocity, m/s
x = coordinate in x direction, m

zone modeling, which is rather common in direct injection (DI) diesel engines, is difficult to apply in the IDI diesel engine due to the continuous mass and energy exchange between the two chambers and the multiplicity of parameters involved. For the calculation of the heat transfer in both the main chamber and prechamber, a consistent turbulence model is incorporated (Launder and Spalding, 1972; Kouremenos et al., 1988).

For combustion modeling, special care is given to representing the air movement and fuel spray movement inside the prechamber and its later progression into the main chamber through the connecting throat, both before and after impingement, as explained in the pertinent sections describing the burned zones in the two chambers.

The following assumptions are made:

(*a*) Spatially uniform pressure and composition in each control volume.

(*b*) Working medium considered as a perfect gas mixture containing in general eleven species (O_2, N_2, CO_2, H_2O, H_2, OH, H, NO, N, CO, O). For the dissociation of the chemical species, the chemical equilibrium calculational scheme of Vickland et al. (1962) is used.

(*c*) Instantaneous mixing of incoming stream into any control volume.

(*d*) For mass exchange between any control volumes, one-dimensional, quasi-steady, compressible flow has been used (Ferguson, 1986; Heywood, 1988).

(*e*) Inside the main chamber and the prechamber two zones are considered, a burning one consisting of air plus fuel and burned products and an unburned one consisting of pure air, each zone possessing its own temperature and composition.

(*f*) Blowby has been considered by using a model (Kouremenos et al., 1987e) developed by the present authors, although its effect has been proved to be of minor importance.

(*g*) The modeling of the fuel injection system follows the analysis of Kouremenos et al. (1989b).

The basic indirect injection engine geometry considered here is depicted in Fig. 1.

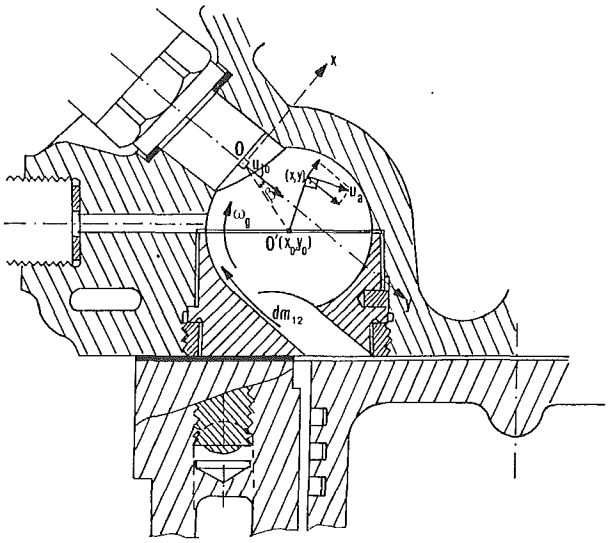

Fig. 1 Prechamber geometry

Conservation Equations

The conservation equations for the total mass and fuel (dodecane) mass in each control volume ($i=1, 2, 3, 4$) is applied. Specifically for the main chamber ($i=1$) and the

Nomenclature (cont.)

x' = exponent in prechamber jet penetration equation
x_{mix} = mixing length of main chamber jet, m
y = coordinate in y direction, m
y_{mix} = mixing length of prechamber jet, m
z = chemical delay coefficient, ms•bar$^{2.5}$
α = convective heat transfer coefficient, W/m^{2}K
β = injector nozzle inclination, rad
γ_i = cone angle of radial wall jet, rad ($i=5$ or 6)
δ_i = wall jet thickness, m ($i=5$ or 6)
δ_{oi} = wall jet initial thickness, m ($i=5$ or 6)
ΔP = injection pressure difference, N/m^2
ϵ = viscous dissipation rate per unit mass, W/kg
ζ = turbulence coefficient
ϑ = cone half angle of free jet, rad
ϑ_a = angle between air and jet velocities, rad
λ = thermal conductivity, W/mK
ρ = density, kg/m^3
Φ = equivalence ratio = $(AFR)_{st}/(AFR)$
ω = angle between jet axis and piston surface at the point of impingement, rad
ω_g = angular velocity of swirling flow in prechamber, rad/s

Subscripts

1, 2, 3, 4, = pertaining to main, prechamber, inlet, and exhaust manifolds, respectively
5, 6 = referring to left and right radial wall jets
a = air
b = burned
bu = mass entrained from unburned to burned zone
f = fuel
g = gas
i = index denoting control volume or left/right radial wall jets
in = incoming
inl = inlet
j = index denoting any other control volume
j = jet
mac = macromixed quantity
mic = micromixed quantity
o = initial value
t = throat
tot = total
u = unburned
w = wall
x = index referring to x coordinate
y = index referring to y coordinate

Dimensionless numbers

Nu = Nusselt number
Pr = Prandtl number
Re = Reynolds number

Abbreviations

°CA = degree crank angle
A = after
B = before
BMEP = brake mean effective pressure
BSFC = brake specific fuel consumption
BDC = bottom dead center
EVO = exhaust valve opening
IVC = inlet valve closing
ISFC = indicated specific fuel consumption
TDC = top dead center

prechamber ($i=2$), the mass conservation principle is applied also between the unburned and the burned zone (Kouremenos et al., 1988). It is to be noted that in the prechamber and up to the time when the flow reverses direction, from the prechamber into the main chamber, the burned zone has covered the area around the connecting passageway, while other parts of the prechamber may be still occupied by the air zone (Meintjes and Alkidas, 1982; Pinchon and Guillot, 1985).

The energy conservation and the perfect gas state equations are applied for both zones of each chamber ($i=1, 2$), together with the volume constraint equations, to yield five differential equations (Rakopoulos, 1986) with five unknowns, T_{iu}, T_{ib}, V_{iu}, V_{ib}, and P_i. Dissociation is taken into account, and the internal energy terms in the energy equations are functions of mass, temperature, and composition (Rakopoulos, 1988). Internal energies include the sensible part measured from 0 K and the energy of formation there, so that the heat of combustion is thus taken into account implicitly (Benson and Whitehouse, 1979).

Combustion Model

Combustion Mechanism. The combustion model described in this section is applied to both the prechamber and the main chamber. It is based on both mechanisms that control combustion, i.e., evaporation of liquid fuel (which is in the form of droplets) and mixing with the entrained air into the burning zone to form a combustible mixture (Kouremenos et al., 1987b, 1987f). Burning is modeled via an Arrhenius formula (Obert, 1973; Whitehouse and Way, 1969–70).

Evaporation Model. Fuel is assumed to enter the zone in the form of droplets having a diameter d equal to the Sauter mean diameter SMD (Benson and Whitehouse, 1979; Hiroyasu et al., 1983)

$$\text{SMD} = 23.9\Delta P^{-0.135}\rho_g^{0.12}B^{0.131} \tag{1}$$

and an initial temperature T_{lo}. The droplets then heat to the saturation temperature and evaporate.

Basically the model proposed by Borman and Johnson (1962) is followed. The injected fuel is divided into packages of SMD, in intervals of a unit time step, and calculation is made of the temperature and diameter of each group, taking into account the fact that the gas pressure and temperature are variable with time, thus affecting the properties of the liquid droplets in both chambers.

When the droplets enter the main chamber they continue to heat up and evaporate until they are all evaporated. The model follows the position of each group inside the burned zone of the prechamber in order to know the time of their entering the main chamber, where they are also followed inside the burning zone of the main chamber.

Mixing Model. The evaporated fuel must further mix with the surrounding air to form a combustible mixture. The mixing rate is controlled by turbulent diffusion. The evaporated fuel and the air entrained into the zone are divided into two portions, a macromixed and a micromixed one (Khan et al., 1971; Hodgetts and Schroff, 1975). When a mass of fuel evaporates or a mass of air enters the burned zone it is considered as macromixed, and when these two mix together they are then considered micromixed. The corresponding rates are described by the following equations:

$$\left.\begin{aligned} \dot{m}_{f\text{mic}} &= D_t(u)\cdot(m_{f\text{mac}} - m_{f\text{mic}}) \\ \dot{m}_{a\text{mic}} &= D_t(u)\cdot(m_{a\text{mac}} - m_{a\text{mic}}) \\ D_t(u) &= a_m \cdot u^{b_m} \end{aligned}\right] \tag{2}$$

where a_m and b_m are constants chosen in a way to give the best fit in maximum pressure (during combustion) between the calculated and the experimental pressure time diagrams.

In equations (2), $D_t(u)$ is a turbulent diffusivity constant, which, for the purpose of this work, is considered as a function of the relative velocity u of the burned zone element with respect to the surrounding air. Therefore mixing is implicitly effected through air–fuel motions.

Ignition Delay (Chemical) Model. Before the mixture ignites, it undergoes a delay period that has two components, a physical and a chemical one (Wakil et al., 1956). The chemical delay is modeled following Kadota et al. (1976), where the ignition delay of a droplet in high-pressure and temperature environments is considered. The degree of completion of chemical preparation is characterized by the integral S_{pr}, given by

$$S_{pr} = \int_0^t \frac{1}{zP_g^{-2.5}\Phi^{-1.04}\exp(5000/T_g)}dt \tag{3}$$

Ignition initiates when the previous integral becomes equal to one, having started from a zero value when the fuel first appeared in the gaseous form.

Burning Model. Burning is modeled by an Arrhenius equation of the form (Hodgetts and Schroff, 1975; Whitehouse and Abughres, 1975)

$$\dot{m}_{fb} = \begin{cases} K\dfrac{(m_{f\text{mic}} - m_{fb})}{\sqrt{T}}e^{-E_c/T}P_{O_2}, & \text{if (AFR)} > \text{(AFR)}_{st} \\ K\dfrac{(m_{a\text{mic}} - m_{ab})}{(\text{AFR})_{st}\sqrt{T}}e^{-E_c/T}P_{O_2}, & \text{if (AFR)} < \text{(AFR)}_{st} \end{cases} \tag{4}$$

where K is a constant chosen to give the desired, compared to experimental, burning rate.

The mass of unburned fuel entering the main chamber is a portion of the fuel injected in the prechamber. Since the flow entering the main chamber from the prechamber has been assumed of uniform composition (of the prechamber's burned zone), the mass of fuel (number of droplets evaporated or not) that enters the main chamber is given by

$$dm_{1f} = \frac{dm_{12}}{m_{2b\text{tot}}}m_{2f\text{tot}} \tag{5}$$

Chemistry of Combustion. Combustion is assumed to be perfect only in a first approximation, the real products being defined by dissociation considerations. For the C–H–O–N system the complete chemical equilibrium scheme proposed by Vickland et al. (1962) is used. The following 11 species are included in the calculation: N_2, O_2, CO_2, H_2O, CO, H_2, NO, OH, N, H, and O.

Description of Burned Zone in the Main Chamber

The gases flowing out of the prechamber into the main chamber to form a burned zone consist of fuel, air, and combustion products. The transient jet formed here is more complicated, in comparison to the one formed in a DI diesel engine from the injector, because of its continuously changing conditions at the throat exit.

In the present work the jet formation and mixing process is modeled based on the conservation equations for mass and momentum, so that the jet is represented via a transient equivalent jet. If during a time step dt_i at time t_i an element of mass dm_i enters the main chamber having a velocity of u_i and a density ρ_i, then at time t, since the moment of first mass entrance ($t_o=0$), the following amounts of mass and momentum have entered the main chamber:

$$J_{in} = \sum_t (\rho_i u_i dV_i) = \sum_t u_i dm_i,\ m_{in} = \Sigma dm_i \tag{6}$$

If during this time period an equivalent jet existed at the throat with an initial velocity u_o, an equivalent diameter d_{eq}, and a uniform density ρ_o equal to the instantaneous one of the burned zone, the following equations would apply ($J_{\text{jet}} = J_{in}$ and $m_{\text{jet}} = m_{in}$):

$$\left.\begin{aligned} J_{\text{jet}} &= A_{eq}\rho_o u_o^2 t \\ m_{\text{jet}} &= A_{eq}\rho_o u_o t \end{aligned}\right] \rightarrow u_o = \frac{J_{\text{jet}}}{m_{\text{jet}}} \rightarrow u_o = \frac{J_{in}}{m_{in}} \tag{7}$$

$$A_{eq} = \frac{m_{\text{jet}}}{\rho_o u_o t} = \frac{m_{in}}{\rho_o \frac{J_{in}}{m_{in}} t} = \frac{m_{in}^2}{\rho_o J_{in} t} \tag{8}$$

In order to calculate the rate at which the jet entrains air from its surroundings, a velocity distribution on its axis is assumed similar to that of a transient turbulent jet (in an open chamber) (Williams, 1973; Hiroyasu et al., 1983), i.e.,

$$u(x) = \begin{cases} u_o, \text{ if } x \le x_{\text{mix}} \\ u_o \left(\dfrac{x_{\text{mix}}}{x}\right)^n, \text{ if } x \ge x_{\text{mix}} \end{cases} \tag{9}$$

where x_{mix} is the mixing length and n a constant chosen by trial and error equal to 0.5 in order to give the best results concerning reasonable jet cone angle and air entrainment rate values.

From equations (9) we get

$$x = \begin{cases} u_o t, \text{ for } 0 < t \le t_o \\ [(1+n)u_o x_{\text{mix}}^n (t - t_o) + x_{\text{mix}}^{n+1}]^{\frac{1}{n+1}} + u_o t_o, \text{ for } t \ge t_o \end{cases} \tag{10}$$

where $t_o = x_{\text{mix}}/u_o$.

Therefore in order to calculate the air entrainment rate, which is given by the increase of volume of the jet $dm_{1bu} = \rho_o \cdot dV_{1bu}$, the equivalent cone half angle ϑ of the jet must be calculated. To achieve this, the momentum conservation equation during the time period t can be applied, i.e.,

$\vartheta = 0$ deg, for $0 \le x \le x_{\text{mix}}$

$$J_{in} = A_{eq} x_{\text{mix}} \rho_o u_o + \pi \rho_o \int_{x_{\text{mix}}}^{x} u_o \left(\frac{x_{\text{mix}}}{x}\right)^n \left(x - x_{\text{mix}} + \frac{r_{eqo}}{\tan \vartheta}\right)^2 \tan \vartheta \, dx, \text{ for } x > x_{\text{mix}} \tag{11}$$

Relation (11) is a second-order equation with respect to tan ϑ. By solving this equation, mean values of about $\vartheta = 10$ deg are found for all cases concerned, which are in good agreement with values reported in the literature concerning turbulent jets (Chiu et al., 1976; Spalding, 1979; Hiroyasu et al., 1983).

Thus the net entrainment rate of air mass into the jet, by also considering the initially entered one dm_{12}, is given by

$$\frac{dm_{1bu}}{dt} = \frac{dV_{1bu}}{dt}\rho_o - \frac{dm_{12}}{dt} \tag{12}$$

In the calculations, during the major part of this process, it has been observed that the velocity at the throat is almost constant, since the pressure difference between the two chambers changes slightly. Due to this fact, the equivalent diameter is found to be very close to the actual one d; the initial jet velocity u_o is almost constant and very close to the instantaneous throat velocity. Thus it is reasonalbe to believe that any error introduced due to the steady-state consideration is small and in any case the estimates are very close to reality, so that a good prediction of the mixing mechanism is achieved.

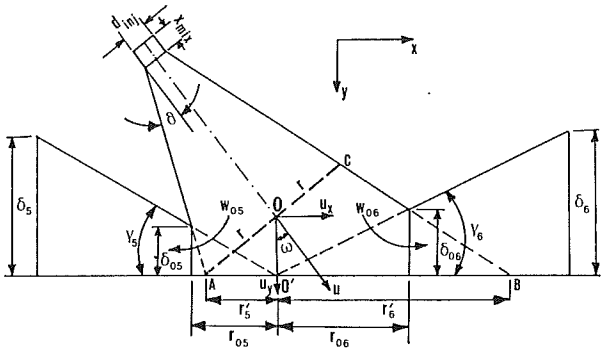

Fig. 2 Main chamber jet trajectory

When the jet hits the piston crown at a certain angle, it generally forms two radial wall jets, a left one and a right one. In order to examine the jet impingement on the piston, the jet is divided as shown in Fig. 2 into two jets, parallel (x) and perpendicular (y) to the piston crown. The equivalent velocities u_x and u_y satisfy the mass and energy conservation equations, i.e.,

$$\left.\begin{aligned} \rho A_x u_x + \rho A_y u_y &= A u \rho \rightarrow u_x \sin\omega + u_y \cos\omega = u \\ \frac{1}{2}\rho A_x u_x^3 + \frac{1}{2}\rho A_y u_y^3 &= \frac{1}{2} A u^3 \rho \rightarrow u_x^3 \sin\omega + u_y^3 \cos\omega = u^3 \end{aligned}\right] \tag{13}$$

where $A = \pi r^2$ and $A_x = A \sin\omega$, $A_y = A \cos\omega$.

The system of equations (13) is solved by incorporating a Newton–Raphson procedure.

The jet corresponding to u_x continues its path parallel to the piston crown surface, while the jet corresponding to u_y is divided equally to the left and right directions. Applying the continuity and energy conservation equations between the overall undeflected jets and the corresponding wall jets, at the transition region, we obtain

$$\left.\begin{aligned} \rho\pi\delta_{05} r_{05} w_{05} &= \rho\frac{A_y u_y}{2}, \qquad \rho\pi\delta_{06} r_{06} w_{06} = \rho\frac{A_y u_y}{2} + \rho A_x u_x \\ \frac{\rho\pi\delta_{05} r_{05} w_{05}^3}{2} &= \frac{\rho A_y u_y^3}{4}, \qquad \frac{\rho\pi\delta_{06} r_{06} w_{06}^3}{2} = \rho\frac{A_y u_y^3}{4} + \rho\frac{A_x u_x^3}{2} \end{aligned}\right] \tag{14}$$

From this set of equations the initial wall jet velocities w_{05} and w_{06} are obtained as follows:

$$\left.\begin{aligned} w_{05}^2 &= u_y^2 \\ w_{06}^2 &= \frac{A_y u_y^3 + 2A_x u_x^3}{A_y u_y + 2A_x u_x} \end{aligned}\right] \tag{15}$$

From this point on, the wall jet theory by Glauert (1956) is considered giving the following downstream values in the wall jet directions:

$$\left.\begin{aligned} w_5 &= w_{05}\frac{r_{05}}{r_5},\ \delta_5 = r_5 \tan\gamma_5 \text{ and } \tan\gamma_5 = \frac{\delta_{05}}{r_{05}} \\ w_6 &= w_{06}\frac{r_{06}}{r_6},\ \delta_6 = r_6 \tan\gamma_6 \text{ and } \tan\gamma_6 = \frac{\delta_{06}}{r_{06}} \end{aligned}\right] \tag{16}$$

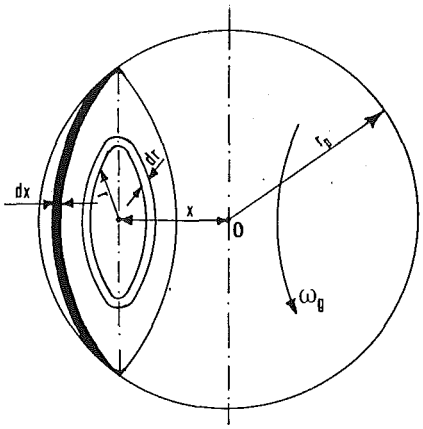

Fig. 3 Swirl structure in prechamber

So there are two additional unknowns for each jet, that is the initial thickness δ_{05}, δ_{06} and the transition length r_{05}, r_{06} (Idoum et al., 1985). These two can be calculated by considering the jet geometry depicted in Fig. 2 and the relevant continuity equations, i.e.,

$$\left.\begin{aligned} \pi r_{05}\delta_{05}w_{05} &= \rho\frac{A_y u_y}{2},\ \tan(\omega-\vartheta)=\frac{r_{05}-r_5'}{\delta_{05}},\\ r_5' &= r\cos\omega\\ \pi r_{06}\delta_{06}w_{06} &= \rho\frac{A_y u_y}{2}+\rho A_x u_x,\ \tan(\omega+\vartheta)=\frac{r_{06}-r_6'}{\delta_{06}},\\ r_6' &= AB-r_5 \end{aligned}\right\} \quad (17)$$

where

$$AB = 2r\cos\omega + 2r\sin\omega\tan(\omega+\vartheta). \quad (18)$$

Combining these equations we obtain two quadratic equations with respect to r_{05}, r_{06}, from which they are calculated by taking also into account that $0'A < r_{05}$ and $0 < r_{06} < 0'B$. Then δ_{05}, δ_{06} are found.

Once the geometry of the wall jet is determined, the entrainment rate is calculated from

$$dm_i = \rho_i dV_i,\quad V_i = \frac{1}{3}\pi\tan\gamma_i(r_i^3 - r_{0i}^3) \qquad (i=5,\ 6) \quad (19)$$

It is observed that the impingement causes a considerable increase in air entrainment rate compared to that of the free jet. The previous calculation is repeated at each time step from the beginning, because the piston moves downward so that there is a considerable change of geometry.

Description of Burned Zone in the Prechamber

In the prechamber there is not the largely transient nature of the main chamber's jet, since the initial fuel velocity can be considered constant throughout the entire injection period. But here an additional problem arises due to the extremely swirling motion of the air and its effect upon fuel air mixing. This mechanism is modeled in the present section to take into account the influence of various operating conditions, such as speed, load, and injection timing, upon combustion. From experimental investigations and extended two-dimensional codes (Dent and Derham, 1974; Morris and Dent, 1976; Mansouri et al., 1982; Meintjes and Alkidas, 1982; Pinchon and Guillot, 1985) considering air motion in the absence of combustion, one can observe that the flow field, up to the time when the flow reverses direction (which is the major mixing interval), is very close to the flow field produced by a rotating solid body. From a turbulence model ($k\sim\epsilon$) (Launder and Spalding, 1972) based on kinetic energy addition (as described in a later section), the mean velocity $\bar{u}$ is calculated inside the prechamber at each instant of time. Eventually, by also considering a solid body flow rotation, an angular velocity ω_g can be calculated that gives the same total kinetic energy. Therefore referring to Fig. 3, we get

$$E_{\text{kin}} = \frac{1}{2}m\bar{u}^2 \quad (20)$$

$$E_\omega = \frac{1}{2}\,2\rho\int_{x=0}^{x=r_p}\int_{r=0}^{r=r_k} 2\pi r dr dx (r\omega_g)^2 \rightarrow$$

$$E_\omega = 2\pi\rho\int_0^{r_p}\int_0^{r_k} r^3\omega_g^2 dr dx \quad (21)$$

Combining these two equations we have

$$\omega_g = \frac{\bar{u}}{r_p}\sqrt{\frac{5}{2}} \quad (22)$$

so that $u_{\max} = \sqrt{5/2}\,\bar{u}$. It should be noticed that the above integral is calculated without taking into account the velocity drop (up to zero value) in the thin boundary layer attached to the prechamber wall. Since the thickness of this boundary layer is relatively small, the error in calculating ω_g should be, in any case, very small.

Having the flow pattern, one can now examine the jet arising from the injector having an inclination β as shown in Fig. 1. From experimental investigations of fuel penetration (Williams, 1973; Hiroyasu et al., 1983) a general equation of the following form is suitable ($c\cong 2.5$ to 3.0 from Morris and Dent, 1976):

$$y = c(\Delta P/\rho_g)^{0.25} d_{inj}^{0.5}\ t^{x'} \rightarrow$$

$$\frac{dy}{dt} = x' c(\Delta P/\rho_g)^{0.25} d_{inj}^{0.5}\ t^{x'-1}$$

$$\rightarrow u_{jy} = \frac{dy}{dt} = \frac{x'[c(\Delta P/\rho_g)^{0.25}\ d_{inj}^{0.5}]^{1/x'}}{y^{(1-x')/x'}} \quad (23)$$

Concerning equation (23), Williams (1973) and Chiu et al. (1976) report values of x' between 0.5 and 0.7. Therefore in the present work we take $1/x' = 1.7$ (i.e., $n=(1-x')/x' = 0.7$ as given in Table 2), so that the calculated penetration agrees with values from the literature (Dent and Derham, 1974; Hiroyasu et al., 1983). The major effort is now concentrated on the calculation of the centerline trajectories (see Fig. 4). To do this, an air velocity distribution on the jet axis is assumed (Hodgetts and Shroff, 1975; Morris and Dent, 1976; Idoum et al., 1985) that has been adopted for the effect of swirl in open chamber diesel engines (see Fig. 1)

$$\frac{dx}{dt} = u_{jx} = \begin{cases} u_{jxo} = 0, \text{ if } 0\le y\le y_{\text{mix}} \\ u_{ax} \text{ if } y > y_{\text{mix}},\ u_{ax} = -\omega_g(y-y_o) \end{cases} \quad (24)$$

$$\frac{dy}{dt} = u_{jy} = \begin{cases} u_{jyo} = c_d(2\Delta P/\rho_f)^{0.5} \text{ if } 0\le y\le y_{\text{mix}} \\ (y_{\text{mix}}/y)^n u_{jyo} + u_{ay} \text{ if } y > y_{\text{mix}}, \\ \qquad u_{ay} = \omega_g(x-x_o) \end{cases} \quad (25)$$

where u_{ax} and u_{ay} are the two components of the air velocity. The expression for u_{jy} is similar to the one derived from equation (23), if swirl were absent. From the term in brackets in

equation (23), using also equation (25), the mixing length is found $y_{mix} = 4.5 d_{inj}$. However, in order to agree with turbulent jet theory (Spalding, 1979), it is taken to be $y_{mix} = 6.5 d_{inj}$ with no serious error, the value of the coefficient n controls the mixing process.

As reported in the literature, the jet cross section in a swirling flow is of a kidney shaped (Whitehouse and Abughres, 1975; Chiu et al., 1976), but it is almost always assumed as an elliptical one with major axis a and minor axis b as shown in Fig. 4.

The rate of spread of the jet is given by the following two equations which are derived from momentum considerations of the jet flow in a swirling field (Whitehouse and Abughres, 1975):

$$\left.\begin{aligned} \frac{da}{ds} &= \frac{c_a}{2}\frac{\sqrt{u_j^2 + 2u_j u_a \cos\vartheta_a + u_a^2}}{\rho_j u_j + \rho_a u_a \cos\vartheta_a}(\rho_a + \rho_j) \\ \frac{db}{ds} &= \frac{c_b}{2}\frac{(u_j - u_a\cos\vartheta_a)}{(\rho_j u_j + \rho_a u_a \cos\vartheta_a)}(\rho_a + \rho_j) \end{aligned}\right] \quad (26)$$

where

$$u_j = \sqrt{u_{jx}^2 + u_{jy}^2},\ u_a = \sqrt{u_{ax}^2 + u_{ay}^2},\ \text{and}\ \cos\vartheta_a = \frac{\mathbf{u}_j \cdot \mathbf{u}_a}{|\mathbf{u}_j||\mathbf{u}_a|} \quad (27)$$

For simplicity in the calculations, an equivalent circular cross section with an equivalent radius r_{eq} given by

$$\pi r_{eq}^2 = \pi ab \rightarrow r_{eq} = \sqrt{ab} \quad (28)$$

is considered. Thus the rate of air entrainment is given as

$$dm_{2bu} = \rho_a dV_{2bu} = \pi r_{eq}^2 ds \rho_a = \pi ab \rho_a \sqrt{dx^2 + dy^2} \quad (29)$$

where dx, dy are given by equations (24) and (25).

When the jet hits the prechamber wall, the angle of impingement, the jet velocity, and the area of the cross section are calculated following the same procedure as adopted in the main chamber wall jet examined before (Idoum et al., 1985). Of course in this case the jet spreads almost entirely toward the swirl direction.

Mass Exchange

One-dimensional, quasi-steady, compressible flow is used to calculate the mass flow rates through the inlet and exhaust valves during the exchange process and for the calculation of mass exchange between the two chambers.

The manifolds are treated as plenums with time-varying temperature, pressure, and composition. Perfect and instantaneous mixing is assumed during the exchange period and reverse flow into the inlet manifold is also considered (Heywood, 1988).

Heat Exchange

Heat Exchange in the Throat. The heat exchange in the throat results in an enthalpy addition to the mass passing through it. This effect has proven to be very small, considering the very small area F_t. The value of enthalpy addition h_{tr} is thus given by ($dm_t = dm_{12}$)

$$h_{tr} = \frac{dQ_t/dt}{dm_t/dt} = \frac{\alpha_t F_t (T_{wt} - T)}{dm_t/dt} \quad (30)$$

where inside the throat passageway the flow is always undeveloped. Depending on whether this flow is laminar or turbulent, the appropriate formula (Incropera and DeWitt, 1985) for the Nusselt number is used, for calculating a_t in equation (30).

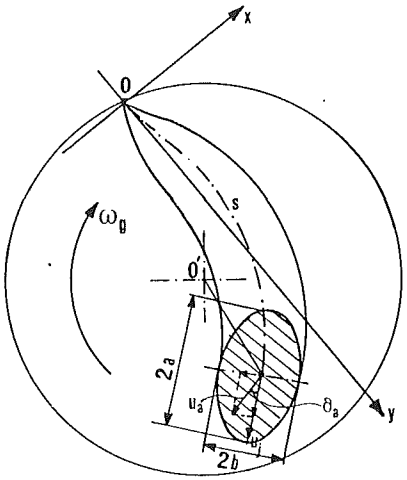

Fig. 4 Prechamber jet development

Heat Exchange in the Main Chamber and in the Prechamber. For calculating the heat exchange between gas and walls, in both chambers, the relevant characteristic velocity and length are calculated by setting up a zero-dimensional energy cascade turbulence model (Launder and Spalding, 1972; Mansouri et al., 1982; Kouremenos et al., 1988).

Mean flow kinetic energy E_i is supplied to the prechamber through the throat, and to the main chamber through the throat as well as the inlet and exhaust valves. The energy supplied to the volume i (= 1 or 2) is

$$E_i = \sum_j \frac{1}{2}\left|\frac{dm_{ij}}{dt}\right| u_{\text{inl},j}^2,\ \text{where}\ u_{\text{inl},j} = \frac{dm_{ij}}{dt}\frac{RT}{P}\frac{1}{A_j} \quad (31)$$

The mean flow kinetic energy E_i supplied to each chamber is converted to turbulent kinetic energy k_i through a turbulent dissipation process, producing turbulent kinetic energy at a rate $\dot{P}_{tk}$. Turbulent kinetic energy is then converted to internal energy through viscous dissipation at a rate of $m \cdot \epsilon$. Thus for the present examination the following equations apply (Kouremenos et al., 1988):

$$E = \frac{1}{2} m u_d^2 \ \text{and}\ k = \frac{3}{2} m u'^2\ \text{(isotropic turbulence)} \quad (32)$$

$$\frac{dE}{dt} = \frac{1}{2}\frac{dm}{dt} u_{\text{inl}}^2 - \dot{P}_{tk} - \frac{E}{m}\frac{dm}{dt} \quad (33)$$

$$\frac{dk}{dt} = \dot{P}_{tk} - m\epsilon - \frac{k}{m}\frac{dm}{dt} \quad (34)$$

For the viscous dissipation rate ϵ and for the turbulent kinetic energy production rate $\dot{P}_{tk}$ (Mansouri et al., 1982; Kouremenos et al., 1988)

$$\epsilon \cong u'^3/l_i \rightarrow \epsilon = \left(\frac{k}{1.5m}\right)^{1.5}\frac{1}{l_i} \quad (35)$$

$$\dot{P}_{tk} = \mu_{\text{tur}}\left(\frac{du_d}{dy}\right)^2 = \mu_{\text{tur}}\zeta_i\frac{u_d^2}{l_i^2} \quad (36)$$

where ζ_i is an adjustable constant selected, by trial and error, to match the experimental compression line.

In the above expressions the characteristic length l_i and the characteristic size of the large-scale eddies are both identified with the macroscale of turbulence, assumed to be equal to the diameter d_p in the prechamber and to the instantaneous main chamber height in the main chamber.

Furthermore the turbulent viscosity μ_{tur} is given by (Launder and Spalding, 1972)

$$\mu_{\text{tur}} = \rho\sqrt{k} l_i \quad (37)$$

Table 1 Engine basic specifications; type: one-cylinder, naturally aspirated, four-stroke, indirect injection, swirl prechamber diesel (Ricardo E-6, Comet MK. V)

Bore	76.2	mm
Stroke	111.2	mm
Connecting rod length	240.5	mm
Displacement volume	536	cm^3
Main chamber dead volume	13.5	cm^3
Prechamber dead volume	11.5	cm^3
Compression ratio	21.5	
Prechamber diameter (spherical)	28	mm
Throat cross section area	0.64	cm^2
Throat length	10	mm
Throat perimeter	25.1	mm
Inlet valve opening	BTDC	8 deg
closing	ABDC	36 deg
Exhaust valve opening	BBDC	43 deg
closing	ATDC	7 deg

Taking into account equations (31), (32), and (35), (36), (37), equations (33) and (34) take the final form

$$\frac{dE}{dt}=\frac{1}{2}\left(\frac{dm}{dt}\right)^3\left(\frac{RT}{PA}\right)^2-\zeta_i\rho\sqrt{k}l_i\frac{2E}{m}\frac{1}{l_i^2}-\frac{E}{m}\frac{dm}{dt} \tag{38}$$

$$\frac{dk}{dt}=\zeta_i\rho\sqrt{k}l_i\frac{2E}{m}\frac{1}{l_i^2}-m\left(\frac{k}{1.5m}\right)^{1.5}\frac{1}{l_i}-\frac{k}{m}\frac{dm}{dt} \tag{39}$$

These two equations are integrated simultaneously, giving finally

$$\tilde{u}=\sqrt{\bar{u}_a^2+u'^2} \tag{40}$$

Therefore the heat transfer coefficients (α_1, α_2) for the two chambers, assuming similar conditions for fully developed turbulent flow over a flat plate, are (Gebhart, 1971; Kamel and Watson, 1979; Kouremenos et al., 1988)

$$\alpha_i=0.037\mathrm{Re}^{0.8}\mathrm{Pr}^{0.33}\lambda_i/l_i \quad (i=1,2) \tag{41}$$

Thus in both chambers and for both zones (burned and unburned), the heat flux through the wall surface to the zones is given by

$$dQ_i/dt=F_i[\alpha_i(T_{w_i}-T_i)+c_i'(T_{w_i}^4-T_i^4)] \quad (i=1,2) \tag{42}$$

where the surface F_i for heat exchange is calculated, for both zones, by considering the jet geometry and the relevant geometry of the chamber before and after impingement. T_{wi} are selected so as to match the experimental maximum compression pressures.

Solution Procedure: Computer Program

The differential equations stated in the previous sections, describing the change of state of the gas in the two chambers, are solved simultaneously for each time step, via a computer code written in FORTRAN 77, which is executed on a CYBER CDC computer.

The integration method used is a combination of the Euler and Predictor-Corrector methods. The additional control volume in the present work (prechamber) makes convergence to a solution much more difficult than in the case of an open chamber diesel engine. The biggest time step used corresponds to $d\varphi=0.33$°CA (degree crank angle) and the smallest one to 0.10°CA, being automatically determined by the program depending on the value of dT/dt. The calculation starts at inlet valve closure. At this point an estimation (initial values) of temperature, pressure, and composition for all control volumes is made, and then a series of cycles is performed until the point where the variables do not change, from cycle to cycle, beyond a certain limit set for accuracy. In the present work convergence was achieved inside three engine cycles.

Experimental Setup and Investigation

To test the model's predictive ability, a detailed experimental investigation was conducted on a single-cylinder, Ricardo E-6, IDI diesel engine fitted with a Comet MK.V swirl prechamber. The basic engine data appear on Table 1. In the experiments the effect of various operating parameters upon engine performance was considered. Specifically, the effect of load, speed, and injection timing was studied. The engine was operated from 40 to 100 percent of full load (corresponding to an air-fuel ratio of 17:1) at each speed and injection timing selected. For all experiments the air inlet temperature was kept constant at 22°C (±1°C), the oil temperature at 65°C (±1°C), and the cooling water inlet temperature at 67°C (±1°C).

An important goal of these experiments was the accurate measurement of pressure indicator diagrams, in both the main chamber and the prechamber, under firing and motoring conditions. These were measured by using flush-mounted, water-cooled, piezoelectric "Kistler" transducers coupled to "Kistler" charge amplifiers. Special attention was paid to the calibration of these transducers, since the accuracy required for such measurements is high, considering the small pressure differences existing between the two chambers. The pressure traces were continuously monitored on a memory "Tektronix" oscilloscope, connected to a "Polaroid" camera, and were recorded using a signal-sampling system of a laboratory data-processing computer (Kouremenos et al., 1989c). Mean values from 20 consecutive runs were taken.

The experimental measurements were conducted at four speeds of 1000, 1500, 2000, and 2500 rpm, at three static injection timings of 35, 38, and 41 deg BTDC and various loads in the range of 40 to 100 percent of full load. All possible combinations of these three operating parameters values were examined.

The engine brake power output was measured via a "Laurence-Scott" NS Type, swinging field, a-c dynamometer connected to the engine, which was also used to motor the engine for determining the mechanical losses at various speeds. Since the measured values of power output and of specific fuel consumption resulting from it are "brake," a relation was incorporated into the model that gives the mean effective pressure of mechanical losses. This relation was taken from Millington and Hartless (1968) and refers specifically to the engine examined in the present work, i.e.,

$$\bar{P}_{mf}=0.123\cdot\mathrm{CR}+4.774\times10^{-4}\ \mathrm{N\ (bar)} \tag{43}$$

where the first coefficient has been adjusted so that the values derived from it agree with the measured ones. A third term included in the original formula (Millington and Hartless, 1968) is omitted here, since it refers to the pumping losses in the cycle, which are calculated separately by the gas exchange model. As can be seen, the present engine has a poor mechanical efficiency, which is due to special experimental features, such as variable compression ratio mechanisms, heavy duty construction, etc. (Ricardo, 1968).

Theoretical and Experimental Results: Comparison and Discussion

In Fig. 5 one can see the comparison between the theoretical and experimental pressure traces under motoring conditions, immediately after the engine has run for a long period at full load conditions (at 1500 rpm). It can be observed that the error is negligible, having a maximum of ±0.5 bar (the same also applies for the other speeds). The maximum pressure occurs before TDC due to the heat transfer process. The calibration of the heat transfer model was based upon these motoring experiments.

If it is required to set up a model with reasonable predictive

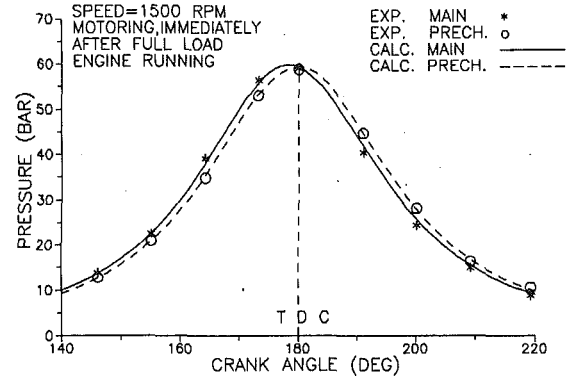

Fig. 5 Pressure versus crank angle diagram

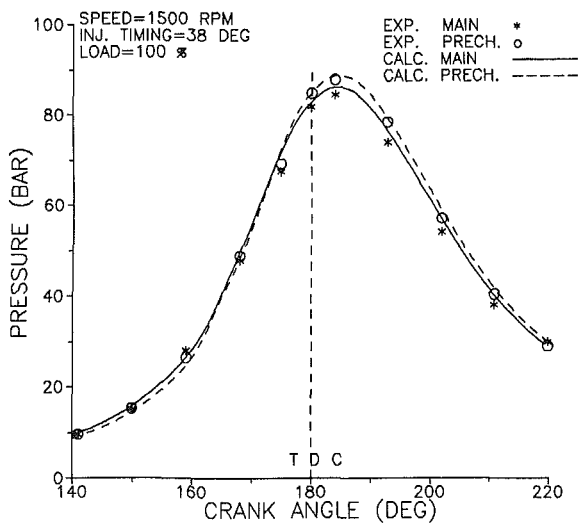

Fig. 6 Pressure versus crank angle diagram

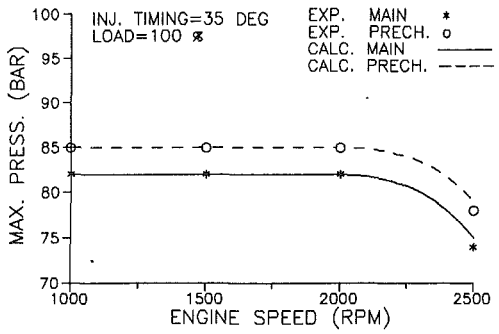

Fig. 7 Effect of speed on maximum pressure

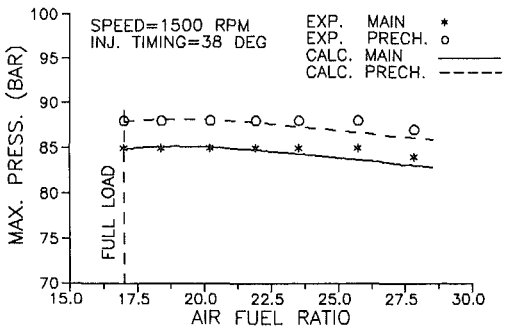

Fig. 8 Effect of AFR on maximum pressure

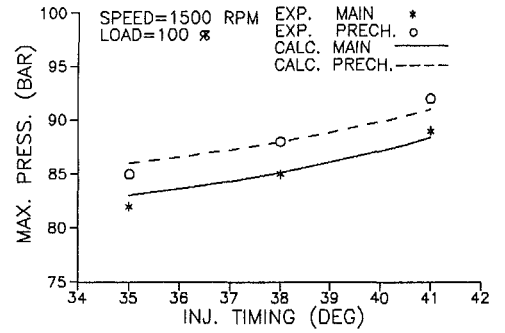

Fig. 9 Effect of injection timing on maximum pressure

abilities, it must at first be insured that the compression phase (before ignition) is well modeled, since any error introduced at the prediction of its final state is likely to be propagated and magnified later in the cycle (during combustion and expansion).

Figure 6 shows the comparison between the theoretical and experimental pressure crank angle diagrams under full load conditions, at 1500 rpm and 38 deg BTDC injection timing. The model's calibration constants, summarized in Table 2, are held constant for the whole range of operating parameters variation. As can be observed, the agreement is very good for both chambers.

Figures 7, 8, and 9 show the effect of speed, air–fuel ratio (load), and injection timing, respectively, on maximum pressure in both chambers. As shown in Fig. 7, from 1000 to 2000 rpm the maximum pressure is not effected, but from 2000 rpm up to 2500 rpm there is a slight drop. This is due to the fact that ignition delay has a significant effect on maximum pressure. When speed is increased from 1000 to 2000 rpm, the time available for fuel preparation (physical and chemical) would be reduced, causing an increase of ignition delay (in °CA), if it had not been offset by the increasing temperature (due to diminishing heat losses). When speed increases further from 2000 to 2500 rpm, the increase of temperature cannot completely counteract the effect of decrease of available time causing the ignition delay to increase, thus resulting in lower maximum pressures.

Figure 8 shows that the load (i.e., AFR) does not seriously affect the maximum pressure. This is due to the fact that at lower loads the droplet SMD is smaller, as shown by equation (1), and so with the same amount of fuel injected in the prechamber up to the time autoignition occurs (the autoignition period is shorter than the injection period), the amount of fuel evaporated would be a little higher (Spalding, 1979). The relatively lower temperature at lower loads offsets this increase, so that almost the same amount of fuel, at any load, is prepared by the time autoignition occurs. It is this amount of fuel burned (during the stage of premixed combustion), almost at constant volume, that causes the maximum pressure. It is shown clearly in Fig. 16 that the mass of fuel burned in the prechamber is almost constant at any load. The effect of injection timing on maximum pressure can be seen in Fig. 9, where the maximum pressure is shown to increase with increasing injection timing. This is due to the fact that at high injection timings ignition occurs far before TDC.

Figure 10 gives the relation (almost linear) between brake power output and engine speed at full load. The agreement between experimental and theoretical values is very satisfactory. Figure 11 shows the effect of engine AFR (i.e., load) on power output at 1500 rpm and 38 deg injection timing, where calculated and experimental values are in very good agreement.

Figure 12 presents the effect of engine AFR (load) on brake specific fuel consumption. There is a minimum at around 80 percent of full load. This is due in part to the longer duration of combustion at higher loads, causing mixing to require more

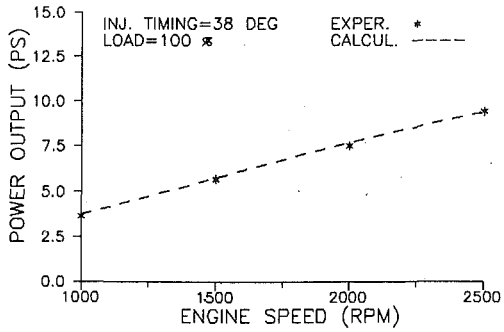

Fig. 10 Effect of speed on brake power output

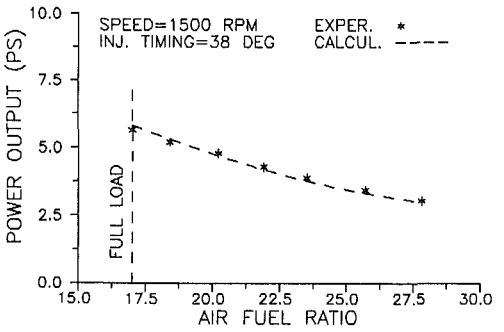

Fig. 11 Effect of AFR on brake power output

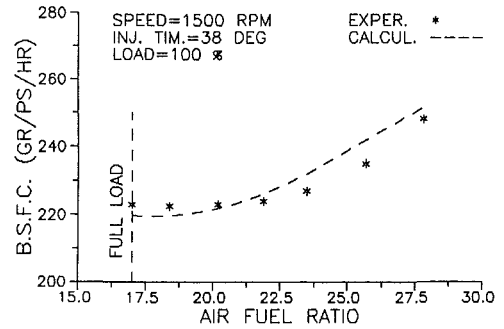

Fig. 12 Effect of AFR on brake specific fuel consumption

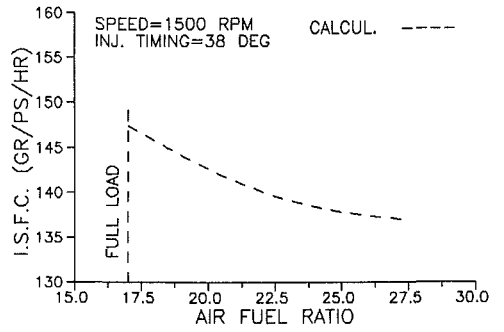

Fig. 13 Effect of AFR on indicated specific fuel consumption

time, so that combustion occurs later (and so less effectively) in the cycle and in part to the increasing mechanical losses (on a percentage basis) at lower loads, resulting in poor brake efficiency.

One can see this mechanism quite clearly by observing Fig. 13, where it is shown that indicated fuel consumption decreases with decreasing load. However at the same time the mechanical losses increase more as a percentage of power output, resulting eventually in an increase of BSFC. The model predicts therefore the engine performance, under varying loads, with satisfactory accuracy.

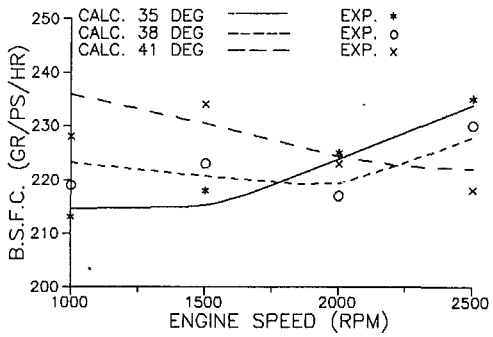

Fig. 14 Effect of speed on brake specific fuel consumption at full load

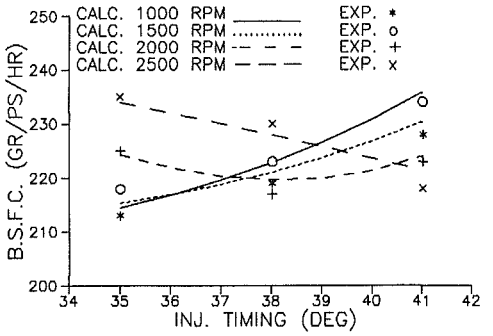

Fig. 15 Effect of injection timing on brake specific fuel consumption at full load

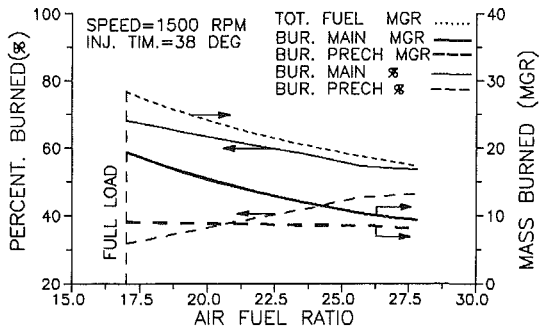

Fig. 16 Effect of AFR on total fuel burned in each chamber

Figure 14 shows the effect of engine speed upon the engine BSFC at three different injection timings: 35, 38, and 41 deg BTDC. The agreement between prediction and experiment is good. As expected the minimum in BSFC is shifted toward higher injection timings with increasing speed. On average the injection timing of 38 deg BTDC gives the best BSFC for the whole speed range, as also suggested by the manufacturer (Ricardo, 1968).

Figure 15 gives the effect of injection timing on BSFC at four different speeds. The agreement between calculated and experimental values is very good for all speeds examined. For 1000 rpm, BSFC increases with increasing injection timing. This is due to the fact that at this speed the ignition delay is small, so that as injection timing increases from 35 to 41 deg there is an early ignition and the piston consumes a great amount of work (negative). For 1500 rpm the same effect exists as for 1000 rpm, since this speed is still comparatively low for an IDI engine. At 2000 rpm the optimum value of BSFC is at 38 deg. As revealed by the model, the 35 deg injection timing causes ignition to occur very near TDC, resulting in poor efficiency. When injection timing is set to 41 deg, there is an early ignition (far before TDC) with the results mentioned above (negative work). Finally for 2500 rpm, as shown, the lowest BSFC appears at 41 deg, because at this injection tim-

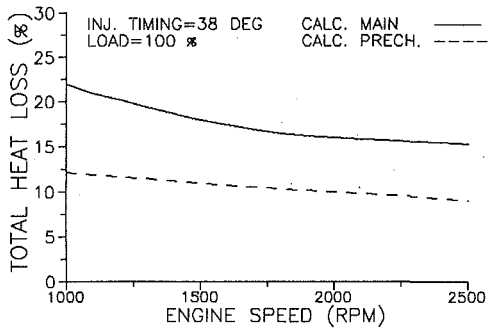

Fig. 17 Effect of speed on total heat loss in each chamber

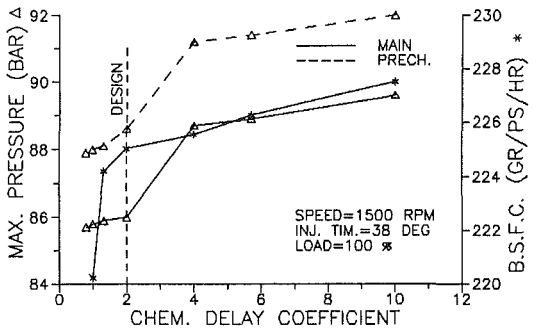

Fig. 18 Sensitivity analysis with chemical delay coefficient

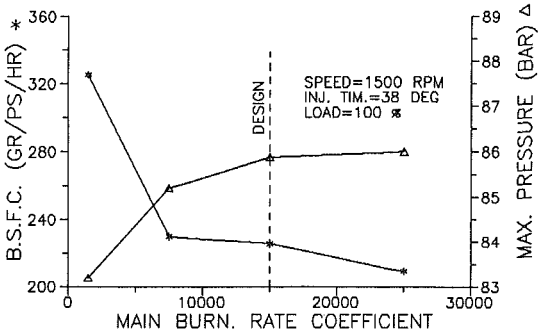

Fig. 19 Sensitivity analysis with main chamber burning rate coefficient

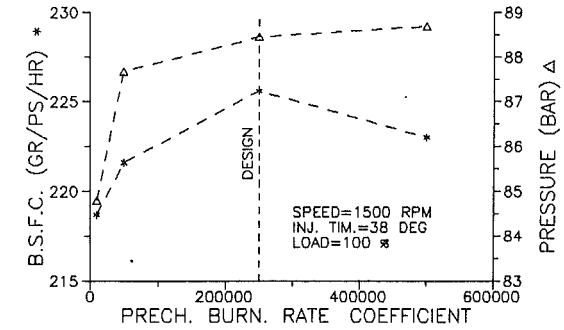

Fig. 20 Sensitivity analysis with prechamber burning rate coefficient

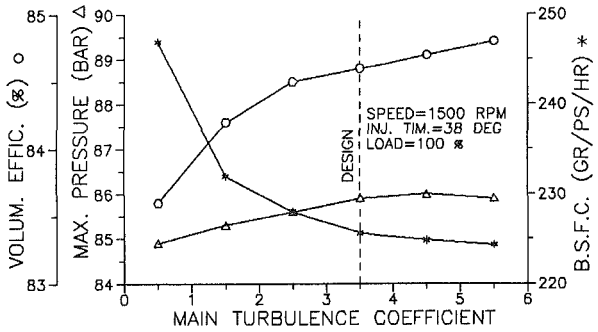

Fig. 21 Sensitivity analysis with main chamber turbulence coefficient

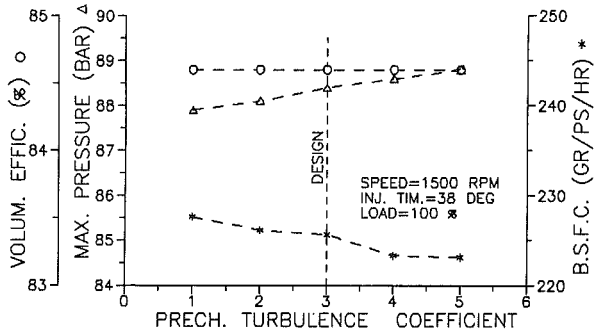

Fig. 22 Sensitivity analysis with prechamber turbulence coefficient

ing ignition starts before TDC. For injection timings lower than 41 deg there is ignition at or after TDC resulting in poor efficiency and increased BSFC.

In Fig. 16 one can see the effect of engine AFR (i.e., load) on the percentage and the mass (per cycle) of fuel burned in each chamber. The amount of fuel burned in the prechamber, as a percentage of total fuel, increases with decreasing load, while it remains constant on a mass (absolute) basis, as was also mentioned during the discussion of Fig. 8.

Figure 17 represents the effect of speed upon heat loss as a percentage of total energy introduced with the fuel in each chamber. As expected, with increasing speed there is a decrease of heat loss in each chamber. This is due to the decrease of available time with increasing speed, which has a major effect as compared to the counteracting effect of increasing gas temperature and heat transfer coefficient.

The remaining figures, Figs. 18–22, show examples of the sensitivity of the overall model predictions when changing the values of the model calibration constants. The logic is to keep in each figure the calibration constants set at the values ("design point" of model) indicated on Table 2, by changing only one calibration constant at a time.

For operation of the engine at full load, 1500 rpm and 38 deg injection timing, Figs. 18, 19, 20, 21, and 22 show the effect, on various overall model predictions, of the chemical delay coefficient z, the burning rate coefficients K_m, K_p, and the turbulence coefficients ζ_m, ζ_p, respectively (m = main, p = prechamber). The figures show a rather high insensitivity of the overall model predictions to a wide variation of the values of these calibration constants.

Table 2 Values of model calibration constants

Combustion

$K_p = 2.5 \times 10^5$ ($K^{1/2} \cdot bar^{-1} \cdot s^{-1}$)
$K_m = 1.5 \times 10^4$ ($K^{1/2} \cdot bar^{-1} \cdot s^{-1}$)
$E_{cm} = 8000$ (K)
$E_{cp} = 6000$ (K)
$a_m = 3.0$
$b_m = 1.2$
$z = 2.0$ (ms·bar$^{2.5}$)

Jet

$n_p = 0.7$
$n_m = 0.5$

Mass exchange between chambers

$c_{d_{1\to 2}} = 0.75$
$c_{d_{2\to 1}} = 0.80$

Turbulence

$\zeta_m = 3.5$
$\zeta_p = 3.0$

Conclusions

A thermodynamic model has been developed that predicts

the performance of an IDI diesel engine fitted with a swirl prechamber. Special attention has been given in setting up the equations expressing the combustion, evaporation, and mixing processes in both chambers.

The two-zone model proposed for each chamber proves to be very efficient in predicting engine performance and specifically the effect of the three major operating parameters, speed, load, and injection timing, upon it. The analysis results are encouraging, since they follow satisfactorily the real engine behavior over a large variety of operating conditions changing in a quite wide spectrum. The same set of calibration coefficients was used throughout. This is essential if the model is to be used for different engines for diagnostic purposes.

It can be concluded that the proposed model describes the cycle of an IDI engine with success, being theoretically sound and containing a minimum of calibration constants.

This is corroborated by the relative insensitivity of the overall model predictions when the values of the calibration constants are changing widely, as well as by its successful extension into the emissions domain as reported by the present authors (Kouremenos et al., 1989a).

References

Benson, R. S., and Whitehouse, N. D., 1979, *Internal Combustion Engines*, Pergamon Press, Oxford, United Kingdom.

Borman, G. L., and Johnson, J. H., 1962, "Unsteady Vaporization Histories and Trajectories of Fuel Drops Injected Into Swirling Air," SAE Power Plant Meeting, Paper No. 598C, Philadelphia, PA.

Butler, T. D., Cloutman, L. D., Dukovicz, J. K., and Ramshaw, J. D., 1981, "Multidimensional Numerical Simulation of Reactive Flow in Internal Combustion Engines," *Progress Energy Combust. Sci.*, Vol. 7, pp. 293-315.

Chiu, W. S., Shahed, S. M., and Lyn, W. T., 1976, "A Transient Spray Mixing Model for Diesel Combustion," SAE Paper No. 760128.

Dent, J. C., and Derham, J. A., 1974, "Air Motion in a Four-Stroke Direct Injection Diesel Engine," *Proc. Inst. Mech. Engrs*, Vol. 188, No. 21/74, pp. 269-280.

Ferguson, C. R., 1986, *Internal Combustion Engines*, Wiley, New York.

Gebhart, B., 1971, *Heat Transfer*, 2nd ed., McGraw-Hill, New York.

Glauert, M. B., 1956, "The Wall Jet," *J. Fluid Mech.*, Vol. 1, pp. 625-643.

Heywood, J. B., 1988, *Internal Combustion Engine Fundamentals*, McGraw-Hill, New York.

Hiroyasu, H., Kadota, T., and Arai, M., 1983, "Development and Use of a Spray Combustion Modelling to Predict Diesel Engine Efficiency and Pollutant Emissions," *Bulletin JSME*, Vol. 26, pp. 569-575.

Hodgetts, D., and Shroff, J. D., 1975, "More on the Formation of Nitric Oxide in a Diesel Engine, in: *Combustion in Engines*, Inst. of Mech. Engrs, pp. 129-138.

Idoum, A., Packer, J. P., Wallace, F. J., and Charlton, S. T., 1985, "An Experimental and Analytical Study of Jet Impingement and Wall Jets in High Swirl DI Diesel Engines Using the Hydraulic Analogy," SAE Paper No. 850263.

Incropera, F. P., and DeWitt, D. P., 1985, *Fundamentals of Heat and Mass Transfer*, Wiley, New York.

Kadota, T., Hiroyasu, H., and Oya, H., 1976, "Spontaneous Ignition Delay of a Fuel Droplet in High Pressure and High Temperature Gaseous Environments," *Bulletin JSME*, Vol. 19, p. 130.

Kamel, M., and Watson, N., 1979, "Heat Transfer in the Indirect Injection Diesel Engine," SAE Paper No. 790826.

Khan, I. M., Greeves, G., and Probert, D. M., 1971, "Prediction of Soot and Nitric Oxide Concentrations in Diesel Engine Exhaust," in: *Air Pollution Control in Transport Engines*, Inst. of Mech. Engrs., pp. 205-217.

Kort, R. T., Mansouri, S. H., Heywood, J. B., and Ekchian, A., 1982, "Divided-Chamber Diesel Engine, Part II," *SAE Trans.*, Vol. 91, pp. 121-135.

Kouremenos, D. A., and Rakopoulos, C. D., 1986, "The Operation of a Turbulence Chamber Diesel Engine, With LPG Fumigation, for Exhaust Emissions Control," *VDI Forschung im Ingenieurwesen*, Vol. 52, No. 6, pp. 185-190.

Kouremenos, D. A., Rakopoulos, C. D., and Hountalas, D., 1986, "Modelling of Spray Mixing in a Quiescent Chamber Diesel Allowing for Jet Wall Impingement," *Proc. Intern. AMSE-France Conf.*, Naples, Sept. 29-Oct. 1, Vol. 3.3, pp. 199-206.

Kouremenos, D. A., Rakopoulos, C. D., and Hountalas, D., 1987a, "Predicting the Nitric Oxide and Soot Emissions From Compression Ignition Engines by One-Zone and Two-Zone Combustion Modelling," *Proc. Intern. AMSE-France Conf.*, Karlsruhe, July 20-22, Vol. 3.B, pp. 49-57.

Kouremenos, D. A., Rakopoulos, C. D., and Karvounis, E., 1987b, "Thermodynamic Analysis of Direct Injection Diesel Engines by Multi-zone Modelling," *ASME Winter Annual Meeting*, Boston, MA, Dec. 13-18, AES-Vol. 3.3, pp. 67-77.

Kouremenos, D. A., Rakopoulos, C. D., and Hountalas, D., 1987c, "Simulation of the Cycle of a Motored Precombustion Chamber Diesel Cylinder," *Proc. 16th IASTED IMS Intern. Conf.*, Paris, June 22-24, ACTA Press, pp. 116-120.

Kouremenos, D. A., Rakopoulos, C. D., Karvounis, E., and Kotsos, K., 1987d, "Preliminary Results From a Two-dimensional Model of Flow in Internal Combustion Engines," *Proc. Intern. AMSE-France Conf.*, Karlsruhe, July 20-22, Vol. 3.B, pp. 39-47.

Kouremenos, D. A., Rakopoulos, C. D., Kotsos, K., and Hountalas, D., 1987e, "Modelling the Blowby Rate in a Reciprocating Internal Combustion Engine," *Proc. 16th IASTED IMS Intern. Conf.*, Paris, June 22-24, ACTA Press, pp. 465-468.

Kouremenos, D. A., Rakopoulos, C. D., and Karvounis, E., 1987f, "Droplet Evaporation Versus Gas Jet Mixing for Combustion and Pollutants Formation Modelling in Diesel Engines," *Proc. Intern. AMSE-France Conf.*, Karlsruhe, July 20-22, Vol. 3.B, pp. 59-69.

Kouremenos, D. A., Rakopoulos, C. D., and Hountalas, D., 1988, "Thermodynamic Analysis of a Divided Combustion Chamber Diesel Engine," *VDI Forschung im Ingenieurwesen*, Vol. 54, No. 3, pp. 73-81.

Kouremenos, D. A., Rakopoulos, C. D., and Hountalas, D., 1989a, "Computer Simulation With Experimental Validation of the Exhaust Nitric Oxide and Soot Emissions in Divided Chamber Diesel Engines," submitted for presentation at the ASME Winter Annual Meeting, San Francisco, CA, Dec. 10-15, AES Session.

Kouremenos, D. A., Rakopoulos, C. D., Hountalas, D., and Kotsiopoulos, P., 1989b, "Modelling the Fuel Injection System of Diesel Engines," 8th IASTED MIC Intern. Conf., Grindelwald, Switzerland, Feb. 7-10, Paper No. 6-1.

Kouremenos, D. A., Rakopoulos, C. D., and Kotsiopoulos, P., 1989c, "Performance and Emission Characteristics of a Diesel Engine Using Supplementary Diesel Fuel Fumigated to the Intake Air," *Journal of Heat Recovery Systems and CHP*, Vol. 9, in press.

Launder, B. E., and Spalding, D. B., 1972, *Mathematical Models of Turbulence*, Academic Press, London-New York.

Lavoie, G. A., Heywood, J. B., and Keck, J. C., 1970, "Experimental and Theoretical Study of Nitric Oxide Formation in Internal Combustion Engines," *Combustion Sci. and Technol.*, Vol. 1, pp. 313-326.

Mansouri, S. H., Heywood, J. B., and Radhakrishnan, K., 1982, "Divided-Chamber Diesel Engine, Part I," *SAE Trans.*, Vol. 91, pp. 89-120.

Meintjes, K., and Alkidas, A. C., 1982, "An Experimental and Computational Investigation of the Flow in Diesel Prechambers," *SAE Trans.*, Vol. 91, pp. 137-154.

Millington, B. W., and Hartless, E. R., 1968, "Frictional Losses in Diesel Engines," *SAE Trans.*, Vol. 77, pp. 2390-2406.

Morris, C. T., and Dent, J. C., "The Simulation of Air Fuel Mixing in High Swirl Open Chamber Diesel Engines," *Proc. Inst. Mech. Engrs*, Vol. 190, No. 47/76, pp. 503-513.

Obert, E. F., 1973, *Internal Combustion Engines and Air Pollution*, Intext Educ. Publ., New York.

Pinchon, Ph., and Guillot, B., 1985, "Thermodynamic and Flow Analysis of an Indirect Diesel Combustion Chamber by Modelling," SAE Paper No. 851686.

Rakopoulos, C. D., 1986, "One-Zone Versus Two-Zone Modelling of the Closed Cycle in a Gasoline Engine Including Comparison With Experimental Results," *Proc. Intern. AMSE-France Conf.*, Naples, Sept. 29-Oct. 1, Vol. 3.3, pp. 229-237.

Rakopoulos, C. D., 1988, "Ambient Temperature and Humidity Effects on the Performance and Nitric Oxide Emission of Spark Ignition Engined Vehicles in Athens/Greece," *Solar & Wind Technology*, Vol. 5, No. 3, pp. 315-320.

Ricardo, H. R., and Hempson, J. G. G., 1968, *The High Speed Internal Combustion Engine*, Blackie & Son Ltd., London.

Spalding, D. B., 1979, *Combustion and Mass Transfer*, Pergamon Press, Oxford, United Kingdom.

Vickland, C. W., Strange, F. M., Bell, R. A., and Starkman, E. S., 1962, "A Consideration of the High Temperature Thermodynamics of Internal Combustion Engines," *SAE Trans.*, Vol. 70, pp. 785-793.

Wakil, M. M., Myers, P. S., and Uyehara, O. A., 1956, "Fuel Vaporization and Ignition Lag in Diesel Combustion," *SAE Trans.*, Vol. 64.

Watson, N., and Kamel, M., 1979, "Thermodynamic Efficiency Evaluation of an Indirect Injection Diesel Engine," SAE Paper No. 790039.

Whitehouse, N. D., and Abughres, S. M., 1975, "Calculation of Fuel-Air Mixing in a Diesel Engine With Swirl for the Purpose of Heat Release Prediction," in: *Combustion in Engines*, Inst. of Mech. Engrs., pp. 147-154.

Whitehouse, N. D., and Way, R. J. B., 1969-70, "Rate of Heat Release in Diesel Engines and Its Correlation with Fuel Injection Data," *Proc. Instn. Mech. Engrs.*, Vol. 184, Part 3J, pp. 17-29.

Williams, T. J., 1973, "Parameters for Correlation of Penetration Results for Diesel Fuel Sprays," *Proc. Inst. Mech. Engrs.*, Vol. 187, 69/73, pp. 771-774.

Yoshida, M., Harigaya, Y., and Sato, K., 1982, "Variation of Heat Flux Through a Combustion Chamber Wall of Prechamber Type Diesel Engine," *Bulletin JSME*, Vol. 25, pp. 426-437.

A New Heat Transfer Correlation and Flow Regime Map for Tube Bundles

Y. A. Hassan
Associate Professor.

T. K. Blanchat
Research Assistant.

Department of Nuclear Engineering,
Texas A&M University,
College Station, TX 77843-3133

A RELAP5/MOD2 computer code model for a once-through steam generator has been developed. The calculated heat transfer in the nucleate boiling flow was underpredicted as shown by a predicted superheat of only 11°C (20°F), whereas plant values range from 22–30°C (40–60°F). Existing heat transfer correlations used in thermal-hydraulic computer codes do not provide accurate predictions of the measurement-derived secondary convective heat transfer coefficients for steam generators because they were developed for flow inside tubes, not tube bundles. The RELAP5/MOD2 flow regime map was modified to account for flow across bundles. This modified flow regime map predicts better transition criteria between bubbly-to-slug and slug-to-annular flow. Consequently, improved saturated conditions for the fluid flow at the entrance to the boiler were obtained. A modified Chen-type heat transfer correlation was developed to predict the boiling heat transfer for steam generator tube bundle geometries. This correlation predicts better superheat.

Introduction

The steam generator is a major component in pressurized water reactors (PWR). Predicting the response of a steam generator during both steady-state and transient conditions is essential in studying the thermal-hydraulic behavior of a nuclear reactor coolant system. Therefore, extensive analytical and experimental research has been performed to investigate the thermal-hydraulic behavior of the steam generators during operational and accident transients. The objective of this study is to predict the behavior of the secondary side of the once-through steam generator (OTSG), using the RELAP5/MOD2 computer code and, in particular, to obtain a better prediction of heat transfer coefficients in bundles.

The RELAP5/MOD2 code (Ransom et al., 1985) is a new version of the RELAP5 thermal-hydraulic code series. This light water reactor transient analysis code was developed for the United States Nuclear Regulatory Commission, to provide an advanced best-estimate predictive capability for use in a wide spectrum of applications in support of the regulatory evaluation and licensing process. The principal new feature of RELAP5/MOD2 is the use of the full six-equation, two-fluid, nonequilibrium, and nonhomogeneous model.

There is abundant information available on boiling in tubes, but unfortunately, information on flow boiling in tube bundles is scarce. This study focused on the flow regime map and the heat transfer correlations for tube bundles. Steady-state conditions were predicted with the current version of the RELAP5/MOD2 (cycle 36.05) code, and compared with experimental plant data. The code predictions consistently underpredict the degree of superheat. With no code modifications, the code currently predicts an 11°C (20°F) superheat, in comparison to a 22–33°C (40–60°F) superheat suggested by plant test data (Turk et al., 1988). The cause for the inaccurate OTSG predictions is that "tube bundle" flow differs from "tube" flow. A steam generator is composed mainly of tube bundles; however, the code currently uses round tubes or pipes as component volumes in addition to using round tube thermal-hydraulic correlations in shellside calculations.

Once-Through Steam Generator

The once-through steam generator (OTSG), is a vertical, straight-tube, straight-shell, counterflow heat exchanger with shell-side boiling. Figure 1 shows the OTSG flow schematic. Primary reactor coolant enters the steam generator through a nozzle in the upper level, flows down through more than 15,000 Inconel-600 alloy tubes, and exits at the bottom head through two outlet nozzles. On the secondary side, subcooled feedwater is sprayed downward into the annulus between the shell and the tube-bundle shroud, where it is heated to saturation by direct contact with steam aspirated from the tube bundle. The saturated feedwater enters the bottom of the tube bundle where nucleate boiling begins. After reaching 100 percent quality at about the midbundle elevation,the steam is superheated in the upper half of the bundle, flows down through the steam annulus, and exits through two steam oulet nozzles. The tubes are located on a triangular pitch, and the spacing between tubes is maintained along the length of the bundle by the tube support plates (TSP). The plates support each tube at equally spaced points around the circumference, while allowing most of the tube surface to be contacted by the secondary fluid. It should be noted that there is approximately a 50 percent reduction in flow area at the TSP in the tube bun-

Contributed by the Nuclear Engineering Division for publication in the JOURNAL OF ENGINEERING FOR GAS TURBINES AND POWER. Manuscript received by the Nuclear Engineering Division January 25, 1989.

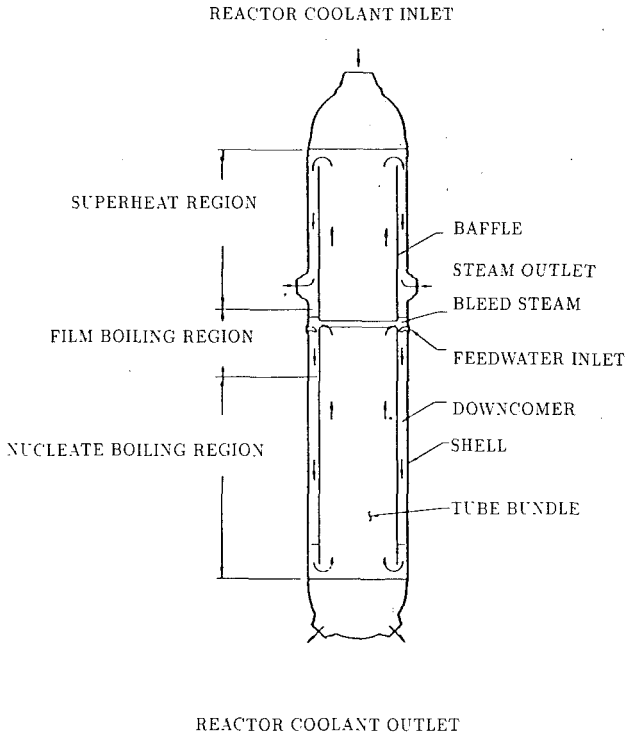

Fig. 1 Once-through steam generator flow schematic

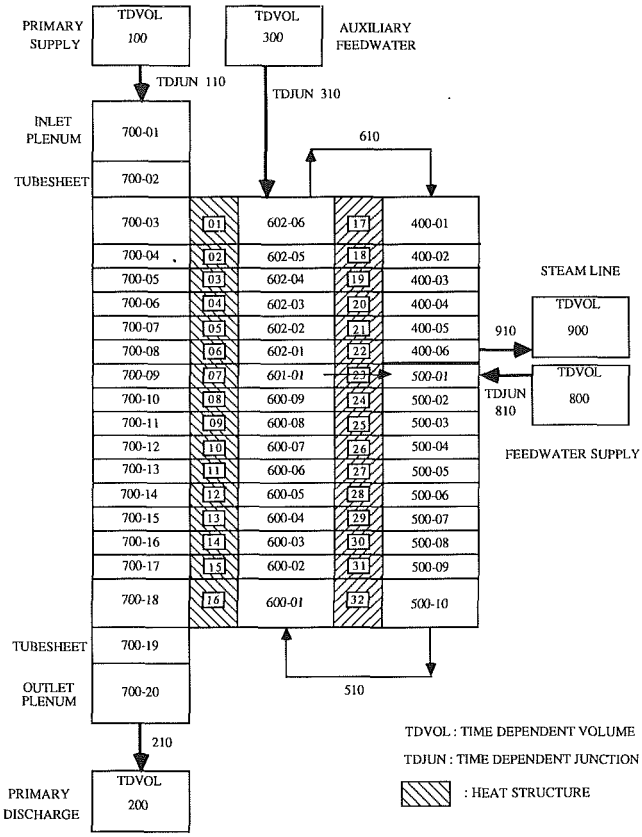

Fig. 2 RELAP5/MOD2 once-through steam generator nodalization

dle region. In addition, the subcooled feedwater should have reached a saturated condition at the bottom of the tube bundle.

The RELAP5/MOD2 model of the OTSG depicting main components and flow paths is shown in Fig. 2. The primary side of the steam generator was modeled by a pipe component consisting of 20 hydrodynamic volumes (700) and 16 heat structures. The inlet to the primary was modeled, using a time-dependent volume (100) and junction (110), which forced the primary mass flow at 15.22 MPa (2208 psia) and 316°C (601°F) in the steam generator inlet plenum. The primary coolant from the outlet plenum was discharged to a time-dependent volume (200) at 15.17 MPa (2200 psia). The tube heat structure dimensions were based on 15,531 tubes with an inner diameter of 1.4147 cm (0.0464 ft) and a wall thickness of 0.0864 cm (0.0028 ft).

The secondary side of the steam generator is divided into three major regions: the incoming feedwater annulus (500) (pipe component with ten hydrodynamic volumes), the tube bundle or "boiler" region, and the steam outlet annulus (400) (pipe component with six hydrodynamic volumes). The tube bundle region consists of two pipe components (600 and 602) and a branch component (601), for a total of 16 hydrodynamic volumes. This allows the placement of 15 reduced internal junction flow areas that model the internal tube support plates (TSP). In addition, the branch component is necessary to model an aspirator flow from the tube bundle region to preheat the incoming subcooled feedwater. An additional 16 heat structures are used to model the vertical cylindrical baffle, which connects the tube bundle region to the feedwater annulus and the steam outlet annulus.

Nomenclature

C = arbitrary constant
c_p = specific heat
D = diameter
F = Reynolds number factor
g = gravitational constant
h = convective heat transfer coefficient
H_2O = water
j = superficial velocity
K = rod bundle flow transition coefficient
k = thermal conductivity
P = pressure
P_{tube} = tube bundle pitch
Re = Reynolds number
S = suppression factor
U, V = velocity
X_{tt}^{-1} = Martinelli flow parameter
α = void fraction
ΔP = pressure increment
ΔT = temperature increment, wall superheat
μ = viscosity
π = 3.14159
ρ = density
σ = surface tension
ϕ_L^2 = liquid-only two-phase multiplier

Subscripts

ann = annular regime
$B-S$ = bubble-to-slug
churn = churn regime
e = hydraulic equivalent
f, l = liquid phase
g = vapor phase
h = hydraulic
mac = macroscopic
mic = microscopic
o = stagnant liquid bubble rise, outer
$S-A$ = slug-to-annular
s = superficial
sat = saturation

Superscripts

m = Reynolds number exponent in the single-phase convective heat transfer correlation
n = Reynolds number exponent in a Blasius-type friction correlation, constant in Biasi CHF correlation
$*$ = dimensionless

The feedwater supply is modeled with a time-dependent junction (810) and volume (800). In addition, at steady-state conditions, the steam exits the steam annulus through a single junction component to a time-dependent volume (900). The steam outlet time-dependent volume pressure is adjusted to maintain a pressure of 6.45 MPa (925 psia) in the steam annulus.

A time-dependent junction (310) and volume (300) is connected to the top of the tube bundle region to model the auxiliary feedwater connections for later transient analysis. No flow is allowed through this junction during the steady-state analysis.

The resulting model is initialized to a steady-state condition based on 100 percent load parameters.

Tube Bundle Flow Regime Map

In gas–liquid flow, the two phases can be distributed in the conduit in a variety of ways. These distributions can vary when changes take place in flow rates, fluid properties, or conduit shape. In these distributions, it has been observed that natural groupings or patterns occur. It is expected that pressure drops, void fractions, heat transfer rates, and other parameters of interest will behave differently as the flow pattern changes (Dukler et al., 1986). Early work in this field showed that the use of empirical correlations that were different for each flow pattern improved the comparison between calculated and measured pressure drops in horizontal pipes (Baker, 1958). Currently, it is believed that it will be necessary to predict the flow pattern that exists in the system of interest to provide accurate predictions of the flow related phenomena.

Very few studies have appeared dealing with flow pattern transitions in a geometry different from a round pipe. However, a review of the literature pertaining to gas–liquid flow pattern transitions for vertical rod bundles has shown thta geometry does affect the flow pattern transition points. Experiments using a 24-rod circular bundle with air–water systems have shown that bubble rise velocities in tube bundles are greater than those in tubes (Venkateswararao, 1981). In addition, Venkateswararao (1981) found that the trend of rise velocity with bubble size, when the bubbles rise in the restricted space of a four-rod cell, is different from that for an infinite medium. There are also observed two types of slug flow patterns in tube bundles. In one, Taylor bubbles occupy the space in a four-rod cell and flow upward, while the liquid flows down as a film along the rods. The cap of the bubble is not penetrated by the rod. This flow pattern is designated "cell type" slug flow. In the second, a large Taylor bubble is formed that spans a number of rods, with each rod penetrating the cap of the bubble. This Taylor bubble can be large enough to occupy the entire test section cross-sectional area. This slug pattern is designated "shroud" slug flow.

Currently, the RELAP5/MOD2 code chooses the bubble-to-slug transition (α_{B-S}) criterion for the vertical flow regime map as

$$\alpha_{B-S}=\text{MAX}\left\{0.25\ \text{MIN}\left[1.0,\ \left(\frac{D^*}{22.2}\right)^8\right],\ 0.001\right\} \tag{1}$$

for low mass fluxes ($G\leq 2000$ kg/m^{2}s). D^* is the limiting dimensionless tube diameter allowing the presence of bubbly flow

$$D^*=D_h\left[\frac{g}{\sigma}(\rho_f-\rho_g)\right] \tag{2}$$

where g is the gravitational constant and σ is the surface tension. This is the criterion that RELAP5/MOD2 has been choosing, since the mass flux is approximately 190 kg/m^{2}s for the OTSG model. This transition equation does not work well for tube bundles. D^* for the OTSG is approximately 12, which corresponds to $\alpha_{B-S}=0.002$ by equation (1). This implies that any void fraction formation immediately places the flow into a slug regime.

Dispersed bubbles are observed to concentrate in the open space defined by the four rod cell. Bubbles that originate in the gap between rods migrate to the open region as a result of the pressure driving force that exists due to the lower velocity that exists between adjacent rods as compared to the open area. It is suggested that the transition flow in a bundle array takes place when the "local" voids over the area of the open space reach 0.25. However, the calculated "average" voids at the transition will be lower and will depend on pitch-to-diameter ratio (P_t/D_{tube}) (Venkateswararao, 1981). The average void fraction for the bubble-to-slug transition can be determined from

$$\alpha_{B-S}=0.25\frac{\left[\sqrt{2}\left(\frac{P_t}{D_{\text{tube}}}\right)-1\right]^2}{\frac{4}{\pi}\left(\frac{P_t}{D_{\text{tube}}}\right)^2-1} \tag{3}$$

where P_t is the tube pitch and D_{tube} is the tube outer diameter. Equation (3) suggests that the bubble-to-slug transition for the OTSG bundle configuration should occur at

$$\alpha_{B-S}=0.1604 \tag{4}$$

for the OTSG values of P_t and D_{tube}. This is less than the conventional bubble-to-slug transition value of 0.25 for flow inside tubes.

A modified version of RELAP5/MOD2 was created to check the utilization of the two new input parameters, tube bundle pitch and tube outer diameter, and also equation (3). The steam exit annulus, feedwater downcomer annulus, and primary tube volume's pitch and tube o.d. were set to 0.0 and the secondary tube bundle region's pitch and tube o.d. were set to 2.221 cm (0.072 ft) and 1.774 cm (0.052 ft), respectively. If RELAP5/MOD2 determined that a volume's pitch was equal to 0.0, then the bubble-to-slug transition (α_{B-S}) criteria was chosen as before with no modification. If RELAP5/MOD2 determines that a volume's pitch was not equal to 0.0, then the code chose equation (3) as the new bubble-to-slug transition criteria. Little difference was noted, however, in the secondary temperature profile since this transition occurs in the first "tube bundle" volume.

The literature review also suggests churn-to-annular transition for tube bundles occurs at a lower value than that for a circular tube geometry (Venkateswararao, 1981; Collier, 1981; Carey et al., 1986). The RELAP5/MOD2 computer code combines the churn regime with the slug regime. It uses a slug-to-annular transition α_{S-A} for the vertical flow regime map based on the critical vapor velocity required to suspend a liquid droplet developed by Taitel and Dukler (Ransom et al., 1985). Equation (5) shows the criterion used in the code

$$\alpha_{S-A}=\text{MAX}\left\{0.75,\ 1.4\frac{[\sigma g(\rho_f-\rho_g)]^{1/4}}{V_g\rho_g^{1/2}}\right\} \tag{5}$$

It also places a limit on the range of the slug-to-annular transition

$$0.75\leq\alpha_{S-A}\leq 0.96 \tag{6}$$

Two points need to be noted. First, the coefficient 1.4 was chosen since it gave better code results to experimental data for "tube" geometry. Second, the same reason was used to place a lower limit (0.75) on the slug-to-annular transition point. Experiments show that churn-to-annular transition for vertical rod bundles occurs at values of α_g less than that for tube geometry (Venkateswararao, 1981). It was determined

Table 1 K values for equation (7)

Geometry	K	Characteristic dimension D
Tube	0.35	Tube diameter D
Rod bundle	$0.35+0.8\left[1-\frac{D_e}{D_o}\right]^3$	Equivalent diameter D_e

that the theoretical churn-to-annular transition for flow in vertical rod bundles occurs at lower values of the gas superficial velocity than for pipe flow. Experimental results for flow in rod arrays also show that the transition occurs at lower void values than that for inside tubes (Venkateswararao, 1981; Bergles et al., 1968; Williams et al., 1978).

Jones and Zuber have examined this transition for various geometries. The recommended equation for churn-to-annular flow transition uses a factor that takes into account the hydraulic equivalent diameter for a rod bundle (Collier, 1981). The transition criterion has the form

$$j_g^* = 4\left(\frac{\rho_g}{\rho_f}\right)^{1/2}[j_f^* + K] \tag{7}$$

where the nondimensional superficial velocities are given by

$$j_f^* = j_f \rho_f^{1/2}[gD(\rho_f - \rho_g)]^{-1/2} \tag{8}$$

and

$$j_g^* = j_g \rho_g^{1/2}[gD(\rho_f - \rho_g)]^{-1/2} \tag{9}$$

The values for the coefficient K and the characteristic dimension D are presented in Table 1 where D_o is the tube outer diameter. It can be shown that use of this factor reduces the transition point below that for a tube geometry.

Another study on annular film-flow boiling in a vertical channel with offset strip fins (geometry similar to tube bundles) also concludes that the transition occurs at a value of void fraction below that for tubes (Carey et al., 1986).

In terms of the parameter j_g^* defined by Wallis, the transition occurred at j_g^* equal to 0.5, whereas Wallis suggested a value of j_g^* equal to 0.9 for normal tube geometries (Collier, 1981).

The following theoretical equations have been developed for predicting void fractions in the churn regime (α_{churn}) based on the holdup model, and in the annular regime (α_{ann}) based on an overall force balance on the gas and liquid flowing in a four-rod cell (Venkateswararao, 1981). The void fraction in the curn regime is given by

$$\alpha_{\text{churn}} = \frac{U_{gs}}{1.15(U_{gs} + U_{ls}) + U_o} \tag{10}$$

where U_{gs}, U_{ls}, and U_o are superficial vapor velocity, superficial liquid velocity, and stagnant liquid bubble rise velocity, respectively. The void fraction in the annular regime is given by

$$\alpha_{\text{ann}} = 1 - \frac{\frac{0.0025}{CD_{\text{tube}}\alpha_{\text{ann}}^3}[1+2g(\alpha_{\text{ann}})][1+300g(\alpha_{\text{ann}})]\rho_g U_{gs}^2 + \frac{0.0025}{CD_{\text{tube}}(1-\alpha_{\text{ann}})^3}\rho_l U_{ls}^2}{(\rho_l - \rho_g)g} \tag{11}$$

where

$$C = \frac{1}{\pi}\left[\left(\frac{P_t}{D_{\text{tube}}}\right)^2 - \frac{\pi}{4}\right] \tag{12}$$

and

$$g(\alpha_{\text{ann}}) = \frac{[1+4C(1-\alpha_{\text{ann}})]^{0.5} - 1}{2} \tag{13}$$

It is suggested that the transition occurs at the intersection of equations (10) and (11) where $\alpha_{\text{churn}} = \alpha_{\text{ann}}$, and this defines

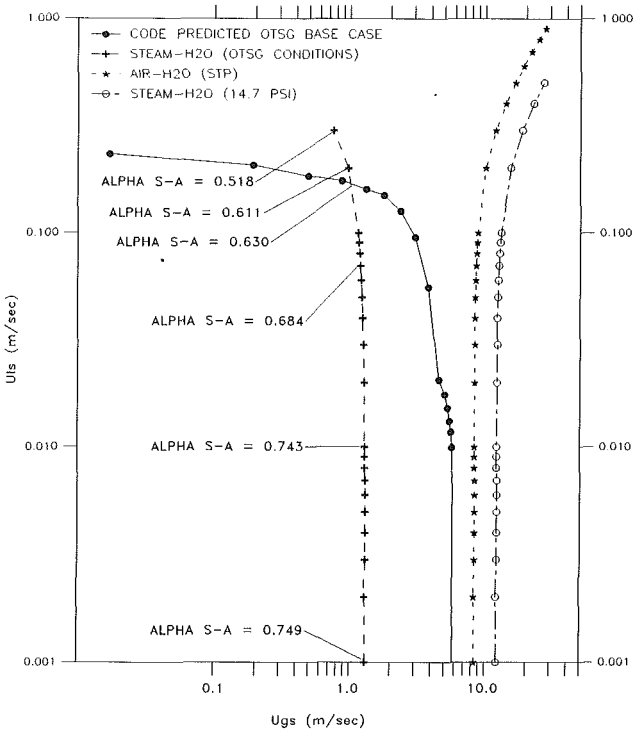

Fig. 3 Theoretical churn-to-annular transition lines

the locus of the U_{gs}, U_{ls} pairs, at which transition takes place (Venkateswararao, 1981). Setting pitch, tube o.d., and the fluid properties to meet the conditions of Venkateswararao's experiment, a steam-water system at atmospheric pressure, and also the OTSG's environment, generated the three theoretical churn-to-annular transition lines shown in Fig. 3. These transition lines were produced by choosing various values of U_{gs} and solving for U_{ls} with equations (10), (11), (12), and (13). This figure also plots the RELAP5/MOD2 code-predicted superficial phase velocity values (each node in the tube bundle region) for the OTSG base case. The intersection of code-predicted superficial phase velocity data with the transition curve for the OTSG shows the slug-to-annular point for the OTSG

$$\alpha_{S-A}(\text{OTSG}) = 0.63 \tag{14}$$

Implementing equation (14) in the code for the tube bundle region lowered the slug-to-annular transition point one node.

Tube Bundle Heat Transfer Correlations

The accuracy of predicted heat transfer coefficients in flow boiling is important for the design and optimization of heat exchange equipment and the prediction of steady-state and transient behavior of steam generators. There are various correlations proposed for flow boiling. Most of these correlations are based on experimental results inside tubes. The heat transfer correlations used in RELAP5/MOD2 underpredict the heat transfer coefficients for tube bundle flow. Much larger boiling coefficients have been obtained on the secondary side of tube bundles in the Semiscale steam generator (Boucher, 1987). Measurement-derived secondary heat transfer coefficients were as high as 62,346 W/m^2-K (3.0

Btu/sec-ft^2-°F), whereas the Chen correlation predicted 13,703 W/m^2-K (0.66 Btu/sec-ft^2-°F). The Chen correlation was developed primarily from data for flow inside an externally heated tube. Flow mechanisms are different for flows inside internally heated tube bundles. It is believed that the bundle geometry causes the flow behavior to be significantly different from flow inside tubes. Studies of boiling heat transfer in a horizontal tube bundle in upward crossflow with R-113 also indicate the need to develop new correlations for tube bundle geometry (Jensen et al., 1987). Bubble rise velocities are greater in tube bundles. In addition, Venkateswararao (1981) observed that few bubbles move in the space between rods but migrate to the open area that exists within an array of four rods. This "sweeping" or "sliding" of bubbles from the rod walls to the open area in the cell induces circulation and increases turbulence. This results in heat transfer enhancement. Furthermore, it is postulated that heat transfer will also be enhanced by the additional turbulence created in the tube bundle flow by the tube support plates. Accordingly, understanding the basic mechanisms of tube bundle flow is of great importance in the design and analysis of more efficient heat exchangers.

The RELAP5/MOD2 computer code uses the Dittus–Boelter correlation to calculate heat transfer coefficients for single-phase forced liquid convection

$$h = C\frac{k_f}{D_e}\mathrm{Re}_f^{0.8}\mathrm{Pr}_f^{0.4} \tag{15}$$

where $C = 0.023$. This correlation was originally derived for smooth flow in tubes. Weisman (1959) has studied available heat transfer data for water (single-phase) flowing parallel to tube bundles. The data were correlated using the form of the Colburn equation as a basis. The constant C in equation (15) was replaced by a function of the pitch-to-diameter ratio (P_t/D_{tube}) and for the OTSG triangular pitch arrays is given by

$$C = 0.026\frac{P_t}{D_{\text{tube}}} - 0.006 \tag{16}$$

Also, Kim and El-Genk (1988) recently found that the turbulent heat transfer data for triangularly arrayed, uniformly heated rod bundles was in good agreement (±15 percent) with Weisman's correlation.

Evaluating equation (16) for a typical OTSG, $C = 0.0304$, which is a 32 percent increase over the Colburn value of 0.023. The RELAP5/MOD2 code was modified so that the constant 0.023 in equation (15) was replaced with the constant predicted by equation (16) for tube bundle components. However, since single-phase forced liquid convection flow was never predicted in the OTSG tube bundle region, this modification had no effect on the predicted temperature profile. Note that equation (16) would also be used for single-phase forced vapor convection.

The Chen correlation is used in RELAP5/MOD2 for subcooled and saturated nucleate boiling (Chen, 1963), i.e.,

$$h = h_{\text{mac}} + h_{\text{mic}} \tag{17}$$

$$h_{\text{mac}} = 0.023\frac{k_g}{D_e}\mathrm{Re}_f^{0.8}\mathrm{Pr}_f^{0.4}F \tag{18}$$

$$h_{\text{mic}} = 0.00122\frac{k_f^{0.79}C_{pf}^{0.45}\rho_f^{0.49}}{\sigma^{0.5}\mu_f^{0.29}h_{fg}^{0.24}\rho_g^{0.24}}\Delta T_{\text{sat}}^{0.24}\Delta P_{\text{sat}}^{0.75}S \tag{19}$$

The parameter F is the Reynolds number factor $(\mathrm{Re}_{TP}/\mathrm{Re}_f)^{0.8}$, and has a purely hydrodynamic nature; it takes into account the enhancement of heat transfer due to an increase in vapor quality (mixture quality) and was derived from tube flow data. The parameter S is the suppression factor due to the ratio of effective-to-wall superheat, which takes into account the nucleate boiling suppression by forced convection

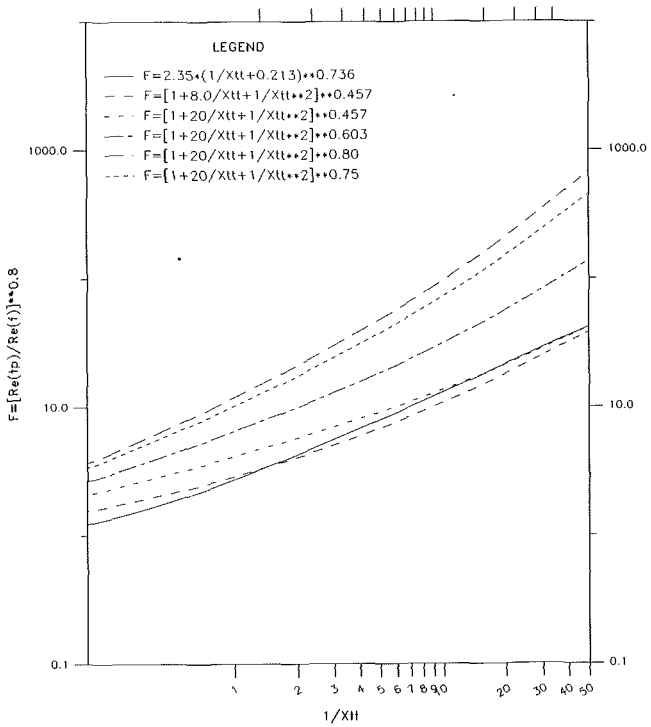

Fig. 4 Reynolds number factor F equations

because of the reduction in the thermal boundary layer thickness. Currently, RELAP5/MOD2 calculates F from

$$F = 1.0 \qquad X_{tt}^{-1} \le 0.1 \tag{20}$$

$$F = 2.35(X_{tt}^{-1} + 0.213)^{0.736} \qquad X_{tt}^{-1} > 0.1 \tag{21}$$

where X_{tt}^{-1} is the Martinelli flow parameter

$$X_{tt}^{-1} = \left(\frac{\alpha_g\rho_g V_g}{(1-\alpha_g)\rho_f V_f}\right)^{0.9}\left(\frac{\rho_f}{\rho_g}\right)^{0.5}\left(\frac{\mu_g}{\mu_f}\right)^{0.1} \tag{22}$$

The RELAP5/MOD2 code was modified to choose a different heat transfer correlation if the volume had a pitch not equal to zero. The first modification was to insert the Weisman C factor (equation (16)) into equation (18) in place of 0.023. The result was a superheat increase of 1.1°C (2°F).

The Reynolds number factor F can be described with a two-phase friction multiplier through the use of a momentum analogy, with the resulting expression for F given by

$$F = (\phi_L^2)^{\frac{m}{2-n}} \tag{23}$$

where ϕ_L^2 is the liquid-only two-phase friction multiplier, m is the Reynolds number exponent in the single-phase convective heat transfer correlation, and n is the Reynolds number exponent in a Blasius-type friction correlation for the tube bundle. An expression was developed by Ishihara et al. (1980) for ϕ_L^2 based on the data from a variety of tube banks

$$\phi_L^2 = 1 + \frac{8.0}{X_{tt}} + \frac{1.0}{X_{tt}^{2.0}} \tag{24}$$

The Reynolds number factor F was modified with various combinations of constants and exponents to increase heat transfer coefficients to the range determined experimentally by Boucher (1987). Figure 4 details these changes along with the results. A simple equation for F has been derived that predicts heat transfer coefficients similar to that determined experimentally

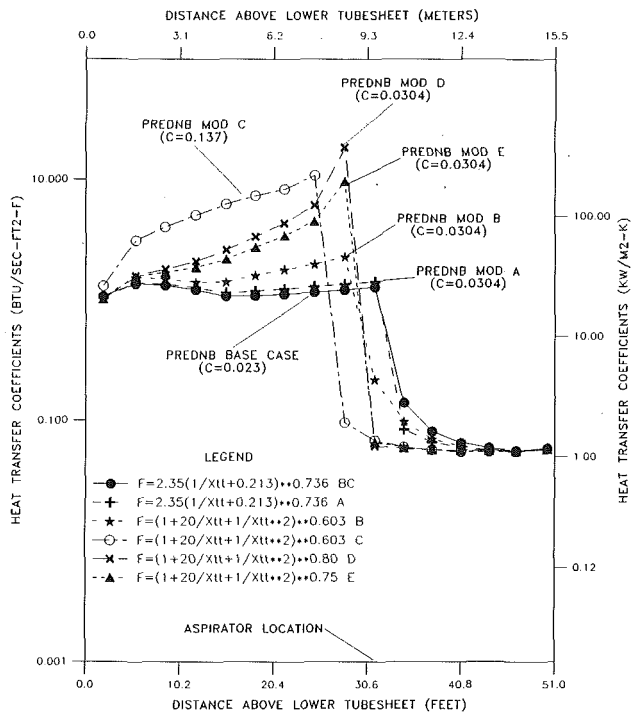

Fig. 5 Tube bundle heat transfer coefficients

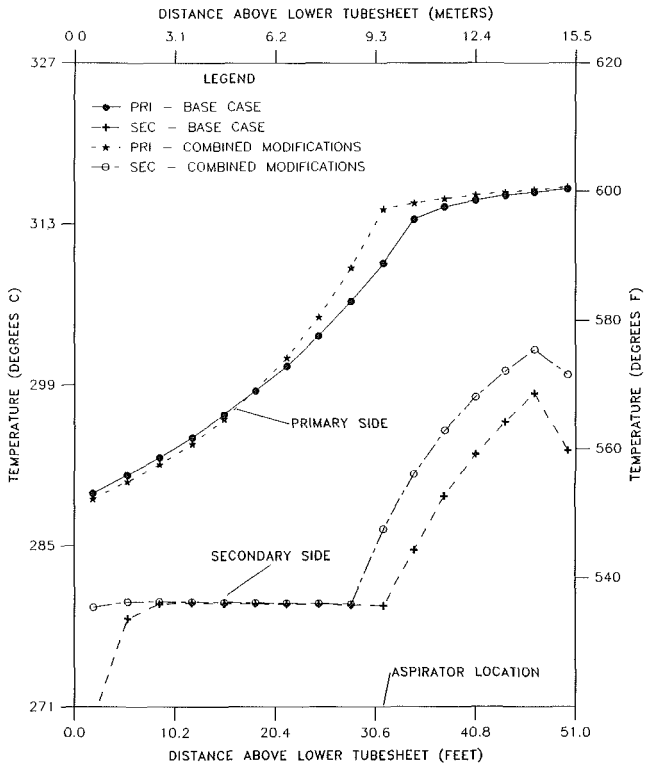

Fig. 6 OTSG temperature distribution comparisons

$$F=\left[1+\frac{20.0}{X_{tt}}+\frac{1.0}{X_{tt}^{2.0}}\right]^{0.75} \tag{25}$$

Note that for a typical OTSG, X_{tt}^{-1} ranges from 0.2 to 50.0 in the nucleate boiling region.

Figure 5 compares the base secondary side heat transfer coefficients to those predicted from various modifications. PREDNB mod A replaced 0.023 in equation (18) with equation (16). PREDNB mod B used PREDNB mod A changes, and replaced equation (21) with

$$F=\left[\frac{1+20.0}{X_{tt}}+\frac{1.0}{X_{tt}^{2.0}}\right]^{0.603}$$

PREDNB mod C replaced 0.023 in equation (18) with the constant 0.137 determined by Jenson et al. (1987) along with the F change as in PREDNB mod B. PREDNB mod D and mod E used the Weisman correlation as in PREDNB mod A, with the F change as in PREDNB mod B, except that the exponents used in the equation for F were changed to 0.80 and 0.75, respectively.

Note that the modification to the Chen correlation is only used in the subcooled and saturated nucleate boiling heat transfer regimes. Also, if single-phase forced vapor convection were to occur on the secondary side of the steam generator, the Dittus-Boelter correlation (equation (15) with vapor properties) would have been used with the constant C replaced with that constant predicted by equation (16).

The correlations for film boiling and inception of DNB(CHF) used in the code were not modified. A transition Chen correlation (Chen et al., 1977; Ransom et al., 1985) is used for transition film boiling, and modified Bromley (Bromley, 1950; Ransom et al., 1985) and Dougall-Rohsenow (Dougall and Rohsenow, 1963; Ransom et al., 1985) correlations are used with film boiling. Two CHF correlations are utilized in RELAP5/MOD2: Biasi for high flow CHF, and a modified Zuber for low flow CHF (Ransom et al., 1985). For the OTSG conditions, the Biasi correlation was employed.

Figure 6 compares the base case (with no modifications) tube bundle temperature profile with the profiles obtained when using the combined modifications to the flow regime map and the heat transfer correlations. The modifications to the flow regime map used equations (3) and (14) for the "tube bundle" volumes, and for the "tube" volumes the slug-to-annular transition point was set to 0.75 The modifications to the heat transfer correlations used equations (16) and (25) for the "tube bundle" volumes. These changes have produced an increase in superheat by 8°C (15°F). This figure shows that

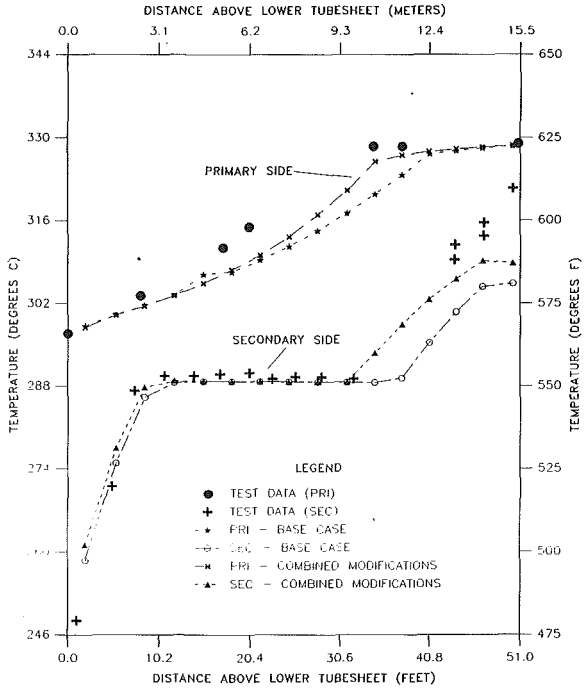

Fig. 7 19-tube OTSG temperature comparisons

typically the first volume, or node, is subcooled for the base case, but close to saturated conditions are achieved with the use of the combined modifications. This is followed by saturation conditions until the aspirator location is reached. Critical heat flux or burnout is then achieved, as indicated by a marked temperature increase above the saturation line. The static quality and vapor void fraction predicted by the code at CHF are approximately 0.9 and 0.99, respectively. The influence of the CHF is also observed in the primary flow by the large change in slope in the temperature profile.

Comparisons between the temperature profile test data for the 19-tube integral economizer OTSG test facility (Hassan, 1988) and the RELAP5/MOD2 predicted values for both a base case and a combined modifications run on a 19-tube RELAP5/MOD2 model were performed. Better agreement is obtained as shown in Fig. 7.

Conclusion

An accurate, realistic RELAP5/MOD2 model for the once-through steam generator has been developed. Literature searches have shown that tube bundle flow differs from the tube flow that RELAP5/MOD2 was developed for. RELAP5/MOD2 has been modified to allow the use of a tube bundle geometry and to choose a flow regime map and heat transfer correlation appropriate for bundle geometry. The flow regime map was modified for flow in bundles and appropriate changes were made in the code. This flow regime map predicts better transition for bubble-to-slug and slug-to-annular flow for the OTSG. Consequently, improved saturated conditions for the fluid flow at the entrance to the boiler were obtained. Heat transfer correlations have been developed to produce similar heat transfer coefficients obtained experimentally in a scaled U-tube steam generator. These correlations have caused superheat values to be increased by 8°C (15°F) to a new superheat value of 19°C (35°F), which is still short of the measured 22-30°C (40-60°F) values. Comparisons between the 19-tube integral economizer OTSG test facility and a RELAP5/MOD2 model were performed. Better agreement is obtained with the modified tube bundle correlations.

Acknowledgments

The authors are indebted to the B&W Nuclear Support Group for many helpful discussions and comments that initiated this project. Partial support for this research was provided by the Center for Energy and Mineral Resources, Texas A&M University, College Station, Texas.

References

Baker, O., 1958, "Multiphase Flow in Pipelines," *Pipeline News.*

Bergles, A. E., Roos, J. P., and Bourne, J. G., 1968, "Investigation of Boiling Flow Regimes and Critical Heat Flux," NYO-3304-13, Dynatech Corporation, Cambridge, MA.

Boucher, T. J., 1987, "Scale Model Test Results for an Inverted U-Tube Steam Generator Witli Comparisons to Heat Transfer Correlations," presented at the ASME Winter Annual Meeting, Boston, MA, Dec.; Paper No. 87-WA/NE-16.

Bromley, L. A., 1950, "Heat Transfer in Slab Film Boiling," *Chemical Engineering Progress*, No. 46.

Carey, V. P., and Mandrusiak, G. D., 1986, "Annular Film-Flow of Liquids in a Partially Heated Vertical Channel With Offset Strip Fins," *International Journal of Heat and Mass Transfer*, Vol. 29, No. 6.

Chen, J., 1963, "A Correlation for Boiling Heat Transfer to Saturated Fluids in Convective Flow," ASME Paper No. 63-HT-34.

Chen, J., et al., 1977, "A Phenomenological Correlation for Post-CHF Heat Transfer," TS-774, Department of Mechanical Engineering, Lehigh University.

Collier, J. G., 1981, *Convective Boiling and Condensation*, 2nd ed., McGraw-Hill, New York.

Dougall, R. S., and Rohsenow, W. M., 1963, "Film Boiling on the Inside of Vertical Tubes With Upward Flow of the Fluid at Low Qualities," MIT Report 9079-76.

Dukler, A. E., and Taitel, Y., 1986, "Flow Pattern Transitions in Gas-Liquid Systems: Measurement and Modeling," *Multiphase Science and Techology*, Vol. 2, Hemisphere Publishing Corporation, Washington, DC.

Hassan, Y. A., 1988, "Assessment of Boiling Heat Transfer Correlations for Once Through Steam Generators," *Nuclear Technology*, Vol. 81, No. 3.

Ishihara, K., Paleo, J. W., and Taborek, J., 1980, "Critical Review of Correlations for Predicting Two-Phase Flow Pressure Drop Across Tube Banks," *Heat Transfer Engineering*, Vol. 1.

Jensen, M. K., and Hsu, J. T., 1987, "A Parametric Study of Boiling Heat Transfer in a Tube Bundle," *Proceedings ASME-JSME Thermal Engineering Joint Conference*, Honolulu, HI.

Kim, S. H., and El-Genk, M. S., 1988, "Experimental Heat Transfer Studies for Low Flow of Water in Rod Bundles," *Proceedings of the 1988 National Heat Transfer Conference*, Vol. 2, ASME HTD-Vol. 96.

Weisman, J., 1959, "Heat Transfer to Water Flowing Parallel to Tube Bundles," *Nuclear Science Engineering*, Vol. 6.

Williams, C. L., and Peterson, A. C., Jr., 1978, "Two Phase Flow Patterns With High-Pressure Water in a Heated Four-Rod Bundle," *Nuclear Science Engineering*, Vol. 68.

Ransom, V. H., Wagner, R. J., Trapp, J. A., Feinauer, L. R., Johnsen, G. W., et al., 1985, *RELAP5/MOD2 Code Manual*, NUREG/CR-4312, EGG-2396, EG&G Idaho, Inc.

Turk, C. H., Guill, P. F., Burchfield, J. E., Davidson, E. H., Irani, A., et al., 1988, Private Communication, B&W Owners Group.

Venkateswararao, P., 1981, "Flow Pattern Transition for Two-Phase Flow in a Vertical Rod Bundle Array," Ph.D. Thesis, University of Houston, Houston, TX.